ResearchGate

See discussions, stats, and author profiles for this publication at: https://www.researchgate.net/publication/324602867

Characterization of Self-Powered Autonomous Embedded Systems for Complementary Balanced Energy Harvesting

Thesis · January 2018

DOI: 10.13140/RG.2.2.29768.42242

CITATIONS
0

READS
435

1 author:



Yannick Verbelen
University of Bristol
23 PUBLICATIONS **39** CITATIONS

SEE PROFILE

Some of the authors of this publication are also working on these related projects:

Reconfigurable Logic View project

Energy Harvesting for Embedded Systems View project

All content following this page was uploaded by Yannick Verbelen on 19 April 2018.

The user has requested enhancement of the downloaded file.

VRIJE
UNIVERSITEIT
BRUSSEL

Faculty of Engineering
Department of Industrial Engineering Sciences

Characterization of Self-Powered Autonomous Embedded Systems for Complementary Balanced Energy Harvesting

Dissertation submitted in fulfillment of the requirements for the degree of Doctor in Engineering Sciences

Jury approved 28 November 2017

Yannick Verbelen

January 2018

Promoters: Prof. Dr. Ir. Abdellah Touhafi
Prof. Dr. Ir. Kris Steenhaut

This work is licensed under the Creative Commons Attribution-NonCommercial-ShareAlike 4.0 International License.

In loving memory of my grandmother, who
believed more than anyone else in the potential of
this work, but passed away before it could be
completed.

Jury

The jury assessing the quality of the work presented hereafter:

Chairman: prof. dr. Noshin Omar (VUB)
Vice-chairman: prof. dr. Roger Vounckx (VUB)

Promoter: prof. dr. Abedellah Touhafi (VUB)
Co-Promoter: prof. dr. Kris Steenhaut (VUB)

Members: prof. dr. Carlos Valderrama (UMons)
dr. Wenke Weinreich (Fraunhofer IPMS)
prof. dr. David Bol (UCLouvain)
prof. dr. Jacques Tiberghien (VUB)
prof. dr. Vincent Ginis (VUB)

Preface

Natural resources and energy are tightly intertwined concepts, since the energy that powers our society is directly generated from natural resources through technological advancements. Whether it requires digging up coal to burn in thermal power stations, or mining rare earth materials to construct solar panels, energy and resources are either way inseparable from each other. It is well known that our current financial and economic system is fundamentally flawed however, relying on an unsustainable exponential growth to secure its continuity, and therefore ever increasing pressure on the natural resources of this planet. As this broken economic system by its very design continues to exhaust resources at an ever increasing rate, it accelerates towards its own demise, predicted by economists to happen within the next 20 years. While the majority of the population remains oblivious or in denial and others anxiously await the inevitable collapse of the current worldwide financial and economic systems, it is up to the scientists and engineers of today to develop sustainable alternatives for the mistakes of the past. With the clock ticking, several solutions to current problems have already been invented, for example cryptocurrencies as a sustainable and inflation immune alternative to paper currency. It is unquestionable that the economy of a sustainable future will be highly automated and autonomous, and powered by renewable energy generated by equally sustainable technologies. Impressive technological advancements have been made in megawatt scale electrical power generation systems, which are the key to powering the next generation of manufacturing facilities and transport systems. Comparably little attention has been given so far to milliwatt scale power generation, to supply the world's growing collection of wireless electronic devices. These smart, autonomous electronic devices will be indispensable, which is why it is paramount to develop the required technologies to make them possible already today. And that is exactly what this thesis is about: building sustainable electronic systems with a minimal environmental footprint, but with the potential to last a lifetime. It aims to address all the individual fallacies and pitfalls that made the design of such systems so cumbersome, and is therefore intended as a guide for embedded systems designers, providing hardware and software support to aid in each step of the design process from concept to finished prototype.

All the design resources discussed in this thesis are open source, and publicly available free of charge without limitations, to encourage widespread adoption of the presented technologies. References can be found in the Appendix. Readers are encouraged to actively contribute to the hardware and software developed for this work by forking existing designs and extending them with novel ideas and insights, and adapting them to new harvesters as they are invented. Let this thesis be a cornerstone in the development of sustainable, autonomous electronic systems.

This work was only made possible with the support of many, without whom this thesis would never have been written. Whereas electronic design is an exact science, embedded software development unfortunately is not. It is the ingeniousness, determination and endurance of Bob W., who spent hundreds of hours developing firmware for the AEM modules, that resulted in working prototypes. Almost driven

to insanity in the process, only Bob's contributions could bring the hardware to life, and his proficiency in embedded C/C++ and Python resulted in the most elegant code to have ever been written for an open source project.

At least equally important and complementary of nature, were the unrelenting emotional support and encouragement from my girlfriend Ulrike Haller, who never lost faith in me even in the most difficult times, and made countless personal sacrifices to ensure this thesis and the research that led to it were completed. My own mental sanity would not have survived if Ulrike wouldn't have been there to safeguard it and inspire me.

On the hardware side I relied on the continued technical support and advice of prof. dr. ir. Abdellah Touhafi, who served as mentor throughout this journey and applied to daily life Richard Branson's famous quote *"if somebody offers you an amazing opportunity but you are not sure you can do it, say yes – then learn how to do it later!"*. By doing so, Abdellah taught me to dare take on challenges and projects against all odds, which often failed more than they succeeded, but either way enabled both of us to gain new knowledge and experience in the process.

My parents and grandparents also played a key role by providing the necessary logistic support, allowing me to dedicate a maximum of my time to the research and development of technology. My grandmother Simonne in particular fiercely believed in the potential and importance of this project, and gave the last years of her life to create the best possible conditions for me to complete it. She sadly passed away before the prototypes were completed, and could not witness herself the beauty and elegance of the countless circuit boards that saw the light of day thanks to her support. This thesis is a tribute to her dedication and confidence in me, and in Science.

Finally, I would like to thank the Brussels University, VUB, for giving me the budget and accommodations to complete this research for the sake of mankind, the future of the planet we all share, and for the benefit of this generation and all the ones to follow. The teaching opportunities provided by the VUB enabled me to acquire profound knowledge in many different fields, including robotics, digital and analog electronic design, and circuit board design. It brought me great joy to share this knowledge with students and fellow researchers, and together build the Electronics Department to what it is today. My closest colleagues Laurent Segers, Lieven Standaert, Ronald Van Ham, Ann Peeters, An Braeken, Maxime Frooninckx and many others each allowed me to grow professionally and personally over the course of the past 8 years, and their help and impact on many aspects of my time at the VUB will never be forgotten. Niek Blondeel and Sam De Winne's help with testing energy harvesters and building equipment also made the work much easier. It is impossible to list everyone who directly or indirectly made this project possible, so may this thesis serve as a token of appreciation to all of you.

Yannick Verbelen, December 2017



Characterization of Self-Powered Autonomous Embedded Systems for Complementary Balanced Energy Harvesting

The contents of this thesis are irrevocably published under a Creative Commons Attribution-NonCommercial-ShareAlike 4.0 International License, giving anyone the right to read, distribute, adapt and republish it within the scope allowed by the license. Freedom of information should be a fundamental right for everyone.

All hardware, software, and datasets are published under their respective open source licenses, as specified in their repositories. References to these repositories can be found in the Appendix.

For inquiries about content reuse or purchase of a hard copy, please mail to yannick.verbelen@inventati.org.

Abstract

The underlying technology for energy harvesting has been thoroughly researched and documented, and harvesters for nearly any type of ambient energy have been developed, yet their adoption remains largely limited to selected iconic use cases. The economic potential of energy harvesting reaches far beyond solar powered calculators or shakable flashlights, however. As improving semiconductor technology becomes less power hungry, innovative power conversion circuits are designed and new energy storage devices are developed, the power balance of currently battery powered systems may shift favorably towards energy harvesters. Low power, highly integrated microcontrollers and SoCs, solid state batteries and low leakage EDLCs combined with efficient MEMS sensors and LoRa long range radio reduce power consumption while enabling new functionality. New market opportunities arise in industrial, domestic and public sectors, but the discontinuous nature of power produced by energy harvesters makes the design of reliable yet cost effective self-powered embedded systems difficult. As a result, batteries with considerable negative environmental impact are often still used in applications where energy harvesters may provide added value in terms of functionality or autonomy. Fortunately, ample incentives towards energy harvesting technology exist in each sector: industrial battery powered applications suffer from high maintenance costs, whereas consumers demand longer life time and performance than is possible with current state-of-the-art primary batteries. The most difficult challenge remaining is not the development of harvesters, energy storage devices, or low power electronics individually, but their optimal integration.

The present research aims to unlock the full economic and environmental potential of energy harvesters as an addition to, or a replacement of, primary batteries in wireless autonomous embedded systems. To select the best harvester(s) for a specific application and to dimension their size(s) optimally, an innovative methodology is presented that is founded on 4 key phases: 1) the parametrization of energy harvesters under different environmental conditions, 2) the measurement of the power consumption and energy budget of a specific embedded system, 3) the power storage and conversion needs, and 4) the characterization of ambient environments through benchmarking hardware using state-of-the-art sensors and energy harvesters.

Traditionally established models for energy harvesters, aiming at predicting their behavior as accurately as possible, are too complex for practical use by embedded system designers. In the first phase, simplified models are developed for photovoltaic, thermoelectric and piezoelectric energy harvesters. For each harvester type, experimental setups for benchmarking have been designed and implemented, to parametrize the characteristics of commercially available energy harvesters as they are currently used in embedded systems. Models are subsequently derived from the obtained benchmarking results as proof-of-concept for state-of-the-art energy harvesters.

Secondly, the performance of energy storage devices with high number of charge/discharge cycles, most notably EDLCs and solid state batteries, is discussed in function of the DC/DC topologies most

suitable to control them. As IPS has currently vanished from the market, and Cymbet on-die solid state batteries remain too expensive for large scale use, the effort was focused on EDLCs in roles of energy storage and peak power sources.

The most important variable in the energy harvester selection/dimensioning problem is the availability of ambient energy in the environment in which the device is intended to be deployed. Different types of ambient energy may be available, all varying in amplitude and characteristics over time. Benchmarking the ambient environment is a critical factor in the energy harvester optimization problem to maximize performance and reliability, and simultaneously reducing costs. In the presented research, a modular and portable ambient energy monitor (AEM) was developed as benchmarking platform, enabling quantization of ambient light, vibrations, thermal and RF power. Each module operates independently, equipped with state-of-the-art sensors and energy harvesters to enable sensor fusion and efficiency measurements. All hardware and related embedded software is open source, and released under appropriate Creative Commons licenses.

Each step of the presented strategy is illustrated with matching use cases demonstrating the added value of energy harvesters, either on their own, or fused in complementary balanced energy harvester topologies.

Contents

Preface **v**

Abstract **ix**

Contents **xi**

1 Introduction **1**
1.1 History . . . 1
1.2 Renewable Energy . . . 2
1.2.1 Sustainability . . . 2
1.2.2 Environmental Impact . . . 3
1.3 Energy Harvesting . . . 4
1.3.1 Harvesting vs. Scavenging . . . 4
1.3.2 Early Applications . . . 5
1.4 Challenges . . . 5
1.5 Solution . . . 6
1.5.1 Harvester Characterization . . . 6
1.5.2 Ambient Energy Benchmarking . . . 6
1.5.3 Energy Budget Estimation . . . 7
1.5.4 Power Path Design . . . 8
1.6 The Foundations of Autonomous Electronics . . . 8
1.6.1 Energy Harvesters . . . 8
1.6.2 Sensors . . . 8
1.6.3 Processing . . . 9
1.6.4 Power Path . . . 10
1.6.5 Actuators . . . 10
1.7 Limitations . . . 11
1.8 Structure . . . 13

2 Energy Harvesters **15**
2.1 Photovoltaics . . . 15
2.1.1 Efficiency . . . 16
2.1.2 Cell Types . . . 17
2.1.3 PV Harvesting . . . 17
2.2 Thermoelectrics . . . 17

2.2.1 Efficiency . . . 18
2.2.2 TEGs . . . 18
2.3 Piezoelectrics . . . 19
2.3.1 Reliablity . . . 19
2.3.2 Efficiency . . . 19
2.4 Triboelectrics . . . 20
2.4.1 Efficiency . . . 20
2.4.2 Reliability . . . 20
2.5 Pyroelectrics . . . 21
2.5.1 Reliability . . . 21
2.5.2 Efficiency . . . 21
2.6 Betavoltaics . . . 22
2.6.1 Efficiency . . . 22
2.6.2 Half Life . . . 22
2.7 Kinetic . . . 22
2.8 RF . . . 23
2.8.1 Efficiency . . . 23
2.9 Chemical . . . 23
2.10 Conclusion . . . 24

3 Resource Considerations **25**
3.1 Decentralization and Grid Connectivity . . . 25
3.2 Batteries vs. Energy Harvesters . . . 26
3.3 Natural Resources . . . 27
3.3.1 Photovoltaics . . . 27
3.3.2 Thermoelectrics . . . 28
3.3.3 Piezoelectrics . . . 29
3.4 Resource Supply Restrictions . . . 30
3.4.1 Scarcity and Reserve Distribution . . . 30
3.4.2 Production Concentration and Governance . . . 30
3.4.3 Substitutability . . . 31
3.5 Sustainable Energy Harvesting Strategies . . . 31
3.5.1 Recycling . . . 31
3.5.2 Resources vs. Efficiency . . . 32
3.5.3 Raw Material Mining Issues . . . 32
3.6 Conclusion . . . 33

4 Complementary Balanced Energy Harvesting **35**
4.1 Modeling Harvester Parameters . . . 35
4.1.1 Technological . . . 36
4.1.2 Environmental . . . 36
4.1.3 Application Specific . . . 36
4.1.4 Harvester Power Output . . . 36
4.1.5 Example . . . 37

4.2 Multi Sourced Energy Harvesting . . . 38
4.2.1 Advantages . . . 38
4.2.2 Transition from Single to Multiple Harvesters . . . 39
4.2.3 Regime . . . 40
4.3 Periodic Systems . . . 41
4.4 Energy Storage . . . 42
4.5 Example . . . 42
4.6 Balancing Harvester Sizes . . . 44
4.6.1 Mathematical Feasibility . . . 45
4.6.2 Dual Harvester Model . . . 45
4.6.3 Multiple Harvesters Mode . . . 47
4.6.4 Regime Benchmarking . . . 51
4.7 Harvester Size . . . 53
4.7.1 Scale Limitations . . . 53
4.7.2 Manufacturing Limitations . . . 53
4.7.3 Combining Multiple Harvesters . . . 53
4.7.4 Example . . . 53
4.8 Limitations . . . 55
4.9 Efficiency Parametrization . . . 57
4.9.1 Ambient Energy Quantity . . . 57
4.9.2 Harvester Exposure . . . 58
4.9.3 Environmental Parameters . . . 58
4.9.4 Practical Implications . . . 58
4.10 Conclusion . . . 59

5 Harvester Performance Characterization 61
5.1 Photovoltaic Cells . . . 61
5.1.1 Requirements . . . 62
5.1.2 Implementation . . . 62
5.1.3 Design Verification . . . 67
5.1.4 Comparison of Photovoltaic Cells . . . 68
5.2 TEGs . . . 73
5.2.1 Operation Range and Requirements . . . 74
5.2.2 System Overview . . . 74
5.2.3 Benchmarking Bi_2Te_3 TEGs . . . 76
5.3 Vibration Harvesters . . . 80
5.3.1 Existing Implementations . . . 80
5.3.2 Parametrization Methodology . . . 81
5.3.3 Design . . . 82
5.3.4 Design Verification . . . 85
5.3.5 Harvester Parametrization . . . 86
5.4 Harvester Performance Database . . . 89
5.5 Conclusion . . . 90

6 Power Path **91**
6.1 Energy Storage . . . 91
6.1.1 Motivation . . . 91
6.1.2 Electrical Storage . . . 92
6.1.3 EDLC . . . 93
6.1.4 Solid State Battery . . . 99
6.1.5 Secondary Chemical Cells . . . 102
6.2 Power Conversion . . . 105
6.3 Linear Regulators . . . 105
6.4 Switched Mode Regulators . . . 106
6.4.1 Buck Regulators . . . 107
6.4.2 Boost Regulators . . . 110
6.4.3 Inverting Regulators . . . 111
6.4.4 Monolithic Converters . . . 112
6.5 Power Regulators . . . 114
6.5.1 Multi Channel Design . . . 115
6.6 Power Path Design . . . 118
6.6.1 Influencair . . . 118
6.6.2 Design Considerations . . . 119
6.6.3 Power Supply Design . . . 121
6.6.4 Battery Management . . . 124
6.6.5 Battery Chargers . . . 134
6.7 Conclusion . . . 137

7 Ambient Energy Monitor **139**
7.1 Design Topology . . . 140
7.1.1 Mk I: Monolithic Design . . . 140
7.1.2 Mk II: Modular Design . . . 141
7.1.3 Shared Core . . . 141
7.2 Development . . . 141
7.2.1 Proof of Concept for MEMS Sensors . . . 141
7.2.2 Evaluation . . . 142
7.2.3 OpenObservatory . . . 142
7.3 Modularity . . . 143
7.4 Digital Processing . . . 144
7.4.1 AVR Peripherals . . . 144
7.4.2 Memory Organization . . . 145
7.4.3 Bootloader . . . 146
7.4.4 Sample Synchronization . . . 146
7.5 Aggregator . . . 147
7.5.1 Raspberry Pi Expansion Module . . . 148
7.5.2 Interface . . . 148
7.5.3 RTC . . . 149
7.5.4 Environmental Sensors . . . 149

7.5.5 Automatic Module Identification . . . 150
7.6 Vibration Module . . . 151
7.6.1 Sensors . . . 151
7.6.2 Vibration Energy Harvester . . . 157
7.7 Light Module . . . 161
7.7.1 Diffraction Spectrometer . . . 161
7.7.2 Solid State Spectrometer . . . 163
7.7.3 Sensors . . . 171
7.7.4 Light Energy Harvester . . . 175
7.8 Thermal Module . . . 189
7.8.1 Ambient Temperature . . . 189
7.8.2 Thermocouple . . . 191
7.8.3 Thermal Energy Harvester . . . 194
7.9 RF Module . . . 203
7.9.1 Challenges . . . 203
7.9.2 Tuned Oscillator Receiver . . . 203
7.9.3 Superheterodyne Receiver . . . 204
7.9.4 RF Energy Harvester . . . 215
7.9.5 Digital Control . . . 216
7.10 Conclusion . . . 218

Future Work and Conclusions **219**

List of Publications **223**

Bibliography **225**

List of Figures **251**

List of Tables **259**

List of Acronyms **261**

Appendices **267**
A Design Resources . . . 267
A.1 Hardware . . . 267
A.2 Software . . . 268
B Analog Front-end . . . 269
B.1 Application-specific ADC Selection . . . 269
B.2 AD7689 . . . 269
B.3 Voltage Reference . . . 270
B.4 DAQ Shield . . . 271
B.5 Driver Development . . . 272
B.6 SPI . . . 275
C Connectivity . . . 280
C.1 JTAG . . . 280

C.2 UEXT 281
C.3 UART 281
C.4 USB 282
D Power Supply 283
D.1 Passive Filtering 283
D.2 Performance 284
D.3 Active Filtering 284
D.4 Variants 287
D.5 Alternative Topology 287

Index **288**

Chapter 1

Introduction

1.1 History

Mankind is increasingly becoming aware of the historic mistake that wasting fossil fuels by burning them in thermoelectric power plants is. Whereas these resources were the key that started the industrial revolution two centuries ago, they are now an example of humanity's failure to bring innovation in its electric power generation. Mining fossil fuels has taken on dramatic proportions, of which tar sand exploitation [7, 158], lignite surface mining [269, 280, 337] and shale gas extraction[149, 320] are the most recent examples. Under pressure of a fundamentally flawed and already for decades failing economic model, natural resources are being exhausted at an unsustainable rate [35, 129]. The situation however is changing, with a public opinion slowly shifting favorably towards renewable energy as an alternative to the dead end that non renewable energy sources are [311]. While some of the historic corporate powers anxiously attempt to unethically slow down progress for the sake of their own financial gain, many new initiatives have been born since the start of the third millennium, and work towards a sustainable future economy and society has commenced [84, 111, 259]. Persuaded by overwhelming scientific evidence and rational reasoning, individuals with a vision have united to solve the most pressing problems of society, among which are energy production, energy storage, and transport. Both non profit organizations such as Avaaz and Greenpeace , as well as commercial initiatives from Elon Musk and others, are now inspiring a generation to leave the mistakes of the past behind and work towards a sustainable future [98, 251].

Renewable energy is not a new concept, rather on the contrary. Before ignorance about its environmental and health consequences allowed fossil fuels to dominate energy production, kinetic energy from water had been used for well over a thousand years since the first water mills were invented in classical antiquity after the reign of Alexander the Great, during the golden times of Hellenistic science and technology [79]. Quickly picked up by the Romans, the technology to construct both horizontal and vertical water wheels was implemented in industry and manufacturing, for applications including grinding wheat to flour, crushing mineral ores, stone masonry, and many others [304, 119]. Also wind mills have a long history, dating back to Greek developments in classical antiquity, and Chinese wind mills have been in use since the 4th century. From the 13th century onward, tower and smock wind mills were found everywhere in Europe and the Mediterranean [199], and their significance would have been long forgotten if they would not be featured prominently on so many picturesque Dutch post cards.

1.2 Renewable Energy

As a scientific term, *renewable energy* can be interpreted broadly beyond the extent it was originally intended for. Coal for example could be considered correctly as a renewable energy source, since the material has been generated through geological processes throughout the recent history of the planet, and continues to be produced through these processes until today [81, 137]. Unfortunately, as with most geological phenomena, the rate of generation is very slow relative to a human time scale, and the rate at which the current deposits are being mined far exceeds the rate of generation [19]. Within the scope of human activity, coal (and any other type of fossil fuel) is therefore not a renewable energy source, although it could be theorized that a few dozen million years after the next extinction event wipes out humankind as a species, global coal deposits may reach the same levels as before the industrial revolution started. It is an interesting course of thought, because true renewability has implications on sustainability, which in turn has implications on the constraints to growth [18, 290]. The question of which energy sources are renewable or not is non trivial, if scalability and growth perspectives in a human time line are brought into the equation. Nuclear fission energy from ^{235}U and derivatives (^{239}Pu etc.) is by most people considered a non renewable energy source because of the finite reserves of natural uranium in the Earth's crust [362, 67]. On the other hand, nuclear fusion (^{3}H to ^{3}He) is considered a renewable alternative to fission although the amount of hydrogen on the planet is equally finite as uranium [132], although there is of course an obvious difference in relative abundance [287, 82]. With the water available in Earth's oceans, a Type I civilization on the Kardashev scale could sustain itself over geological time scales [155], while in contrast uranium reserves are already running short after less than a century (since 1940s) of use for energy production purposes. An unsettling number of claims has been made on the renewability of specific energy sources, particularly those anticipating the possible development of new technology (like breeder reactors to extend nuclear fission to ^{238}U [326] for example), some of which the feasibility has not yet been proven. In this thesis, the definition of renewable energy is constrained to those that can be harnessed using technology available today, which for now excludes nuclear fission. The remaining options are energy from the Sun (photovoltaic, but also indirect solar energy like wind and hydro power), and geothermal energy .

1.2.1 Sustainability

Renewable and sustainable are often incorrectly used interchangeably, although the meaning of both terms is largely unrelated. Whereas *renewable* refers to the long term availability of an energy source, *sustainable* refers to limitations in energy conversions, and more specifically the long term consequences of these limitations. These limitations are related to resources required for converting the renewable energy source to electrical energy, and the waste being produced in the process. For example sunlight is a renewable energy source since the expected life time of the Sun will exceed human civilizations, but to convert sunlight to electrical energy directly, photovoltaic cells are needed. The way these cells are manufactured, transported, installed, recovered and disposed of will determine whether photovoltaic energy is sustainable or not. If the manufacturing of these cells fundamentally relies on new natural resources being mined, and the decommissioned cells end up in landfills, then photovoltaic energy may be renewable but not sustainable, since the process of mining raw materials and piling waste onto landfills cannot be sustained indefinitely [243]. For example, a steel or wooden wind turbine *may* be a sustainable energy source since both wood and steel are sustainable materials – wood is renewable on a human time scale, and steel can be recycled an infinite number of times in a closed loop process. However, if a wind turbine were to be built with composite materials containing polyester and fibreglass, a material mixture that cannot currently be completely recycled [151, 305], then the resulting wind energy is not

sustainably being produced since the landfill of decommissioned turbine blades will grow over time, and raw materials need to be expedited to construct new turbine blades over and over again [29]. Such a process would not be fundamentally different from a nuclear power station, which for its operation also requires raw materials to be mined (uranium) and leaves a trail of unrecyclable byproducts (nuclear waste) [220]. When insufficient long term planning precedes renewable energy related development efforts, as the example shows, the environmental impact may be as severe as for non renewable energy applications. A closed resource cycle is a primary requirement for sustainability [222, 124]. In the example above, decommissioned composite wind turbine blades are already being processed into fences and picnic tables, but only as a detour that inevitably still ends on a landfill. As long as these fences or picnic tables cannot be processed back into new turbine blades, the resource cycle is not closed, and the generated wind energy therefore not sustainable [218]. Proponents, often driven by financial incentives, may advocate to use such currently unsustainable methods immediately, anticipating the likely future development of recycling technology to close the cycle. But the same logic was applied to nuclear waste in 1960s, when the choice for temporary storage of nuclear waste in simple steel barrels was made solely on the assumption that waste processing technology would be developed within 10 years. However, over half a century later the anticipated technology still does not exist, and the leaking "temporary" storage tanks have become an environmental hazard on their own [67]. In that sense, the precautionary principle should also be applied to renewable energy technology. Sustainable energy implies it comes from a renewable source, but renewable energy does not necessarily indicate sustainability. Sustainability will be extensively discussed in the chapter on resource management.

1.2.2 Environmental Impact

The environmental impact of electric energy production has been a subject of political and public discussion for decades, and a frequent source of conflicts of interest. Non renewable energy sources self-evidently have the largest and thus best known environmental impact, which also scales with the production capacity. The Garzweiler quarry complex [337], Athabasca extraction site in Alberta [158], and the Deepwater Horizon incident [180, 250] are infamous examples of recent or ongoing environmental disasters, the first two still deteriorating to present day. Renewable energy sources also have environmental consequences, albeit often less visible than with non renewable energy related problems. There are first of all direct environmental and ecological consequences to megaprojects such as the Three Gorges Dam [347, 340] and the planned Qattara Depression Project [254, 92], which flood large areas and can substantially alter local climates. Less apparent are the environmental costs of large scale solar installations for example, for which arable land may be sacrificed. Occupied area is also a resource, like raw materials are, and should also be treated as finite. A developing conflict in renewable energy generation from biomass is the production of that biomass for example [223]. When organic waste is converted into methane through gasification, the resources required remain limited, but when crops are grown with the explicit goal of conversion into biofuels [232], a conflict with traditional land usage such as farm land or meadows is inevitable. These concerns directly affect scalability and sustainability, and complicate the decision making process. [23]

It should be kept in mind that electricity in our current economy, just like hydrogen in a hydrogen economy[37, 298] or methanol in a methanol economy[31, 289], are only "energy carriers" but not "energy sources": they do not occur naturally, and are the result of man-made energy conversion processes. The finite (and often low) efficiency of these conversion processes from a particular renewable energy source to electric energy may be the decisive factor as to whether the conversion is environmentally responsible or not, regardless of technical feasibility.

1.3 Energy Harvesting

Large scale renewable energy projects focus on converting renewable energy sources like wind, solar and hydro power into electrical energy which is then fed into the electrical grid for use in transport, manufacturing, illumination and domestic applications. Such installations are consequentially constructed in areas favorable to renewable energy production, such as in the proximity of rivers for hydroelectricity [55], from where overhead power lines (or undersea HVDC cables) transport electrical power to where it is needed. This is inconvenient since a considerable fraction of generated power is lost in transformation and transport [99], but inevitable because applications like metro trains or laundry machines do not typically have sufficient quantities of renewable energy sources nearby to operate from directly [55]. However, depending on the environment, there may be adequate renewable energy present in the direct environment ("ambient") of the application to generate the electrical power required for operation locally, thus allowing a disconnection from the electrical grid. It is said that these applications *harvest* energy from their immediate environment, leading to the term *energy harvesting*. Energy harvesting essentially refers to decentralized renewable energy generation, specifically for one application [70]. There are several advantages to the approach:

1. If the application does not need to be connected to the grid, it can be wireless (depending on other functionality), which allows it to be easily installed and/or moved.
2. It can operate in areas where grid power is not easily available, such as in remote locations, or where running power cables is inconvenient (tall chimneys or poles, roofs of buildings, ...).
3. It operates reliably when grid power is unreliable (for example in areas with instable power grid, rolling blackouts etc.).
4. It can be designed to operate autonomously, locally generating the power required for its own operation.
5. No high to low voltage AC/DC power supply circuits are necessary, the application can operate from low voltage DC sources which have a favorable affect on life expectancy.

Energy harvesting as an alternative to grid powered applications, does not imply any assumptions regarding achievable power levels. Autonomous applications powered by energy harvesting technology have been constructed with power levels ranging from less than a μW to several kW [74]. Since batteries are produced by converting raw materials using grid power, battery powered devices can essentially be regarded as "disconnected" grid powered with all the additional drawbacks associated with batteries, as discussed in the chapter on resource management.

1.3.1 Harvesting vs. Scavenging

Often incorrectly used interchangeably, energy harvesting and energy scavenging are two related concepts leading to confusion. The difference between energy harvesting and energy scavenging is principally the source of the energy being converted into electrical energy. If the source is naturally present around the application, such as sunlight, vibrations, air flow, etc., some authors prefer the term *scavenging* over *harvesting* to make a distinction with active energy transmitters illuminating the application from a distance. These include RF antennas (for RFID for example)[179], lasers (for concentrated PV)[194] and magnetic fields for power induction [217]. However, such usage is incorrect since these cases in fact describe wireless power transfer rather than energy harvesting. Because the electrical transfer efficiency of such wireless power transfer techniques is low (typically $< 1\,\%$), with the exception of resonant

inductive power transfer between high Q coils, it should not be considered as a viable option unless there are really no other alternatives [288, 113]. It is simply unethical to waste $> 99\,\%$ of power in the wireless transfer, so these wireless power transfer techniques are intentionally excluded from this thesis (with RFID being an exception to this rule). In what follows, *scavenging* is thus referred to as *harvesting* for the sake of convenience, and applications with non ambient energy sources are referred to as *wireless power transfer*.

1.3.2 Early Applications

Despite the recent popularization of the term *energy harvesting*, it is nowhere near a recent concept. Crystal radios were one of the earliest applications of energy harvesting [235], emerging in the 1920s - 1930s, and kits for crystal radios for children with an interest in electronics were for sale until the 60s. Other early examples include dynamos on bicycles, harvesting mechanical energy to power front and rear bicycle lights. In cutting edge technology, energy harvesting was essential to the Space Race: in 1958 the United States launched the first satellite equipped with solar panels, the Vanguard 1 [244], and solar panels have since then become the *de facto* standard power source for satellites in orbit. [154] Only 3 years later, in 1961, the first satellite using thermoelectric energy harvesting was developed and launched. The technology pioneered in the Transit 4A would prove to be essential for deep space exploration in the 60s and 70s [27, 28, 74]. During the Soviet era, the same thermoelectric energy harvesting technology powered by α decay of a ^{238}Pu core, was indispensable to keep 132 lighthouses operational during cold and dark arctic winters far above the pole circle [224]. Although they have been decommissioned since Glonass took over the responsibility for navigation above the arctic circle, some of the original energy harvesters have been repurposed and remain operational to date. These examples are only a small selection from the countless energy harvesting applications that were developed before the actual term *energy harvesting* was introduced, and development of the various energy harvesting technologies were largely developed independently from advancements in electronics. Only by the end of the 1970s was the first consumer product powered by energy harvesting released to the market, a solar powered calculator [258, 352], using the then newly developed amorphous silicon solar cells designed for indoor use. With an electrical efficiency of only 2-3 % at the time [118], the performance was abysmal compared to modern day amorphous cells ($12\,\%$), but the autonomous calculators without batteries became an instant hit. Since the early calculators, more electronic applications using energy harvesting have been developed, enabled by advancements in auxiliary technologies including storage, power conversion, and microcontroller electronics. The enabling factors are discussed in the next chapter.

1.4 Challenges

The most difficult aspect of energy harvesting as an alternative to grid power or battery power is that there is no one-fits-all kind of solution that works for a wide range of applications. Since energy harvesting depends on ambient energy present in the environment of the application itself, the design constraints of such applications are location dependent, and the possibilities tied to specific environments. Unsurprisingly, the calculators with photovoltaic cells from the example above will perform as expected in a well lit office space, but unsatisfactory in a dark basement. It may also prove to be challenging to scale down solutions on a MW scale to a W scale, mW scale or even μW scale. For example, the design of a 700 MW Kaplan turbine is an extensively studied and well understood subject, but scaling down the technology to design a 700 mW Kaplan turbine for an autonomous water meter is a far less straight forward engineering problem. Depending on the situation, a Pelton, Banki, Francis or even Gorlov turbine could offer a better efficiency on a small scale, trade-offs requiring time consuming and often costly engineering work.

And even if a CFD simulation can shed light on the most favorable solution, questions about the actual performance of the solution in the field remain: what about the reliability or degradation of performance over time? And how can the output power be interfaced with the water meter electronics? Would there be enough power available to measure continuously?

1.5 Solution

The goal of this thesis is to provide a comprehensive answer to the questions above from the perspective of an electric engineer or embedded systems designer. It aims to offer a methodology for developing autonomous applications, regardless of their scale, following a novel approach: **Complementary Balanced Energy Harvesting** (CBEH). This newly developed methodology is specifically designed to streamline and simplify the design of applications powered by energy harvesting technology. It is modular, allowing the design work load to be split into manageable tasks and larger engineering teams, and can be applied to industrial, civil and consumer applications. It consists of 5 steps: ambient energy benchmarking, harvester characterization, power supply optimization, energy budget estimation, and finally harvester selection and dimensioning. Complementary Balanced Energy Harvesting is a methodology designed to completely replace the previous ad-hoc design process of ambient energy powered systems with a systematic approach that does not require profound knowledge of harvester physics but instead relies on engineering data obtained through benchmarking.

The 4 steps in the Complementary Balanced Energy Harvesting design methodology are shown in figure 1.1. It consists of harvester characterization (1), ambient energy benchmarking (2), energy budget estimation (3) and finally, power path design (4). In sequence, the design process provides answers to the 3 questions: which energy harvester(s) work best in a specific environment, how large they should be, and which power path (including local storage) is necessary to combine harvester(s) and electronic system.

1.5.1 Harvester Characterization

Countless energy harvesters are commercially available, and more are being released to the market daily. Manufacturers often publish very little performance data however, and if they do so, data are constrained to one or few specific situations. Solar cell datasheets, for example, most notoriously only provide performance data for outdoor use, but nothing is said about indoor use under a specific type of artificial light source. This lack of data makes it nearly impossible to correctly compare energy harvesters with each other, and obstructs the harvester choice decision making process. To solve this problem, a new approach for parametrization of energy harvesters is presented in chapter 4, allowing the performance characterization of energy harvesters independently from their environment or size to grant more accurate performance comparisons. Several implementations of a low cost apparatus for energy harvester characterization are discussed in chapter 5.

1.5.2 Ambient Energy Benchmarking

Which types of ambient energy are available in an environment is not always a question with trivial answers. The quantities may vary in time, and the variations may be very subtle: a light source may change in spectrum, and the vibration frequency of a pneumatic hammer may vary depending on compressor settings, etc. These variations impact the performance of harvesters, and determines those who are suitable for certain environmental conditions. Complementary Balanced Energy Harvesting presents the first integrated solution to this problem with the Ambient Energy Monitor (AEM), an automated benchmarking

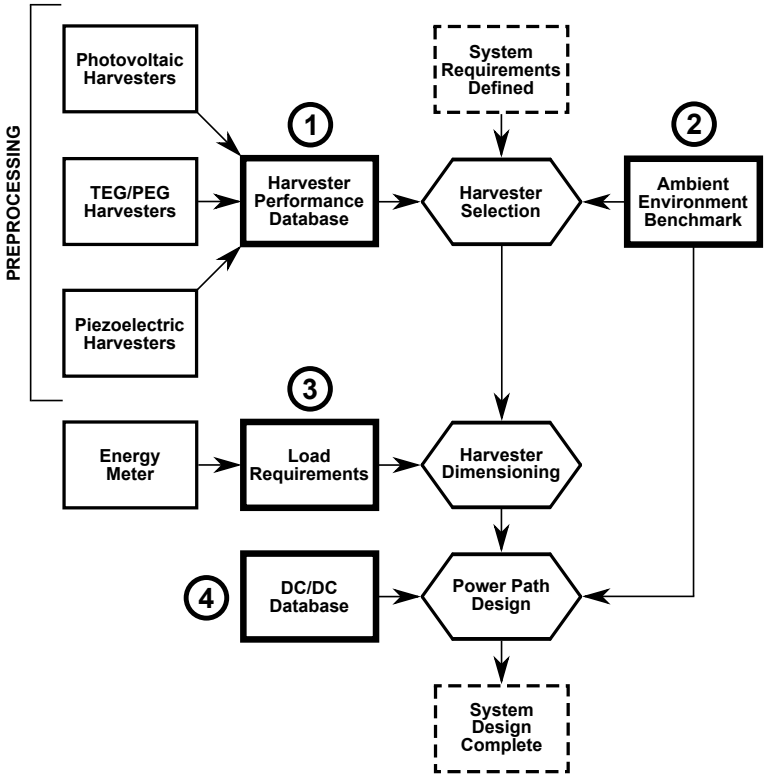

Figure 1.1: The 4 steps to complete the design of an autonomous system powered by ambient energy: harvester characterization (1), ambient energy benchmarking (2), energy budget estimation (3) and power path design (4).

system specifically designed to acquire data on ambient energy with the explicit purpose of optimizing the choice of energy harvesters. The AEM is presented in chapter 7.

With a database of harvester performance characteristics at hand, in combination with a data set of available ambient energy, an algorithm can be developed to match harvester(s) with that specific environment. This solves the first problem: selecting the most optimal harvester(s) for that environment, as shown in figure 1.1.

1.5.3 Energy Budget Estimation

To dimension the harvester(s) appropriately, the energy consumption profile of the attached system must be estimated. This can be done with a datasheet based calculation, as demonstrated in chapter 6. For complex systems it may be cumbersome to make a theoretical estimation of the power consumption variations over time, and measurement with specialized energy meters is necessary. The majority of existing applications is simple enough to allow a modular breakdown of the power requirements, enabling a less accurate but faster estimation of the application's energy budget. An energy budget estimation methodology to make the estimations is presented in chapters 4 and 6 and applied to the Complementary Balanced Energy Harvesting work flow.

Combining the energy budget requirements of the powered system with the selected harvester performance solves the second problem: dimensioning the chosen energy harvester(s). Chapter 4 assesses the reliability requirements and modifications necessary to handle periodic systems and harvester profiles.

1.5.4 Power Path Design

Since there is a financial and resource cost attached to energy harvesters, it is beneficial from an economic and ecological perspective to minimize their size. Proper design of the power path, choice of local energy storage and power management are essential, and discussed in chapter 6. The latest developments regarding voltage regulation and power management technology are applied to intelligent power path design for energy harvesting applications, with a discussion of an autonomous air quality measurement station as a case study serving as example of proper design.

The power path is the last essential piece to complete the puzzle that the design of an autonomous, ambient energy powered system is. It solves the third and last problem: attaching energy harvester(s) to the system it/they are intended to supply power to. Several approaches for harvester-specific power paths are implemented and discussed on a circuit level in chapter 7.

1.6 The Foundations of Autonomous Electronics

The design of autonomous electronic systems relies on 5 key elements, also referred to as the *5 pillars of autonomous electronics* [319]. Technological improvements made in each of these fields enable new applications, usually through improvements in energy efficiency or life time. The 5 pillars are energy harvesters, sensors, processing, power path and actuators. Maximizing the life time and autonomy of a system while simultaneously minimizing its economic and environmental cost, requires each of the 5 pillars to be optimized individually. Poor design choices for even one of the pillars could multiply the cost or decimate autonomy of a design. The importance of addressing each of the pillars individually can not be emphasized enough, and it should not surprise that each of the pillars is discussed in the next chapters.

1.6.1 Energy Harvesters

Energy harvesters are self-evidently the backbone of any autonomous system, since no current energy source exists that can power an electronic system reliably for 20 years, 30 years or even longer, perhaps with the possible exception of RTGs, but these have their own drawbacks. The eventual goal is to make electronic systems completely self-sufficient, allowing them to be installed and, in a manner of speaking, forgotten. This allows them to be embedded into concrete constructions for structural monitoring for example, or in locations where maintenance is impossible such as in nuclear reactor vessels. Although ambient power levels are predictable, such as natural sunlight, the inevitable wear of the harvesters needs to be taken into account to guarantee adequate longevity of the application. A significant portion of this thesis is dedicated to discussing the potential and limitations of various energy harvesters, their scaling, their reliability, and their resource management.

1.6.2 Sensors

The concept “sensor” as input to an autonomous embedded system can be broadened to any kind of input, including human interaction such as buttons or touch interfaces. In many cases, harvesters can be

used as sensors at the same time (for example, vibration harvesters acting as accelerometers, or photovoltaic cells as light sensors). Wireless switches are already on the market that capture sufficient energy from the switch activation event to transmit a wireless signal to a receiver of choice. Interesting opportunities are offered by such combined functionality, where a device can measure, power and control the system at the same time, by triggering dormant logic using a wake-up interrupt for example. With a harvester and sensor in one device, system designs can be made very compact, which in turn lowers their environmental cost. Not all input can be linked to harvesting energy unfortunately: if the purpose of a system is to monitor the humidity and temperature in a greenhouse and open the roof window automatically, then an additional harvester will be required to power those sensors. The size of the harvester will be directly proportional to the power consumption of those sensors, so selecting sensor types with a low power consumption could be equally important as choosing sensors with a good accuracy. Progress made in MEMS technology offers opportunities here, particularly in fields where previously power hungry electrochemical sensors were the only viable option. In addition to their improved reliability, the extra initial investment in MEMS technology will be returned by smaller energy harvesters later on in the design process. MEMS accelerometers, gyroscopes, gas sensors, humidity sensors etc. are already commercially available, and outperform their traditional counterparts with longer life times and lower power consumption.

1.6.3 Processing

In the signal path of traditional electronics, any systems between input and output circuitry could be designated as signal processing. In modern embedded electronic systems, microcontrollers are often chosen for this purpose to reduce cost, since all functionality can be implemented in software on a microcontroller with adequate hardware (i.e. availability of a good ADC and/or DAC, serial or parallel transceivers for I/O etc.). Several manufacturers have tailored microcontroller series specifically to these application ranges, by packing simple processors with extensive hardware functionality, to the point where even reconfigurable logic cells are included. Examples are the PIC XLP series from Microchip, the ESP series from Espressif, or the EFM32 series from Silicon Labs. The applications of PIC XLP and ESP8266 are discussed in detail in this thesis, with a worked out case study for the ESP8266 as microcontroller for intelligent autonomous sensing systems presented in chapter 6.

Although microcontrollers can be made very energy efficient by disabling unused functionality and reducing the clock frequency, they remain fundamentally power hungry devices because of the inherent complexity associated with the design of a microcomputer, regardless of the complexity of its instruction set. Microcontrollers are too often seen as a solution to every embedded problem, and discrete alternatives are dismissed or overlooked. In the example of the greenhouse monitoring scenario above, there really is no need for a microcontroller: monitoring MEMS sensors with analog output voltages can also be done with a simple comparator, enabling power to a servo motor whenever the humidity or temperature goes out of range. Using modern opamps or comparators to construct relatively simple signal paths such as PID controllers and filters will result in a power consumption that will be 1 to 2 orders of magnitude lower than if a solution with identical functionality were to be implemented on a microcontroller. The TLV8802 from Texas Instruments (320 nA), MAX44264 from Maxim Integrated (750 nA) and OP281 from Analog Devices (3 μA) are examples of low power opamps suitable for applications with high energy efficiency demands. Dedicated comparators are even more efficient than opamps because their output stage does not require continuous linear biasing, and can be used to trigger events or generate wake-up interrupts for other hardware.

1.6.4 Power Path

Modern power path design is more than a linear voltage regulator on a battery, and underestimating the importance inevitably leads to dire consequences for overall system efficiency and cost. Similarly to the wide variety of microcontrollers on the market, there is an even larger selection of power conversion solutions available. These range from LDOs with low quiescent current, to efficient buck-boost or SEPIC controllers with integrated flyback diode and power switches, to complete switched power path solutions with active supply monitoring and load balancing functionality. Although linear regulators *may* still be a part of an efficient power path design, there are likely optimizations possible with intelligently switched power branches to enable or disable power to specific hardware dynamically. Although X317 and X1117 class regulators are a favorite for many system designers because of their simplicity and proven reliability, they should be regarded as electronic archaeology, and no longer considered for new designs. Chapter 6 extensively discusses dynamic power rail generation.

A backup power supply, to secure an RTC for example, will often be indispensable in power paths for embedded systems. The choice between a standard elco, an EDLC or solid state battery is not trivial however, and the options are discussed in chapter 6 with the necessary attention to size, reliability and (environmental) cost. Charge controllers and cell management circuitry are an essential aspect of any local energy storage solution to maximize the life time. Overcharge or overdischarge protection, current limiting and trickle charge functionality have a decisive effect on storage reliability in autonomous systems with a long life time.

1.6.5 Actuators

An important advantage of harvesting ambient energy to power a system, as opposed to the classic approach of powering it with batteries, is that the available energy in the scope of most practical situations is infinite. That means it is no longer required to supply all the necessary energy the system will need over the course of its life time as an initial injection (a battery), but instead can be harvested continuously during its operation. This allows more freedom in the power budget, and enables interactivity in many applications. In the same greenhouse example, the controller could be equipped with an e-ink display showing the real-time temperature and humidity on screen, or perhaps send an RF pulse at predetermined frequency to alert other windows they should also open or close. Or it could be equipped with a rain sensor, to automatically close windows whenever it starts raining, etc. Such additional functionality would possibly be unaffordable on a classic battery powered energy budget, but achievable using energy harvesters as power source. There are countless applications imaginable where such relatively simple and straight-forward added functionality immediately leads to a significant improvement in user friendliness, or contributes to the perception of an “intelligent” system.

Using capacitors or EDLCs as local storage allows systems to draw peak power levels exceeding those achievable with batteries by 1 to 3 orders of magnitude. This allows the design of autonomous systems that make use of high power brushless DC motors, solenoids, etc., at least for a short period of time. This enables new applications, such as opening or closing valves quickly, unlocking gates, releasing moderator rods in a nuclear reactor vessel, or controlling a railway switch in remote locations.

An actuator class of particular interest of energy harvesting applications is those of wireless transceivers. Since the goal of an autonomous system is to make it independent of external power to save the effort of installing power cables, it would be pointless if cables still need to be installed for data communication. Autonomous systems that need to communicate with other systems, for example by cooperatively

storing data into a blockchain or reporting a status in a decentralized network architecture, will need some kind of wireless communication. Countless solutions have been developed for this purpose, but not all are equally suited for all applications. There are major variations in transmission power, range and throughput, and as one of the 5 pillars, wireless transceiver selection should also be tailored to the requirements of the application itself. Promising wireless communication systems are for example BLE, Z-Wave, LoRa, Narrowband 4G, Dragonlink RC etc. The last 3 options are particularly interesting because they have a long range, which usually allows direct (point to point) communication instead of the complex multi-hop routing strategies that were required before their introduction to route data across a mesh network. This in turn simplifies the rest of the system, and with simplicity does not only come elegance in the case of ambient energy powered systems, but usually also favorable power budgets.

An important consideration with wireless transceivers is the standardization of the underlaying technology. If a system with support for wireless communication is designed with an autonomy of 30 years in mind, then it will only live up to these expectations if another transceiver supporting the same protocol remains available over the entire duration of that time span. Technology in electronics however tends to change rapidly. As a comparison, the *de facto* standard interface for computer expansion cards 30 years ago was the ISA slot, which has meanwhile been superseded by PCI and PCI-e. Finding the necessary hardware to use ISA cards becomes more challenging every year, and many ISA cards have already been decommissioned because hardware and software support for them is no longer available. When selecting wireless technology, the same considerations should be kept in mind. Although the nRF5 modules from Nordic Semi are a very popular wireless communication interface for example, they use proprietary technology that is incompatible with any other wireless system, creating a major liability in the supply chain if Nordic Semi were to file bankruptcy or otherwise discontinue their product(s). Following the same logic, LoRa and Sigfox offer comparable wireless performance, but LoRa is the superior choice because the technology is implemented by different vendors (Semtech, Microchip, HopeRF) instead of relying on a single company as is the case with Sigfox.

Simple solutions are usually the most energy efficient solutions as well, and that statement is nowhere else as true as for wireless communication. Most standardized wireless protocols require considerable overhead (the so-called “protocol stacks”) which make more powerful microcontrollers imperative. This is often ultimately unnecessary to implement the desired functionality in an application. In the greenhouse example, if all windows need to be opened or closed on a wireless command, there are much simpler solutions than a Z-wave or BLE transceiver. The two commands (open and close) can be easily encoded, for example a 20 ms RF pulse at 70 MHz can be the signal to open windows and same length pulse at 75 MHz could be the command to close them again. A Colpitts oscillator at the transmitter side and broadband opamp with dual band analog filter at the receiver side is all that is required to implement such FSK functionality, without requiring any microcontroller with excessively complex protocol stack at all. The resulting implementation is very energy and cost efficient, simple in layout (thus creating the durability required to operate 30 years), and most importantly, compatible technology can be implemented at minimal effort with standardized components at any time in the future. The Rad1o Badge as SDR development kit discussed in chapter 7 is an example of this philosophy.

1.7 Limitations

Despite the rising awareness of developers about the opportunities provided by energy harvesting to prolong the autonomy of their applications, too often energy harvesting is simply seen as a replacement for batteries. This is evidenced by the numerous integrated energy harvesting capable modules currently

existing on the market, such as those commercially distributed by EnOcean [88, 156, 300, 334] and PowerCast [174, 140, 226]. Many system engineers seek for off-the-shelf energy harvesting solutions. Recently, plug&play energy harvesting solutions have drawn significant attention from the industry and energy harvesters having the form factor of AA or AAA batteries are often seen as ideal situations [321].

To maximize the power harvested from them, however, ambient energy sources demand designers to think beyond the conventional battery – electronics concept. Rather than seeing the energy harvester as a replacement for batteries, it is a necessity to adapt the application to the environment it is designed to operate in, and engineer the electronics with the harvester as foundation. Consequently, sales of these off the shelf energy harvesting solutions have in most cases been disproportional to the enthusiasm with which they were received. Ironically, on the other side of the spectrum, stand alone harvesters have seen a greater success despite their lack of integration.

The possibilities of energy harvesting are not only limited by the quantities of ambient energy available, but also by the environment itself. Practical limitations may prevent harvesters to be installed in an optimal way, or partly obstruct access to ambient energy. Even the most accurate and elaborate energy harvester model can not cope with this kind of factors, which leads to misconceptions and disappointments. Discussed below are several examples of recent hoaxes, able to propagate beyond reasonable proportions, often based on crowdfunding campaigns supported by poorly informed contributors.

- **Solar Roadways** is an ongoing "smart highway" initiative, envisioning the replacement of current asphalt or concrete roads with solar panels covered by a thick layer of tempered glass. Before reputable researchers and experts in the field could express their doubts about the concept, the project had already collected $ 2 M worth of funds on crowdfunding platform Indiegogo, and government R&D grants worth another $ 1.25 M. The difficulty of designing a scratch resistant tempered glass surface, able to withstand mechanical strain from braking vehicles, was one of the major problems cited. Supporters rejected the most evident solution, placing the panels on a roof above the road instead, even after thorough debunking efforts of the hoax. [209]
- **iFind** claimed to be an RF energy harvesting powered item location tag, acting as an active BLE node powered by ambient RF energy. Despite the lack of evidence and experimental data from the supposed inventors, the project raised over $ 500 k on crowdfunding platform Kickstarter. With a maximum RF power density of around 20-35 nW/cm^2, in areas with high GSM, 3G and 4G network density, the claim could easily be debunked based on the physical size limitations of the tag itself. Funding for the project was suspended in 2014. [125, 12]
- **ThermoLife** claimed to have a prototype of a new micro TEG based on a zT$>$10, although the largest currently reported is zT=3. A prototype was demonstrated that looks suspiciously much like a coin cell battery of which the engravings were removed with sandpaper, supposedly generating 111 μW at a temperature difference of 5°C. The prototypes were promised by 2007, but no patents have currently been filed for the new technology. [245]
- **Fontus** was an initiative using a solar panel to drive a thermoelectric cooler (TEC) to generate drinkable water from the air by accelerating condensation on the cold side of the TEC. After peer review, the designers admitted that the 500 ml/hour yield promised was assuming "optimal environmental conditions", i.e. very humid climates. In the arid desert climates for which the device was designed, condensation would be minimal because of the very low dew point in these areas. [336]
- **Rayton Solar** started a crowdfunding campaign to finance a particle accelerator to slice silicon wafers to the minimum 200 μm thickness required for optimal solar cells. According to the inventors, it would allow a 25 % more efficient solar cell at 60 % lower cost. Despite the high profile

advertisement campaign, in which even Bill Nye was involved, no prototypes could be demonstrated to prove the 25 % efficiency gain. [242]

- **Batterizer** filed a patent in 2010 for a boost regulator designed to extend the life time of 1.5 V alkaline batteries by allowing them to be discharged to a lower voltage. The crowdfunding campaign that followed raised over $ 300 k, or 10 times the original set goal of $ 30 k. The usefulness was quickly contested, when D. Jones and others demonstrated that existing portable devices operate reliably down to 1.1 V, and below that threshold have an output impedance prohibiting the use of a boost regulator. [102]

The examples above illustrate that infeasible or impossible claims can debunked with moderate ease using common sense, and keeping the law of Conservation of Energy into the equation. The complementary balanced energy harvesting methodology can help to identify such hoaxes before too much effort and/or funding is wasted on them.

1.8 Structure

The relationship between harvester size, ambient energy and the system's energy needs is essential to understanding the fundamental problems with ambient energy powered autonomous system design. The energy harvesters themselves are the starting point of the design. Chapter 2 presents an overview of current state-of-the-art energy harvesting technologies, with a side track on emerging technologies expected to make a breakthrough in the upcoming years. Resources required for the construction of energy harvesters may be a limiting factor in the large scale deployment of energy harvesting technology however, and the energy needed for the production and distribution of energy harvesters has environmental costs just as with other power sources. The purpose of chapter 3 is making a distinction between what is technologically possible, and what is environmentally responsible based on longevity and power efficiency of energy harvesters. Since economic and technical feasibility does not take ecological footprints into consideration, the environmental cost of different energy harvesting solutions may vary greatly despite having a marginally different electrical power output.

With an overview of energy harvesting technology in mind, chapter 4 proceeds with discussing the theoretical perspective of Complementary Balanced Energy Harvesting: splitting harvester performance into peak power, size, and harvester efficiency. This parametrization approach offers 3 individual parameters, corresponding respectively to the harvester performance in a specific environment, its size, and the available ambient energy in that environment. Applications are illustrated with appropriate examples. Another point of attention is the source of the ambient energy that is being converted. In the case of a floating oceanographic measurement station using wave energy, for example, the energy source is the waves themselves [170], and there are no noticeable consequences to the ocean by extracting a small fraction of energy from these waves. In contrast, a thermoelectric energy harvester on a steam pipe converts heat flux into electrical power [213], so the harvester will intrinsically cool down the steam pipe, potentially altering its functionality. The trade-offs are are also discussed in chapter 4.

The first parameter, harvester performance, is determined through harvester performance characterization. Techniques to obtain harvester performance and fill a database with harvester characteristics are presented in chapter 5, suggesting low cost testing apparatus to automate harvester benchmarking.

Determining the types and quantities of available ambient energy in a specific target environment is probably the most interesting aspect of Complementary Balanced Energy Harvesting, and no suitable

methods are available that allow measurement of ambient energy in the field, and measure harvester performance at the same time. The Ambient Energy Monitor project (AEM) aims to measure both at once, offering a compact, low cost and portable framework for automated ambient energy benchmarking. The open source hardware and software developed in the context of the AEM project is presented in chapter 7.

Finally, with ambient energy and harvester characteristics known, the optimal harvesters can be selected, dimensioned and designed into the autonomous system. Depending on the periodicity of the available ambient energy and the continuity of system operation, local energy storage may be required depending on system demands. Chapter 6 discusses possibilities regarding power storage, including solid state batteries and capacitors, with particular attention to longevity, cost and performance, without neglecting the environmental factors. After selection of local storage, if needed, chapter 6 proceeds to DC/DC converter selection and power path design, using a case study to illustrate the complete Complementary Balanced Energy Harvesting design methodology work flow.

Chapter 2

Energy Harvesters

Any device converting ambient energy into electrical energy is an *energy harvester*, regardless of the type of source energy. Since energy harvesters obey the Law of Conservation of Energy, they can only output as much power as they can physically capture. Intuitively, larger energy harvesters have the potential to convert more power than their smaller counterparts. There are losses in the conversion process however: not all ambient energy captured by the energy harvester will be converted into electrical energy – in fact, the most efficient commercial harvesters convert less than 50 % of ambient energy into electrical energy, which means the other half is converted into unusable thermal energy (heat) and thus lost from the perspective of the powered system.

Photovoltaics (PV), wind and hydro energy harvesting are the best known to a broad public, mostly in MW scale installations, but energy harvesters exist for nearly any type of ambient energy imaginable. This means almost any kind of ambient energy available can be converted into electric energy, although the available energy density may very small in practical situations. When harvesting energy from vibrations, variations in air pressure, electromagnetic radiation (RF), and many other weak sources, expected power output levels for matching energy harvesters can be expected to be in the range of mW down to nW, depending on harvester size, construction and installation. As processing units, sensors, and actuators become more energy efficient, as with MEMS gyroscopes and e-ink displays for example, those weak ambient energy sources become interesting in specific applications. Unsurprisingly, many different types of energy harvesters have resulted from the arduous work of countless enthusiastic research groups, some of which employ highly unusual and exotic strategies or clever tricks to tap into previously unusable ambient energy sources.

This chapter aims to provide an overview of the current (as of 2018) state-of-the-art in energy harvester technology, discussing existing harvesters and anticipated future trends. It does not intend to be a complete glossary of all energy harvesters in existence to date, since such a list would be encyclopedic and impractically long. A selection was made based on current research and trends towards the foreseeable future, focusing on technologies particularly scalable to μW and mW output power levels.

2.1 Photovoltaics

Photovoltaic energy harvesting (PV) can refer to any type of energy harvester that converts light into electric energy. The source of light may be of natural or of artificial origin, so depending on the spectral sensitivity of the PV cell, they can work with (outdoor) sunlight or (indoor) lamps as energy source [93].

Solar irradiation at the Earth's surface (*insolation*) has been extensively studied and data on variations with seasons, altitude, and location on the planet are readily available for most large cities, including average values for expected insolation at a specific location [144, 83]. This is an important advantage of PV since, if used outdoors, the environment does not have to be measured/benchmarked anymore, and development of an autonomous system using PV can be accelerated. The drawback of sunlight is of course the inevitable day and night cycle, so for systems that need to operate around the clock, energy need to be stored during the day for use at night. An extensive example of calculation for PV cell sizes and local storage capacity is given in chapter 6.

When using PV for indoor applications, benchmarks will point out that the luminosity indoors may be 3 to 4 orders of magnitude smaller than natural sunlight. Depending on the type of room, indoor luminosity may vary from about 50 lx in a dark corridor to nearly 1 klx for precision workshops or surgery tables. In contrast, outdoor luminosity can be expected between 10^3 and 10^4 lx. This difference of scale means that an application must be specifically developed for indoor or outdoor use [13]. The dynamic range of the human eye is deceiving, so actual benchmarking is required to correctly characterize indoor environments, as discussed in chapter 7.

2.1.1 Efficiency

PV cells only absorb photons with an energy that corresponds to the band gap sensitivity of the cell, that is the energy required to liberate an electron from the valence band. For Si, the energy required is 1.1 eV, so depending on the construction of the cell (doping, materials, etc.) the PV cell will have a different wavelength sensitivity. Greater band gaps reduce efficiency because few photons will possess the necessary energy to liberate an electron, whereas lower band gaps liberate many electrons but also convert the difference in photon energy and band gap energy into heat [323]. The band gap thus is a trade-off, and should be chosen in function of the spectrum of the environment in which the cell will be used. For instance, pc-Si and mc-Si cells (polycrystalline and monocrystalline silicon) have a band gap of 1.1 eV, InP and GaAs have a band gap of 1.4 eV, CdTe of 1.6 eV and a-Si (amorphous silicon) 1.7 eV [324, 262]. The earliest Ge cells have the lowest band gap, around 0.6 eV [166]. The band gap trade-off also dictates that there is a maximum efficiency for single junction PV cells, which is for sunlight around 33.7 % for a band gap of 1.34 eV, a limit called the *Shockley-Queisser* limit [277, 252]. For Si based PV (band gap of 1.1 eV), currently the dominant technology, the theoretical maximum efficiency is thus slightly lower, around 32 %. The best single junction PV cell to date (September 2017) is a Si HIT cell developed by Kaneka with an efficiency of 26.6 % in sunlight [267]. Si HIT efficiency surpassed mc-Si efficiency in 2014, and the best mc-Si cell to date has an efficiency of 25.3 % developed by Fraunhofer ISE in 2016 [118]. The difference between the ca. 32 % theoretical maximum efficiency and actual 26.6 % achieved efficiency is caused by incomplete absorption (reflection) and other practical issues. [76, 329, 183, 261]

To get around the Shockley-Queisser limit, multiple PV cell junctions with different band gaps can be stacked on top of each other [176, 44]. With an infinite number of junctions, a theoretical limit of 86.8 % may be achievable, but the current maximum for multi junction cells is 38.8 % for a 4 junction cell by Boeing-Spectrolab [64], designed for aerospace applications. Further improvements may be made by using lenses and other optical techniques to concentrate light onto a smaller PV surface, so-called concentrated PV. The current world record cell dates from 2015 and is a 4 junction cell with concentrator designed by Fraunhofer ISE with a top efficiency of 46.0 % [32]. It should be noted however that, although the technology exists and has been independently verified by NREL, such concentrated

PV systems are likely too expensive and complex to be used for general purpose energy harvesting applications for the foreseeable future.

2.1.2 Cell Types

Since all semiconductor materials are photosensitive, it should not be a surprise that a large number of cells have been designed, manufactured and tested, with a wide range of materials in use. Important developments in PV are CIGS (22.6 % efficiency, [147]), CdTe (22.1 % efficiency, [162]), DSSC (11.9 % efficiency, [192]), $CaTiO_3$ perovskite (22.1 % efficiency, [266]) and CZTSSe (12.6 % efficiency, [329]). None of these satisfy all the requirements for eligibility in autonomous applications: life span, commercial availability and environmental impact. With the exception of CdTe, which anyway should not be used because of the health risks involved with Cd as discussed in chapter 3, the market is currently dominated by Si based PV: mc-Si (25.3 % efficiency, [118]), pc-Si (21.9 % efficiency, [296]) and a-Si (14.0 % efficiency, triple junction cell, [264]). Scalability and environmental impact related to PV cell choice are discussed in chapter 4, performance analysis of Si PV in chapter 5.

2.1.3 PV Harvesting

Since PV cells are non-linear elements, the load lines of PV cells are also non-linear and the power curve is parabolic. The local maximum of the power curve is the maximum power point (MPP), which corresponds to the cell voltage at which the extracted power is maximum. To maximize efficiency, the cell should be operated as close as possible to its MPP, which can be dynamically adapted using circuits known as maximum power point trackers (MPPT). The MPP shifts slightly with temperature, but is usually between 70 % and 80 % of the cell's open circuit voltage V_{oc}. Depending on the nominal power rating of the cell, adding a MPP to the circuit may or may not result in an overall efficiency improvement [349, 36]. PV cells behave as DC current sources.

2.2 Thermoelectrics

Thermoelectric energy harvesting makes use of a temperature difference between a hot and cold surface to create a heat flow/flux through a suitable harvester called a thermoelectric generator (TEG). The principle is based on the Seebeck effect, the phenomenon of charge carrier diffusion as a result of a heat flow. It occurs in both semiconductors and metallic conductors, but is too small in metals to be of practical use. The best thermoelectric materials are doped semiconductors. The flow of charge carriers in turn results in a voltage difference over the TEG [5]. This mechanism thus directly converts thermal power (a heat flow) into electrical power, with the major advantage over other methods such as Sterling engines being that a TEG is a solid state device without moving parts (and thus potentially a long life time), and that it works with any temperature difference [184]. All thermally and electrically conductive materials exhibit the Seebeck effect, but the effect is usually insignificantly small. There are few exceptions, the best known materials being Bi_2Te_3, $Ca_2Mn_3O_8$ [11], PbTe [338], SnSe [356], $Mg_2Si_{0.55}Sn_{0.4}Ge_{0.05}$ [159] and SiGe [145]. The efficiency of a material as TEG is expressed as the *figure of merit* zT [282]:

$$zT = \frac{S^2 \varsigma T}{\kappa} \tag{2.1}$$

where S is the Seebeck coefficient, κ the thermal conductivity, ς the electrical conductivity and T the absolute temperature. Since metals have both a high ς and a high κ, they have a very low zT [107, 238]. Current thermoelectric materials such as Bi_2Te_3 and PbTe have a zT$\approx$ 1 [108], which can be improved

by either increasing the Seebeck coefficient S or reducing the thermal conductivity κ by making use of nanostructures instead of solid semiconductor materials. The temperature cannot be increased arbitrarily since TEG materials melt at relatively low temperatures: 450 K for semiconductor based materials (alloys of Bi, Sb, Te or Se), 850 K for alloys of Pb [237, 133], and up to 1300 K for SiGe. The environmental concerns associated with Pb TEGs are discussed in chapter 3.

Since proven by Venkatasubramanian et al. that the figure of merit (zT) can be increased to values greater than 1, thermoelectrics have gained increased attractiveness for energy harvesting purposes due to the higher thermal efficiencies available. Although a thermal efficiency close to the Carnot efficiency requires zT$= \infty$ and there is no theoretical upper limit for its value, there are currently no known materials with zT$\geq$3 [308]. The Carnot efficiency corresponds to the amount of useful work that is output for a given amount of heat energy input. The maximum efficiency is therefor

$$\eta_{max} = 1 - \frac{T_c}{T_h} \tag{2.2}$$

where T_h is the absolute temperature of the hot source and T_c that of the cold sink, measured in K.

These advancements allow for commercial implementations of thermoelectrics for energy generation, as available from *Nextreme* and *Micropelt*, a spin-off from Fraunhofer IPM.

2.2.1 Efficiency

Typical efficiency of TEGs is between 5-8 %, depending on the materials used. Thermal contact with the heat or cold source can be challenging, particularly since pipes tend to have a circular diameter, whereas TEGs have a flat surface. TEGs have been developed in conjunction with collets specifically designed to be mounted around high temperature pipes, but these collets add thermal resistance and lower the efficiency. In practical TEGs there are always 2 materials used, and the maximum efficiency is given by

$$\eta_{max} = \frac{T_H - T_C}{T_H} \frac{\sqrt{1+zT} - 1}{\frac{1+zT}{+} \frac{T_C}{T_H}} \tag{2.3}$$

with the zT for the combination material being

$$zT = \frac{(S_p - S_n)^2 T}{\left(\sqrt{\rho_n \kappa_n} + \sqrt{\rho_p \kappa_p}\right)^2} \tag{2.4}$$

with ρ being the electrical resistivity.

2.2.2 TEGs

Commercial TEGs have a wafer structure, consisting of thermopiles (stacks of thermoelectric material) sandwiched between 2 electrically insulating but thermally conductive ceramic plates. Because of the low output voltage per pile, several piles are usually combined and electrically wired in series but thermally in parallel. Combinations can be made by stacking multiple TEGs on top of each other etc. A TEG behaves as a low voltage DC source, and requires a step-up converter (voltage booster) [339], as discussed in chapter 7. TEGs continue generating power as long as the temperature difference between the hot and cold side is maintained, to keep a heat flux flowing. When using a TEG on a hot surface, the heat flux through the TEG will also quickly heat up the cool side, reducing the temperature difference

ΔT and thus reducing the output power. The most difficult aspect of using a TEG is therefore maintaining the temperature difference, since either passive or active cooling of the cold side will be necessary to maintain a sufficient temperature gradient. In environments where a large temperature gradient is available (for example steam pipeline in an outdoor environment) then natural air flow may be sufficient to cool down the cold side to maintain a sufficient temperature difference. When the initial temperature gradient is already small, for example when powering a smart watch with human body heat, then a rather bulky heat sink is required to maintain a minimum temperature difference.

2.3 Piezoelectrics

The piezoelectric effect occurs when a crystal shape is physically altered under mechanical strain, causing repolarization inside the crystal, and as a result, a voltage appears over the crystal. The voltage changes in polarity depending on the direction of strain (i.e. whether the crystal is being compressed or allowed to expand), and a sequence of successive compression and expansion cycles therefore results in an AC voltage [350]. Piezoelectric energy harvesters are commonly used to convert mechanical vibrations or shocks into electrical power. Because piezoelectricity is a phenomenon occurring in a three-dimensional crystal structure, the effect can not be described with a linear equation but requires 2 constitutive equations [52]:

$$\begin{cases} T_p = C_{pq}^E S_q - e_{kp} E_k \\ D_i = e_{iq} S_q + \epsilon_{ik}^S E_k \end{cases} \tag{2.5}$$

with c_{pq}^E the material's Young modulus, e_{kp} its piezoelectric coefficient, and ϵ_{ik}^S its clamped permittivity. The equations assume an electromechanical equilibrium where the electric field E and mechanical strain S are both constant. The piezoelectric effect can be observed in many materials, both of natural (quartz, tourmaline, sugar, bones, mineral salts) and synthetic origin [203]. The most used piezoelectric materials in commercial cantilever energy harvesters are PZT (lead zirconate titanate, $Pb(Zr,Ti)O_3$, [48]), $BaTiO_3$ [265], PVDF (polyvinyldifluoride), $(Na,K)_{0.5}NbO_3$ [89] and ZnO. PVDF is more flexible and responds better to high g conditions and vibration frequencies up to 80 kHz. ZnO in particular is of interest because nanostructures can be manufactured with it, such as ZnO nanowires with a strain coefficient of ca. 10 pC/N. [148]

2.3.1 Reliablity

Under stress of the vibrations applied to piezoelectric energy harvesters, mechanical deterioration inevitably occurs. Although PZT has the highest power density, it is poorly suited for high accelerations because of the lower robustness that eventually leads to fracturing of the material. But also at lower vibration amplitudes, fracturing eventually occurs. The piezoelectric properties of the materials stabilize logarithmically with age, stabilizing over time, and manufacturers of piezoelectric energy harvesters often specify the performance of the harvester after a well defined period of time. To increase reliability, the surface of the harvester may be increased to compensate for fracturing, or a more flexible material such as PVDF can be chosen over stiffer materials such as PZT.

2.3.2 Efficiency

The absolute conversion efficiency of a piezoelectric energy harvester is given by

$$\eta = \frac{2(1-k^2)}{k^2} \cdot \left(\frac{1}{Q} + \frac{k^2}{2(1-k^2)} \right)^{-1} \tag{2.6}$$

with k^2 the coupling factor and Q the quality factor of the harvester. The efficiency of PZT cantilevers has been theoretically estimated to 50-90 %, measurements indicate efficiencies around 7-10 % however. The record efficiency for PZT cantilever in its resonance frequency is 26 %, the record for PVDF nanofibers, 21.8 % [350]. Cantilever or impact based piezoelectric energy harvesters are strongly affected by variations in their mechanical resonance frequency however, which is given by

$$\omega_r = \sqrt{\frac{k}{m}} \tag{2.7}$$

where k is the spring constant and m the tip mass of the harvester [211]. The resonance frequency can thus be tuned, within practical limits, by adjusting the tip mass of the cantilever. [350]

2.4 Triboelectrics

Triboelectricity is an alternative to piezoelectricity to convert mechanical movement into electrical energy directly without the need for magnets [331]. Triboelectric generators (TENG) use the triboelectric effect, which occurs when a material that charges positively comes into friction contact with a material that charges negatively, as with the famous examples of fur rubbing over a glass rod or running a plastic comb through hair [61]. Although the effect has been known to occur for centuries, the results remained unpredictable, and thus too inconvenient to construct a harvester with. Until 2012, when prof. Zhong Lin Wang's team at the Georgia Institute of Technology developed the first practical implementation of a TENG [327, 328]. Since 2012, TENG output has been improved by 5 orders of magnitude, reaching a power density of 313 W/m^2 and a volume density of 490 kW/m^3. The technique is similar to reverse electrowetting as described by Krupenkin et al., with the difference that no external potential is necessary [177]. The potential can be calculated as

$$U_{TE} = -\frac{\varsigma d}{\eta_0} \tag{2.8}$$

with ς the triboelectric charge density, η_0 the vacuum permittivity, and d the interlayer distance at a given state. Modern TENGs are constructed with a stack of organic and inorganic films that exhibit opposite triboelectric polarity. By causing friction between the films, an electric potential is thus generated. TENGs are the only energy harvesters to date, with the exception of emerging organic PV cells, using organic materials in their construction.

2.4.1 Efficiency

The conversion efficiency depends on the contact mode between the two films, for which there are 3 options: vertical contact-separation mode [189], lateral sliding mode [357], and single electrode mode [348] as a cantilever. The mode should be chosen as a function of the application itself, i.e. the mechanical direction of movement available. Depending on the construction of the TENG, efficiencies up to 60 % are achievable for vertical contact-separation [94], and 72 % for lateral sliding mode [246, 246].

2.4.2 Reliability

With the exception of single electrode mode, TENG deployment requires an electrode to be connected to both films, which practically infers one on a static substrate and one leading to a moving object [358]. The flexible conductor that makes the connection is also susceptible to the movement, and vulnerable to excessive mechanical strain which may cause it to fail prematurely. TENGs have a long life time and

are reliable since the contact mode can be tightly controlled, for example between kapton and PMMA [122, 341, 160]. The difficulty in implementation is that the harvester needs to be shaped to fit onto the moving object, and a stationary substrate must be available for the other film [65, 94].

2.5 Pyroelectrics

The pyroelectric effect is similar to the piezoelectric effect, but induced by temperature variations instead of mechanical strain variations [69, 68]. Piezoelectric materials are often also pyroelectric, as is the case with ferroelectric materials such as titanates ($PBTiO_3$, $BaTiO_3$ etc.) and non-ferroelectric materials such as tourmaline, ZnO and AlN [71, 342]. Not all piezoelectric materials are pyroelectric; quartz and langasite are examples of good piezoelectric materials that are not pyroelectric [148, 161]. Pyroelectric energy harvesters (PEG) produce an output voltage when the temperature of the harvester is changed. The phenomenon is defined by the pyroelectric coefficient p_i [71]:

$$p_i = \frac{\partial P_{S,i}}{\partial T} \tag{2.9}$$

hence, the polarity of the output voltage changes with dT/dt: heating the material will result in a positive output voltage, cooling it in a negative output voltage. A continuous cycle of heating and cooling results in an AC voltage appearing over the pyroelectric energy harvester, but since the frequency of a heating/cooling cycle is typically low, the power output is also low in comparison to piezoelectric energy harvesters since less energy can be converted within the same time interval. The choice between a TEG and PEG depends on the stability of the heat or cold source: a constant temperature (difference) can be converted in a constant heat flux and favors a TEG, when the temperature is variable then a PEG may be a better choice. Materials for pyroelectric generators are PZT, $CaTiO_3$, $LiTaO_3$,$Na_{0.5}Bi_{0.5}TiO_3$ [200], (Pb,La,Zr,Sn)TiO_3 [359, 249], TGS (triglycine sulfate) [275] and PVDF [219, 353, 172]. The figure of merit is zT is given by [39]

$$zT = \frac{p_i}{c_v \eta_0 \eta_r} \tag{2.10}$$

where p_i is the pyroelectric coefficient, c_v the thermoelectric capacitance, and $\eta_0\eta_r$ the electrical permittivity.

2.5.1 Reliability

As with piezoelectric energy harvesters, the constant exposure to thermal stress may lead to fracturing in the materials, particularly solid crystal structures [270]. However, since PEGs can be constructed from ceramic materials unlike TEGs which are constructed from semiconductors with lower melting point, PEGs offer the advantage that they can operate at temperatures up to 1200 K for titanates and tantalates [40]. Progress made with synthetic materials specifically designed for pyroelectric energy harvesting such as GaN and $CsNO_3$ which improves reliability at a cost of lower operation temperature. Since pyroelectric energy harvesters are also solid state devices without moving parts, they also have a better reliability than heat engines and Sterling engines.

2.5.2 Efficiency

In an Ericsson heat cycle, pyroelectric energy harvesters can reach efficiencies up to 50 %, but only for the pyroelectric effect itself [271]. Losses from heating and cooling the substrate of the harvester

and heat transfer losses lower the effective efficiency [231]. In many applications where a PEG should outperform a TEG, the choice is still made for a TEG because it is easier to implement [178]. To measure the potential of pyroelectric energy harvesters, the same benchmarking module as for TEGs can be used (see AEM Thermal in chapter 7).

2.6 Betavoltaics

Betavoltaic energy harvesting is the direct conversion of ionizing radiation into electrical energy, as opposed to RTGs which first convert ionizing radiation into heat, which is then converted into electrical energy through TEGs [38]. The operation principle of a betavoltaic energy harvester is identical to a PV cell, with only a different source of radiation. Materials with a different band gap are chosen, depending on the type of ionizing radiation, such as GaN [136, 197], InGaP [49] and ZnO [355]. The radiation source can be natural (β decay of mineral ores) or artificial from decaying shorter lived isotopes such as ^{90}Sr [77], ^{90}Y, ^{63}Ni [49] and ^{3}H (tritium). When an isotope is combined with a PV cell into a single device operating as a betavoltaic energy harvester, it is referred to as a nuclear battery. Betavoltaics potentially offer long life times, which is why betavoltaic batteries were already used in pacemakers and other high reliability, long life time medical applications [229]. Betavoltaic energy harvesting has specific applications in the monitoring of underground long term storage of nuclear waste, where no other practical sources of ambient energy are available.

2.6.1 Efficiency

Identically to a PV cell, betavoltaic energy harvesters are also subjected to a theoretical maximum limit similar to the Shockley-Queisser limit [165]. The theoretical maximum efficiency can be approximated by [77]

$$\eta_{max} = \frac{E_g}{2.8E_g + 0.5} \tag{2.11}$$

where E_g is the bandgap of the semiconductor material being used. The thickness of the PV cell determines its stopping power and thus absorption coefficient, values range from 150 μm (40 % absorption) to 265 μm ($> 90\,\%$ absorption). The overall efficiency is below 10 % [77].

2.6.2 Half Life

By definition, after each half life of an isotope, its output power from β decay will also halve. Unless there is a constant replenishment of the isotope source, the estimated average half life should be taken into account when dimensioning the PV cell. When using a known isotope as a source, the half life is also known and the calculation becomes trivial. However, when relying on natural decay or sources from nuclear waste with variable composition, benchmarking the ambient environment is required. Methods are discussed in chapter 7. As with PV cells, betavoltaics generate a DC current source, although additional boost circuitry may be necessary because of the low output amplitude [57, 121].

2.7 Kinetic

Kinetic energy includes any source that can be harvested with classic induction type energy harvesters based on Faraday's induction law [101]. This includes all sources of movement, except high frequency

vibrations [240], which have already been covered by piezoelectric energy harvesters although there is of course an overlap region between the two. Kinetic energy may come from the movement of vehicles, animals [272] (including humans), or machinery [273]. Examples typically include monitoring of mechanical integrity on revolving machine parts, such as helicopter propellers or wind turbine blades. Other sources of kinetic energy are nearby fluid flows in a liquid [263, 175] or gas [188, 335] state. This kinetic energy can be converted into electrical power using appropriate turbines, for example micro wind turbines to harvest energy from air flows in ventilation shafts, or water flow as power source for an autonomous domestic water meter [257]. The design of generators and/or turbines to harvest mechanical energy must be tailored to the energy source and the intended application, so it is pointless to make estimations or predictions on the efficiency of such devices [1].

2.8 RF

Energy harvesting from ambient electromagnetic energy only requires a suitable antenna and a rectification circuit to operate. The range of frequencies that can be harvested depends on the physical construction of the antenna (equivalent antenna length equal to $\lambda/2$), and complementary balanced energy harvesting techniques can be applied to harvest energy from multiple antennas tuned to different frequency ranges simultaneously [306, 46]. The surface covered by the antenna is directly proportional to the output power, and various antenna designs for energy harvesting, specifically broadband antennas, are discussed in chapter 7. The interface between antenna and power path is an RF suitable rectifier called *rectenna* [51], which may be combined with voltage doublers or multipliers [2].

2.8.1 Efficiency

The efficiency of RF harvesting is 50 % peak, with subtraction of rectification and power regulation losses, the figure is usually below 2 % efficiency [236]. When optimized for wireless power transfer, rectenna designs in microwave range can reach a conversion efficiency of 85-90 % [354]. Harvesters can be low cost however, since theoretically any conductive object can act as a suitable antenna for RF energy harvesting. RF energy harvesting is only a viable option in densely populated areas with a high concentration of wireless communication, in particular cellular communication in the 900 MHz - 1.2 GHz band and 1.8 - 1.9 GHz band [146], and wireless video broadcast transmissions. Although energy can theoretically be harvested from any band, higher frequency bands (assigned to modern telecommunication protocols) are less efficient because the contained RF power levels are too low [198]. As a general rule, the older the technology used for RF communication, the higher the power levels [87], and the more profitable RF energy harvesting is [225]. There is an ethical aspect to RF energy harvesting, however: since harvesting RF signals reduces the signal strength "behind" the harvester's antenna, the ISP or telco may be required to increase the transmission power to also reach these users.

2.9 Chemical

Harvesting energy from chemical sources requires a bioharvester [150], currently using specifically engineered proteins to convert chemical compounds with a high caloric value, such as sugars, directly into electrical energy [127, 142]. The technology is being sought after for wearable electronics in particular and medical implants such as pacemakers or prosthesis monitoring inside the body. Although bioharvesters have been developed, the life span is currently unsatisfactory because the proteins necessary

for the conversion process decay after 2 to 3 years, or are reclaimed by the body itself. Similar bioharvesters have been developed for waste water [112, 292], trees (such as the Voltree project[253]) and other sources of chemical energy of organic origin, for monitoring remote biomes and forests. No commercial harvesters are available on the market unfortunately, which excludes their use in the scope of this thesis.

2.10 Conclusion

The ambient environment determines which energy harvester(s) will fulfill the power demands of a specific application the best. When selecting a harvester based on tech reports and datasheets, it should be kept in mind that the optimal test conditions leading to the maximum performance documented in datasheets can rarely, if ever, be replicated in a real world application. Minor variations in ambient energy, such as a slight deviation in vibration frequency or light spectrum, may have significant consequences for the power output of a harvester. Comparing maximum power ratings of different harvesters with each other, as is historically a tradition in literature, is therefore pointless, since no correct comparison yields usable results. Instead, it is necessary to benchmark the performance of harvesters in both favorable and unfavorable conditions so an accurate prediction of power output can be made in a known ambient environment – which also needs to be benchmarked for that reason. Strategies for benchmarking energy harvesters and ambient environments are discussed in the next chapters.

Chapter 3

Resource Considerations

The previous chapter presented a summary of energy harvesting technology to date, emphasizing on technological feasibility and state-of-the art. Technical reports on prototype performance, usually constructed and measured in a laboratory, unfortunately often only spotlight conversion efficiency and omit resource considerations either because they are considered unimportant in the context or remain unknown at the time of publication. This shortsightedness causes a negative bias in the design process of electronic systems powered by energy harvesters, with negative environmental consequences. Resources are the decisive factor for economic and ecological feasibility however, and the matter is complicated because economic profitability and environmental responsibility are not always aligned goals. Deploying a specific energy harvesting technology may be economically profitable but not environmentally responsible and vice versa. Projected life time, available ambient energy, alternative energy sources, harvester installation, and all aspects related to production and transport play a role in the decision making process.

Only a minority of the discussed solutions is also commercially available for use in autonomous systems powered by energy harvesters. The 3 major technologies, covering $> 87\,\%$ of the energy harvesting market, are in order of significance photovoltaics (PV) for natural and artificial light, thermoelectrics (TEG) for harvesting energy from temperature gradients, and piezoelectrics (PZ) for vibration harvesting [72]. Although developments in PEG and TENG technology have been omitted in the resource management discussion, most of the conclusions are applicable to pyroelectric and TENG energy harvesters as well since they largely share the same materials for their construction.

The aim of this chapter is to provide an overview of commercially available energy harvesters, a small subset of the technology tree presented in the previous chapter. Energy harvesters are presented from the perspective of environmental cost rather than mere harvester efficiency, to provide a more nuanced overview of design choices for sustainable electronics than the narrowminded comparisons usually found in technical publications.

3.1 Decentralization and Grid Connectivity

Before delving into resource management for energy harvesters, the trade-offs between local (decentralized) energy harvesting and grid connected (centralized) energy harvesting deserve to be discussed. Large scale power generation systems, such as solar farms or hydroelectric dams, are usually more efficient than small scale (decentralized) implementations of the same harvesting technology. For example, a roof top mc-Si PV panel array aimed under a favorable angle at the sun, will generate on average more

power per m^2 of panel surface than if the same mc-Si panels were used indoor to power a connected ceiling mounted smoke detector directly. Not only are the conditions for a roof top installation superior to indoor light harvesting, secondary losses in transformers, power inverters etc. can also be reduced by scaling them up. Because the equivalent PV surface required to power the same smoke detector will thus be larger for a decentralized than for a centralized energy harvesting approach, the choice for or against decentralized energy harvesting becomes a rather complex engineering optimization problem: at which point do the combined costs of a roof top PV panel and the required cabling efforts exceed the added size of a local PV panel? The answer to the question is not straight-forward, since a multitude of factors play a role. Aside from the manufacturing cost of PV in kg CO_2/m^2 resp. the cost of copper wiring in kg CO_2/m, the environmental costs also encompass the amounts and types of natural resources used, the waste produced (for example acids used in the silicon purification process), and energy spent on transport. Generally speaking however, in most stationary locations in close proximity of a power grid connection, decentralized energy harvesting solutions cannot compete with their centralized counterparts.

Aside from measurable environmental costs, there are also concurrent unmeasurable factors to be reckoned with: in buildings with a historic value such as UNESCO protected cultural heritage, it may simply not be possible to drill holes in walls to pull power cables through, or the installation of such cables would have a too detrimental effect on the aesthetic value of the construction. In these cases, the choice for decentralized energy harvesting may be made regardless of how unfavorable their environmental costs are.

A common misconception in the debate is the supposed added cost in human resources to perform the installation of cables. Comparing the cost of a PV cell against manpower is incorrect however, because the production of PV cells currently requires consumption of non-renewable natural resources, and generates non-regenerative waste in the process. Manpower is a renewable resource in contrast, and abundantly available. From the perspective of structural construction it can be considered infinite, and the combined effects of overpopulation and automation will make even more manpower available in the future. Installation costs should therefore not be taken into account in the cost balance when solving the decentralization vs. grid connectivity problem in a per case approach.

3.2 Batteries vs. Energy Harvesters

In unfavorable conditions, efficient non-rechargeable batteries can easily outperform energy harvesters economically and environmentally. For example, in an application that remains in idle state for most of its life, is expected to undergo maintenance after 5 years for a scheduled sensor replacement, and is required to remain active at any time within a $> 3\sigma$ reliability interval, it is unlikely that a harvester based solution can compete with a NiMH or Li-ion battery with a self-discharge of 2 %-3 % per month. Continuous operation for shorter periods and low average power requirements are favoring rechargeable batteries, while discontinuous/non critical applications with high average power requirements lean towards energy harvesting based solutions. It is important to point out in this context that modern rechargeable batteries can be recharged hundreds of times, therefore outlasting energy harvesters by an order of magnitude of lifetime. Secondly, rechargeable batteries are simpler in construction than energy harvesters like PV cells of TEGs, making them easier an thus less costly to recycle.

The conditions influencing the decision making process can be very subtle in practical applications, and the balance can easily shift in either direction if not all constraints are considered. Although no solutions should be explicitly excluded, only the most efficient energy harvesting solutions can generally be expected to compete against a grid connected or rechargeable battery powered alternative.

3.3 Natural Resources

3.3.1 Photovoltaics

Being the leading technology for solid state energy harvesting on both small and large scale for over 2 decades, silicon based PV have gained a share of over 93 % among light harvesters because of the exclusive use of silicon PV in kilowatt and megawatt scale installations [45]. Unsurprisingly, most existing resource related problems are directly or indirectly related to the production of silicon based solar cells (mc-Si, pc-Si and a-Si).

Silicon has historically been used as the substrate for conventional photovoltaics (PV), and has the advantages of being non toxic and abundantly available in the Earth's crust [260][294]. However, silicon has a low photon absorption coefficient, requiring a substrate thickness of 0.2 mm to achieve solar cells with high efficiency, equivalent to 9 g silicon per m^2 [45, p. 31][75]. This is half the quantity required in 1990, but between 2006 and 2016 there have been no further optimizations in Si economization. The relative Si usage per W_p has decreased from 11 g/W_p down to 5 g/W_p due to improvements in Si PV cell efficiency [45, p. 31]. Unfortunately, refining silicon from sand and purifying it to solar grade material is an energy intensive process. This elevates the cost of the raw material, resulting in a high price for silicon based PV. In 2013, silicon PV reached a share of 92 % in total PV production, of which 62 % pc-Si and 24 % mc-Si. Adding another 2 % market share for thin film a-Si, the total Si PV share rises to 94 %. [45, 208]

Research for thin film photovoltaics is an effort to reduce the amount of raw materials needed to manufacture PV. For large installation, thin film panels require two layers of glass instead of 1 layer for mc-Si/pc-Si as cover, but glass can be efficiently recycled. Despite none having the 25.3 % efficiency reached by mc-Si cells, advancements have been made in CdTe and CIGS technologies. With an NREL demonstrated efficiency of 22.1 %, CdTe is currently less efficient than mc-Si/pc-Si PV, but can be manufactured at lower costs. The presence of cadmium makes the technology not RoHS compliant because of the element's high toxicity [106], with the concentration of Cd in CdTe cells roughly equivalent to a C-cell NiCd battery [105] per m^2 of CdTe PV. The increasing market prices for Te impose further production and deployment problems. The SnO_2 and CdS in these cells lead to toxic waste when disposed at end of life. CIGS is regarded as an improvement over CdTe since the use of Cd reduced to CdS only. CIGS cells commonly reach 18.7 % efficiency, with efficiencies up to 22.6 % reported by NREL [63]. The technology relies on the rare elements indium and gallium for its development (chemical composition $Cu(In,Ga)Se_2$), increasing costs and obstructing a market introduction [3, 116]. Dye sensitized cells (DSSC) face the same problems because of their need for ruthenium and platinum, aside from their lower efficiency of 11.9 % [66].

Emerging technologies attempting to solve the issues above include organic PV and graphene PV. Research for organic photovoltaic materials have increased the efficiency of these cells from 3 % in 2000 to 8 % in 2012, and Pandey et al. demonstrated efficiency improvements for copper phthalocyanine (CuPc)

and C_{60} [234].

Finally, the most recent developments with high expectations were made with graphene and/or perovskite based PV cells, with as notable advantages over other technologies the wideband frequency sensitivity, and the high efficiency of energy conversion due to its capability to convert one photon into multiple electrons [301][115][210]. An efficiency of 8.6 % has been reported [210]. Since the recent discovery of low cost manufacturing methods for graphene by reduction of graphite oxide and arc discharge, the technology is expected to have a large impact on the PV industry in the next 10 years, reducing the environmental cost of PV cell manufacturing [330]. Both graphene and perovskite have the advantage to be non-toxic and practically insoluble in water, posing no threat to aquatic life if decommissioned improperly. As a material, perovskites (general composition ABO_3, most commonly $CaTiO_3$) are naturally available in abundant quantities, or can be synthesized as a composite material [20, 248].

Because of the increasing production capacity of PV worldwide, the demand for copper, silver and aluminum far exceed the supply from recycled sources. These resources currently need to be mined, along with the quartz used as a source of pure SiO_2. The quartz is subsequently heated to temperatures above 1400 °C, above the melting temperature of Si, and reacted with graphite to reduce the quartz to Si, and produce CO as a byproduct of the reduction process. The following purification steps, using the trichlorosilane method for example, involve treating the reduced Si with HCl, creating $SiHCl_3$ and a list of toxic chlorinated byproducts that need to be recycled or disposed of. Conversion of Si to $SiHCl_3$ takes place at temperatures above 300 °C, making these 2 initial steps responsible for the majority of CO_2 emission equivalent environmental cost of the PV manufacturing process. Current pc-Si PV panels have an energy payback of 3 to 4 years, depending on the insolation and installation execution. With an assumed life expectancy of ca. 30 years, this means a panel produces 8 to 10 times more energy than is consumed during the manufacturing process. For indoor energy harvesting, as in the smoke detector example mentioned above, the energy payback will likely never break even considering the 2 to 3 orders of magnitude lower light intensity in this environment, even with generous lifetime estimates of 50 - 60 years. Other environmental costs, including production waste management, mining consequences and recycling, are not even included in this environmental cost balance. This should be fuel for thought before considering choosing for PV as energy source in PV unfavorable environments. [167, 360, 8]

3.3.2 Thermoelectrics

Whereas many semiconductors yield measurable thermoelectric effects, traditional elements have been constructed using bismuth and tellurium. Elements of Bi_2Te_3 currently dominate the market, with chemistries based on Sb_2Te_3 and $CoSb_3$ emerging [157]. Bi_2Te_3 elements currently have the highest efficiency at room temperatures and a stability up to 250 °C, making them a preferred choice in many low temperature applications such as vehicles and aircraft [173, 126].

As discussed in the photovoltaics context, Te suffers from severe supply problems, causing its market price to have increased tenfold in the last 5 years (see figure 3.1). This makes Te based thermoelectrics unattractive because of their high Te content in comparison to CdTe photovoltaics (resp. 47.8 % by mass in Bi_3Te_3 and 61.1 % in Sb_2Te_3) [182]. The low voltage per cell requires many cells to be stacked in series to produce a usable output voltage, causing high market prices for Te based thermoelectric elements (TEGs). These evolutions have accelerated the development of alternatives with a lower Te content such as PbSeTe/$CoSb_3$ (30.8 % by mass) with a reported $zT = 3$ at 500 K [128].

Despite the lower Te content of PbSeTe/PbTe or PbSeTe/$CoSb_3$ thermoelectrics, the fundamentally limited supply of Te prevents their application for renewable energy harvesting on a large scale. A second problem is the geographically heterogeneous distribution of worldwide Sb reserves, most of them located in China. This further reduces the resource's supply reliability required for large scale production of Pb/Te based thermoelectrics from a political perspective [3, 116].

Advances in nanotechnology open up the possibility for higher efficiencies by increasing zT, allowing future replacement of Bi, Te and Sb with more common materials. Research in quantum dots [10][227], superlatices [312] and nanowires [135] have demonstrated the practical feasibility of constructing thermoelectrics using these technologies, however production costs are prohibitive for large scale implementations [343]. Good results have also been demonstrated for thermal to mechanical conversion using bimetallic structures [247]. All still rely heavily on Bi, Te and Sb however.

The first sustainable alternative to Te based thermoelectrics was presented by Hosono et al. in 2003, using Mg_2Si to construct thermoelectric generators [138]. Since both Mg (13.9 %) and Si (15.1 %) are abundantly available components of the Earth's crust [294], these elements allow large scale production of low cost thermoelectric generators independent of political or geographical limitations. A $zT > 1.5$ is achievable for Mg_2Si thermoelectric generators, and higher values are expected in the next 2 to 3 years. Aside from the relative abundance of magnesium and silicon, both elements also have the advantage of being non toxic and light weight, the latter an important aspect for applications in aircraft [50].

3.3.3 Piezoelectrics

Many materials are known to have piezoelectric properties, which all can be exploited to construct piezoelectric transducers for actuation or energy harvesting. The most well know and well studied material is PZT with chemical composition $PbZr_{0.52}Ti_{0.48}O_3$. This ceramic material has a very high electromechanical coupling ability but is also very brittle which limits the strain it can endure [284]. Solutions for this problem include application as thin film with chemically adjusted properties by addition of lanthanum as described by Liu et al. [195].

Other piezoelectric materials used for transducer construction are $PbTiO_2$, $BaTiO_3$, $PbZrO_3$ and $LiNbO_3$ [221]. The materials required for the synthesis of these compounds are common, with Ti and O in the top 10 of most abundant minerals in the Earth's crust. In the case of $LiNbO_3$, it has been shown that Li can be substituted with Na [153]. Possible bottlenecks are zirconium and niobium. The global Zr supply is a byproduct of titanium mining, with a yearly production of 52 kt of ZrO_2. Yearly Nb production tops at 63 kt as a result of newly discovered ore deposits despite being only the 33th most common element with an occurrence of 20 ppm [86], but large scale extraction and purification using HF leads to environmental concerns.

An organic alternative was discovered in 1969 in polyvinyldifluoride (PVDF), $(CH_2CF_2)_n$). The material has the advantage of high flexibility in contrast to the ceramic compounds mentioned above, but its negative d_{33} coefficient makes direct substitution in other piezoelectric applications difficult [284][58].

MEMS research is particularly important for piezoelectric transducers, resource consumption can be reduced by use of micro cantilever arrays and nanowires. Common materials include zinc based (ZnO and ZnS) and nitride based (InN and GaN) compounds. As with many types of energy harvesters, graphene also receives attention for the construction of piezoelectric transducers [181].

3.4 Resource Supply Restrictions

Aside from the scarcity of a resource, 5 other factors also affect the supply of a specific resource: its production concentration, its reserve distribution, its recycling rate, substitutability, and governance [116, 3].

3.4.1 Scarcity and Reserve Distribution

The scarcity of a resource is determined by the relative abundance of a certain element in the Earth's crust and the geographic concentration in ores. For the most abundant elements, such as Si, Ti, Fe, Mg etc. an extensive supply exist because massive quantities are present in the Earth's crust. However, the concentration of said elements must be high enough in a certain ore for it to be mined economically. Specific elements are generally extracted from minerals that contain them, which are in turn mined from a mineral ore deposit that concentrates large quantities of these minerals in a geographically constrained area (e.g. quarry or mine)[34]. Elements as Cu, Zn, Ti, Fe etc. are mined this way. Elements without concentrated ore deposits are considered rare, despite their relative abundance in the crust. Examples include Te, which occurs naturally as a spore element in sphalerite and galena (Zn and Pb ores), but occurs nowhere in sufficient concentrations to allow for Te specific extraction. Being a byproduct of Zn and Pb production, Te is moderately cheap despite it being rare. However, its production rate is tied to Zn and Pb production, and cannot be increased easily to satisfy demand. A predicted Te shortage is an important factor in the search for alternatives to CdTe thin film PV and Bi_2Te_3 TEGs. Around 137 t of Te was produced in 2007, while current CdTe PV technology requires 93 t/GW of the element. This indicates a clear bottleneck. A second element suffering this problem is Zr, a byproduct in the production of Ti and Sn. Unlike Te, Zr has many industrial applications, making its market price highly vulnerable to speculation, and its reliability for large scale energy harvesting applications low. Between 2003 and 2007, the price of Zr has doubled because of this supply limitation.

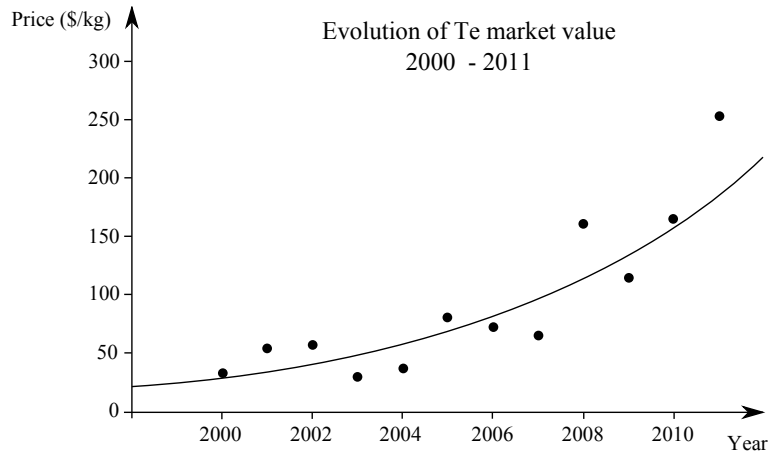

Figure 3.1: Evolution of Te market prices in the last decade, showing a near exponential increase of the element's market value. [255]

3.4.2 Production Concentration and Governance

Whereas some resources are widespread across the planet such as uranium ores, others are concentrated in a smaller geographic region. One notable example is Nb, which is produced for 75 % of the world's

supply by only 2 extraction sites in Brazil [86]. This severely limits the scalability of the extraction industry, making it challenging to satisfy demand of the PZ industry would $LiNbO_3$ be implemented as a large scale vibration energy harvester. In case of political instability in the region, worldwide Nb supply would possibly be compromised. For these reasons, resources with highly concentrated production are poor candidates for large scale energy harvesting applications.

3.4.3 Substitutability

The substitutability of a resource represents the ease of its replacement by another resource with comparable results. Examples include substitution of Ag conductor strips with Al strips for Si based PV, and the substitution of Li with Na in $LiNbO_3$ perovskites as transducers in piezoelectric and pyroelectric energy harvesters. A resource with higher substitutability is less likely to face supply difficulties because alternatives exist for it. Hence, the higher an element's substitutability in a certain application, the more suitable it is for large scale implementations.

3.5 Sustainable Energy Harvesting Strategies

It is possible to avoid the expected supply shortages of the resources discussed above and evolve to a sustainable energy harvesting industry by focusing on recycling, resource minimization and sustainable resource acquisition techniques.

3.5.1 Recycling

As mentioned briefly in chapter 1, the concept of truly sustainable renewable energy implies that not only the energy source is renewable, but that also its harvesters can be renewed. Practically, harvesters must be able to be collected and recycled at the end of their projected life time to recover their resources and optionally construct the next generation of harvesters from them with a negligible small or no influx of new natural resources. Currently, the life cycle of most harvesters is not yet entirely closed because of numerous reasons. Firstly, the necessary technology does not yet exist to recover $> 99\,\%$ of resources from any harvester. Plastics and composite materials are notoriously difficult to reuse or recycle. Secondly, current harvesters are optimized for performance instead of for sustainability, making recycling efforts more expensive and lowering recovery yield substantially. Finally, waste still most often does not find its way towards recycling installations but instead tends to be incinerated or disposed of in landfills. Only a fraction of domestic waste is currently recycled, including the first generation of solar cells that will reach its end of life in the next few years. Government's incompetence at organizing battery collection and recycling demonstrates that public sensibilization and large scale efforts must be made to improve waste collection and recycling rates. From all gaps in the cycle, this one is the most difficult to close.

As illustrated by operational landfill mining operations, resource reuse from decommissioned harvesters can provide economic as well as environmental benefits over mining more natural resources. Advancing technology including manufacturing techniques reduces the amount of resources required to construct every new generation of harvesters [45]. This can compensate for recycling inefficiencies, allowing harvesters to be constructed entirely from their predecessors. This is particularly true for silicon PV, where technological advances have reduced substrate thickness from 400 μm to 200 μm since 1990 [45]. Newer silicon PV cells with thinner substrates can thus be manufactured entirely from silicon recovered from their predecessors [207]. Solar grade silicon prices are expected to drop steadily due to increased

production and the large quantities of silicon recovered from decommissioned PV cells. This illustrates how recycling can provide a cheap supply of an otherwise expensive resource. Recycling also directly benefits the environment due to Si PV cell's 8 years return of energy investment. First Solar and others have already started pilot plants for recycling PV cells, and demonstrated the practical feasibility of recovering glass, Si, Cd and Te from PV cells [104, 204, 30].

3.5.2 Resources vs. Efficiency

In the highly competitive renewable energy market, harvester manufacturers most often focus on improving the power conversion efficiency of their products regardless of the required resources. This prevents large scale applications of these technologies because historic reserves and mining efforts can no longer satisfy demand, causing prices to spiral out of control. Current rises in Zr and Te market prices are examples of this effect, and may cause the premature deaths of energy harvesting technologies manufactured with them.

Chapter 2 already discussed the feasibility of constructing harvesters for any of the 3 most promising ambient energy sources (PV, TEG/PEG, PZ/TENG) without requiring significant quantities of resources with limited supply. Solar cells using graphene, Mg_2Si based thermoelectric harvesters and PVDF film piezoelectric materials allow application of these energy harvesters on a nearly unlimited scale. The harvesters can be truly sustainable, produced with low costs on a large scale, without adverse health or environmental effects. Rather than trying to increase the efficiency of harvesters, investments must be made in improving their sustainability. This seems not yet a priority for the industry in 2017, however, a-Si PV cells have already demonstrated that harvesters with a lower efficiency than the industry best can also be economically successful because of their lower manufacturing costs.

3.5.3 Raw Material Mining Issues

Because of the poor organization of recycling efforts to date, almost all constructed harvesters are manufactured using newly mined raw materials. While this is inevitable to provide an initial supply of a resource, mining is not sustainable since it depletes ore deposits. Assuming improvements in recycling rates combined with landfill mining in the nearby future, the need for new raw materials will be reduced. However, expansion of the installed electric capacity will still require a stable supply of new materials. Three strategies to supply these materials in a sustainable way are discussed below.

Firstly, it must be noted that resources currently produced as a byproduct of another resource, such as Te in Zn production from sphalerite, are recovered with suboptimal yields because they were/are considered of marginal value. Until the introduction of CdTe PV and Bi_2Te_3 TEGs, Te had few industrial uses, causing the build up of historic reserves at a rate proportional to that of Zn mining. Te production rates can be increased with minimal efforts by optimizing the processes to recover Te from Zn or Pb smelter slag material.

Following the example of Te and others, the same historic reserves of these elements have reduced prospections of ore deposits to a minimum. Consequently, undiscovered deposits of these elements are likely to exist. In the case of Te, Hein et al. suggested the global occurrence of Te rich ferromanganese crusts on the ocean floor, enough to supply the worldwide demand for these resources [131]. The exact amount of these resources is unknown however, nor whether or not it is possible to recover them at depths between 400 and 4000 m without repeating the mistakes made during current deep water oil

drilling [180].

Recovery of minerals dissolved in sea water gains popularity due to advancements in absorbent technology [216]. Simulations have shown that sea water has the potential to supply humanity with all the rare resources it needs. This has been demonstrated with the case study of uranium as fuel for nuclear fission reactors worldwide. The high cost of the absorbents makes minerals recovered from sea water more expensive than their traditionally mined equivalents. Recovery from sea water has the advantage of being able to be fully automated, unlike traditional mining operations, and to be sustainable due to the large quantity of sea water covering the planet. [314]

3.6 Conclusion

Benefits in system autonomy and ease of installation aside, deploying decentralized energy harvesting as an alternative to grid connected devices or rechargeable batteries does not necessarily prove to be a benefactor for the environment, as the combined environmental costs of consumed natural resources, CO_2 emitted during production and transport, and waste produced during production, can exceed the cost of grid powered installations or batteries under many conditions. Longevity of the intended application in combination with the newest manufacturing techniques is the key to reaching a break even.

When selecting energy harvesters for large scale deployment, considering resource management and related limitations are a key perspective for scalability. To avoid creating undesirable economic stimuli for unsustainable harvester manufacturing, it is crucial to examine the environmental costs for each energy harvesting technology with inclusion of production, transport, maintenance and end-of-life management. Closed loop resource management for sustainable and scalable solutions should be a requirement in the selection process of suitable energy harvesters.

Chapter 4

Complementary Balanced Energy Harvesting

The highly volatile nature of ambient energy sources, combined with the requirement to tune harvesters to these sources, prevents the construction of energy harvesting black boxes. Selecting the optimal harvester for an application and integrating it into the environment is a complex matter, and electronics developers often lack knowledge of the physical principles on which energy harvesters are based, further obstructing the integration of ambient energy harvesters in electronic appliances.

A solution to the complexity of harvester operation is reducing its numerous parameters to a manageable number, that could be regarded as degrees of freedom. In the presented model for complementary balanced energy harvesting, harvesters are parametrized as a product of 3 factors: the normalized maximum output power of the harvester, its size, and its efficiency of operation depending on available ambient energy and environmental conditions. The goal is to disconnect the fundamental principles of operation from the harvesters technological properties to make the application of the energy harvesters more transparent from an engineering perspective.

4.1 Modeling Harvester Parameters

Consider any harvester h that is able to capture ambient energy from its environment and convert it into electrical energy. The power output of h is P_h, equal to the voltage over h multiplied by the current that it is able to deliver at that voltage. Since the amount of ambient energy ϕ tends to vary, the harvesters power $P_h(t)$ is also a function of the time. The function $P_h(t)$ makes it considerably more difficult to engage in the dimensioning of a system powered by h since the boundaries of $P_h(t)$ (its minimum and maximum value) are unknown. To overcome this issue, it is necessary to break P_h apart in a set of parameters, and then model these parameters individually to build up a practically usable model of $P_h(t)$.

When comparing datasheets of harvesters of different types, it immediately becomes apparent that the number of parameters that influences P_h is very large: the size of the harvester, its type, the amount of energy in its range, the temperature and humidity it is operating in, the efficiency with which it is able to convert ambient energy into electricity, the position of the harvester with respect to the ambient energy source etc. Needless to say, practical calculations of ambient energy powered embedded systems will become increasingly complicated when hogging all these parameters into the equations, which does not

help the simplification of the problem forward.

The proposed approach, *Complementary Balanced Energy Harvesting*, attempts to model $P_h(t)$ as a function of 3 parameters, each grouping the influences of a specific nature together. A distinction is made between technology, environmental and application specific parameters.

4.1.1 Technological

A collection of technology specific parameters such as the type of materials used in the construction, the quality of the materials, the scientific principles on which the harvester is based, etc. are not subject to change by the application designer using the harvester in an application. These parameters are decided by the harvesters manufacturer or limited by physical barriers, and determine the maximum amount of power p_h a harvester h is able to capture in the most optimal conditions. The variable p_h is a property of the harvester that must be specified by the manufacturer, or can be tested by measuring the power output of a harvester under reference conditions.

Within the scope of the design process of a single application, p_h will be constant. However, as technology progresses and advances are made in the manufacturing processes of harvesters, p_h gradually increases. An important practical consequence of this is that it is useless to create a "final" list of p_h values per ambient energy type.

The value of p_h as parameter is only useful when it is normalized because within a group of harvesters for the same type of ambient energy, the size of the harvester can vary between manufacturers. This results in a harvester power p_h corresponding to the specific maximum power per unit of size, e.g. per m^3 for volume oriented harvesters or per m^2 for surface oriented harvesters.

4.1.2 Environmental

The environment specific parameters unite all external influences on the harvester, such as changing atmospheric conditions and fluctuations in the ambient energy ϕ. The parameters affecting ϕ are elaborated below, and determine the efficiency of the harvester η_h. As will be demonstrated, η_h strongly varies in time, and is responsible for the reliability issues often associated with ambient energy powered systems.

4.1.3 Application Specific

The designer of an ambient energy powered electronic system cannot influence technology specific parameters defined by p_h, nor influence environment specific parameters referred to with η_h. There is however one parameter the designer is able to modify, specifically for the application itself, being the size of the chosen harvester μ_h. It is important to note that a correlation between p_h and μ_h exists because the performance of a harvester design depends on its size. Since it is technologically easier to make power conversion mechanisms more efficient on a larger scale, the specific harvester power will be a function of its total size denoted by $p_h(\mu_h)$.

4.1.4 Harvester Power Output

Let ς be the size reference for harvesters, defined as $1\,m^2$ for surface oriented harvesters (PV cells, TENGs, ...) and $1\,m^3$ for volumetric harvesters (such as micro turbines). An overlap between them is

inevitable, as with TEGs which rely on a particular contact surface with a cold or heat source, but can be stacked in a threedimensional pile to increase output power. Since $[p_h] = \frac{\mathrm{W}}{\varsigma}$, $[\mu_h] = \varsigma$ and η_h is a dimensionless efficiency, these parameters express the power of the harvester as shown in equation (4.1) with $[P_h] = W$.

$$P_h(t) = \mu_h p_h(\mu_h)\eta_h(t) \tag{4.1}$$

In this equation, p_h denotes the normalized maximum harvester power per unit of size, μ_h denotes the size of the harvester, and hence $p_h\mu_h$ corresponds to the total maximum power a harvester of size μ_h can produce. Figure 4.1 shows an example of this mechanism for the case specific power output of a fixed size photovoltaic cell in natural lighting conditions. The maximum output is reached when the harvesters efficiency η_h equals 1. This expression can now be used to investigate the limitations of a single harvester powered system. Note that the notation of μ_h, using ς, is a simplification with the sole purpose of formulating a single equation to incorporate both surface oriented and volumetric harvesters.

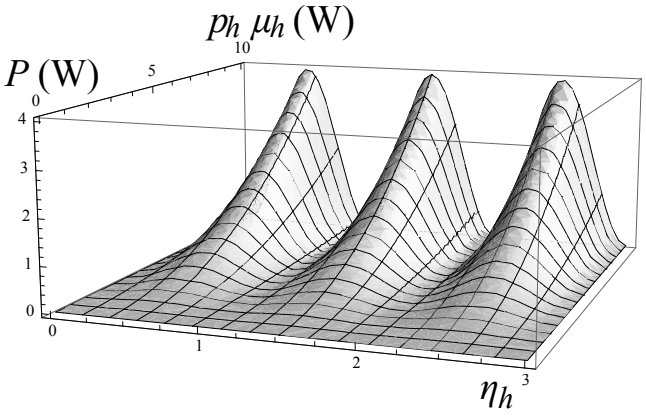

Figure 4.1: Yield of a photovoltaic cell as a function of the efficiency μ_h which varies over a 3 day time interval. The applicate denotes the output power P for any harvester size μ_h assuming the maximum power output p_h is constant ($\mu_h p_h \in \Re^+$).

This approach allows to compare the performance (i.e. conversion efficiency) of a harvester in specific environmental conditions independently of their size. For example, a 10 cm^2 monocrystalline PV cell can be compared to a 250 cm^2 amorphous cell, or to a 20 cm^2 PVDF TENG, and the harvester that makes optimal use of the available surface in that specific environment can be selected.

4.1.5 Example

Assume in a subway station, it is desired to count the number of passengers that enter through a certain entrance to obtain an overview of rush hours in that specific station. After benchmarking, it is determined that the most prominently available ambient energy source is kinetic energy from the moving passengers [212][276]. A comparison is made between 3 harvesters for kinetic energy, denoted as h_1, h_2 and h_3.

Harvester h_1 has a maximum rating of 200 mW and a nominal maximum output of 182.5 mW $\pm$ 10 % and a rated output voltage of 150 VAC for a volume of 0.821 dm^3 [17]. This allows the power p_1 of this harvester to be calculated, assuming linear extrapolation, to p_1 = 222.3 $\mathrm{W/m}^3$ $\pm$ 10 %. A second harvester, the AR01 from Arveni, h_2 has a rated energy output of 2.1 mJ per pulse for a force of 3.4 N in

a volume of 15 mm x 62 mm x 10 mm. With a pulse with of 250 ms this results in a yield of 8.4 mW for a volume of 9.3 cm^3 which is equivalent to a power $p_2 = 91 \cdot 10^2$ W/m^3 [202]. Finally, an experimental prototype with unspecified thickness has an energy yield of 0.4 μJ/mm^2. The authors cite a pulse duration of 0.1 s $\pm$ 0.05 s [177, Fig. 2], which, again assuming linear extrapolation, gives a power $p_3 = 4$ W/m^2 $\pm$ 2 W/m^2.

Depending on the requirements *in situ*, this helps to compare the size of the harvesters for a given output, since the excitation η_h will be nearly identical as long as all three are deployed in the same environment and are harvesting from the same energy source. When the power consumption of the embedded system is known, this readily allows computation of the required minimum harvester sizes. In a practical situation, factors such as harvester cost and life time will also affect the decision making process.

4.2 Multi Sourced Energy Harvesting

4.2.1 Advantages

From a physical perspective, a large variety of different energy types are available in any environment. In an urban outdoor environment for example, various types of energy are present. Energy can be harvested from sunlight, wind, vibrations (from traffic or noise), heat from vehicle exhaust pipes etc. In contrast, most ambient energy powered outdoor systems described in literature case studies are limited to a single energy source, being sunlight. Sunlight has notable advantages, such as its high energy potential, matured and widely available harvesters. However, it also has the obvious disadvantage of unavailability during night and cloudy moments, when covered by leaves in autumn or snow in winter. The classic solution applied to these problems is incorporating a battery to bridge the nights, and a solar cell with double size to charge the battery during the day while powering the connected system simultaneously. Often the total surface of the solar cells is over-dimensioned to compensate for uncertainties.

A second drawback of this approach is the uncertainty involved with modular energy harvesting solutions. When deploying a harvester with a guaranteed nominal power, the targeted environment is often unverified for the particular energy source. Harvester manufacturers provide power ratings, but seldom an exact relationship between the power output and the available ambient energy is published. This makes the integration of a harvester in a new design research intensive and a project on its own. Strong efforts are necessary to translate the harvesters specifications into a usable model. As a consequence, ambient energy powered systems based on a single harvester are currently only considered an option for applications which do not require high reliability.

The from an energetic point of view most viable solution for the problems above is the extraction of energy from multiple energy sources in the systems environment. When proper power conditioning circuitry is applied, the system can profit from the power generated by a multitude of harvesters simultaneously. For a system with a single energy harvester, a stable operation is only assured when the consumed power of the system P_h is smaller than or equal to the power generated by the harvester $P_h(t)$ as expressed in Equation 4.1 and the efficiency of the power conditioning circuitry η_p:

$$P_h \eta_p = p_h \mu_h \eta_h \eta_p \geq P_s \tag{4.2}$$

When η_h decreases due to a drop of the amount of ambient energy the harvester is able to extract from the environment, then the system will cease to function correctly, i.e. when $\eta_h < \frac{P_s}{p_h \mu_h \eta_p}$. In a practical

situation this will causes the system to lose state, e.g. any microcontroller present will reboot, any data in volatile memory will be lost, and interrupts or incoming data may be glitched.

4.2.2 Transition from Single to Multiple Harvesters

When n harvesters are attached to the power conditioning circuitry, this introduces n (largely) independent efficiencies η_h:

$$\eta_p \sum_{k=1}^{n} p_h^k \mu_h^k \eta_h^k \geq P_s \tag{4.3}$$

This implies the threshold at which the system fails is now dependent on the share of the dropped harvester in comparison with the other harvesters and their respective powers:

$$\eta_h^i < \frac{1}{p_h^i \mu_h^i} \left(\frac{P_s}{\eta_p} - \sum_{k \in [1,n] \setminus \{i\}} p_h^k \mu_h^k \eta_h^k \right) \tag{4.4}$$

Hence, by increasing the variety of connected harvesters n, the stability of the system can be increased assuming $p_h^1 \mu_h^1 \eta_h^1 \approx p_h^2 \mu_h^2 \eta_h^2 \approx ... \approx p_h^n \mu_h^n \eta_h^n$. To protect the system from the scenario that $x \leq n$ harvesters fail completely or experience a drop of η_h with more than 90 % (in the latter situation the power conditioning circuitry will be unable to convert the harvester output into usable energy), the size of all harvesters must be increased accordingly with a factor f:

$$f \sum_{k=1}^{n-x} p_h^k \mu_h^k \eta_h^k = \sum_{k=1}^{n} p_h^k \mu_h^k \eta_h^k \tag{4.5}$$

Since it was also previously assumed that all n harvesters have an output power of a comparable magnitude, denoted by $p_h^1 \mu_h^1 \eta_h^1 \approx p_h^2 \mu_h^2 \eta_h^2 \approx ... \approx p_h^n \mu_h^n \eta_h^n$, the expression above can be simplified to

$$f(n-x)(p_h \mu_h \eta_h) = (n-x)(p_h \mu_h \eta_h) + x(p_h \mu_h \eta_h) \tag{4.6}$$

with $x \leq n$. Dividing the previous equation by $p_h \mu_h \eta_h$ and rearranging the terms gives an expression for the correction factor f:

$$f = \frac{n}{n-x} \tag{4.7}$$

Substitution of (4.7) in (4.3) expresses how every harvester in a system with n harvesters must be over dimensioned to compensate for the failure of x harvesters.

$$\eta_p \frac{n}{n-x} \sum_{k=1}^{n} p_h^k \mu_h^k \eta_h^k \geq P_s \tag{4.8}$$

In a real situation however, the previously made assumption that all harvesters have a comparable output power, is a rough simplification. The calculated f is consequently an underestimation of the actual f required for system stability. Since

$$\lim_{n \to \infty} f = \lim_{n \to \infty} \frac{n}{n-x} = 1 \tag{4.9}$$

for a finite x, the reliability of the systems power supply can be increased by increasing the variety of harvesters n, assuming no strong correlation exists between energy sources. Note however that the method of decreasing the failure threshold in case of a single harvester blackout consists of increasing the power of every harvester by a factor $\frac{n}{n-1}$, which in practical situations corresponds to the increase of the harvesters size μ_h. And even in this situation the operation of the system is not guaranteed, since for a finite n, an $x+1$ failing harvester will still result in the failure of the system. Since n is very limited in reality, as suggested in the previous chapters, this leaves an open problem for which a solution is suggested below.

4.2.3 Regime

A second point of attention is the power consumption of the system, P_s. Previously P_s has been considered constant, which is often not true for a real world electronic system. For example, a sensor along a railway to detect the passing of trains will require more power during the day since more trains tend to pass, and thus more signals must be sent to the control room. On the other hand, during the day also more energy is available due to the presence of sunlight and the frequent passing of trains. Hence, when the size of the harvesters μ_h^i needs to be calculated, it is necessary to correlate the power requirements of the system with the ambient energy available to the system. Using the worst case power consumption of the system $P_{s,max}$ will lead to an overestimation of the required harvester sizes and hence a higher cost and overall size of the system. Equation (4.2) shows that in case of a proportional correlation of P_s and the efficiency of the harvester η_h, the size of the corresponding harvester may remain constant. This is unfortunately not true for most harvesters, which yield a high η_h for short periods of time followed by comparably long periods of η_h approximately equal to zero. Figure 4.2 demonstrates the energetic advantage of using multiple uncorrelated environmental energy harvesters.

The classic solution for both problems is the dimensioning of the harvester sizes based on average power consumption. Due to the Law of Conservation of Energy, this implies that a storage medium for energy must be introduced into the power conditioning circuitry, altering η_h. Since $dW = Pdt$, the introduction of the time element necessary to allow averaging, shifts the equation center from *power* to *work*, changing Equation (4.3) into an expression for the systems energy balance:

$$\eta_p \sum_{k=1}^{n} \int_T p_h^k \mu_h^k \eta_h^k dt \geq \int_T P_s dt \tag{4.10}$$

In Equation 4.10, T represents the period of the system. To be 100 % reliable it is required that $T = \infty$, the energy storage device has an infinite capacity. It should also provide energy without having it previously stored. Obviously this is practically unfeasible as well as unnecessary since many real world electronic devices know a far shorter period grafted on environmental factors. A day or week are common periods, since these correlate strongly to natural and human behavior.

Since T depends on environmental factors it cannot be calculated, however it can be fairly easily estimated based on benchmarking of the desired environment and cross referencing with common periods (day, week, etc.). Chapter 7 presents a complete hardware solution for the benchmarking of ambient environments using the Ambient Energy Monitor (AEM).

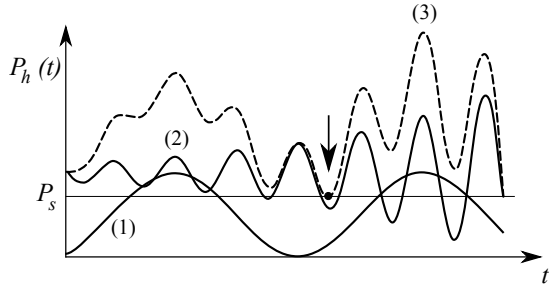

Figure 4.2: A system with 2 independent harvester outputs P_h^1 (1) and P_h^2 (2) profits from the harvested energy from both harvesters simultaneously (3), decreasing its dependency on a single harvester and increasing the systems reliability.

4.3 Periodic Systems

In the previous section, it was for simplicity assumed that the power consumption of the system P_s is highly irregular. By contrast, typical electronic applications do show a regular period, either triggered by interaction or by self timed operation (e.g. RTC clock). With the drawback of introducing uncertainty into the energy balance, Equation 4.10 can be further simplified by assuming the system knows two states: an active state in which a power P_{active} is consumed during a time d, and a standby state during which a standby power P_{sleep} is required. Examples of systems with these patterns include mobile phones (state during calls vs. stand by state), automated sensor modules (state during sampling of the sensor(s) and transmitting this data vs. sleep state), mp3 player (state during which music is played vs. turned off state) and many others. This does not necessarily mean that the left and right side of Equation 4.10 conduct the same period. For example, a solar powered traffic counter has a harvester period of a day (the day and night cycle), while the period of the system is the average time between passing vehicles. Hence it is necessary to make a distinction between both. Let T_1 be the least common multiple period of all harvesters and T_2 the period of the system. Equation 4.10 can then be rewritten to keep the balance between produced and consumed energy:

$$\eta_p \sum_{k=1}^{n} \int_{T_1 T_2} p_h^k \mu_h^k \eta_h^k dt \geq \int_{T_1 T_2} P_s dt \tag{4.11}$$

To avoid calculation of the least common multiple, the integration takes place over the product of the two periods $T_1 T_2$. Using the previously described elaborated regime model, the following simplification is derived:

$$\eta_p \sum_{k=1}^{n} \int_{T_1 T_2} p_h^k \mu_h^k \eta_h^k dt \geq \frac{T_1}{T_2} \left[P_{active} d + P_{sleep}(1-d) \right] \tag{4.12}$$

A notable advantage of this trade off becomes apparent considering that the discrete values P_{active} and P_{sleep} can be found by summing the power consumptions of all system components in only 2 situations. Simulation tools such as SPICE (Simulation Program with Integrated Circuit Emphasis) can be used to accurately determine the power consumption of analog circuitry, while the power consumption of digital components can be found in their respective datasheets. This makes solving the right side of the equation considerably easier, assuming T_1 and T_2 are known through benchmarking. For systems with more than 2 discrete power states, a more elaborate solution for power management is presented in chapter 6.

4.4 Energy Storage

Equation 4.2 shows that the power transfer to the storage element P_{store} is equal to

$$P_{store} = p_h \mu_h \eta_h \eta_p - P_s \tag{4.13}$$

When

- $P_{store} > 0$: the harvesters produce more energy than the system requires, and the power P_{store} is used to charge the storage medium.
- $P_{store} = 0$: all energy produced by the harvesters is consumed by the system.
- $P_{store} < 0$: the system requires more energy than the harvesters can provide, the storage medium now provides P_{store} and discharges.

The value of a storage medium is illustrated in figure 4.3, showing how the addition of a storage medium can reduce the required size of harvesters. The storage medium thus acts as a buffer between the harvesters and the system. In a perfectly balanced system, according to Equation 4.10, during one period T an equal quantity of energy must be produced and consumed:

$$\int_T P_{store} dt = 0 \tag{4.14}$$

This does not take any losses in power conversion and charge/discharge losses of the storage medium into account. Whereas modern lithium-ion batteries can be charged with efficiencies between 80 % and 90 % [309], it is important to note the high penalty for charging capacitors mainly due to series resistance (ESR). Although this suggests the exclusive use of rechargeable batteries to keep the size of the harvesters to a minimum, rechargeable batteries have the disadvantage of sustaining a limited number of charge-recharge cycles before their capacity drops steeply to the point of complete failure. Typically, lithium ion cells retain between 75 % and 95 % of their original capacity after 100 charge-discharge cycles, imposing severe limitations on the use of batteries in application with a long autonomous life time, as discussed in chapter 6. Charging and discharging capacitors at a reduced charge current may provide a solution. Chapter 6 elaborates on trade-offs between rechargeable batteries and capacitors.

Projecting these battery benchmarks on the theoretical recharge cycle frequencies from the previous paragraph, assuming common periods from as little as a day up to a week or more, this implies equally many charge-recharge cycles and thus a battery lifetime that can be as small as a few months.

4.5 Example

Despite a theoretical approach to the problem, the presented theory can be easily applied to real world situations. Consider for example a sensor module attached to the metallic parts of the support beams of a roller coaster construction to monitor structural integrity. Logically it can be expected that all major construction elements are equipped with such sensor modules. When wired solutions are chosen, this translates to a lengthy cable installation. Exposed to the weather elements, such a setup would be prone to random errors, making a wireless solution a better choice. When roller coaster parts are swapped for maintenance, no cables need to be disconnected, directly lowering maintenance costs. To achieve autonomy, the module must retrieve its power from the surrounding environment.

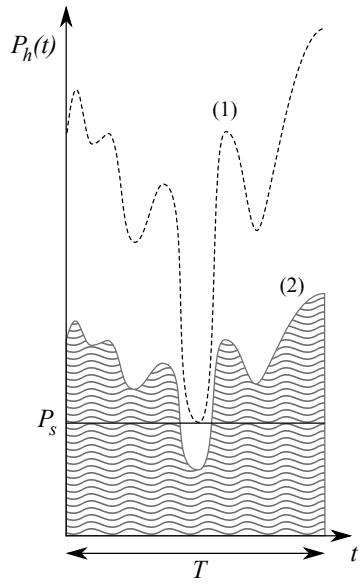

Figure 4.3: Effect of adding a storage medium to the system; both curves represent a harvester of the same type with same η_h but different μ_h since a system without storage (1) must generate at least as much power as required by the electronics (P_s) while for the version with storage (2) the average is sufficient.

A quick analysis of the system uncovers three essential elements: a wireless transmitter, a corrosion sensor, and a microcontroller unit to collect measurements and transmit them wirelessly. Located in an outdoor environment, a large variety of environmental energy sources are available. In this particular situation, two sources with high potential might be identified: sunlight and track vibrations.

Sunlight, which can be harvested with a photovoltaic cell, provides a steady but relatively low supply of power during the day. The efficiency η_h of the harvester will be at maximum around noon, and nearly zero between sunset and sunrise. After benchmarking the efficiency of the solar cell η_h^s, it may for example be found that $\eta_h^s(t) \approx e^{\sin(\frac{\pi}{720}t-1)}$ (with t in minutes). The track vibrations on the other hand, harvestable using piezoelectric harvesters, will provide a high power spike with a very short duration. This happens when a train passes on the track segment which is monitored by the module. The efficiency of the piezoelectric harvester η_h^v may be determined as $\eta_h^v(t) \approx \csc^2\left(\frac{t}{24\pi}\right)$. Note that the expressions for $\eta_h^s(t)$ and $\eta_h^v(t)$ are rough approximations of how the parameter η_h would evolve in time for a solar cell and a vibration harvester. For the sake of demonstration these behaviors were simplified to functions, whereas in actual applications η_h would be measured by the AEM, and thus be represented by a discrete sequence of samples instead.

Neither environmental energy source is suitable to power the entire system independently. When only a photovoltaic cell would be used, its constant but low power output would prohibit high power wireless transmissions, necessitating additional local storage in capacitors and complex power path management. With only a piezoelectric harvester, high power wireless transmissions will be possible, but the sensor would remain unpowered during the dead time between two passing trains. Of course this problem can be solved by over dimensioning either harvester and accumulating enough charge into batteries or capacitors to perform the desired action, but this would increase the cost and size of the module significantly.

The presented theory can easily provide a solution here.

By combining both harvesters, their respective output powers can be added up to power the system as demonstrated in Equation 4.11. Assume for the purpose of demonstration for the solar cell a period of 1 day ($60 \cdot 24$ min) and for the vibration harvester a train passing by every 4 minutes. The system acquires a measurement and transmits it every 30 minutes, requiring a power of 2 W for 1 s and remaining in a 20 mW sleep state the rest of the time. Finally, let the power path circuitry have a realistic efficiency $\eta_p = 0.8$. This is enough information to solve the problem. Following expressions for the right and left side of Equation (4.11) can be derived:

$$\int_{T_1 T_2} P_s dt = \frac{60 \cdot 24}{30} \left[2\frac{1}{1800} + 20 \cdot 10^{-3} \left(1 - \frac{1}{1800} \right) \right] \tag{4.15}$$

and

$$\eta_p \sum_{k=1}^{n} \int_{T_1 T_2} p_h^k \mu_h^k \eta_h^k dt = 0.8 \left[p_h^s \mu_h^s \int_0^{1440} e^{\sin(\frac{\pi t}{720} - 1)} dt + p_h^v \mu_h^v \int_0^{1440} \csc^2 \left(\frac{t}{24\pi} \right) dt \right] \tag{4.16}$$

The harvester parameters p_h^s and p_h^v are characteristic for the solar cell or piezoelectric harvester, respectively, and may be treated as constants within the scope of this application. This leaves the harvester sizes μ_h^s and μ_h^v the only variables in the equation. These variables can be found by choosing either μ_h^s or μ_h^v, and calculating out the other by solving the equation. Mathematically it does not matter which parameter is chosen, but in practical situations the quantization of available harvesters will play an important role. For example, piezoelectric harvesters and solar cells can be manufactured to fit any shape or surface area, but a standard size and shape will significantly reduce cost of the harvesters. In the example above, the best solution may be found by selecting one or more piezoelectric harvesters with a combined size μ_h^v that is as close as possible to satisfying the peak power requirements of the system. The photovoltaic cell surface μ_h^s required to satisfy the rest of the power requirements can then be calculated by substituting μ_h^v in the equation and solving it for μ_h^s. Further examples are provided in chapter 6.

4.6 Balancing Harvester Sizes

In a system powered by complementary balanced energy harvesting, the combined power output of n harvesters must be equal or greater than the power requirements of the system, as shown in Equation 4.3. Since the parameter p_h represents the maximum output of the harvester in ideal circumstances and η_h the varying environmental factors, the only factor that can influence the harvesters power output is its size, μ_h.

Considering $\mu_h \geq 0$; $1 \geq \eta_h \geq 0$ and $p_h > 0$, a minimum output P_s can be generated by choosing the sizes accordingly. Assume n harvesters with sizes μ_1, μ_2 ... μ_n and provided that corresponding efficiencies η_1 ... η_n have no common zero point, e.g. $\forall t \in [0, T] : \sum_{k=1}^{n} \eta_h^k(t) > 0$.

In this case, the sizes of the n harvesters can be chosen so that at any given time at least the minimally required power P_s is generated. A technologically optimal solution exists when the combined size of all the harvesters is minimal, which minimizes resource requirements, cost, weight and volume in the process. The optimal size of every harvester at any given time in a single period of system operation

depends on the power requirement of the system, on the relative power output of the harvester, and on the relative power outputs of the $n-1$ other harvesters feeding the system. For n harvesters, the problem can be expressed as

$$\sum_{k=1}^{n} p_h^k \mu_h^k \eta_h^k (t) \geq P_s \tag{4.17}$$

4.6.1 Mathematical Feasibility

The harvesters maximum outputs $p_1, p_2, ..., p_n$ and the systems power requirement P_s can be treated as constants within this scope. This leaves n variables, $\mu_1, \mu_2, ..., \mu_n$ subject to optimization. For every $t \in [0, T]$ the combined output of all harvesters $\sum_{k=1}^{n} P_h^k$ must equal or greater than P_s so that the total harvester size $\sum_{k=1}^{n} \mu_h^k$ is minimal. Since t is continuous in $[0, t]$ this presents a mathematical problem with $n+1$ variables and an infinite number of constraints, known as a *semi-infinite programming problem* [134]. Solutions for this type of problems can be found using advanced optimization theory, but the mathematical complexity of these methods make them too cumbersome for frequent use in energy harvesting applications. However, harvesters in real world applications have discrete rather than continuous sizes (e.g. installing a solar cell of arbitrary size would be prohibited by the cost to manufacture such a custom cell). This has proven advantageous to simplify the problem. The following sections present a solution that is less computation intensive, can easily be implemented in an algorithm, and is also easy to tweak to specific needs.

4.6.2 Dual Harvester Model

Because of the large number of parameters in a system with $n \in \mathbb{N}_0$ harvesters, the relationships between the parameters for a system with 1 ($n = 1$) and 2 ($n = 2$) harvesters must be discussed before presenting the generalized solution for n harvesters. In the context of complementary balanced energy harvesting, a large n is impractical due to the overhead of each harvester. For one ($n = 1$) or two ($n = 2$) harvesters, the problem can be sufficiently simplified to allow analytic solutions.

For the situation where $n = 1$, Equation 4.17 can be simplified to $p_h \mu_h \eta_h \geq P_s$ which essentially is the simplest form of the energy balance earlier discussed, and also the simplest topology of an ambient energy powered system despite not truly being a case of complementary harvesting. If in the period T the minimum efficiency of the harvester η_h, and thus the corresponding power output $p_h \eta_h$, occurs at a $t_m \in [0, T]$ with $\forall t \in [0, T] : \eta_h(t_m) \leq \eta_h(t)$ then the size of the harvester can be calculated as

$$\mu_h \geq \frac{P_s}{p_h \eta_h (t_m)} \tag{4.18}$$

on the condition that $\forall t \in [0, T] : \eta_h(t) > 0$ and thus $\eta_h(t_m) > 0$.

If $n = 2$, the sum of the generated power depends on 2 harvesters h_1 and h_2 with each corresponding p_h, μ_h and η_h parameters. Both η_{h_1} and η_{h_2} are functions of t but statistically independent. The energy balance can be written as

$$\mu_{h_1} p_{h_1} \eta_{h_1}(t) + \mu_{h_2} p_{h_2} \eta_{h_2}(t) \geq P_s \tag{4.19}$$

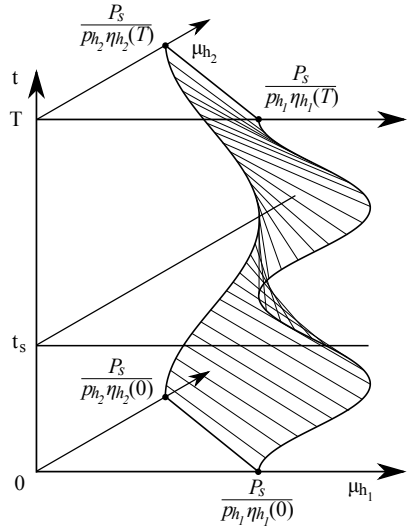

Figure 4.4: Three-dimensional representation of the optimization problem as function of time t and the two harvester sizes μ_{h_1} and μ_{h_2}. Any cross section at any given time t_s is a line with equation $\mu_{h_1} p_{h_1} \eta_{h_1}(t_s) + \mu_{h_2} p_{h_2} \eta_{h_2}(t_s) = P_s$.

again assuming that $\forall t \in [0, T] : \eta_{h_1}(t) + \eta_{h_2}(t) > 0$ as condition for a solution to be found. Since the problem to solve here is finding the sizes of the harvesters μ_{h_1} and μ_{h_2}, the equation has 3 variables μ_{h_1}, μ_{h_2} and t. A graphical representation can be seen in Figure 5.24. For every slice in the horizontal $\mu_{h_1}\mu_{h_2}$ plane, the variable t is held constant at $t = t_s$ and the equation of the intersection is

$$\mu_{h_1} p_{h_1} \eta_{h_1}(t_s) + \mu_{h_2} p_{h_2} \eta_{h_2}(t_s) \geq P_s \tag{4.20}$$

Transforming (4.20) in function of μ_{h_1} to retrieve the edge line equation gives

$$\mu_{h_1} = \frac{P_s}{p_{h_1}\eta_{h_1}(t_s)} - \frac{p_{h_2}\eta_{h_2}(t_s)}{p_{h_1}\eta_{h_1}(t_s)}\mu_{h_2} \tag{4.21}$$

which is the equation of a falling line with slope $-\frac{p_{h_2}\eta_{h_2}(t_s)}{p_{h_1}\eta_{h_1}(t_s)}$. The intersection point with the μ_{h_1} axis is at $\left[0, \frac{P_s}{p_{h_1}\eta_{h_1}(t_s)}\right]$ and with the μ_{h_2} axis at $\left[\frac{P_s}{p_{h_2}\eta_{h_2}(t_s)}, 0\right]$. This line graphically represents all combinations of μ_{h_1} and μ_{h_2} for which the harvesters h_1 and h_2 have a combined power output of P_s at any given time $t_s \in [0, T]$. An optimal solution is found when both μ_{h_1} and μ_{h_2} are minimal. This point can be found by constructing a minimum curve $m(\mu) = \mu_{h_1} + \mu_{h_2}$ and solving it for either variable. This results in 2 equations $i(\mu_{h_1})$ and $j(\mu_{h_2})$:

$$\begin{cases} i(\mu_{h_1}) = \mu_{h_1} + \dfrac{P_s}{p_{h_2}\eta_{h_2}(t_s)} - \dfrac{p_{h_1}\eta_{h_1}(t_s)}{p_{h_2}\eta_{h_2}(t_s)}\mu_{h_1} \\ j(\mu_{h_2}) = \mu_{h_2} + \dfrac{P_s}{p_{h_1}\eta_{h_1}(t_s)} - \dfrac{p_{h_2}\eta_{h_2}(t_s)}{p_{h_1}\eta_{h_1}(t_s)}\mu_{h_2} \end{cases} \tag{4.22}$$

The equations $i(\mu_{h_1})$ and $j(\mu_{h_2})$ are lines in the first quadrant where a minimum positive value must exist; these minimum values represent the most optimal size configuration of μ_{h_1} and μ_{h_2}. As example for $i(\mu_{h_1})$ this yields in

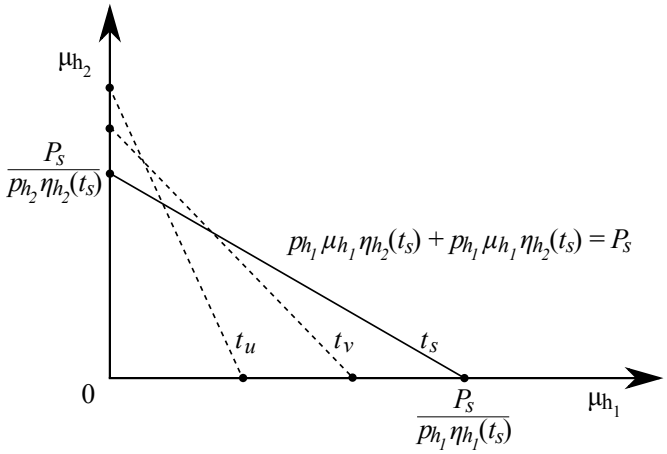

Figure 4.5: Optimization problem for 3 cross sections at $t_s, t_u, t_v \in [0, T]$, with equation of the line given for t_s.

$$\forall \mu_{h_1} < \frac{P_s}{p_{h_1}\eta_{h_1}} : i(\mu_0) \leq i(\mu_{h_1}) \Rightarrow \begin{cases} \mu_{h_1,m} = \mu_0 \\ \mu_{h_2,m} = i(\mu_0) \end{cases} \tag{4.23}$$

with $\mu_{h_1,m}$ and $\mu_{h_2,m}$ the minimum sizes of h_1 and h_2 respectively. This equation proves that at any moment t_s in the systems period, the harvester with the highest efficiency is to be maximized in size, while all harvester with lower efficiency will be nullified. This is expected because this harvester also dominates the energy balance, and yield information for the harvesters is the remainder of the period is omitted, thus missing an infinite number of additional critical constraints. An approximation that includes constraints from the entire period $[0, T]$ is presented hereafter. While useless in the continuous domain, the technique is essential for solving the optimization problem in the discrete domain, as will be demonstrated below.

4.6.3 Multiple Harvesters Mode

Knowing the relative performance of each harvester in a system powered by n harvesters is a requirement for determination of the optimal size combination. In order to obtain representative results, the influence of each harvesters size μ_{h_i} must be eliminated. For simplicity, the harvester size is held constant at unity ($\mu_{h_i} = 1$) throughout the following paragraph.

Regime Influence

Assuming the n harvesters powering the system are statistically independent, the optimal size of a specific harvester h_i will be determined by 3 factors:

- the power ratio of the harvester with respect to the other $n - 1$ harvesters;
- the magnitude of the average power output;
- the stability of the power output over the entire period T.

The first and most significant factor is the ratio of a harvesters power output in comparison to the combined output of the other harvester at any given time. When the combined output power of all the other

harvesters is low in comparison to a single harvester, the relative importance of its contribution to the power balance of the system is high. Conversely, when a harvesters output is low in comparison to the other harvester, then its significance is lowered proportionally.

For a harvester h_i the power ratio κ_1 can be expressed as

$$\kappa_1 = \frac{1}{T}\int_0^T \frac{p_h^i \eta_h^i(t)}{\sum_{k\in[1,n]\setminus\{i\}} p_h^k \eta_h^k(t)} dt \tag{4.24}$$

If h_i has a constant output power of 0 then $\kappa_1 = 0$. Because $0 \leq \kappa_1 < \infty$, the factor κ_1 is a useful first indication for the significance of a harvester in the power balance of the system. A second factor κ_2 is the magnitude of the average power output of the harvester. Harvesters with high average power output have a higher contribution to the power balance of the system. Considering $\frac{1}{T}\int_0^T p_h^i \eta_h^i(t)dt$ the average power output of a harvester h_i, κ_2 can be expressed as

$$\kappa_2 = \int_0^T p_h^i \eta_h^i(t)dt \left((n-1) \sum_{k\in[1,n]\setminus\{i\}} \int_0^T p_h^k \eta_h^k(t)dt \right)^{-1} \tag{4.25}$$

The third factor κ_3 represents the degree of fluctuations of power output within a period of the system. It makes use of a continuous time standard deviation to quantize how much the harvesters power output changes, as expressed in Equation 4.26:

$$\kappa_3 = \left[1 + \frac{1}{T}\int_0^T \left(p_h^i \eta_h^i(t) - \frac{1}{T}\int_0^T p_h^i \eta_h^i(t)dt \right)^2 dt \right]^{-2} \tag{4.26}$$

In Equation 4.26 the standard deviation is easily recognizable, with $\frac{1}{T}\int_0^T p_{h_i}\eta_{h_i}(t)dt$ representing the average power output of the harvester from which to calculate the deviation. The inner square ensures that only positive deviations are summed, so that positive and negative deviations do not cancel each other out. The total deviation is increased by 1 so that κ_3 approaches unity when the deviation with respect to the average power output approaches 0, e.g. when the h_i has a constant power output. Since the standard deviation is a positive value, κ_3 will also be a positive value with $0 < \kappa_3 \leq 1$.

Harvester Coefficient

The three factors κ_1, κ_2 and κ_3 can now be combined to attribute a value to a harvester h_i as part of a system powered by n harvesters. This defines the *harvester coefficient* θ_i for any harvester h_i as

$$\theta_i \equiv \prod_{k=1}^{3} \kappa_k[h_i] \tag{4.27}$$

which corresponds to the product of the three factors κ_1, κ_2 and κ_3 introduced above. In this product, κ_1 and κ_2 will act as positive modifiers, e.g. higher values represent a better harvester performance. The factor κ_3 is a negative modifier causing a decrease in θ if the deviation of the harvester output with respect to its average increases. Because κ_1, κ_2 and κ_3 are all positive values, also θ will be a positive value which, however, does not directly reflect the size of the corresponding harvester in the system. The

examples below illustrate the effectiveness and interpretation of θ.

Example 1. Consider 2 harvesters h_1 and h_2 with respective efficiencies η_{h_1} and η_{h_2}. To demonstrate the effect of θ, the output power of both harvesters will be held at unity ($p_{h_1} = p_{h_2} = 1$). Assume η_{h_1} a square wave with period 1 and duty cycle of 50 %:

$$\eta_{h_1}(t) = \begin{cases} 0.9 & \text{if } t < \frac{k}{2} \\ 0.1 & \text{if } t > \frac{k}{2} \end{cases} \quad \forall k \in \mathbb{N} \tag{4.28}$$

and

$$\eta_{h_2}(t) = \sin\left(t + \frac{\pi}{5}\right) \tag{4.29}$$

In this example, the period of the system will arbitrarily be assumed 2. κ_1 can now be calculated for h_1 and h_2:

$$\kappa_1[h_1] = \frac{1}{2}\int_0^2 \frac{\eta_{h_1}(t)}{\eta_{h_2}(t)}dt = 0.602 \tag{4.30}$$

$$\kappa_1[h_2] = \frac{1}{2}\int_0^2 \frac{\eta_{h_2}(t)}{\eta_{h_1}(t)}dt = 4.612 \tag{4.31}$$

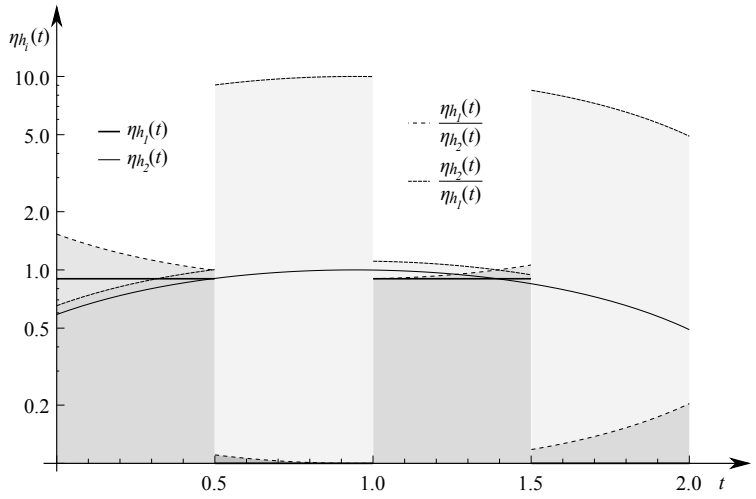

Figure 4.6: Graphical representation of the optimization problem for a system powered by 2 harvesters with output efficiencies following a square wave and a sine arc. As shown, $0 \leq \eta_{h_1}, \eta_{h_2} \leq 1$ and $\mu_{h_1}, \mu_{h_2} = 1$. Continuous curves represent η_{h_1} and η_{h_2} while dotted curves correspond to the power ratios. Note the high values on a log scale for $\frac{\eta_{h_2}}{\eta_{h_1}}$ as a result of division by a very small value during the low period halves of the square wave.

The corresponding surfaces of the ratios between η_{h_1} and η_{h_2} are shown in Figure 4.6. Comparing the results for κ_1 shows a significantly higher value for $\kappa_1[h_2] = 4.61$ than for $\kappa_1[h_1] = 0.602$. In this example, this is attributed to the averagely higher efficiency of h_2 and the very low efficiency of h_1 during the low period halves of the square wave. Proceeding to the calculation of κ_2 for h_1 and h_2 results in

$$\kappa_2[h_1] = \frac{\int_0^2 \eta_{h_1}(t)dt}{\int_0^2 \eta_{h_2}(t)dt} = 0.595 \tag{4.32}$$

and

$$\kappa_2[h_2] = \frac{\int_0^2 \eta_{h_2}(t)dt}{\int_0^2 \eta_{h_1}(t)dt} = 1.650 \tag{4.33}$$

Again the value of $\kappa_2[h_2]$ is higher because the average power output of h_2 is higher than that of h_1. Finally, calculating κ_3 for h_1 and h_2 results in

$$\kappa_3[h_1] = \left[1 + \frac{1}{2}\int_0^2 \left(\eta_{h_1}(t) - \frac{1}{2}\int_0^2 \eta_{h_1} dt\right)^2 dt\right]^{-2} = 0.641 \tag{4.34}$$

$$\kappa_3[h_2] = \left[1 + \frac{1}{2}\int_0^2 \left(\eta_{h_2}(t) - \frac{1}{2}\int_0^2 \eta_{h_2} dt\right)^2 dt\right]^{-2} = 0.942 \tag{4.35}$$

The value of $\kappa_3[h_2]$ is lower than $\kappa_3[h_1]$ in this case because the output of h_2 is more constant than the output of h_1. Combining the values obtained for κ_1, κ_2 and κ_3 for both h_1 and h_2 results in

$$\theta_1 = \prod_{k=1}^{3} \kappa_k[h_1] = 0.23 \tag{4.36}$$

$$\theta_2 = \prod_{k=1}^{3} \kappa_k[h_2] = 7.3 \tag{4.37}$$

The values for the harvester coefficients θ_1 and θ_2 differ by more than a factor 30. This indicates that harvester h_2 is the better choice and the preferred candidate for size optimization. Since for either harvester $0 < \theta_i$, both are able to support the system autonomously, and since neither harvester has zero points in its power output, neither is critical.

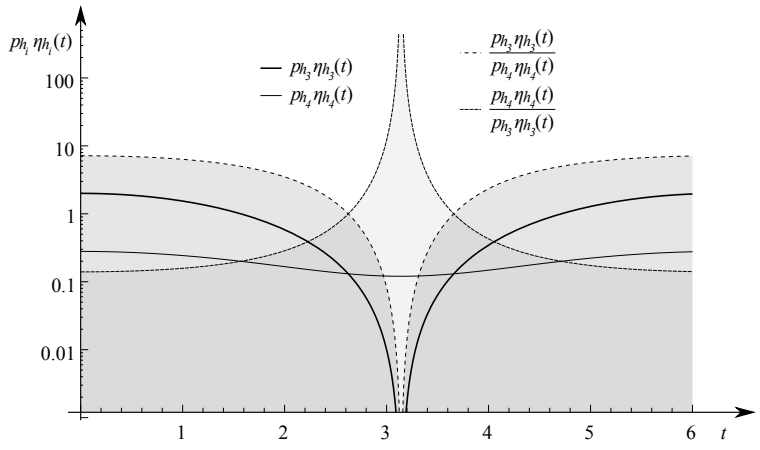

Figure 4.7: Graphical optimization problem for 2 harvesters, one having a zero point within the interval. Note the logarithmic scale.

Example 2. As a counter example, consider 2 harvesters h_3 and h_4 with power outputs $p_{h_3}\eta_{h_3} = \cos(t) + 1$ and $p_{h_4}\eta_{h_4} = \frac{0.1}{2\pi}\cos(t)$, as shown in Figure 4.7. In this example, $p_{h_3} \geq 1$ so that $0 \leq$

$p_{h_3}\eta_{h_3} < \infty$. Furthermore, $p_{h_3}\eta_{h_3}$ has a zero point. Calculating the factors κ_1, κ_2 and κ_3 for h_3 and h_4 in a periodic interval $[0, 6]$ results in the values below.

	κ_1	κ_2	κ_3	θ
h_3	4.186	4.857	0.311	6.330
h_4	440.8	0.206	0.991	89.95

Due to the complexity of the integral calculations, shown values are approximated using Wolfram Mathematica. It is clear that the harvester coefficient θ_4 of harvester h_4 dominates the balance, indicating a strong advantage for h_4. The presence of a zero point in $p_{h_3}\eta_{h_3}$ which causes κ_1 to asymptotically reach infinity at this point, and the large spread in harvester power, both contribute to this result. It is important to note here that, due to the continuous time integral for the calculation of the ratio surfaces, κ_1 does not result in infinity because of the asymptote to the zero point. A high value for θ may be result of a zero point for other harvesters, but may also be a result of a low average output of other harvesters.

Example 3. Whereas the previous 2 examples demonstrated the ease of use of the presented methodology for a system with 2 harvesters, the example below illustrates feasibility with 3 harvesters. Systems with $n > 3$ follow an identical approach. Assume 3 harvesters h_5, h_6 and h_7 with respective power outputs $p_{h_5}\eta_{h_5} = \dfrac{t^2}{5} + 0.1$, $p_{h_6}\eta_{h_6} = \pi\dfrac{\sin\left(\pi - t^2\right)}{\pi - t^2} + 1$ and $p_{h_7}\eta_{h_7} = \cos(t) + 1.5$, as shown in Figure 4.8. The systems period will be assumed 5, making the interval of interest $[0, 5]$. Note that the attenuated impulse excitation of h_6 corresponds to a typical response of a piezoelectric harvester, while h_7 could represent a periodic system such as a solar cell. Calculating the harvester coefficient for the three harvesters results in the following values for θ:

	κ_1	κ_2	κ_3	θ
h_5	0.459	0.588	0.084	0.023
h_6	0.700	0.551	0.351	0.135
h_7	0.545	0.378	0.923	0.190

The values for θ_5, θ_6 and θ_7 are relatively low because there are more than 2 harvesters in the system (reducing κ_1 and κ_2 and because no two harvesters have a common low point (which would increase the third harvesters κ_1). The low value of θ_5 in comparison with θ_6 and θ_7 indicates that in an energy optimized system, this harvester will not contribute significantly to the balance unless its size must be increased drastically. Since the values for θ_6 and θ_7 are close, in this example, a near fifty/fifty combination may be the best choice since neither harvester has zero points. Further optimization is possible by repeating the calculation for a system powered by h_6 and h_7, without h_5. Performance differences of this magnitude will likely not translate to a better optimized system in a real world situation due to the discrete sizes of common harvesters.

4.6.4 Regime Benchmarking

While an analytical approach as presented in the previous paragraph is useful for harvesters with a very complex power output regime, in practical situations this may often not be necessary. Many real world harvesters show rather slow variations in their power output. Commonly used examples exhibiting this behavior are solar cells, TEGs, and so on. For a system powered by these harvesters, it is not necessary to construct continuous functions of their power output and calculate their harvester coefficients. Instead, it is more efficient to use acquired samples from benchmarking the environment of future deployment directly. Chapter 7 presents strategies to acquire this data.

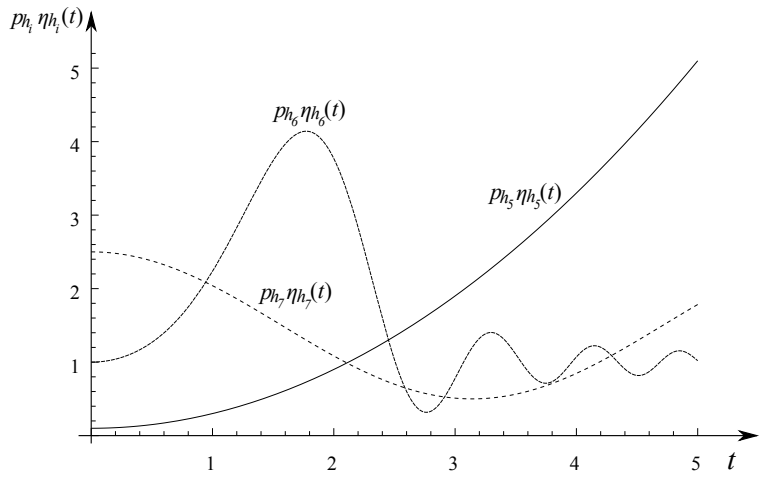

Figure 4.8: Optimization problem for 3 harvesters: h_5 has an exponential output, h_6 an attenuated impulse and h_7 a sinusoidal output.

θ in Discrete Time Domain

The equations (4.24), (4.25) and (4.26) can be ported to the discrete time domain by discarding the intervals between samples from the balances. Where in continuous time domain integrals have the function of calculating the surface under the curves, in discrete time domain the same can be done by summing the known samples. Because this eliminates integrals from the equations all together, the computation of θ becomes mathematically much simpler. This allows the calculation to be done on an embedded sensor node for benchmarking of the environment, for example.

If the discrete time domain measurement of the power output of a harvester h_i results in j samples for $p_{h_i}\eta_{h_i}$, then the equations for κ_1, κ_2 and κ_3 can be expressed as follows:

$$\kappa_1 = \frac{1}{j}\sum_{m=1}^{j}\frac{\left[p_h^i\eta_h^i\right]_m}{\sum_{k\in[1,n]\setminus\{i\}}\left[p_h^k\eta_h^k\right]_m} \tag{4.38}$$

An equal number of samples needs to be taken for every harvester for the calculation of κ_1.

$$\kappa_2 = \left[(n-1)\sum_{k\in[1,n]\setminus\{i\}}\sum_{m=1}^{j}\left[p_h^k\eta_h^k\right]_m\right]^{-1}\sum_{m=1}^{j}\left[p_h^i\eta_h^i\right]_m \tag{4.39}$$

$$\kappa_3 = \left[1+\frac{1}{j}\sum_{m=1}^{j}\left(\left[p_h^i\eta_h^i\right]_m - \frac{1}{j}\sum_{l=1}^{j}\left[p_h^i\eta_h^i\right]_l\right)^2\right]^{-2} \tag{4.40}$$

Implementation of the equations above as algorithms in software is very straight forward since every κ can be calculated by means of basic arithmetic functions, and the sum functions can directly be translated into software loops. The memory footprint of an embedded implementation can remain small because samples are manipulated sequentially, and no backtracking or recursion is necessary. In this regard it should be noted that in the discrete time domain, the problem of harvester size optimization

is no longer a semi-infinite computation problem because the number of constraints is now finite and equal to the number of samples. However, as obtaining a solution through this method would require a vast set of equations to be solved, the method presented above is more friendly to implementation on embedded systems.

4.7 Harvester Size

As mentioned before, it is realistically unfeasible to integrate harvesters with arbitrary size into the system because of economic and practical limitations.

4.7.1 Scale Limitations

Although some harvesters scale very well to smaller or larger sizes, such as solar cells, other harvesters will be subjected to minimal physical sizes (such as mechanical turbines). Others only scale with natural multiples of a basic harvester block, such as TEGs. This should be kept in mind when solving the optimization problem to avoid excessive deviations between calculated and practical total harvester sizes.

4.7.2 Manufacturing Limitations

While in large volume applications it may be economically feasible to manufacture harvesters with custom sizes to precisely fit the needs of a specific electronic system, this may only rarely be the best option. Aside from the higher cost of custom harvester sizes, it is wise to over-scale the harvesters to compensate for reduced harvester output due to wear over prolonged periods of time. In this regard it is deemed more practical to select an off-the-shelf harvester with the next higher harvester output compared to the values obtained through mathematical calculation of the minimally required size.

4.7.3 Combining Multiple Harvesters

When designing a system, care must be taken so that all harvesters are placed in an optimal configuration. For example, a system deployed in a cubic enclosure and powered with solar energy should not be coated on all 6 sides with $\frac{1}{6}$ of the calculated solar cell surface, since for obvious reasons only 1 side will receive an optimal energy flux at any given time. Figure 4.10 shows an example.

There are, however, many combinations that may turn out to be profitable from an energetic and economic perspective. A magnetic vibration harvester may for example be enclosed in a box together with the systems electronics, while the outside of the box is coated with piezoelectric or photovoltaic cells. Even photovoltaic and piezoelectric cells can be stacked since only the photovoltaic cells need to be exposed to light, as shown in Figure 4.10. Listing all possible combinations would be pointless because of the application specific nature of this problem. Consequentially it should be understood that the specific requirements involved with the design of an ambient energy powered system extend far beyond limited mathematical calculations.

4.7.4 Example

To illustrate the practical usefulness of the presented theory, consider and embedded systems as example. This system consists of a state of the art ultra low power microcontroller, an ESP32 from Espressif, and an SD Card to allow data storage. It is also equipped with a humidity sensor to allow monitoring of indoor

humidity through the year. The sensor node is mounted to a heater, facing a window on the other side of the room. The system must be powered by environmental energy using integrated energy harvesters.

As discussed above, the unknowns in this problem are the power consumption of the system P_s, the types of harvester(s) used, their nominal power p_n, sizes μ_n and efficiency η_n. Using Equation 4.12, the problem can be split in 2 halves that can be resolved separately: power consumption and power generation.

Power consumption

To sample, process and store the actual humidity value once per day, the system will remain active for only 250 ms per day, spending the remainder of the time dormant. From application nodes and data sheets, the active current consumption of the sensor is 5 mA, of the ESP32 at 2 MHz ca. 500 μA, and the flash SD Card 60 mA. In dormant mode (sleep with RTC enabled) the sensor and flash card are powered off and the ESP32 consumes 1 μA. At a system voltage of 3.0 V, the energy required over the entire period of one day is 308.3 mJ and assumed independent of the time of the year.

Power generation

Through benchmarking it is determined that the two most prominently available environmental energy sources are heat (from the heater the system is attached to) and ambient light (from natural and artificial light sources). The 3 parameters p, μ and η must be determined for these 2 harvesters. Firstly, the parameter η can be found either through the same benchmarking process or by consulting literature. Artificial light intensity is, with a small error, nearly constant while natural light intensity changes with the time of the year. Literature [187] shows an average daylight function of $H(t) = 8.5 \sin(0.017t - 1.35) + 12$. After scaling to match efficiency, an approximate efficiency for photovoltaic harvester h_1 is obtained:

$$\eta_1(t) = \frac{1}{19} \cdot 8.5 \sin(0.017t - 1.35) + 12 \tag{4.41}$$

The efficiency of TEG h_2 is less complex because its efficiency is a function of the heaters activity and the room temperature. In summer it is completely turned off but acts as a heat sink, allowing reverse heat flux to flow. In winter, on the other hand, the temperature difference is high and will only see a slight drop when the room heats up. Thus, the efficiency can be expressed as a square wave signal, and approximated using a Fourier series to allow easier numeric computation. For simplicity, a 5th order approximation is used:

$$\eta_2(t) = \frac{5}{2}\left(1 + \frac{4}{\pi}\sum_{k=1}^{5}\frac{\sin\left[0.003 \cdot 2\pi(2k-1)(t-300)\right]}{2k-1}\right) + 0.1 \tag{4.42}$$

This information can now be used to calculate the values of κ_1, κ_2 and κ_3 for both harvesters, as shown below:

	κ_1	κ_2	κ_3	θ
h_1	2.602	1.005	0.153	0.400
h_2	4.191	0.995	0.099	0.412

Due to the complexity of the integrals, calculations were numerically approximated using Wolfram Mathematica. With only 3 % difference in value between θ_1 and θ_2, it can be concluded that, in this specific configuration, both harvesters have a comparable efficiency and neither has a clear advantage over the

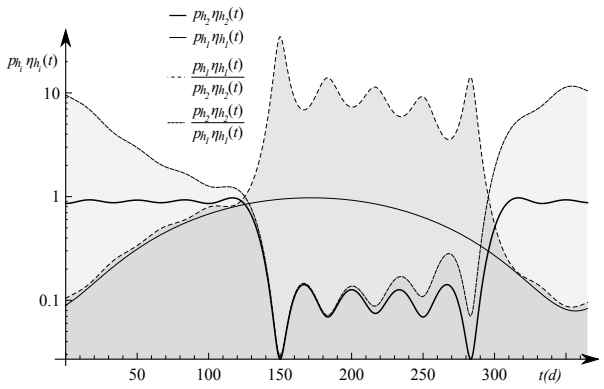

Figure 4.9: Approximated evolution of harvester efficiency over a one year period.

other. Both values are also fairly low, indicating that both harvesters are able to power the system independently of the other if necessary. This can also be seen in graph 4.9, where solid lines represent the efficiencies of h_1 and h_2 as $\eta_1(t)$ and $\eta_2(t)$ for a constant p.

The given harvesters can be operated complementary, and balance each others minimal and maximal output values. This can also be found when calculating the difference of both functions, since for perfect complementation, $\frac{d}{dt}\left(\eta_1(t) + \eta_2(t)\right) = 0$.

With the environment and the magnitude of its ambient energy sources known, the harvesters can now be dimensioned. To harvest light, a photovoltaic cel from *First Solar* [322] is selected with a nominal power of 60 W$\pm$8.3 % for a cell surface of 60 x 120 cm. This corresponds to a power p_1= 83 W/m^2. As thermoelectric harvester, an eTEG HV37 [143] was selected with an extrapolated power of 222 mW at its maximum temperature difference of 200 K. With a volume of 4.3 mm^3, the harvester power is $p_2 = 51.7$ kW/m^3.

Based on these figures and the values of θ_1 and θ_2 calculated for each harvester previously, the most optimal configuration for this particular case is a (near) equal power distribution among the harvesters. To generate 308.3 mJ over its period of one day, a combined average harvester power of 5.9 μW is required for power conversion efficiency of 60 %. This can be optimally generated with 3.5 cm^2 solar cells (keeping in mind day-night cycle and reduced indoor efficiency) and a single eTEG HV37 (considering $\Delta T \approx 10$ K).

4.8 Limitations

To maximize the efficiency of energy harvesters, design considerations of these harvesters form the guidelines for the entire system, and it is essential that the system is designed from the ground up with energy harvesting in mind.

Energetically the most relevant property of harvesters is their normalized yield, e.g. the generated maximum power per unit of volume (m^3) or surface (m^2) p_h, as well as the minimum volume/surface needed per harvester due to overhead. These concepts can be applied to a generic system by assuming it has a volume V bound by a closed surface S. This volume V is filled with a volume oriented harvester,

and by definition $V = \mu_{hv}$. The surface is coated with a surface oriented harvester, by definition of size $S = \mu_{hs}$. The power output of such a system can be mathematically written as

$$P = \iiint_V p_{hv}\eta_{hv}dV + \oiint_S p_{hs}\eta_{hs}dS \tag{4.43}$$

where the first term in this polynomial accounts for the power generated by a volume oriented harvester filling V completely, and the second term representing the power generated by the surface oriented harvester covering the external closed surface of V, corresponding to S. To obtain a real model, several losses must be recorded as well:

- the overhead V_{ho} or S_{ho} per harvester that represent rectifiers, DC/DC converters and other power conditioning circuitry;
- the volume of the electronic part of the system V_s (including battery or storage capacitor where necessary.

The energy balance of the system can then be expressed as

$$P_s \leq \iiint_{V_h} p_{hv}\eta_{hv}dV + \oiint_{S_h} p_{hs}\eta_{hs}dS \tag{4.44}$$

with $V = V_{ho} + V_s + V_h$ and $S = S_{ho} + S_h$. Interestingly, equation 4.44 knows a single solution in any given environment because in said environment only one most efficient volume oriented harvester and one most efficient surface oriented harvester exists, while the sizes of the respective overheads are known. The easiest way to find this solution is through iteration, e.g. filling in all the ambient energy sources into the equation using their respective p_h and η_h properties, and searching the shape for V that has the smallest size, which often also implies the lowest manufacturing cost. Note that for many practical situations the shape will be constrained prior to the design process, which greatly simplifies the number of possibilities. Since most applications prefer cuboid shapes, the calculation of the integrals is often also reduced to basic multiplications since the closed surface integral for a cuboid equals $S = 2xy + 2xz + 2yz$ and its volume $V = xyz$.

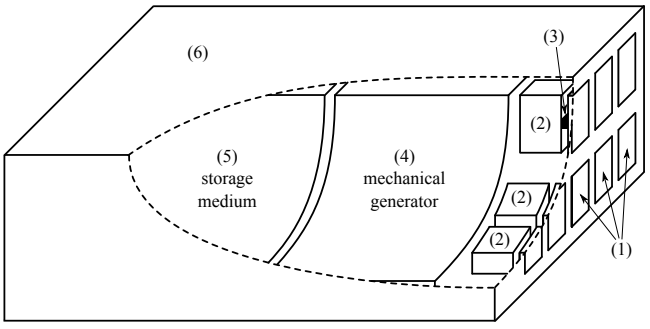

Figure 4.10: Cross section of a generic ambient energy powered embedded system using a combination of different energy types and harvesters. The outside surface of the system is covered with photovoltaic cells (1) which are mechanically joined (3) to piezoelectric film to generate energy from impulses on the systems surface. The inside volume is not critical, and can be filled with RF or magneto-mechanical harvesters (4). Room for a capacitor or battery for energy storage is also provided (5).

Equipping a system with multiple harvesters (with low correlation between their respective η_h) is profitable because it increases the systems reliability and decreases the required battery or capacitor capacity. However, with the introduction of overheads per harvester, this figure does not add up linearly, and a trade-off must be made between adding harvesters together with their respective V_{ho} or S_{ho} in favor of a reduction in battery or capacitor size. Although also in this respect a straight forward solution exists, in practical situations economic considerations will often get priority since harvesters are more expensive than storage capacity.

For a system with multiple harvesters, the constraining equations are

$$V = \sum_{k=1}^{p} (V_{hk} + V_{hok}) + V_s \tag{4.45}$$

$$S = \sum_{k=1}^{q} (S_{hk} + S_{hok}) \tag{4.46}$$

with $p + q = n$.

4.9 Efficiency Parametrization

The efficiency η_h of a harvester is one of three parameters determining the total power output of a harvester – the other two being the harvesters normalized maximum output p_h and its size μ_h. To answer the question which parameters influence η_h, the harvester must be placed in the environment from which it is supposed to extract ambient energy. Parametric dependencies can be reduced to 3 categories:

1. the amount of ambient energy the harvester is able to capture;
2. the fraction of the harvester exposed to the energy source;
3. variations of environmental parameters outside the regular harvester scope.

During normal operation the maximum power p_h and the harvester size μ_h will remain constant, making η_h the variable that determines the total amount of energy the harvester produces since $P_h = p_h \mu_h \eta_h$. To ensure stable operation of the system, it is necessary to know the function $\eta_h(t)$ as precisely as possible, which is immediately the most sensitive and complex problem in the design process of an ambient energy powered system. The AEM presented in chapter 7 is specifically designed to solve this problem.

4.9.1 Ambient Energy Quantity

The amount of ambient energy in range of the harvester ϕ is the primary factor that determines η_h, for a harvester with a constant size μ_h. The value of ϕ is independent of the harvesters size, and solely a function of external factors, making ϕ the main reason why η_h cannot be calculated by conventional means but must be experimentally determined.

In most cases ϕ follows patterns that can be approximated, but in some applications ϕ may prove to be relatively constant, for example the temperature gradient between a steam pipe in a power plant and the surrounding air. When captured with an appropriate harvester such as a TEG or PEG, the resulting power output P_h will be stable since p_h and μ_h are also constant. Conditions like these are exceptional

however, and in any other situation the careful determination of $\eta_h(t)$ proves to be the most difficult aspect of the design of an ambient energy powered system.

4.9.2 Harvester Exposure

In contradiction with a common perception involving the dimensioning of harvesters, the exposure of the harvester to the ambient energy source is subject to change. In this situation both μ_h and ϕ remain constant, but external factors reduce the amount of energy the harvester is able to capture. Examples include a micro turbine getting stuck because of dust/debris in the fluid stream, or the angle of a light source changing over α degrees with respect to a photovoltaic cell and reducing its yield with a factor $\sin\left(\frac{\pi}{2} - \alpha\right)$.

A second case exists when the yield of the harvester does not scale up linearly with μ_h. This happens when the harvester is composed of k different units with each a discrete size μ, where $\mu_h \geq k\mu$. When calculating the harvesters size, this implies no arbitrary μ_h can be chosen as it should be a multiple of μ. The discrepancy between both, $\mu_h - k\mu$ can de facto be considered a part of the harvester that is not exposed to the energy source, with $k = \lfloor \frac{\mu_h}{\mu} \rfloor$. Practically, harvesters which exhibit this behavior, such as pyroelectric crystals for instance, will make note of μ and the maximum power that corresponds to it, allowing further calculation using the formulas above nonetheless.

4.9.3 Environmental Parameters

Changing environmental parameters can be caused either by external phenomena, from which weather is the most variable, or by the system itself. Aside from very few exceptions, these system induced changes are exclusively related to warming up due to heat dissipation in hermetically sealed containers with an external energy input. Unfortunately, the system induced changes in environmental conditions are negligible compared to influences of weather, humans or natural causes. As these parameters have an unpredictable nature and are only obtainable by means of exhaustive benchmarking and field testing, it is advisable to protect the harvester against external variations or make it immune to them. TENGs are for example known to be very resistant to dust, moisture etc. because they can be constructed from highly resistant materials such as kapton and PMMA.

As a side note, it is important to point out that those influences having a detrimental effect on the harvesters performance usually also shorten the life time of the harvester, effectively providing two reasons to shield them against changing environmental parameters.

4.9.4 Practical Implications

Reviewing existing energy harvesting applications gives the impression that η_h is continuously fluctuating in time, making it responsible for a harvester power output $P_h(t)$ that is also function of time. Despite being a valid generalization and proving to be effectively true in most known situations, there are also cases imaginable where η_h is constant. Assume for example that a TEG is installed between a pipe of hot and cold water in a continuously operated power plant, relying on a temperature gradient to generate electric power. In this case, the temperature gradient will be constant after a certain amount of time after startup of the cycle, the fraction of the TEG in thermal contact with the pipes does not change, and the effects of environmental effects are negligible in this indoor location. Since all three parameters influencing η_h are constant, the TEG will effectively produce a constant output power.

4.10 Conclusion

Through parametrization of energy harvesters as a product of 3 factors, normalized harvester power output p_h, harvester size μ_h and environment dependent conversion efficiency η_h, a harvester model is obtained that is suitable for use in a design methodology for autonomous systems because the 3 factors can be adjusted individually. The harvester model offers a simple relationship between harvester output power, its harvesting potential, its size, and the effects of possible environments it could be deployed in. This chapter presented the theoretical feasibility of complementary balanced energy harvesting as a flexible approach to harvester fusion, demonstrating the potential added value of combining multiple energy harvesters in the same autonomous system.

Secondly, the power output of energy harvesters obtained through this model can be easily matched to the load requirements of an attached electronic system, estimating energy budgets over one or multiple operation periods for periodic systems and periodic energy harvester regimes.

Chapter 5

Harvester Performance Characterization

Energy harvesters act as power transducers, they convert ambient energy in their direct environment into an electrical form, which can then be temporarily stored in a battery or capacitor, or used directly in an electronic circuit. The harvesters output power is, as discussed in the previous chapters, dependent on environmental factors (available ambient energy, installation of the harvester) but also on the harvester itself. Although some energy harvesters, PV cells in particular, have been accurately modeled, it remains a cumbersome task to develop new models or adapt existing models whenever improvements in harvester technology offer enhancements in harvester performance. To evade the tedious task of harvester model development, characterizing energy harvesters by measuring them under various circumstances is a more scalable and automateable approach. This chapter focuses on the development of appropriate test apparatus for PV cells, TEGs and vibration harvesters which enable automated acquisition of harvester characteristics.

5.1 Photovoltaic Cells

Since PV manufacturers primarily focus on outdoor applications, the behavior of PV cells under natural sunlight is usually documented in datasheets, or can be obtained through replication of the solar spectrum using appropriate light sources. The necessary measurement equipment is commercially available, and therefore not the bottleneck in the design of light powered autonomous systems. For energy harvesting applications, however, PV cell performance under both natural sunlight and artificial light sources is of interest. Since no adequate test equipment is available to measure the performance of small PV cells under combinations of artificial light sources, the goal of the PV cell test apparatus described below is to simulate a configurable indoor environment. Rather than testing the state-of-the-art cells, which have higher photoelectric efficiencies but are not commercially available and too expensive for practical use, this research aims to focus on benchmarking the performance of PV cells and modules that are readily available on the market. The proposed approach consists of a specialized test chamber where PV cells and modules can be exposed to different indoor light sources with varying intensity to emulate lighting conditions in any practical real world indoor environment [25]. Combining the test chamber with specifically developed data processing algorithms allows fully automated testing of cell characteristics, including determination of critical cell parameters such as open loop voltage, short circuit current, and maximum power point of the cell (MPP). A maximum power point tracker (MPPT) is implemented for this purpose [313].

5.1.1 Requirements

As discussed in the previous section, existing efforts mainly focus on performance testing of large solar panels for outdoor use under natural sunlight conditions. This makes the design of energy harvesters for light to electric energy conversion a burdensome task since necessary constraints are completely absent. The type of PV cell, the light intensity, its size and the spectrum of the ambient light will all affect the power output of the cell, however, existing environments do not allow to vary each of these 4 parameters to quantize the performance of the cells under worst case scenarios. Instead, commercial testers are limited only to ideal lighting conditions (sun light on a cloudless bright day), and benchmarkings as described by Stephan et al. measure the power output for a specific combinations of light intensity and spectrum [206].

For maximum flexibility, a test environment must allow the 4 parameters to be changed dynamically to measure nominal and worst case power outputs, the latter is paramount in applications where high reliability is required and the PV harvester is the only power source. Hence, different types of cells with different sizes should be testable under varying light intensity and spectrum. The load of the cells must also be configurable to emulate realistic loads and power path design of embedded systems powered by ambient energy. Finally, the test environment must include power point tracking and power measurement. As individual cells are not only difficult to acquire but also inconvenient to integrate in electronic products, the efforts will focus on commercial modules consisting of on or more individual cells in series or parallel, or combinations thereof. Key parameters to test are the voltage in the MPP, the maximum current in the MPP, and the power output for different illumination levels. To be of any practical use, the results must be presented in such a way that the comparison of different cells is convenient for embedded systems designers.

5.1.2 Implementation

Reproducing Indoor Light Spectra

Testing PV cells or modules for outdoor applications requires a specialized light source, a xenon or metal halide lamp, which resembles the spectrum of the sun as closely as possible. Spectral filters may be applied to tune this light source to atmospheric conditions, i.e. panels that are targeted to the East or West are exposed to a slightly different spectrum than panels targeted to the South, as light from a rising or setting sun travels a longer path through the atmosphere than in zenith, causing wavelengths towards the blue side of the spectrum to be absorbed by the atmosphere. Because these parameters are well documented in literature, however, fitting light sources and filters are readily available, albeit expensive. For indoor lighting conditions, the spectral information of the light source is usually not known because lamp manufacturers rarely specify these characteristics. When following the same approach as for testing under natural lighting conditions, it is thus necessary to measure the spectrum as well as the illumination (in lx). A spectrometer is required for this purpose. Secondly, the measured spectrum ought to be reproduced by the test chamber. This can be done subtractively using a single light source and a set of different filters to remove undesired wavelengths, or additively by combining multiple light sources with different spectral characteristics. Figure 5.1 compares both techniques. The subtractive approach is cumbersome and expensive due to the high cost of the heterogeneous lamp (i.e. a reasonably “flat” spectrum) and the specialized filters, as well as the optical or mechanical hardware required to switch them in and out. Using the additive approach to mimic natural sunlight is nearly equally complex, but fortunately indoor lighting allows simplification while retaining adequate accuracy.

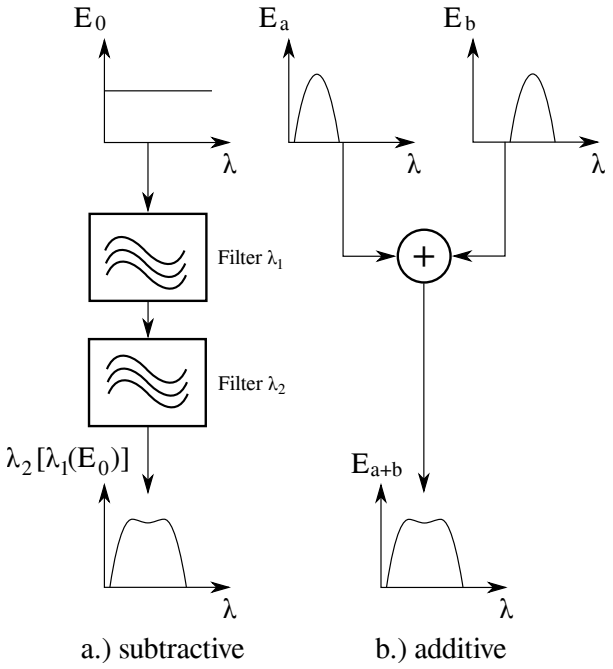

Figure 5.1: Reproduction of indoor light spectra by subtraction using filters (a) or by addition (b). The resulting spectra a discrete and not identical, ideally $\lambda_2 \left[\lambda_1 \left(E_0\right)\right] \approx E_{a+b}$.

A solution can be found by simplifying the problem twofold: firstly, it is assumed that the cell under test (DUT) is only exposed to artificial light in its intended application, thus ruling out influences of direct sunlight. The luminosity of scattered sunlight is typically 3 orders of magnitude lower than direct sunlight, attributing to an error which is deemed acceptable. The resulting spectrum can thus be reproduced easily using commercially available, off-the-shelf lamps or combinations thereof. Secondly, it is assumed that the spectral characteristics of lamps of the same type are congruential, i.e. there are few differences between 6000 K "cool white" fluorescent lamps of different manufacturers, for example. Keeping both assumptions into consideration, any real world indoor lighting situation can now be recreated by mixing lamps of different types with weighted luminosities. Although an infinite number of spectral combinations are possible, they can all be emulated by varying the relative intensity of a few discrete light sources. This is a much more convenient method than measuring the spectrum using a spectrometer and reproducing it, since it will practically almost always be possible to quickly determine the type of artificial light source(s) in the PV cells intended environment, which can then be replicated in the test chamber. Such a solution shifts a complex optical problem to a set of electronic problems with can be solved more reliably and at lower cost. A combination of a 120 W incandescent source, 100 W halogen source, 16 W LED source (8 W "warm" and 8 W "cold") and 36 W fluorescent light source was selected, because these light sources are the most popular in 2017. However, the modular construction of the light source allows specific light bulbs (i.e. ultraviolet fluorescent sources as used in indoor entertainment environments for example) to be added with minimal cost or efforts. This approach was published in [313].

Spectral Composition

An arbitrary spectral composition of the light source is achieved by modulating the relative intensities of the different sources it is composed of. While LEDs and incandescent lamps can be modulated using

digital pulse width modulation (PWM) but halogen lamps require a precise bias current to make them accurately dimmable. Fluorescent lamps include an inductor (either a ballast or electronic gyrator) for ignition, and the phase shift between voltage and current makes it notoriously difficult to control the exact ignition when using phase edge modulation. Industrial light source specific dimmers were chosen for this purpose to ensure consistency in the modularity of the design. For the fluorescent lamp, a specific OSRAM dimmer of type *Quicktronic Intelligent Dim T8* was integrated in the design. As with other industrial dimmers, these devices support dimming of light sources with an analog control input in a range of typically 1 - 10 V. Connected lamps in a power range between 5 W and 350 W are supported, making this dimmer universally applicable and more than sufficient for the intended usage.

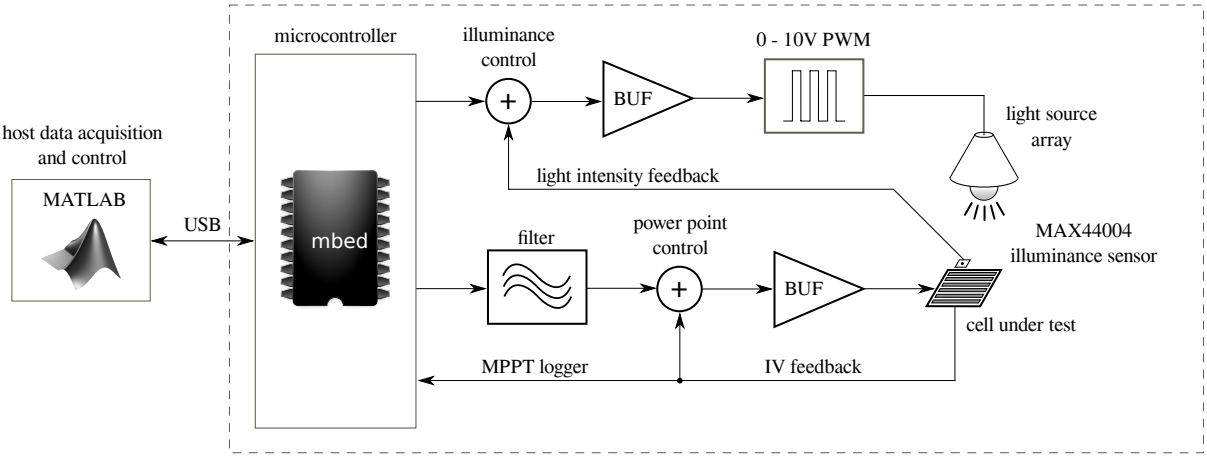

Figure 5.2: Block diagram of the test chamber. The logic is implemented on the embedded development platform *mbed* based on an LPC1768 microcontroller running at 50 MHz. The primary control loop stabilizes the illuminance using a MAX44004 lux sensor. The secondary loop controls the load impedance of the cell, allowing the measurement of the cells voltage and current to calculate the instantaneous power output. The experiments are controlled by Mablab software, responsible for execution of the experiment and collecting data.

Source Intensity Feedback

There are numerous factors affecting the effective intensity of the light reaching the surface of the cell being tested. Variations in dimmer performance, degradation of the lamps and temperature, among others, are factors that significantly alter the light intensity under influence of external or unknown circumstances. Such variations cannot be stochastic and as such do not lead to random errors in measurements but to systematic errors, hence they are undesirable. Because said variations are very difficult to model and compensate, it was chosen to instead employ a feedback system to regulate the light intensity reaching the photovoltaic cell by adjusting the light intensity of the different light sources. A key component in this scheme is an adequate light sensor. Various types of light sensors exist, the simplest being light dependent resistors (LDR). Despite their favorable cost, these devices suffer from high component spread in production and are sensitive to variations in temperature. They also need to be individually calibrated, and therefore either a calibrated light source or meter is still required. Both are expensive and require a cumbersome calibration procedure, making LDRs an undesirable solution in this application. The inherent photosensitivity of semiconductor materials makes on-chip VLSI light sensors possible, and their large scale production offers a viable alternative to discrete light sensors. The MAX44009 is

an integrated ambient light sensor with an integrated analog to digital converter (ADC). It includes 2 light sensors, one for ambient light and another for optional infrared light compensation. Its ADC has a resolution of 16 bit and feeds data directly to a serial communication interface though I^2C after being processed by an internal DSP unit. Every device is individually factory calibrated by its manufacturer Maxim Integrated, and this configuration is stored in the on board non volatile memory of the device. This eliminates additional calibration steps for the user. Maxim Integrated ensures calibrated measurements in a wide luminosity range between 45 mlux and 188 klux, more than sufficient for any indoor lighting environment. The MAX44004, a variant of the MAX44009, was eventually chosen for its better spectral response. The complete block diagram is shown in figure 5.18.

Power Measurement

Its nominal power rating aside, the most important property to know of any photovoltaic cell is its maximum power point (MPP). The MPP is the point on the load curve of the cell where the product of voltage and current is maximum, thus where the rectangle constructed from the current and voltage at any given point has a maximal surface. Because the MPP is determined by the forward voltage drop over the cells internal pn-junction, the MPP varies with temperature, illumination, light spectrum and cell type. The MPP determines the ideal cell voltage, which the power management circuitry must be able to handle. Assemblies of photovoltaic cells with MPP voltages too far above or below the intended system voltage will cause DC/DC conversion (buck or boost) to be inefficient, thus wasting any power gains made by operating the cell in its MPP. The easiest way to determine the MPP of any photovoltaic cell, under a specific luminosity, is by varying the resistive load between open and short circuit, and measuring the corresponding voltage for each load. The MPP can then be found by calculating the product of current and voltage, and searching the voltage where this value is maximal. Consequentially, measuring the MPP of a cell requires accurate measurement of both voltage and current, as shown in the circuit of figure 5.3. [36]

Accurate Current Measurement

Unlike voltages, which can be measured with satisfactory accuracy using any ADC with a resolution of 12 bit or higher in a range between 0 and the open cell voltage, measurement of the current requires more complex solutions. The order of magnitude of short circuit current (the maximum for which the system should be designed) is 500 mA. However, this is assuming outdoor lighting conditions on a module with a reasonably large surface. In indoor conditions, on smaller cells/modules, currents less than 1 mA should be expected. This wide input disparity makes the choice of a suitable shunt resistor difficult: for low currents, the accuracy will be insufficient while for high currents the burden voltage (voltage drop over the shunt resistor) will be too high. A solution for this problem was proposed by Dave L. Jones, by switching between different shunt resistors [152]. This approach is well suited to this application since there are no continuity requirements: measurements may be interrupted for an unlimited period of time while the shunt resistor is electronically changed and the system stabilizes from the step response. Electronic or mechanical switches (relays) are both viable options for this purpose. A second problem is the low voltage over shunt resistors, which must be amplified before being fed to an ADC. Noise susceptibility is a significant problem, and the chosen option to negate this error source is by keeping the shunt as close as possible to the amplifier and ADC into a monolithic package. Several semiconductor manufacturers offer such commercial current sensors, examples include the LTC2990 from Linear Technology and the INA226 from Texas Instruments, among others. In this application the INA226 was the most optimal choice because it is capable of both high side and low side current measurements and incorporates a 16 bit ADC for voltage (with a resolution of 1.25 mV) and for current (with a resolution of 2.5 μV), the latter configurable for any current range with an external shunt resistor. In this configuration, the INA226

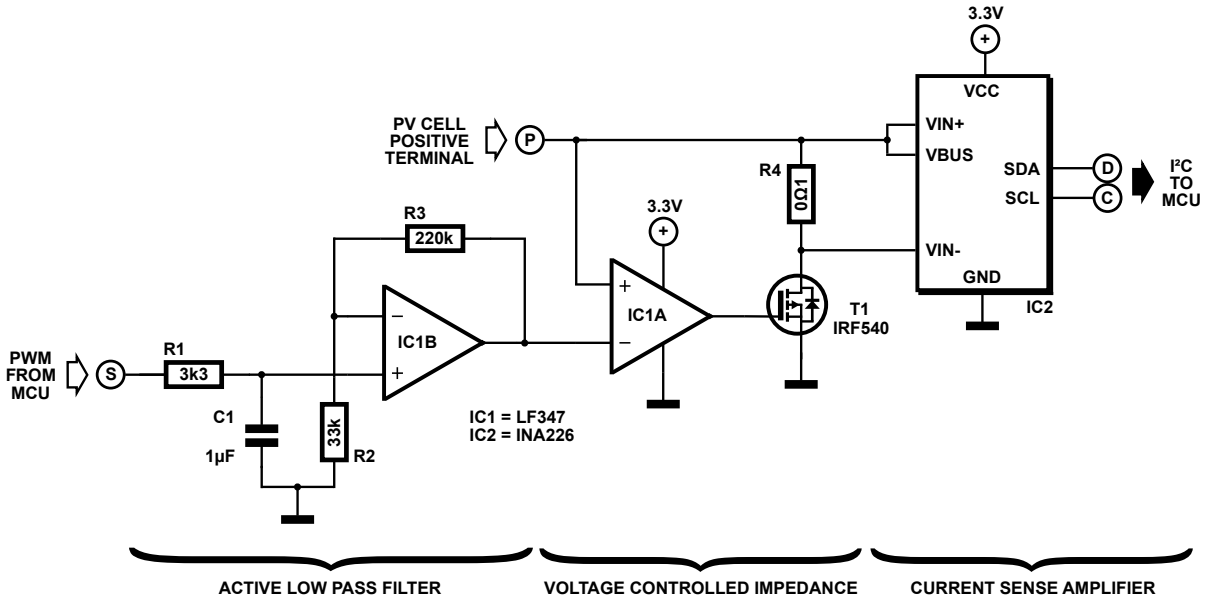

Figure 5.3: Detail of the variable impedance generator used to load the cell under test. A PWM signal generated by the microcontroller (left) is actively filtered (IC1B) to set the desired cell voltage. The signal is fed into a comparator (IC1A), causing the partial conduction of an N-MOSFET which acts as a variable resistance. The current through the MOSFET's drain-source channel is measured as a voltage over a low value shunt resistor (R4) and digitized by high side current sense amplifier INA226 (IC2). The current measurements are sent back to the microcontroller (right).

can work in conjunction with shunt switching in function of its current ADC overflow flag. The INA226 offers digital I/O over I^2C with 2 configurable address bits, thus able to operate on the same bus as the MAX44004 used for luminosity sensing. This architecture allows simplification of the hardware and increases reliability and accuracy by reducing noise on analog lines.

Variable Load

Several different approaches are possible to apply a variable load to a photovoltaic cell. The best known technique is by using a potentiometer. Unfortunately, many off the shelf digital potentiometers have a limited accuracy and/or current load capability. In case of the TP0401 from Texas Instruments, one of the considered types, only 128 different positions are possible and the maximum pulsed load current is 20 mA. Both are unsatisfactory for this application. Digital potentiometers with higher current capabilities exist but are prohibitively expensive. The most straight forward analog technique is by using a bipolar transistor as controlled current source, thereby immediately controlling the current through the cell. The cell voltage of a single cell is unfortunately insufficient to reach a transistor's minimum collector emitter voltage, causing it to saturate and unable to regulate current. A practical solution for this problem is using a MOSFET instead of a bipolar transistor, and biasing it in its linear operation mode to give it a controllable finite ohmic resistance. This is done by means of a feedback loop with a comparator and a reference voltage, as shown in figure 5.3. Feedback from the current sensor is then used to keep the MOSFET precisely in its linear operation mode, simultaneously eliminating any influence of temperature or component spread in MOSFET or offset in the comparator.

Control Logic

The controller must comply to three requirements: (1) it must be capable of analog I/O to control the dimmers, (2) it must support a digital I^2C bus interface and (3) it must support the USB protocol as a bidirectional communication link for control signals and for data transmission. Many microcontrollers, such as the PIC18F4550 or PIC18F2550 from Microchip, are possible choices and there is no decisive criterion that differentiates between them. For this application, an LPC1768 from NXP Semiconductor has been chosen because of its synergy with the MBED development platform that allows transparent USB communication and straight forward local data storage, as well as reconfiguration of the device. Figure 5.18 shows the block diagram of the test chamber. The MBED supports 2 separate I^2C buses in addition to a USB interface, is capable of analog input and output, and 6 digital pulse width modulation (PWM) outputs. The LPC1768 is equipped with a 32 bit ARM Cortex-M3 processor, a necessity to handle USB communication, control and data acquisition in real time. The software was written in C++ and makes use of a Matlab API to interface with Matlab running on the host computer. The PID control logic requires a fast feedback loop to keep the load MOSFET biased in linear mode, and has been implemented in software on the Cortex-M3. The stabilization of the PID controller is shown in figure 5.4.

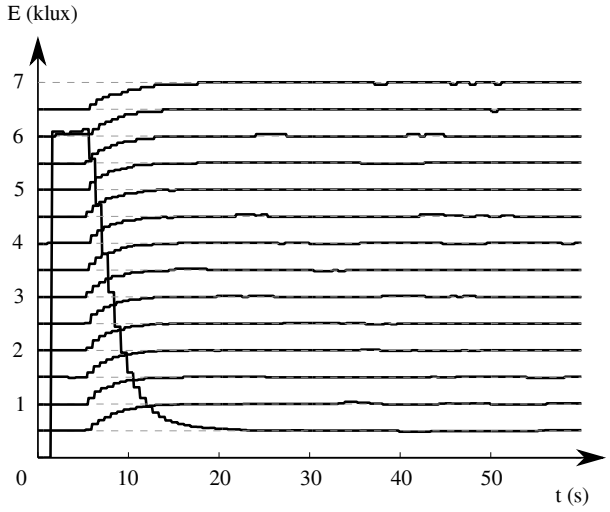

Figure 5.4: Stabilization of the illumination in the test chamber as a response on a step function of 500 lx. Stabilization time (less than 1 % error over 10 samples) is up to 85 % longer for the 6.5 klx - 7.0 klx step than for the 0.5 klx - 1.0 klx step. Since illumination higher than 2 klx rarely occur in indoor environments, these delays are not a problem. The initial step to 0.5 klx experiences an overshoot of approx. 5.6 klx due to instability of the dimmers at low illumination levels. At very low illumination levels ($<$ 150 lx) this effect may cause longer stabilization delays.

5.1.3 Design Verification

The distance between the light sources and the cell under test is determined by the angle of the different light sources. The source with the smallest angle determines this distance, about 30 cm. However, an unintentional side effect is that wide angle sources will radiate a significant fraction of their output power to the walls of the chamber. The walls have been coated with a reflective film to minimize local dark spots and redistribute scattered light evenly over the test surface. Ideally, the light intensity must be homogeneous over the entire surface of the photovoltaic cell being tested. This was verified using a

spectrometer and cross-checked using automated measurements with an array of MAX44004 ambient light sensors. An example of a distribution map is shown in figure 5.5.

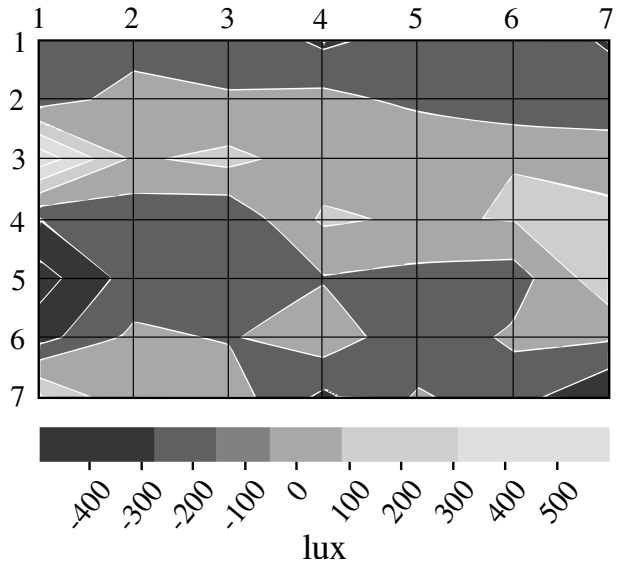

Figure 5.5: Illumination distribution map for an incandescent light source at an intensity of 7 klx, expressed as deviations to the average illumination level. The largest deviation accounts for approx. 1 klx, corresponding to an error of up to 14 %. Care must be taken when positioning the cell under test to keep the error to a minimum. Larger cells will suffer from uneven energy distribution. x and y units are physical measurement points, distributed over the entire active surface of approx. 30 x 30 cm.

For low luminosities the variations in luminosity are so low that they are difficult to measure. To amplify the variations, tests were performed on high luminosities of 6000 lux and above. The maximum relative error for incandescent light is found to be 16 %, for halogen light 61 %, for LEDs 26 % and for fluorescent light 15 %. However, these errors only apply for PV modules covering the entire surface of the test chamber. Smaller modules or cells can be easily located in an area with uniform distribution as seen in figure 5.5 where the error is significantly smaller. A software routine keeps track of the expected error based on the size of the cell under test to compensate for these variations. An algorithm for anomaly detection has not yet been implemented in the software.

5.1.4 Comparison of Photovoltaic Cells

Maximum Power Point

The presented software implementation provides automated test procedures for maximum power point measurements and for illumination sweep testing. The procedure for maximum power point measurements performs a sweep over the entire load line of the PV module, varying the load of the module between open loop voltage and short circuit. At each point, the current is measured and multiplied with the voltage set point to obtain the module's output power. The relation between module output power and voltage is a curved load line, as shown in figure 5.6.

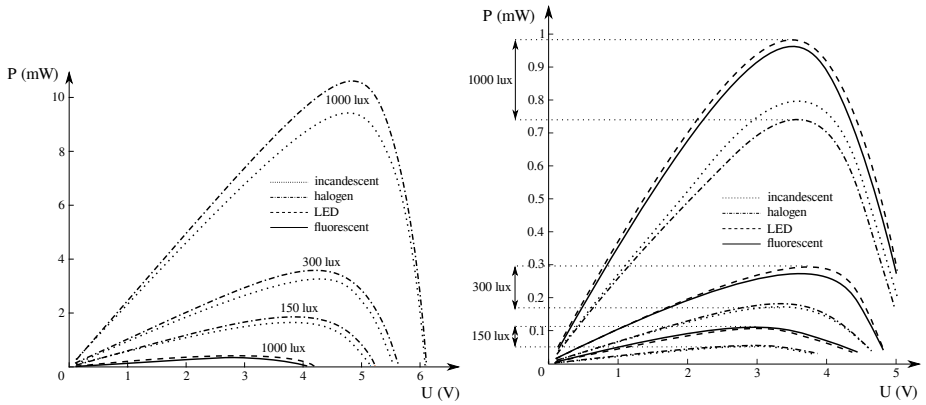

Figure 5.6: Comparison of the behavior of a monocrystalline cell of type SLMD960H121 (active area: 1200 mm^2) in the left graph, with an amorphous cell of type Panasonic AM-1815 (active area: 2408 mm^2) in the right graph, for different types of artificial light, under 150 lx, 300 lx and 1000 lx.

The top of each curve corresponds to the respective maximum power point (MPP) of each cell, for a specific combination of illumination and light source type. For any combination of illumination and light source type, the MPP specifies the cell voltage at which the power transfer to the load is maximum. In practical applications, the power electronics responsible for extracting energy from the harvester, must be calibrated to keep the cell voltage as close as possible to this value. For the majority of commercially available cells, significant variations in MPP voltage can be observed, as seen in figure 5.6. MPP voltages typically vary with illumination level, where higher illumination levels result in higher MPP voltages. For example, for a monocrystalline cell of type SLMD960H12L, the MPP voltage increases by 0.9 V for an increase in illumination level of 850 lux (150 lx to 1000 lx). It is usually not possible to find simple mathematical relations between MPP voltage and illumination levels, posing a challenge for embedded implementations since look-up-tables (LUTs) will be required. Figure 5.6 shows two examples, for a monocrystalline cell (left graph) and an amorphous cell (right graph), both exhibiting the same behavior.

Aside from determining the optimal cell or module voltage for energy harvesting power path electronics, combining load lines for different types of artificial light in the same graph immediately allows comparison of cell performance under various indoor light types. Depending on the chemistry of the cell, completely different behavior can be observed. Amorphous cells, such as the AM-1815 in the bottom graph of figure 5.6, show a power output in the same order of magnitude regardless of the type of light source they are illuminated by. Variations of 40 % $\pm$ 15 % can be observed, with a maximum performance under LED light and minimum performance under halogen light bulbs. In contrast, the monocrystalline SLMD960H12L performs nearly 2200 % better than the amorphous AM-1815 under incandescent or halogen light sources (proportional to their respective active surface areas). However, its power output collapses under LED or fluorescent (TL) light sources, performing worse than the AM-1815 for a 64 % higher cost. It can be concluded that the MPP load lines derived from automated testing under different types of artificial light sources are a valuable, yet easily interpretable tool for comparing PV module types and selecting the best type for a specific indoor environment.

Although the power output of amorphous (a-Si) cells is not as strongly dependent on the type of light source as it is for crystalline (monocrystalline and polycrystalline) cells, significant performance differences can nonetheless be observed when comparing a-Si cells of different types. In figure 5.7, a-Si

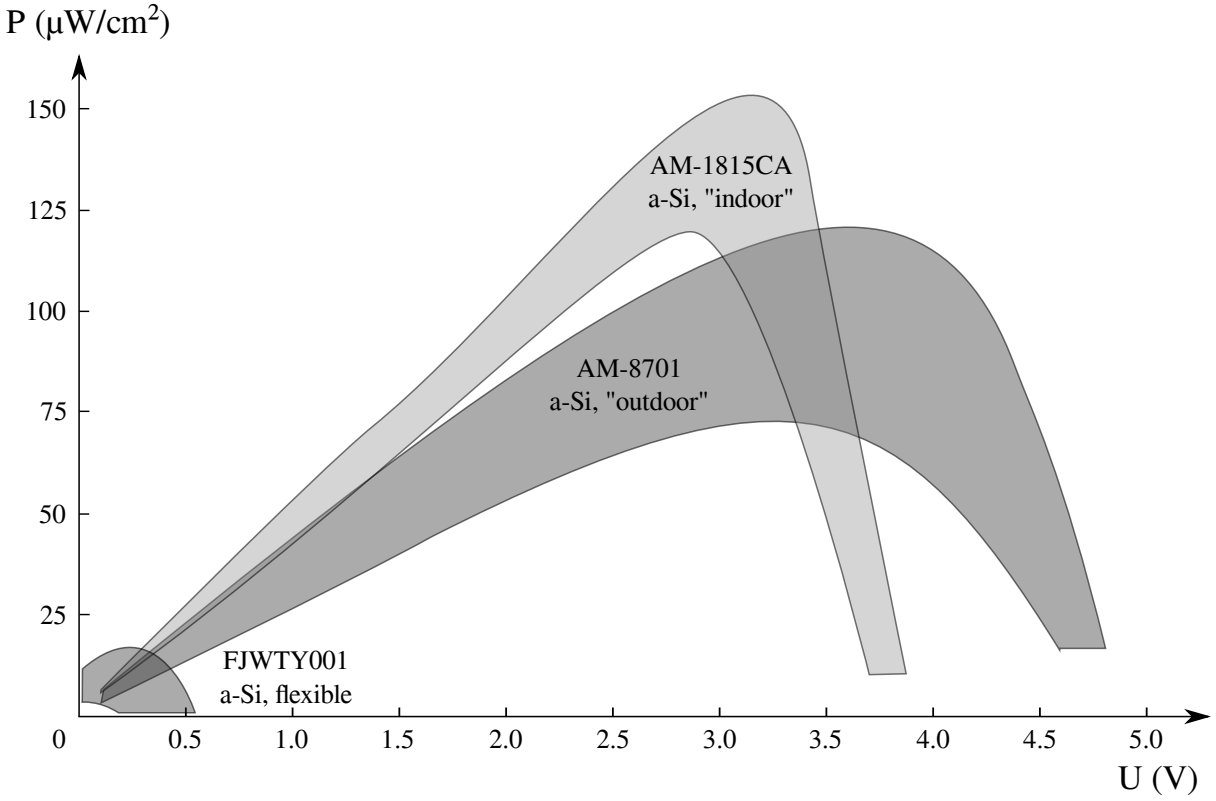

Figure 5.7: Performance difference for different types of a-Si cells under 300 lx: a FJWTY001 flexible cell, a Panasonic AM-1815 marketed as “indoor” cell and a Panasonic AM-8701 marketed as “outdoor” cell.

cells of 3 different types are compared: a Panasonic AM-1815 cell marketed for indoor use, a Panasonic AM-8701 cell marketed for outdoor applications, and finally a flexible cell of type FJWTY001. The power outputs have been scaled to compensate for the differences in active surface area ($24 \cdot 10^2\,\mathrm{mm}^2$, $29 \cdot 10^2\,\mathrm{mm}^2$ and $70 \cdot 10^2\,\mathrm{mm}^2$ respectively). Although the curves for individual light bulb types have been omitted in figure 5.7 for clarity, the ranges nonetheless show significant performance differences between cell types. As suggested by their manufacturer, AM-1815 and AM-8701 exhibit a notable performance difference under 300 lux. The AM-1815 marketed as “indoor” cell effectively shows a higher performance than its counterpart designated for outdoor use. It should be noted that both cells have a MPP voltage between 3.0 V - 4.0 V, which allows efficient design of the power path through DC/DC conversion because input and output voltages of these converters will be close. For the AM-1815 in particular it may be possible to power modern microcontrollers directly from the cell without any power path electronics at all, since its MPP voltage occurs below 3.6 V which is the typical maximum for 3.3 V logic devices. Such systems can thus be designed more energy efficient and at lower costs. Despite their recent surge in popularity, the flexible cell has a comparatively inferior performance at the same illumination of 300 lux for any type of artificial light. With a MPP voltage between 0.2 V - 0.3 V, these cells require energy inefficient step-up converters to power electronic systems, or alternatively, a considerably large surface area is required to connect cells in series.

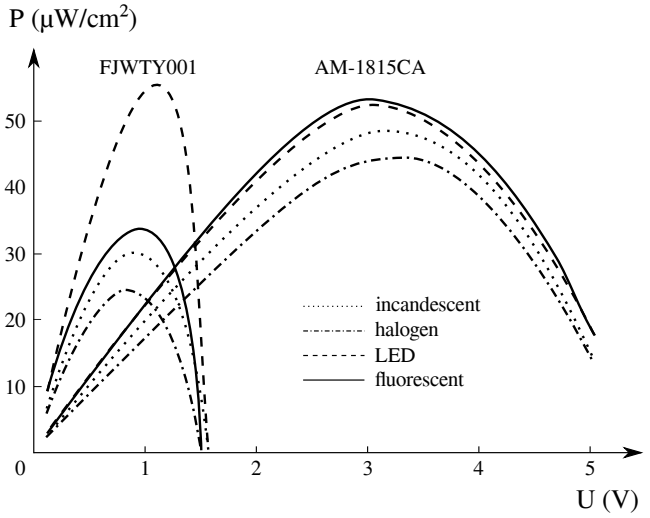

Figure 5.8: Performance difference between a rigid a-Si cell for indoor use (AM-1815CA) and a flexible a-Si cell (FJWTY001) at 2000 lx.

At higher power levels, the performance of a-Si cells appears to converge, as can be seen in figure 5.8 for a flexible and rigid a-Si cell under 2 klx of incandescent, halogen, LED or fluorescent light. Under LED light, the performance of both cells is nearly identical, relative to the active surface area of both cells. For other types of artificial light, the performance of the rigid cell is congruent with figure 5.6, but the performance of the flexible cell drops sharply to roughly 50 % of its power output under LED light. Despite the cell voltage in the MPP climbing to approx. 1.0 V$\pm$0.2 V, a step-up converter (switched capacitor or switched inductor) will still be necessary for most practical applications, since state of the art microcontrollers still require approx. 1.2 V for reliable operation. It should also be noted that illumination levels of 2 klx are very rare in indoor environments, the graph in figure 5.8 is without a doubt an optimistic scenario. Further experiments with other types of flexible a-Si cells indicate a similar performance, thus it can be concluded that for indoor applications in particular, rigid cells are advantageous in comparison to flexible cells, at least where the latter flexibility is not a necessity.

The software developed also allows reading out IV-curves, the traditional representation of load lines. Figure 5.9 shows an example for a monocrystalline cell of type SLMD960H12L under illumination of 150 lx of different types of artificial light. The MPPs are marked on the curves with dots, indicating the respective power rating and the corresponding currents. Absolute numeric values allow evaluation of the cell in a specific environment with known light bulb types and illumination levels (by measuring with a lx meter). Unlike in outdoor environments, where clouds, trees, birds, planes, leaves etc. can cast shadows on cells, the illumination level for an indoor cell will likely only have 2 states: fully illuminated or dark. The energy density of scattered (i.e. indirect) light is two orders of magnitude smaller than of direct light, and hence will not contribute any useful energy because the resulting cell voltage will be too low to be of any practical use. In these cases, the power output in the MPP of figure 5.9 will be close to the actual average power output of the cell, assuming it is operated in its MPP. If the (average) power consumption of the electronic application is known, determination of the cells viability as a power solution becomes trivial.

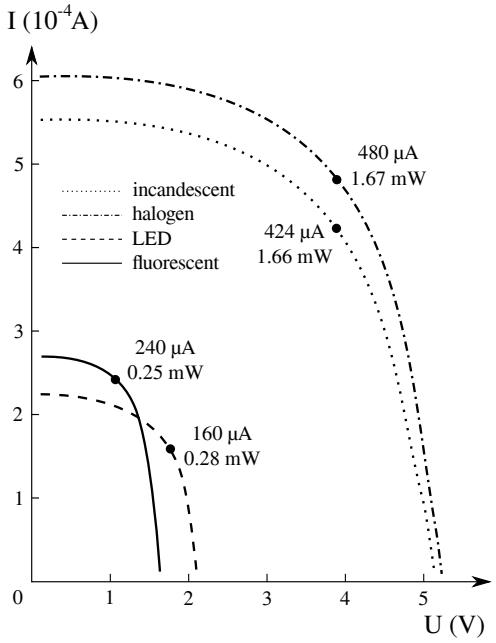

Figure 5.9: Comparison of IV curves for a SLMD960H12L monocrystalline cell under 150 lx.

Sweep Tests

Finally, the presented system also allows to execute automated illumination sweep tests instead of measuring load lines at discrete illumination intervals. A sweep test starts with a dark test chamber, after which the illumination sweeps from ca. 100 lux to a configurable upper limit, typically 500 lx or 1000 lx. The power output at each illumination level is measured in the MPP and plotted in a graph as shown in figure 5.10. Again, a comparison is made between a crystalline cell (SLMD960H121) and an amorphous cell (AM-1815). Despite their differences in performance, there is a near linear correlation between the illumination level and the power output of the cell. Large variations in performance are possible however, the crystalline cell performs poorly under fluorescent light, which is consistent with previous observations. Due to the approximately simple mathematical relation between illumination level and power output, it is straight forward to calculate the illumination gap for a given application and environment. This information can then be used to increase illumination levels by, for example, adjusting the angle between the cell and its primary energy source.

Both cell types show a much higher angle of inclination at low power levels. This is caused by secondary effects. The performance of PV cells is inversely proportional to their temperature, and despite the presence of forced air cooling in the test chamber, an increase in cell temperature is inevitable due to direct infrared emissions. This temperature increase is responsible for the saddle points occurring in the curves between 200 lx and 300 lx for both cells.

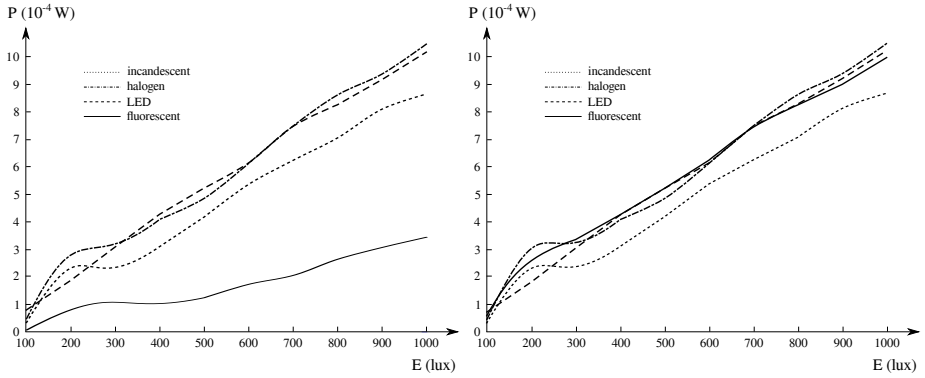

Figure 5.10: Power output in the MPP for a crystalline cell of type SLMD960H121 (left graph), and an amorphous cell of type AM-1815 (right graph) for an illumination sweep between 100 lx and 1000 lx.

5.2 TEGs

Traditional solid state thermoelectric coolers are entirely bidirectional from a thermoelectric perspective because of the Seebeck effect on which they rely, and can be used both as cooling devices or as thermoelectric generators (TEGs). When a temperature difference is applied to a junction of two materials with a different thermoelectric constant, a small potential difference will be created over this junction. The voltage is a function of the thermoelectric materials being used, and the temperature difference that is applied. As heat flows through the device from the "hot" side of the junction to the "cool" side, a heat flux is effectively converted into electric power [53]. The maximum thermodynamic power available [103] is given by

$$P_{max} = \frac{\Delta T^2}{4T_0(K_c + K_h)} \tag{5.1}$$

For TEGs, the heat flux to electric power conversion depends on the Seebeck coefficient S, the thermal conductivity κ, the electrical conductivity σ and the temperature difference ΔT [97, Eq. 1], and can be approximated as the dimensionless figure of merit zT [109][117, p. 190]:

$$zT = \frac{S^2 \Delta T}{\sigma \kappa} \tag{5.2}$$

Higher Seebeck coefficient and temperature difference, and better thermal and electrical conductivity of the material, will result in better heat flux to power conversion. The figure of merit zT as shown in equation 5.2 is a parameter of thermoelectric efficiency. Although zT is straight forward to model, the thermal (κ) and electrical (σ) conductivity of thermoelectric materials is difficult to measure, especially at elevated temperature differences because of the Thomson effect [317].

From the perspective of an embedded systems designer, looking to make use of TEGs as a replacement for primary chemical cells in electronic applications, the complexity of TEG operation at a fundamental physical level prohibits straight-forward integration. The lack of sufficiently detailed datasheets and the necessity of a power conversion stage between TEG and electronic system, are posing serious barriers to large scale TEG adoption. The large variety of semiconductor materials that may be used in TECs, and the performance dependence on specific construction details (i.e. material depositing techniques, thin film, MEMS etc.) make theoretical performance predictions a difficult and research intensive task.

Currently, many applications make use of reference designs based on case studies [317], which are most likely suboptimal for other applications. A better method for testing the performance of commercial TECs as energy harvesters is therefore necessary.

5.2.1 Operation Range and Requirements

Depending on the physical construction of the junction, the voltage over a common Bi_2Te_3 TEC junction can be expected between -228 μV/K [361, p. 85] and -287 μV/K [293]. As a material with relatively high zT, still a significant number of junctions must be thermally placed in parallel but electrically in series to generate a useful voltage. As a result, in order to be practically usable, either a large surface (i.e. more elements in series) or a large temperature difference is required for practical operation.

Fortunately, as embedded electronic devices are improving, their power requirements and operating voltages are also dropping [317]. That is particularly for TEG powered applications a favorable evolution: less power conversion circuitry will be required, and the electrical conversion efficiency will be higher. It also allows representative testing of TEGs and their power conversion circuitry together, resulting in power figures that are more accurate than measuring the TEG output with MPP and the power circuitry separately. For this research, the focus was primarily on Bi_2Te_3 TEGs since they are the most widely available commercial heat flux energy harvesters and have good performance. However, it should be noted that other TEG types may be better suited for complementary balanced energy harvesting applications. For use in domestic applications, industrial temperatures are never reached, and thus a maximum high side temperature of 100 °C (boiling water) was chosen as upper limit, since this is the maximum temperature that can commonly be achieved in office or home heating appliances without pressurization. For the same reason, since active "cold" sources are rare in conjunction with heat sources, we will focus on ambient air cooling instead of forced cooling. A heat sink is used for this purpose. Considering an average indoor temperature between 20 °C for office buildings and 22 °C - 25 °C for home environments, the maximum temperature difference considered is ca. 80 °C. However, this assumes the heat sink would be able to keep the cold side of the TEG at room temperature, which would require the heat sink to be impractically large. Since 3.3 V power rails are standard for low power embedded devices, a maximum voltage of 5 V was chosen for harvester/power conditioning circuitry output.

5.2.2 System Overview

The system consists of 3 major parts: a heated bed of 25 cm by 25 cm with integrated temperature sensor (1), a heat sink with optional forced air cooling using a fan (2) and a control unit for data acquisition and communication with a computer (3), as seen in figure 5.11. Heat sink and heated bed are monitored with an industry standard LM35 temperature sensor from Texas Instruments (figure 5.11, insert), and the heating power is modulated to achieve a desired temperature difference over the TEG being tested (DUT). For higher temperature differences, passive cooling is not sufficient at room temperature for TEGs with a good thermal conductivity, and forced air cooling with a fan may be necessary to maintain the temperature difference. Temperature stabilization is implemented with a PID controller in software on a PIC24F16KA102 microcontroller from Microchip. The microcontroller reads the temperature of hot and cold side of the TEG, computes the temperature gradient ΔT and adjusts the heated bed power to increase or decrease the temperature on the hot side if necessary. The temperature difference is considered stable if 150 successive measurements fall within an error margin of ± 1 °C. The accuracy is limited by the LM35, causing a larger error on measurements at low temperature gradients, as seen in figure 5.12.

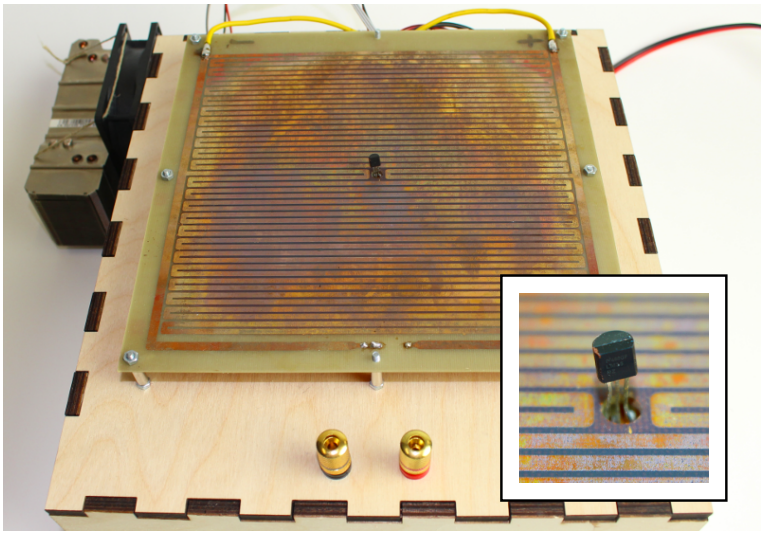

Figure 5.11: Heated bed constructed with a PCB trace on standard 1.6 mm FR4 as planar resistor. TEG and forced air cooled heat sink are dismounted, heat sink visible on the left of the setup. Insert: a close-up of the LM35 temperature sensor monitoring the hot side of the TEG, fitting into a cavity of the ceramic plate (not shown) on which the TEG is mounted.

Power Measurements

When a stable temperature gradient is reached, the data acquisition (DAQ) module is notified to measure output voltage and current. To ensure optimal stability and eliminate any interference between control and DAQ, measurements are performed by a separate microcontroller, also of type PIC24F16KA102. The current is measured over a 100 mΩ shunt resistor using an INA226 high side current/power monitor. In the INA226, the voltages on each side of the shunt resistor are fed to an integrated analog to digital converter (ADC) separately and then subtracted rather than using an analog differential amplifier topology. The advantages are twofold: the device can be used for both high and low side measurements (i.e. load connected to power rail or to ground), and the load voltage is measured simultaneously with the current, allowing direct computation of output power. The INA226 thus acts as a 4 wire sensing device. The primary reason for choosing an ADC with integrated switch is the better noise immunity in comparison to topologies with separate differential amplifier and ADC stages. The SMbus/I^{2}C interface also allows easy interfacing with the microcontroller responsible for DAQ, and ensures the measured power reaches its 0.1 % gain error and 10 μV offset specs. The electrical connectivity diagram is shown in figure 5.13.

Maximum Power Point Tracking

For maximum power point tracking (MPPT), the perturb & observe algorithm has been implemented. By sweeping the load between open circuit voltage (V_{oc}) and short circuit current (I_{sc}), the UI-curve of the TEG can be obtained, which allows to compute the maximum power point. The variable load has been implemented with a linear drive of an N-channel MOSFET [25] of type IRF540 from International Rectifier (IR). However, instead of using a passive filter to control the MOSFET as in [25], a digital to analog converter (DAC) of type MCP4921 from Microchip was chosen instead because of its better transient response and stability. The non-existing ripple also simplifies the feedback loop and allows it to be implemented in software on the same microcontroller that is doing the DAQ. Current/power

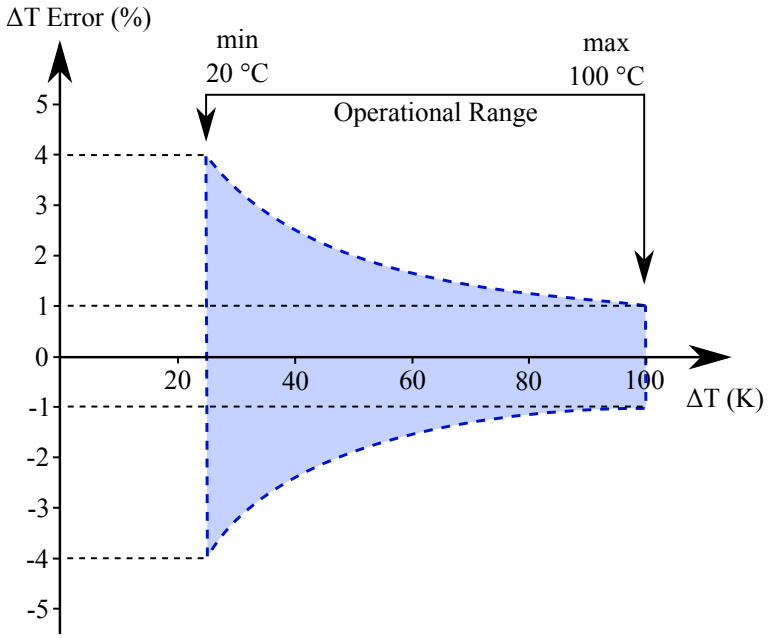

Figure 5.12: Relative error on the temperature measurement over the operational range between room temperature.

measurements do not interfere with stabilization because the INA226 is connected over I^2C while the DAC uses a faster SPI connection, as shown in figure 5.13. The output of the DAC is compared to the drain voltage of the MOSFET with an OPA1644 opamp so that the channel impedance is adjusted to match the voltage over the channel with the MCP4921 output voltage. The voltage drop over the current shunt resistor does not have to be compensated for because it is measured by the INA226 and can thus be subtracted in the software feedback loop. Feedback from the high side (VIN+) is not possible with INA226 because it is unable to measure the voltage on the high side separately. Therefore, feedback from the low side (VIN-) has been implemented.

Control logic

Both PIC24F16KA102 microcontrollers are interfaced with a computer over a USB connection with CDC driver to implement a virtual UART connection using an MCP 2200 integrated I/O controller. The software on the computer side is written in C#, and responsible for temperature stabilization and data management. The control loop first stabilizes the TEG at the desired temperature difference and waits until 150 successive measurements indicate time invariance. When stable, the power measurement is then started following the procedure presented above. After completing sufficient measurements to generate an UI-curve, the software renders the data points and saves them to disk. This method was published in [317].

5.2.3 Benchmarking Bi_2Te_3 TEGs

As proof of concept, measurements were performed on a series of Bi_2Te_3 coolers (TECs) used as generators, with an experimental setup similar to figure 5.14. The goal is to demonstrate the usability of

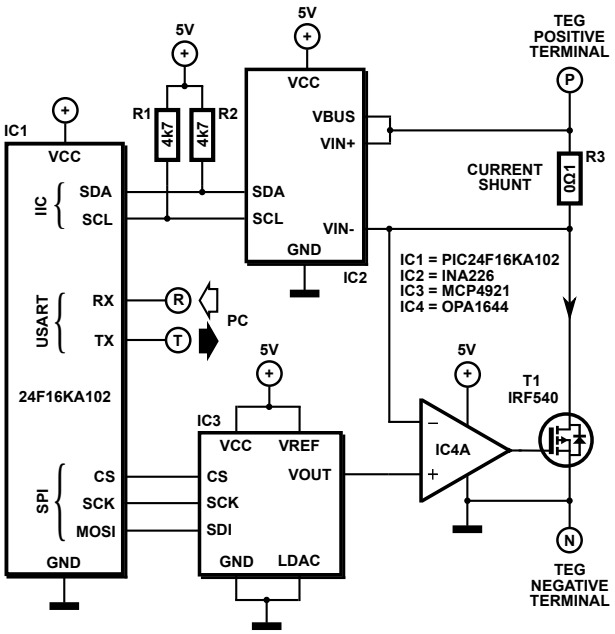

Figure 5.13: Schematic diagram of the DAQ module, showing digital control (PIC24F16KA102), a current sense amplifier (INA226) connected over I^2C, and a DAC (MCP4921) connected over SPI. A local feedback loop is implemented with a OPA1641/OPA1644A opamp as direct MOS driver.

the presented solution with commercial, off-the-shelf Peltier elements rather than dedicated application-specific thermoelectric generators as sold by Marlow, Nextreme, Micropelt and others. The tested types are TEC1-12706, CP2-12706 and TEC2-19006, which are available through third party distributors. A comparison of the physical and electrical properties of these TEGs is shown in Table 5.1. The test

Table 5.1: Comparison of TEC1-12706, CP2-12706 and TEC2-19006 TEG properties.

Parameter	TEC1-12706	CP2-12706	TEC2-19006
Semiconductors	Bi_2Te_3	Bi_2Te_3	Bi_2Te_3
Ceramics	Al_2O_3	Al_2O_3	Al_2O_3
Solder	BiSn	BiSn	BiSn
# thermocouples	127	127	190
Dimension (mm)	40 x 40	62 x 62	40 x 40
Thickness (mm)	3.9	4.572	6.4
Volume (cm^3)	6.24	17.57	10.24

setup allows two types of tests: a static test at a constant temperature gradient to measure the maximum power point (MPP) by performing a sweep and constructing a load line, and a dynamic test where the temperature is varied to determine the maximum power output in a specific temperature range.

Measuring MPP

To measure the MPP, as previously elaborated, the load is swept from short to open circuit by varying the channel impedance of the MOSFET between $R_{DS(on)} << 0.1\,\Omega$ (short circuit) and $R_{DS} >> 1\,\mathrm{M}\Omega$ (open circuit). For every impedance value, voltage-current pairs are measured and multiplied to obtain

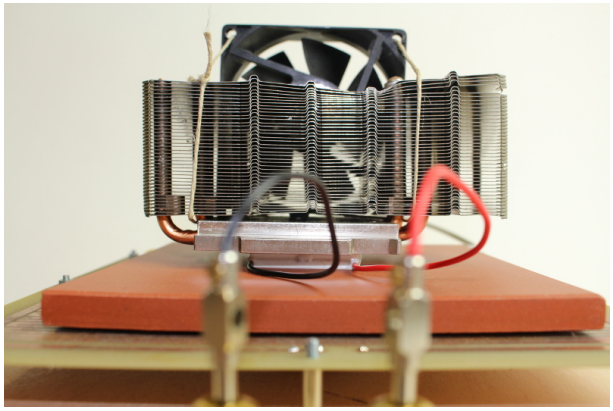

Figure 5.14: Experiment in progress (side view): a two stage TEG mounted between a stone heated bed (hot side) and an aluminum heat sink with heat pipes and forced air cooling (cold side). Electrical connections visible in the foreground.

a power curve. For a static test at 30 °C, the results are shown in figure 5.15 for the 3 TEGs. Parabolic

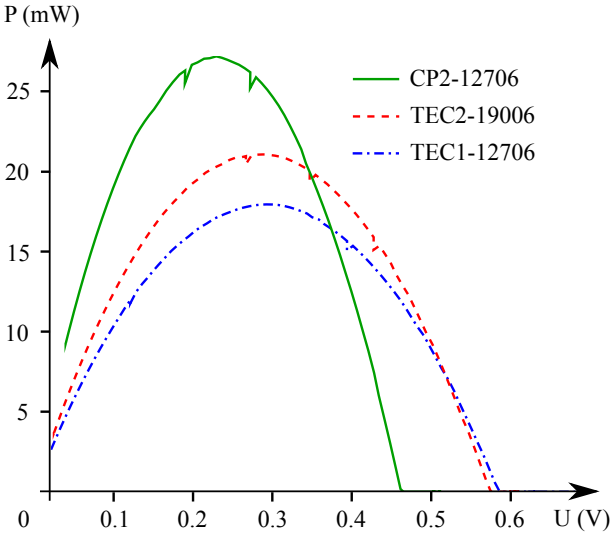

Figure 5.15: Visualization of maximum power point (MPP) for 3 commercial TEGs. Note that the MPP is roughly equal to half the open circuit voltage V_{oc}.

power curves are characteristic for TEGs, and the MPP is found in $\frac{V_{oc}}{2}$. However, it should be noted that for consumer grade TEGs, the power output is not proportional to the TEG's volume, as shown in Table 5.2. The differences can be attributed to variations in construction, thermal conductivity (i.e. differences in heat flux), mechanical composition, and optimization for higher or lower temperature differences. From datasheets alone, it is impossible to choose the most optimal TEG because the data does not allow for an adequate comparison. However, the presented test setup allows to mimic the target temperature difference at the intended environment of deployment, and enables the extraction of necessary data without much user interaction.

Table 5.2: Power density analysis for three commercial, consumer grade TECs.

	TEC1-12706	CP2-12706	TEC2-19006
P_{max} (ΔT = 30°C, mW)	17.9	27.2	21.1
Volume (cm^3)	6.24	17.57	10.24
Power density (mW/cm^3)	2.8	1.5	2.1

Measuring DC/DC Power Output

Even more important than estimating the MPP is making actual measurements of a TEG in conjunction with power conditioning circuitry. The low output voltage of a typical TEG prohibits powering an embedded electronic system directly, and a boost stage ("DC/DC step-up converter") is almost always necessary. Although any boost stage topology may be used as long as MPPT is enabled, the low cold start voltages tend to favor transformer based designs such as the LTC3108. Impedance matching through a transformer is difficult however, and the varying MPP in function of ΔT will pose a challenge to operate the TEG at high efficiency. This results in electrical conversion efficiencies below 30 % for cold start voltages below 45 mV. Alternatively, if a threshold between 250 mV and 400 mV is reached, cold starting a transformerless boost stage is possible. Several such solutions exist on the market: LTC3105 (250 mV cold start) from Linear Technology, BQ25504 (330 mV cold start) from Texas Instruments and AEM10940 (380 mV cold start) from E-peas. Unfortunately, quiescent power consumption as well as power switches in active mode result in a lower end-to-end power transfer than what may be estimated from DC/DC conversion losses alone. A second purpose of the presented test setup is measuring end-to-end power output *after* the DC/DC stage, aiming to provide embedded systems designs with power ratings that are directly usable to calculate the system's power budget and its associated parameters. Figure 5.16 shows a comparison of the power generated by a TEC2-19006 under varying temperature

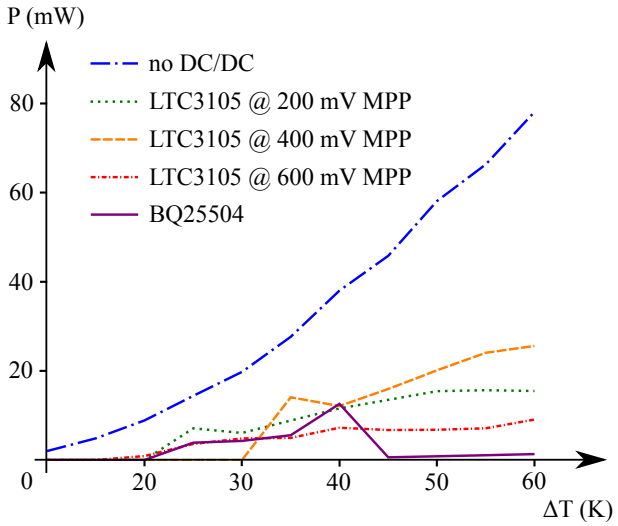

Figure 5.16: DC/DC conversion stage effect on end-to-end power output for a TEC2-19006.

differences. As expected, the highest output power is available when the maximum power point tracking is done externally by the test setup itself, rather than by an integrated maximum power point tracker. Although discrete MPPT systems exist, the choice is most often made for integrated MPPT controllers to save cost, PCB area, and benefit from better performance because of the typically higher switching

frequencies. Unfortunately, the overhead caused by the DC/DC conversion stage is significant, as shown in figure 5.16, with overall conversion efficiencies below 50 %. Neither the LTC3105 nor the BQ25504 offer good performance, despite their difference in topology. The LTC3105 supports a fixed MPPT which can be set with an external bias resistor. Figure 5.16 shows an average efficiency of ca. 40 - 50 % when set to 400 mV, implying an open circuit voltage for the TEG of around 800 mV. Unfortunately, as temperature changes, the MPP shifts accordingly, causing the LTC3105 to drift away from its MPP operation. Fortunately, as DC/DC conversion becomes more efficient as the voltage difference between input voltage and desired output voltage decreases, the performance hit can be slightly offset, resulting in an output power (orange in figure 5.16) that is surprisingly proportional to the input power (blue in figure 5.16) regardless of variations in temperature. For operation points too far from the actual MPP however, the output power converges to a maximum regardless of input power (green and red in figure 5.16). The test setup presented in this work can resolve this problem by measuring the MPP for a given operating environment beforehand, thus illustrating its usefulness for thermal embedded energy harvesting applications. It has been observed that the BQ25504 performs worse in terms of end-to-end conversion efficiency than the LTC3105, despite being equipped with a dynamic MPPT instead of the static one. For dynamic MPPT, the MPP is set as a fraction of the open circuit voltage instead of a fixed point set by a bias resistor. Only at a temperature difference of 40 K does the BQ25504 meet the performance of the LTC3105, but never exceeds it. The higher power requirements of the dynamic MPPT logic itself could be a cause of this overhead, but differences in input impedance between LTC3105 and BQ25504 may also contribute to the performance difference. At higher temperature differences (corresponding to higher input voltages), the BQ25504's dynamic MPPT algorithm appears to lose track, causing the power output to drop off sharply beyond $\Delta T > 40\,K$. This is unexpected for a device that is explicitly marketed as a boost converter for low power energy harvesting applications supported by TEGs. As a final note, it is important to observe the cold start in figure 5.16. Neither converter is able to start up at temperature differences $\Delta T < 20\,K$. For applications with passive cooled cold sides at room temperature (20 °), the limiting boundaries are around 0 °C and 40°C. Immediate implications are the inherent incompatibility of the measured TEC2-19006 TEG for harvesting human body heat for example, as the temperature gradient is too low to start up any DC/DC power conversion stage.

5.3 Vibration Harvesters

A major difficulty with vibration energy harvesters is that the power output is a function of multiple parameters, making vibration energy harvesting a multidimensional problem [302]. The amplitude of the vibrations, their frequency spectrum, the shape of the harvester, its orientation and even the strategy used to mechanically connect it to the vibration source, all influence the harvesters power output.

5.3.1 Existing Implementations

Numerous implementations of test setups for vibration energy harvesters have been discussed in literature. In [345], Yang et al. describe a shaker based implementation for testing electrodynamic vibration energy harvesters with planar coils [345, fig. 6, p. 5]. An accelerometer is used as feedback. A similar approach is suggested by Challa et al. using a function generator and amplifier to create a variable vibration source [56, fig. 7, p. 6]. Unfortunately, automated frequency sweeps are not possible with such a setup. Korla et al. apply partial automation, and focus on low frequency vibrations for a compact harvester using a very large shaker as vibration source [169, fig. 3, p. 267]. Leland et al. [186] and Ertruk et al. [90] use a vibrometer in conjunction with an accelerometer for contactless vibration measurements. To measure generated power, Liu et al. propose two strategies: direct dissipation in a load resistor and

indirect power measurement through the Joule effect (1), and AC measurement through a full bridge rectifier [193, fig. 5, p. 804](2). Other sources confirm this approach [169], although optimizations are possible by using Schottky or tunnel diodes instead of silicon diodes [169, fig. 2a, p. 267]. Since a shaker offers the most flexible frequency and amplitude range [283], this is the approach of choice for the implementation described in this article.

5.3.2 Parametrization Methodology

Due to the large discrepancy between properties of electromagnetic and piezoelectric harvesters, this work exclusively focuses on cantilever based piezoelectric harvesters, as bistable vibration harvesters are covered by He et al. in recent literature [130]. For cantilever piezoelectric harvesters, p_h corresponds to the normalized power rating when a sinusoidal excitation at the harvesters resonance frequency is applied that leads to the maximal tip displacement [163]. As material properties of p_h, both the resonance frequency and maximal tip displacement are harvester properties that can be found in harvester datasheets.

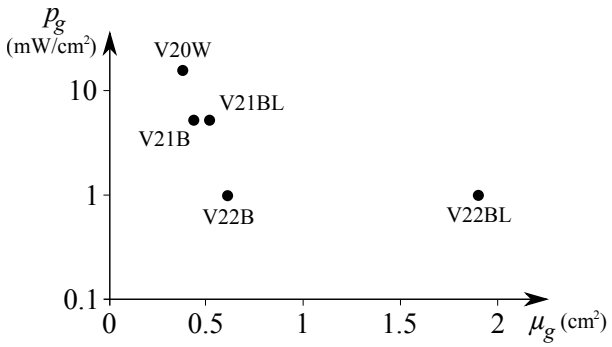

Figure 5.17: Comparison of the power outputs of various Mide vibration energy harvesters under a load of 1 g at their respective resonance frequencies.

Unlike other harvesters, such as photovoltaic cells, the power output of vibration harvesters at maximum excitation and tip displacement ($\eta_h \approx 1$) is not only a function of the material properties of p_h and the size of the harvester μ_h, but also strongly depends on the geometry of the harvester. This geometry is in turn a determining factor for the harvesters resonance frequency. Figure 5.17 shows a comparison of the normalized output power p_h at an excitation of 1 g for various vibration energy harvesters in their respective resonance frequencies. Since all harvesters are composed of identical piezoelectric material operated at identical excitation in their respective resonance frequencies, the differences in p_h are solely attributed to the differences in harvester geometry. Resonance frequencies are also shown to illustrate that the differences cannot be traced to the disparity in harvestable energy at different frequencies. While a somewhat accurate mathematical correlation between harvesters of similar geometry can be deducted, the methodology is excessively complicated because harvester geometry is a subjective parameter that makes adequate comparison between harvesters from different series or manufacturers difficult. The energy harvester parametrization methodology described in is fortunately flexible enough to be adapted to these specific constraints. When η_h is retained as a metric for the offset between the ideal excitation amplitude/frequency combination and the actual operating conditions, the parameters p_h and μ_h can be combined to represent the harvesters specific maximum power output, taking into account the harvesters material composition, geometry and size. This simplification is in fact an extension of the

methodology in as a special case where $\varsigma \neq 1\,\mathrm{cm}^2$, but instead ς equals the size of the harvester itself. Following the complementary balanced energy harvesting methodology, the dependence on a specific $\varsigma \neq 1\,\mathrm{cm}^2$ can be expressed as

$$P_h(t) = [\mu_h]_\varsigma \, [p_h]_\varsigma \, \eta_h(t) \qquad [\mu_h]_\varsigma \in \mathbb{N}^+ \tag{5.3}$$

where $[p_h]_\varsigma$ represents the normalized maximum power output of a single harvester of a specific type, model, geometry etc., and $[\mu_h]_\varsigma$ is the total harvester area expressed as a number of harvesters of that specific type, model and geometry. Therefore $[\mu_h]_\varsigma$ is a positive natural number. The conclusion that μ_h is a constant multiple of the intrinsic harvester size is a result of the demonstrated effect of harvester geometry which cannot be transparently quantized and must subsequently be excluded from the equation to allow further modeling.

Variables related to η_h are parameters that can be varied: most notably excitation amplitude, frequency range, mechanical adhesion and harvester orientation. A testing environment must be able to vary these variables to mimic real environmental conditions in which the harvester might be used.

5.3.3 Design

A test apparatus for piezoelectric cantilever vibration energy harvesters must be capable of modulating the variables affecting η_h, most notably the amplitude of the vibration measured in g (with $1\,\mathrm{g} \approx 9.81\,\mathrm{m/s}^2$) and the frequency of the vibration measured in Hz. To eliminate anomalies caused by variations in mechanical adhesion and orientation, harvesters must be mounted in a known standardized position. This section discusses the design considerations and implementation of a low cost test apparatus for piezoelectric cantilever vibration energy harvesters, and how this can be integrated in the harvester parametrization methodology presented above. The proposed design consists of a closed loop vibration generator using a commercial shaker as vibration source and an accelerometer as the necessary sensor providing frequency and amplitude feedback. The harvester is then mounted on the vibration generator with a variable impedance as load to measure its power and maximum power point, and enable simulation of impedance matching with loads such as buffer capacitors or DC/DC converters. Figure 5.18 shows a block diagram of the test setup.

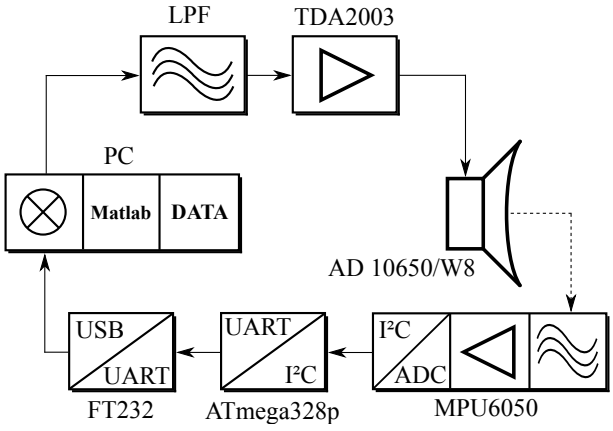

Figure 5.18: Block diagram of the benchmarking platform with an AD 10650/W8 subwoofer as vibration source, TDA2003 as amplifier and MPU6050 as vibration sensor.

Vibration Generator

Three potential vibration generators were compared: a DC motor with asymmetric load as commonly used in game controllers and mobile phones, a piezoelectric material with a voltage applied to it, and finally a traditional speaker. Experiments quickly ruled out the first two options. Both DC motors and piezoelectric crystals are not suitable as generators for this application because the amplitude with which they vibrate is either too variable or too small, respectively. Speakers in heavy duty implementation ("shaker"), commonly used as subwoofers in the audio industry, are considerably better suited since both the amplitude and the frequency are easily controllable. This design choice is consistent with literature describing shakers in similar applications as vibration sources [295, fig. 9a, p. 4], [56], [90].

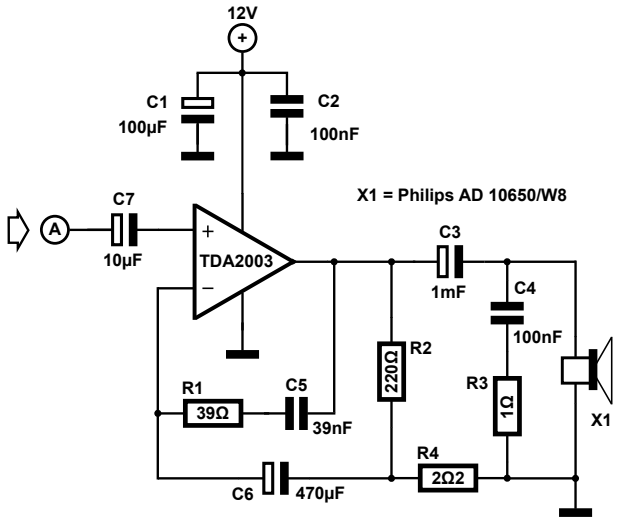

Figure 5.19: Schematic diagram of the TDA2003 based amplifier circuit driving the subwoofer.

A type AD 10650/W8 from Philips with a diameter of 10 inches and nominal impedance of 8 Ω was selected as shaker based on its favorable impedance and wide frequency response. A standard TDA2003 10 W audio amplifier was connected to drive it with sinusoidal excitation signals. This amplifier has a bandwidth of nearly 15 kHz (40 Hz to 15 kHz at -3 dB attenuation for an output power of 1 W in a load of 4 Ω) and a maximum gain of 40 dB, while keeping distortion low at typically 0.15 % at 1 kHz. These properties greatly simplify the amplifier design because the TDA2003's frequency response in conjunction with the shaker's natural attenuation of higher frequencies eliminates the need of extensive input and output filtering to remove harmonics. Figure 5.19 shows the schematic diagram of the amplifier design.

A recurring issue with commercial shakers is the irregular frequency response that is insufficiently flat to qualify as excitation source for vibration harvester benchmarking. One possible solution to this problem is measuring the frequency response, as shown in figure 5.20 and then compensating it in software by means of a look up table (LUT) in which the inverse frequency response is stored. While this works adequately for a short period of time, mechanical wear and decay of the shaker's membranes cause a continuous slow drift of the frequency response which in turn leads to a constantly increasing error decreasing the compensation's effectiveness. Since it is a cumbersome task to measure or model this wear over time and adjust the LUT accordingly, it was chosen to use a closed loop feedback instead of open loop amplitude regulation. For this purpose an accelerometer was selected as low cost vibration sensor.

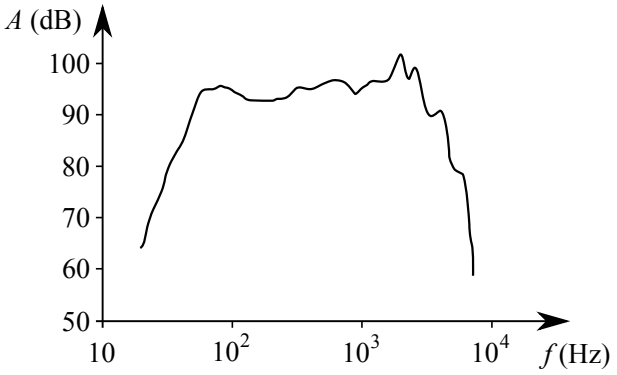

Figure 5.20: Frequency response of the Philips AD 10650/W8 subwoofer.

A platform was manufactured in ABS plastic using additive 3D printing technology to accommodate accelerometers and piezoelectric DUTs, and was attached to the conus of the shaker using epoxy glue.

Accelerometer Selection Criteria

The accelerometer must be selected with care, as accelerometer performance is paramount to a vibration with stable amplitude and frequency. The responsiveness is of particular importance for the frequency sweeps used in automated testing, as discussed below. Modern MEMS accelerometers are very low cost due to their widespread use in mobile gadgets such as mobile phones, game controllers and drones, and nearly all except the cheapest ones have specifications that generously exceed the requirements for this apparatus. Accelerometers with a range up to 16 g are readily available, often with selectable sensitivity. To eliminate noise contamination of analog output signals, a MEMS accelerometer with integrated ADC is advised. As of 2016, MEMS accelerometers with an I^2C interface are becoming the norm, surpassing older devices with three analog output channels. The MPU6050 from InvenSense has dynamically reprogrammable sensitivity ranging from ± 2 g up to ± 16 g. At 16 bits resolution, the highest sensitivity corresponds to 16384 LSB/g which exceeds the sensitivity of commercial sensors for comparable purposes such as the LOG-0002-025G-PC from Mide (0.0008 g resolution at 16 bit ADC) for only a fraction of the cost.

While low cost MEMS accelerometers have adequate resolution, sensitivity, and sample frequency (up to 1 kHz for MPU6050) a recurringly cited drawback is the noise on measurements reducing actual resolution of 16 bit devices to 14 bits or less. The low cost of these devices allows them to be combined into arrays, however, creating kinematically redundant sensor systems. Output can be processed by averaging values from different devices to eliminate random noise, or advanced accelerometer array algorithms can be implemented. A diagram of the test bench setup is shown in figure 5.21.

Software

A PC has been chosen as data processing unit to reduce the cost of external hardware and to take advantage of Matlab as DSP platform and user control interface. Data from the accelerometer is sampled at 512 Hz and transmitted to the PC, using an FT232 UART to USB bridge well documented in literature [318]. A standard ATmega328p microcontroller was chosen to configure the accelerometer using its I^2C interface and to read out its data. Accelerometer samples are transmitted to the PC and processed in

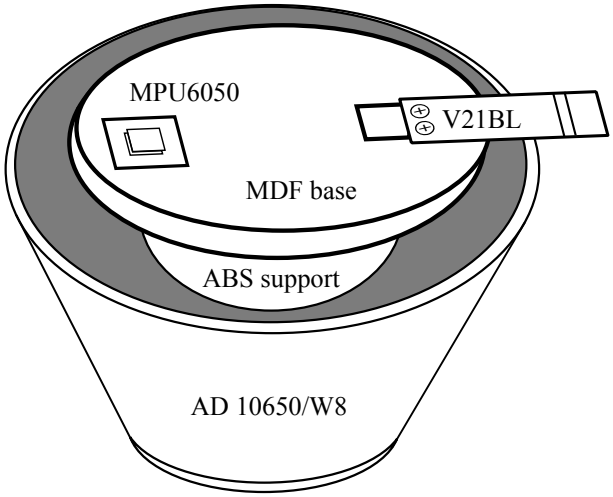

Figure 5.21: Test bench setup with subwoofer and accelerometer.

Matlab with a Fast Fourier Transformation (FFT) to extract amplitude and frequency information from a series of 512 samples (1 s data) at a time. Choosing a multiple of 2 ($512 = 2^9$) speeds up the FFT computation which benefits the response time of the control loop. Figure 5.18 shows the different hardware blocks and their respective connection protocols. An example output of the FFT operation in Matlab is shown in figure 5.22 for a 25 Hz sinusoidal signal with an amplitude of 0.35 g.

5.3.4 Design Verification

The properties of the implemented test bench must be checked and verified prior to the measurement of actual energy harvesters. It is particularly important to quantize the errors on amplitude and frequency of the asserted signal, and ensure that second order effects such as harmonics, noise and distortion are within the acceptable accuracy margins. This can be achieved by verifying the shaker's frequency response, whose irregularity is compensated in software by means of a proportional regulator. The output amplitude of the sinusoidal control signal for the shaker will automatically be adjusted to compensate for its attenuation of low and high frequencies, ideally resulting in a constant vibration amplitude regardless of the frequency. This is an essential requirement for testing since both amplitude and frequency are independent factors that influence η_h and thus must be treated as variables in the equation. An automated calibration and test routine was implemented in Matlab to generate a frequency sweep from 1 Hz up to 500 Hz with an accuracy of 1 Hz. Below a frequency of 15 Hz it was discovered that the attenuation of the shaker prohibits a satisfactory linear amplitude selection in the range from 0 to ± 3 g with a minimum accuracy of 0.01 g. However, a cut-off frequency of 15 Hz is acceptable because all commercially available cantilever piezoelectric vibration energy harvesters are designed to operate at frequencies higher than 15 Hz. An example analysis at a frequency of 25 Hz is shown in figure 5.22, with the accelerometer data in both time and frequency domain. The error on the amplitude is less than 1 % over the entire frequency spectrum between 15 Hz and 200 Hz in a range ± 3 g. Minor spectral leakage can be seen in figure 5.22 around the center frequency of 25 Hz as a result of the finite 512 sample input window for the FFT. Figure 5.23 demonstrates the frequency response from the perspective of the shaker. A near linear correlation exists between peak to peak input voltage (Vpp) and vibration amplitude for all frequencies in the 25 Hz - 200 Hz range, but the response for center frequencies (most notably 125 Hz - 150 Hz) is

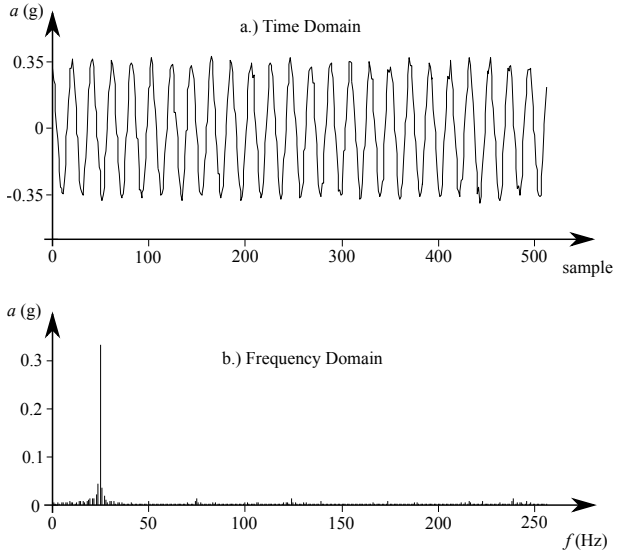

Figure 5.22: Frequency response of the subwoofer as accelerometer samples in time domain (top graph, a.) and in frequency domain (bottom graph, b.).

over three times stronger than limit frequencies for the same input Vpp. Measurements were verified with a second accelerometer of type MMA7361. The method was presented at ICRERA 2016 [318].

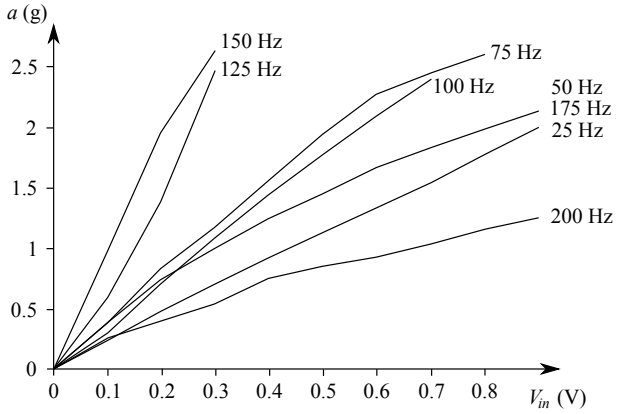

Figure 5.23: Frequency response of the subwoofer as function of the input voltage for different frequencies.

5.3.5 Harvester Parametrization

Amplitude - Frequency Sweep Analysis

With the intended operation of the test apparatus verified, actual cantilever piezoelectric vibration energy harvesters can be tested under varying vibration amplitude and frequency to determine their power output. A Matlab algorithm was developed that sweeps frequency and amplitude over independently configurable ranges with a step of choice. The function takes 6 arguments: the lowest frequency, frequency

step, highest frequency, lowest amplitude, amplitude step and highest amplitude. The generated power is then rectified and buffered with a capacitor to allow the measurement of average power instead of peak power, and finally dissipated in a digitally controlled potentiometer of type MCP4151. With a maximum voltage of 5.5 V, resistance of 100 kΩ and a resolution of 8 bits, the load can be adjusted with increments of approx. 390 Ω which is sufficiently accurate to represent the load of a real world DC/DC converter. Using the load impedance, the measured output voltage is converted in a power rating using Ohm's Law since the load is a purely resistive impedance. Figure 5.24 shows the result of a frequency and amplitude sweep for a V21BL vibration energy harvester from Mide, captured in its maximum power point (MPP) as shown in figure 5.25. Note that unlike vibration amplitude or frequency the operation point on the load line cannot be considered a true variable of η_h since the power path will often contain a form of MPPT to ensure operation in the MPP on the load line. For real world harvester applications, the power point may for this reason be excluded from η_h, simplifying Equation 5.3. The relatively constant load impedance presented to the harvester by a DC/DC converter will make a continuous load impedance sweep largely obsolete. The MCP4151 can subsequently be replaced with a constant load resistor to operate the harvester in its maximum power point without inducing errors in the power output measurements.

Modelling the Power Output

Matlab generates threedimensional diagrams as a graphical representation of the amplitude and frequency sweep data for a specified load impedance. Every load impedance results in a separate graph.

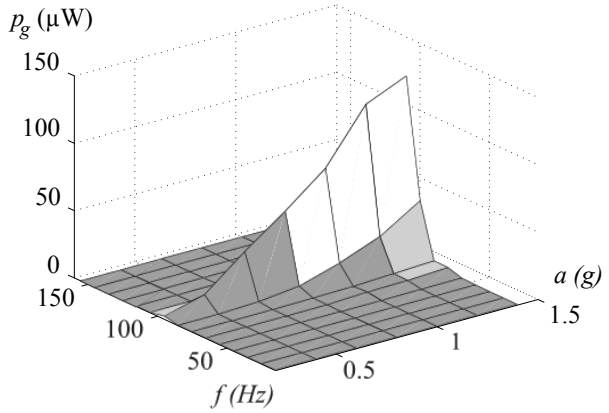

Figure 5.24: Power output of a V21BL vibration harvester as a function of vibration amplitude and frequency.

It is immediately apparent that the harvester only generates useful output power when operated at its resonance frequency or very close to it. For any other frequencies, the harvester does not produce significant output power. Before modeling η_h as a function of amplitude a and frequency f, it is a requirement to determine whether a correlation exists between a and f. Fortunately, the correlation between both variables is insignificant, determined by numerical correlation computation. It can also directly be deducted from figure 5.24 that both variables do not influence each other with statistical significance. This allows the effect of a and f to be modeled independently. For a constant load Z in the harvesters MPP, η_h can be expressed as

$$\eta_h\left(a, f, Z\right) = \frac{a}{a_0} \cdot \frac{f}{f_0} \tag{5.4}$$

with a_0 the excitation amplitude at which maximum output power occurs and f_0 the frequency at which maximum power point occurs.

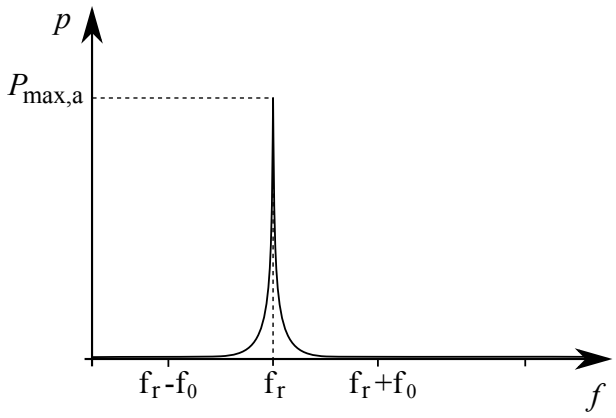

Figure 5.25: Exponential approximation of the resonance frequency f_r with maximum power output $P_{max,a}$.

At any given vibration a, the power output of the harvester resembles a narrow peak with steep slopes, shown in figure 5.25. Since this curve is a cross section of figure 5.24 across the y axis, the maximum of the curve occurs at the resonance frequency f_r with an amplitude equal to the maximum power output of the harvester at a vibration a, $P_{max,a}$. Using regression to prove curve symmetry and data point correlation, the slope approximates an exponential curve with negative exponent of the form e^{-bf} where b determines the steepness and shape (with $b > 0$), and f is the frequency variable. From the symmetry around the resonance frequency f_r the equation of the curve in figure 5.25 can be modeled as

$$P_{o,a,f} = P_{max,a} \cdot e^{-b|f-f_r|} \tag{5.5}$$

The parameter b must be obtained by calculating the equation of an exponential trend line on the slope of any cross section as seen in figure 5.25, based on experimental data points. Similarly a cross section along the x axis yields a curve representing the power output for a frequency f at any amplitude a. This curve can be approximated by a linear relation between the power output at that frequency $P_{max,f}$ and the excitation amplitude a. The equation of this curve follows directly from linear trigonometry:

$$P_{o,a,f} = P_{max,f} \frac{a}{a_{max}} \tag{5.6}$$

Expressions 5.5 and 5.6 can now be combined to obtain a model for η_h since

$$\frac{a}{a_0} = \frac{P_{o,a,f}}{P_{max,a}} = e^{-b|f-f_r|} \tag{5.7}$$

and

$$\frac{f}{f_0} = \frac{P_{o,f,a}}{P_{max,f}} = \frac{a}{a_{max}} \tag{5.8}$$

due to a and f being uncorrelated variables. Combining these equations with Equation 5.4 results in an expression for $\eta_h(a, f)$ and in turn a power output for the harvester in the model for harvester parametrization presented in [316]:

$$P_h\left(t, a, f\right) = \left[\mu_h\right]_\varsigma \left[p_h\right]_\varsigma \frac{a}{a_{max}} e^{-b|f-f_r|} \tag{5.9}$$

With all limiting factors described in datasheets or deductible from statistical analysis of benchmarking data, this equation serves as a harvester specific expression of output power as a function of vibration amplitude and frequency.

5.4 Harvester Performance Database

When performance data is collected, it is stored in the appropriate dataset per type of harvester. As such, a dataset is created for photovoltaic cells, TEGs, piezoelectric energy harvesters, and so on. Each dataset consists of the superposition of the individual harvester performance datasets. The dimensionality of harvester type dataset is the same as the individual datasets. For TEGs it is one-dimensional (temperature), for piezoelectric harvesters two-dimensional (frequency and amplitude), and for photovoltaic cells 5-dimensional (illuminance under 4 artificial light sources + natural sunlight).

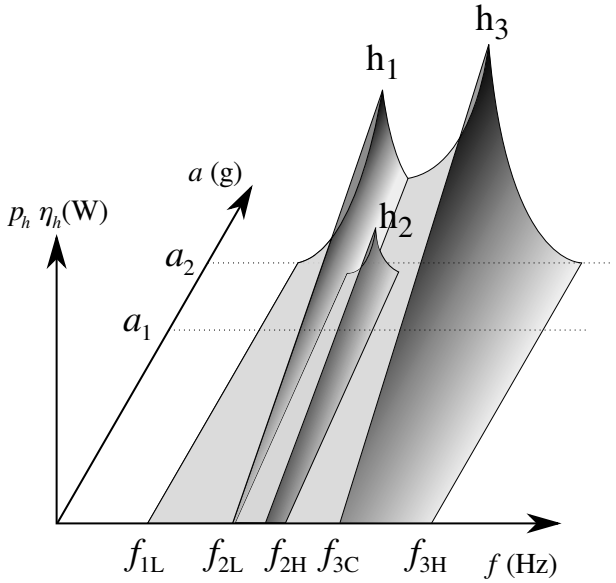

Figure 5.26: Database example for piezoelectric energy harvesters, with 3 harvesters $h_1..h_3$ displayed as overlapping point clouds.

A visual representation of the dataset for 3 piezoelectric energy harvesters is shown in figure 5.26. The x and y dimensions represent respectively vibration frequency response and amplitude response, and the z dimension is accordingly a point cloud with normalized output power $p_h\eta_h$. For each combination of frequency and amplitude, only one harvester in the dataset can have the highest $p_h\eta_h$ response, and as such, the combined dataset is a surface $p_h\eta_h(a, f)$, referred to as $D(a, f)$. In other words, $D(a, f)$ is the union of the surfaces of the individual harvester datasets. Hence, the formal definition of $D(a, f)$ is

$$D(a,f) = \begin{cases} h_1(a,f) \cup h_2(a,f) \cup h_3(a,f) \\ \\ \forall p_h^i \eta_h^i : p_h^i \eta_h^i \geq \{p_{h_1}\eta_{h_1}, p_{h_2}\eta_{h_2}, p_{h_3}\eta_{h_3}\} \end{cases} \tag{5.10}$$

Although $D(a, f)$ is defined for each value of aa and f in the range that was benchmarked, the resulting surface is not necessarily continuous or closed. This is illustrated in figure 5.26 as a comparison between

3 harvesters, of which 2 (h_1 and h_3) are able to withstand vibrations with an amplitude up to a_2, while harvester h_2 has a maximum amplitude of a_1. Since no performance data for h_2 exists for acceleration amplitudes beyond a_2, a discontinuity occurs in the surface where $f_{2L} \leq f \leq f_{2H}$ and $a = a_1$, where f_{2L} and f_{2H} are respectively the lower and upper frequency where h_2 dominates $D(a, f)$.

From a data management perspective, $D(a, f)$ is a union of points, each having 3 parameters in the case of a piezoelectric energy harvester dataset, as shown in figure 5.26:

- coordinates $\{a, f\}$;
- normalized power output $p_h \eta_h$ at coordinate $\{a, f\}$;
- harvester part number or identifier of which dataset the sample belongs to.

When the ambient environment is benchmarked, as discussed in chapter 7, and the benchmark reveals that the vibration source vibrates at a center frequency f_0 with a maximum amplitude a_0, then the most optimal harvester can be found by looking up which harvester part number corresponds to $D(a_0, f_0)$ in the vibration energy harvester dataset. Since $D(a, f)$ consists of collection of discrete points rather than a continuous function definition, it is likely that $D(a, f)$ is undefined at the exact coordinate $\{a_0, f_0\}$. In that case, cubic extrapolation can be used to find the closest best fit. Mathematically, the closest fitting harvester $h_s(a_s, f_s)$ to the environmental conditions is

$$\forall p_h^i \eta_h^i : \sqrt{(a_s - a_0)^2 + (f_s - f_0)^2} \leq \sqrt{(a_i - a_0)^2 + (f_i - f_0)^2} \tag{5.11}$$

following Pythagoras' theorem.

5.5 Conclusion

Too many different energy harvesters exist to make manual comparisons of harvester performances practical, particularly since multiple parameters must be taken into account. This chapter presented strategies to develop low cost benchmark apparatus for the most promising 3 types of energy harvesters: PV, TEGs and piezo. The automated benchmarking procedures are characterized by a better repeatability than would be the case with manual performance testing, and the digital interfaces allow measured datasets to be integrated directly into a centralized harvester performance database. Only little manual intervention remains necessary when harvesters need to be connected to the benchmark apparatus.

After combining datasets of multiple energy harvesters, the most optimal harvester type for a specific environment can be selected automatically based on environmental benchmarking data, obtained with the Ambient Energy Monitor discussed in chapter 7.

Chapter 6

Power Path

There are few practical scenarios in which an energy harvester can directly be connected to a load, simply because a typical energy harvester is far from an ideal voltage source. The output power of an energy harvester is either too high, too low, too irregular or has too much ripple to be eligible as a direct power source for systems with high demands regarding power supply. Every electronic design powered by energy harvesters inevitably requires circuitry for power conversion, be it increasing or decreasing the voltage, adapting input to output impedances, or storing energy for future use. The collective circuit design responsible for extracting power from one or more energy harvesters and generating the necessary voltage rail for an electrical or electronic system, is called the systems *power path*. The power path can be split into 3 major blocks:

1. harvester power extraction, optionally with maximum power point tracking;
2. energy storage and monitoring;
3. power conversion, voltage and/or current regulators.

Harvester power extraction, featuring specialized ICs for energy harvesting purposes, is covered in the next chapter. The purpose of this chapter is to explore energy storage and power conversion strategies specifically useful to energy harvesting. It may undoubtedly be tempting to simply throw an integrated power path controller onto the PCB, like the famous AXP209 for example, but these solutions are designed to be *as general purpose as possible* which is also their weakness: they contain undesired functionality that still consumes power, which can be saved by composing the critical components of the power path more carefully.

6.1 Energy Storage

6.1.1 Motivation

In a complementary balanced system, the combined power production of all connected harvesters is at any time greater than or equal to the power consumption of the embedded electronic system, as discussed in chapter 3. When using a single harvester, this axiom implies that the harvester must generate at any time the power required to supply the system. If the amount of available environmental energy is highly discontinuous however, or exhibits significant amplitude variations over time, calculation of the required harvester will yield large harvester sizes to satisfy the energy balance equations. Consider as example trajectory scanners on a highway, which are deployed to catch speeding vehicles by measuring the time they take to travel a fixed distance and calculate their average speed. These systems are

equipped with a camera to capture license plates and identify individual vehicles, and often deployed on highway overpasses and bridges, or other places where power is not readily available or would require substantial infrastructure work. Powering them with energy harvesters makes maintenance and deployment cheaper but also more effective since they can be easily moved to new locations. To power such scanners, there are 3 obvious candidates: solar, wind, and vibrations from vehicles. Each of these are unfortunately discontinuous:

- *Solar cells* generate power efficiently during the summer months at day time, but generate very little at night unless they are in the direct proximity of a street lamp. In winter, there is a risk of being covered by snow for multiple consecutive days.
- *Wind turbines* only generate power when wind is available, which is also during day time when heat from the sun causes pressure differences and air to flow from high to low pressure zones. Fewer wind is available at night or when the area is in the center of a high or low pressure zone.
- *Vibration harvesters* only generate power when a vehicle is passing at a sufficient speed to generate vibrations. In case of a traffic jam, many vehicles will pass but little power will be produced.

Evidently, complementary balanced energy harvesting is the solution here: by combining the different harvesters, reliability of the system will improve since scenarios in which all harvesters fail to produce power simultaneously are less likely to occur. For example, when the solar cells are covered by fallen leaves in autumn or by snow in winter, the wind turbine or vibration harvester can complement to supply power to the system. With each harvester added, the reliability in a probability distribution function (PDF) shifts right, decreasing the probability of system failure due to failure of all harvesters simultaneously (assuming there is no correlation between the harvesters, which there is in reality: PV and wind are both related to the sun etc.). Each added harvester also adds an additional cost to the system design, so the marginal utility of each added harvester decreases since its added cost remains as high as the previously added harvesters, but the right shift in the probability distribution function is smaller. Depending on the system, its power consumption and requirements, it may require impractically large (and expensive) harvesters to get far enough to the right in the probability distribution function to achieve a $99.\overline{9}$ % reliability (however many digits are required for the application). In these situations, instead of adding more harvesters, it is likely beneficial to add local storage instead.

6.1.2 Electrical Storage

When energy storage is discussed in this chapter, the term is constrained to electrical energy storage, and disregarding any other types of local storage. A well known example of non-electrical storage is heat storage, where a medium with a high thermal capacity such as water is heated or cooled when it is in a hot resp. cold ambient environment, and then transported to an environment with different ambient temperature. The temperature difference between the heated or cooled medium and the ambient temperature can then be converted back into electrical energy with a TEG or PEG energy harvester. This technique is used in aviation industry, where aircraft components are routinely exposed to large temperature differences. A TEG can also be used as TEC to actively heat or cool the medium, but with a TEG/TEC efficiency of 6-8 % this is hardly an energy efficient approach. Another option is the combination of a hydrogen fuel cell and electrolysis cell, using hydrogen as storage. Although such a system complies to the definition of a battery (since electrical energy can be converted in hydrogen through electrolysis and back to electrical energy in the fuel cell), it is inconvenient because of the difficulties of hydrogen gas storage. Research is ongoing to store the hydrogen as metal hydrides instead of in a gaseous form, but the technology is not yet to the point where it can be considered reliable enough to power an autonomous electric or electronic system for more than 15 years without maintenance. The

only technologies which can potentially provide this order of magnitude of longevity are EDLCs, solid state batteries and secondary chemical cells (i.e. rechargeable batteries).

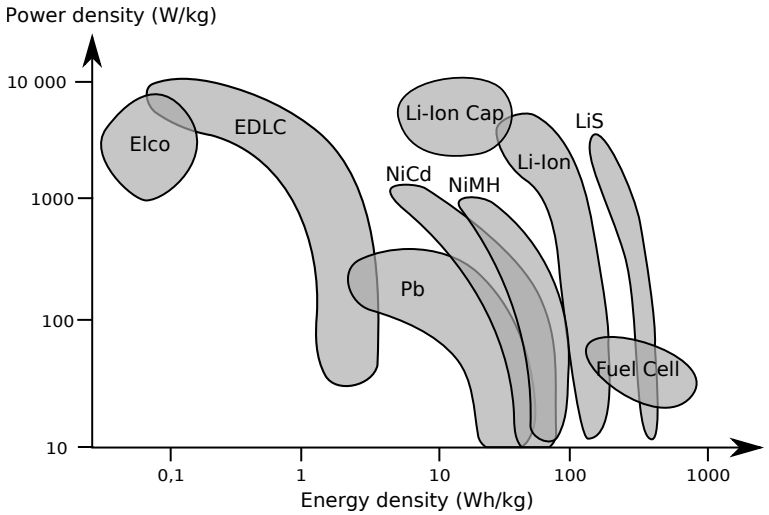

Figure 6.1: Ragone chart comparing power density and energy density for different energy storage devices. Elcos refer to aluminum electrolytic capacitors or tantalum capacitors [291, 141, 164, 110, 21, 214, 114, 228].

6.1.3 EDLC

Electrolytic Double Layer Capacitors have long been sought after as an energy storage solution combining the capacity of traditional rechargeable batteries and the longevity of and high charge/discharge rate of regular electrolytic capacitors. EDLCs can have an energy efficiency of up to 95 % and a power density of 300-500 W/kg [201]. The energy density is between traditional electrolytic capacitors (elcos) and batteries, ca. 3-5 Wh/kg [201]. The position of EDLCs in a Ragone chart is shown in figure 6.1. EDLCs are commonly used in applications where either a rapid discharge is required (peak current supplier in a defibrillator for example) or where rapid charging is necessary (to recover braking energy from electric vehicles etc.). Aside from high power applications, they are also interesting for electronic systems powered by energy harvesters as an energy storage medium, for 7 reasons:

- They do not require a charge curve to be followed, nor can they be charged too fast. Charging can be done with a simple switched mode regulator to match the impedance of the energy harvester(s) to the very low input impedance of the EDLC.
- EDLCs can not be overdischarged, an UVLO (under voltage lock-out) can be omitted.
- Life time is measured in time rather than number of charge/discharge cycles, it is only affected by overcharging and temperature.
- EDLCs have a rated voltage of 2.7 V or 5.5 V, which are convenient values to operate switched mode regulators from.
- EDLCs do not have a liquid electrolyte that can freeze, and thus perform well in subzero environments (i.e. outdoors in winter).
- EDLCs can be constructed from environmentally friendly materials (for example, the carbon used in commercial capacitors is made from coconut shells [16]), and can be disposed without hazards.
- The lack of a liquid electrolyte allows EDLCs to be hermetically sealed, improving their ruggedness.

As with regular electrolytic capacitors, an EDLC rarely undergoes catastrophic failure under normal operational conditions but rather experiences a degradation of performance. An EDLC is considered end-of-life (EoL) if its rated capacity has decreased by 20 % or if its ESR has increased by 200 %, whichever comes first [171]. However, both problems can be dealt with at design time. Table 6.1 shows a comparison of several EDLCs suitable for energy harvesting applications.

The EDLCs listed in table 6.1 are all commercially available types, ranging in capacitance between 33 mF and 3.4 kF. The maximum working voltage determines the amount of energy that can be stored, calculated in J. Exceeding the maximum working voltage rapidly decimates lifetime, so the given values for V_{max} are hard limits. Leakage current is a determining factor for self discharge and thus critical for energy storage applications over a longer period, but a function of temperature and thus can not be listed as a scalar point in the table. To provide a comparison with better known batteries, the equivalent capacity of a 3.6 V Lithium Ion battery is also shown in Ah. EDLCs with an energy storage capacity equal to Lithium Ion batteries are commercially available, though replacement is not always economically feasible. For example, the Maxwell BMOD0500 with a capacitance of 500 F and working voltage of 16 V is roughly the equivalent of 2 Lithium Ion 18650 cells (2 x 2.5 Ah), but the cost of this EDLC bank is ca. 400 EUR. On the other hand, the closest equivalent to the 268 mAh Lithium Ion battery in the Influencair example below is the Cornell EDLSD334V5R5C EDLC, with a cost of 70 cents in volumes of 1000 pcs, which is less than the actual battery would cost. This of course assumes the EDLC could be completely discharged, which is not the case in practical circuits. Nonetheless, the comparison indicates that EDLCs can be a practical and economically viable alternative to batteries, with the advantages listed above. [185]

Table 6.1: Comparison of EDLCs for local energy storage. Last column showing an equivalent battery capacity for a 3.6 V Lithium Ion battery.

Device	Manufacturer	V_{max}	Capacitance	ESR	Energy	Bat. Eq.
BZ055A333ZSB	AVX	5.5 V	33 mF	250 mΩ	0.5 J	39 μAh
DSK-3R3H224U	Elna	3.3 V	220 mF	200 Ω	1.2 J	93 μAh
KR-5R5C104-R	Eaton	5.5 V	100 mF	75 Ω	1.5 J	116 μAh
EEC-F5R5H104	Panasonic	5.5 V	100 mF	100 Ω	1.5 J	116 μAh
EDLF104A5R5C	Cornell	5.5 V	100 mF	100 Ω	1.5 J	116 μAh
EDLSD334V5R5C	Cornell	5.5 V	330 mF	75 Ω	5.0 J	386 μAh
JUWT1155MPD	Nichicon	2.7 V	1.5 F	3 Ω	5.5 J	424 μAh
ESHSR-0003C0	NessCap	2.7 V	3 F	55 mΩ	11 J	849 μAh
BCAP0003	Maxwell	2.7 V	3.3 F	290 mΩ	12 J	926 μAh
DH-5R5D105T	Elna	5.5 V	1 F	30 Ω	15 J	1.2 mAh
FT0H105ZF	Kemet	5.5 V	1 F	3.5 Ω	15 J	1.2 mAh
ESHSR-0005C0	NessCap	2.7 V	5 F	35 mΩ	18 J	1.4 mAh
BCAP0005	Maxwell	2.7 V	5 F	170 mΩ	18 J	1.4 mAh
HV0830-2R7605	Eaton	2.7 V	6 F	40 mΩ	22 J	1.7 mAh
EEC-S0HD224V	Panasonic	5.5 V	220 mF	75 Ω	33 J	2.5 mAh
BCAP0010	Maxwell	2.7 V	10 F	75 mΩ	36 J	2.8 mAh
PAS1220LA3R0905	Taiyo	3 V	9 F	200 mΩ	41 J	3.2 mAh
MAL222090003E3	Vishay	2.7 V	15 F	30 mΩ	55 J	4.2 mAh
HV1325-2R7156	Eaton	2.7 V	15 F	30 ,mΩ	55 J	4.2 mAh
JUMT1226MHD	Nichicon	2.7 V	22 F	200 mΩ	80 J	6.2 mAh
SCCU25B256MRB	AVX	2.7 V	25 F	27 mΩ	91 J	7.0 mAh
HV1625-2R7256	Eaton	2.7 V	25 F	27 mΩ	91 J	7.0 mAh
256DCN2R7Q	Illinois	2.7 V	25 F	30 mΩ	91 J	7.0 mAh
HB1635-2R5356	Eaton	2.3 V	35 F	30 mΩ	93 J	7.2 mAh
EEC-HW0D506	Panasonic	2.3 V	50 F	100 mΩ	132 J	10 mAh
ESHSR-0050C0	NessCap	2.7 V	50 F	14 mΩ	182 J	14 mAh
BCAP0050	Maxwell	2.7 V	50 F	20 mΩ	182 J	14 mAh
MAL219691214E3	Vishay	5.6 V	15 F	2.4 Ω	235 J	18 mAh
JUWT1826MHD	Nichicon	2.7 V	82 F	100 mΩ	299 J	23 mAh
XV3550-2R7307	Eaton	2.7 V	300 F	4.5 mΩ	1.09 kJ	84 mAh
BCAP0350	Maxwell	2.7 V	350 F	3.2 mΩ	1.28 kJ	99 mAh
BCAP0650	Maxwell	2.7 V	650 F	800 μΩ	2.37 kJ	183 mAh
BCAP3000	Maxwell	2.7 V	3 kF	290 μΩ	10.9 kJ	841 mAh
BCAP3400	Maxwell	2.7 V	3.4 kF	280 μΩ	12.4 kJ	957 mAh
BMOD0500	Maxwell	16 V	500 F	2.1 mΩ	64 kJ	4.94 Ah

Output Regulation

Since the voltage over an EDLC is proportional to the charge it holds, large voltage variations will result from changes in state-of-charge (SoC). For EDLCs with a V_{max} of 2.7 V, a boost regulator is necessary to raise the voltage level to the 3.3 V typically required by modern embedded systems. Of particular importance is the cold start voltage, which is the minimum voltage necessary to start the boost regulator. General purpose regulators like the ISL9111 from Intersil (0.9 V), MCP1640 from Microchip (0.8 V) and TPS61220 from Texas Instruments (0.7 V). Boost efficiency drops with the input voltage, so it is usually not profitable to discharge EDLCs below half their rated voltage, i.e. 1.35 V for 2.7 V rated EDLCs, since at 1.35 V only 25 % of the total maximum energy will remain. Because of the low output impedance of EDLCs, a boost regulator may be connected directly. The drawback of this approach is that, if the EDLC is completely discharged (0 V), the system will not start up until the EDLC is charged to the minimum voltage (i.e. 0.7-0.9 V. An intelligent (switched) power path architecture may circumvent this shortcoming.

Power Regulation

A key feature of EDLCs is that they are capable of delivering a higher power output regardless of SoC or temperature, unlike batteries. This property qualifies them for systems which draw high peak power. Due to the low V_{max} of EDLCs it is not possible to power high current loads directly from EDLCs because the resistance in the circuit will limit the maximum current drawn. Boosting the EDLC voltage to higher voltage levels seems a trivial solution, as explained in the previous section for electronic loads, but the output power of monolithic boost controllers is limited to 1-2 A maximum. To provide higher power levels, a more complex solution is required. Consider as example the ventilation exhaust of the containment building of a nuclear power station. Under normal operation it remains open to allow air circulation, but the exhaust is at any moment monitored for ionizing particles by a geiger counter, which could be an autonomous system powered by energy harvesting (by solar power outside, or the kinetic energy of the airflow itself). As a small embedded system with only a solid state geiger counter, a voltage reference and threshold detection comparator circuitry (and possibly an optional RF transceiver to signal the control room), the power consumption is low enough to implement the power path between EDLC and embedded system with a single boost regulator, as discussed above. However, when radioactive contamination of the exhaust air is detected, it is essential that the exhaust is closed as fast as possible to avoid release of radioactive materials into the environment. To close off the exhaust, an aperture or iris driven by a BLDC motor can be implemented, drawing a power up to 50 - 60 W for a duration of a few 100 ms. BLDC motors in this power class operate at at least 12 V, so a power path needs to be implemented that is able to boost the 2.7 V EDLC voltage to 12 V with an output power of at least 50 W. A solution is presented below.

Voltage Booster

Two distinct strategies for high power voltage boosters from EDLC sources were attempted to satisfy the requirements listed above: an isolated converter using a custom transformer, and a synchronous polyphase flyback converter. A functional comparison between the two is shown in figure 6.2.

The isolated converter measures the current through the primary winding of the transformer for current control feedback, and output voltage coupled back with a linear optocoupler for voltage control feedback. The transformer is custom designed specifically for this application, and constructed by specialized transformer manufacturer Ranlo Corp, with a primary/secondary winding ratio of 1:25 and a

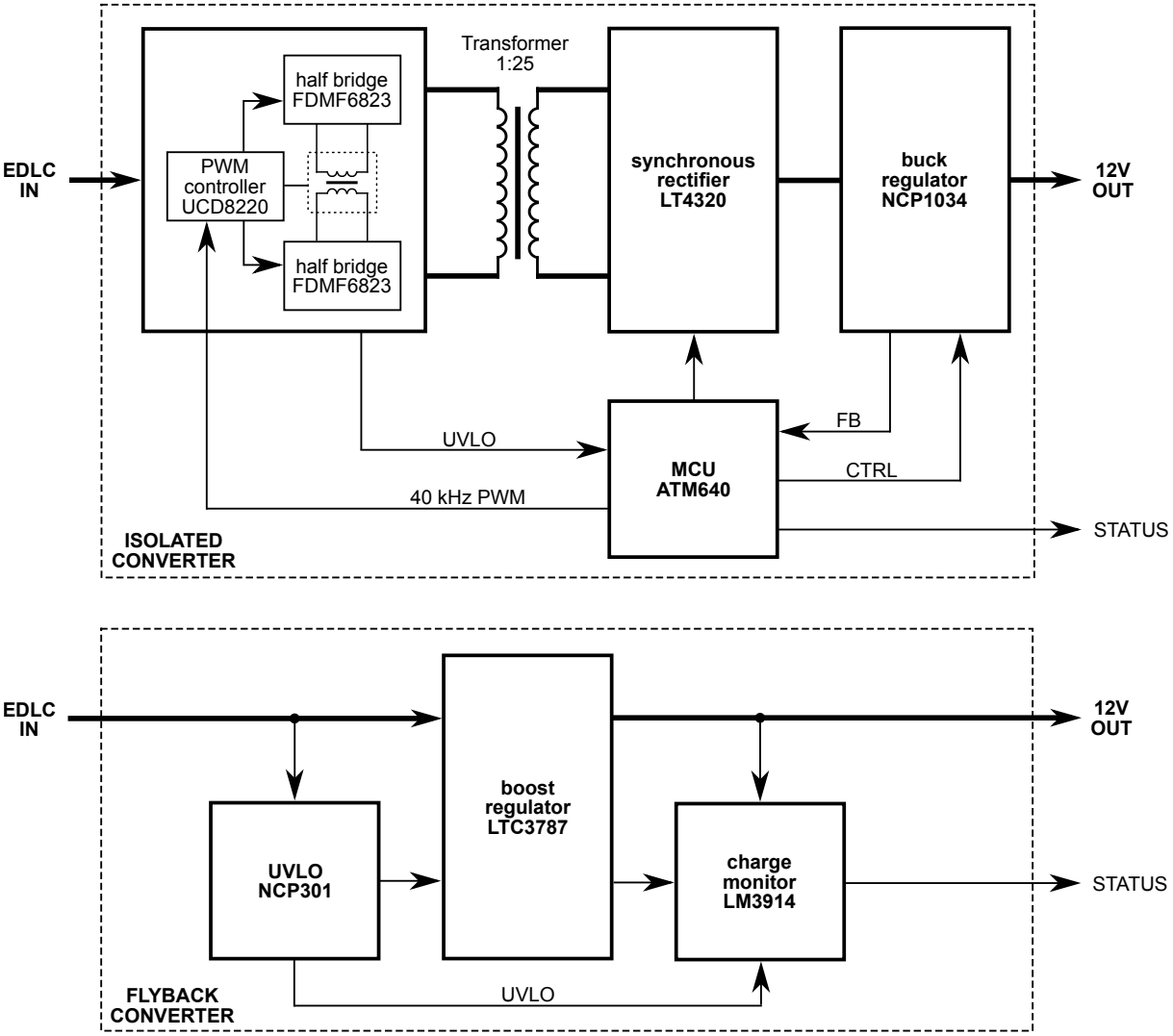

Figure 6.2: Block diagrams of isolated converter with transformer (top) and synchronous polyphase flyback converter (bottom).

rated primary current of 22 A. It is driven in a full bridge consisting of 2 integrated half bridges and at a PWM frequency of 40 kHz. Control is implemented in a general purpose microcontroller to make output voltage and related functionality adjustable in software. The secondary winding of the transformer is rectified using a synchronous rectifier followed by an optional buck stage for lower output voltages, and a 2nd order LC filter for ripple suppression. The design is shown in figure 6.3.

During development it became evident that such an approach is inefficient: the cost of the components (most notably the custom high frequency (pulse) transformer and current transformer) in combination with the relative size of the design, reduce the usefulness in practical energy harvesting applications. It was decided that a cost/size trade-off in favor of a smaller and cheaper design that operates from 2 to 4 EDLC cells rather than a single EDLC cell would be beneficial. This led to the development of the second approach, using a synchronous polyphase flyback converter. This design swaps out the microcontroller from the isolated converter for 2 separate integrated switched mode regulator controllers: a dual phase

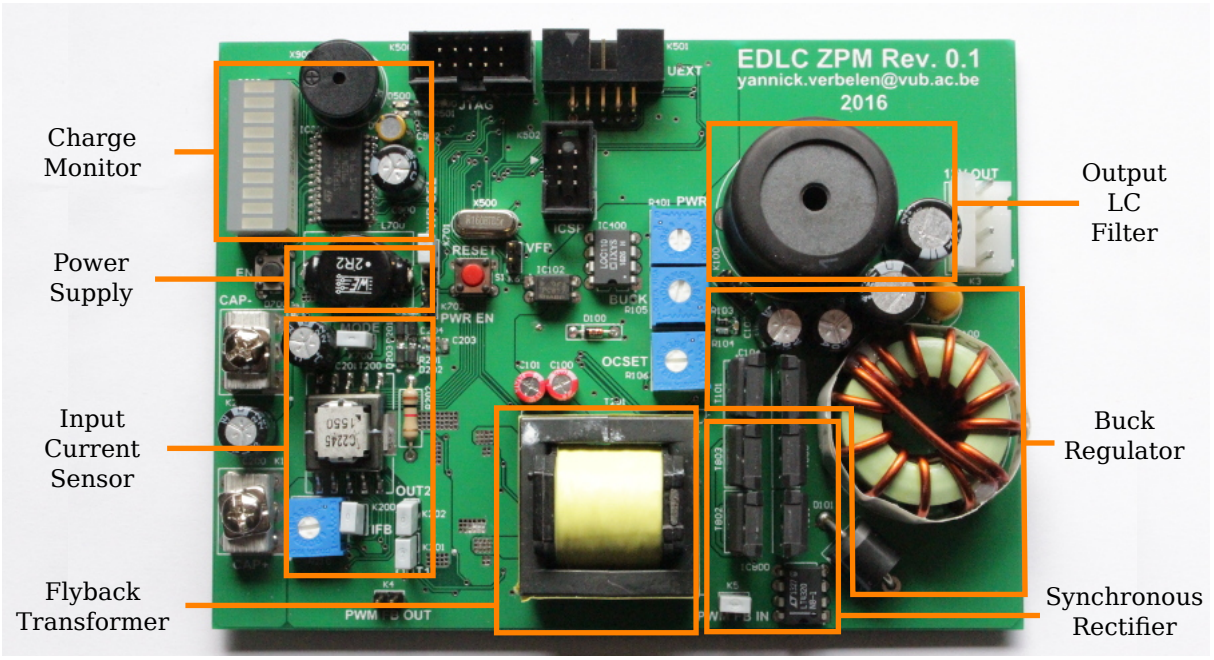

Figure 6.3: First prototype of the EDLC voltage booster. From left to right: LED bar for visual charge indication and controller, local 5 V buck regulator, input current transformer and rectification, custom Ranlo flyback transformer, N-MOSFET synchronous rectifier, single channel buck regulator with push-pull N-MOSFET power stage and passive flyback diode, and LC output filter. For hardware reference and BOM, see Appendix A.

PWM controller with integrated current and voltage feedback operating down to 2.5 V input voltage, but with a cold start of at least 4.5 V. To improve performance, a second buck-boost regulator with integrated power switches is added, allowing cold start-up from 1.5 V. The chosen chipset is a combination of a Linear Technology LTC3787 and a Texas Instruments TPS55065, along with logic for dynamic support of 2, 3 and 4 EDLC cells in series. The synchronous dual phase flyback regulator circuit is shown in figure 6.4.

To reduce cost, the current transformer from the first attempt was swapped for a much cheaper 4 mΩ shunt resistor to allow direct current feedback without requiring additional passives for current transformer signal conditioning. The output voltage is set through a voltage divider and configurable by a trimpot. Because of the higher switching frequency (800 kHz instead of 40 kHz), the peak current through the inductors and MOSFET switches is smaller and more easily handleable, standard power inductors of 5.6 μH can be used in combination with a push-pull N-MOS bridge using PSMN95 power MOSFETs.

For cold start-up, the TPS55065 implements a standard buck-boost regulator with start-up voltage of 1.5 V, boosting it to a 5 V supply voltage for analog and digital circuitry as well as the LTC3787. A single 33 μH power inductor with 1 A current rating and 2 4.7 nF capacitors for a dual mode charge pump are sufficient for operation. The schematic diagram is shown in figure 6.5.

Two versions were designed, the first version supporting only 2 EDLC cells in series (input voltages between 1.5 V and 5.5), while in the second version support for 3 and 4 cells in series was added, as well as additional circuitry for a more graceful shutdown at UVLO around 1 V. A rotary switch was added to

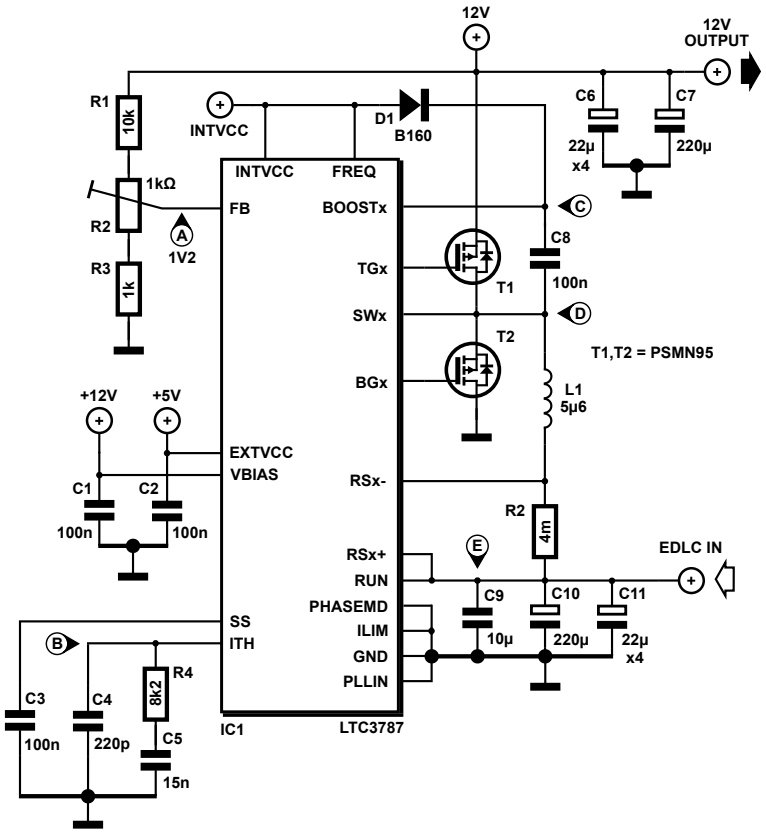

Figure 6.4: Synchronous boost converter stage based on Linear Technology's LTC3787 controller, featuring constant voltage control (feedback input, point A) and constant current control (shunt resistor R2). There are 2 identical channels 180° out of phase, and the pins duplicated in the second channel are marked with an **x**: BOOSTx, TGx, SWx, BGx and the differential shunt inputs RSx. T2 acts as the primary switch to charge up inductor L1, and T1 acts as a synchronous rectifier (ideal diode) to decrease losses in the usual flyback diode. D1 and C8 form a bootstrap circuit to allow a half bridge with all 2 N-channel MOSFETs.

set the number of cells connected at the input, and the visual charge indicator was also adjusted to operate with different cells in series. A standard multicolor LED bar driven by an LM3914 was chosen for this purpose to replace the LM3916 from the first version. In the transformer based design, the same LED bar was driven directly from the controlling microcontroller. Both board revisions are shown in figure 6.6.

6.1.4 Solid State Battery

Solid state batteries differ from classic rechargeable batteries because, as the name suggests, both the electrodes and electrolytes are in a solid state. High ionic conductivity minimizes internal resistance of the battery, which improves its power density, while at the same time high resistance reduces the self-discharge rate of the battery. Both properties are particularly favorable for energy harvesting applications.

As shown in table 6.2, solid state and thin film batteries (terms used interchangeably by manufacturers) are less prominently available in the market than their EDLC or traditional battery counterparts, in fact there are only a handful of manufacturers who have released commercial solid state or thin film batteries

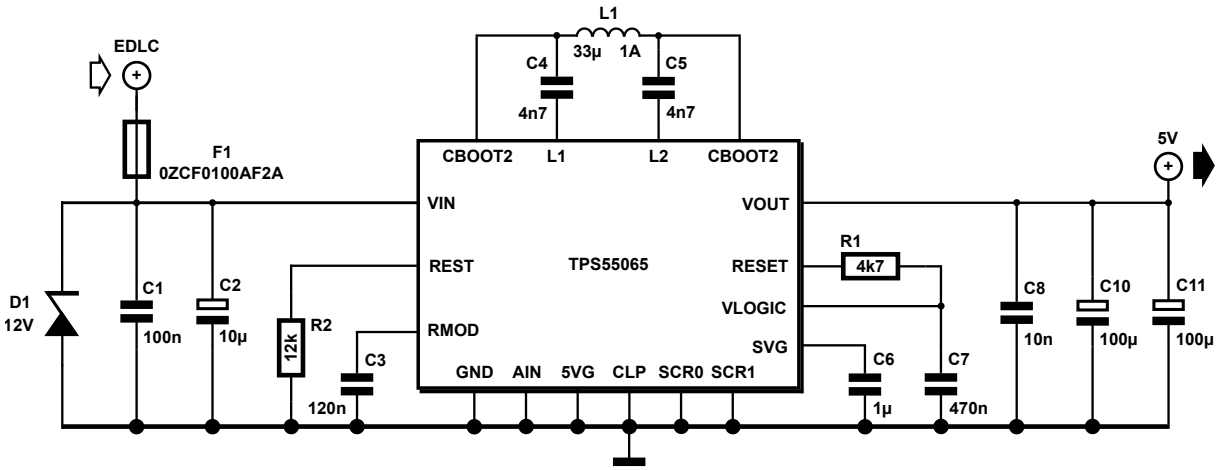

Figure 6.5: Buck-boost regulator built around the Texas Instruments TPS55065 switched mode controller with integrated H-bridge. Capacitors C4 and C5 are part of a dual bootstrap circuit for an N-channel H-bridge. Booststrap diodes are integrated in the IC.

to date. A distinction should be made here between true thin film batteries, which are made with thin film manufacturing processes (as opposed to thick film processes), rather than traditional batteries which are made "thin" to fit into modern handheld devices. Since solid state batteries do not degrade as much per charge/discharge cycle as traditional batteries, the life time can exceed 10 000 cycles for thin film cells, and Cymbet even claims up to 100 000 cycles until the point of 20 % capacity degradation. Cymbet is the only manufacturer to date who has released commercial on-die energy storage using a standard silicon semiconductor process, and their batteries are also packaged in a surface mount (reflow compatible) chip package. From a power path perspective, the 2 most important drawbacks of solid state and thin film batteries is that they do have an UVLO voltage that needs to be respected, and their ESR is 2 to 3 orders of magnitude higher than EDLCs of comparable capacity. The introduction of printed thin film batteries may initiate a revival of solid state batteries, but so far it appears the technology is stagnant and losing to EDLC technology which is developing more rapidly. With the notable exception of ST Microelectronics, which have released a single solid state battery (the EFL700A39) in 2014, few new battery types are released to market, and Infinite Power Solutions (IPS) in particular has completely vanished from the sector although their Thinergy series of solid state batteries has been used in designs powered by energy harvesters [22, fig. 2][303].

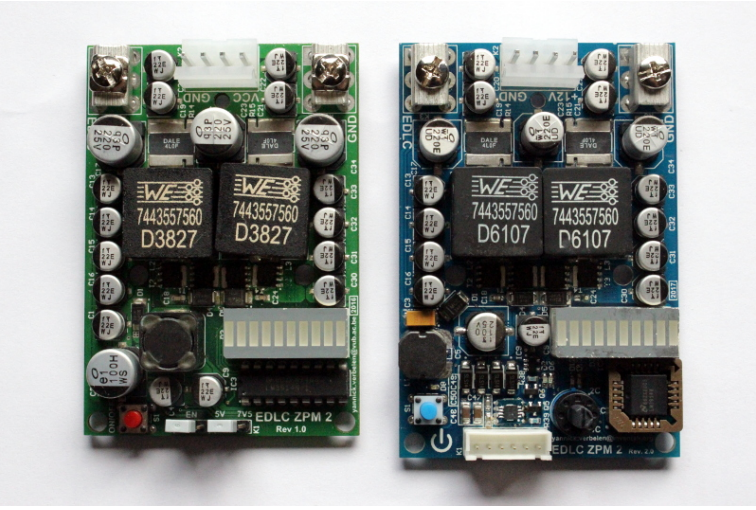

Figure 6.6: Transformerless ELDC booster prototypes. Rev. 1.0 (left) requires manual configuration with jumpers at the bottom of the board. Improved version Rev. 2.0 (right) features automatic range adjustment, rotary switch for cell configuration, and JST output connector for digital and analog control. Charge controller is a PLCC on the lower right of the board.

Table 6.2: Comparison of solid state and thin film batteries.

Device	Man.	V	Charge	ESR	Energy
CBC3112-D7C-TR1	Cymbet	3.3 V	12 μAh	10.7 kΩ	143 mJ
CBC012-D5C	Cymbet	3.8 V	12 μAh	10.7 kΩ	164 mJ
CBC3150-D9C-TR1	Cymbet	3.3 V	50 μAh	2.3 kΩ	594 mJ
CBC050	Cymbet	3.8 V	50 μAh	2.3 kΩ	684 mJ
MEC225	IPS	4.1 V	0.13 mAh	260 Ω	1.8 J
MEC220	IPS	4.1 V	0.4 mAh	120 Ω	5.5 J
EFL700A39	ST	3.9 V	0.7 mAh	100 Ω	9.8 J
MEC201	IPS	4.1 V	1 mAh	45 Ω	14 J
MEC202	IPS	4.1 V	2.2 mAh	20 Ω	32 J
UMAL201421A012TA01	Renata	2.3 V	12 mAh	200 mΩ	99 J
452229-14XT	BrightVolt	3.0 V	14 mAh	50 Ω	151 J
452229-17XT	BrightVolt	3.0 V	19 mAh	60 Ω	205 J
452229-25XT	BrightVolt	3.0 V	25 mAh	75 Ω	270 J
CP042350	Renata	3.0 V	25 mAh	30 Ω	270 J
452229-35XT	BrightVolt	3.0 V	35 mAh	35 Ω	378 J
454523-35XT	BrightVolt	3.0 V	35 mAh	35 Ω	378 J

6.1.5 Secondary Chemical Cells

Secondary chemical cells, colloquially known as rechargeable batteries, have been used to power wireless electronic devices as a stand-in for non-rechargeable batteries, often by consumers who remove batteries in standard form factors (AA, AAA etc.) and recharge them in dedicated chargers before returning them to duty. NiMH batteries remain popular in this role, because their 1.2 V cell voltage is close enough to traditional alkaline batteries (1.5 V) to operate as a stand-in without requiring modifications to the power path circuits [26]. NiMH batteries have the advantage that they do not suffer from degrading performance from deep discharge (the so-called *memory effect*), and are tolerant to overcharge and overdischarge conditions. The cell voltage of 1.2 V is also their most significant drawback however, since a single cell is too close to the UVLO threshold of most boost regulators to offer a reasonable reliability interval of operation. A few specialty applications like the *Joule Thief* aside, requirements in practical designs will impose a minimum of 2 NiMH cells in series to achieve a more reasonable 2.4 V nominal voltage for the boost circuitry of a power path. While series connections of chemical cells do not pose problems in steady state operation, the recharging process is made more difficult because of the requirement for cell charge balancing: to maximize the life time of rechargeable batteries in a battery pack, they should ideally be maintained at equal SoC. For removable rechargeable batteries in products like TV remote controls, the problem is solved by the external battery charger which can charge the individual cells separately up to their maximum charge, after which they are returned to their device as part of a maintenance cycle. For autonomous systems, this kind of maintenance is undesirable of course, and thus the on-board power path needs to take care of cell balancing itself during the charge process. In its simplest form, such a battery management system (BMS) consists of a switch matrix and charge pump to transfer charge from one cell to another, or a shunt in parallel to each cell to discharge the highest charged cells to the same level as the lowest charged cell. Because of the limited efficiency of cells (typically 80 % - 90 %), each transfer of charge inevitably wastes energy, which may be acceptable if the charger is powered by a mains outlet, but not when an (expensive) energy harvester supplies the input power. This is one of the 2 reasons why lithium ion batteries have become popular in wireless devices, the other being their higher power and energy density. The nominal cell voltage of most lithium ion batteries is 3.6 V to 3.7 V or equivalent to 3 NiMH batteries in series. This allows series of NiMH cells to be replaced by a single Li-Ion cell in most applications. Unfortunately, Li-Ion batteries do suffer from abuse like overdischarge, overcharging and overheating, so a battery management circuit is necessary to keep charge and discharge under control in order to maximize the life time of a lithium ion battery. With the notable exception of the 18650 form factor, unlike alkaline and NiMH batteries, there have never been standards defined for form factors of lithium ion batteries, and their ease of construction makes them available in every shape and size imaginable. This offers opportunities for system design, since lithium ion batteries can quite literally be shaped to fit into an enclosure instead of the traditional way of designing an enclosure around (a set of) AA or AAA batteries. Table 6.3 lists battery chemistries rather than commercial devices.

Table 6.3: Comparison of secondary chemical cell types with wet electrodes. Self discharge is indecated per month.

Chemistry	Cutoff V	Nom. V	Max. V	E. Efficiency	Wh/kg	Cycles	Self-discharge
NiZn	0.85 [346]	1.65 [332]	1.85 [95]	80 % [123]	60 [123]	100	<20 %
NiFe	1.2 [215]	1.4 [190]	1.65 [190]		25 [9]	5000	20-40 %
NiH_2	1.0 [281]	1.55 [6]		65 % [230]	65 [233]	20000	
NiMH	0.9 [168]	1.2 [168]	1.4 [168]	75 % [139]	80 [201]	1000	30 %
LiS	1.7 [78]	2.5 [78]			500 [286]	1500	<5 %
$LiCoO_2$	2.5	3.7 [297]	4.2	90 % [139]	150 [297]	750	5-10 %
$LiFePO_4$	2.0	3.3 [139]	3.65	95 % [139]	130 [201]	2000	3 % [59]
$LiMn_2O_4$	2.5	3.7 [139]	4.2	90 % [139]	150	500	2-10 % [60]
$LiNiCoAlO_2$	3.0 [268]	3.6	4.3 [54]		220	1250	5-10 %
$LiNiMnCoO_2$	2.5	3.6	4.2		205	5000	

Although toxicity is relative when it comes to batteries, there is a medical consensus on the effects of the metals and compounds used in the batteries listed in table 6.3. Since every battery needs to be disposed of eventually, toxicity of its compounds should be one of the decisive factors when choosing a battery type. For example, lithium based batteries are considered of low toxicity to the environment, lithium compounds do not accumulate in the human body and therefore, unless large quantities are ingested, acute cases of lithium poisoning are rare. It is routinely prescribed as part of bipolar disorder treatment, and considered safe in most conditions. Unfortunately, lithium ion batteries often contain other compounds (manganese and cobalt oxides) which are far more harmful. Lithium iron phosphate batteries, with a $LiFePO_4$ cathode and graphite cathode, are considered the safest since $LiFePO_4$ is practically insoluble in water (and thus not absorbed by living organisms). Lithium iron phosphate batteries therefore deserve a strong preference, and are the *de facto* recommended battery chemistry in this thesis. [205, 274, 4]

Nickel, on the other hand, is a known carcinogenic metal and associated with increased risks of lung and breast cancer, cardiovascular diseases, elevated blood pressure, kidney failure, and a variety of neurological problems. In metallic form (as used in coins etc.) it does not pose much harm because it has a low solubility, and thus low absorption in the body. However, nickel batteries contain the much more soluble nickel oxide hydroxide, which is also faster absorbed in the blood stream where radicalization leads to oxidative damage. Although nickel batteries are still widely used, they should be generally avoided in favor of lithium iron phosphate batteries. [62, 73, 85, 15, 100, 14]

Since the extreme toxicity of cadmium has never been in question, NiCd batteries were deliberately omitted from the comparison in the table above.

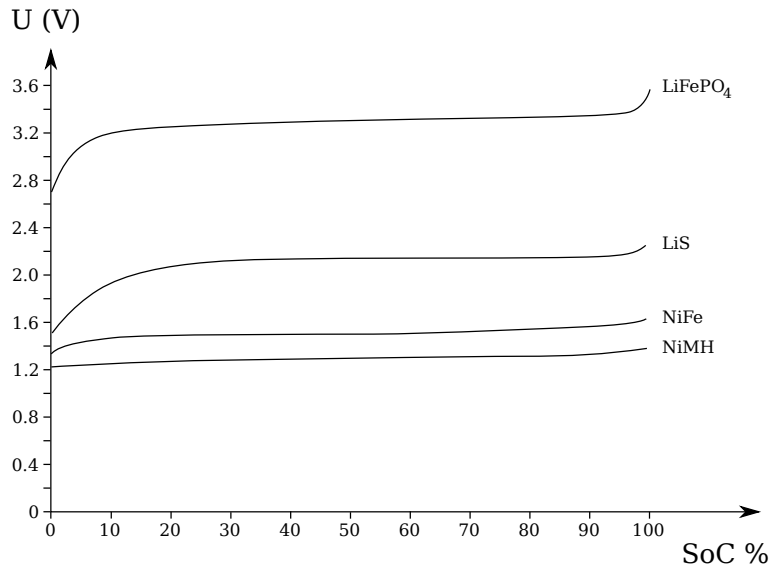

Figure 6.7: Typical discharge curves for popular secondary cell types: $LiFePO_4$, NiFe, LiS and NiMH. [299, p. 639, fig. 11][278, p. 34, fig. 5][239, p. 270, fig. 1][344, p. 109, fig. 3]

Primary chemical cells, i.e. non-rechargeable batteries, are not discussed here because they offer no perspective of long term autonomy for smart electronic systems powered by energy harvesting. It is often argued that non-rechargeable batteries still have a place in the smart systems of the future because

they have low self discharge rates and thus hold their charge 10 to 15 times longer than rechargeable batteries can. However, if the power requirements of a system are so small that a non-rechargeable battery can power it for 15 years or longer, then there can only be few reasons why replacement by energy harvesters and EDLCs or solid state batteries is not an option. Hence, non-rechargeable batteries are a relic of the past and should be considered obsolete technology when designing new autonomous systems.

6.2 Power Conversion

One of the most persistent and widespread misconceptions on energy harvesting is that it implies applications with low power levels. While this is true for embedded systems powered by primary (non rechargeable) batteries which a finite energy reserve, the energy balance equation does not impose any limitations on power levels. Rather the contrary is true, since energy harvesters continuously convert ambient energy into electrical energy and draw from a reserve that is replenished over time, the energy reserves can be regarded as infinite from the perspective of a constrained autonomous device. As long as harvesters are appropriately dimensioned, nearly any system can be powered as long as the energy balance equations are satisfied. This concept enables two key applications:

1. **Extension** of existing battery powered applications with constrained functionality. Example: a device like the SHA2017 badge [191], equipped with a monochromatic e-ink display to conserve battery life, could be retrofitted with an LCD display, improving the frame rate and enabling colors.

2. **Creation** of new applications that are impractical with conventional battery powered technology. Example a bicycle rental station can be made wireless and autonomous, given enough power to operate its control terminal, rental holders, RFID readers and wireless communication.

Aside from differences in order of magnitude of absolute power levels, an important secondary factor is the peak power that the power supply system needs to be able to deliver. In the previous example of the bicycle rental station for instance, the average stand-by power may be limited to 5-10 W to power a microcontroller in a low power mode, an LCD display and a touch controller interface. When a bicycle needs to be unlocked by a solenoid however, a peak current of 10 A or more may be drawn by the solenoid to ensure the bicycle is released regardless of variations in friction caused by dirt in the mechanism. Hence, for a few hundred milliseconds, power levels will soar above 100 W. If the facility is designed to support the rental of multiple bicycles in parallel, the power supply system needs to be properly designed to ensure reliable operation at all times. Scalability of power conversion with linear and switched mode DC/DC converters will be discussed below.

6.3 Linear Regulators

Linear regulators have been extensively discussed in literature and historically used in countless designs, so their operation should not need to be discussed in this context. A widely propagating misunderstanding about these regulators is that they supposedly have been made obsolete by more efficient switched mode regulators, and that point does need correction to give linear regulators the credit they deserve. Practically, linear regulators function by biasing a switching element such as a bipolar junction transistor in its linear mode of operation. Regardless of the complexity of the other regulator circuitry for noise suppression, loop compensation etc. there are always one or more power transistors or FETs that need to be actively biased to maintain proper regulation. The bias current required for that lowers the overall

efficiency however. Since the input current of the regulator equals the output current and a bias current, the power lost over the regulator is

$$P_{\text{lost}} = (V_{\text{in}} - V_{\text{out}})I_L + V_{\text{in}}I_B \tag{6.1}$$

where V_{in} and V_{out} are the input and output voltages of the regulator respectively, I_L is the load current, and I_B is the bias current for the linear element, for linear regulators more or less equal to the quiescent current I_Q. Since for a given transistor the relation between collector and base current is given by β (h_{FE}), a linear regulator with a higher maximum output current will result in a physically larger output stage element and thus a larger I_Q. For output currents over 30 - 50 mA, I_Q will become substantial (considering that for power transistors, $\approx 50 < \beta <\approx 100$). For example, for a standard X1117 LDO with a maximum output current of 1 A, I_Q may vary between 1.5 mA and 12 mA. This may result in adverse and unexpected effects on the system's power consumption in total. Consider as example a thermostatic valve in a domestic heating application. Such a circuit typically contains an analog temperature sensor and a few opamps to amplify the temperature input signal and compare it to a fixed voltage reference. In this idle state, the combined consumption of the temperature sensor, voltage reference and opamps may be as low as a few μA. However, when the valve needs to be adjusted, using a small DC motor for example, the consumption of the system will for a short time peak to 500 mA. To deliver such an output current during a brief period, it may be tempting to choose for an X1117 with a maximum output current of 1 A, which will indeed satisfy the current requirements of the DC motor. As long as the DC motor is running, assuming worst case scenario, I_Q for the X1117 will rise to 12 mA, or about 2.4 % of the total system consumption, which is acceptable. However, when the valve is adjusted and the motor is turned off again, the system returns to an idle state, but the LDO will still draw an I_Q between 50 μA and 1.5 mA, which is one to three orders of magnitude higher. Since the system can be expected to spend most of its operational time in such a dormant state, the losses caused by the LDO can certainly not be ignored, and will necessitate an energy harvester that must also generate an order of magnitude more power, and thus possibly is a factor 10 larger in size and cost. There are several solutions to this problem, the most effective one being parallelization of voltage regulators. In the thermostatic valve example, one could opt for a TPS797XX with a maximum output current of 10 mA and an $I_Q \leq 2\,\mu$A for the sensing circuitry, which through a comparator enables an LM2594 to supply the output current for the DC motor, at a temporary $I_Q \leq 20$ mA. Many modern LDOs are equipped with a fourth pin for Enable/$\overline{\text{Shutdown}}$ functionality to implement this. In summary, in applications with a very low current consumption, LDOs have the potential to outperform switched mode regulators because of the lower I_Q. To maximize efficiency, the difference between V_{in} and V_{out} should be minimized for LDOs, which is less critical for switched mode regulators. When designing the rest of the power path it is also important to realize that all linear battery chargers, including the popular and widespread CN3065 from Consonance or the TP4056 from NJTPAC, also behave as linear regulators. While charging, the power loss will be the same as for a linear regulator with output voltage equaling the battery cell voltage.

6.4 Switched Mode Regulators

Switched mode voltage regulators, commonly incorrectly known as DC/DC converters (since linear regulators also convert a DC voltage into another DC voltage, thus causing ambiguity), have enjoyed a rise in popularity over the last 15 years because their control logic – most notably oscillators – have become more power efficient. This has enabled the design of switched mode regulators with an improved efficiency, surpassing linear regulators in any application with maximum current output over 30 mA - 50 mA, and rivaling linear regulators in the lower segment in applications where ripple current is of lesser importance. This immediately leads to the design trade-off in power supply circuits: efficiency vs. output

voltage ripple. Switchers with an output power over 1 W and a high $\frac{di}{dt}$ benefit from switching frequencies between ca. 250 kHz (for example, the classic LM2596) up to ca. 2 MHz (for the SX1308). This enables the use of smaller inductor values (typically between 4.7 μH and 33,μH, which are physically smaller and thus take up less board space). As power consumption scales with the square of the oscillator frequency, the I_Q of switched mode controllers also scales up with oscillator frequency. A VCO with or without PLL for frequency multiplication would be ideal to adapt the switching frequency dynamically. The alternative is increasing the inductor value, which also leads to an increase of output voltage ripple. For digital logic, such as microcontrollers running in a stand by mode, a bounded ripple on the digital power rail may have little effect on circuit operation, as long as the ripple remains between the maximum input voltage and brown-out voltage, evidently. For analog circuitry, combination with a linear regulator to eliminate the excessive digital ripple can be a favorable strategy from a power supply efficiency perspective, as for example in the design in figure 61. Commercial examples include the LTC1174 with a switching frequency of 85 kHz, using a single inductor of 82 μH to ca. 100 μH. Switched inductor voltage regulators are essentially always constructed with the same 5 elements: an oscillator, voltage reference, comparator, PWM-controller, and output switching element such as a MOSFET. The switching element may be internal to the controller, as is customary for low power controllers, or can be required to be external for high power density designs. In addition, 4 passive components are also required: an tank capacitor on input and output, a flyback diode and of course the inductor that gives switched inductor voltage regulators their name. Depending on the configuration of the diode, inductor and switching element, different topologies of regulators can be constructed: buck regulators, boost regulators, and inverting regulators. A comparison is shown in figure 6.8.

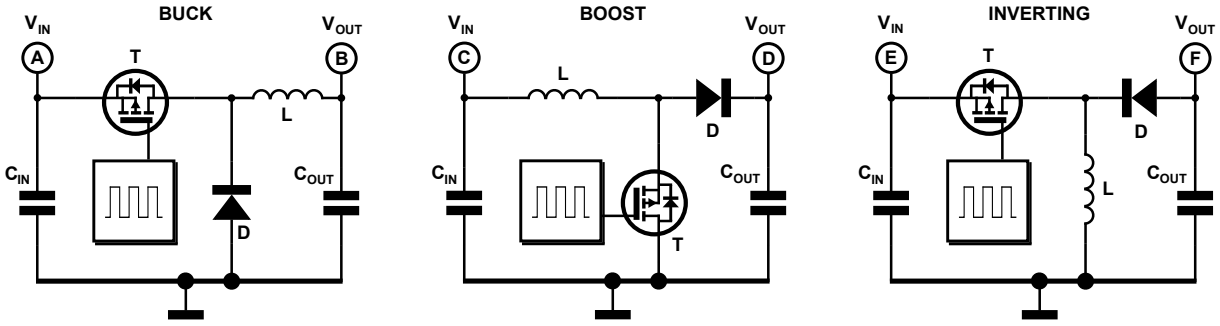

Figure 6.8: Topologies of buck, boost and inverting regulators with a single switch and PWM controller. Note that for buck and inverting regulators P-MOSFETs are commonly preferred over N-MOSFETs for high side switching to avoid bootstrap circuits.

6.4.1 Buck Regulators

Buck regulators (also informally called step-down converters) use a high side switching element in series with the output inductor. High side switching thus requires a less efficient P-channel MOSFET or PNP transistor, or a bootstrap circuit with an N-channel MOSFET. The input is physically disconnected from the output when the PWM duty cycle is 0, and shorted to the output when the duty cycle is 100 % (usually triggering an internal current limiting circuit or a fuse). The switching element is typically controlled by a simple flipflop, as seen in figure 6.9. The flipflop is set on a rising edge of the oscillator, turning on the switching element and ramping up the current through the inductor. As charge is transported from the input capacitor to the output capacitor, the voltage over the output capacitor will rise, eventually exceeding a reference voltage. The comparator flips, resetting the flipflop and turning off the switching

element until the next rising clock edge occurs. When the switching element is turned off, the energy stored in the inductor is discharged into the output capacitor. The inductor thus behaves as a charge pump, forward biasing the flyback diode and acting as a current source in parallel with the output capacitor. On the next rising oscillator edge, the process restarts. Since the (idealized) switching element cycles between saturation and cut-off, it does not contribute to power losses, allowing buck regulator designs with an efficiency of (theoretically) 100 %. In practical circuits, there are 4 factors contributing to power losses, pulling down the efficiency:

1. **resistive losses**: ESR of input and output capacitor, and of the inductor;
2. **magnetic losses**: saturation of the inductor;
3. **linear losses**: voltage drop over the conducting flyback diode;
4. **control losses**: supply current of the regulator itself.

Each of these loss factors must be individually addressed to maximize regulator efficiency.

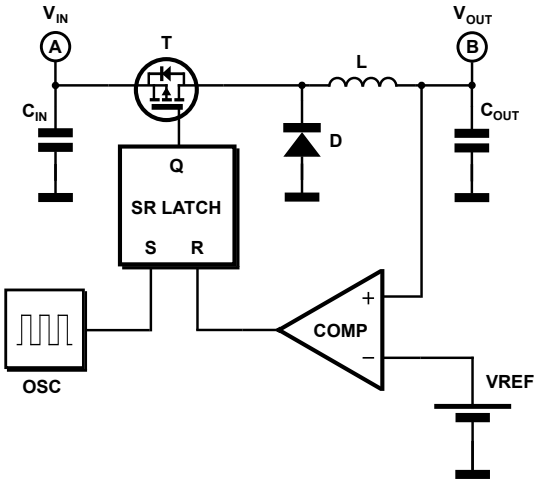

Figure 6.9: Principal components of a buck regulator: input capacitor C_{in}, output capacitor C_{out}, MOSFET, inductor and flyback diode. Comparator and voltage reference provide voltage mode feedback to adjust PWM duty cycle of the MOSFET switch.

ESR

The Equivalent Series Resistance of an inductor is simply the resistance of the wire, and thus proportional to the length of said wire and its diameter. Since the length depends on the number of turns around the core, which is dictated by the desired inductance, ESR increases with inductance value. The design will thus often boil down to a trade-off between inductor value and oscillator frequency: higher oscillator frequencies cause more current consumption on the controller side but enable lower inductor values and decrease ESR losses accordingly, and vice versa. To minimize both, a low oscillator frequency can be combined with a high value inductor, wound with a large diameter wire. However, this in turn increases the cost and size of the solution. In any application using a buck regulator, the choice must be made to either favor cost, or favor efficiency (which may in turn affect secondary issues like heat dissipation in inductors and switching elements for example). At high switching frequencies, the skin effect may

dominate ohmic ESR, and for these applications there are inductors on the market by Würth Electronics and others that use wire with a rectangular cross section (large circumference) rather than a circular cross section (minimal circumference to surface area ratio).

The ESR of capacitors can be minimized by the creation of capacitor banks with multiple smaller value capacitors adding up to the desired capacitance value. By connecting 2 identical capacitors in parallel, regardless of type, the equivalent capacitance will double but the ESR will halve. This technique offers designers some control over ESR, again at the cost of higher board area. Solid state capacitors (niobium, ceramic, film, polymeric, tantalum capacitors) typically have lower ESR than electrolytic capacitors (aluminum capacitors and EDLCs), but again at a higher cost for equivalent capacitance. A combination of electrolytic capacitors and ceramic capacitors often offers the best trade-off regarding cost and board area. Most regulators are designed for single ended topologies, the LM2596/LM2577 duo for example, while others also support isolated flyback topologies (XL6009 from XLSemi and others).

Inductor Saturation

Saturation occurs in all inductors with a ferromagnetic core, which practically means all inductors for switched mode voltage regulation applications. Saturation occurs when an increase in current does not result in a further increase in magnetic flux, because all the elementary poles of the material are already aligned. The materials permeability is an indication for the capacity, and higher permeability results in a conventionally higher maximum flux density. Depending on the physical construction of the core material, reaching magnetic saturation may result in magnetization of the area in the immediate surrounding of the core material, often a magnetically impermeable material such as plastic, or air. This results in a burst of EMI to be transmitted by the inductor and also cause a drop in the core's permeability, contributing to the effect in a positive feedback mechanism. Although there are applications that rely on saturation for their operation, the effect should be avoided in switched mode voltage regulators. This can be done by either choosing a core with a sufficient amount of physical core material (i.e. a larger core) or by choosing a ferromagnetic material with a higher permeability.

Flyback Diode

Just as inductors, the flyback diodes must be rated to the peak current rather than the average output current of the power supply circuit. Since the voltage drop over Schottky diodes is highly nonlinear but increases with forward current through the diode, instantaneous power losses in the flyback diode may contribute substantially to an efficiency drop of the regulator. For example, with a B130 Schottky diode having a forward voltage drop $V_F = 500\,\text{mV}$ at $I_F = 1\,\text{A}$, charging up the 3.3 V output capacitor in flyback mode will only have an instantaneous efficiency of $\eta = 1 - \frac{0.5}{3.3} \approx 85\,\%$. Unlike with capacitors and inductors, adding more diodes in parallel is an ineffective solution since the V_F curves of all diodes will slightly diverge, causing uneven distribution of the current load over all parallel diodes. A single larger diode rectifier is often the best solution. Alternatively, it may be beneficial to eliminate the flyback diode completely and choose for active rectification instead of passive rectification. The switching element in this case is usually an N-channel MOSFET with internal body diode for spike suppression.

Regulator Supply Current

Different OEMs have the inconvenient habit of using the terms supply current and quiescent current interchangeably, making it difficult to streamline comparisons between chip sets. Usually, the supply current is defined as the current consumed by the regulator in active regulation minus the load current

through the MOSFET. Following this definition, the supply current can be estimated as the sum of the oscillator, analog circuitry, and current to charge and discharge the gate of the MOSFET every cycle. The latter cannot be easily reduced because the current to charge and discharge the gate depends on the MOSFET's gate capacitance, which in turn scales with properties such as $V_{DS(max)}$ and $I_{DS(max)}$, usually critical to the application's context. For example, Suosemi defines 3 parameters in the datasheet for the SX1308 as *shutdown current* when the Enable pin is pulled low, and makes a difference between I_Q with and without switch. As a general rule of thumb, physically larger MOSFETs also have higher gate capacitances, resulting in yet another trade-off when selecting the MOSFET. Choosing a physically small MOSFET reduces gate capacitance but increases $R_{DS(on)}$ and vice versa, although MOSFET technology is developing rapidly and no longer making $R_{DS(on)}$ a problem. Trench MOSFETs from Nexperia and Vishay in particular are designed for switching regulators, and attempt to minimize both $R_{DS(on)}$ and gate capacitance simultaneously. Since the MOSFET's gate must be charged and discharged every cycle, the average charge current is proportional to the oscillator frequency. The gate current is often the only parameter scaling with oscillator frequency, and thus dominates the supply current of the regulator. The definition of the quiescent current I_Q is more variable, some OEMs consider I_Q as the current drawn when the device is in a shutdown state (i.e. its Enable or $\overline{\text{Shutdown}}$ pin pulled low), while others add also the supply current of the device when no switching occurs (which may incur oscillator activity etc.). The I_Q is important in applications that reside the majority of their lifetime in a dormant state, and only periodically wake up to execute actions as triggered by an internal timer or initiated by the user or another external event. It is rarely possible to shut off power to the system completely because that would inhibit data retention in RAM and disrupt any RTC operation for time keeping purposes. In these cases, the system's current consumption will be reduced to whatever a watchdog, RTC or low power sensor require, and a parallel LDO can usually take over the power path temporarily. The I_Q of the switched regulator however will still load the harvester or power source. In applications with rechargeable chemical cells, this poses a particular problem since there is a risk of overdischarging the battery even when the system is dormant, by the I_Q of the regulator(s) alone. Adequate counter measures must be taken to prevent this from happening, as will be discussed in the Influencair example below.

6.4.2 Boost Regulators

Boost regulators increase the output voltage (referred to as *step-up*) rather than decreasing it, and are necessary for energy harvesters with an output voltage typically below the required voltage level as is the case for TEGs. Another use case for boost regulators is the end regulation of single rechargeable cells, for example Li-Ion or Li-Ion-Polymer. The components required to build a boost regulator are identical to a buck regulator, only their arrangement is different: MOSFET, flyback diode and inductor have switched places in the circuit topology. In this mode of operation, the MOSFET acts as a current shunt, tying the high side of the inductor to ground whenever it is enabled, thus charging it up. When the MOSFET is turned off, the inductor acts as a charge pump, and the voltage over the inductor rises to a level at which the flyback diode is forward biased and the output capacitor is charged with the energy stored in the inductor. The feedback mechanism works identically to a buck regulator, adjusting the PWM duty cycle to control the amount of energy that is stored in the inductor when the MOSFET is turned on. Although functionally identically to buck regulators, a fundamental difference is the power path between input and output capacitor. In case of a boost regulator, there is no inline switch such as with a buck regulator, but only a series inductor and diode. This causes an overflow effect when the input voltage would rise above the desired output voltage, in which case the regulator logic cannot prevent the input voltage to forward bias the flyback diode and charge up the output capacitor. When this occurs, there may be fatal consequences for sensitive downstream circuitry. A typical situation is

3.3 V logic powered by Li-Ion batteries. A charged battery has a cell voltage of ca. 3.6 V, and the voltage rating of low voltage circuitry is commonly rated to 3.6 V to allow it to be powered by a single battery directly without requiring a buck regulator. The cell may discharge down to 2.7 V however, which is often insufficient for reliable operation at the rated maximum frequency, and a boost stage is therefore required between battery and system. When the battery is being charged, the cell voltage may rise above 4.1 V, which would forward bias the flyback diode and create a conductive path between input and output. At low currents, the forward voltage drop over a Schottky diode may be as low as 200 mV, leaving 3.9 V on the output capacitor, which exceeds the rated voltage limit of 3.6 V and may irreversibly damage the circuitry. A common solution to this problem is cascading a boost and buck regulator.

Buck-boost Regulators

It is possible to cascade a boost and buck regulator, the order being important to eliminate the effect of the boost regulator's flyback diode voltage drop in buck regulation mode. An independent boost and buck regulator may be used, since the buck regulator will create a conductive channel if the input voltage is too low, and the boost regulator will do the same if the input voltage is too high. For any given input voltage, only one of the regulators will be in active regulation, the other being bypassed by design because it is turned off by its internal comparator. There are controller ICs on the market which integrate 2 separate controller stages which may either be used as 2 buck regulators, 2 boost regulators, or to build a buck-boost regulator. This flexibility requires external power switches, and is consequentially not available for low power integrated buck or boost controllers with an internal power switch. Solutions exist, such as the TPS55065 demonstrated in figure 6.5. These controllers feature a complete control path for a buck and boost stage together with the required low and high side switches. They are easily recognizable because the inductor is directly connected to the control IC on both sides, instead of with one side as is the case for buck, boost or inverting regulators, as shown in figure 6.8. An improvement to the direct cascading of a boost and buck regulator, is synchronizing the oscillators of each stage and adding a capacitor between the two stages to couple them. This approach potentially offers 2 benefits: it can be constructed using a single power switch instead of 2 separate switches, and the capacitor acts as an open circuit to DC so this topology is more resistant against short circuits. This topology is referred to as SEPIC – Single Ended Primary Inductor Converter. The main drawback is the additional capacitor, which is often bulky and costly since it must be bipolar type with a low ESR.

6.4.3 Inverting Regulators

As the name suggests, the use case of inverting regulators is mainly limited to create a negative power rail or negative bias voltage. Inverting voltage polarity was seen as the holy grail of power path design before the invention of switched mode regulators, since it cannot be done without the charge pump mechanics offered by switching an inductor on and off. It is not more complex or expensive to construct than a buck or boost regulator (see figure 6.8) and requires an identical set of components. The only difficulty is the inability to provide direct voltage feedback from the output to the control stage, since the polarity of the output is negative, which cannot be measured by the controller which is supplied with a positive power rail. Additional level shifting is necessary, but this can be done with a modified resistor divider instead of requiring active components. The most common strategy is constructing a voltage divider between a fixed positive reference voltage and the (negative) output voltage, which needs to be dimensioned so that the feedback pin is at a zero potential (or a potential between ground and the positive reference voltage). Because of their convenience, inverting regulators are commonly used to generate a symmetric power supply from an asymmetric one (a single battery cell for example) which allows to eliminate the input offsets of ADCs and opamps completely. When used as a bias rather than a power rail, the current drawn

may be small enough to enable end regulation with a negative linear voltage regulator (such as 79XX series regulators) to decrease switching regulator oscillator frequency and improve efficiency. When decoupled, in a topology similar to the previously discussed SEPIC regulators, it is possible to design a combined regulator that can generate a positive or negative output voltage depending on the duty cycle of the internal switch. The complexity of the circuit is similar to a SEPIC regulator, but they are rarely used since there are few practical applications which require alternation between positive and negative voltage levels.

It should be noted that also switched capacitor voltage regulators exist, which can be used as voltage multipliers to generate bias voltages as an alternative to diode/capacitor bootstrap circuits for example. Since their uses are limited in the scope of energy harvesting applications, they will not be further discussed. A second consideration to make is that all discussed switched mode voltage regulators can also be used as constant current sources instead of constant voltage sources by switching from voltage feedback to current feedback using a single shunt resistor instead of a voltage divider.

6.4.4 Monolithic Converters

Whereas regulators with higher power levels ($>$ ca. 15 W) typically require external MOSFET switches and flyback diodes, regulators for low power levels can be highly integrated. Such devices are referred to as *monolithic* DC/DC converters or voltage regulators, and include all semiconductor components to construct a switched mode voltage regulator: PWM or PDM generator, oscillator, power switch(es) and flyback diode(s). The advantage of this approach is of course the reduced component count, and therefore smaller PCB footprint. Typically required external components are input and output capacitor, inductor(s), and optional passives for configuration of oscillation frequency or output voltage. Their ease of use has resulted in high popularity for electronic designs, and the large production volumes have brought down costs significantly. However, performance differences can be observed, and it is difficult to compare the performance of different devices objectively. Comparing conversion efficiency is difficult because this parameter varies with output current, the second most important parameter as discussed previously is the supply current or quiescent current, depending on the manufacturer, while the device is in active regulation. A comparison of devices from different manufacturers is shown in table 6.4.

Table 6.4: Performance comparison of monolithic DC/DC converters.

Device	Manufacturer	Type	$V_{in,min}$	$V_{in,max}$	$V_{out,min}$	$V_{out,min}$	I_{out}	I_Q
SL8009	Silergy	Buck	3 V	5.5 V			1.5 A	80 μA
XC6206	Torex	LDO		6 V	1.2 V	5.0 V	200 mA	1 μA
ME2149	MicrOne	Buck-Boost	0.9 V	6 V	1.5 V	6.5 V	2 A	25 μA
SX1308	SuoSemi	Boost	2 V	24 V		28 V	2 A	1.6 mA
TD6817	TechCode	Buck	2.5 V	5.5 V			2 A	20 μA
LC3406	LeadChip	Buck	2.6 V	7.0 V			1.2 A	46 μA
AP5100	Diodes Inc.	Buck	4.75 V	24 V	0.8 V	15 V	1.2 A	0.4 mA
AOZ3103	A&Ω	Buck	4.5 V	18 V	0.8 V		3 A	0.8 mA
RT8258	Richtek	Buck	4.5 V	24 V	0.8 V	15 V	1.2 A	0.55 mA
LT3757	Linear	Buck-Boost	2.9 V	40 V		24 V	2 A	1.6 mA
XL6009	XLSemi	Buck-Boost	5 V	32 V		60 V	2 A	2.5 mA
LM2596	TI	Buck		40 V	1.2 V	37 V	3 A	5 mA
MAX5035	Maxim	Buck	7.5 V	76 V	1.25 V	13.2 V	1 A	270 μA
MP1484	MPS	Buck	4.75 V	18 V	0.925 V	20 V	3 A	1.3 mA
XL4015	XLSemi	Buck	8 V	36 V	1.25 V	32 V	5 A	2.1 mA
AP1509	Diodes Inc.	Buck		22 V	1.23 V	18 V	2 A	5 mA
LM317	TI	LDO		40 V	1.2 V	37 V	1.5 A	3 mA
LM2576	OnSemi	Buck		40 V	1.23 V	37 V	3 A	5 mA
LSP5522	Lite-On	Buck	4.5 V	23 V	0.925 V	18 V	2 A	1.4 mA
TPS54332	TI	Buck	3.5 V	28 V	0.8 V		3.5 A	82 μA
PAM2863	Diodes Inc.	Buck	4.5 V	40 V			2 A	0.6 mA
NCP1595	OnSemi	Buck	4.0 V	5.5 V	0.8 V		1.5 A	1.7 mA
TD1583	TechCode	Buck	3.6 V	28 V	1.22 V	26 V	3 A	3.6 mA
MP2307	MPS	Buck	4.75 V	23 V	0.925 V		3 A	1.3 mA
MIC4680	Micrel	Buck	4 V	34 V	1.25 V		1 A	7 mA
MT3608	AeroSemi	Boost	2 V	24 V		28 V	2 A	1.6 mA
G5177B	GMMT	Boost	3.3 V			5 V	2 A	70 μA
RT9293	Richtek	Boost	2.5 V	5.5 V		46 V	100 mA	2 mA
XR2203	XYSemi	Boost	2.3 V	6 V		26 V	1.4 A	75 μA
LM1117	National Semi	LDO			1.25 V	13.8 V	800 mA	5 mA

The large majority of the devices listed in table 6.4 are buck regulators, some with an optional buck-/boost or SEPIC configuration. There are 3 to 4 orders of magnitude difference in the supply current consumption of monolithic regulators, and 1 order of magnitude difference in maximum output current. The graph in figure 6.10 shows the relation between maximum output current and supply or quiescent current, as specified by manufacturers in datasheets.

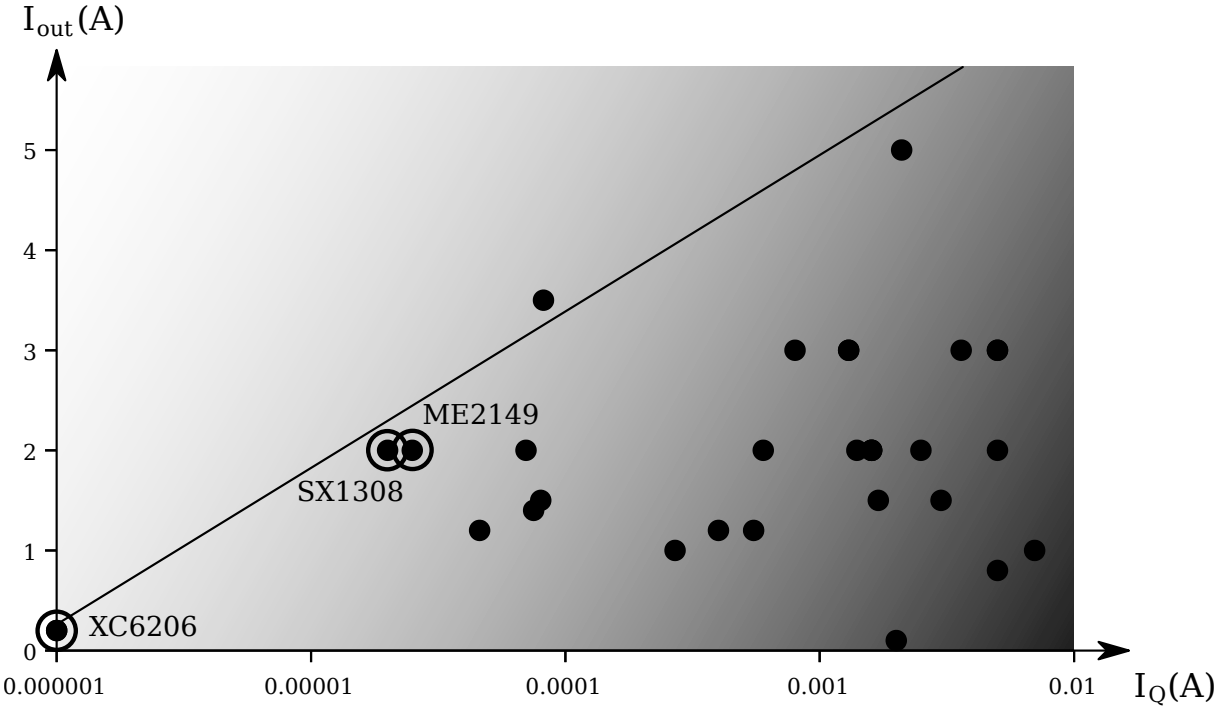

Figure 6.10: Supply current in active regulation in comparison to maximum output current of monolithic DC/DC converters. Gradient indicates power efficiency, with devices in lightly shaded areas performing better than devices in strongly shaded areas. The line approximates the current state of the art for monolithic DC/DC converters for different output current magnitudes.

6.5 Power Regulators

Because the control logic of switched mode regulators is getting more efficient, the market for highly integrated switched mode controllers has boomed in the last 10 years, and many of these low cost controllers have integrated power switches and flyback diodes, and preset output voltage configurations. A fully functioning switched mode regulator can be built with only the controller, a power inductor, and 2 external capacitors on input and output. The popular SX1308 boost controller from Suosemi for example is available from 5 cents in high volumes. Buck regulator equivalents, such as the LC3406 or AX2002 from LeadChip and Axelite respectively, are available in the same price range. At a higher cost, modules with integrated planar inductors have also been designed by Linear Technology, such as the LTM4603. These only require an input and output capacitor, and a few smaller passives to set oscillator frequency and output voltage. The additional cost of VLSI construction of planar inductors is substantial however, due to a multiplication of the required silicon area, and unless board area is a critical parameter for optimization, external wire wound inductors are usually a better cost-performance trade-off. To achieve higher power levels, the options are either the use of a galvanically isolated approach using a transformer

– the solution of choice for net adapters – or a multi channel single ended design. A fundamental flaw of the transformer approach is the use of series power path with a single power switch. Upon failure of this switch, the entire system ceases to function, and with it also the downstream circuitry that is being powered. Although a power supply circuit may have a MTBF of up to a million hours by definition if the design complies to the recommended characteristics, it is difficult to predict the exact life time under influence of other factors. Although the life expectancy of the MOSFET cannot be reliably statistically modeled for expectancies beyond 1 million hours of operation, it is known that other components such as capacitors have a shorter life time and affect MOSFET operation indirectly through varying ripple currents for example. Increasing ESR over time also reduces efficiency, increases heat dissipation, and degrades MOSFET life time at elevated operation temperatures. These factors make it extraordinarily difficult to make theoretical estimations about the life expectancy of a MOSFET in an actual circuit design. To circumvent the problem, a multi channel single ended power supply topology may offer a solution by intrinsically adding redundancy to the design.

6.5.1 Multi Channel Design

The example of an autonomous bicycle rental station given at the beginning of this chapter is an excellent case to illustrate the design criteria and trade-offs often encountered in autonomous systems which require high reliability and low maintenance. In this application, unlocking a bicycle with a solenoid powered by an EDLC requires a high surge current of 10 A or more for a short duration of time. No other types of voltage or current regulators can offer this peak power, requiring the use of a power regulator appropriately dimensioned for these requirements. It may be tempting to power the solenoids from the EDLC bank directly, but since the EDLC voltage is highly variable depending on its state of charge (SoC), the surge current generated at full charge would be detrimental to solenoid life time itself. Assume that, for the sake of the example, it would be a design requirement to be able to unlock 3 bicycles simultaneously. The corresponding output current at the solenoids rated voltage would then be 30 A, or an instantaneous power output of 360 W at a solenoid voltage of 12 V. Designing for reliability and redundancy, a good choice is a 4 channel synchronous buck regulator with a supply current of 10 A per channel. Simply stated, each channel individually is capable of unlocking a bicycle, but since the load current is shared among 4 channels instead of 3, each channel only operates at 75 % of its maximum capacity, improving its lifetime. By design, even if one of the channels fails, the remaining 3 channels would rebalance the load and turn to 100 % capacity each without endangering the operation of the system.

Multi Phase Oscillator

The block diagram of the solution is shown in figure 6.13. It consists of 4 indentical synchronous buck regulators designed with buck controllers and an N-channel MOSFET half bridge, an external flyback diode per channel, and a shunt resistor to enable current feedback. The 4 channels are synchronized with a multiphase oscillator acting as a double quadrature signal generator (4 channels with a 90° phase shift between each channel). The chosen type, an LTC6902 from Linear Technology, is configurable for 2, 3 or 4 phases, and supports spread spectrum frequency modulation to reduce EMI emitted by the inductors at a single switching frequency and instead spreading EMI over a wider frequency band to reduce its impact on adjacent circuitry. The schematic is shown in figure 6.11.

The operation frequency is set to ca. 1.5 MHz, which generates 4 phase shifted channels at ca. 375 kHz. The channels are used as clock signals for the buck controllers, replacing their integrated oscillators to ensure a proper synchronization with a 90° phase shift.

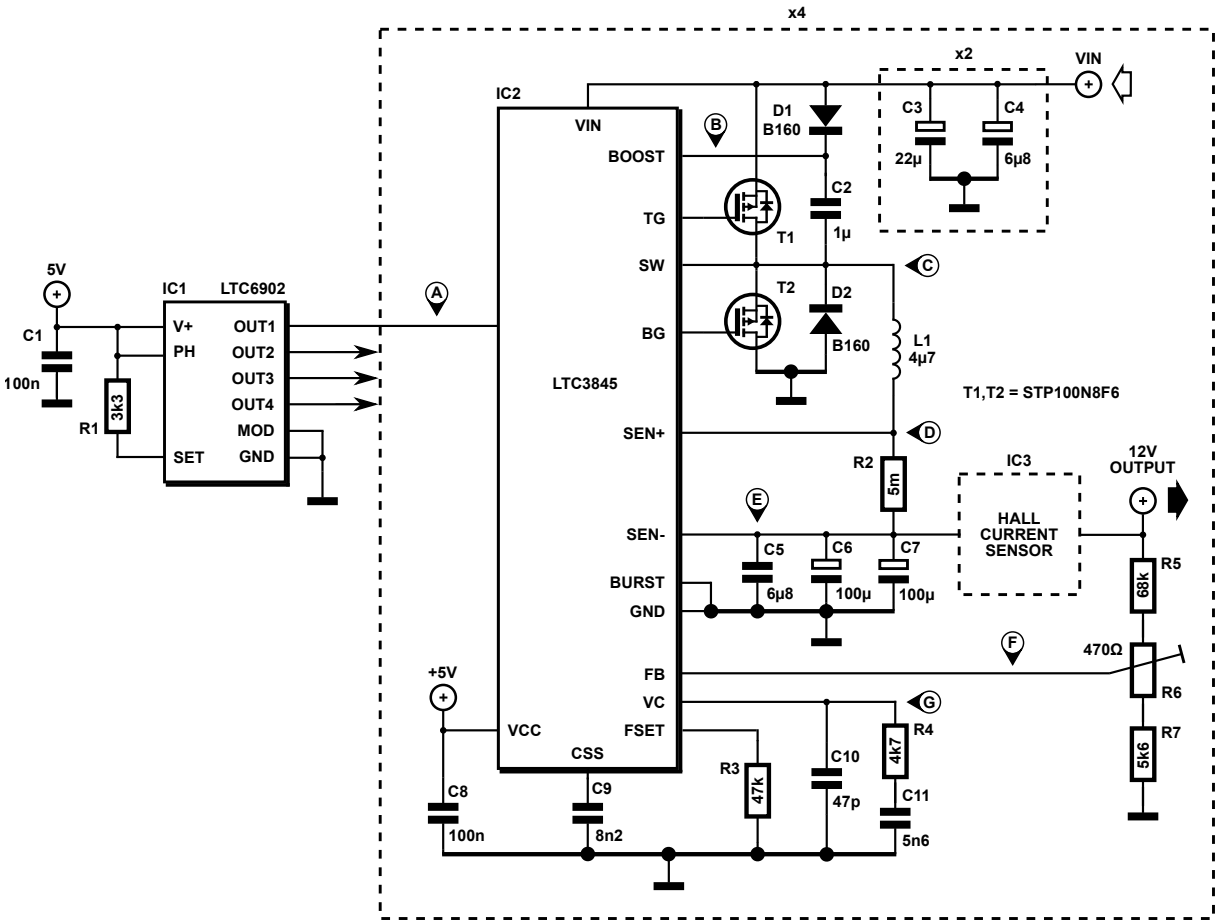

Figure 6.11: A 4 phase synchronous oscillator (LTC6902) feeding a clock signal to 4 identical, 90° phase shifted buck stages with an LTC3845 controller and N-MOS half bridge for synchronous rectification. The Hall sensor based current sensing is shared among the 4 buck stages.

Buck Stage

The 4 buck channels, using an LTC3845 as integrated controller, use a dual N-channel half bridge built up with STP100N discrete power MOSFETs, each with a rated $I_{DS(max)}$ of 100 A. The high side is the actual power switch for the buck regulator topology, the low side acts as synchronous rectifier replacing the flyback diode. Both MOSFETs may also be used in a push-pull configuration, depending on the configuration of the LTC3845. A bootstrap circuit, a voltage doubler with a 1 μF capacitor and B160 Schottky diode, supplies the gate voltage for the high side N-MOSFET. Capacitor banks are overdimensioned and also include redundancy, since electrolytic capacitors are prone to ESR increase and premature failure though evaporation of electrolytes, or leaking of electrolytes. The inductor is a 4.7 μH power inductor with a flat rectangular cross section from Würth Electronics, with top side shielding for improved EMI reduction. Passives are used to configure frequency compensation for the control loop. A 5 mΩ shunt resistor in series with the power inductor allows current feedback to minimize current spikes through the MOSFETs, increasing their lifetime, although the primary regulation method is constant voltage control using a voltage divider feedback loop. Output voltage feedback is taken further downstream of the output capacitor bank and after a Hall current sensor to avoid adverse premature triggering by inrush currents through inductors. The hall sensor replaces fuses for output circuit protection, since non-resettable fuses

require maintenance and resettable fuses (PPTCs) are unreliable for this current magnitude. The voltage drop over PPTCs also decreases conversion efficiency, a drawback not shared by hall sensors. The chosen type here is an Allegro ACS722 with an analog output signal proportional to the current, thus behaving similar to a shunt resistor. The circuit is shown in figure 6.12.

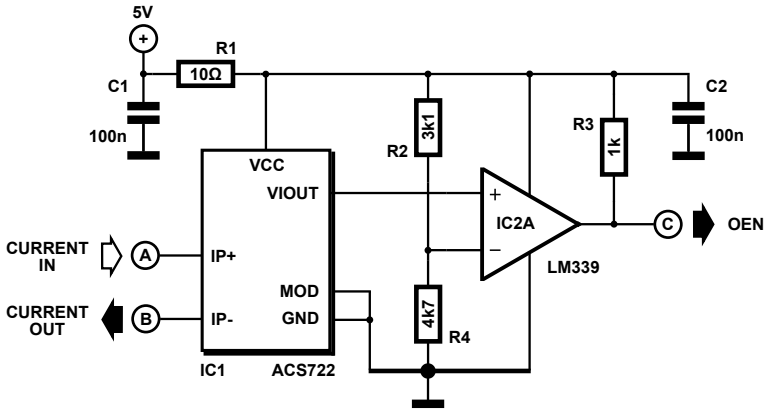

Figure 6.12: A 40 A over current detection module using an ACS722 hall sensor.

The hall sensor output is compared to a fixed voltage reference derived from the power rail by a standard LM339 comparator, and used to disable the power stage in the event of a short circuit. Pulse extender and hysteresis circuitry are omitted for clarity. The voltage feedback for the buck stages is taken after the hall sensor to compensate for voltage drops over that sensor, and voltage drops over individual current shunts. Interestingly, since solenoids generate a force on their plungers electromagnetically, and the magnetic field is determined by the current flowing through the solenoid, one may be tempted to favor current control rather than voltage control for this application. In this case it would be impossible to balance the load current with a single stage however, requiring either a topology where each solenoid is powered by its own buck regulator and/or an additional switch matrix to get the redundancy required for reliability back into the system. The additional power switches or relays would in turn lower the overall reliability again, making this solution an unwise choice. The only part for which no redundancy is built in, is the multi phase oscillator circuit generating the clock signals for the 4 buck regulators. If this oscillator fails then the individual buck regulators will automatically fall back to their own oscillators, but synchronization (and load sharing) functionality will be lost. Because of the 33 % overdimensioning (i.e. 4 channels instead of 3), the design can meet its performance requirements even if this situation occurs.

Synchronous Rectifier

The input voltage of the system is up to 30 V, easily accommodating 10 EDLC cells in series to build an EDLC bank for more efficient storage. The ESR of existing EDLC power banks is low enough to allow direct interfacing with the discussed input. The presented system can be easily adapted to work with AC sources as well, in which case an additional rectifier bridge is necessary. To minimize losses, active rectification is the method of choice, using 4 identical N-channel MOSFETs to replace the diodes in a classic full rectifier bridge, as shown in figure 6.14. The MOSFETs are controlled with a LT4320, a control IC specifically designed for synchronous rectifier applications. As long as the MOSFETs are operational, the efficiency is improved because the voltage drop over the conducting MOSFET channel is lower than that over a forward biased Schottky diode, therefore reducing the Joule effect. It is self sustainable and redundant because the body diodes of the MOSFETs are polarized identically to the diode

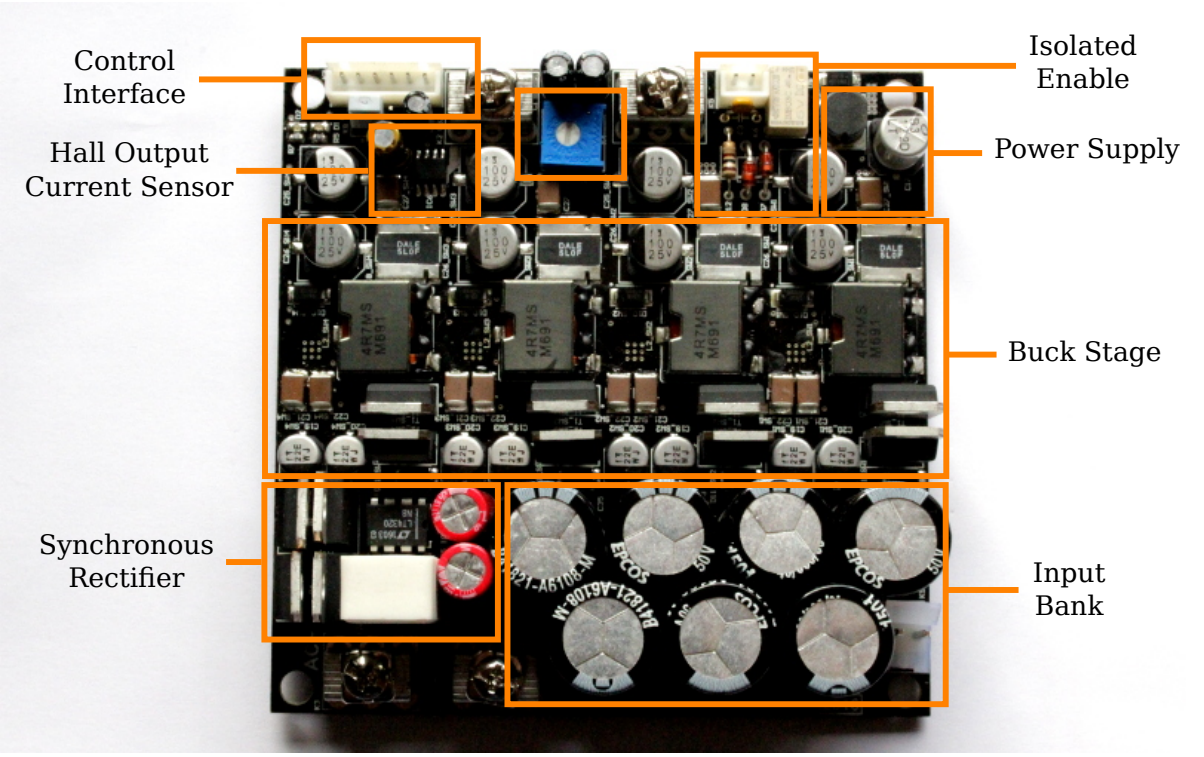

Figure 6.13: Top side of the prototype. Left to right: digital and analog control interface (output voltage and current, as 6-pin JST connector, galvanically isolated enable input, ACS722 hall current sensor, local 5 V buck regulator, 4 phase buck stage (oscillator on bottom side of the PCB), synchronous rectifier with 4 N-channel MOSFETs and ceramic dump resistor, and input tank capacitor bank.

configuration of a classic full rectifier bridge, so in other words, the MOSFET channels short the diodes when the controller is active. The circuit of figure 6.14 also works without the LT4320 controller inserted in its socket, solely relying on the conductance of the MOSFET body diodes. If either the controller or one of the MOSFETs would fail, the rectification can continue passively instead of actively.

6.6 Power Path Design

Depending on the types of harvester(s) chosen, their power ratings, the necessity of an active maximum power point tracker, the choice for local storage and load matching networks, and the different voltage rails with individual power ratings each, there are more possible solutions for power paths than can possibly be discussed in a thesis on energy harvesting. Power path design for energy harvesting applications is a topic that rightfully deserves more than one thesis on its own, so instead of discussing a seemingly endless list of possible topologies and power path architectures, the design procedure for a typical low power autonomous system will be illustrated below with the design of a stand-alone embedded system.

6.6.1 Influencair

Air quality, particularly in urbanized areas, is a serious concern that has gained interest from the scientific community in recent years, and interest from the general public in its wake. Preliminary research on the health effects of air pollution suggests that citizens living in polluted areas may see their average life

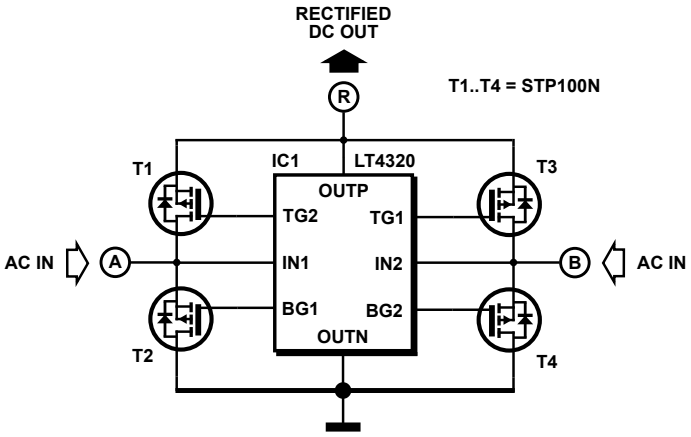

Figure 6.14: LT4320 based synchronous rectifier with 4 N-MOSFETs providing superiorr efficiency over passive full bridge rectifiers.

expectancy reduced with as much as 2 to 5 years, depending on the severeness of the pollution and the estimation metrics. These results inevitably stirred up the necessary attention, but unfortunately, air quality monitoring by official governmental measurement stations is wholefully inadequate. In the city of Brussels, covering an area of 161 km^2, there are only 13 measurement stations, and none are located in the proximity of logical hot spots such as busy intersections or highways. This is likely an intentional choice by governmental institutions, trying to keep the population in the dark about the actual air pollution in the city to avoid social unrest and uproars. The independent organizations Open Knowledge Belgium and Civic Labs Brussels have concluded that air pollution monitoring by the government is inadequate, and an independent, decentralized, crowd sourced alternative is necessary. The Influencair project was launched in 2017 with the explicit goal to develop low cost autonomous measurement stations that are compatible with the Luftdaten.info network previously developed by Hackerspace Stuttgart, and upload their data to a map overlay powered by OpenStreetMap. The sensor of choice is the SDS011, able to measure airborne particles between 0.3 μm and 10 μm (resp. PM2.5 and PM10). The German sister project already acquired extensive field experience with this sensor, so a statistical analysis of its reliability had already been done. The existing prototype relied on a 5 V power bank or USB power for operation, and the primary goal of the project was to develop fully autonomous sensor stations. Two variants were designed, one for mobile use on a bicycle (using the generator of the bicycle to supply the necessary power) and one for stationary use, to be installed on poles or antennas in the immediate vicinity of areas suspected of poor air quality. Since the power path design of the mobile station is straight-forward (a passive full rectifier bridge and LM2596 based buck regulator), only the stationary variant using solar panels is discussed below, which was the designed specifically for this thesis.

6.6.2 Design Considerations

The architecture block diagram for the Influencair system is shown in figure 6.15.

The choice for the ESP8266 is a consequence of its community support as an IoT microcontroller, and it comes with a preconfigured bootloader that makes programming or reprogramming more transparent. The bootloader is internally protected against tampering, making the software side resistant against tampering and bricking, and thus improving reliability. The ESP8266 does not have an integrated USB interface, so for programming purposes, a CH340G USB/UART bridge has been included. The CH340G

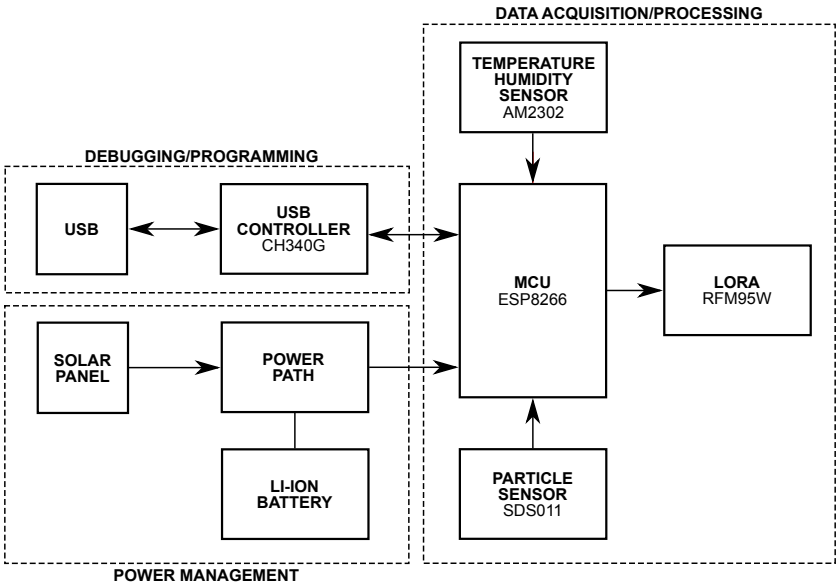

Figure 6.15: Embedded architecture of the Influencair air quality sensing module, with an ESP8266 as general purpose IoT MCU and SDS011 particle sensor.

is powered through USB, so remains in a powered down state during normal operation of the system, and can be excluded from the energy budget. The main sensor module is an SDS011 from Nova, which requires a 5 V supply for its integrated CCD, acquisition logic, and on board fan cycling air through the sensor module. Current consumption varies between 2 mA in idle mode up to a maximum of 220 mA (ca. 1 W), making it by far the highest rated power consumer in the design. In contrast, the ESP8266 consumes 15 mA at 3.3 V in active mode, and 20 μA in sleep mode. Finally, an Aosong AM2302 combo humidity and temperature sensor is chosen for air quality compensation in function of varying weather conditions. An overview of power requirements of the primary system components are shown in table 6.5.

Table 6.5: Power consumption of the active components in the Influencair design.

Device	Supply V	Active I	Active P	Idle I	Idle P
ESP8266	3.3 V	15 mA	50 mW	20 μA	66 μW
AM2302	3.3 V	500 μA	1.7 mW	15 μA	50 μW
RFM95W	3.3 V	120 mA	0.4 W	0.2μA	0.66 μW
SDS011	5 V	200 mA	1 W	2 mA	10 mW
DW01-P	4.2 V	3 μA	13 μW	3 μA	13 μW
SX1308	4.2 V	1.6 mA	7 mW	1 μA	4.4 μW
ME2149F	4.2 V	4 mA	16.8 mW	0.5 μA	2.1 μW
XC6206P282	4.2 V	1 μA	4.2 μW	1 μA	4.2 μW

Tempting as an easy solution to the power supply probem is to keep all components active at all times. The total power consumption of the system is in that case the sum of all components in active mode. This estimation is confirmed by measurements of the Luftdaten prototype, which remains powered by USB or power bank at all times, and uses a 3.3 V LDO to derive the 3.3 V power rail from the 5 V power

rail. The power consumption can be estimated as

$$P_{act} = 5\,\mathrm{V} \cdot (15\,\mathrm{mA} + 200\,\mathrm{mA} + 120\,\mathrm{mA} + 0.5\,\mathrm{mA}) \approx 1.68\,\mathrm{W} \tag{6.2}$$

Note that it does not make a difference in the equation whether the device is powered from the 3.3 V or 5 V power rail since the LDO only drops the voltage at a constant current. For 3.3 V devices, the power loss from 5 V is simply split between the LDO and the devices themselves.

When adapting to energy harvesting, more specifically solar energy, there are several possible optimizations to reduce the power consumption and make it more cost-effective to switch to energy harvesting, as a solution to make the air quality monitoring station fully autonomous. Most significantly, the time span in which components operate in their active mode – and draw active current – can be reduced by making measurements discontinuous. Based on measurements by the Irceline network, an interval of 5 minutes was chosen. With 12 samples per hour, the effect of phenomena like rush hours, traffic jams and weather can be measured, which is the environmental evolution most of interest. Because of sensor limitations, it is not possible to make the active time arbitrarily short: the SDS011 requires at least 10 seconds for air inside the sensor to be refreshed and evenly dispersed, and the AM2302 also takes 2 seconds to make a measurement. Transmitting data over LoRa to the Wireless Belgium network also takes time to power up the transceiver, establish a connection to the remote cellular tower, make a transmission, and receive the acknowledgement. A generous estimate of 5 seconds for LoRa was used in the calculations. The power consumption of the system over a period of 300 seconds is shown in figure 6.16.

To make a more accurate estimation of the efficiency gain, initially assume that any power rail can be generated from another by a regulator (either linear or switched mode) with an efficiency of 100 %. This is purely an assumption since neither LDOs nor switched mode regulators are close to 100 %, but it will allow a dissection of the power consumption per device. For example, the power consumption with all devices in active mode is then

$$P_{act} = 5\,\mathrm{V} \cdot 200\,\mathrm{mA} + 3.3\,\mathrm{V} \cdot (15\,\mathrm{mA} + 120\,\mathrm{mA} + 0.5\,\mathrm{mA}) \approx 1.45\,\mathrm{W} \tag{6.3}$$

Usage of switched mode regulators alone offers a potential 13.7 % reduction in power consumption, assuming all devices are constantly running in active mode. As expected from table 6.5, the SDS011 is responsible for the highest peak during its active time, accounting for 1 W (69 %) of total power consumption. When enabled asynchronously with LoRa, this rises to 95 %. The last 2 seconds of its active sensing time, the AM2302 is also activated to obtain a humidity and temperature measurement that is synchronized with the moment the actual air quality sample is taken. At this point, the sensors are disabled, and since the SDS011 is the only component on the 5 V power rail, this power rail can be disabled completely. In stand-by, the SDS011 would otherwise draw a constant 2 mA, a stand-by power waste of 10 mW. After disabling sensors, the sample will be transmitted, for which the RFM95W LoRa transceiver is enabled, drawing up to 120 mA in highest transmission power settings. The total consumption of the system with LoRa active is then 450 mW. After the transmission period of 5 s the system returns to stand-by, drawing 117 μW from the battery.

6.6.3 Power Supply Design

Figure 6.17 shows a comparison between active and idle (= stand-by) mode, a useful tool to identify the facets where a power consumption reduction can be gained.

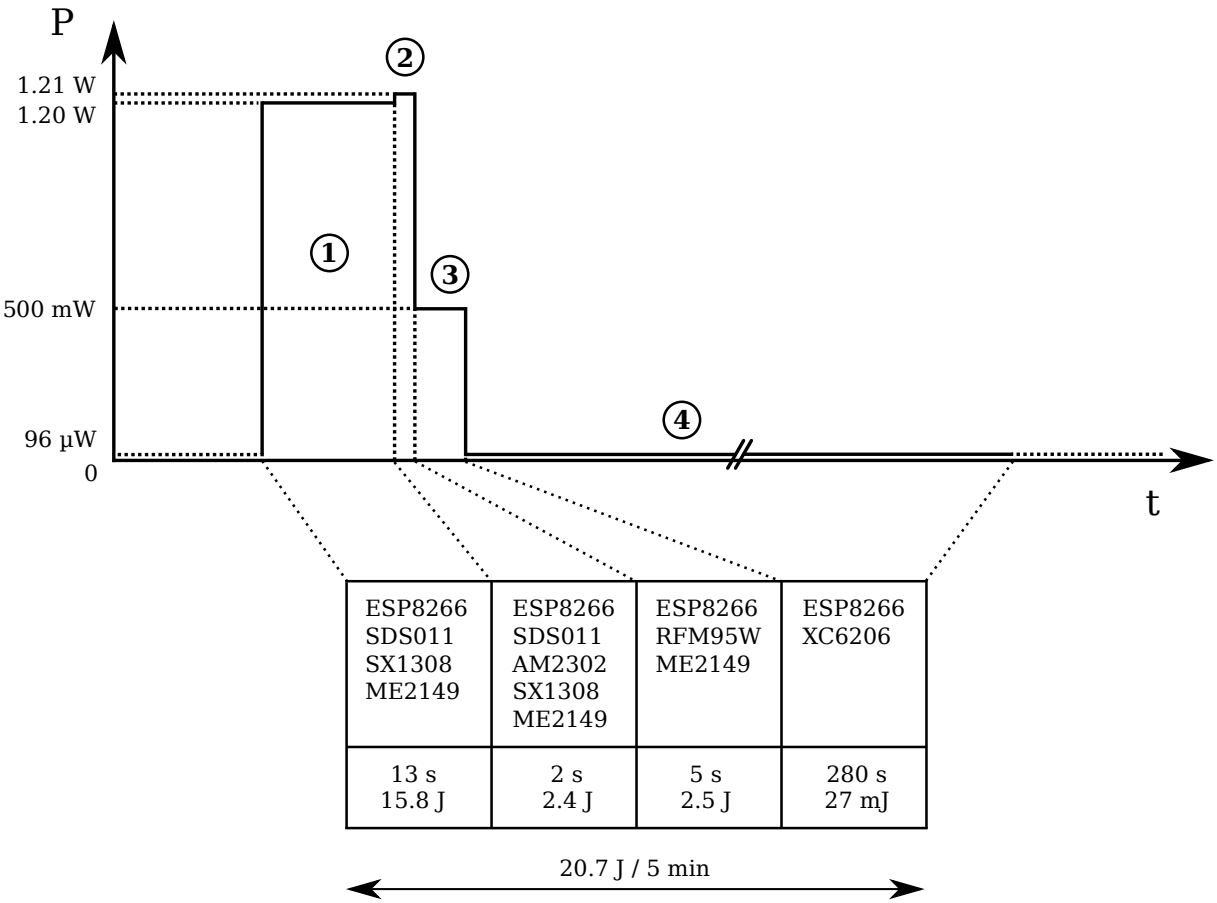

Figure 6.16: The 4 principal power consumption modes of the Influencair module: ① refreshing SDS011 particle sensor, ② particle, humidity and temperature measurement, ③ wireless LoRa transmission, ④ idle state of minimal power consumption.

In both active and stand-by mode, the SDS011 is the largest consumer, and disabling it completely instead of putting it into stand-by is paramount for power reduction. ESP8266, AM2302 and RFM95W are energy efficient in a power down mode, but require 3.3 V for operation. From a Li-Ion battery ranging between 3.0 V and 4.2 V this implies the necessity of a buck-boost regulator to either increase or decrease the battery voltage depending on its state of charge (SoC). A buck-boost controller like the ME2149F draws 4 mA supply current in active regulation, and it would have to be permanently active. The supply to load ration (SLR) is then

$$SLR = \frac{16.8\,\mathrm{mW}}{16.8\,\mathrm{mW} + 66\,\mu\mathrm{W} + 50\,\mu\mathrm{W} + 0.66\,\mu\mathrm{W}} = 99.3\,\% \tag{6.4}$$

The next step for further optimization is logically disabling the buck-boost regulator when its operation is not necessarily required. This is possible during time when only the ESP8266 is active, since this microcontroller can run on supply voltages between 2.5 V and 3.6 V. Because of the previously discussed *flow-over* effect when charging a battery, it is not possible to connect the ESP8266 directly to the battery, since it would get damaged when the battery is being charged. Since the maximum current drawn by the ESP8266 in stand-by mode is only 20 μA, a tiny LDO can be used to power the ESP8266 in stand-by mode. Modern LDOs like the XC6206 series from Torex Semi have a supply current of only 1.0 -

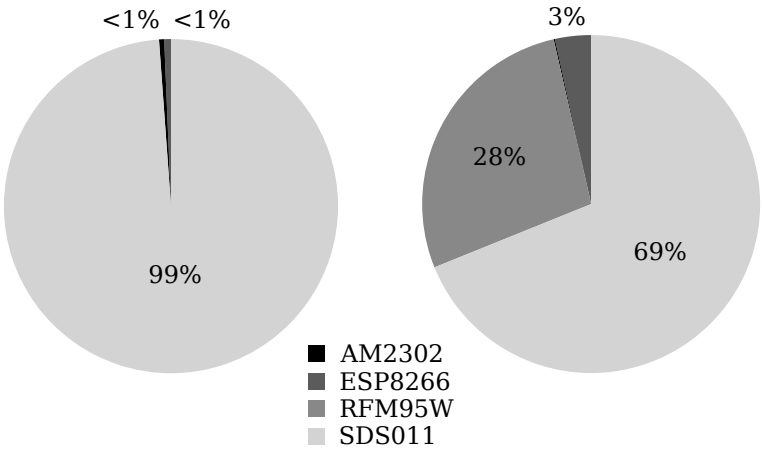

Figure 6.17: Comparison of active power consumption proportions (right) and idle power consumption (left) for the active components.

3.0 μA, or expressed as a SLR to the ESP8266 in stand-by

$$SLR = \frac{1.0\,\mu\text{A}}{20\,\mu\text{A}} = 5\,\% \tag{6.5}$$

The datasheet of the XC6206 mentions 3 μA as the supply current at the maximum output current of 500 mA, for a meager output current of 20 μA it can be expected that the supply current is closer to the minimum of 1 μA, resulting in a more acceptable SLR of 5 % instead of the 99 % for an architecture with a continuously enabled buck-boost regulator. Combining these elements together, the 5 V power supply in the prototype, using a 3.3 V LDO to power all devices on the 3.3 V power rail, can now be optimized by splitting the power supply design in 3 branches:

1. A boost regulator using a Suosemi SX1308 controller to generate the 5 V power rail for the SDS011 from the 4.2 V battery voltage, can be disabled through its Enable pin;
2. A buck-boost regulator using a MicrOne ME2149F controller in a SEPIC configuration, can be disabled through its Shutdown (CE) pin;
3. A Torex Semi XC6206 LDO to supply the ESP8266 in stand-by mode.

The relative performance of the three devices is marked in figure 6.10. It is the ESP8266 itself, the only device that is permanently enabled, that controls the boost and buck-boost regulators to turn on and off the 5 V and 3.3 V power rails as necessary. The LDO itself does not have an enable pin, but a trick can be used to *hand over* the supply of the ESP8266 when the buck-boost regulator is turned on, by choosing the output voltage of the LDO below the output voltage of the buck-boost regulator.

When tied together through a MOSFET, as shown in figure 6.19, the supply voltage of the ESP8266 is automatically raised to 3.3 V as soon as the buck-boost regulator is enabled. This further increases efficiency (since a switched mode regulator is more efficient than an LDO) and eliminates the need for level shifters on digital IO lines or complex analog voltage reference circuitry. The operation is simple: by using a P-MOS with its gate tied to ground, an ideal diode is constructed. The MOSFET will conduct if its $V_{GS} < V_{GS(th)}$ and in this operation a P-MOSFET with $V_{GS(th)}$ should be chosen so that -3 V $\geq V_{GS(th)} \geq$ -3.3 V. When the buck-boost regulator is disabled, $V_{GS} \approx 0$ and the MOSFET will not

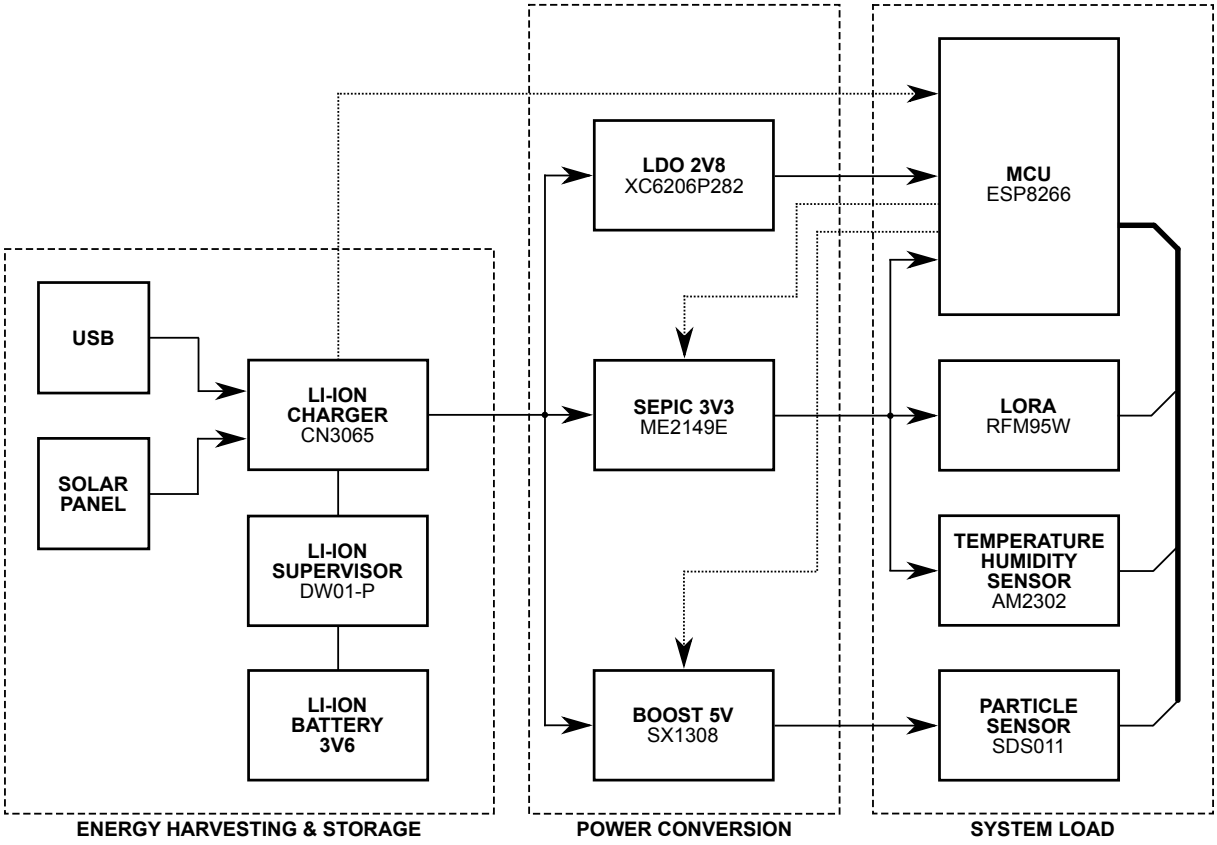

Figure 6.18: Detailed architecture with PV energy harvester, Li-ion battery charger and supervisor system, triple voltage regulator with LDO and SEPIC for 3.3 V generation and boost regulator for 5 V regulation, and the system load as presented in figure 6.15. Dotted lines denote control and monitoring, the right side connections represent a data bus between sensors, actuators, and the ESP8266 microcontroller (top right).

conduct, isolating the LDO from the buck-boost 3.3 V rail. When the buck-boost regulator is enabled, V_{GS} drops to below the $V_{GS(th)}$ and the MOSFET will form a conductive channel between the LDO and buck-boost 3.3 V rail, automatically disabling the LDO since its feedback voltage will be increased to 3.3 V. Several MOSFETs can be cascaded if the current flowing through the MOSFET body diode is a problem. A few BSS84s can suffice for this purpose. The complete power supply is shown in figure 6.20.

6.6.4 Battery Management

When the power supply is solved, the next problem to be tackled is the battery management itself. While it is technically possible to attach the power supply circuitry directly to the battery, it is unwise to do so because there is no protection against short circuit or over discharge conditions. When no solar power is available to recharge the battery, for example because it is covered by a layer of snow for multiple consecutive days, it is possible that the battery is discharged below its minimum voltage. Such a deep discharge reduces the capacity of the battery irreversibly, and thereby reduces its lifetime. On the other hand, short circuit conditions are a risk in this application since water intrusions are possible at any time. Finally, care should be taken to not overcharge the battery either, since that also incurs a reduction in battery life, overheating of the battery, and in a worst case scenario leakage of battery electrolyte. There

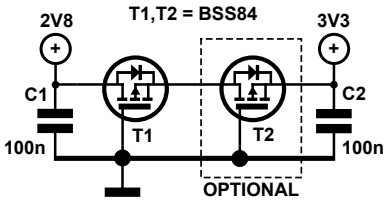

Figure 6.19: Tying 2.8 V LDO output and 3.3 V SEPIC outputs together through a passively controlled P-MOSFET bridge.

are fortunately numerous solutions available, most of them designed for monitoring single cell lithium ion batteries. A trade-off will often need to be made between a single cell and a multi cell battery.

- **Single cell** batteries are easy to charge, but require more advanced power supply design (such as a buck-boost regulator) because the cell voltage may vary above or below the desired system power rails.
- **Multi cell** batteries allow a simpler power supply design because of the higher pack voltage, typically allowing only buck regulators. Aside from charging, these packs require cell balancing to maximize battery life, which is more complex in design and wastes power if done through shunt balancers instead of switched balancers.

For most electronic applications, a single lithium cell will suffice, as is the case for the Influencair project. For cell management itself, an integrated monitor like the DW01-P from Fortune Semi is a low cost and easily implementable solution. It features internal voltage references designed to trigger on overcharge or overdischarge, as well as on short circuit conditions. Two cascaded N-MOSFETs are used to isolate the battery from the system in case any of these faults occurs. The current drawn when powered down is 0.1 μA, so that it does not further deplete a battery close to the overdischarge threshold. The circuit diagram is shown in figure 6.21.

To charge the battery, there are multiple options. Interestingly, the battery can be connected directly to the solar cell through a diode, since the DW01-P will automatically disconnect the battery from the solar cell if the charge current exceeds the preconfigured value. Unfortunately, this offers little control over the charge process, and disregards the benefits of a maximum power point tracker on the solar cell. To streamline the solution, the energy harvesting and battery management should be solved together. There are many commercial solutions for charge controllers with integrated maximum power point tracking, such as the LTC3105, SPV1040 or BQ25570 discussed in the next chapter. Although efficient at higher currents (100-200 mA), where the switched regulators work optimally, they also come at a substantial cost. An interesting alternative is offered by linear chargers, for example the TP4062 or CN3065, which act as configurable constant current sources, but at a fraction of the cost of switched battery chargers. The CN3065 in particular is an interesting option because it supports USB operation, allowing a discharged battery to be quickly charged through the USB port for debugging and programming if desired. The controller supports a configurable charge current, settable through its ISET output using a single bias resistor, which can also be used to throttle back the charge current if the solar cell is overloaded – creating an external feedback loop as maximum power point tracker. The mechanism is shown in figure 6.21 using an LM10, a low power 200 mV reference and amplifier used as comparator.

For small solar cells, the maximum power point voltage is typically fairly constant, with only minor variations resulting from cloud coverage or temperature. The maximum power point voltage (MPPV) can then be fixed to around 70 % of the open circuit voltage of the cell, which can be easily measured with

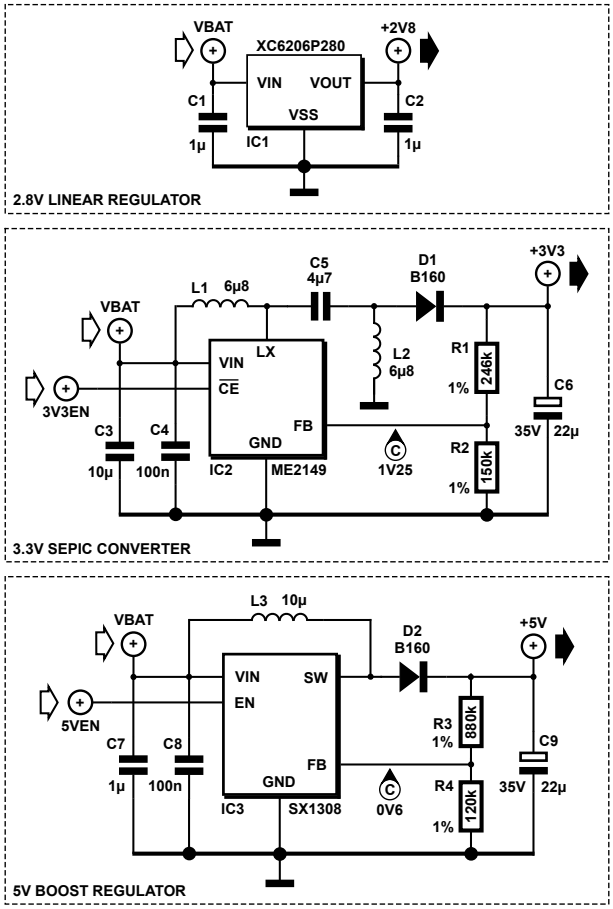

Figure 6.20: Linear, SEPIC and boost regulators for power rail generation. On battery side only ceramic capacitors are used to minimize leakage losses.

a multimeter. This rule of thumb is valid for most monocrystalline and polycrystalline solar cells. Since the CN3065 is a linear current regulator, optimal efficiency is achieved when the voltage drop over the CN3065 is at its minimum. Adding the dropout voltage over the CN3065 to the battery charge voltage of 4.2 V, an optimal value of ca. 4.4 V is a target setting for the maximum power point voltage of the solar cell. Suitable cells are the SLMD121H9L or SLMD960H09L from Ixys, or the AM-8801 or AM-8804 from Panasonic. The maximum charge current in mA can be set by calculating the ISET resistor using

$$I_{charge} = \frac{0.2\,\mathrm{mV}}{R_{iset}} \cdot 900 \tag{6.6}$$

The charge current of the battery is therefore linearly proportional to the value of R_{iset}: higher resistor values will lead to a decrease in charge current and vice versa. This can be used to throttle back the charge current using an additional transistor with a $V_{CE(sat)}$ below 200 mV, such as a DSS20201, as shown in figure 6.21. A proportional fraction of the solar cell voltage is compared to a reference and used to control a transistor in series with R_{iset}. If the solar cell voltage drops below its preconfigured maximum power point voltage, the base current of the transistor will be reduced, decreasing its collector current, and as a result decreasing the charge current of the battery. This causes the solar cell voltage to increase again until it reaches a stable set point that keeps the solar cell voltage close to its maximum power point voltage. When the transistor is saturated, the charge current will top off at the maximum configured by R_{iset}, and any further rise in solar cell voltage will result in an increase of dropout voltage over the CN3065.

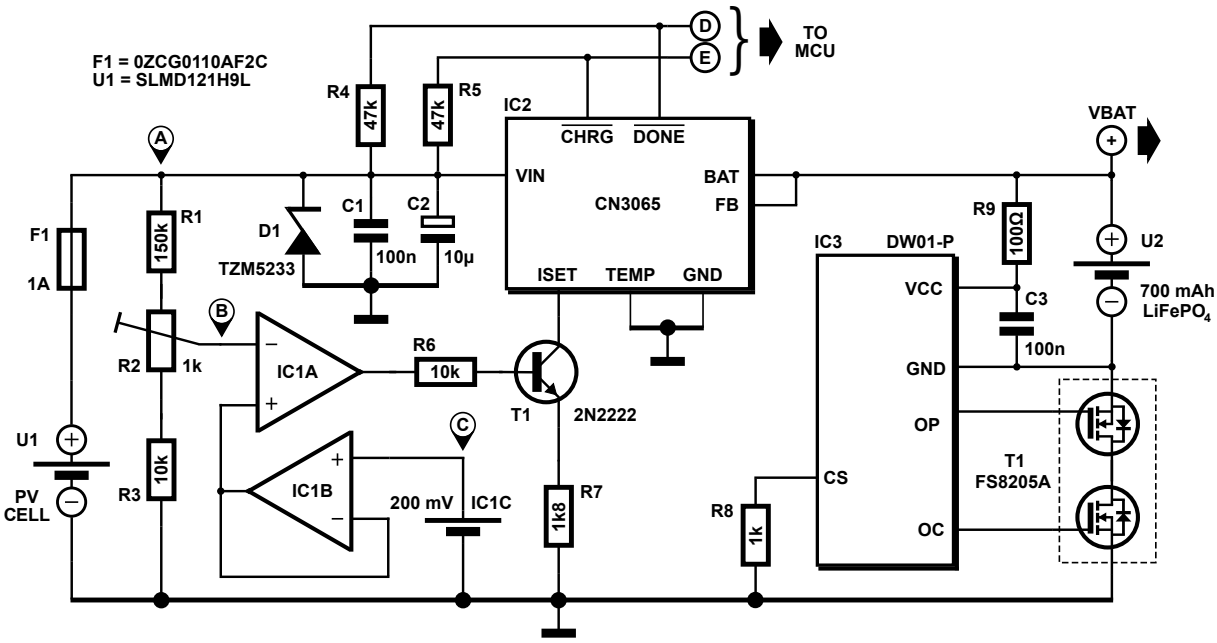

Figure 6.21: CN3065 Li-ion battery charger with DW01-P battery monitor. An external MPPT circuit is implemented by controlling the charge current of the CN3065 with a feed-forward LM10.

Energy Balance

The energy balance, an essential part of the complementary balanced energy harvesting theory, requires power generation to be greater or equal to consumption at any time, provided that no local storage is used. Since the choice was made for a battery here, supply and consumption are buffered by the battery reserves, and do not need to match. This allows to design an autonomous system with only a solar cell, if sufficient energy is stored during the day to sustain continuous operation at night as well. To calculate the capacity of the battery, the total energy consumption per period/cycle of the system needs to be estimated first, and efficiency of the power supply needs to be added to the equation.

As discussed in the previous chapters, the energy demand for a system s over a period or cycle T is equal to

$$E_s = \int_T P_s(t)dt \tag{6.7}$$

In this equation, P_s represents the time variable power consumption of the system, as the sum of the different power rails. In a system with n voltage regulators supplying n power rails, at any time, all regulators have a state defining whether they are enabled or disabled. The set R, representing all regulators, thus consists of two subsets R_i and R_0, respectively enabled and disabled regulators. The power consumption of a disabled regulator is equal to its quiescent current multiplied by the source voltage, $V_s I_{Q,n}$, where $I_{Q,n}$ is the quiescent current for regulator n. Active regulators draw a supply current $I_{s,n}$ from the supply rail, a power consumption intrinsic to the enabled regulator, and an additional power equal to the sum of whichever devices are connected to the supply rail. For k connected devices, the power drawn by the regulator is then

$$P_{R,n}(t) = V_s I_{s,n} + \frac{V_{R,n}(t)}{\eta_{R,n}(t)} \sum_{a=0}^{k} i_a(t) \tag{6.8}$$

where $\eta_{R,n}$ is the efficiency of the regulator, varying in time depending on the sum of the currents drawn by k connected devices. At any point in time, the power of the entire system may be expressed as the sum of all regulators and their attached loads:

$$P_s(t) = \sum^{n} \left(R_n(t) \left[V_s I_{s,n} + \frac{V_{R,n}}{\eta_{R,n}(t)} \sum_{a=0}^{k} i_a(t) \right] + (1 - R_n(t))\, V_s I_{Q,n} \right) \tag{6.9}$$

In this equation, $R_n(t)$ expresses a unity step or box function for regulator n with $R_n(t) = 1$ if the regulator is enabled on time t, and $R_n(t) = 0$ if the regulator is disabled at time t. Since $P_s(t)$ is a continuous function, the energy budget for a complete period or cycle T can be found by integrating P_s over the entire period:

$$E_s = \int_T \sum^{n} \left(R_n(t) \left[V_s I_{s,n} + \frac{V_{R,n}}{\eta_{R,n}(t)} \sum_{a=0}^{k} i_a(t) \right] + (1 - R_n(t))\, V_s I_{Q,n} \right) dt \tag{6.10}$$

The generalized equation can be applied to any system regardless of complexity, number of regulators or number of devices. It is somewhat cumbersome to calculate however, since the integration requires continuous functions for currents drawn from devices, and regulator efficiency as a function of those currents. In many practical situations, it may be acceptable to simplify the equation by assuming both variables are instead constants within a well defined mode of operation of the system. This is shown in figure 6.16, where the current drawn within a block or section is nearly constant, resulting in a square shaped power consumption graph. A convenient consequence is that for each block or section, the conversion efficiency of each regulator $\eta_{R,n}$ can be looked up in a datasheet. Most regulator datasheets provide graphs with $\eta_{R,n}$ as a function of V_s and $V_{R,n}$, respectively the supply voltage (e.g. input voltage) and the output voltage of the regulator, and in function of various output currents drawn. When the cycle is split up in such blocks of constant operation, with a total of S sections, then the integral may be expressed as a discrete sum instead, which is easier to calculate:

$$E_s = \sum_{S} \left[\sum_{n}^{R \backslash R_0} \left(V_s I_{s,n} + \frac{V_{R,n}}{\eta_{R,n}} \sum_{a=0}^{k} i_a \right) + \sum_{n}^{R_0} V_s I_{Q,n} \right] \Delta t \tag{6.11}$$

In this equation, $R \backslash R_0$ is the set of enabled voltage regulators, and R_0 the set of disabled voltage regulators. While the equation assumes switched mode regulators with an efficiency $\eta_{R,n}$, it can also be expanded for use with linear regulators, eliminating the efficiency term:

$$E_s = \sum_{S} \left[\sum_{n}^{R \backslash R_0} V_s \left(I_{s,n} + \sum_{a=0}^{k} i_a \right) + \sum_{n}^{R_0} V_s I_{Q,n} \right] \Delta t \tag{6.12}$$

Combinations can of course also be used, interchanging the terms depending on the type of regulator n being considered. With the sets know for each section, the total energy consumption per period or cycle can now be calculated from the data in table 6.5. Splitting up the consumption in the 4 sections shown in figure 6.16, each section S_1 to S_4 can be calculated separately. For S_1, the ME2149 (switched 3.3 V rail) and SX1308 (switched 5 V rail) are active, while the XC6206 is in a shutdown state:

$$\begin{aligned} E_{S_1} = &\left[4.2\,\mathrm{V} \cdot 4\,\mathrm{mA} + \frac{3.3\,\mathrm{V}}{92\,\%} (15\,\mathrm{mA} + 15\,\mu\mathrm{A} + 0.2\,\mu\mathrm{A}) \right] \cdot 13\,\mathrm{s} \\ &+ \left[4.2\,\mathrm{V} \cdot 1.6\,\mathrm{mA} + \frac{5\,\mathrm{V}}{88\,\%} \cdot 200\,\mathrm{mA} + 4.2\,\mathrm{V} \cdot 1\,\mu\mathrm{A} \right] \cdot 13\,\mathrm{s} \end{aligned} \tag{6.13}$$

The power profile for S_2 is identical to S_1, but with the AM2302 added to it:

$$E_{S_2} = \left[4.2\,\mathrm{V} \cdot 4\,\mathrm{mA} + \frac{3.3\,\mathrm{V}}{92\,\%}(15\,\mathrm{mA} + 500\,\mu\mathrm{A} + 0.2\,\mu\mathrm{A})\right] \cdot 2\,\mathrm{s} + \left[4.2\,\mathrm{V} \cdot 1.6\,\mathrm{mA} + \frac{5\,\mathrm{V}}{88\,\%} \cdot 200\,\mathrm{mA} + 4.2\,\mathrm{V} \cdot 1\,\mu\mathrm{A}\right] \cdot 2\,\mathrm{s} \quad (6.14)$$

In S_3, the SX1308 is powered down because the switched 5 V power rail is no longer necessary, only the ME2149 remains active to power ESP8266 and LoRa transceiver:

$$E_{S_3} = \left[4.2\,\mathrm{V} \cdot 4\,\mathrm{mA} + \frac{3.3\,\mathrm{V}}{92\,\%}(15\,\mathrm{mA} + 120\,\mathrm{mA} + 15\,\mu\mathrm{A}) + 2 \cdot (4.2\,\mathrm{V} \cdot 1\,\mu\mathrm{A})\right] \cdot 5\,\mathrm{s} \quad (6.15)$$

Finally, all switched regulators are turned off, and the system remains in a dormant state until the end of the period, with the ESP8266 in a sleep state and powered by the XC6206:

$$E_{S_4} = [4.2\,\mathrm{V} \cdot 0.5\,\mu\mathrm{A} + 4.2\,\mathrm{V} \cdot 1\,\mu\mathrm{A} + 4.2\,\mathrm{V}\,(1\,\mu\mathrm{A} + 20\,\mu\mathrm{A})] \cdot 280\,\mathrm{s} \quad (6.16)$$

To obtain the total energy, the individual sections are summed together:

$$E_s = \sum_S = E_{S_1} + E_{S_2} + E_{S_3} + E_{S_4} = 15.8 + 2.4 + 2.5 + 0.027 = 20.7\,\mathrm{J} \quad (6.17)$$

Consumed over an entire period of 5 minutes, the average power consumption is then

$$\overline{P_s} = \frac{E_s}{T} = \frac{20.7\,\mathrm{J}}{300\,\mathrm{s}} \approx 70\,\mathrm{mW} \quad (6.18)$$

During the entire duration of operation, regardless of which state (i.e section) the system is in, the battery management circuitry of the power path also remains active. The energy consumption of the power path, E_{pp}, then equals

$$E_{pp} = \int_T V_s \sum_{a=0}^{k} i_a dt \quad (6.19)$$

where V_s is the supply voltage as above, and i_a represents the current drawn by k devices in the power path. It can also be written in its discrete form

$$E_{pp} = T \cdot V_s \sum_{a=0}^{k} i_a \quad (6.20)$$

if the consumption of the power path $\sum_{a=0}^{k} i_a$ remains constant over the entire period T, which is often the case in practical designs. For the presented design, the number of devices is limited to only one, the battery management system DW01-P, since both the CN3065 and LM10 are powered by the solar cell directly and thus do not present a load on the battery if there is no incoming solar power. Filling in the data from table 6.5 yields

$$E_{pp} = 300\,\mathrm{s} \cdot 4.2\,\mathrm{V} \cdot 3\,\mu\mathrm{A} \approx 3.8\,\mathrm{mJ} \quad (6.21)$$

From a battery management perspective, the SLR is

$$SLR = \frac{E_{pp}}{E_s} = \frac{3.8\,\mathrm{mJ}}{20.7\,\mathrm{J}} \approx 0.18\,\% \quad (6.22)$$

which is a very acceptable figure for battery management, in comparison to the complete system consumption.

Storage

If $P_s(t)$ is the power consumption by the system, $P_{pp}(t)$ the power consumption of the power path itself, and $P_h(t)$ the power produced by the energy harvester(s), then at any moment in time the power budget must be in balance:

$$P_s(t) + P_{pp}(t) \leq P_h(t) \tag{6.23}$$

With local storage such as a battery or EDLC, the difference between the two equation sides determines whether energy is being stored or retrieved. The local stored energy is thus an accumulation of the power difference between harvester, system and power path over time:

$$E_{bat}(t) = \int (P_h(t) - P_s(t) - P_{pp}(t))dt \tag{6.24}$$

If exactly dimensioned to the requirements of the system, then power storage equals retrieval over a large number of cycles:

$$\int_{-\infty}^{\infty} (P_h(t) - P_s(t) - P_{pp}(t))\, dt = 0 \tag{6.25}$$

As such, not all energy required for the operation of a complete period or cycle needs to be stored locally into a battery or EDLC, only a buffer. The minimum capacity of the local storage can be found by calculating the local minima and maxima of $E_{bat}(t)$, which corresponds extremum values in energy storage (peaks or dips). The values t at which a peak or dip in $E_{bat}(t)$ occurs can be found by solving

$$\frac{\partial E_{bat}(t)}{\partial t} = 0 \tag{6.26}$$

The minimal capacity of the local storage is then the largest value of a local minimum or maximum in $E_{bat}(t)$. The total energy stored in the battery during a period is ideally identical to the total amount of energy retrieved:

$$E_{bat,T} = \frac{1}{2} \int_T \sqrt{[P_h(t) - P_s(t) - P_{pp}(t)]^2} dt \tag{6.27}$$

Because the efficiency with which batteries can store energy is not 100 %, it is necessary to keep the battery charge and discharge efficiency into account when calculating the power that needs to go into the battery for $E_{bat,T}$ to be available during T. It is assumed that the charge and discharge efficiency η_{bat} are equal:

$$E_{ch,T} = \frac{1}{2\eta_{bat}^2} \int_T \sqrt{[P_h(t) - P_s(t) - P_{pp}(t)]^2} dt \tag{6.28}$$

This equation provides an estimation of the energy penalty resulting from using a battery with an efficiency of η_{bat}.

Energy Harvester

The intermediate step to calculate the battery size and ultimately the solar cell, is the characterization of the ambient environment to benchmark the amount of power that is available in the environment in which the Influencair device is planned to be deployed. The power generated by the solar cell $P_h(t)$ can

then in turn be used to calculate the battery size, depending on the ripple on $P_h(t)$ (as a side note: if the ripple on $P_h(t)$ would be zero, the harvester power and load would be exactly matched, and there would be no need for storage). To benchmark the environment, the AEM project was developed, as will be discussed extensively in the next chapter. However, since only a single harvester is chosen here and deployed in an already known environment (since solar irradiation is closely monitored for large scale PV installations), the benchmarking step can be skipped in this situation because benchmarking data is already available. In Brussels, the solar irradiation is highly variable throughout the year, as shown in figure 6.22, with an average monthly minimum irradiation of ca. 0.66 kWh/m^2 in december, and a maxiumum of 5.02 kWh/m^2 in June. The figures are for a flat (horizontal) solar cell mounted on the top side of the Influencair device.

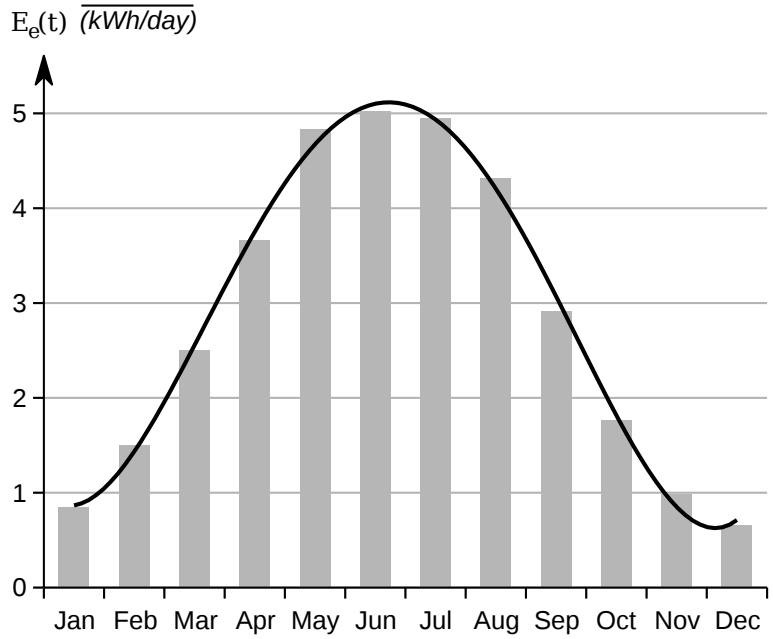

Figure 6.22: Variation of average insolation levels in Brussels as a function of the seasons.

Following the complementary balanced energy harvesting theory, the period of such a harvester would thus be 1 year, following the cycle of the astronomical calendar. An good polynomial fit exists, with a 4th order polynomial expressing the average monthly irradiation

$$E_e(t) = 5.28 \cdot 10^{-3}t^4 + 0.132t^3 + 0.938t^2 - 1.40t + 1.45 \tag{6.29}$$

and $R^2 = 0.997$. The term $E_e(t)$ denotes energetic irradiation, to avoid confusion with photometric quantities. Assuming a year would be used as a period for the system and calculating out the capacity following the equations in the previous section, results in an expected maximum charge to be reached between September and October, and the battery would be close to depletion between March and April. Storing the required amount of energy to operate over the span of an entire year, without taking self discharge of the battery into account, would add up to ca. 703 kJ (assuming a near sinusoidal irradiation variation). For a single cell lithium ion battery (3.6 V), this translates into a battery capacity of 51 Ah $\pm$ 4 Ah, roughly equivalent to a battery pack of 17 individual 18650 lithium ion batteries. The cause of this large size is of course the SDS011 which accounts for the majority of power drawn by the system. For less power hungry systems it may be a plausible strategy to store energy in summer for use during

winter, but at an average power consumption of 70 mW that is not realistic for Influencair. The alternative approach is taking a day/night cycle as the period of the energy harvester rather than a full year, in this case assuming a worst case scenario of 0.66 kWh/m^2 to estimate solar cell yield. [325, 333, 41]

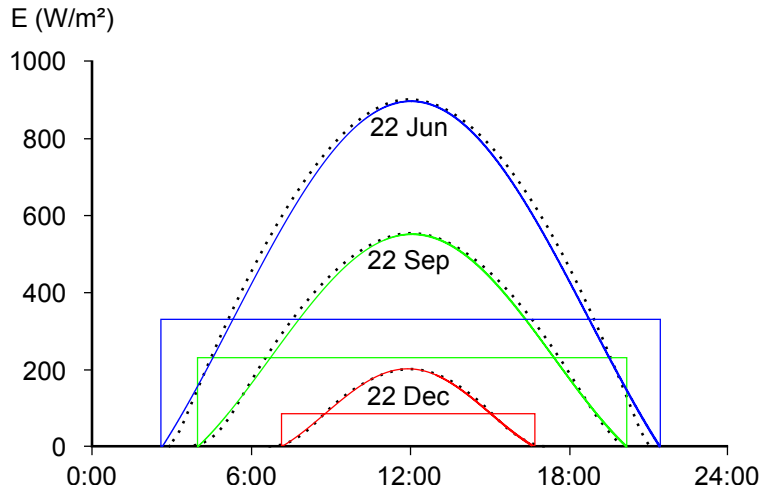

Figure 6.23: Comparison of insolation levels in Brussels, Belgium, in different seasons. Dotted line represent measured averages, colored curves a sinusoidal fit through the measured data. Horizontal lines denote half sines.

To calculate the capacity of the battery, the insolation variations over the entire period (i.e. day and night cycle) need to be considered. Figure 6.23 shows a proportional comparison of solar insolation during the day and night cycle for different seasons. The lower insolation graph for December is of interest to this application. There are multiple approximation strategies for insolation, and the most accurate is a sinusoidal approximation, which correlates well to insolation regardless of the time of the year. The dotted curves in figure 6.23 denote the actual insolation data, while the solid curves correspond to a sinusoidal regression fit. The boundaries of the curve are $\frac{-\pi}{3}$ and $\frac{4\pi}{3}$, corresponding to a total daylight period of ca. 10 hours. Extrapolating to the entire day corresponds to a range of 4π for 24 hours, hence the function for winter insolation can be expressed as

$$E_e(t) = \begin{cases} 0 & \text{if } \frac{-3\pi}{2} \leq t < \frac{-\pi}{3} \\ A\left[\sin(t) + \frac{\sqrt{3}}{2}\right] & \text{if } \frac{-\pi}{3} \leq t \leq \frac{4\pi}{3} \\ 0 & \text{if } \frac{4\pi}{3} < t \leq \frac{17\pi}{6} \end{cases} \tag{6.30}$$

The vertical correction $\frac{\sqrt{3}}{2}$ is found from the function at its boundaries, i.e. $\sin\left(-\frac{\pi}{3}\right) = -\frac{\sqrt{3}}{2}$. With the total insolation for winter known to be 0.66 kWh/m^2 (= 2.376 MJ), the amplitude of the sine wave can be calculated from

$$0.66\,\text{kWh/m}^2 = \int_T E_e(t)dt = \int_{-\frac{\pi}{3}}^{\frac{4\pi}{3}} A\left[\sin(t) + \frac{\sqrt{3}}{2}\right] dt \tag{6.31}$$

which after integration and solving for A yields an amplitude correction factor $A = 4.29 \cdot 10^3$. Filling the value for A into the equation for insolation above gives an accurate representation of the insolation

for any time of the day. [47, 42]

As discussed in the previous chapters, the available environmental energy $E_e(t)$ must be converted to electrical energy with an energy harvester as specialized transducer for this purpose, with again a finite electrical efficiency. Although any type of solar cell can be used in an outdoor environment, there are limitations on the lifetime of amorphous and polycrystalline silicon cells. Both types degrade over time, amorphous cells under influence of UV light, and polycrystalline silicon cells as a result of impurities that are intrinsic to the cell construction. Where amorphous cells harvest between 300 nm and 600 nm, and polycrystalline cells between ca. 500 nm and 1100 nm, monocrystalline silicon cells can harvest the widest spectrum (300 nm to 1100 nm). They have the added advantage of being resistant against performance degradation, making them a favored choice for applications where a long autonomy is desired without maintenance. Depending on the monocrystalline cell construction, conversion efficiency is ca. 22 % ± 2 %, with the highest cells close to 25 % conversion efficiency. This corresponds with the efficiency η_g which is given by

$$\eta_g = \eta_{ref}\left[1 - \beta_0(T_c - T_{ref})\right] \tag{6.32}$$

with $\beta_0 = 4 \cdot 10^{-3}\,\mathrm{K}^{-1}$ for monocrystalline silicon cells [80]. Keeping this efficiency in consideration, the output power of the solar cell on an average December winter day in Brussels is

$$P_h(t) = E_e(t)\mu_g\eta_g = E_e(t)\mu_g\eta_{ref}\left[1 - \beta_0(T_c - T_{ref})\right] \tag{6.33}$$

In this equation, which is derived directly from the energy harvester model for complementary balanced energy harvesting systems, the parameter μ_g denotes the size of the harvester, which is a factor relative to 1 m^2 since the insolation is referenced to a surface of 1 m^2. For a battery with 100 % charge/discharge efficiency, the matched energy balance is

$$\int_T P_h(t)dt = \int_T \left[P_s(t) + P_{pp}(t)\right] dt \tag{6.34}$$

Since the period of the system and its power management (5 minutes) is small compared to the period of the energy harvester (a day), the right side of the equation can be simplified by filling in the discrete power levels directly:

$$\int_T E_e(t)\mu_g\eta_g(T_c)dt = \frac{24 \cdot 60 \cdot 60\,\mathrm{s}}{T}(E_s + E_{pp}) \tag{6.35}$$

This can then be solved for μ_g since μ_g is a constant (i.e. the size of the solar cell as a factor proportional to the reference of 1 m^2:

$$\mu_g = \frac{24 \cdot 60 \cdot 60\,\mathrm{s}}{T \cdot \eta_g(T_c)}\left(\int_T E_e(t)dt\right)^{-1}(E_s + E_{pp}) = 1.056\,\mathrm{m}^2 \tag{6.36}$$

with the previously calculated values for $E_s = 20.7\,\mathrm{J}$ and $E_{pp} = 3.8\,\mathrm{mJ}$, monocrystalline efficiency of 22 % at room temperature operating at 5°C. In other words, a PV panel with an area of 1 m^2 is necessary to ensure the system can continue operation even in winter.

Battery

With $P_h(t)$, $P_s(t)$ and $P_{pp}(t)$ know, it is finally possible to calculate the required capacity of the battery. This can be done by solving equation 6.25 and finding its maximum and minimum using equation 6.26:

$$\left(4.29 \cdot 10^3\left[\sin(t) + \frac{\sqrt{3}}{2}\right] \cdot 1.056 \cdot 0.2376\right) - \frac{1}{300}(20.7 + 3.8 \cdot 10^{-3}) = 0 \tag{6.37}$$

The roots of equation 6.37 are

$$t = \begin{cases} 2\pi n + \pi - \sin^{-1}\left(\dfrac{7963}{108900000} - \dfrac{\sqrt{3}}{2}\right) & \text{with } n \in \mathbb{Z} \\ 2\pi n - \sin^{-1}\left(\dfrac{7963}{108900000} - \dfrac{\sqrt{3}}{2}\right) & \text{with } n \in \mathbb{Z} \end{cases} \tag{6.38}$$

Within the boundaries $\left[-\frac{\pi}{3}; \frac{4\pi}{3}\right]$, the values for the minimum and maximum are

$$E_{bat,T} = \left[\int (P_h(t) - P_s(t) - P_{pp}(t))dt\right]_{t_{min}}^{t_{max}} \approx 3.478\,\mathrm{kJ} \tag{6.39}$$

which corresponds to the energy that needs storage in the battery to get through the night. To store this energy, a battery with a capacity of 0.9661 Wh is required, for a 3.6 V lithium ion battery that equals a battery capacity of minimum 268 mAh. The fraction of the energy that passes through the battery in a period T is

$$E_{bat,T}\left(\int_T P_h(t)dt\right)^{-1} = \frac{3.478\,\mathrm{kJ}}{5.227\,\mathrm{kJ}} = 66.5\,\% \tag{6.40}$$

If the battery efficiency $\eta_{bat} < 100\,\%$ then the harvester size that was calculated is an underestimation, since charge and discharge losses in the battery require a higher $P_h(t)$ than first estimated. The correction factor can be found by calculating the fractional losses in the battery [310]:

$$1 + R\left(\frac{1 - \eta_{bat}^2}{\eta_{bat}^2}\right) \tag{6.41}$$

With a charge/discharge efficiency between 80 % and 90 % for lithium ion batteries, the required solar cell size can be corrected:

$$\mu_g = \mu_{g,0}\left[1 + R\left(\frac{1 - \eta_{bat}^2}{\eta_{bat}^2}\right)\right] \approx 1.448\,\mathrm{m}^2 \tag{6.42}$$

A square monocrystalline solar panel with sides of 1.2 m will thus suffice to power the Influencair sensor system year round, using a single cell lithium-ion battery of 268 mAh to store energy during the night. This concludes the calculation of the Influencair example, whose behavior is deterministically characterized at any point in time. As demonstrated, the presented power path management and complementary balanced energy harvesting theories are sufficiently generalized to be applicable to a wide range of energy harvesting related design problems, but at the same time also flexible enough to be applied to a specific problem like the Influencair system with relative ease.

6.6.5 Battery Chargers

During the design of the Influencair power path, the choice for a battery charger controller of type CN3065 from Consonance was made, although this may seem an odd choice since both the battery and the load are attached down stream of the CN3065. Since there is no load balancing (i.e. intelligently switched power path), the maximum charge current sourced by the CN3065 is divided between the attached embedded system and the battery itself. When the consumption of the system is high, the

maximum current as set by the ISET resistor in figure 6.20 will be reached. In this topology, the actual charge current is therefore always lower than the theoretical maximum charge current as set by the ISET resistor. This is not usually a problem since if properly dimensioned, the maximum charge current of the battery will be higher than the maximum current supplied by the PV panel, and the MPPT circuit will throttle back the charge current to keep the output voltage of the solar cell in its MPPV.

As a linear device, the CN3065 acts as programmable constant current source with integrated hand-over between constant current and constant voltage charging. Similar devices like the TP4056 rely on identical operation principles, and such linear devices can be easily recognized in circuit by the absence of an inductor. The low overhead in terms of required circuitry makes this approach particularly favorable if the input and output voltage are very close to each other, with a minimal drop-out voltage to minimize ohmic losses. The higher the charge current, or the larger the difference between solar cell voltage and battery voltage, the greater the losses in a linear regulator will be. A solution to this problem is, analogous to voltage regulator, migrating from a linear battery charger to a switched mode battery charger. The required circuity to implement such a solution is more complex, and an example is shown in figure 6.24 using the Consonance CN3306, which could be considered the switched mode variant of the CN3065.

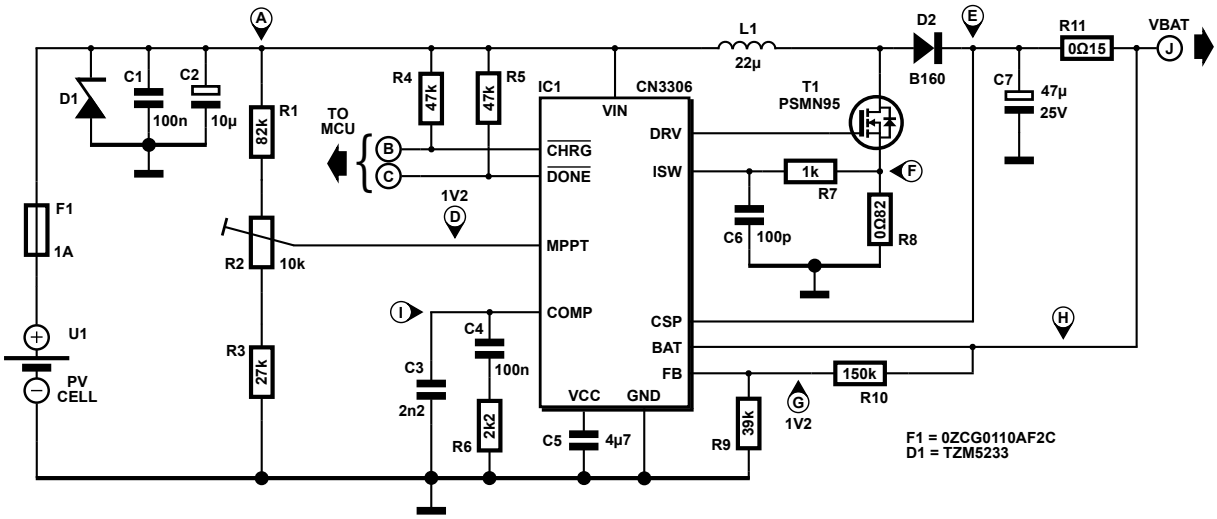

Figure 6.24: Switched mode battery charger with a CN3306 charge controller implementing a boost regulator and integrated MPPT.

The circuit implementation shares the same elements as the CN3065 shown in figure 6.20: a charge controller, MPPT voltage divider on the input, circuit protection, and battery voltage feedback to terminate the charging cycle. Unlike the CN3065 however, the CN3306 includes the necessary MPPT circuitry, and the external LM10 can therefore be omitted. The CN3306 internal voltage reference used for MPPT and battery feedback is 1.205 V, so the set point of the solar panel MPPV is straight forward using the 70 % V_{oc} rule of thumb. A trimmer (R2) is provided for precise calibration of the MPPV.

With MOSFET T1, series inductor L1 and flyback diode D2, a classic boost topology can be immediately recognized, with the CN3306 acting as the boost controller. The current through the MOSFET, which allows the peak current through L1 to be measured, is captured using a small shunt resistor (R8) in the MOSFET source path. The signal is filtered using R7/C6 as LPF and then fed back to the CN3306 to adjust the duty cycle of the DRV output. The actual charge current is sensed using a second shunt

resistor R11, and the burden voltage is measured differentially using the CSP and BAT inputs. The maximum charge current for this implementation is equal to 120 mV/R11, which for a 750 mAh battery would correspond to ca. 1 C to maximize battery life time. The feedback pin (FB) is used to set the constant current/constant voltage threshold: when the voltage on this pin approaches 1.2 V, the CN3306 will switch from constant current to constant voltage mode and continue charging until the charge current (measured as the voltage over R11, points E and H) drops below 10 % of the set charge current. A loop compensation network (C4, R6 and C3) is required to ensure stability, the compensation slope of the CN3306 is fixed to $4.49 \cdot 10^4$ V/s, and the values for C4, R6 and C3 are calculated following specifications in the datasheet.

Since the supply current of the CN3306 is 30 % higher than the CN3065, a trade-off exists depending on the difference between solar panel output voltage and battery voltage, and is also affected by the charge current. At low charge currents, the supply current to keep the CN3306 in active regulation is no longer negligible, and should be accounted for when calculating the charge efficiency of the the battery. Figure 6.25 shows a comparison of the CN3065 and the CN3306.

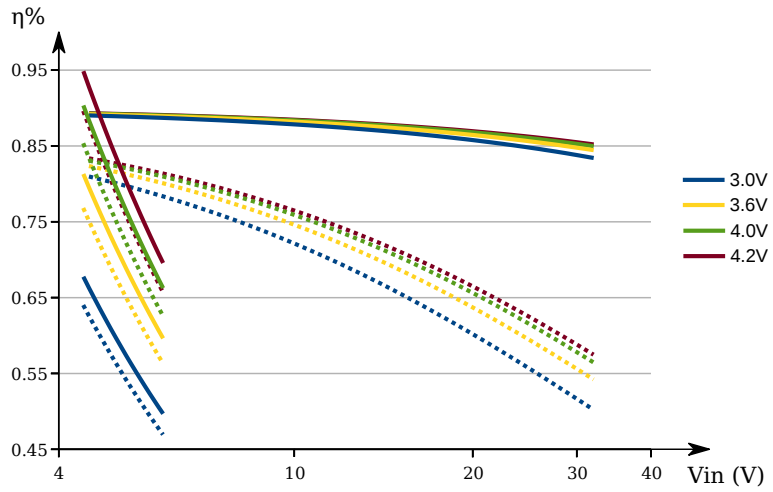

Figure 6.25: Charge efficiency comparison between the linear CN3065 (left steep curves) and switched mode CN3306 battery chargers. Solid curves show a charge current of 100 mA, dotted curves a charge current of 10 mA.

Because the CN3065 is a linear device and dissipates the power difference between input and output as heat, the voltage range of operation is only 4.4 V to 6 V, and the associated efficiency curves are shorter in comparison to the CN3306 which supports input voltages up to 32 V. In the graph, 2 separate curve sets are shown: solid lines denote efficiency for a 100 mA charge current, while dotted lines represent a 10 mA charge current. When the solar panels output voltage is close to the battery voltage, corresponding to the curves for 4.0 V and 4.2 V, the CN3065 is more efficient because the losses resulting from a linear regulation approach are smaller than those inferred by the overhead of a switched mode solution. Likewise, for small charge currents, the CN3065 outperforms the CN3306 for the same reason, but this is only a fraction of about half of its operation range. At higher currents (solid curves), the fixed switching efficiency of the CN3306 ($>$90 % for I$\leq$500 mA) makes it a more energy efficient solution. For sources with a wide output voltage range, the CN3306 is also the only viable option since the linear CN3065 would burn up due to excessive heat dissipation.

When choosing the most optimal battery charger type for a specific application, other factors should also be kept into the equation: linear regulators tend to have a longer lifetime than switched mode regulators because of the lower peak currents, switched mode regulators require more external components (inductor, MOSFET, flyback diode, frequency compensation networks), and the cost is higher in terms of component investment and required PCB area.

6.7 Conclusion

As demonstrated with the Influencair case study, the design of the power path interfacing harvester(s) with system electronics is as important as optimizing the rest of the circuit architecture is. The potential gains of highly efficient harvesters or microcontrollers with low idle power consumption can be lost entirely in the power path, if the latter isn't properly designed to match the power requirements of the system to the supply of the harvester(s). Linear and switched mode DC/DC converters have their own role in the power path, and separation of power rails is a favorable topology that allows to switch on and off circuit parts as desired, thus saving energy. Voltage regulators or switched mode controllers have Enable inputs, it is time to start using them.

In environments where ambient energy levels are discontinuous, and harvesters are unable to power the system directly over the course of its entire period, intermediate storage is required. While non-rechargeable batteries do not have a future, rechargeable batteries may be an acceptable solution for applications with a high power consumption and infrequent but lengthy interruptions of ambient energy supply. The battery type and capacity needs to be selected appropriately to compensate for degeneration of capacity over time, and ensure the desired number of charge/discharge cycles is chemically feasible. In specific applications there may be better alternatives: EDLCs have a nearly unlimited life time and can deliver high power peaks into a load due to their low ESR. On the other side of the storage spectrum, solid state batteries can retain a charge in the order of magnitude of a few mAh, but have cycle times comparable to EDLCs and combine it with the low self discharge advantage of non-rechargeable batteries.

Chapter 7

Ambient Energy Monitor

Two critical factors in the design and implementation of any autonomous ambient powered embedded system are the available ambient energy and the efficiency at which it can be converted to electrical energy to power the system.

Consider as example an autonomous CO detector for domestic use in boiler rooms, powered by ambient energy. Electrochemical CO sensors that do not require their sensing element to be heated have emerged on the market, such as the TGS5342 from Figaro Engineering, reducing the power consumption of such a system by over 2 orders of magnitude in comparison to traditional electrochemical sensors. Designs using a transimpedance amplifier and comparator as analog front end have been proven possible to last up to 5 years on a few coin cell batteries. In combination with a low power microcontroller for sensor EOL detection, basic user interface and buzzer control, the hardware topology of such a CO detector fits into the scheme described in the previous chapter.

Since the sensor life time outlasts the battery life in existing implementations, the battery needs to be replaced multiple times during the life time of the product, resulting in maintenance costs and toxic battery waste that needs to be collected, managed and recycled. Energy harvesting clearly offers an advantage in such applications because, when following the proper design methodology dictated by the complementary balanced energy harvesting theory presented earlier, an adequately reliable system can be designed without batteries at all. In such a design, not the power source will limit the life time of the detector, but the sensor itself. This is, however, a considerable improvement because the TGS5342 can be replaced when mounted in a suitable socket, just like batteries, but does not contain hazardous substances and can be disposed of safely without harming the environment. The question still remains, if such an autonomous CO detector must be designed to work on ambient energy, which types of ambient energy would have the largest potential, in combination with which harvesters, and how large should said harvesters be?

In practical applications, it is up to the embedded systems designer(s) to determine the best harvester type and size, but the tools to achieve this goal are currently lacking. Sensors are abundantly available to measure any type of ambient energy imaginable, but the process of measuring the available energy in an environment – the ceiling of a boiler room, in the example above – is a cumbersome and labour intensive process. It may for example be straight forward to measure the light intensity using an off-the-shelf lux meter, for example, but this remains a snapshot and does not provide any information on the continuity of the energy source, nor its characteristics. Given the wavelength sensitivity of solar cells, a snapshot of the light intensity level at a given location is useless without accurate spectral data and their evolution

in time. This issue may self-evidently be resolved by using more expensive measurement instruments hooked up to high end data acquisition systems, but needless to mention, it would be impractical and costly to install such systems on the ceiling of a boiler room for the sole purpose of selecting and dimensioning solar cells. An easy to use solution for the characterization of ambient environments is therefore paramount to enable adoption of energy harvesters as replacements for batteries.

This chapter is dedicated to resolving the problem of measuring ambient energy in the field. The proposed solution is an Ambient Energy Monitor, abbreviated to AEM, of which the design as an open source energy harvesting development platform is the most important realization of this work.

7.1 Design Topology

The design goals of the AEM system aim to provide answers to the following questions:

- Which types of ambient energy are available?
- What are their characteristics?
- What is their continuity?
- How will actual harvesters behave in the environment?

The AEM therefore fulfills 3 major roles:

- Characterizing the ambient energy available in an environment
- Providing a platform to test how energy harvesters behave in the environment
- Evaluating the performance of state of the art power conversion circuitry

7.1.1 Mk I: Monolithic Design

The first version of the AEM was designed as a monolithic system with numerous sensors, energy harvesters and DC/DC converters connected to a switch matrix to dynamically construct power paths for different types of ambient energy. Equipped with an AllWinner A20 processor, Raio RA8875 graphics processor and touch screen user interface, the system was designed to be portable and easy to install. After the informal presentation of the blueprints at the 2015 IDTechEx Conference on Energy Harvesting and Storage, the design was received with mixed critical feedback. The most significant issues with a monolithic design are the substantial cost due to the complexity of the hardware, while only certain subsystems can be used at any given time since not all energy types are available in every environment.

Secondly, it became apparent that the usefulness of such a device would be severely limited in time due to rapid and ongoing evolutions in power path and DC/DC converter technology. As these components are integrated in a monolithic design, considerable design efforts are periodically required to update them to the most recent technology. The highly interconnected nature of a monolithic design complicates this kind of updates, and it would likely be obsolete by the time this work is published – or soon afterwards, without the continuous maintenance required to keep it up to date. Extensibility and refactoring are key targets, but made difficult by a monolithic design layout. The monolithic approach was therefore abandoned in the design phase in favor of a modular design. The design files have been published and are available under an MIT license for reference.

7.1.2 Mk II: Modular Design

As a solution to the previously discussed shortcomings of a monolithic design topology, a modular topology was chosen instead. The custom central processing block (A20 + RA8875) was swapped out in favor of a standard single board computer with a mezzanine interconnect to interface different daughter boards for each type of ambient energy. The choice for UEXT as a standard communication interface between mezzanine hardware enables compatibility across different versions of hardware modules and firmware revisions.

Additionally, instead of a closed hardware design in the professional EDA package Altium Designer, which complicates refactorability, it was instead chosen to support the CircuitMaker initiative. CircuitMaker launched in 2015 as a free to use cloud centric edition of Altium Designer, targeted at the maker community. All hardware designs are open source and stored in a git version control system that is publicly available. The AEM hardware is released under a Creative Commons license which allows forks and modifications of the individual modules, thus encouraging an ecosystem of harvester boards for which the initial framework is provided, but ultimately supported by the community interested in energy harvesting. As part of the AEM project on CircuitMaker, over 500 electronic components and parts were contributed to the CircuitMaker community vault in the context of this work. This includes the framework with microcontrollers and common ADCs, as well as other parts shared between boards (power supply, filtering, connectivity etc.).

7.1.3 Shared Core

Individual AEM modules, specific for different types of ambient energy, share a central processing unit responsible for the acquisition of data samples, time stamp management and preprocessing. As of 2017, there are 4 different AEM modules available for respectively vibrations, light, heat, and RF. Up to revision 2, they have an ATmega2560 8 bit microcontroller with bootloader programming interface in common, and from revision 2.2 onwards, a USB interface based on a CH340G/T USB controller. The primary ADC is the AD7689 from Analog Devices, an 8 channel, 16 bit, 250 kS/s ADC with SPI interface, which can be used in single ended or differential mode. The shared core structures will be discussed below. The modular design was presented at SHA2017 [319].

7.2 Development

7.2.1 Proof of Concept for MEMS Sensors

To ensure a sufficiently accurate comparison between ambient energy influx and harvester output, fitting sensors for various types of ambient energy must be selected. The choice of sensors for any type of ambient energy is plentiful, and both technical and practical factors play a role in the decision making process. To evaluate the potential of several sensor types for use within the AEM ecosystem, it was decided to design a sensor evaluation platform and deploy it in various environments to gain experience with different types of sensors. The evaluation platform, branded as a weather station, ought to provide insights in three aspects:

- Accuracy and repeatability;
- Calibration, including drift and decay, automatic recalibration, and EOL prediction;
- Interfacing and data acquisition, including software driver development;
- Estimation of development time.

Because its ease of verification, environmental temperature was chosen as measurable parameter, and 3 sensors were selected to compare measurement accuracy: a Bosch BMP180 digital temperature sensor with I2C interface, a DHT-11 digital temperature sensor with one wire interface, an analog semiconductor NTC sensor (which could be swapped for an LDR if desired), and the internal temperature sensor of a PIC microcontroller as integrated sensor. The block diagram of the board is show below.

The PIC microcontroller is responsible for reading out both digital sensors, and acquiring samples from the analog NTC using its internal 12 bit ADC. Since temperature variations in a climate chamber can be kept stable, sample acquisition rate could be kept low at 1 S/s. Aside from the microcontroller, the platform was equipped with an MCP2200 USB to serial controller to allow an interface with data acquisition software on the computer side. The electronics are powered through the USB port, for which an integrated power supply is included on the board.

To speed up the evaluation process, 50 boards were manufactured in house. The PCBs were ordered from EuroCircuits, assembled with a TM220A benchtop pick and place machine from NeoDen, and reflowed in a standard LPKF Zelflow reflow oven. No wave soldering took place: the through hole components were soldered on manually in a collaborative effort with students, to enhance their soldering skills, under supervision of lab management staff. This drew attention and interest of the students, and boards were distributed among second year engineering students as a programming and data visualization exercise, with as goal to implement computer side software in a high level programming language to extract environmental data from the boards and visualize it in a graphical user interface (GUI). Since the use case of the sensor evaluation platform is quite similar to the AEM itself, feedback on its ease of use was collected together with the experience on sensors itself.

7.2.2 Evaluation

Despite the diversity in sensors on the board, it was found that calibration was the most difficult challenge for all of them. Temperature readings strongly differed between boards, and even between sensors on the same board. The accuracy of factory calibrated sensors (BMP180, DHT-11) was inadequate, and recalibration of sensors necessary. This is surprising, since Bosch claims that no user calibration ought to be necessary. No built in amenities for dynamic reconfiguration/recalibration were provided however, in hindsight a poor design choice under pressure of cost limitations. Secondly, the lack of on board storage for data was experienced as a flaw because the board needed to be connected to a computer (desktop or embedded) at all times. A third conclusion from this test was the satisfactory reliability of the platform, even without a custom housing for it. No critical failures were reported, and only 2 boards (4 %) were returned partially defective. One board, connected to a Raspberry Pi single board computer, operated continuously in an outdoor environment for the duration of 2 months, collecting data on temperature, pressure and humidity to make weather forecasts. Based on this evaluation, a second version was designed to resolve problems with the first version of the evaluation platform, as the next step in development of the AEM.

7.2.3 OpenObservatory

In an attempt to improve the flexibility and refactorability of the first version and resolve its flaws, numerous improvements were made based on user feedback. The topology of the system was completely redesigned, with the exception of the USB interface and power supply. Most importantly, the PIC24F16KA301 microcontroller of the first version was swapped out for an ATmega328p and equipped

with a bootloader that enables dynamic reconfiguration of firmware. As an open source project, the hardware was designed in CircuitMaker, and the firmware published on Github. A C++ header file for the board was written and published to enable users to develop custom firmware, which can be uploaded without the need of a programmer by means of the bootloader. The USB-interface doubles as a programming interface, serial debugger, and data output. A decisive argument for the choice of the ATmega328p as replacement for the PIC is its incorporation of 1 kbyte EEPROM memory, enabling local storage of calibration data and dynamic recalibration if necessary. The design was presented at CCC 2015 for peer review [91].

In addition to the existing sensors, the board contains a Si1145 triple photo diode light sensor and an MQ-135 electrochemical sensor capable of measuring airborne pollutants. It therefore acts as a reference for many different electrochemical sensors, as for example the TGS5342 CO sensor in the example at the beginning of this chapter. To allow local storage of data, a standard SD card slot was added as well, allowing local storage of sample data in a CSV format in file systems with a capacity up to 4 GB. Thus, it is possible to run the board autonomously without any computer connected to it, as long as 5 V is supplied through its USB port. An additional on board LED indicates local data logging, and data is written to a new file whenever the reset button is pressed.

The flexibility provided by the bootloader allows quicker software development. Care was taken to make the board 100 % compatible with the PlatformIO framework, as embedded systems development add-on for the Atom editor. The board is also compatible with the Arduino ecosystem, and firmware can be compiled and uploaded in 4 ways: with a direct AVR programmer using JTAG, with PlatformIO, from the Arduino IDE or from command line tools AVaRICE or avrdude. Dynamic reconfiguration of the microcontroller is only supported from Linux and OSX due to driver and dependency related issues. Remote reconfiguration over a network connection has been verified with a Raspberry Pi as host.

In addition to the C++ board description header file, 2 firmware versions were developed: one for normal operation, in addition to a program for self-test and recalibration purposes. Both were released as open source content on Github, and the project was released under the name OpenObservatory. When booting with default firmware, the board samples sensors at a configurable interval. This interval can be dynamically changed without having to reboot or reflash the firmware, by means of an AT like command structure. Other functions that can be controlled using similar commands are logging to SD card, turning on or off the heating element of the electrochemical sensor, setting default temperature sensor, etc. Sensor data is sent to the host as plain ASCII text.

The self-test uses advanced microcontroller features like voltage rail monitoring and watchdog timers to scan the hardware on the board and reports the status of all on board functionality to the user over a serial connection. Alternatively, if an SD card is present, the report may also be written to the file system on the card. The robustness of the self-test firmware was verified using known defective boards with missing parts, malfunctioning sensors or solder short circuits. Likely because of the increased complexity of the design, the production yield was lower in the second version of the board, with 5 boards out of 95 manufactured boards failing the self test (6 %).

7.3 Modularity

Based on experiences drawn from the OpenObservatory sensor evaluation board, the modular design for the AEM consists of 3 parts: a Raspberry Pi 3 single board computer with power supply (either USB

powered or from a battery pack), an AEM interconnect board that is mounted on the Raspberry Pi 3 as hat extension module, and to which one or two energy harvesting modules can be connected. At the time of writing, modules have been developed, or are in development, for 4 different types of ambient energy: vibrations, light, heat and RF energy, which will be discussed below.

7.4 Digital Processing

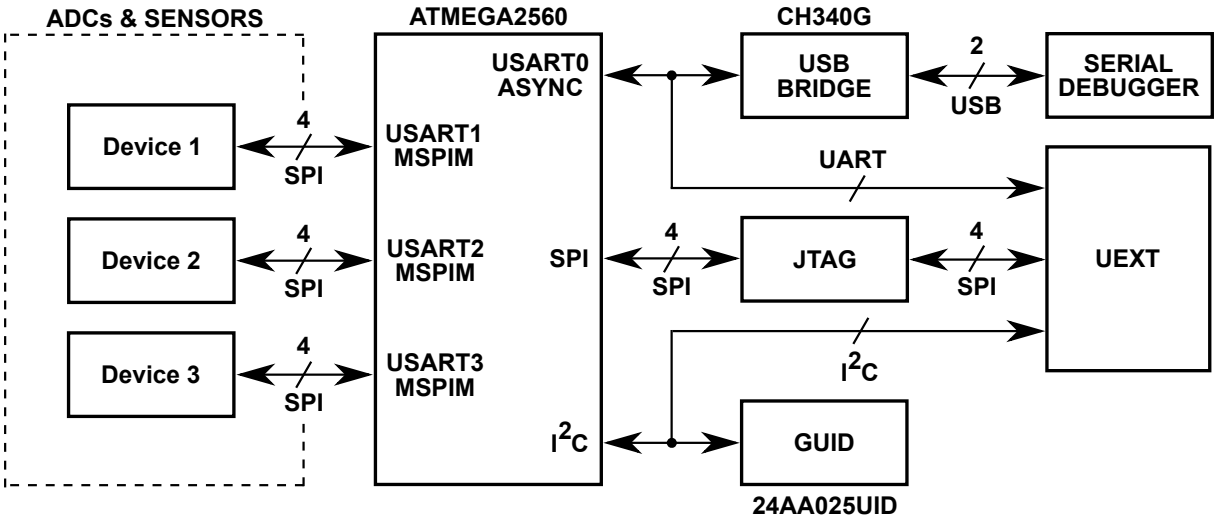

Figure 7.1: Block diagram of the digital control systems common to all AEM modules. The central Atmega2560 AVR interfaces with analog parts (left) and retrieves samples, time stamps them, adds a unique ID and subsequently transmits them to the host over a UEXT interface. JTAG is provided for bootloader programming. Once a bootloader is in place in the designated memory space (see figure 7.2), debugging and reprogramming can be done over USB (top right).

The central processing unit on all AEM modules is an AVR microcontroller from Atmel of type ATmega2560. This 100 pin device in TQFP package provides the necessary IO to interface the AEM-Aggregator with the ADCs and other hardware peripherals on each module. The block diagram of the digital logic is shown in 7.1, identifying the AVR and the ADCs and sensors connected to it as key components on AEM modules. In addition, a memory module of type 24AA025UID provides 2 kbit EEPROM and a unique serial number (GUID) with a length of 4 bytes. The GUID is guaranteed to be unique by the device's manufacturer Microchip, in contrast with the serial number of the microcontroller which is not. The purpose of such a unique serial number on the AEM modules is to ensure data integrity: it allows a global index of AEM modules in existence, together with their module specific calibration data. Samples are recorded together with a time stamp and the module's serial number, allowing them to be traced back to uniquely identified hardware at any given moment in the future. It also enables correlation of data across different modules and/or revisions of hardware. All AEM modules report their GUID to a serial debugger, and every dataset is preceded by it to eliminate any chance of confusion. The host keeps an index of all GUIDs and their respective module types, to match data with a module template.

7.4.1 AVR Peripherals

The Atmega2560 AVR microcontroller is based on a single core 8 bit microcontroller complemented by peripherals. Of relevance for AEM modules are the 4 hardware USART controllers, an SPI controller,

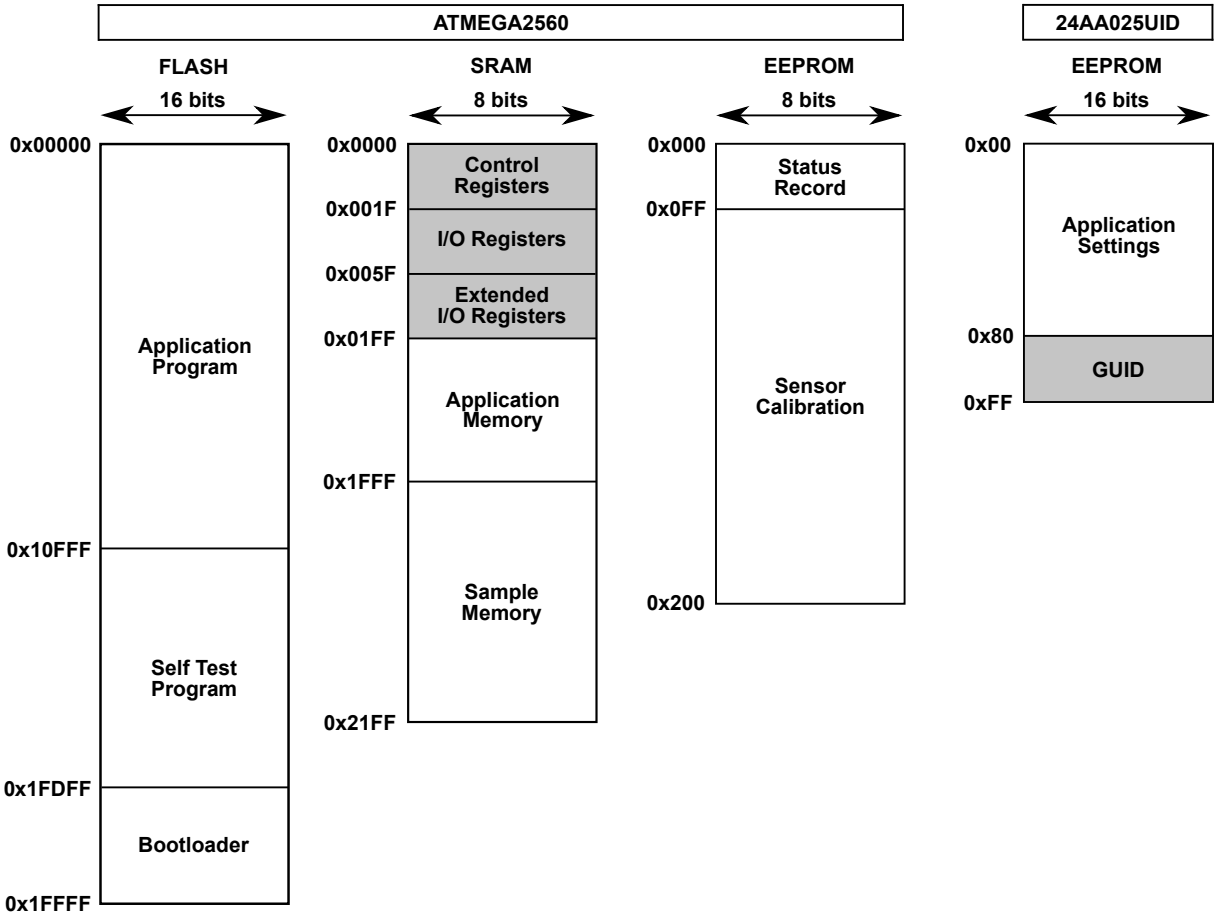

Figure 7.2: Organization of memory space on the AEM modules, with Atmega2560 on the left and 24AA025UID on the right. Ca. 256 kB flash memory and 8 kB SRAM is available on the AVR, complemented by 512 bytes EEPROM internally and another 512 externally in the 24AA05UID. Blocks are not to scale.

and an I^2C controller. These are wired as shown in figure 7.1. Of the 4 USART controllers, the first one (USART0) is operating asynchronously, and the remaining 3 synchronously, as discussed in section B. The synchronous UART connection is interfaced to the UEXT connector, explained in section C. The UART interface is used for serial programming and debugging, but is physically implemented as a USB connection to make usage more practical. The SPI controller is used as a slave, interfacing with UEXT to transmit data to the host system. Unlike any USART core on the device, the SPI controller is able to operate in slave mode, thus enabling communication with a master external to the AEM module. The SPI lines are multiplexed with a JTAG interface, with which SPI is compatible on a hardware level. A JTAG state machine is implemented in the AVR to enable debugging and programming, as discussed in section C.

7.4.2 Memory Organization

The memory map of AEM modules is shown in figure 7.2, and the total address space is divided between the two physical devices the Atmega2560 (left) and 24AA025UID (right). The largest fraction of the address space, 256 kB, is implemented as flash memory organized in 16 bit words. Flash memory is divided in 3 blocks, respectively for the application program memory, a self test for hardware, and the

boot sector containing the bootloader. Integrated flash memory is guaranteed by Atmel to support up to 10 000 read/write cycles. The available SRAM on the Atmega2560 is only a 16th of the flash size, and the address space is shared between user allocatable memory and system reserved memory. The first block from 0x0000 to 0x01FF contains control and I/O registers used for device configuration. The integration of control registers into the SRAM address space simplifies control, although not all addresses are writable within this address space. The remaining memory, from 0x0200 to 0x21FF, is available to the running application. When running AEM firmware, the first sectors from 0x0200 to 0x1FFF are used for storage of application specific variables and objects, while the last sectors from 0x2000 to 0x21FF are used as a buffer for samples. In self test mode, the last sectors remain unused. EEPROM is available on both the Atmega2560 and 24AA025UID, but their memory structure is different. The EEPROM memory on the Atmega2560 is primarily used to store calibration data for sensors and ADCs on board, the absence of which was one of the reported shortcomings of the OpenObservatory board. The first 256 bytes are reserved for recording the state of the board, including life time, to streamline periodic recalibration. The lifetime of the board is recorded by periodically incrementing a non volatile counter value. On the 24AA025UID, the available memory is organized in 16 bit words instead of 8 bit words, and may be used to store application specific settings. The memory is too slow to be used as cache for samples. The last sectors, from 0x80 to 0xFF, contain the 32 bit unique ID, which remains the primary reason the 24AA025UID device was included on every AEM module. A driver for the 24AA025UID device was developed in C++ and released under a Creative Commons license.

7.4.3 Bootloader

The bootloader used on AEM modules is a modified version of Optiboot, recompiled for the Atmega2560. Optiboot offers numerous advantages over other bootloaders for the AVR platform such as STK500 from Jason Kyle or 1Kboot, most importantly its reduced size. With inline optimizations enabled, Optiboot is only a quarter the size of STK500, and compiles to less than 256 bytes of flash memory. This fits into the minimum boot sector size of 512 bytes on the Atmega2560. When the necessary fuses are set for operation in bootloader mode, the device will boot from address 0x1FE00 instead of 0x00000, starting the bootloader routine. If no programming data is received over the serial connection within 250 ms, the bootloader will exit and launch the main application from address 0x00000. Alternatively, the bootloader may be compiled to use the watchdog timer (WDT) with a time-out of up to 1 s, which triggers a full reset when no data is received. When the bootloader gets corrupted, an automatic fallback to 0x00000 occurs when the instruction pointer reaches the end of flash address space, 0x1FFFF. Alternatively, the bootloader can jump to address 0x11000, containing a second block of program memory holding a self test routine. This self test is based on the one used on OpenObservatory, which proved its usefulness for diagnosing hardware errors.

7.4.4 Sample Synchronization

Correlating samples across different AEM modules connected to the same Aggregator, or comparing multiple identical AEM modules deployed in the same physical environment, requires accurate time synchronization of samples. For fast changing signals such as vibrations in particular, it is essential to synchronize them properly to enable correct post data analysis. Two separate mechanisms are implemented, respectively on AEM module level, and on Aggregator/host level.

Time Stamping

The Atmega2560 has an internal clock with microsecond accuracy. Dividing the 16 MHz clock with 4 divider stages results in a precision clock signal with a period of 1 mus. This clock signal is fed into a 32 bit counter, which automatically starts up when the device boots (either in bootloader mode or in regular application memory space). Whenever a measurement is made by one of the connected ADCs or sensors (see figure 7.1), the value of the counter is recorded along with the value. Since all samples are stored as floating point values with 32 bit precision (6 digits precision), the total memory space required to store a sample is 8 bytes: 4 for the 32 bit time stamp, and 4 for the 32 bit floating point value. An additional bytes uniquely identify the source of a sample. The first 4 bits of this 9th byte mark the origin (0 being reserved, 1 - 3 referencing USART1 - USART3, and 4 - 15 referencing other devices on the board, i.e I^2C sensors. The second nibble of 4 bits points to the channel within the device, since the AD7689 can read from up to 8 different channels. Upon transmission, a 10th byte is added to identify the source of the sample, as a CRC of the 32 bit GUID of each board.

Central Clock

When samples are sent to the Aggregator, synchronization between different AEM modules poses a second problem. To resolve it, an RTC module is present on the Aggregator board, as discussed in section 7.5.3. During boot phase, and before data is communicated between AEM modules and host, the host requests the value of the 32 bit counter from each module and associates it with the absolute RTC time. These timing associations are stored in memory of the host. When samples are received, the 32 bit time stamp of each sample is subsequently expanded to an absolute time stamp including date and time, with microsecond accuracy. The host keeps track of the overflow period of the 32 bit counters on each AEM module, which is around 1 hour and 11 minutes, to ensure time stamps remain in sync.

The analog front-end, communications, and power supply are discussed in appendices B - D.

7.5 Aggregator

Only 8 kB of memory is available on each AEM module – 10 kB with the 2 kB flash memory counted in. This limited local storage space urges rapid transmission of data to the host, which can be any computer system with a UEXT interface. For measurements in the field, it is inconvenient to place a laptop next to the AEM module(s), particularly in outdoor environments, because of their size and power supply requirements. A low power single board computer, such as a LIME2, BeagleBone, CHIP, PINE64 or Raspberry Pi is better suited for these applications. Countless different single board computers are available at prices ranging from less than 10 EUR to well over 150 EUR, and it would be pointless to make a list because by the time of publication of this thesis, it would already be outdated. Specific features such as non standard video interfaces or high speed USB aside, many boards will typically feature an ARM CPU with integrated RAM and internal or external flash memory to install a linux distribution onto. Although host platforms with UEXT connector exist, most notably from Olimex, few have more than a single UEXT connector, and those that have one are generally poorly supported. AEM development originally started on a LIME2 board with a single UEXT connector, equipped with an AllWinner A20 dual core A7 CPU and 4 GB on board flash memory, but as development progressed it turned out documentation for this platform was limited. Rather than taking the risk of having to fiddle around endlessly with poorly documented hardware, it was instead decided to move to the much better supported Raspberry Pi platform. As the high end computering counterpart of what Arduino is

for microcontroller development, Raspberry Pi boards are well documented and broadly supported. An additional advantage is that software libraries are available for the platform, speeding up development. The only disadvantage of the Raspberry Pi ecosystem is that its hardware is not open source, unlike LIME2, Beaglebone or PINE64. The development boards however are more widely available than the aforementioned open source counterparts, which is an advantage that could be considered significant enough to offset the drawback of it being closed source.

7.5.1 Raspberry Pi Expansion Module

The Raspberry Pi Rev. 3 offers a 40 pin GPIO header with a pitch of 2.54 mm, which is compatible with former IDE ribbon cables and IDC connectors. Alternatively, an expansion module may be mounted directly on top of the Raspberry Pi 3, as seen in figure 7.4, using a 40 pin board to board connector. As the Raspberry Pi side offers a male header, the mating connector is a Harwin M20-7832046 female header mounted on the bottom side of the module. Cut-outs were provided for other IO interconnects of the Raspberry Pi, as well as mounting holes to mount the expansion module (called a *hat* in Raspberry Pi jargon) onto the host board using spacers. Since the purpose of the module is to collect data on energy harvesters and sensors and centralize them, the module was nicknamed AEM-Aggregator, following the naming convention of other AEM modules.

7.5.2 Interface

Only a few pins of the 40 GPIO pins are used by AEM-Aggregator, most notably those related to digital bus interfaces used by UEXT: SPI for data transfer, I^2C for status communication and calibration, and UART for serial debugging and programming. AEM-Aggregator and any other AEM modules connected to it, are powered directly from the Raspberry Pi. Figure 7.3 gives an overview of the connections between Raspberry Pi and AEM-Aggregator.

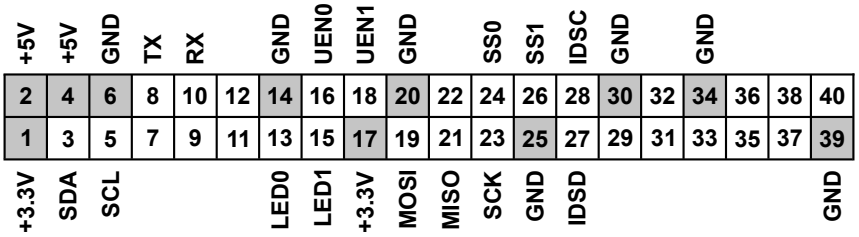

Figure 7.3: Digital interface between Raspberry Pi 3 host and AEM Aggregator add-on module. Used pins are marked, grey pins indicate power connections. Redesigning AEM-Aggregator for use with different host systems is trivial as long as the same IO pins are available.

Since Raspberry Pi 3 provides a master SPI bus that can be shared by 2 devices, it allows 2 UEXT modules to be connected to the AEM-Aggregator. The MOSI, MISO and SCK pins (19, 21 and 23 respectively) are tied together, and 2 separate SS signals are provided on pins 24 and 26.

Although the I^2C bus of two simultaneously connected AEM modules may theoretically be shared, allowing both modules to communicate with each other as well, this would result in a multi master configuration in normal operation, when both AEM modules address sensors on their respective boards. This could lead to instabilities, since the I^2C controller of the Atmega2560 does not formally support multi master I^2C operation. The solution implemented on AEM-Aggregator is splitting the I^CC bus, and only

connecting one of both UEXT modules with the host at any given time. A PCA9542A I^2C multiplexer is responsible for this task. It can be controlled directly through the I^2C bus itself.

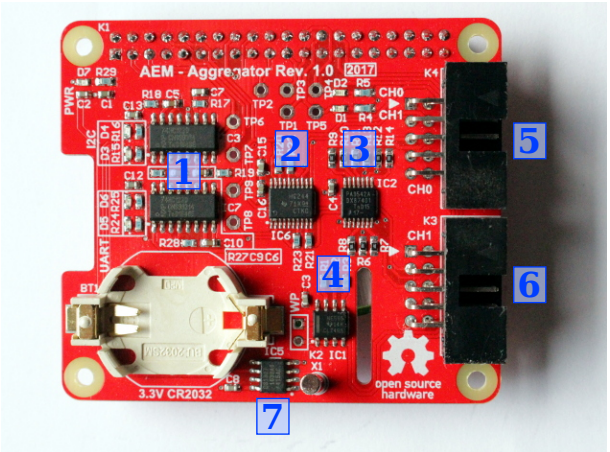

Figure 7.4: Rev. 1.0 of the AEM Aggregator prototype. ① transceivers for channels 1 and 2, ② I^2C multiplexer controller ③ UART multiplexer controller, ④ flash memory with UUID, ⑤ channel 1 IDC connector, ⑥ channel 2 IDC connector, ⑦ RTC with backup battery holder (not mounted).

UART does not provide the opportunity to be multiplexed, and a tri state buffer on each line in each direction controls access to the shared UART resource of the Raspberry Pi. A standard 74 series tri state buffer of type SN74HC244 was selected for this task. The enable pins of the buffer are wired to pins 16 and 16, for channel 0 and 1 respectively, and active low. When either pin is pulled low, the corresponding AEM module's UART is connected to the UART resource of the Raspberry Pi. If both are left floating, for which pullup resistors are provided on the board, UART remains disconnected.

7.5.3 RTC

To enable synchronization of data across AEM systems deployed in different physical locations, accurate timing is essential. The Raspberry Pi 3 is not equipped with a real time clock module (RTC) so an additional RTC based on the Maxim DS1307 is included on AEM-Aggregator for time keeping purposes. A 1620 silver oxide coin cell with terminal voltage 3.0 V is included as back-up battery to ensure RTC continuity when the power to the Raspberry Pi itself is disconnected. A precision crystal of 32.768 kHz is used as oscillator. Its low frequency allows a power favourable 15 stage frequency divider to be constructed to generate a precision clock signal of 1 Hz. The DS1307 RTC controller is connected to the host over I^2C, and bidirectional communication is supported to set the time or read it back. The RTC time is synchronized whenever it is connected to the Internet, using internet time servers available within the linux operating system.

7.5.4 Environmental Sensors

To allow sensor values of AEM modules deployed in different environments to be correlated and compared objectively, it is necessary to record in which environmental conditions the measurements were made. This allows anomalies in sensor readings to be identified, and measurements that are potentially out of range of the sensor's calibrated operation range, to be rejected. The standard conditions for sensors across all AEM modules are a pressure of 10^5 Pa (standard pressure as defined by IUPAC in 1982) and

25 °C room temperature. Additionally, the relative humidity is also monitored.

To measure air pressure, the Bosch BMP180 air pressure sensor was inherited from the OpenObservatory project, where it proved its reliability. The accuracy of its pressure measurements is ±12 Pa. The integrated temperature sensor of the BMP180 did not excel in stability, however, so the temperature sensor of the BMP180 was not used. Instead, the Sensirion SHT31 was chosen as combined temperature and humidity sensor. The SHT31 comes factory calibrated with a temperature accuracy of ±0.3 °C and humidity accuracy of ±3 % RH (relative humidity) in the range between 10 % RH and 90 % RH. At very low or high humidity levels, the accuracy may drop below ±7 % RH, but since these conditions occur rarely, this is not considered an issue. Both the BMP180 and SHT31 are equipped with an I^2C interface, which is shared with the I^2C bus of the UEXT interface of whichever AEM module is connected. The sensors operate at 3.3 V from the digital Raspberry Pi power rail.

The environmental sensors are not available on AEM-Aggregator Rev. 1, but added to Rev. 2.

7.5.5 Automatic Module Identification

Since the I^2C bus of each individual AEM module is routed through UEXT to AEM Aggregator, the unique ID codes of each AEM module can be read out by the Raspberry Pi independently of the firmware running on the AEM module, even if the module MCU were bricked or otherwise disabled. This allows automatic identification of connected modules by the Raspberry Pi. Since the pull-up resistors for the I^2C bus are located on AEM modules themselves, and the Aggregator board features a very high pull-down resistor on both SCL and SDA (330 kΩ), the floating high I^2C lines are used to implement a hot swap mechanism with plug & play support, similar to computer monitors. These also feature an I^2C bus integrated in VGA, DVI or HDMI cables to allow the host to identify the connected monitor and automatically detect its display modes. On AEM Aggregator, a logic high SCL and SDA line signals an AEM module was connected to the respective Aggregator channel. After a configurable time-out to mitigate start-up effects, the 24AA025UID on the AEM board is subsequently polled for its unique 32 bit ID by the Raspberry Pi. This ID uniquely identifies the AEM board type.

Automatic identification requires a complete list of AEM module IDs to be available at Raspberry Pi level or above. Since the system is conceived to be open source and easily modifiable/adaptable by third party hardware developers contributing to the AEM project, a decentralized database with unique AEM module IDs is required. The best way to implement this is by using a blockchain, which acts as a public ledger of existing AEM boards and provides legitimization. The proposed blockchain uses Proof of Stake (PoS) instead of Proof of Work (PoW) to reduce the computation load for implementations on embedded systems such as the Raspberry Pi. A secure authentication protocol suitable for embedded systems is described in [315].

7.6 Vibration Module

The purpose of the vibration energy harvesting module, abbreviated to AEM-Vibrations, is to provide a platform for testing cantilever based piezoelectric vibration energy harvesters. Connectivity is provided to interface an external piezoelectric energy harvester, and a MiniSense-100 piezoelectric harvester is mounted on the board as reference for vibration measurements. To correlate measurements with actual vibrations the module is exposed to, 6 vibration sensors are integrated on the module:

- 2 Kionix KX122-1037 accelerometers, with a dynamic range between ± 2 and 8 g and a maximum sample frequency of 12.8 kHz with a 12 bit resolution. Sensors are sensitive in three dimensions, and have been mounted with a difference to allow anomaly detection by correlating data from both sensors.
- MiniSense 100 vibration sensor, a cantilever type vibration sensor loaded with a tip mass, mounted on the edge of the board. The active sensor area is shielded for improved RFI/EMI, and consists of a PVDF film on a flexible carrier.
- Tilt sensor of type 801S
- PVDF transducer for airborne vibrations (i.e. sound)
- 2 Murata PKGS-00LDP1-R shock sensors
- Piezo disc sensor

7.6.1 Sensors

With the aim of refactorability and supply chain management (i.e. sourcing parts), care was taken during the selection process of the sensors to ensure adequate commercial availability.

KX122-1037

The Kionix KX122-1037 is a 3D digital MEMS accelerometer with 3 discrete sensitivity levels (± 2 g, ± 4 g and ± 8 g respectively), resolution of 14 bits and sampling frequency up to 12.8 kHz. This allows to measure sinusoidal vibrations up to 6.4 kHz, in compliance with the Shannon-Nyquist sampling theorem, but structural vibrations in this frequency range are rare in industrial and domestic environments. The lower energy content of frequencies above 2 kHz makes harvesting energy from these vibrations inefficient unless the amplitude is significant, but since frequencies above 2 kHz are audible to humans and at high amplitudes experienced as irritating, such situations will rarely occur in real world applications. The KX122-1037 provides integrated processing of vibration data, including detection of free fall and processing of board orientation, in addition to a 2 kB embedded data buffer. The sensor is factory calibrated and includes self-test functionality to ensure its correct operation. However, the sensor is not immune to noise, as are all MEMS accelerometers, and drifts may occur when the sensor is subjected to large shocks. It was therefore decided to mount 2 sensors of type KX122-1037 on the AEM-Vibrations module, to reduce the effect of noise and drift, by rotating the sensors with a 90 ° angle towards each other. This allows detection of anomalies and EOL. The sensors are equipped with a dual I^2C (max. 3.4 MHz) and SPI interface (max. 10 MHz). On AEM-Vibrations Rev. 2, both sensors share the same I^2C bus, but are assigned a different address, set by pulling the ADDR pins high and low respectively. Addresses are respectively 0x1E and 0x1F. The resolution of measurements is 14 bit in ± 2 g range, 13 bit in ± 4 g range and 12 bit in ± 8 g range. The range is adjustable through the I^2C interface. The sensor shows excellent stability, with only 0.01 % temperature drift per °C, and ± 0.6 % non-linearity. As a MEMS device, the mechanical resonance frequencies are ca. half the maximum range in x and y direction (3.5 kHz) and ca. a quarter in z direction (1.8 kHz). Other sensors on the AEM-Vibrations

module with different resonance frequencies are available to ensure continuity of measurement when the KX122-1037 sensors are subjected to vibrations too close to their resonance frequency.

MiniSense 100

The MiniSense 100 from Measurement Specialties is a cantilever type vibration sensor that also acts as a piezoelectric energy harvester. It consists of a PVDF film coated on a flexible carrier, acting as the sensing area. The active area is shielded to improve RFI/EMI rejection, and the device is designed to retain its integrity even in conditions of high shock overloads. This sensor was chosen for its excellent linearity ($\pm 1\,\%$) in the range from 0.1 mg to 1 g, providing a high dynamic range. With a resonance frequency of 75 Hz with the supplied tip mass of 0.3 g, the frequency range is specified from ca. 1 Hz up to 42 Hz (+3 dB over the baseline response). The open circuit output voltage is 1.1 V/g for a sinusoidal vibration, and up to 6 V/g at the resonance frequency of 75 Hz. Electrically, the MiniSense 100 behaves as a sinusoidal voltage source in series with a 244 pF capacitor, corresponding to an ESR of ca. 650 MΩ at a frequency of 1 Hz. The high impedance poses challenges in the PCB layout, since unshielded signal traces are prone to picking up noise. A secondary concern is the input impedance of the ADC, which forms a high-pass RC filter in conjunction with the internal 244 pF capacitor of the sensor itself. For this purpose, a buffer with high input impedance was chosen. The LTC6088 from Linear Technology is a rail-to-rail CMOS amplifier/buffer with a maximum input bias current of 15 pA and a capacitive load of 4.2 pF. The equivalent circuit is shown in figure 7.5, with a transfer function equal to

$$H(s) = sR\frac{C_1 + sRC_1C_2}{(1 + sRC_2)^2 + sRC_1} \tag{7.1}$$

where R=73 GΩ, C_1=244 pF and C_2=4.2 pF. The circuit acts as a high pass filter with -3 dB frequency at $8 \cdot 10^{-6}$ Hz, which in far below the frequency range in which the sensor is designed to be used (1 Hz - 42 Hz). For applications in industrial environments (i.e. vibrating machines), the sensor will

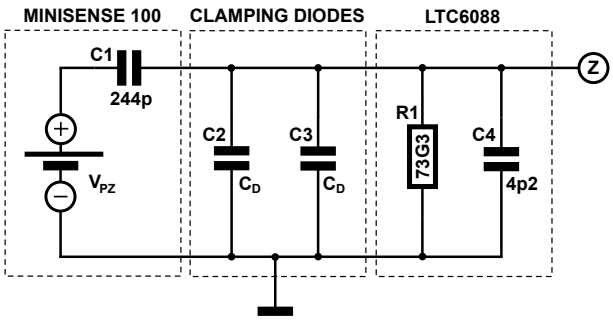

Figure 7.5: Equivalent circuit for MiniSense 100 connected to an LTC6088 buffer, with clamping diodes.

be subjected to a single dominant frequency to which the tip mass should ideally be tuned. In this case, it would be possible to use an envelope detector as for AM demodulation to reduce the AC signal to a DC signal. Any information on frequency components with smaller amplitude however is lost in this process, which is undesirable. Therefore, it was decided to feed the LTC6088 buffer output directly into an ADC. Care must be taken to constrain the input signal amplitude for large excitations, in which case the input signal may exceed 2 Vpp, and damage the buffer. Clamping diodes are therefore necessary on the input signal. The diodes each add an additional parasitic capacitance C_D to the equation, which

must be accounted for as follows:

$$H(s) = sR\frac{C_1 + sRC_1(C_2 + 2C_D)}{(1 + sR(C_2 + 2C_D))^2 + sRC_1} \tag{7.2}$$

Schottky diodes are necessary to ensure the forward voltage drop is below that of the internal body diode of the LTC6088 buffer. The 1PS70SB84 dual schottky diode from Nexperia has a stray capacitance of 15±3 pF (measured at 1 MHz). The VF of this diode remains below 200 mV at currents up to 100 μA, which is adequate since piezoelectric devices are unable to deliver a higher current.

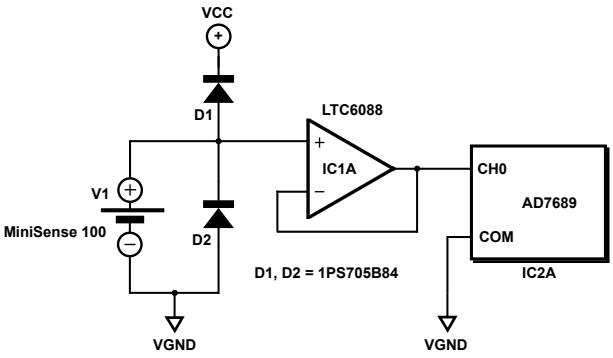

Figure 7.6: Interfacing the MiniSense 100 to the AD7689 ADC using a virtual ground to allow postive and negative input voltage swings.

CEB-20D64

The CEB-20D64 is a ceramic piezoelectric diaphragm mounted on a brass disc with a diameter of 20 mm and a thickness of 0.43 mm. It is developed by Cui, Inc. as a piezo transducer and buzzer, but also acts as a low-cost vibration sensor. This allows it to be mounted on a vibrating object that is too small to accommodate the entire AEM-Vibrations module, would be dampened by it, or otherwise undesirably affected. The CEB-20D64 does not have a dampening mass and, consequentially, a much higher resonance frequency than the MiniSense 100 described above (6.5 ± 0.5 kHz as opposed to 75 Hz for the MiniSense 100). The specifications are very similar to those of the MiniSense 100 otherwise, except notably the internal capacitance C_1 which is considerably higher, 13 nF $\pm$ 30 % (measured at 120 Hz with output amplitude of 1 V). The response of the CEB-20D64 is linear between 2 kHz and 8 kHz with a non-linearity of max. 5 %, requiring an anti aliasing filter. This is implemented as an active low pass filter with cut-off frequency of 5 kHz. The transfer function is

$$H(s) = H_i(s) \cdot \left[2 - \frac{1}{sRC + 2}\right] \tag{7.3}$$

where $H_i(s)$ is equal to equation 7.2. Measurement of frequencies lower than 2 kHz requires careful calibration.

1005919-1

The 1005919-1 is an omnidirectional broadband piezoelectric transducer with a cylindrical 30 μm thick PVDF film as sensing element. These devices have a bandwidth up to 80 kHz. The low resonance Q value of 5 enables fast response times by decreasing the rise and decay times of sensed signals. The

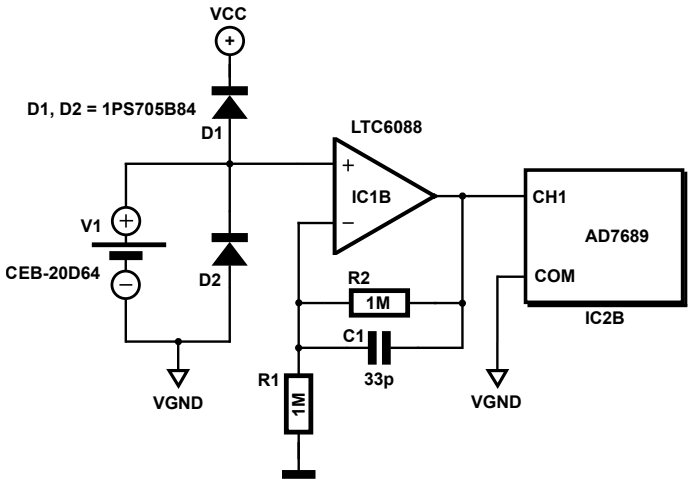

Figure 7.7: Interfacing the CEB-20D64 with the AD7689 ADC. Amplification and a low pass filter is required due to the higer frequency response but smaller amplitude than the MiniSense 100.

resonance frequency is between 80 - 90 kHz depending on the installation of the device, which is far beyond the range of interest for energy harvesting, and thus not posing a problem. The sensitivity is 300 μV/Pa pressure difference. The corresponding sound pressure level is

$$SPL = 10 \log \frac{1^2}{p} = -20(\log 2 + \log 10^{-5}) = 100 - 20 \log 2 \approx 94\,\mathrm{dB} \tag{7.4}$$

A SPL of 94 dB corresponds to sound sources like heavy traffic or a pneumatic jackhammer. Amplification is necessary to make optimal use of the entire input range, which is 2.048 V full range, as discussed below. The required amplification is

$$A_{\mathrm{CL}} = \frac{2^{11}}{10^3 \cdot (3 \cdot 10^{-4})} \approx 6.8 \cdot 10^3 \tag{7.5}$$

The LTC6088 has a gain bandwidth product of 14 MHz, which limits the bandwidth for a single amplifier stage to 2.1 kHz. This is too close to the underside of the desired sensitivity bandwidth to be comfortable, so a dual stage amplifier topology is necessary. With 2 identical inverting amplifiers with a gain A_{CL}=82, the total amplification factor is 6724 with a bandwidth of 171 kHz, which is more than sufficient. 82 is an E12 series resistor value, making implementation easier. The amplifier circuit is shown in figure 7.8, implementing 2 cascaded active low pass filters with a cut-off frequency of 5 kHz (390 pF in parallel to 82 kΩ corresponds to a -3 dB of 4.98 kHz), the upper limit of the useful range for energy harvesting. A buffer stage is still necessary because of the internal 200 pF series capacitance of the transducer, which would otherwise form an undesired low pass filter. The transfer function is

$$H(s) = \frac{H_i(s)}{\left[R_1 C(sR_2C + 1)\right]^2} \tag{7.6}$$

where R1=1 kΩ, R2=82 kΩ and C=390 pF. Unlike the other sensors, the 1005919-1 is designed for specific acoustic applications in the ultrasound range, and therefore more difficult to acquire than the other sensors on the board. It is unavailable at DigiKey, and sourced from Mouser instead. Ultrasound energy transfer has already been demonstrated to work in laboratory environments. The uBeam project developed a wireless transfer of 1.5 W over a distance of 4 m in 2017 at an SPL of 145 - 155 dB and a

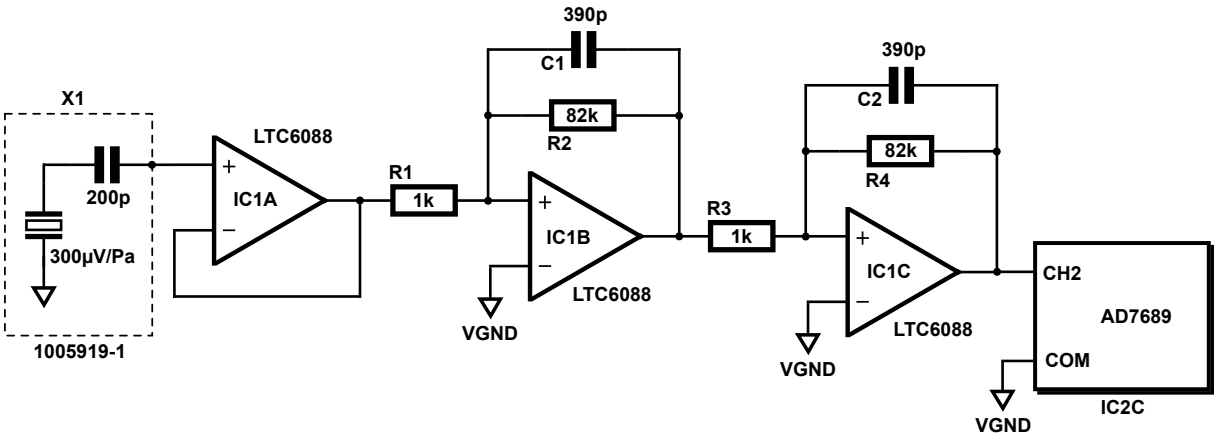

Figure 7.8: Input buffer and double stage amplifer for the 1005919-1 ultrasonic acoustic vibration sensor.

frequency of 60 kHz. With a power fall-off of 3 dB/m in air, depending on temperature and humidity, the transfer efficiency ranges between ca. 12.5 % at 1 m distance down to 1.56 % at 4 m. At the highest SPL of uBeam, the 1005919-1 will produce output levels that cause the amplifier output to saturate. In such cases, it is necessary to reduce the amplification factor. However, it should be noted that an SPL of 155 dB in the ultrasonic frequency range exceeds the WHO safe sound level by three orders of magnitude. It is therefore unlikely that such levels are encountered by accident. [241]

When assembling the board, capacitors must be chosen carefully with microphonics in mind. Ceramic capacitors with $BaTiO_4$ as dielectric in particular are microphonic, since $BaTiO_4$ is a piezoelectric material itself. When electric signals are applied to these capacitors, they may vibrate and produce sound in the same frequency range, resulting in an undesirable source of noise for the 1005919-1.

PKGS-00LDP1-R

The PKGS-00LDP1-R is a piezoelectric shock sensor manufactured by Murata for applications in warranty void circuits, particularly for hard drives. It consists of a piezoelectric element sandwiched between two layers of ceramic substrate. The device has a theoretical sensitivity of 1.10 mV/g, but acts as a current source for all practical applications. It is rated up to 10 g (98.1 m/s^2), at which a typical charge of 85.7 pC/g is produced. Unfortunately, the low cost of the sensor comes with a disadvantage regarding accuracy, with a maximum error of 15 %. However, the excellent linearity (non-linearity max. 5 %) and high resonance frequency (typically 20 kHz) makes it well complementary to the other sensors on the board. Its series capacitance was found to be in the range of similar piezoelectric transducers, 770 pF $\pm$ 30 %. A drive circuit was developed by Linear Technology, which was adapted to the transimpedance amplifier shown in figure 7.9. As with the PVDF 1005919-1, the cut-off frequency was aimed at around 5 kHz (12 pF in parallel to 2.4 MΩ yields a -3 dB of 5.5 kHz). The matching network improves the linearity of the response, acting as a notch filter.

801S

The 801S is a heavy duty shock sensor from ElectronInvest consisting of a sensing element in a gold alloy plated cylinder able to withstand up to $6 \cdot 10^7$ shock cycles, with a stable response over time. It is omnidirectional and able to detect vibrations as low as 15 mg. However, it has poor linearity, and therefore

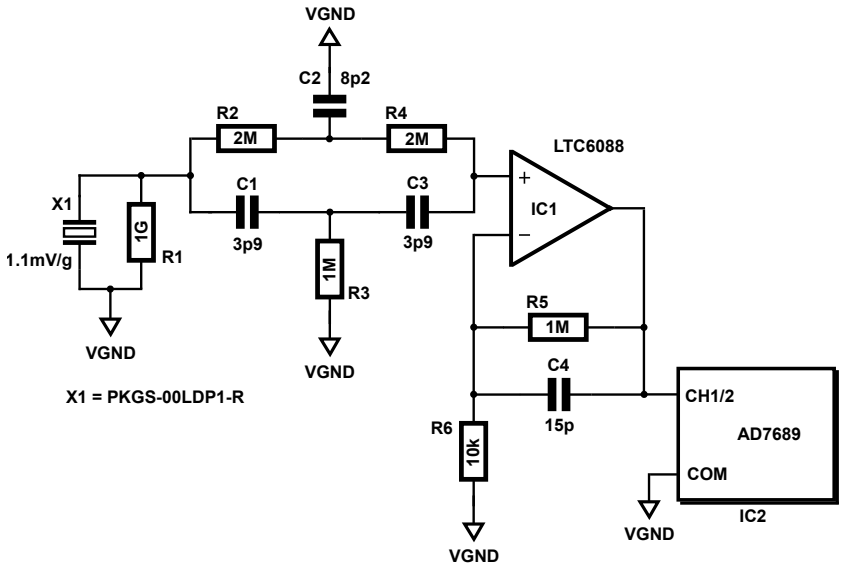

Figure 7.9: Amplifier and filter front-end for the PKGS-00LDP1-R shock sensors.

serves only as a reference for EOL detection of other sensors. To achieve this functionality, the response of the 801S is compared to that of the other sensors on AEM-Vibrations at regular intervals. When a drop in output amplitude or frequency sensitivity is detected when comparing another sensor with the 801S' response, it can be concluded that this sensor reached the end of its life, and should be decommissioned. This change in status is recorded in on-board non-volatile memory The amplifier circuit was adapted from the datasheet, and shown in figure 7.10. Because of the mechanical construction of the sensor, its frequency range is limited to max. 1 kHz, the amplifier therefore includes an active low pass filter with that cut-off frequency to suppress noise (15 pF in parallel with 100,kΩ yields a -3 dB of 1.1 kHz).

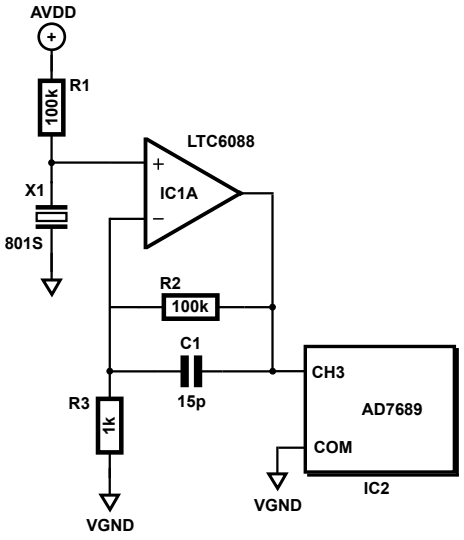

Figure 7.10: Bias and active filter for the 801S high durability shock sensor.

SW-520D

Finally, the SW-520D is a mechanical ball tilt sensor serving as an optional wake-up mechanism for the board. When subjected to vibrations, the steel sphere inside the cylinder makes contact with two electrodes, sending a digital pulse as wake-up interrupt to the board's main microcontroller. Although present, this functionality is not yet implemented as of AEM-Vibrations Rev. 2.2.

7.6.2 Vibration Energy Harvester

The AEM-Vibrations module supports connectivity of an external piezoelectric vibration energy harvester, and is equipped with an LTC3588 chipset from Linear Technology. The LTC3588 is DC/DC converter with integrated full bridge rectifier, designed for piezoelectric energy harvesting applications. The device supports input voltages between 2.7 V and 20 V, with integrated shunt zener diode to protect the device from overvoltage conditions. The rectified input voltage is stored in an external capacitor, from which power is drawn into a buck regulator to reduce the stored charge to the desired output voltage. The output voltage is configured by setting 2 digital inputs of the device, allowing selection between 4 discrete output voltages. With D0 set high and D1 set low, the LTC3588 targets an output voltage for its buck converter stage of 2.5 V. Without the need for an external voltage divider to set the output voltage, the quiescent current in regulation drops to 1 μA, or about half of that in UVLO conditions. The LTC3588 contains the necessary provisions for impedance matching to maximize the output power.

Revision 1

In a first experiment to measure the output power of the energy harvester directly, a high side current sense amplifier of type MAX4373 was used to measure the output current, when at the same time output voltage was measured by another AD7689 channel. While this approach worked reasonably well in simulation for ideal voltage sources, it failed for actual vibration energy harvesters because of the large output voltage and small current they produce. Accurate measurement of current requires a large dynamic range and a shunt resistor of 1 kΩ or more in series with the energy harvester. Such an approach significantly alters the characteristics of the circuit, which was deemed unacceptable. This approach was therefore abandoned.

Revision 2

An indirect approach to measuring the output power of a vibration energy harvester is by loading the output of the LTC3588 by drawing the maximum power permitted before the output voltage falls off, which forces the LTC3588 into its maximum power point to draw maximum power from the harvester. A precision electronic load is constructed with an Analog Devices OP07D low offset, low noise opamp and a P-channel MOSFET. The OP07D is specifically designed for instrumentation applications, particularly current shunt measurements. The maximum noise level is specified at 0.25 μVpp, which is about 2 orders of magnitude below the resolution of the AD7689 with a 2.048 V reference, about 31 μV. The circuit is shown in figure 7.11, and based on the work of Van Belle et al. [25]. The opamp closes the feedback loop, adjusting conductivity of the MOSFET to keep it in its pseudo-linear operation mode. In this mode, the MOSFET is used as an adjustable resistive load. Conductivity is regulated such that the output voltage of the LTC3588 is pulled to 2.048 V, below its target of 2.5 V. With the output voltage tied to 2.048 V and the output current measured over a precision shunt resistor of 1 kΩ, the output power can be calculated.

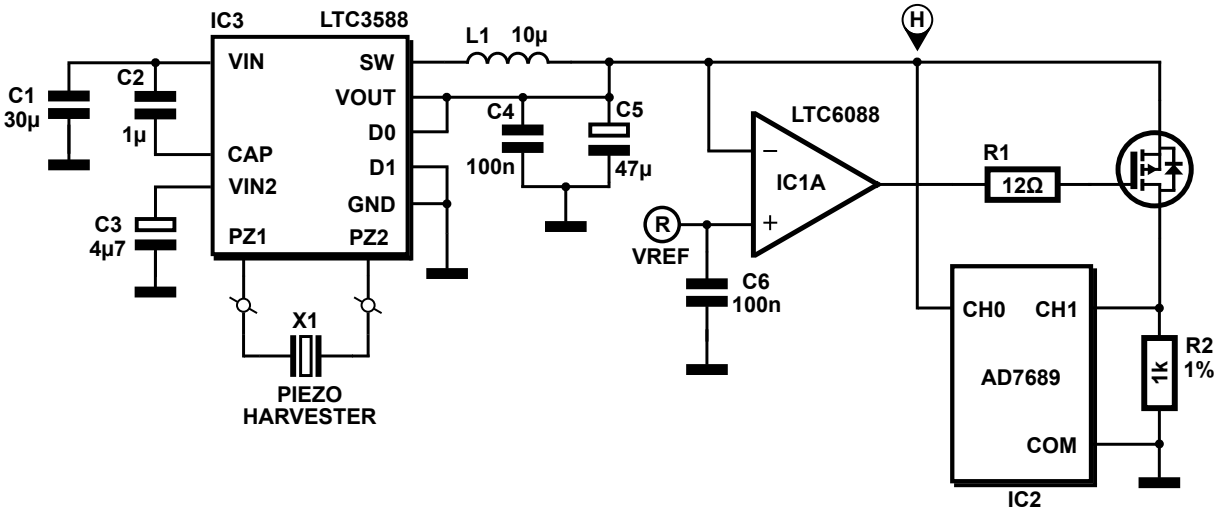

Figure 7.11: Vibration energy harvester based on LTC3588 set to 2.5V output voltage, with precision electronic load to measure .

Revision 3

The approach taken in Rev. 2 shows unpredictable behavior when connected to a high impedance load. The cause for this instability is the inherent self-regulation of the LTC3588: it switches from burst mode to UVLO as the input capacitor is discharged below the threshold (300 mV above the target output voltage). This approach caused the circuit to alternate between saturation and UVLO. Although it is still possible to calculate the average output power of the energy harvester under these discontinuous conditions, it is undesirable. To resolve the instability, a second external feedback loop was added, monitoring the voltage over the input capacitor. The block diagram is shown in figure 7.12. The voltage

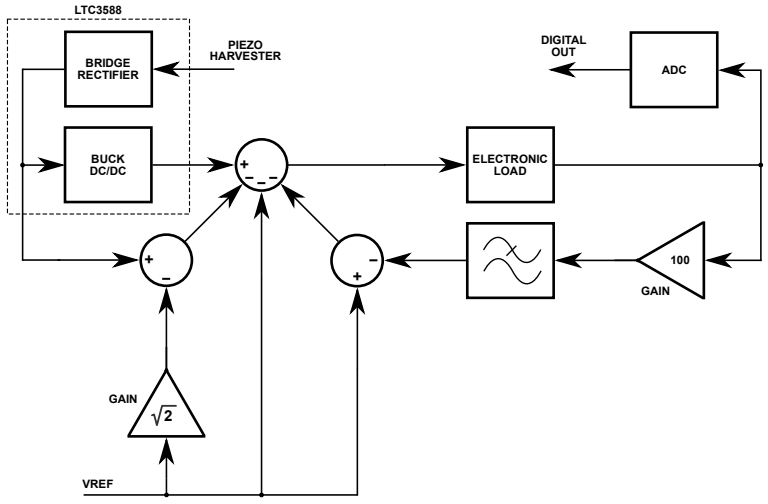

Figure 7.12: Block diagram of the improved electronic load control system.

over this capacitor is held at the minimum threshold above UVLO, in this application ca. 2.9 V. This reference is derived from the on board 2.048 V reference voltage. When the input capacitor voltage drops below 2.9 V, the reference voltage for the electronic load controller is pulled slightly above 2.5 V to allow the input voltage to recover. The solution is shown in figure 7.13. Choosing 10 kΩ for one half

of the voltage divider, the second resistor is calculated as follows:

$$v_{out} = 2.6 = 2.048 + (3.3 - 0.6)\frac{10}{10 + R} \rightarrow R = 38.913 \approx 39 \tag{7.7}$$

Again, 39 kΩ is a convenient E12 series value, simplifying implementation.

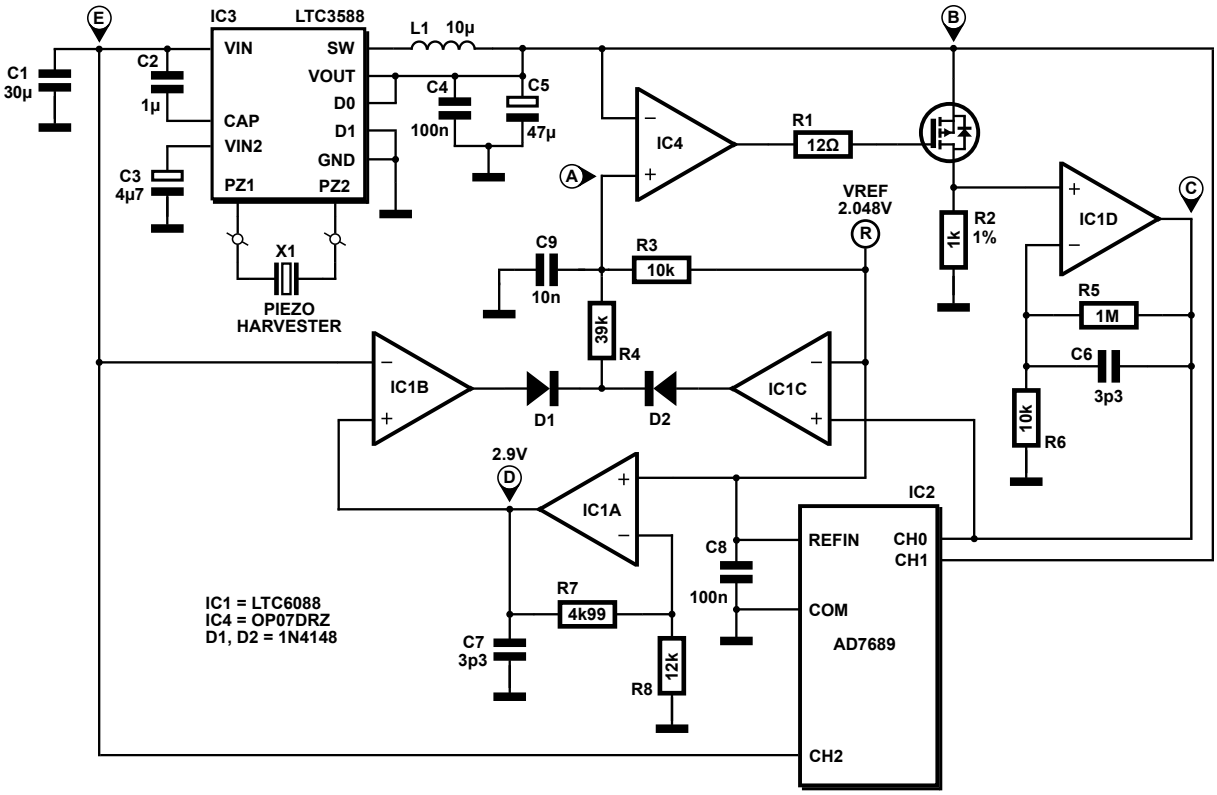

Figure 7.13: Vibration energy harvester based on LTC3588 set to 2.5V output voltage, with precision electronic load to measure.

Diodes D1 and D2 form a logic NOR gate for comparators IC1B and IC1C, going logic high if either comparator output is high, thus pulling up point A from the reference voltage of 2.048 V to 2.9 V. IC1B evaluates the input capacitor voltage by comparing it to 2.9 V, whereas IC1C compares the input to the ADC with the reference to ensure the amplified ADC input does not exceed the 2.048 V reference. The LTC3588 includes a buck regulator, switching at a frequency of 1.2 MHz, which causes a ripple at that frequency on the output. Since this frequency is much higher than any vibration frequencies on the full bridge rectified input signal, they can be removed with a low pass filter. This filter is constructed around IC1D which both acts as a non inverting amplifier with $A_{CL} = 100$ and as active LPF with cut-off frequency 50 kHz. It should be mentioned that, ideally, the voltage at point B should be a DC voltage around 2.048 V. The complete block diagram of the signal path is shown in figure 7.12, demonstrating the feedback mechanism for output voltage regulation. Because of the flexible and device-independent design layout, this topology for a precision electronic load can be directly reused in conjunction to other DC/DC converters for vibration energy harvesters, with minor or no modifications at all. It is worth noting that the value of the shunt resistor R6, which must be a precision resistor with high thermal stability, should be adjusted to the expected power of the harvester to achieve maximum range on current

measurements. At a value of 1 kΩ, the maximal measurable current is ca. 2 mA due to resistive losses in the NVF2955T1G MOSFET.

7.7 Light Module

Characterizing a light source of natural or artificial nature for the purpose of harvesting energy from it, is a complex endeavor in comparison to vibration or thermal energy harvesting. Whereas a temperature gradient is only one dimensional (the magnitude of temperature difference itself) and vibration are two dimensional (the magnitude of the vibration and its frequency), light adds a third dimension of complexity because it consists of a continuous spectrum of wavelengths with each a different magnitude. Unlike for vibrations or temperature, for which there are countless sensors readily available, there is no such thing as an off-the-shelf low cost sensor able to measure the spectral characteristics of a light source pseudo real time. Designing AEM-Light thus requires the problem of sensing the light spectrum to be solved first.

7.7.1 Diffraction Spectrometer

The first approach to solving the problem, in line with literature, is implementing an optical spectrometer using the classic diffraction strategy to split a light source into monochromatic beams which are then measured separately. While dedicated spectrometer CCDs are notoriously expensive, as are the devices themselves, there are low cost alternatives on the market as well. As a side effect of the increasing popularity of portable gadgets, including but not limited to smartphones, CCDs have emerged from a niche market position, and several types are currently being mass produced for use in those gadgets. The very competitive nature of the smartphone/consumer electronics market has driven technology development forward, and devices with adequate response speed, resolution and noise immunity are currently commercially available in low volumes. Examples of linear CCDs considered for AEM-Light are the Toshiba TCD1703 and TCD1304, the Sony ILX511B, and the On Semi KLI-4104. The TCD1304 in particular has been used as CCD in mid range spectrometers, and in order to verify its performance, an Ocean Optics USB2000+ spectrometer was acquired for this research. As the name suggests, this spectrometer conveniently interfaces through USB with a host computer, and is supplied with the necessary software to read out spectra. In experiments with LEDs, incandescent light sources and fluorescent light sources, the accuracy proved to be sufficient to differentiate between the type of light source, and measure their relative intensity. With a proof of concept in place, it was decided to replicate the USB2000+ optical parts as a low cost spectrometer, using commercially available components and 3D printing techniques.

Linear CCD

To select the best suited linear CCD for the application, the models listed above were compared as shown in table 7.1.

The 4 CCD sensors show very competitive characteristics, most notably in terms of electrical specifications. Non-linearity and noise (measured as dark signal) are within acceptable boundaries. There are however significant differences in dynamic range, which is defined as the ratio between saturation output voltage and the dark signal. The Toshiba TCD1703 emerges as CCD with the best specifications from this comparison: nearly double the resolution (number of pixels) of its predecessor, best linearity, and a 74 dB dynamic range due to its lowest dark signal/noise and highest saturation level. Although it is less commonly available than its TCD1304 predecessor, and around 50 % more expensive (depending on the chosen supplier), the performance outweighs these drawbacks. Considering the fact that Ocean Optics was able to design a spectrometer capable of distinguishing light source types from each other using the TCD1304, the superior TCD1703 was chosen with confidence for the design of a spectrometer for use on AEM-Light.

Table 7.1: Comparison of 4 linear CCDs as potential candidates for a spectrometer.

CCD Model	ILX511	KLI-4104	TCD1703	TCD1304
Manufacturer	Sony	On Semi	Toshiba	Toshiba
Pixels	2048	4134	7500	3648
Pixel size	14 μm x 200 μm	10 μm x 10 μm	7 μm x 7 μm	8 μm x 200 μm
Pixel pitch	14 μm	10 μm	7 μm	
Saturation	4 mlx·s	$121 \cdot 10^3$ e$^-$	130 mlx·s	4 mlx·s
Sat. Voltage	0.8 V	1.7 V	2.0 V	0.6 V
Output Sens.	200 V/lx·s	14 μV/e$^-$		160 V/lx·s
Dark signal	3 mV	7 fA	1.2 mV	2 mV
Dyn.c range	56 dB	60 dB	74 dB	57 dB
Non linearity	5 %	5 %	3 %	10 %
Price	ca. € 8/pc.	ca. € 503/pc.	ca. € 9/pc.	ca. € 6/pc.

Optics

The prisms used for diffraction in traditional spectrometers have drawbacks which makes them an unfavorable choice for AEM-Light: they are bulky, expensive, and susceptible to shocks which may cause them to get damaged or shatter. In comparison, plastic diffraction gratings have the advantage of being thin, low cost and immune to shocks, but with the disadvantage of having a finite resolution. As a compromise, linear diffraction gratings from Rainbow Symphony with a resolution of 1000 slits/mm were chosen for the prototype. With a grating, longer wavelengths (red) are diffracted more than shorter wavelengths (violet) in comparison to the refraction effect of a prism, an effect which has to be accounted for in calibration. An additional requirement is that the slits of the grating must be wider than the wavelengths of interest for diffraction to occur. The gratings from Rainbow Symphony are not the most ideally suited diffraction gratings on the market, but are widely available and inexpensive, which are also factors to be taken into consideration for an open source project intended for large scale deployment like the AEM modules.

Light enters the 3D printed case through a narrow aperture (1) and passes a collimator lens (2) before being reflected onto the diffraction grating (4) with a strip of aluminum foil serving as a mirror (3). The diffracted light is then reflected again on a second strip of aluminum foil (5) acting as a lens, focusing it on the TCD1703 CCD. The diffraction grating is mounted on a rotatable drum, allowing the beams alignment to be adjusted. The drum rotates between 2 bearings that are friction locked in the casing, and can be locked in place with 2 screws. The design is inspired on a spectrometer design by Frattaroli et al. (2013) with 3 modifications: the mirrors are replaced with strips aluminum foil to lower costs and make the design immune to shock, and the collimator mirror in the original design was replaced by a collimator lens designed for indoor LED lighting applications. The entire structure was meant to be monted in a 3D printable ABS casing with mounting holes, allowing it to be screwed to a PCB for integration. This design was inspired by Serranon et al. (2016) who proved that 3D printable casings are possible for spectrometer applications.

To read out the TCD1703, the software is an adaptation on the software driver for the TCD1307 written by Esben Rossel for a Raman spectrometer, but modified to run on an STM32.

Evaluation

Although the structure of the proposed design was very similar to several others documented in literature, tests with a white power LED with known spectral response were unsatisfactory. The test was performed in a dark room, and variations were tried with and without collimator lens, and with aluminum strips and actual mirrors. In none of the experiments was the measured spectrum anywhere close to the expected spectrum of the white LED. Inclusion of a collimator lens or polarization filter in the light path before diffraction grating did not make a noticeable improvement in the response. The experimental setup also proved to be highly susceptible to shocks, as kicking the table caused the optical components to move, and the readings of the TCD1703 to change.

Construction of a spectrometer with the specified components should theoretically be possible, as demonstrated by the CCD selection comparison of table 7.1 and the existing designs documented in literature. However, a longer than anticipated development cycle seems to be necessary to accomplish the stated goals, including significant time required to optimize alignment of optical components, calibration, and shock resistance. The author is convinced that a low cost spectrometer may be built following the optical approach, but the magnitude of such a project is too far outside the scope of solving the AEM problem to be justifiable within the ongoing research. It was therefore decided to abandon the idea of a PCB mounted spectrometer for the time being.

7.7.2 Solid State Spectrometer

Infrared Spectrometry

When the spectrometer experiments discussed above were in progress, Consumer Physics launched their crowdfunding campaign for the SCiO, an experimental infrared spectrometer targeted at food analysis applications. Turning a desktop based Raman spectrometer into a handheld device, the underlaying technology used by SCiO is proprietary, but reverse engineering of their 3rd prototype, acquired through their Developer Program, reveals the use of solid state IR sensors. These measurements are subsequently processed by comparing them to a cloud based database of known signatures for specific categories of food products, such as fruits, vegetables or dairy items. A similar approach to SCiO can be used to identify light sources, and can be implemented simpler because no external light source is necessary to illuminate the sample as is the case for the SCiO.

Sensor Fusion

On a semiconductor level, light absorption is wavelength dependent because molecules and crystal structures absorb wavelengths that are characteristic of their structure, which means absorption occurs most at their resonance frequency. The mass of the atoms in the semiconductor material, the molecular potential energy surface and the vibronic coupling are all factors that also influence the rate of absorption. Since all semiconductors are light sensitive, but their doping characteristics are different, it is trivial that as a result, their light absorption characteristics will also be different. Comparison of the specific wavelength sensitivity for light sensors of different manufacturers, or even different sensors from the same manufacturer, reveals a difference in sensitivity that can be exploited to determine spectral composition.

In a real world application, each sensor, or more precisely every photodiode in each sensor, outputs a scalar value V that is a function of the spectrum of the light illuminating the sensor $\Phi(\lambda)$ and the spectral sensitivity $S(\lambda)$ of the sensor itself. In a traditional spectrometer, as discussed above, the spectral

sensitivity $S(\lambda)$ is typically known though benchmarking, and $\Phi(\lambda)$ is the function that is being measured. The problem here is that the scalar V is does not give a direct point on the $\Phi(\lambda)$ curve because V is determined by the specific sensitivity of the sensor as well. A spectrometer solves the problem by breaking down the light sample into its spectral components, which are then measured individually by an array of photodiodes. Since each sensor returns only a single scalar value, it is impossible to construct a continuous spectrum $\Phi(\lambda)$ from these samples, unless a large number of photodiodes is being used like with the TCD1703. However, measuring a continuous spectrum is unnecessary for the purpose of energy harvesting, where it is only relevant to know which type (or types) of natural or artificial light source is/are illuminating the solar cell in question. Unless very exotic light sources are being used to harvest energy from, the spectral composition of the source will be a combination of the spectra of one or more light sources, natural or artificial. These are the spectra that provide the boundary condition to solve the problem, because the spectral characteristics of sunlight and any commercial light bulb are relatively constant and documented in literature. In other words, $\Phi(\lambda)$ is composed of the weighted spectra of the individual light sources:

$$\Phi(\lambda) = A \cdot f_{sun}(\lambda) + B \cdot f_{TL}(\lambda) + C \cdot f_{LED}(\lambda) + ... \tag{7.8}$$

The functions $f(\lambda)$ denote the spectral compositions of each light source, and the coefficients $A, B, C, ...$ represent the weighing factors differentiating between light source types. For example, in the sequence above, the combination $\{2, 0, 0\}$ would indicate an outdoor environment with only natural sunlight, while the combination $\{0, 1, 1\}$ rather indicates an indoor environment with mixed fluorescent and LED sources. There is no limit to the number of light types that can be added to $\Phi(\lambda)$, each additional light type will result in another unknown coefficient. It is important to point out that the functions $f(\lambda)$ are known, either through literature or benchmarking, and thus the function $\Phi(\lambda)$ only has as many unknowns as there are different types of light sources. The coefficients $A, B, C, ...$ are furthermore also scalar, and can therefore be treated as variables. In a generalized form, for n different light sources, $\Phi(\lambda)$ can be expressed as

$$\Phi(\lambda) = \sum_{i=1}^{n} A_i \cdot f_i(\lambda) \tag{7.9}$$

From the sensor's perspective, the output signal V is determined by the relative spectral sensitivity as well, but this function is constant and a sensor parameter that can either be measured or obtained from sensor datasheets. Each sensor k has a different sensitivity function $S_k(\lambda)$. Since each wavelength is absorbed independently from other wavelengths, and the rate at which photons are converted to free electrons, the output signal V is essentially the weighted sum of the responses for each individual wavelength. This means that for a sensor k with output signal V_k, the response is determined by the combination of the spectra:

$$V_k = \int_{-\infty}^{\infty} \Phi(\lambda) \cdot S_k(\lambda) d\lambda \tag{7.10}$$

Substituting equation 7.9 into equation 7.10 results in

$$V_k = \int_{-\infty}^{\infty} S_k(\lambda) \left[\sum_{i=1}^{n} A_i \cdot f_i(\lambda) \right] d\lambda \tag{7.11}$$

It is important to note that the integral in equation 7.11 is definite, the integration occurs over the entire relevant wavelengh spectrum. Practically, the interval for λ will be typically $[100 - 1100]$ nm. This

means that solving the integral in equation 7.11 removes the wavelength λ as variable from the equation, leaving the sensor response V_k as a function of the coefficients A_i. Since for n light sources there are n coefficients $A_1 ... A_n$ as unknowns in the equation, they can not be solved. However, as discussed above, each sensor has a different sensitivity $S_k(\lambda)$, which means that for each sensor k the response can be expressed as a different equation following the same structure as equation 7.11. If $n = k$, a system of k independent equations can be expressed with n variables in each, which means the the system can be solved for each coefficient $A, B, C, ...$ etc. Since the number of different light source types is small in real world energy harvesting applications, the number of different sensors necessary to make the equations solvable is also small. The implications are significant, because it means that the combination of different sensors (colloquially called *sensor fusion*) enables AEM-Light to indirectly measure ambient light spectra without the need for any optical components. Ambient light will be predominantly composed of natural sun light, fluorescent light (TL), LED light, incandescent light and halogen light, which means that the spectral composition can be measured by as few as 5 physical photodiodes with different spectral responses.

Proof of Concept

No literature describing the technique discussed above to estimate the spectal composition of a light source with known spectral components exists as far as the author is aware. This new and undocumented approach to solving the problem thus requires a profound proof of concept to enable evaluation of the constraints of practical implementation. The Si1145 from Silicon Labs is well suited for this purpose. It is marketed as a low cost, general purpose proximity sensor with UV and ambient light measurement capabilities, designed for consumer electronics and industrial automation. It contains 3 separate physical photodiodes, 2 with sensitivity peak in the IR wavelength range and one for visible light. The device is able to calculate the UV index and proximity to a near field object directly, and the three sensors can be individually wired to an ADC using the internal analog switches, then read out separately. Because of this flexibility, the Si1145 was selected as one of the 4 sensor devices to be included on the OpenObservatory hardware (3rd revision only). At design time, the Si1145 had only recently been released (2014), and no appropriate software driver existed for it. Only the UV index calculation had been verified and documented in literature (Fried et al., 2014). An open source software driver therefore needed to be developed first, and an implementation of the theory discussed below was included.

Si1145 Spectral Response

Although the Si1145 possesses 3 physical photodiodes, the 2 infrared diodes have a nearly identical spectral response. As a test case, only the large infrared diode (IR) and visible light diode (VIS) were used, since their spectral responses are the farthest apart. With 2 independent photodiodes, the number of distinguishable light sources is limited to 2. This is the minimum for a proof of concept, and allows to distinguish for example natural sunlight from an artificial light source of choice, or a combination of the two.

The normalized spectral response of the photodiodes, f_{IR} and f_{VIS} respectively, was acquired directly from the Silicon Labs documentation of the sensor. The response of either diode is continuous but irregular, and does not match any existing elementary mathematical function. Is was therefore chosen to approximate the spectral response of the diodes as polynomial functions. Using Wolfram Mathematica to calculate correlations, the results are shown in figure 7.14. For the infrared diode (to the left), a 4th

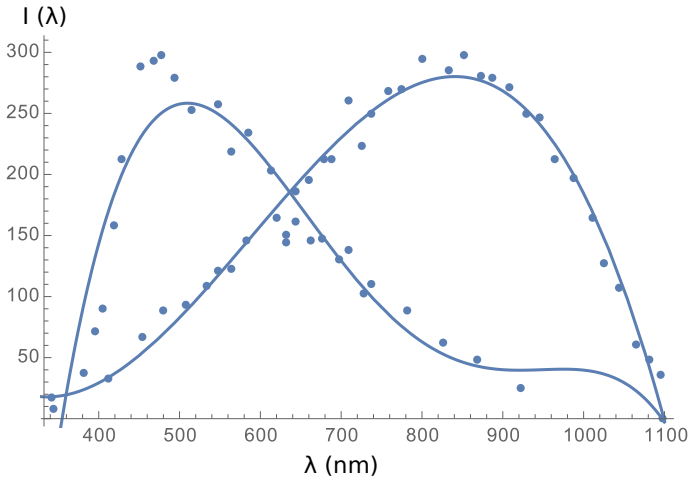

Figure 7.14: Relative sensitivity for both Si1145 photodiodes: visible light (VIS) to the left, and infrared (IR) to the right.

order polynomial fits well, with a regression coefficient $R^2 = 0.98$:

$$f_{IR}(\lambda) = -1.393 \cdot 10^{-10}\lambda^4 - 3.729 \cdot 10^{-6}\lambda^3 + 0.007\lambda^2 - 3.336\lambda + 504.557 \tag{7.12}$$

In comparison to $f_{IR}(\lambda)$, the visible light photodiode correlates poorly with a 4th order polynomial function, with $R^2 = 0.87$. However, higher order polynomials would be considerably more difficult to solve on a microcontroller, where memory resources are limited. Although this is not much of a problem on more advanced microcomputer systems, the MCU on OpenObservatory is only an 8 bit microcontroller with 4 kB RAM which need to be shared among the processing routines for all sensors on the board. Optimal usage of the limited resource is therefore desirable. Figure 7.15 shows the relative regression in function of the polynomial order.

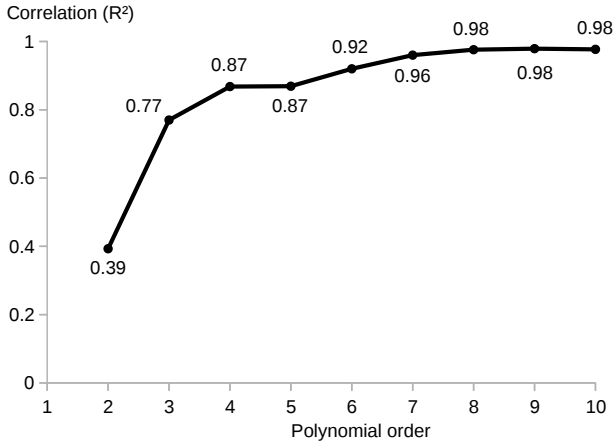

Figure 7.15: Regression fit for the Si1145 visible light (VIS) photodiode, for polynomials with order 2 to 10.

Moving from a 3rd to 4th order polynomial yields a notable gain in R^2, but there is no improvement when moving to a 5th order polynomial. In the scope of a proof of concept, it was therefore decided to

limit the polynomial order for both f_{IR} and f_{VIS} to 4:

$$f_{VIS}(\lambda) = -1.834 \cdot 10^{-8}\lambda^4 + 5.882 \cdot 10^{-5}\lambda^3 - 0.068\lambda^2 + 33.553\lambda - 5637.498 \tag{7.13}$$

To convert normalized spectral response curves to absolute spectral response curves, a correction must be made to account for relative sensitivity and physical photodiode size. This correction factor ψ is documented in the device's datasheet, with $\psi = 0.282$ ADC counts/lx for the VIS and $\psi = 14.7$ ADC counts/lx for IR. This immediately also allows to correlate a raw ADC value to a lx. To apply the correction, the spectral response curves are multiplied with the correction factors:

$$S_k(\lambda) = \psi f_k(\lambda) \tag{7.14}$$

Since the curves and the ψ correction factors are constant, the correction can be done in advance instead of at execution time by multiplying each coefficient for the 4th order polynomial separately and storing the multiplication results instead of the original coefficients.

Light Source Signatures

After identification of $S_k(\lambda)$ as first unknown, the light source spectra also must be identified individually. Figure 7.16 shows a comparison of the spectra of several types of ambient light sources. Since only the proportions of the ambient light mixture are of interest, the absolute magnitude is irrelevant for the light source spectra, in graph 7.16 they have been normalized.

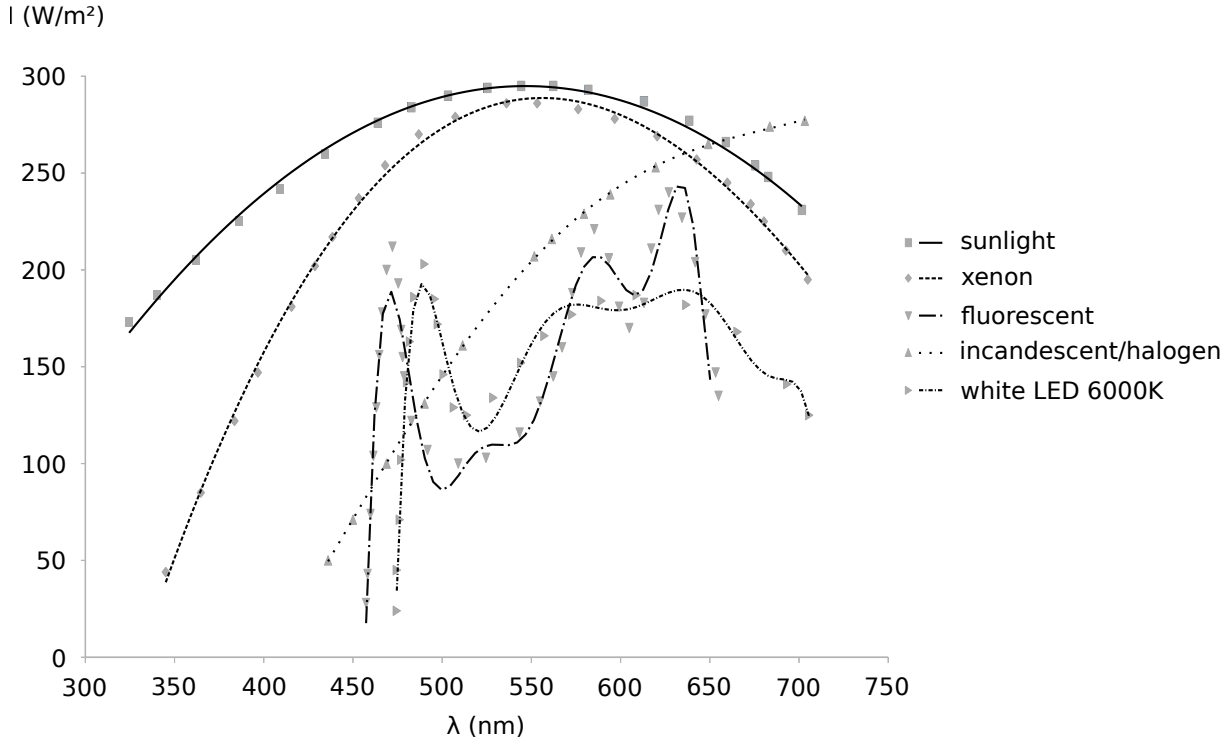

Figure 7.16: Relative spectra of ambient light sources, including natural sunlight and 4 artificial sources: xenon lamps, fluorescent lamps (TL/CFL), incandescent lamps with tungsten filament (including halogen bulbs) and cool white LEDs with light temperature of 6000 K.

Taking the same approach as above, the curves were approximated as polynomial equations. As suggested by figure 7.16, the curves for sunlight, xenon and incandescent (tungsten filament) sources closely resemble parabolas, and can be approximated with a 2nd order polynomial with $R^2 > 0.99$. However, the spectra of fluorescent sources (CFL or TL) and white LEDs are highly irregular and require higher order polynomials for a good fit. Figure 7.17 shows the correlation of LED and fluorescent spectra with 2nd to 13th order polynomials.

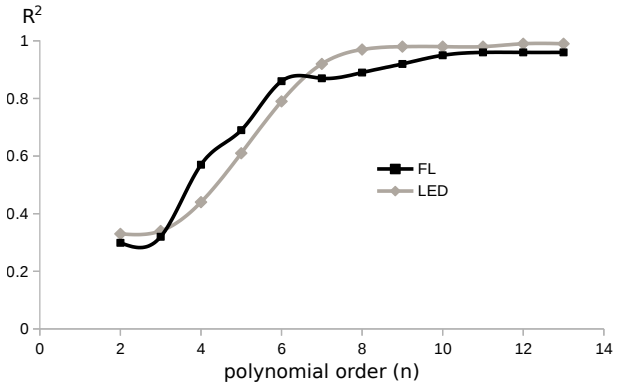

Figure 7.17: Regression fits for fluorescent light sources (FL) and white LEDs, showing polynomial orders between 2 (parabola) and 10.

It is possible that for specific light sources not included in the comparison, another fit than polynomial functions may yield a better regression. However, solving the integral of equation 7.11 with discrete computation methods requires polynomials, and it is therefore not recommendable to attempt other types of fits. Although there is no theoretical maximum limit to polynomial order for a feasible computation, the multiplication of $\Phi(\lambda)$ with $S_k(\lambda)$ causes fractional higher order terms to be formed. For example, if the order of $\Phi(\lambda)$ were m and the order of $S_k(\lambda)$ were n, additional terms with orders up to λ^{n+m} will be generated. Although these may practically be discarded if too small, they do increase the memory usage of the algorithm. As a trade-off, the order of light spectra has therefore been limited to 10. The coefficients are listed in table 7.2. As expected, the coefficients for $\lambda^3 - \lambda^{10}$ are small for sunlight, xenon and incandescent sources since these already fit properly with a 2nd order parabole.

With light sources types and sensor sensitivity identified, it is now possible to calculate the relative intensity of the composing light sources. With 2 sensor diodes, a maximum of 2 different light sources can be identified, and thus

$$\Phi(\lambda) = A f_{sun}(\lambda) + B f_{LED}(\lambda) \tag{7.15}$$

Substituting the curves listed in table 7.2 into equation 7.15 gives the polynomial for $\Phi(\lambda)$:

$$\begin{aligned}\Phi(\lambda) = A\left(a_{sun}\lambda^{10} + b_{sun}\lambda^9 + ... + i_{sun}\lambda + j_{LED}\right) \\ + B\left(a_{LED}\lambda^{10} + b_{LED}\lambda^9 + ... + i_{LED}\lambda + j_{LED}\right)\end{aligned} \tag{7.16}$$

The coefficients a-j correspond to those listed in table 7.2 for λ^{10}-λ^0. The sensitivity of the Si1145 sensor diodes is also characterized, as discussed above, and their responses shown in equations 7.12 and 7.13. Their form is respectively

$$S_{1,2}(\lambda) = a_{s_{1,2}}\lambda^4 + b_{s_{1,2}}\lambda^3 + c_{s_{1,2}}\lambda^2 + d_{s_{1,2}}\lambda + e_{s_{1,2}} \tag{7.17}$$

Table 7.2: Calculated coefficient table for light source types as 10th order polynomial fits.

n	Sunlight	Xenon	Incandescent	Fluorescent	LED
λ^{10}	$6.18 \cdot 10^{-21}$	$6.52 \cdot 10^{-21}$	$4.35 \cdot 10^{-20}$	$7.59 \cdot 10^{-17}$	$4.22 \cdot 10^{-18}$
λ^{9}	$-3.13 \cdot 10^{-17}$	$-3.41 \cdot 10^{-17}$	$-2.54 \cdot 10^{-16}$	$-4.18 \cdot 10^{-13}$	$-2.43 \cdot 10^{-14}$
λ^{8}	$7.06 \cdot 10^{-14}$	$7.99 \cdot 10^{-14}$	$6.63 \cdot 10^{-13}$	$1.00 \cdot 10^{-9}$	$6.28 \cdot 10^{-11}$
λ^{7}	$-9.38 \cdot 10^{-11}$	$-1.10 \cdot 10^{-10}$	$-1.00 \cdot 10^{-9}$	$-1.51 \cdot 10^{-6}$	$-9.57 \cdot 10^{-8}$
λ^{6}	$8.11 \cdot 10^{-8}$	$9.91 \cdot 10^{-8}$	$1.03 \cdot 10^{-6}$	$1.45 \cdot 10^{-3}$	$9.54 \cdot 10^{-5}$
λ^{5}	$-4.77 \cdot 10^{-5}$	$-6.06 \cdot 10^{-5}$	$-7.13 \cdot 10^{-4}$	$-9.50 \cdot 10^{-1}$	$-6.49 \cdot 10^{-2}$
λ^{4}	$1.93 \cdot 10^{-2}$	$2.55 \cdot 10^{-2}$	$3.40 \cdot 10^{-1}$	432	60.6
λ^{3}	-5.33	-7.33	-111	$-1.34 \cdot 10^{5}$	$-9.83 \cdot 10^{4}$
λ^{2}	956	$1.37 \cdot 10^{1}$	$2.36 \cdot 10^{4}$	$2.73 \cdot 10^{7}$	$2.06 \cdot 10^{6}$
λ^{1}	$-1.01 \cdot 10^{5}$	$-1.50 \cdot 10^{5}$	$-2.97 \cdot 10^{6}$	$-3.29 \cdot 10^{9}$	$-2.55 \cdot 10^{8}$
λ^{0}	$4.74 \cdot 10^{6}$	$7.37 \cdot 10^{6}$	$1.67 \cdot 10^{8}$	$1.78 \cdot 10^{11}$	$1.41 \cdot 10^{10}$

The equation for sensor 1 can now be expressed as

$$\begin{aligned} V_{s_1} = \int_{\phi_0}^{\phi_1} (&a_{s_1}Aa_{sun}\lambda^{14} + a_{s_1}Ab_{sun}\lambda^{13} + a_{s_1}Ac_{sun}\lambda^{12} + ... + a_{s_1}Aj_{sun}\lambda^{4} \\ &+ a_{s_1}Ba_{LED}\lambda^{14} + a_{s_1}Bb_{LED}\lambda^{13} + a_{s_1}Bc_{LED}\lambda^{12} + ... + a_{s_1}Bj_{LED}\lambda^{4} \\ &+ b_{s_1}Aa_{sun}\lambda^{13} + b_{s_1}Ab_{sun}\lambda^{12} + b_{s_1}Ac_{sun}\lambda^{11} + ... + b_{s_1}Aj_{sun}\lambda^{3} \\ &+ b_{s_1}Ba_{LED}\lambda^{13} + b_{s_1}Bb_{LED}\lambda^{12} + b_{s_1}Bc_{LED}\lambda^{11} + ... + b_{s_1}Bj_{LED}\lambda^{3} \\ &+ ...+ \\ &+ e_{s_1}Aa_{sun}\lambda^{10} + e_{s_1}Ab_{sun}\lambda^{9} + e_{s_1}Ac_{sun}\lambda^{8} + ... + e_{s_1}Aj_{sun} \\ &+ e_{s_1}Ba_{LED}\lambda^{10} + e_{s_1}Bb_{LeD}\lambda^{9} + e_{s_1}Bc_{LED}\lambda^{8} + ... + e_{s_1}Bj_{LED})d\lambda \end{aligned} \quad (7.18)$$

A large number of linear terms is generated by multiplication, and same order terms can be grouped together to simplify the equation as follows:

$$\begin{aligned} V_{s_1} = \int_{\phi_0}^{\phi_1} (&(a_{s_1}Aa_{sun} + a_{s_1}Ba_{LED})\,\lambda^{14} \\ &+ (a_{s_1}Ab_{sun} + a_{s_1}Bb_{LED} + b_{s_1}Aa_{sun} + b_{s_1}Ba_{LED})\,\lambda^{13} \\ &+ ...+ \\ &+ (e_{s_1}Aj_{sun} + e_{s_1}Bj_{LED}))d\lambda \end{aligned} \quad (7.19)$$

Since $\int (a+b)d\lambda = \int ad\lambda + \int bd\lambda$, the integral can be split and each term integrated separately. Thus

$$V_{s_1} = \int_{\phi_0}^{\phi_1} (a_{s_1}Aa_{sun} + a_{s_1}Ba_{LED})\,\lambda^{14}d\lambda$$

$$+\int_{\phi_0}^{\phi_1}\left(a_{s_1}Ab_{sun}+a_{s_1}Bb_{LED}+b_{s_1}Aa_{sun}+b_{s_1}Ba_{LED}\right)\lambda^{13}d\lambda$$
$$+\ldots+$$
$$+\int_{\phi_0}^{\phi_1}e_{s_1}Aj_{sun}d\lambda+\int_{\phi_0}^{\phi_1}e_{s_1}Bj_{LED}d\lambda \quad (7.20)$$

With the integral limits being constant ($\phi_0 \approx 200\,\text{nm}$, $\phi_1 \approx 1100\,\text{nm}$), the integration is reduced to another multiplication term:

$$V_{s_1}=\frac{1}{15}\left(a_{s_1}Aa_{sun}+a_{s_1}Ba_{LED}\right)\left(\phi_1^{15}-\phi_0^{13}\right)$$
$$+\frac{1}{14}\left(a_{s_1}Ab_{sun}+a_{s_1}Bb_{LED}+b_{s_1}Aa_{sun}+b_{s_1}Ba_{LED}\right)\left(\phi_1^{12}-\phi_0^{13}\right)$$
$$+\ldots+$$
$$+e_{s_1}Aj_{sun}\left(\phi_1-\phi_0\right)+e_{s_1}Bj_{LED}\left(\phi_1-\phi_0\right) \quad (7.21)$$

For V_{s_2} an identical equation can be written out. After substituting the parameters with those listed in table 7.2 for the curves, those in equations 7.13 and 7.12 for the sensor sensitivity, and 200 nm resp. 1100 nm for ϕ_1 and ϕ_0, 2 equations are obtained with each only 2 unknowns, A and B. Either unknown can be calculated by simply substituting the equation for V_{s_1} into V_{s_2} or vice versa and solving the linear equation for the remaining unknown. For more than 2 sensors, a system of linear equations is obtained that can be solved computationally with Gauss' method. To find the proportionality of each light source, the fraction can be calculated as a percentage by division: for source A that is $f_A = \dfrac{A}{A+B}$ and for B likewise $f_B = \dfrac{B}{A+B}$. For n light sources, the generalized method is

$$f_{A_i}=A_i\left(\sum_n A_n\right)^{-1} \quad (7.22)$$

Linear Arrays

The simplified solid state spectrometer approach disseminated above, works with any combination of light sensors as long as their relative wavelength sensitivity is sufficiently diverse. Any semiconductor material or combination thereof is sensitive to light, and slight alterations in the composition (i.e. doping) may have significant effects on light absorption. If a linear array like the TCD1703 can be modified so that the cells have different instead of identical responses, for example by adding an additional vapor phase epitaxy step to the manufacturing process, it would be theoretically feasible to apply the strategy to create a spectrometer in the conventional sense of the word. Because the inaccuracies introduced with curve approximation, and the finite resolution of the benchmarking process, such a spectrometer would have a lower accuracy compared to its conventional counterparts, but would not require any optical components to achieve the same wavelength resolution (which depends solely on the number of cells and their range). However, the design of such a device and its manufacturing process is outside the scope of the research, and will therefore not be elaborated here.

7.7.3 Sensors

With feasibility of the approach demonstrated above, both on a theoretical level and in terms of computational implementation, a design for AEM Light can be brought forward by expanding the number of photodiodes from 2 in Si1145 to the required number to measure any combination of ambient light sources. Since there are 3 major artificial light sources (fluorescent, incandescent/halogen and LED) in addition to natural sunlight, a minimum of 4 physical photodiodes is required.

Selection

Although any sensor combination can be used as long as their wavelength sensitivity differs, the best results are obtained when sensors are chosen with a complementary sensitivity, ideally spread out over the entire spectrum of interest. Many sensors are technically qualified for the AEM-Light application, and it would be practically unfeasible to compare them all. For instance, preferential supplier Digikey alone offers 292 different qualified sensors in their inventory. To reduce that number, only devices that are in active production (and thus guaranteed to be commercially available the next 5 - 10 years) and have performance documented in literature were considered. After filtering out devices with inconvenient interfaces or packages (i.e. BGAs), making implementation unnecessarily difficult, a selection of 8 sensors remains. Their characteristics are compared in table 7.3.

Table 7.3: Comparison of commercial light sensors considered for application in AEM-Light.

Device	Manufacturer	# d.	package	interface	€	€/diode
GUVA-S12SD	Roithner	1	DO-214	analog	1.24	1.24
VEML6070	Vishay	1	6-LGA	I^2C	2.43	2.43
Si1145	Silicon Labs	3	10-QFN	I^2C	2.83	0.94
TSL2561	Taos	2	6-DFN	I^2C	2.34	1.17
TSL25911	AMS	2	6-DFN	I^2C	2.58	1.29
VCNL4010	Vishay	2	12-LLP	I^2C	3.09	1.55
TCS3472	Taos	4	6-DFN	I^2C	3.83	0.96
ADPD2212	Analog Devices	1	10-LFCSP	analog	7.90	7.90

The only parameter that can not be easily compared in a table, and also the most important parameter to be taken into consideration, is the relative sensitivity of each photodiode. As seen in figure 7.18, several sensors have strongly overlapping spectra (for example, TLS25911 and TSL2561), while others are sensitive in unique wavelength ranges, such as the GUVA-S12SD.

Although pricing will be a decisive factor for sensor combination selections in commercial implementations of AEM-Light, for the development version it was instead chosen to select sensors with a narrow wavelength sensitivity and an optimal complementarity. This resulted in 6 physical devices being selected: the GUVA-S12SD, ADPD2212, TCS3472, VEML6070, and TSL25911, with a total of 9 individual photodiodes. In addition, a MAX44009 lux sensor was also selected to provide calibrated measurements of absolute luminosity. All digital sensors including MAX44009 share the same I^2C bus, which is also shared with the 24AA025UID GUID/EEPROM IC on AEM-Light. The sensors with analog output, GUVA-S12SD and ADPD2212 respectively, share the same ADC and are interfaced though SPI.

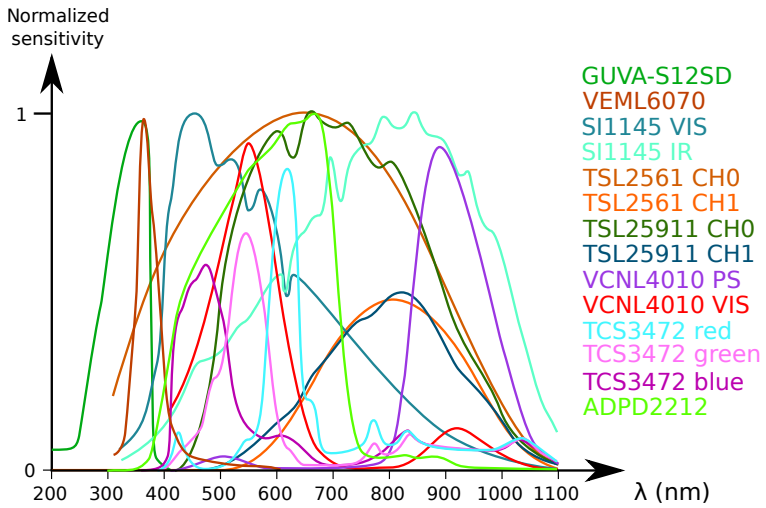

Figure 7.18: Comparison of relative wavelength sensitivity of 8 commercial sensor devices. For devices with more than one photodiode, each diode response is listed separately.

The block diagram of AEM Light Rev. 2 is shown in figure 7.19. As any other AEM module, it consists of a digital block with an Atmega2560 microcontroller as processing unit, with an AD7689 16 bit ADC front-end. Revision 1 used 2 ADCs of type ISL26102 from Intersil, which are 24 bit delta sigma ADCs with integrated programmable gain amplifier. Because the complexity of software development, as discussed in section B.1, newer versions use the AD7689 instead. The 8 single ended input channels of the AD7689 are shared among the 2 light sensors with analog output, GUVA-S12SD and ADPD2212, the voltage outputs of 2 photovoltaic boost converters (LTC3105 and SPV1040, as discussed below), and the current sense input of the electronic load for the connected harvester. An analog switch of type FSA2467, corresponding to a DPDT switch, is controlled by the Atmega2560 to switch the connected photovoltaic cell between the LTC3105 (top signal path) and SPV1040 (bottom signal path). Both share the same electronic load circuit, as shown in figure 7.12. To set the maximum power point (MPP) in each signal path, a digital potentiometer of type MCP4262 from Microchip is used. This device contains 2 potentiometers with a nominal impedance of 50 kΩ which can either be used as potentiometer or rheostat. The connection of the light sensors with digital output, all using I^2C, is trivial, and does not need to be discussed. Interfacing of the analog sensors, GUVA-S12SD and ADPD2212, is elaborated below.

GUVA-S12SD

The GUVA-S12SD is a photodiode in a standard DO-214 (SMB) diode package, and acts as a current source, with an output current proportional to the received light. The sensor is designed for UVA and UVB measurements, which contributes a significant fraction of the energy in natural sunlight. The sensitivity is 113 nA/mW/m^2, which poses a challenge regarding noise susceptibility. The required gain can be calculated from the expected maximum in an outdoor environment with clear sky, around noon, which is ca. 260 mW/m^2. This corresponds to a sensor current of ca. 2.94 nA. Using a current amplifier, as shown in figure 7.20, the required feedback can be calculated as follows:

$$R_f = \frac{V_o}{I_{GUVA}} = \frac{2.048}{2.94 \cdot 10^{-9}} = 3.53 \cdot 10^8\,\Omega \approx 350\,\mathrm{M\Omega} \tag{7.23}$$

The output current is converted into a voltage by the current amplifier shown in figure 7.20.The amplifier consists of 2 stages: the actual current amplifier stage and a non inverting amplifier to scale the output

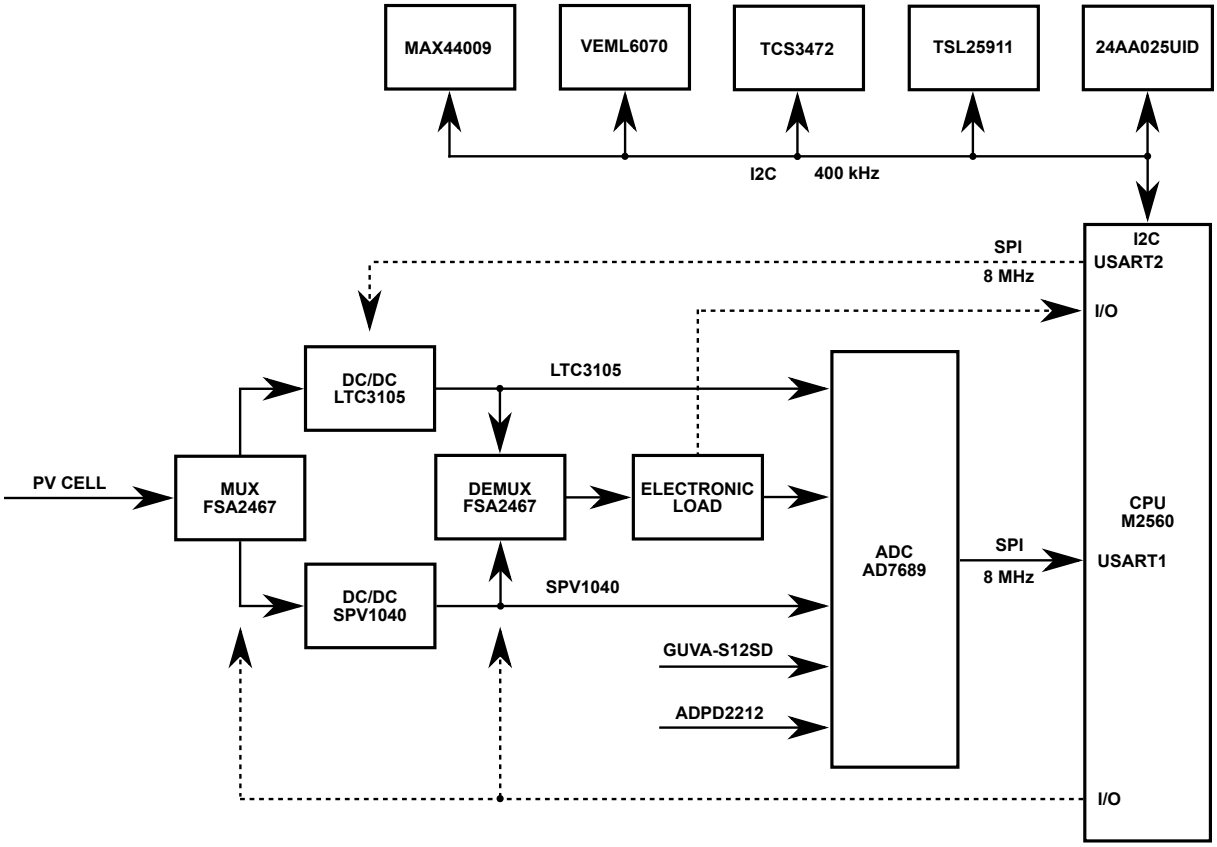

Figure 7.19: Block diagram of AEM Light, with a dual power path for LTC3105 and SPV1040 using analog multiplexers.

voltage of the first stage to the full input range of the ADC.

A resistor value of this magnitude is impractical, and the high impedance nature of the amplifier would easily couple in external noise. A solution is to use a 2 stage topology instead, combining a current amplifier stage acting as a preamp with a non inverting amplifier stage. With a 10 MΩ feedback resistor, as recommended in literature, the full scale output is

$$V_o = R_f \cdot I_{GUVA} = 10\,\mathrm{M\Omega} \cdot 2.64\,\mathrm{nA} = 29.4\,\mathrm{mV} \tag{7.24}$$

For a full scale output to match the reference of 1.024 V of the ADC, the second stage thus needs an amplification factor

$$A_{CL} = \frac{v_o}{v_i} = \frac{1.024\,\mathrm{V}}{29.4\,\mathrm{mV}} = 34.8 \tag{7.25}$$

For a non inverting amplifier, the resistor combination 10 kΩ and 330 kΩ yields an amplification factor of $A_{CL} = +1\dfrac{330}{10} = 34$, which is close enough and has the added advantage that both resistor values are E27 series standard values. Special care must be taken for the selection of the opamps, particularly the one in the current amplifier. Considering the nA range output signal amplitude of the sensor, any input bias current of the opamp will distort the measurement, and thus an opamp with an input bias current as low as possible is necessary. The LMP7721 from Texas Instruments was chosen for this purpose. This

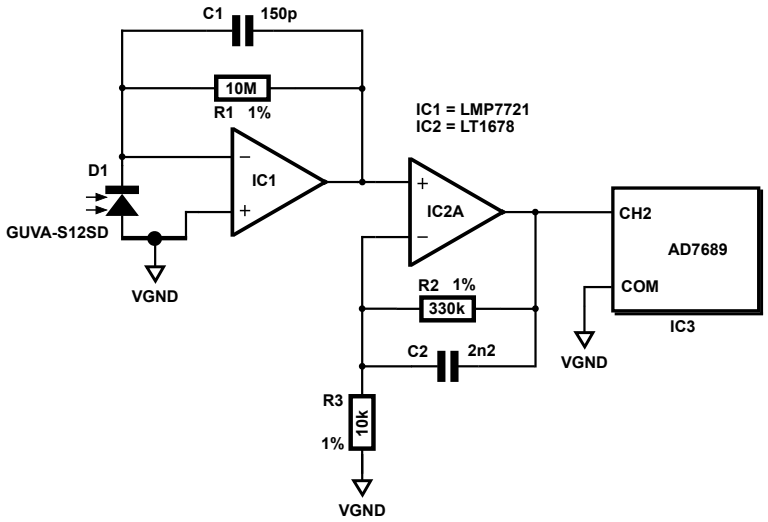

Figure 7.20: Analog front-end for GUVA-S12SD, with current amplifier and second order LPF.

opamp has an input bias current of 3 fA for common mode inputs below 500 mV and a power supply of 3.3 V. With an input offset of $\pm 26\,\mu$V and a gain bandwidth of 17 MHz, it is well suited for this application. For the non inverting amplifier stage, the constraints are less high demanding, and a low noise rail to rail opamp of type LT1678 from Linear Technology was chosen for that purpose.

Due to the exceptionally high input impedance, noise suppression measures must be in place. Both stages are configured as active low pass filters for this purpose. Although the cut-off frequency of the filters may seem unimportant, and might be chosen arbitrarily low, one practical application provides the incentive for more tolerant filters: measuring fluorescent lamp decay. In normal operation, fluorescent lamps emit a primarily UV spectrum which is then converted to visible light by a fluorescent coating on the inside of the tube, which gives the lamp type its name. When the coating deteriorates, not all the produced UV light is converted, and a UV signal pulsing at the net frequency of 50 Hz may be measurable. To allow this application, the first harmonic (100 Hz) was chosen as the cut-off frequency for both low pass filters. For the current amplifier stage with a feedback resistor of 10 MΩ, a capacitor of 150 pF results in a -3 dB frequency of 106 Hz. For the non inverting amplifier stage with a feedback resistor of 330 kΩ, the same cut-off frequency is achieved with a 2.2 nF capacitor. The calculated complex response function is

$$v_o = \frac{R_1(2j\omega C_2 R_2 R_3 + 2R_2 + R_3)}{(j\omega C_1 R_1 + 1)(j\omega C_2 R_2 R_3 + R_2 + R_3)} I_{GUVA} \tag{7.26}$$

which for a DC input signal simplifies to

$$v_o = R_1 \left(1 + \frac{R_3}{R_2}\right) I_{GUVA} \tag{7.27}$$

with I_{GUVA} the output current of the sensor. The SPICE simulation results of noise attenuation characteristics and phase shift as a result of the filter are shown in figure 7.21. The output of the non inverting amplifier is shown in black (second order noise filtering), while the intermediate output of the current amplifier is shown in gray.

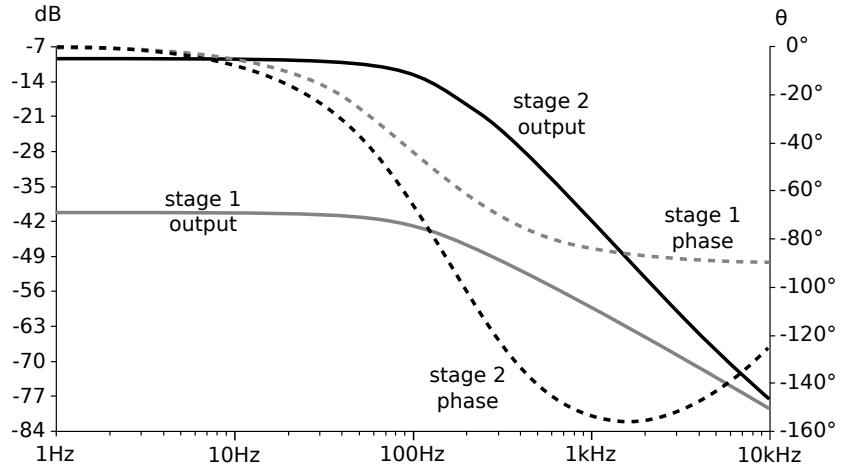

Figure 7.21: Frequency response of the amplifier, showing current amplifier stage in gray and complete amplifier in black. Phase shifts are denoted with a dotted line.

While less important for the second stage, the leakage current for the 150 pF capacitor in the current amplifier feedback is paramount, and a ceramic capacitor with high quality dielectric with long term stability such as C0G is necessary to prevent the capacitor from adversely affecting measurements.

ADPD2212

Like the GUVA-S12SD, the Analog Devices ADPD2212 is a high sensitivity optical sensor with an analog output, but with a wavelength response in the visible light range instead of the in UV range. With a very low noise floor of only 90 fA/$\sqrt{\text{Hz}}$ and an integrated current amplifier, it offers a better accuracy than the GUVA-S12SD, unfortunately at a much higher cost as well. The relatively large active area (2.5 mm^2) results in a physically large package, but also the highest saturation irradiation of any sensor: 1.6 mW/cm^2. Unlike the GUVA-S12SD, the ADPD2212 is an active light sensor with an integrated, 24 dB gain current amplifier. It is internally compensated for non-linearity of its photodiode, and its output thus acts as an ideal current source. At saturation, the output current is 240 μA, so matching the output to the 2.048 V ADC reference requires a shunt resistor

$$R_s = \frac{2.048\,\text{V}}{240\,\mu\text{A}} \approx 85.3\,\text{k}\Omega \tag{7.28}$$

However, unless illuminated by a powerful artificial light source such as a laser, the saturation level will never be reached for practical applications. It was therefore decided to follow the manufacturer's recommendation and use a 100 kΩ shunt resistor instead. The output voltage of the ADPD2212 is limited to VCC - 0.75 V = 2.55 V, which makes any additional input clamping protection redundant.

7.7.4 Light Energy Harvester

To harvest energy from a photovoltaic cell, as discussed in the previous chapters, designers must decide on the maximum power point tracking (MPPT) strategy to be used. Although software algorithms exist for true maximum power point tracking, such an approach is rarely efficient for low power systems since the power consumption of such an algorithm is likely to offset the power gained by its implementation. Since the choice for a fixed or dynamic maximum power point tracker may not be trivial depending on

the conditions of the ambient environment, it was decided to offer both strategies on AEM Light. To implement them, a state of the art controller for each was selected based on existing literature, with a comparison of suitable controllers listed in table 7.4.

Table 7.4: Comparison of commercial PV energy harvesters considered for application in AEM-Light.

Param.	LTC3105	SPV1040	TPS61200	BQ25504	MB39C831	AEM10940
Man.	LT	ST	TI	TI	Cypress	e-Peas
IC	12-MSOP	8-TSSOP	10-VSON	16-VQFN	40-QFN	24-QFN
MPPT	fixed	P & O	fixed	none	fixed	fixed
V_{min}	225 mV	300 mV	300 mV	80 mV	300 mV	100 mV
V_{start}	250 mV		500 mV	330 mV	350 mV	380 mV
V_{max}	5 V	5.5 V	5.5 V	3 V	4.75 V	2.5 V
V_{FB}	1.004 V	1.25 V	500 mV			1.0 V
I_{Q}	24 μA	60 μA	55 μA	330 nA	41 μA	10 μA
I_{max}	500 mA	1.65 A	300 mA	300 mA	200 mA	80 mA
f_{osc}	100 kHz	100 kHz	1.65 MHz	1 MHz	1 MHz	

To compare input voltage, a distinction is made between the minimum input voltage V_{min}, the maximum input voltage V_{max} and the cold start-up voltage V_{start}. For single ended or SEPIC controllers, V_{min} and V_{start} are nearly identical, with small differences attributed to forward diode voltage drops. This is the case for the LTC3105 and MB39C831. Those with a high side switch in the power path need a higher V_{start} to make the high side switch conduct in the first cycle. Once in regulation, the input voltage may drop below V_{start}, with a detrimental effect on efficiency. This effect is notable on the TPS61200, BQ25504 and AEM10940. For the BQ25504, the input voltage may drop even below the forward voltage drop of Schottky junction, because a flyback topology similar to the LTC3108 is used on the input.

Of particular importance for autonomous systems is the quiescent current, which leads to a power loss even when the output current is 0, and consequentially independent of the output regulation efficiency. Ideally, I_{Q} should be minimized, and as with LDOs, I_{Q} is often correlated to I_{max} for boost converters, but also dependent on switching frequency. Higher switching frequencies reduce output ripple and allow smaller inductors, but typically also result in higher I_{Q} losses (for example when comparing TPS61200 with LTC3105). Concluding from table 7.4, LTC3105 was selected as the choice for a PV energy harvester with fixed maximum power point control, because of its favorable V_{min} and V_{start}, and compatibility with cells up to 5 V V_{oc}. An additional advantage of the LTC3105, from a practical point of view, is that it has been reviewed in literature, which reduces design efforts. For dynamic maximum power point tracking, the SPV1040 was chosen because it is the only widely available commercial device for low power energy harvesting with a documented dynamic maximum power point tracking algorithm (perturb & observe).

Topology

To integrate both DC/DC converters into the same signal path, an multiplexer/demultiplexer topology allows dynamic switching, as shown in figure 7.19. As mux/demux, an analog switch from Fairchild Semiconductor of type FSA2467 is inserted before and after the DC/DC converter stages. The FSA2467 was chosen for its low solid state switch resistance, 0.4 Ω per channel. On the input side, compensation for this loss is difficult, and ultimately not necessary since the switch resistance is an order of magnitude smaller than the output resistance of commercial silicon photovoltaic cells. On the output side, the

0.4 Ω is bypassed by measuring the output voltage for both DC/DC converters directly on separate ADC channels, as shown in figure 7.19. The current regulation feedback loop shown in figure 7.13 will automatically compensate MOSFET resistance to offset the additional 0.4 Ω parasitic resistance. The 1 kΩ precision shunt to measure current remains unaltered, but even without compensation, the error would be negligible (0.4 Ω/1 kΩ = 0.0004 %, far below the noise floor of any of the active components in either signal path).

AEM Light does not currently switch between either signal path depending on PV cell characteristics, because the software required to evaluate cell characteristics on a microcontroller level has not yet been developed. The FSA2467 is controlled directly by the microcontroller however, allowing implementation of the functionality with a mere software update. On AEM Light Rev. 2, a micro switch is provided to allow the user to switch between fixed or dynamic power point tracking. Rev. 1 only implements the LTC3105 (fixed power point tracking).

Table 7.5: Comparison of commercial PV cell specifications at illumination of 1 kW/m^2.

PV cell	V_{MPP}	I_{MPP}	P_{MPP}	V_{OC}	I_{SC}	type
KXOB22-12X1F	0.50 V	44.6 mA	18.6 mW	0.63 V	50.0 mA	mono
KXOB22-04X3F	1.50 V	13.38 mA	18.6 mW	1.89 V	15 mA	mono
KXOB22-01X8F	3.40 V	3.8 mA	18.6 mW	4.70 V	4.4 mA	mono
SLMD121H04L	2 V	44.6 mA	89 mW	2.52 V	50 mA	mono
SLMD600H10L	5.01 V	22.3 mA	111 mW	6.3 V	25 mA	mono
SLMD121H08L	4 V	44.6 mA	178 mW	5.04 V	50 mA	mono
SLMD121H10L	5.01 V	44.6 mA	223 mW	6.3 V	50 mA	mono
SLMD481H10L	5 V	178 mA	892 mW	6.3 V	200 mA	mono
SLMD481H12L	6.06 V	178 mA	1.08 W	7.56 V	200 mA	mono
SLMD480H12L	6.06 V	18 mA	109 mW	7.56 V	20 mA	mono
SLMD121H9L	4.5 V	44.6 mA	201 mW	5.67 V	50 mA	mono
AM-1417CA	1.5 V	12.5 μA	18.75 μW	2.4 V	13.5 μA	amorphous
AM-1454CA	1.5 V	31 μA	46.5 μW	2.4 V	35 μA	amorphous
AM-1801CA	3 V	18.5 μA		4.9 V	20 μA	amorphous
AM-5610CAR	3.3 V	5.1 mA	16.8 mW	5.1 V		amorphous
AM-1815CA	3 V	42 μA	126 μW	4.9 V	47 μA	amorphous
AM-5412CAR	2.2 V	39.8 mA	87 mW	3.4 V		amorphous
AM-1816CA	3 V	84 μA	252 μW	4.9 V	94 μA	amorphous
PRT-13782	6.0 V	615 mA	3.69 W	7.0 V		mono
PRT-13781	6 V	378 mA	2 W	7 V		mono
PRT-13784	6 V	1.5 A	9 W	7 V		mono
313070004	5.5 V	100 mA	500 mW	8.2 V		mono
313070003	5.5 V	360 mA	2 W	8.2 V		mono
313070001	5.5 V	540 mA	3 W	8.2 V		mono
313070000	5.5 V	450 mA	2.5 W	8.2 V		mono
310370005	5.5 V	170 mA	1 W	8.2 V		mono
313070002	5.5 V	270 mA	1.5 W	8.2 V		mono
114990248	5.3 V	950 mA	5 W	6.7 V		amorphous
114990058	2 V	500 mA	1 W			flexible
114990247	1.3 V	950 mA	2.5 W	3.1 V		flexible
114990057	2 V	250 mA	500 mW			flexible

2885456	18.1 V	2.75 A	50 W		2.95 A	mono
FIT0333	1.5 V	250 mA	500 mW	2 V	420 mA	flexible
FIT0330	9 V	220 mA	2 W	9.6 V	500 mA	flexible
ECS300	3 V	4.5 μA		4 V	6.5 μA	amorphous
XOB17-04X3	1.53 V	11.7 mA	18 mW	1.89 V	12.6 mA	mono
XOB17-12X1	510 mV	39 mA	20 mW	630 mV	42 mA	mono
XOD17-04B	505 mV	12 mA	6 mW	630 mV	168 mA	mono
XOD17-12B	505 mV	39.6 mA	20 mW	630 mV	42 mA	mono
XOD17-34B	505 mV	111 mA	56 mW	630 mV	120 mA	mono
750-00030	6 V	166 mA	1 W	6.9 V	180 mA	mono
750-00031	9 V	110 mA	1 W	10.4 V	120 mA	mono
750-00032	18 V	580 mA	10 W	21.6 V	640 mA	mono
750-00034	504 mV	5.16 A	2.6 W	600 mV	5.6 A	mono
CBC-PV-01N	800 mV	201 μA		1.2 V	212 μA	amorphous
CBC-PV-02N	800 mV	110 μA		1.2 V	116 μA	amorphous
SLPN005H10	5.5 V	980 mA	5.39 W	6.3 V	1 A	mono
MSL-156-52	500 mV		1.4 W			poly
IHUAX-156-156	530 mV	8.17 A	4.33 W	635 mV	8.693 A	poly

Static Power Point Tracking

The Linear Technology LTC3105 is designed for low voltage input sources with a low output impedance, such as PV cells. It integrates a low voltage start-up sequencer, high side current sensor and maximum power point controller (MPPC) into a single package. The primary output is a boost stage with a configurable output voltage, set through external feedback. It also features an LDO with a fixed 2.2 V output voltage for internal operation. The design has been improved through 3 iterations.

Revision 1 The initial design, implemented on AEM Light Rev. 2, features the LTC3105 in a topology that closely resembles the reference design provided by manufacturer Linear Technology. The circuit is shown in figure 7.22. The PV cell is connected to the board through a 2 pin JST connector, feeding the PV cell output into the LTC3105 (point A). The VIN input powers the integrated 2.2 V LDO (point B), the SW input is the actual switched boost converter input (with an integrated N-channel switch from the SW input to ground, and integrated flyback diode). LDO feedback to ground defaults the output voltage to 2.2 V, but it is not loaded aside from a decoupling and buffer capacitor of 4.7 μF for noise suppression. The output voltage is set to 2.048 V, equal to the reference voltage of the ADC. The internal feedback reference voltage of the LTC3105 is a 1.004 V precision bandgap reference (point E), making calculation of the feedback resistors R1 and R5 trivial. Values for satellite peripherals L1, C1, C2, C3 and C4 were obtained from the LTC3105 datasheet.

The maximum power point tracker consists of a linear feedback loop, regulating the input voltage on the VIN pin to match the voltage set on the MPPC pin. Although a voltage divider can be used, the LTC3105 has an integrated 10μA current source connected to the MPPC pin, which allows setting the MPP voltage with a single resistor to ground. As seen in table 7.5, the minimum MPP voltage for commercial cells is around 500 mV, which is slightly below a pn junction drop. The resistor required to have at least a MPP of 500 mV is

$$R_{MPP} = \frac{V_{MPP}}{10\,\mu\text{A}} = \frac{0.5}{10^{-5}} \approx 47\,\text{k}\Omega \tag{7.29}$$

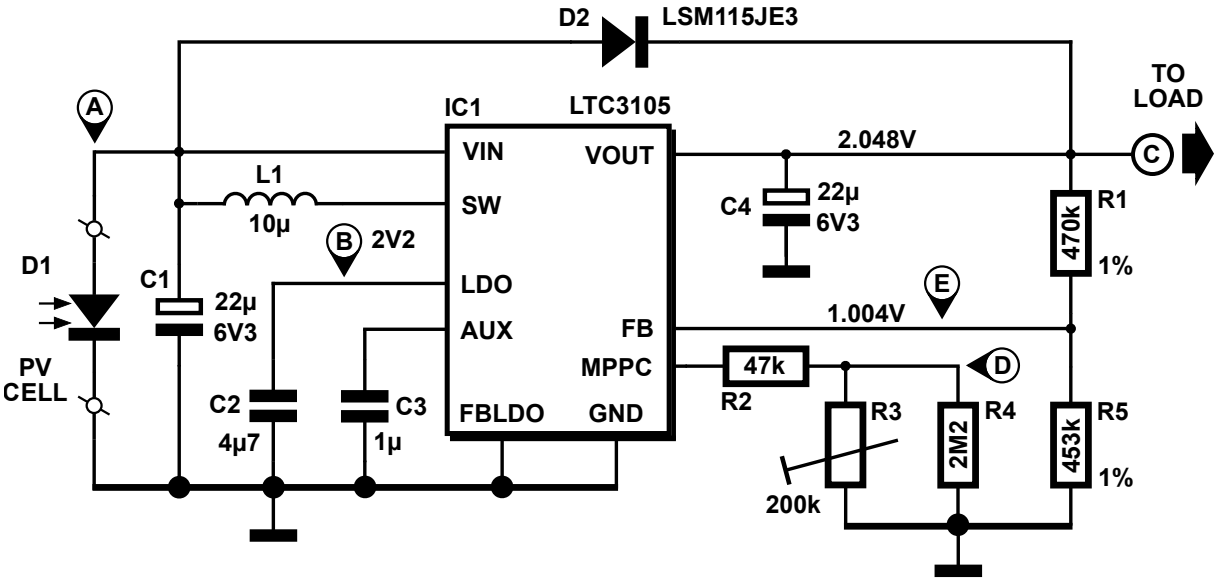

Figure 7.22: Static power point tracking with LTC3105 using trimpot for MPP configuration.

The maximum MPP voltage allowed is the one where the input voltage corresponds to the output voltage of the LTC3105, which is the 2.048 V reference, plus the forward voltage drop over the bypass diode D2. At this voltage, the diode will conduct, and effectively push the LTC3105 out of regulation because the feedback voltage on point E will rise above 1.004 V, disabling the PWM controller of the LTC3105. To make the exact MPP voltage configurable, a trim pot has been included, with a value

$$R_{MPP-TRIM} = \frac{V_{MPP-MAX}}{10\,\mu\text{A}} - 47\,\text{k}\Omega = \frac{V_{REF} + V_D}{10\,\mu\text{A}} - 47\,\text{k}\Omega \approx 183\,\text{k}\Omega \tag{7.30}$$

Since trimmers of 180 kΩ are not available, parallel shunt resistor R4 with a value of 2.2 MΩ was used to rescale a 200 kΩ trimmer (R3) to a full scale of 183 kΩ. The load and measurement circuit was inherited from revision 2 of AEM Vibrations (figure 7.11).

Revision 2 A drawback of the design in figure 7.22 is the inaccuracy of setting the MPP voltage for the LTC3105 by rotating the 200 kΩ trimmer. The lack of grading on the device makes experiments difficult to repeat consistently, and the only improvement would be to turn the trimmer into a full scale potentiometer with calibration markings. Although such an adjustment would trade compactness for accuracy, the problem remains that the maximum power point needs to be set manually. The solution to this problem is using a digital potentiometer, like the MCP4262 from Microchip, instead of a trimmer or potentiometer, as shown in figure 7.23.

The MCP4262 is a low cost device featuring 2 individually configurable potentiometers/rheostats with a nominal resistance of 100 kΩ each. To achieve the full range calculated in the previous example, a minimal variable resistance of 183 kΩ is required, so the two potentiometers are wired in series, with the wiper of device 0 (P0W) connected to terminal A of device 1 (P1A). The wiper of device 1 is then led to ground, while terminal A of device 0 is wired in series with the fixed 47 kΩ resistor. The other components in the design are functionally identical to figure 7.23. The MCP4262 supports a serial SPI compatible interface, and is wired to a USART resource of the microcontroller. The resolution of each potentiometer is 8 bit, so the equivalent resolution of both allows to set a resistance between 0 and 200 kΩ

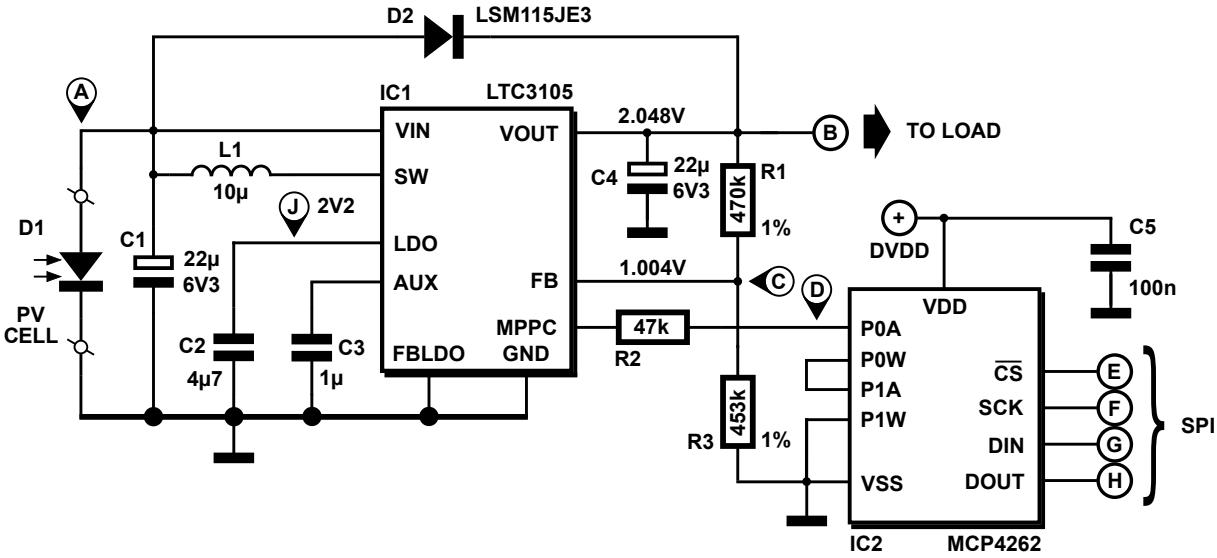

Figure 7.23: Static power point tracking with LTC3105, using a digital potentiometer for MPP configuration.

with an accuracy of ca. 390 $Omega$, which corresponds to a MPP voltage of ca. 4 mV. That is an order of magnitude lower than the MPP drift expected from temperature variations, and therefore adequate for this application.

To set the correct maximum power point voltage for a PV cell of a specific type, a look up table was implemented in the external EEPROM memory of the 24AA025UID external memory on board of AEM Light, as shown in figure 7.24. The USB connection in figure 59 allows the user access to the Atmega2560 microcontroller and set a PV cell type, or alternatively, set a MPP voltage directly. The microcontroller then retrieves the MPP voltage corresponding to that cell type from the 24AA025UID if necessary, and calculates the settings for the MCP4262. The MCP4262 communicates in SPI mode 0 (clock polarity = 0 and clock phase = 0), and the configuration registers are 0x00 (for potentiometer 0) and 0x01 (for potentiometer 1). The volatile configuration is used for both (using 0x00 and 0x01 instead of 0x02 and 0x03). For any given configuration, the resistance of both potentiometers is set to an identical value R_{set}:

$$R_{set} = \frac{1}{2}\left[\frac{V_{MPP}}{10\,\mu\mathrm{A}} - 47\,\mathrm{k\Omega}\right] \tag{7.31}$$

from which the bit value for each register can be calculated as the fraction of the resolution and the nominal value:

$$reg_{0x00,0x01} = \frac{2^8}{2 \cdot 100\,\mathrm{k\Omega}}\left[\frac{V_{MPP}}{10\,\mu\mathrm{A}} - 47\,\mathrm{k\Omega}\right] \tag{7.32}$$

If a value is set that exceeds the maximum MPP voltage (ca. 2.3 V), the resistance is clipped to its maximum allowed value of 183 kΩ.

Revision 3 With a maximum allowed MPP value of 2.048 V, only 39 % of cells listed in table 7.5 can be measured. This was deemed unsatisfactory, because it would exclude most composite monocrystalline PV cells. It was therefore decided to double the allowed MPP voltage from 2.048 V to 4.096 V, allowing

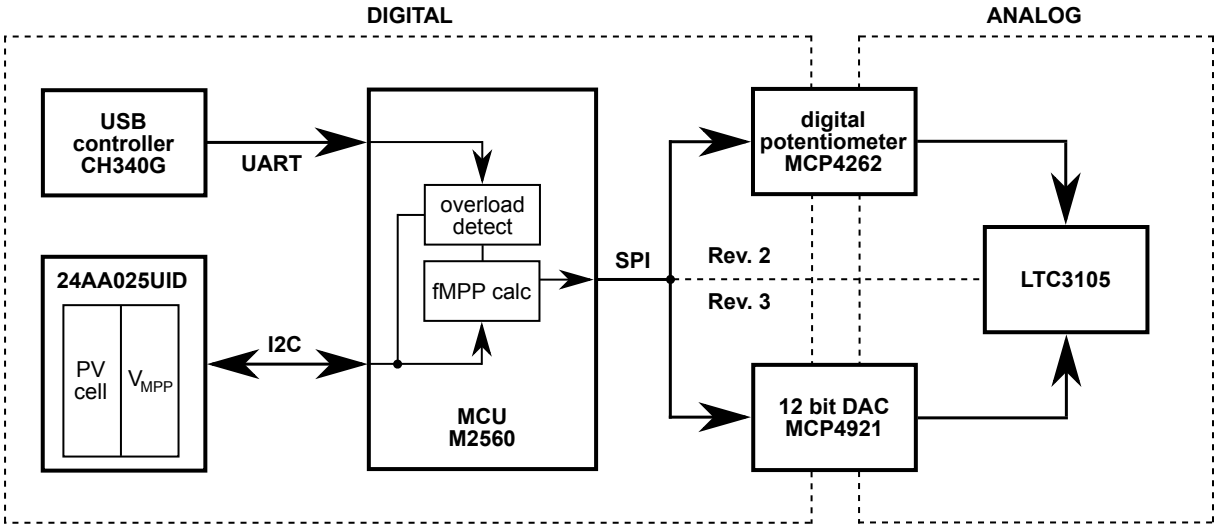

Figure 7.24: Control mechanism for MPP configuration of LTC3105, using digital potentiometer (Rev. 2) and DAC (Rev. 3). A library with MPP voltages for different cells is stored locally in the 24AA025UID EEPROM.

more cells (55 %) to be tested. This improvement however requires several modifications to the design. The modified signal path is shown in figure 7.25.

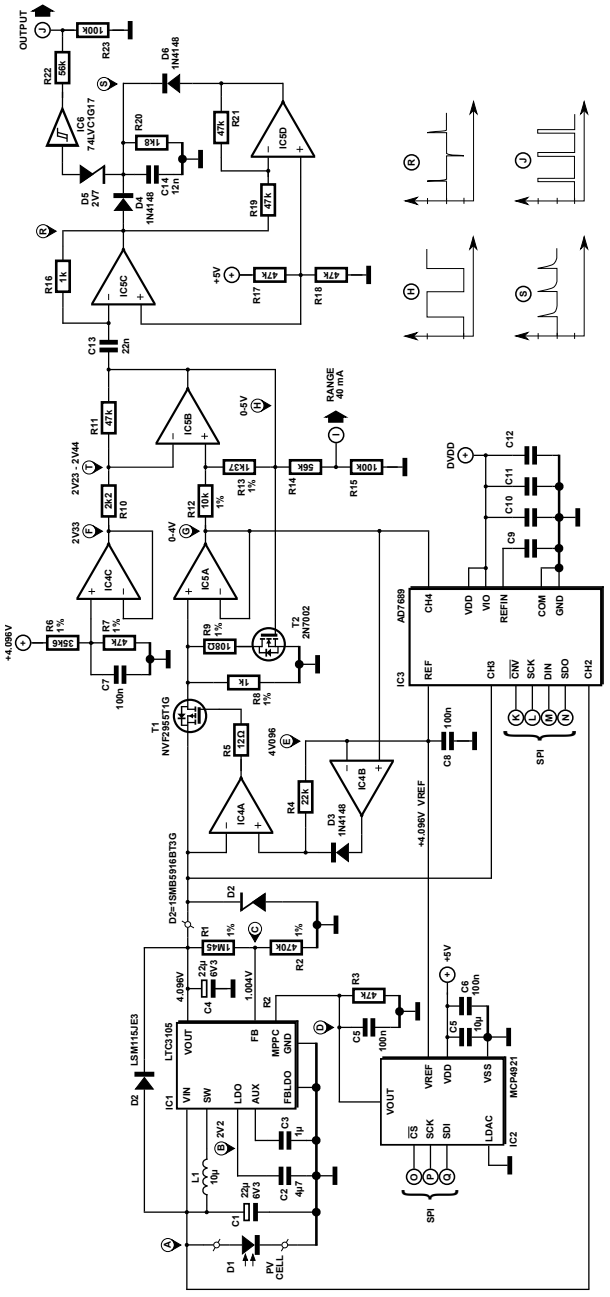

Figure 7.25: Analog front-end for fixed power point tracking using the LTC3105 boost controller. MPP voltage set directly through MCP4921 DAC. Includes overload protection and auto ranging between 4 mA and 40 mA range, with digital outputs for range indication and sampling suspension (I and J). Waveforms for schmitt trigger, integrator, pulse extender and comparator are shown in the lower right corner.

Switching from 2.048 V maximum MPP to 4.096 V maximum MPP simplifies the reference generation, since the AD7689 has an integrated 4.096 V precision reference that can be activated in its configuration. This functionality is implemented in the driver software, discussed in section B.2. The MCP1501 generating the 2.048 V precision reference can therefore be omitted. Unfortunately, setting the MPPC of the LTC3105 to its maximum of 4.096 V would require a digital potentiometer with a value of ca. 350 kΩ, which are expensive and difficult to source. Instead, it was decided to generate the MPPC input voltage directly with a DAC rather than using the integrated 10 μA current source of the LTC3105. The Microchip MCP4921 (IC2 in figure 7.25) is ideal for this purpose, with a 12 bit resolution and rail-to-rail output. Its reference is the 4.096 V reference output generated by the AD7689, which is fed into its VREF input. The configuration of the ADC is set at start-up, or whenever the connected PV cell is changed. Since $2^{12} = 4096$, the accuracy of voltage MPPC configuration is exactly 1 mV. When the board resets, the MCP4921 will also reset, causing the VOUT output to become high impedant, which may result in an MPPC above 4.096 V due to the integrated current source of the LTC3105 on the MPPC pin. R3 is added to keep the MPPC at a single cell when IC2 is disabled or held in reset. The alternative approach to generate a high accuracy reference from the microcontroller, would be to filter a high frequency PWM signal with a 2nd order Sallen-Key filter or similar, as discussed in [351]. However, such an approach would not be simpler nor cheaper, since more passive components are required. More importantly, it also requires a continuous high frequency square wave to be fed into the data acquisition part of the circuit, crossing over from the DGND plane to the AGND plane. This would create a large current return loop, and a significant amount of noise from harmonics. This problem can be avoided by using the MCP4921 which has integrated buffers, and only needs to be configured once. In case the output voltage of the LTC3105 would exceed 4.2 V, zener diode D2 offers protection to the downstream circuitry by clamping the output to 4.2 V.

Automatic Ranging Extending the input voltage range broadens compatibility with a wider variety of different cell types, but the maximum measurable power at a MPP voltage of 4.096 V remains only 17 mW due to the 1 kΩ shunt resistor being used in the current measurement section of the self adjusting precision load. When driven into saturation, the impedance of MOSFET T1 will be negligible compared to the 1 kΩ shunt, and the current will therefore top off at 4 mA. To allow measurements of more powerful cells, it is necessary to devise a solution that allows dynamic setting of shunt resistors. The auto ranging circuit in figure 7.25 was developed for this purpose. It allows the analog front-end to switch from a 1 kΩ shunt resistor to a 100 Ω (equivalent) shunt resistor in real time, and the circuit reports the state as well as switching dead time to the microcontroller to scale measurements accordingly. To adjust the shunt resistor from 1 kΩ (R8) to 100 Ω, a second resistor (R9) is switched in parallel using N-channel MOSFET T2. The required resistor value can be calculated with

$$R_s = 100\,\Omega = \frac{R_8(R_9 + R_{DS(ON)})}{R_8 + R_9 + R_{DS(ON)}} \tag{7.33}$$

Substituting 1 kΩ for R8 and 3.2 Ω for $R_{DS(ON)}$, then solving for R9 yields a value of 108 Ω. $R_{DS(ON)}$ is not a negligible parameter, omitting it results in a calculated resistor value of 111 Ω, corresponding to an error of 2.7 %. When swapping T2 for another type of N-MOSFET, the corresponding value for R9 needs to be recalculated carefully. Resistors with a tolerance of 1 % or better need to be selected for R8 and R9 to achieve adequate measurement accuracy. The voltage over the shunt resistor(s) is buffered by IC5A and sent off to the ADC. IC4B serves as overload protection, comparing the shunt resistor voltage with the 4.096 V ADC reference voltage. If the shunt voltage exceeds 4.096 V, the output of IC4B pulls the reference pin of IC4A up to 5 V, thereby throttling back conductivity of T1, closing the negative feedback loop. This mechanism prevents overloading of the ADC input. This safety only works as long

as the LTC3105 output is below 5 V, which is ensured by clamping diode D2.

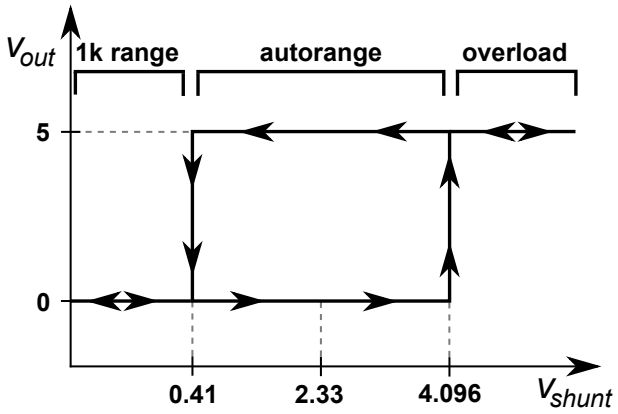

Figure 7.26: Hysteresis mechanism switching between 1 kΩ and 100 Ω shunt resistor.

The shunt configuration, set by either turning on or off T2, is controlled directly by opamp IC5B, which employs a mechanism of both positive and negative feedback to achieve stable regulation. The primary control loop, with a set point determined by R12 and R13, makes use of positive feedback to set trip points of the comparator: when point G reaches 4.096 V (saturation at 4 mA range), the 40 mA range is enabled by turning on T2, and point G drops to 0.4 V accordingly. A stable state is maintained until point G drops below 0.4 V, in which case the 40 mA range is reverted to 4 mA range by turning off T2, and point G jumps to a value between 0.4 V and 4.096 V again. The hysteresis mechanism is shown in figure 7.26. With flip points 0.4 V and 4.096 V, the characteristic equations for IC5B become

$$\begin{aligned} V_x &= 4.096\frac{R_{13}}{R_{12}+R_{13}} \\ V_x &= 0.4 + \frac{R_{12}}{R_{12}+R_{13}}\,(5-0.4) \end{aligned} \tag{7.34}$$

Choosing R12 = 10 kΩ and solving for V_x and R13 results in values $V_x = 2.33$ V and R13 = 1.389 kΩ. An inverting schmitt trigger configuration is required, because the same equation system for a non inverting schmitt trigger results in imaginary values:

$$\begin{aligned} V_x\frac{R_{13}}{R_{12}+R_{13}} &= 4.096 \\ V_x + (5-V_x)\,\frac{R_{12}}{R_{12}+R_{13}} &= 0.4 \end{aligned} \tag{7.35}$$

With 2.33 V as set point and 4.096 V and 0.4 V as flip points, the output of IC5B (point H) toggles between 0 and 5 V, thereby turning on or off T2. The current state of the shunt is also communicated to the microcontroller through point I, with a logic high indicating 40 mA enabled, and logic low representing 4 mA range active. Since IC5B is rail-to-rail, its output level of 0 - 5 V needs to be scaled down to 0 - 3.3 V to prevent MCU internal clamping diodes from conducting. The LTC6088 may source and sink up to 35 mA of current, which is enough to severely damage or destroy the MCU in case of overload.

When the output current of the LTC3105 at MPP is around 4 mA, the autoranging mechanism built up around IC5B is prone to oscillation due to the ringing effect on the shunts, fed through to point

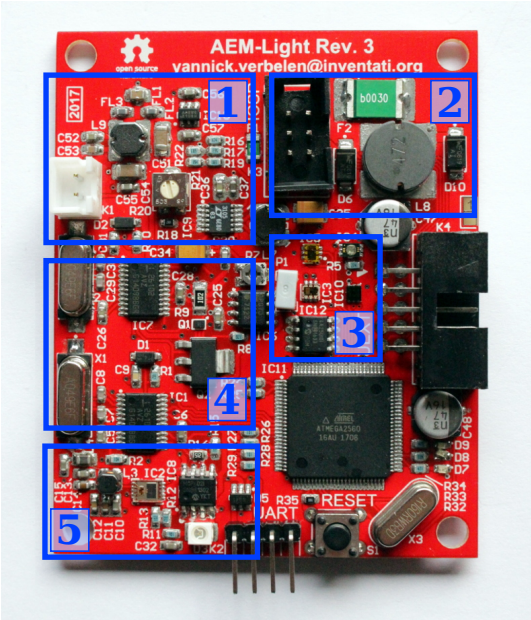

Figure 7.27: Rev. 3.0 of the AEM Light prototype. ① light energy harvester with LTC3105 MPPCT, ② power supply and ESD protection, ③ TCS3472, VEML6070, TSL25911, and MAX44009, ④ analog front-end with precision electronic load, ⑤ GUVA-S12SD with amplifier and ADPD2212.

G by buffer IC5A. To prevent this, negative feedback was added to the Schmitt trigger configuration around IC5B by modifying the set point dynamically instead of fixing it to 2.33 V. Resistor divider R6/R7 derives the previously calculated 2.33 V set point from the 4.096 V reference generated by the AD7689, which is then buffered by IC4C (point F). Using feedback resistor R11, a swing on the inverting input of IC5B is achieved:

$$\begin{aligned} V_1 &= V_F \frac{R_{11}}{R_{11} + R_{10}} \approx 2.23\,\mathrm{V} \\ V_2 &= (5 - V_F) \frac{R_{10}}{R_{10} + R_{11}} + V_F \approx 2.44\,\mathrm{V} \end{aligned} \tag{7.36}$$

Although undesirable oscillations are eliminated, the ringing effect when switching on or off T2 remains. Measurements made at this point will be inaccurate, and should be discarded. To notify the microcontroller when the shunt value has been switched, and thus samples need to be dropped, a secondary control signal is being generated by the right side of the circuit in figure 7.25. The waveforms at the respective points H, R, S and J are shown in the lower right corner. In the first stage, built up as a differentiator around IC5C, transitions on the Schmitt trigger output (point H) are detected and converted into a pulse train (point R). A 2.5 V bias (resistor divider R17/R18) is added to allow both rising and falling edges to be processed. Negative pulses are inverted by IC5D (built up as inverting buffer with R19 and R21), and together with the positive pulses fed into a pulse extender (point S). D4 and D6 act as a logic OR for positive and inverted negative pulses. The length of the pulses is determined by the time constant R20/C14, and should be dimensioned appropriately for the severeness of the ringing effect. In the configuration shown in figure 7.25, a conservative figure of ca. 22 μs ensures no switching noise is included in the valid data. Since light intensity normally only changes slowly, unlike vibrations, 22 μs lost samples are deemed acceptable. From the pulse extender, D5 subtracts the 2.5 V bias voltage again, feeding the difference

into buffer IC6, which converts it into a square wave (point J). With also IC6 powered by the 5 V rail, a second but identical voltage divider R22/R23 is necessary to scale the output signal from 5 V to 3.3 V.

Temperature Compensation Since PV cells exhibit a temperature drift, as all semiconductor materials do, the maximum power point also drifts with changing temperature. The solution suggested by LTC3105 manufacturer Linear Technology, is generating the MPPC input signal by connecting a series of forward biased diodes from the MPPC pin to ground, with as many diodes as there are junctions in series in the PV cell. The 10 μA current source of the LTC3105 ensures the diodes remain forward biased, and if they are thermally coupled to the PV cell (i.e. mounted to the back panel with thermal paste and an appropriate clamping technique), the MPPC input voltage reflecting the maximum power point voltage will more closely approach the actual MPP voltage under varying temperature conditions. However, because the presented design is intended to be compatible with cells of different chemistry (m-Si, p-Si, a-Si, CIGS, DSSC, CdTe, ...) and varying stacks of cells, it is cumbersome to use this approach. The additional complexity caused by the installation requirements of thermally coupled diodes means that they are typically omitted in low power PV application for energy harvesting, and the MPPC input is then set to a constant voltage. An alternative proposed solution is to use the ambient temperature to correct the MPP voltage drift in software, then update the DAC accordingly. The AD7689 includes an integrated temperature sensor specifically for temperature drift compensation, and reading out this sensor is already supported by the driver for the AD7689 developed for the AEM project, and discussed in section B. However, this compensation method is not yet experimentally verified on AEM Light Rev. 3.

Dynamic Power Point Tracking

As concluded from the comparison made in table 7.4, the SPV1040 from ST Microelectronics is the only true dynamic power point tracker, using a separate control loop for voltage and current in a perturb & observe mechanism. The device has 3 modes of operation (soft-start, start-up and MPPT), but only the MPPT mode is used for the purpose of benchmarking energy harvesters, the others only relevant when using the SPV1040 to charge a battery directly. When the SPV1040 starts up, it will immediately enter MPPT mode to search for the MPP. The perturb and observe algorithm either monitors the current supplied by the PV cell so that the PWM signal duty cycle is increased or decreased step-by-step according to the input power trend. In the implemented configuration, shown in figure 7.28, both constant current regulation and constant voltage regulation are used. Shunt resistor R1 = 10 mΩ is used to measure the current, and determines the current regulation set-point. R2, R3 and C3 form a bipolar low pass filter to reduce switching noise from the current regulation feedback loop. The values for these passives are obtained from the ST Microelectronics reference design. The constant voltage regulation loop is controlled by the VCTRL input, and used to regulate the output voltage after the shunt resistor to the desired value, in this case 4.096 V. The internal bandgap reference is 1.25 V, which allows calculation of the feedback voltage divider R4/R5. The precision electronic load circuit is shared between the LTC3105 and SPV1040, as shown in figure 7.19. The divider marker between R1 and D2 in figure 7.25 indicates the divisor: all components to the right of it are shared between LTC3105 and SPV1040.

Overload Protection

For PV panels with $V_{MPP} \leq 4\,\text{V}$ but $V_{OC} > 4.3\,\text{V}$, it is possible that the bypass diode over the LTC3105/SPV1040 will conduct if the MPP is not being tracked. For panels with a considerable output power, this could cause damage to the FSA2467, switching input between LTC3105 and SPV1040, and also potentially overload shunt resistors and/or electronic load zener diode. It is therefore desirable to

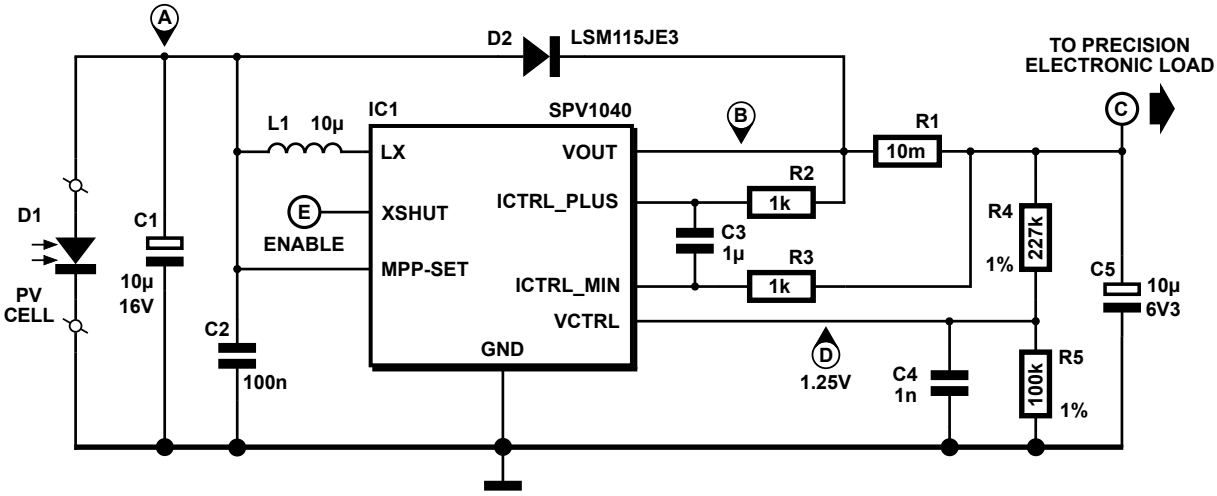

Figure 7.28: PV energy harvesting circuit with true maximum power point tracking (perturb and observe), implemented with an SPV1040 DC/DC converter.

disconnect the solar panel if the maximum voltage is exceeded. A solution is presented in figure 7.29.

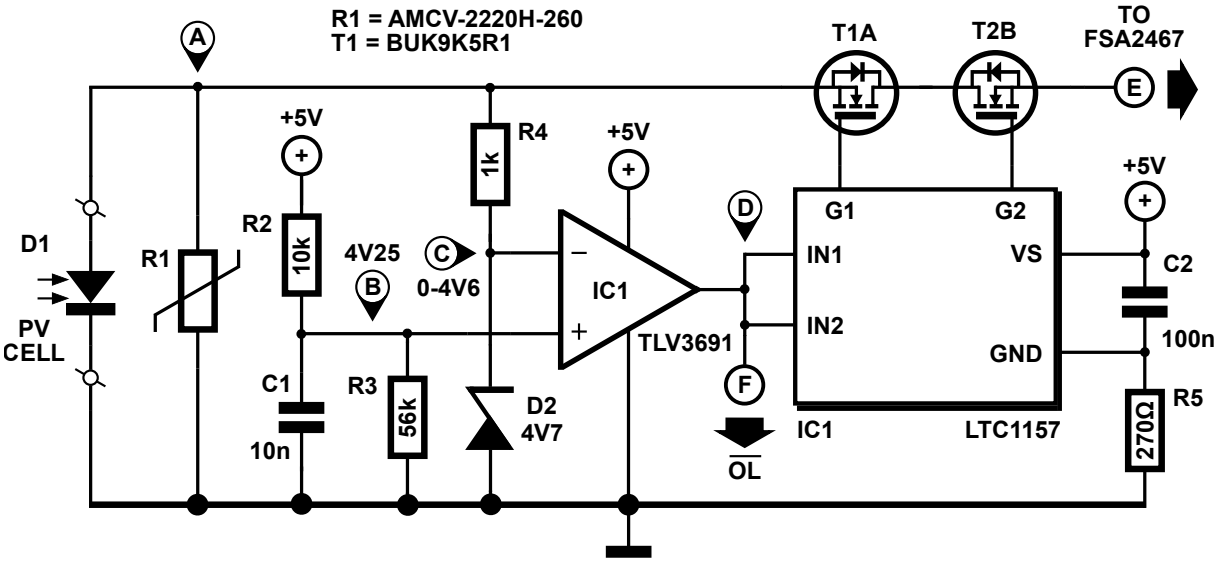

Figure 7.29: Active overload protection with bidirectional N-MOSFET switch, disconnecting DUT above 4.3 V.

The overload protection circuit consists of an active dual N-channel MOSFET acting as a bidirectional switch. The BUK9K5R1 is a matched MOSFET pair in a single package, with $V_{DS(max)} = 30\,\mathrm{V}$ and $I_{DS(max)} = 40\,\mathrm{A}$. When turned on, at $V_{GS} \geq 5\,\mathrm{V}$, the channel resistance is maximum 5.3 mΩ, totaling 10.6 mΩ additional parasitic resistance to be accounted for. With connected drains, the body diodes are in opposition and cannot conduct. The only failure mode exists under conditions where $V_{OC} \geq 30\,\mathrm{V}$, risking a flashover between drain and source. To eliminate this condition, varistor R1 clamps the input voltage to ca. 26 V. This MOV can dissipate a maximum of 7.8 J, but aside from 2 cells in table 7.5, no commercial solar cells or assemblies get close to the breakdown voltage of 26 V, and the

protection is deemed adequate. Since N-MOSFETs require a positive V_{GS} to turn on, for the BUK9K5R1 $V_{GS(th)} \approx 2.45$ V, the gate voltage of T1A and T1B need to be driven above the maximum V_{MPP} allowed by the signal path, which is 4 V. A dual MOSFET driver with integrated voltage multiplier was chosen for reasons of design simplicity. The LTC1157 fits the purprose adequately, doubling the power rail of 5 V internally to 10 V to drive the gates, leaving a generous margin of ca. 3.5 V to accomodate for manfacturing deviations. Both MOSFETs can be controlled individually, but in this application they are tied together and controlled by a single comparator of type TLV3691. The inputs IN1 and IN2 are CMOS compatible, with inputs ranging between 0 and VS, in this case 5 V. Comparator IC1 is used in a classic overload detection topology, comparing a constant maximum voltage reference of 4.25 V generated by voltage divider R2/R3 to the output voltage of the PV cell. As long as the PV cell voltage is lower than 4.25 V (4.096 V + bypass diode voltage drop), then the output of IC1 will be a logic high, instructing IC2 to turn on the MOSFETs. However, if the PV cell output exceeds 4.3 V then the output toggles and the MOSFETs are disabled, effectively disconnecting the PV cell from the analog switch input of the FSA2467. R1 acts as a voltage limiter in this configuration, since the PV cell is now unloaded, and the voltage on the terminals will rise to V_{OC}. To prevent latchup in IC1, the input voltage is clamped to ca. 4.7 V by zener diode D2, with R4 limiting the current through D2 under these conditions. A digital control signal is being generated (point F), notifying the microcontroller of the overload situation.

7.8 Thermal Module

The module for characterization of potential heat or cold sources for energy harvesting purposes, AEM Thermal, is arguably the simplest of the 4 AEM sensor/harvester modules documented in this chapter because a heat or cold source is only one-dimensional: a scalar temperature varying in time relative to the ambient temperature. The ambient air temperature will function as a reference, acting as a heat sink or cold sink to maintain a temperature difference over a TEG. AEM Thermal thus consists of 3 blocks: ambient air temperature measurement for reference, a displaceable thermocouple for measuring the temperature of an active surface, and a boost converter for TEG energy harvesting itself. The block diagram

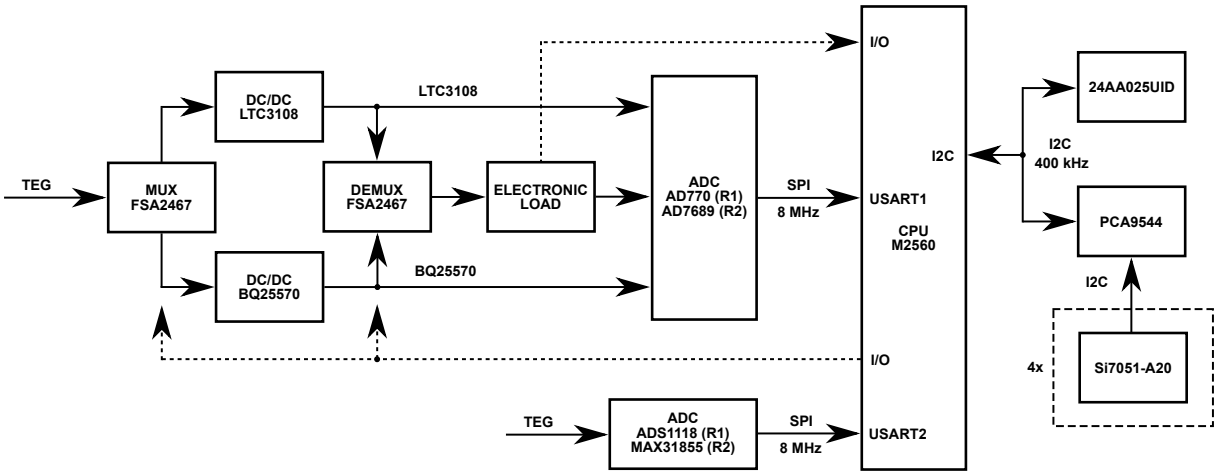

Figure 7.30: Block diagram of Revision 1 (R1) and Revision 2 (R2) of AEM Thermal. On Revision 2, only the LTC3108 signal path is implemented, and the analog switches were omitted. Component selection differences between both revisions are marked where relevant.

for AEM Thermal is shown in figure 7.30 for the 2 revisions of the module. The first revision R1 only supports LTC3108 as harvester, with an Analog Devices AD7705 as analog front-end for energy harvesting. A separate ADC with 18 bits resolution, the ADS1118, is used for the thermocouple specificially. In revision R2, the primary ADC was swapped for an AD7689 to streamline code development and unify the analog front end across all AEM modules. It was also chosen to replace general purpose ADC ADS1118 with a specific thermocouple front end from Maxim, the MAX31855. The design is discussed below.

7.8.1 Ambient Temperature

To measure ambient temperature, which will act as the cold side reference for a heat source or a hot side reference for a cold source, PCB mounted temperature sensors can be used since the AEM Thermal module itself is assumed to be at the ambient temperature, corresponding to the temperature an application is intended to be deployed in. Measuring directly on a heat sink is not representative for generalized thermal energy harvesting conditions, since size of the harvester (and heat sink), as well as any air flow, could influence the thermal conditions of the heat sink itself. However, measurement of ambient conditions is desired to be independent from any harvester or heat sink selection, instead presenting the actual temperature difference between hot or cold source and the ambient environment, thus corresponding to the maximum temperature gradient energy can be harvested from. To select the best temperature sensors for measuring the ambient air temperature, sensors with an accuracy of $\pm 2\,\mathrm{K}$ or better in a temperature range between -40°C and 85°C were compared in table 7.6. For the sensors with an integrated ADC and

digital output, a resolution of 11 to 16 bits is the most common, although actual accuracy greatly differs because of variations in manufacturing processes, calibration, and temperature drift. With additional factors as solderability for prototyping and cost in consideration, the choice was made for the Si7051, with a resolution of 14 bits and accuracy of $\pm 0.25\,\mathrm{K}$ over its temperature range. The 6 pin DFN package has an exposed ground pad for thermal coupling to the PCB, resulting in less skittish temperature measurements. The choice for a Silicon Labs sensor was partially supported by the previous experience with the Si1145 during AEM Light development. To further increase the accuracy of ambient air temperature measurement, and eliminate local hot spots or directionality, 4 separate Si7051 devices were mounted in the 4 corners of the PCB, as far apart as possible, resulting in 4 independent measurements $s_1 ... s_4$. To estimate the error of the average measurement, $\delta\overline{s}$, the average is statistically calculated as follows:

$$\frac{\delta\overline{s}}{\overline{s}} = \left(\frac{\delta(s_1 + ... + s_4)}{s_1 + ... + s_4} + \frac{\delta N}{N} \right) \tag{7.37}$$

with $\delta N = 0$:

$$\delta\overline{s} = \frac{1}{N} \sum_{i=1}^{N} \delta s_i \tag{7.38}$$

Since $\delta\overline{s}$ converges to $\frac{\overline{s}}{\sqrt{N}}$ for $N >> 1$, it can thus be concluded that for a sample size of $N = 4$, the error is $0.25\,\mathrm{K} \geq \Delta\overline{s} \geq 0.13\,\mathrm{K}$. To interface the 4 identical Si7051 devices through I^2C, a bus multiplexer of type PCA9544 functions as the controller, as shown in figure 7.30. Although the I^2C bus supports a maximum of 127 simultaneously connected devices due to its 7 bits addressing scheme, the Si7051s have identical addresses, which prevent them from being addressed individually. The PCA9544 solves this issue by multiplexing the SDA and SCL lines of the I^2C bus to each of the 4 Si7051s. The PCA9544 itself also acts as a device on the I^2C, and the multiplexer functionality can be controlled through I^2C. The address of the Si7051 is 0x40. The PCA9544 supports external configuration of 3 of its 7 address bits, allowing selection of any address in the range between 0xE0 and 0xE7. Since the I^2C bus is shared with the 24AA025UID GUID EEPROM, with address 0x28, there are no address conflicts in this configuration. To cycle through the sensors, the MCU keeps track of an internal counter cnt ranging

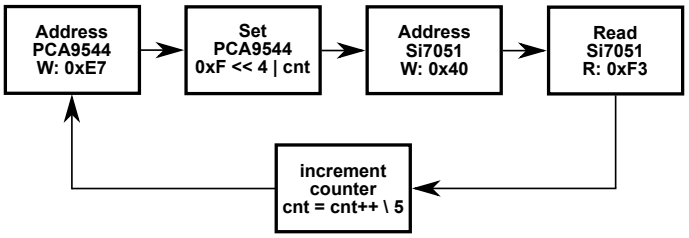

Figure 7.31: Sequence to retrieve ambient air temperature data from 4 Si7051 I^2C temperature sensors.

from 1 to 4, as shown in figure 7.31. The PCA9544 8 bit control register sets the selected channel with the 3 LSB, with 4 MSB reserved for interrupts. In this application, the interrupt functionality of the PCA9544 is not used since the Si7051 does not support interrupt outputs. After setting the channel, the Si7051 is addressed and its temperature value is read out from register 0xF3. At start-up, the MCU cycles through each Si7051 as well for a reset though register 0xFE.

7.8.2 Thermocouple

A distinction must be made between the maximum temperature gradient to which a TEG may be exposed, and the maximum absolute temperature. The latter is bounded by the temperature of physical deformation (lower than the melting temperature) of the semiconductor material the TEG is composed of on the high side. There is no hard limit on the low side, although semiconductors self-evidently lose their properties approaching the absolute zero. For example, for a TEC1-12706, the maximum specified operating temperature is 138°C, while the melting temperatures of its constituents, Te and Bi, are respectively 450°C and 272°C. To measure temperatures in the range between industrial cryogenic conditions (ca. -200°C) to ca. 140°C, several thermocouple types are available. The materials used for the junctions is a determining factor for the temperature range and the sensitivity. A comparison of common thermocouple types is made in table 7.7. The higher the sensitivity, the better the accuracy of temperature measurement, particularly when temperature variations are small. With the exception of type S and R, all thermocouples generously comply with the operating conditions for TEGs in typical industrial or domestic environments. Of the remaining types, types E, J and T have the highest sensitivity, but unfortunately, types E and T are not widely used and therefore expensive. The choice for a commonly commercially available type J thermocouple was made as a result. The 79696030 from Crouzet has the added advantage of being equipped with a bolt ring, enabling easy mounting on a hot or cold surface.

ADS1118

The initial design for AEM Thermal was intended to support two remote temperature measurement points, one for the hot side of the TEG and a second one for the cold side. For this purpose, the ADS1118 was selected as the best suited analog front end. The ADS1118 from Texas Instruments is a 4 channel ADC with integrated PGA and reference temperature sensor, designed to interface 2 type K thermocouples with minimal external parts. The measurement is differential, with the hot side thermocouple connected to channels AIN0 and AIN1, and the cold side thermocouple connected to channels AIN2 and AIN3. The circuit for one thermocouple is shown in figure 7.32.

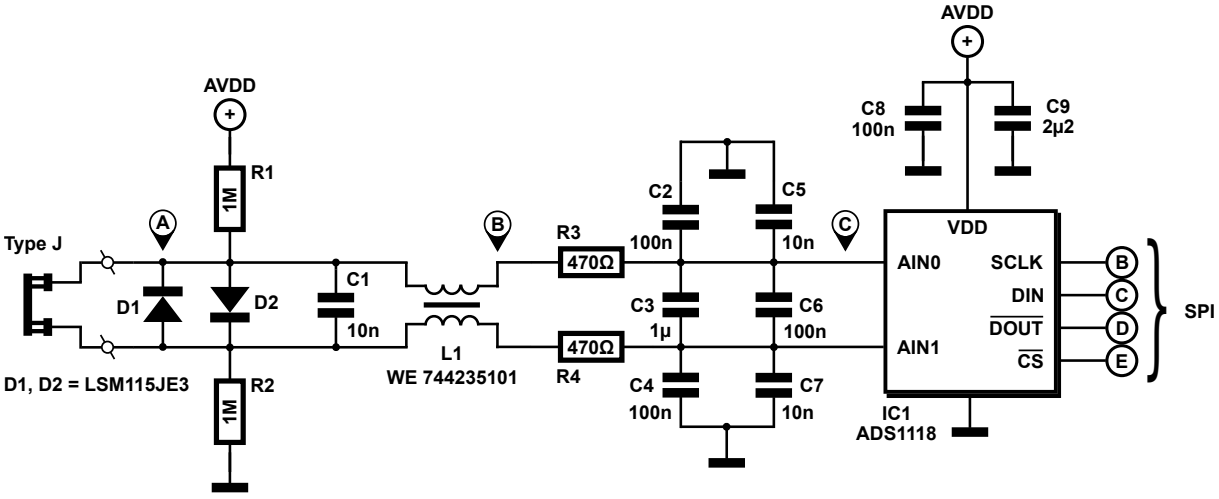

Figure 7.32: Block diagram of Revision 2 (R2) and Revision 3 (R3) of AEM Thermal. On Revision 2, only the LTC3108 signal path is implemented, and the analog switches were omitted. Component selection differences between both revisions are marked where relevant.

Diodes D1 and D2 serve as input protection, clamping the voltage over the thermocouple to $\pm 250\,\mathrm{mV}$ to prevent damage to the ADC. Resistors R1 and R2, with a value of $1\,\mathrm{M}\Omega$ each, serve a dual purpose. Most importantly, they set the bias voltage for the thermocouple at AVDD/2, ensuring both channel inputs are within range. A secondary function is failure mode detection: if the thermocouple junction fails, AIN0 will be pulled up to AVDD and AIN0 pulled down to AGND, an input range that is impossible under normal operation. For noise suppression, the ADS1118 includes a digital filter to attenuate high-frequency noise components, but passive filtering is required for low-frequency noise. The differential LC filter is formed by L1, C3 and C6. At low frequencies, the impedance of common mode choke L1 is too low to provide active filtering, and series resistors R3 and R4 were added for this purpose. The cut-off frequency for the differential mode filter at low frequencies is

$$f_c = \frac{1}{2\pi\,(R_3 + R_4)\,(C_3 + C_6)} \tag{7.39}$$

Capacitors C2, C5, C4 and C7 provide common mode filtering in combination with resistors R3 and R4. Following the rule of thumb, C3 + C6 was chosen a factor 10 higher than C2/C5 and C4/C7 respectively, since mismatches in the common mode capacitors can convert common mode noise into differential mode noise. The characteristics of the filter were obtained through SPICE simulation, using common mode choke model provided by Würth Elektronik. The noise attenuation is shown in figure 7.33.

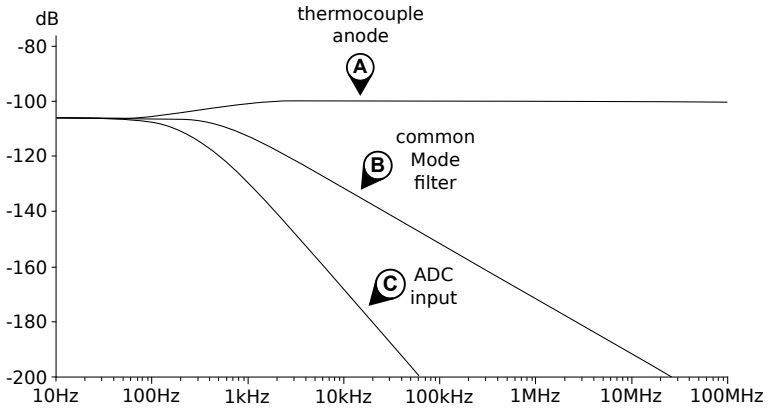

Figure 7.33: Common mode noise attenuation by second order RLC filtering. Points A, B and C refer to nodes in figure 7.32.

MAX31855

With Si7051 temperature sensors available to measure the reference side, i.e. the ambient air temperature, the dual thermocouple approach with an ADS1118 requires unnecessary processing to calibrate the temperature measurements and reference the cold side junction temperature. For measurement of a single thermocouple, the MAX31855 is better suited because it integrates the required amenities for thermocouples of type K and J, without additional computation efforts by the microcontroller. It also supports type J thermocouples, which offer a performance superior over type K in this application. The MAX31855 front-end implements the necessary common and differential mode filtering, simplifying the external filtering circuitry in comparison to the ADS1118. For an experimental validation of the MAX31855 approach to measuring thermocouple characteristics, the circuit in figure 7.34 was implemented and tested in an unrelated open source project [256].

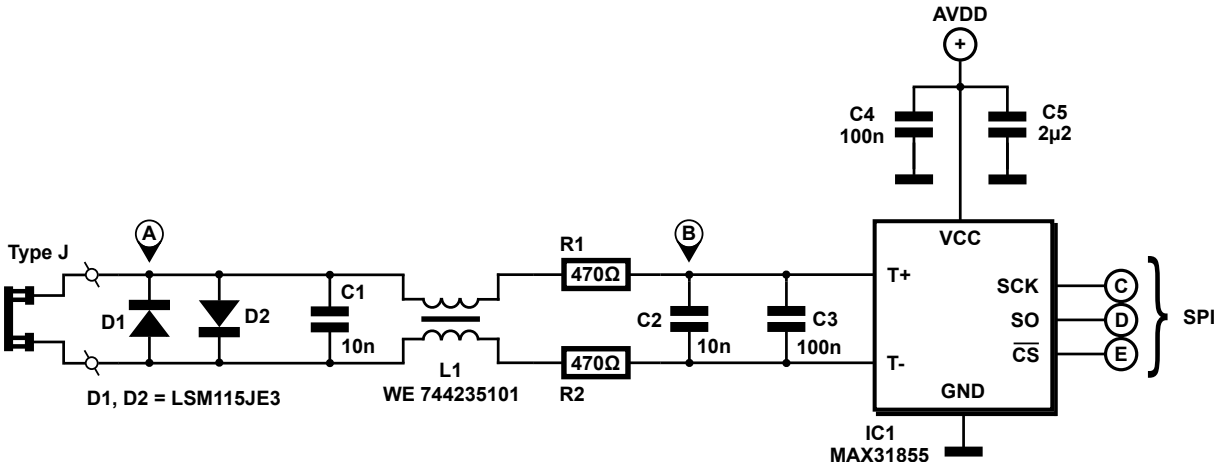

Figure 7.34: Block diagram of Revision 2 (R2) and Revision 3 (R3) of AEM Thermal. On Revision 2, only the LTC3108 signal path is implemented, and the analog switches were omitted. Component selection differences between both revisions are marked where relevant.

A comparison was made between the two implementations, with an infrared thermometer of type ANENG GM550 (-50°C - 0°C: ±3 %, 0°C - 550°C: ±1.5 %) as reference. No statistically significant deviations could be measured, keeping in mind that the accuracy of the ANENG GM550 (±1.5 % - ±3 % depending on temperature range) lowers the confidence interval of measurements.

The accuracy of the Si7051 is specified as ±0.1°C within the -40°C - 125°C temperature range. The accuracy of the MAX31855 is ±2°C over the temperature range between -200°C to 700°C, realistic usage intervals for AEM Thermal. Assuming the 4 Si7051 temperature sensors are normally distributed, and applying the t-distribution to estimate the error, the total error on the temperature gradient calculation can be found:

$$T_{grad} = \Delta T = \sqrt{(T_{TC} - T_{ambient})^2} \tag{7.40}$$

For 4 independent Si7051 sensors, the error estimation on T_{grad} is

$$\eta_{grad} = \frac{\pm 0.1^{\circ}\mathrm{C}}{\sqrt{n}} + (\pm 2^{\circ}\mathrm{C})) = \frac{0.1}{2} + 2 = 2.05^{\circ}\mathrm{C} \tag{7.41}$$

An important consequence of this error is that measurement of small temperature gradients have a low confidence interval, as shown in figure 7.35. For temperature gradients of 5 K, the error on the measurement varies between 41 % for the Si7051 up to 50 % for the Si7050. Only for temperature gradients above 20 K does the relative measurement error drop below 10 %. Hence, for small temperature gradients, care should be taken when interpreting the measurements.

Given the temperature variations to which AEM Thermal is expected to be exposed, thermal noise (Johnson-Nyquist noise) will elevate the noise floor as temperature increases. Without filter capacitors, the signal fed into the ADC for figure 7.34 equals

$$v_{in} = v_t h + \sqrt{4 k_B T R} \tag{7.42}$$

where k_B is the Boltzmann constant: $1.38065 \cdot 10^{-23}$ J/K. Taking the DC resistance of the common mode choke into account, $R_F = 2.0\,\Omega$, the thermal noise equals

$$v_{RMS}^2 = 4 \cdot 1.38065 \cdot 10^{-23} \cdot \Delta T \cdot (470 + 2.0) \tag{7.43}$$

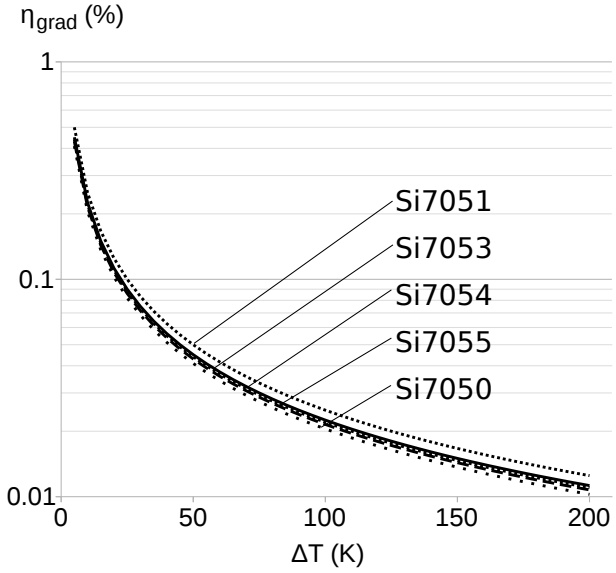

Figure 7.35: Comparison of different Si705X series temperature sensors and their effect on the measurement error of a temperature gradient, in combination with the MAX31855.

Which in the temperature range between -40°C and 160°C corresponds to $2.47 \cdot 10^{-9} < v_{RMS} < 3.36 \cdot 10^{-9}$. With thermocouple output voltages in the order of μV, this means the error caused by thermal noise is in the order of 0.1 %. With filtering capacitors, the noise can be reduced since the DC resistance and 470 Ω series resistors act as a bipolar low pass filter in combination with capacitors C2 and C3. The generated thermal noise is thus reduced following

$$v_{RMS}^2 = k_B \Delta T \left[\frac{1}{10^{-8}} + \frac{1}{10^{-8} + 10^{-7}} \right] \tag{7.44}$$

In the same temperature range, the thermal noise is thus reduced to $3.51 \cdot 10^{-13} < v_{RMS} < 6.52 \cdot 10^{-13}$. This is 6 orders of magnitude below the expected input signal level, and therefore adequate.

7.8.3 Thermal Energy Harvester

For a full scale range between 0 and 2.048 V, the AD7705 ADC was chosen with the same motivation as its inclusion on AEM Vibrations. However, as TEG output voltages are in the order of μV for temperature gradients below 10°C (particularly for TEGs with less than 127 elements in series), the input offset voltage of 10 mV with a drift of 0.5μV/°C prevents it from accurately measuring conditions close to idle state. Since an unquantifyable error caused by an input offset will lead to large errors in efficiency calculations, it is essential that small signals can also be accounted for. One solution to the problem, functionally similar to the switching system used to divert inputs and outputs between different harvesters using the FSA2467, is the insertion of a low offset preamplifier with overload capabilities in a parallel signal path to the ADC. The already included in the BOM low noise, low input offset opamp LTC6088 is well suited for this purpose, with an input offset voltage below 750 μV and a dirft below 5 μV/°C. However, with a gain of 10 - 15 dB, the amplified signal path overloads at temperature gradients typically present for thermal energy harvesting, thus requiring extensive output clamping. The secondary signal to tha ADC input halves the effective data rate, and the discontinuity in singal path requires more complex logic in the MCU. This approach was therefore discarded in favor of a continuous solution, by lowering the absolute reference of the ADC by pulling it below ground level, as shown in figure 7.36.

Table 7.6: Comparison of commercial temperature sensors for ambient air temperature measurement, with an accuracy of ±2 K or better, and temperature range between -40°C and 85°C.

Sensor	Manufacturer	Interface	Resolution	Accuracy	Package
MCP9808	Microchip	I^2C	10 bits	±1 K	8-MSOP
TMP112	TI	I^2C	11 bits	±1 K	6-SOT
TMP275	TI	SMBus	11 bits	±1.5 K	8-VSSOP
LMT70	TI	analog	5.194 mV/K	±0.36 K	4-DSBGA
MAX31725	Maxim	I^2C	15 bits	±0.7 K	8-TDFN
MAX31723	Maxim	SPI	11 bits	±2 K	8-uMax
DS7505	Maxim	I^2C	11 bits	±2 K	8-uMax
LM92	TI	I^2C	12 bits	±1.5 K	8-SOIC
Si7051	Silicon Labs	I^2C	14 bits	±0.25 K	6-DFN
Si7053	Silicon Labs	I^2C	14 bits	±0.3 K	6-DFN
DS18	Maxim	1-Wire	11 bits	±2 K	8-uMax
DS1631	Maxim	I^2C	11 bits	±2 K	8-uMax
DS600	Maxim	analog	6.45 mV/K	±0.75 K	8-uMax
DS28	Maxim	1-Wire	11 bits	±2 K	8-uMax
DS620	Maxim	I^2C	12 bits	±2 K	8-uMax
ADT7410	AD	I^2C	15 bits	±0.7 K	8-SOIC
ADT7310	AD	SPI	15 bits	±1 K	8-SOIC
N018	TE	I^2C	24 bits	±0.5 K	16-QFN
TMP20	TI	analog	11.77 mV/K	±2.5 K	SC-70-5
AS6200	AMS	I^2C	12 bits	±1 K	6-WLCSP
STS-31	Sensirion	I^2C	16 bits	±0.3 K	8-TDFN
MAX30205	Maxim	I^2C	16 bits	±0.5 K	8-TDFN
N003	TE	I^2C	16 bits	±1 K	8-TDFN
LM76	TI	I^2C	12 bits	±1 K	8-SOIC
STS-30	Sensirion	I^2C	16 bits	±0.3 K	8-TDFN
MAX6632	Maxim	SPI	12 bits	±0.8 K	6-TDFN
LM95234	TI	SMBus	10 bits	±0.2 K	14-WSON
STS21	Sensirion	I^2C	14 bits	±0.2 K	6-DFN
ADT7311	AD	SPI	16 bits	±1 K	8-SOIC
Si7055	Silicon Labs	I^2C	14 bits	±0.5 K	6-DFN
MCP9804	Microchip	I^2C	12 bits	±1 K	8-DFN
ADT7420	AD	I^2C	15 bits	±0.6 K	16-LFCSP

Table 7.7: Comparison of common thermocouples for high temperature ranges. Cold-junction sensitivity for range between 0°C and 70°C.

Type	Range (°C)	Sensitivity (μV/°C)	Cold-junction Sensitivity (μV/°C)
K	-270 - 1372	41.276 (0 - 1000°C)	40.73
J	-210 - 1200	57.953 (0 - 750°C)	52.136
N	-270 - 1300	36.256 (0 - 1000°C)	27.171
S	-50 - 1768	9.587 (0 - 1000°C)	6.181
T	-270 - 400	52.18 (0 - 400°C)	41.56
E	-270 - 1000	76.373 (0 - 1000°C)	44.123
R	-50 - 1768	10.506 (0 - 1000°C)	6.158

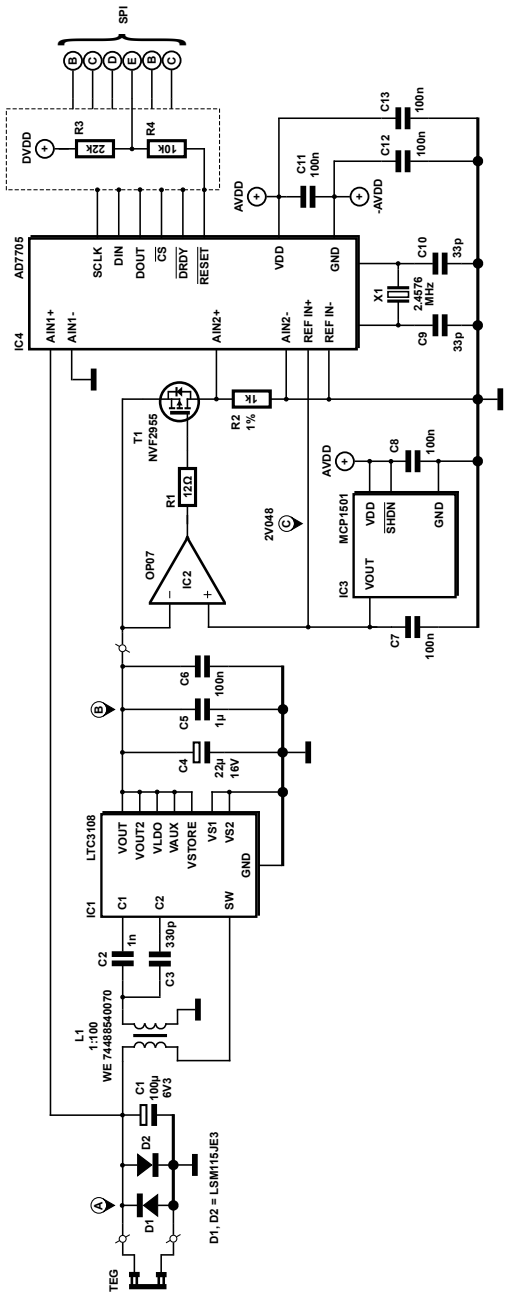

Figure 7.36: Analog front-end for TEG energy harvesting using the LTC3108 as ultra low input step-up converter. The negative bias for the AD7705 ADC is generated by a dedicated power supply, shown in figure 7.37.

In the presented configuration, the AD7705 has its negative reference input REF IN- tied to AGND, which is equal to the negative inputs of channel 1 (AIN1-) and channel 2 (AIN2-). The actual ground connection of the ADC is tied to a negative bias voltage, generated from DVDD with an inverting DC/DC converting with Cúk topology, shown in figure 7.37. This power supply circuit is essentially an inversion of the design in figure 61, but with a Cúk converter (IC1) instead of a boost converter, followed by a negative LDO (IC2) instead of a positive LDO. The Cúk converter is built around a TPS63700 from

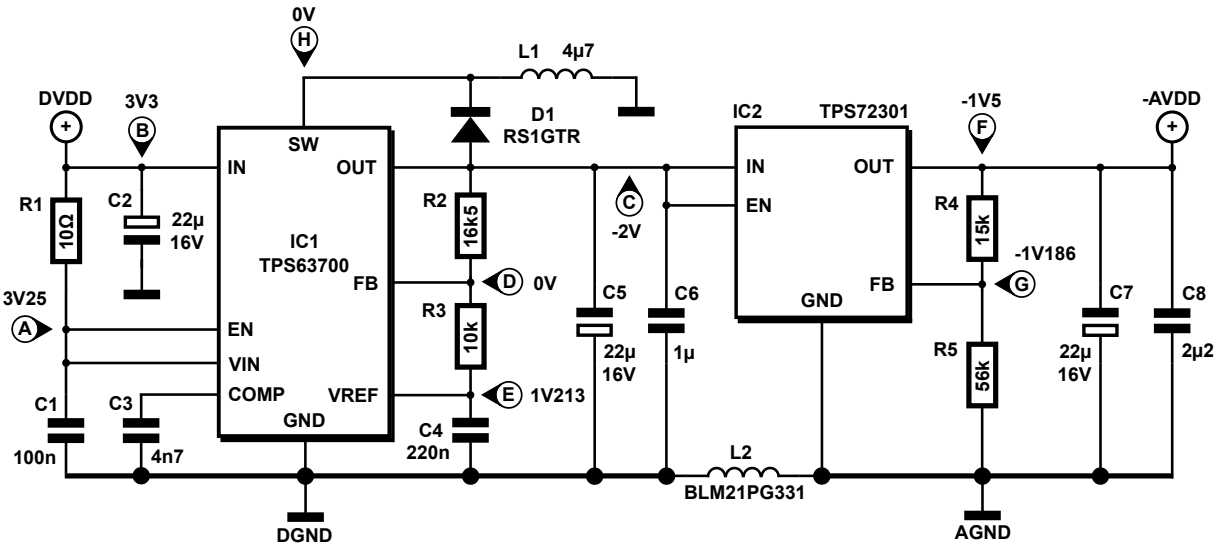

Figure 7.37: Generation of a -1.5 V negative offset bias for the AD7705 ADC, using a switched mode Cúk converter (IC1) followed by a linear regulator (IC2) for ripple removal.

Texas Instruments (IC1), with D1 as flyback diode and L1 as power inductor. The switching node H rests at ground level. The IC provides an internal bandgap reference voltage (point E) which can be used to set the output voltage directly. C4 provides filtering and C3 frequency compensation for the feedback mechanism. From VREF, a voltage divider to the output rail sets the feedback voltage to 0 (point D), from which the output resistor can be calculated with R3 = 10 kΩ as suggested by the manufacturer:

$$R_2 = R_3 \left[\frac{VREF - VOUT}{VREF} - 1 \right] = 10\,\mathrm{k\Omega} \left[\frac{1.213 - (-2.0)}{1.213} - 1 \right] \approx 16.5\,\mathrm{k\Omega} \tag{7.45}$$

The values of R2 and R3 do not need to low tolerance, since the switching stage is followed by a linear stage built up around IC2. The output voltage of IC1 (point C) will be ca. -2 V ±10 %, from which IC2 of type TPS72301 regulates down to -1.5 V. The reference voltage of IC2 is -1.186 V (point G), from which the output voltage can be set through the feedback input, choosing R4 = 15 kΩ:

$$V_{out} = VREF \cdot \left(1 + \frac{R_4}{R_5} \right) = -1.5\,V \Leftrightarrow R_5 = 56\,\mathrm{k\Omega} \tag{7.46}$$

The dropout voltage of the TPS72301 is around 280 mV at its maximum current of 200 mA, but in this application the maximum load is never reached. Under load of 100 mA and worst case temperature drift conditions, the dropout voltage is limited to 175 mV, which leaves a generous 125 mV for ripple elimination from the switching stage. L2 is a ferrite bead from Murata, designed to filter power lines, and used to tie analog and digital ground together to prevent switching noise from the Cúk stage from entering the analog part of the circuit. With a negative bias of -1.5 V and a reference of 2.048 V generated by the MCP1501 as shown in figure 7.36, the full range between 0 and 2.048 V becomes available. For

$\Sigma\Delta$ ADC AD7705 with resolution of 16 bits, the step size and error is a theoretical $\pm 31.25\,\mu$V. In Rev. 2, the AD7705 was swapped for the standardized AD7689, which eliminates the voltage offset problem in exchange for a higher BOM cost. This allowed the inverting power supply circuit to be dropped from Rev. 2 onwards.

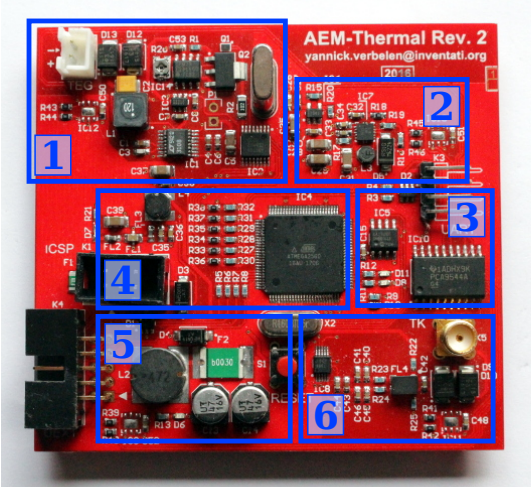

Figure 7.38: Rev. 2.0 of the AEM Thermal prototype. ① thermal energy harvester with LTC3108 step-up converter, ② voltage reference and negative bias supply ③ ambient temperature sensor controller, ④ digital processing, ⑤ digital power supply, ⑥ SMA connector for thermocouple, amplifier and ADC.

LTC3108

The LTC3108 from Linear Technology is a low voltage, switched mode step-up converter using a transformer and resonant LC tank at its secondary side. This strategy allows a cold start from 20 mV, which enables it to be used with small TEGs, or under small temperature gradients (for example, wearables extracting human body heat). The circuit is shown in figure 7.36. The cold terminal of the TEG is tied to ground, the hot terminal (point A) to the secondary side of the transformer. Diodes D1 and D2 provide clamping of the input voltage to prevent overloading the LTC3108 in the event of excessive input voltages, since the transformer's ratio is 1:100, resulting in a considerable gain even under conditions of low Q-factor. C2 and C3 form a resonant tank in combination with the secondary winding of L1. Practically, any transformer with a ratio 1:50 or higher can be used in this application, as long as the resonance frequency is around 100 kHz. WE and Coilcraft provide such transformers in a small form factor, the chosen type is no. 74488540070 by WE, with a footprint of 41 mm^2. LTC3108 comes in 2 variants, the LTC3108 and LTC3108-1. They are functionally identical, except for the preset output voltages that are configurable to the user. The possible output voltages for LTC3108 are 2.35 V, 3.3 V, 4.1 V and 5 V, while for LTC3108-1 they are 2.5 V, 3 V, 3.7 V and 4.5 V. Unlike other controllers in the family (e.g. LTC3105 or LTC3330) there is no voltage divider feedback as is customary with voltage regulators, but the output voltage is fixed and set through configuring 2 IO pins (VS1 and VS2). The intermediate voltage settings (4.1 V and 3.7 V) allow the LTC3108/-1 to charge resp. trickle charge Li-Ion/Polymer batteries directly, provided sufficient output power is available. An optional capacitor can be connected to VSTORE for local storage (for example an EDLC).

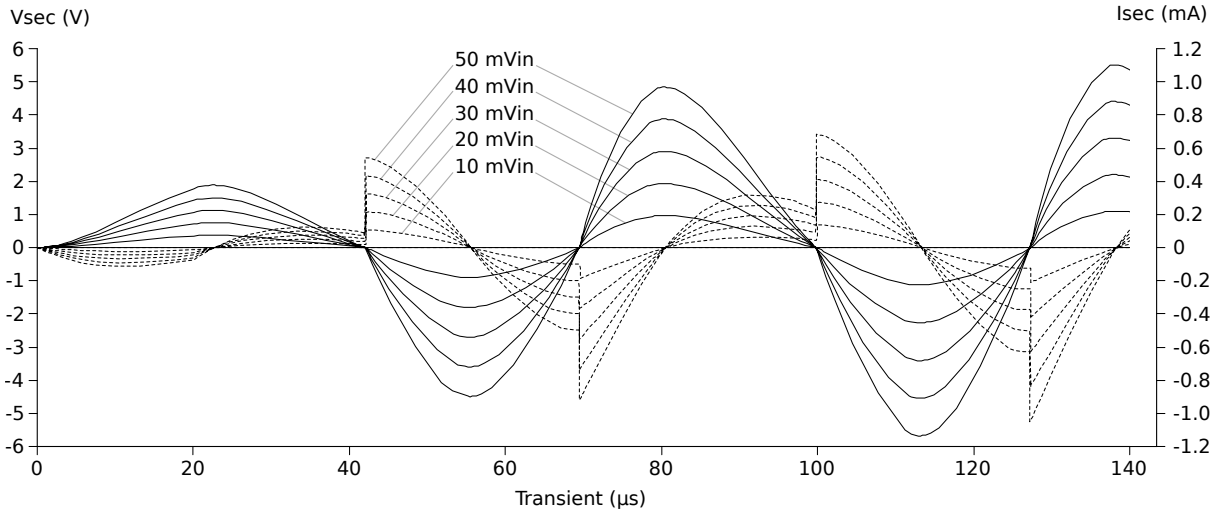

Figure 7.39: Start-up sequence of the LTC3108 with a 1:100 transformer (7.5 μH primary, 75 mH secondary) and capacitor values shown in figure 7.36. The left axis denotes voltage on the transformer secondary in [V], the right side shows the current through the secondary winding in [mA]. Responses shown for TEG input voltages between 10 mV and 50 mV.

Figure 7.39 shows the startup transient response of the LTC3108 for input voltages between 10 mV and 50 mV. The inductances of primary and secondary winding of the transformer are measured at 100 kHz. At voltages below 100 mV the effect of the Q-factor of the transformer is negligible, and as a result, the secondary voltages and currents scale relatively proportionally to the DC input voltage. Note the 90^{circ} phase shift between voltage (solid curves) and current (dotted curves), as well as the boost effect at voltage zero pass causing a discontinuity in the current. When the voltage treshold is reached, the LTC3108 will switch to active regulation instead of passive tank resonance, and the secondary voltage will be prevented from increasing any further.

The transient start-up behavior of the LTC3108 is shown in figure 7.40, with a circuit identical to 7.36 but with a 4.7 μF local storage capacitor connected to VSTORE to show the effect of the charging mechanism. For DC input voltages between 20 mV and 200 mV the LTC3108 is able to perform a cold start, but due to the transformer acting as a charge pump and the fixed resonance frequency of 100 kHz, the charge transported per cycle is independent of the TEGs output impedance. Even when connected to a regulated power supply, at low input voltages, the output capacitors charge slowly, as seen for the 20 mV and 40 mV curves. For input voltages from 100 mV onwards, the VAUX capacitor is charged up to its nominal value of 3.3 V (output voltage) within 10 ms after applying power to the circuit (under zero load conditions). The storage capacitor connected to VSTORE charges linearly, because of the constant charge pump effect, as shown by the dotted curves in figure 7.40. The voltage on VSTORE is internally limited to 5.5 V, shown by the clipping effect in the dotted graphs, which conveniently corresponds to the maximum voltage of commercial dual EDLCs.

BQ25570

As alternative signal path for the LTC3108, the AEM Thermal Rev. 2 also offers the BQ25570 as low voltage step up converter in a parallel signal path. The BQ25570 is a general purpose DC/DC boost

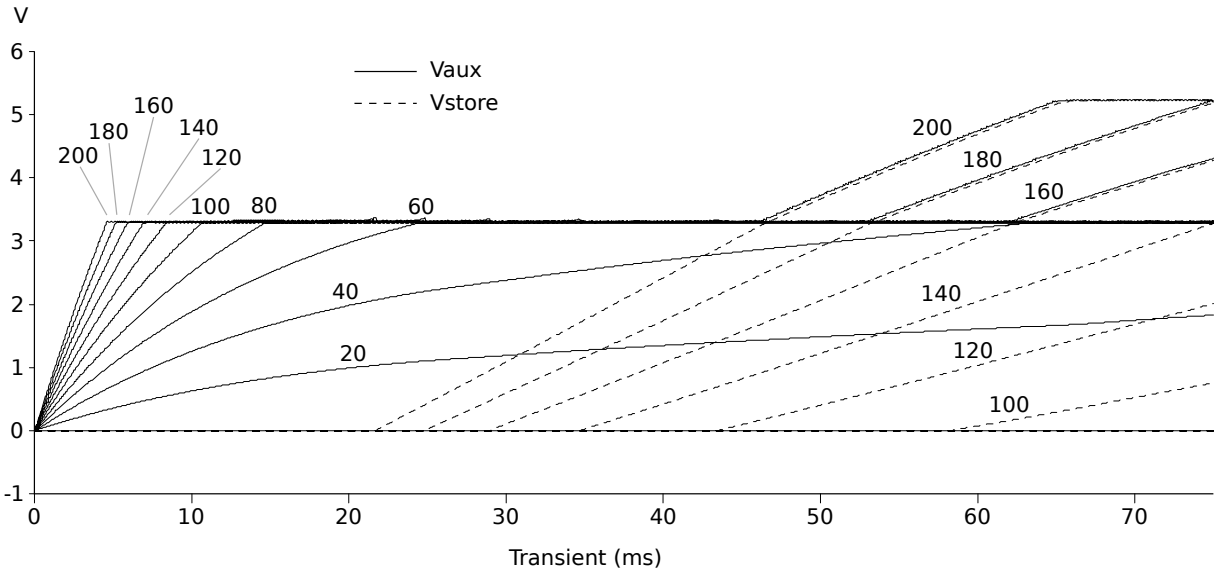

Figure 7.40: Start-up sequence of the LTC3108 with decoupled V_{aux} and V_{store} for faster start-up transient behavior. Solid line shows voltage over a 1 μF capacitor between V_{aux} and ground, dotted line shows the voltage over a 4.7 μF storage capacitor connected between V_{store} and ground. Curves given for DC input voltages between 0 and 200 mV in 20 mV intervals. V_{aux} tracks V_{store} above its output voltage set point, until the LTC3108 rated maximum of ca. 5.5 V (internally limited).

converter designed for applications requiring integrated battery charging, but its operation can be modified to accommodate a TEG. The modularity requires considerably more configuration parameters to be set through external voltage dividers (resistors R1 - R7 in figure 7.41). The values for the configuration resistors were calculated with assistance from a configuration tool provided by manufacturer Texas Instruments. With the values shown, the buck regulator regulates the output voltage to 2.5 V, making its signal path compatible with the LTC3105.

Because flyback diodes are integrated in the BQ25570, there are relatively few external components for a buck-boost topology. Capacitor C5 acts as storage instead of a battery, and a capacity of 100 μF is a minimum for stable operation. The drawback of the buffer between the boost and buck stage is the decreased transient response, i.e. changes in the TEG output power do not translate into a changing voltage on point B as fast as they do in the LTC3108 signal path. The BQ25570 is therefore usable as a general purpose buck-boost converter with low cold start voltage capable of operating from a TEG, but less suitable for harvester benchmarking.

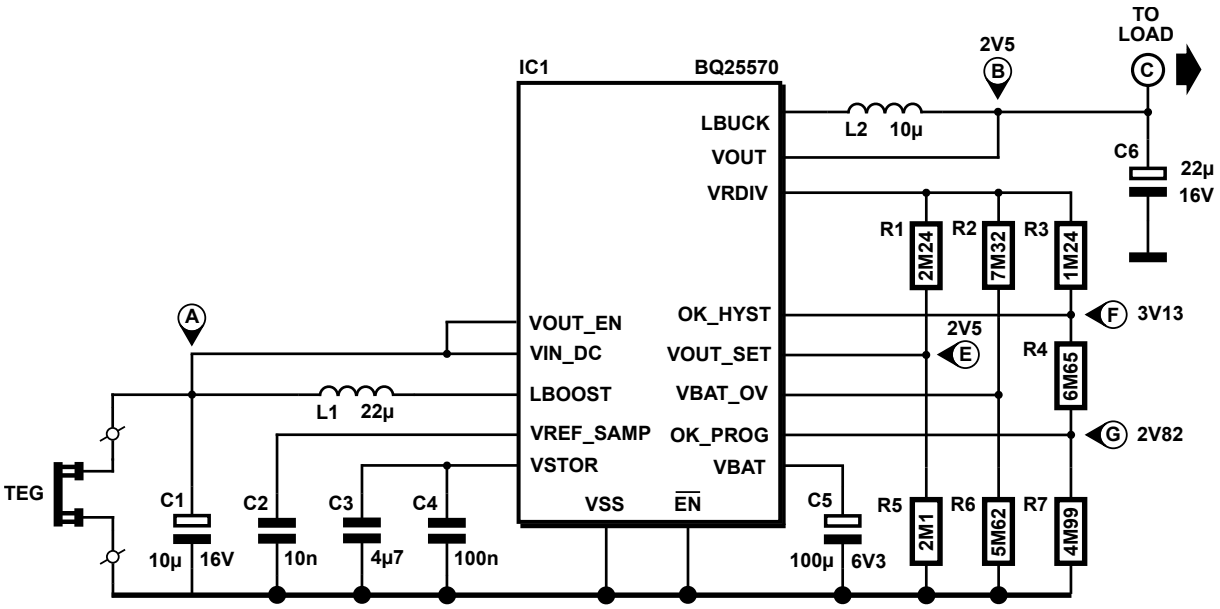

Figure 7.41: Alternative signal path for thermal energy harvesting using a TEG, with the TI BQ25570 as integrated buck-boost DC/DC converter. Capacitor C5 acts as storage element between boost and buck stage instead of a battery.

7.9 RF Module

7.9.1 Challenges

Benchmarking an ambient environment for RF energy harvesting requires the acquisition of spectral data over the entire electromagnetic spectrum, or at least those wavelengths that are most interesting (i.e. highest power density) for energy harvesting applications. The spectral composition then allows to identify the frequency bands with the highest power density, for which an antenna can be designed or optimized to maximize efficiency. However, measuring the electromagnetic spectrum is a non trivial problem because the resolution is a critical parameter. Existing benchmarks documented in literature have reported that most RF communication in urbanized environments is concentrated in narrow frequency bands. For example, Bluetooth operates in 79 frequency bands of 1 MHz each, while BLE (a.k.a. Bluetooth 4.0) doubles the band width to 2 MHz, but halving the number of available bands to 40. For wifi, the bands are respectively 20 MHz on a 2.4 GHz carrier, and 40 MHz on a 5 GHz carrier. For cellular communications, the bands vary in width from as little as 200 kHz per channel for GPRS and EDGE to 3.75 MHz for CDMA and 5 MHz for WCDMA (3G). The assigned frequency bands of 900 MHz and 1800 MHz for cellular communication (LTE bands 3 and 8, respectively) cover only a fraction of the total frequency range reserved for this communication, however. For GSM communication, the majority remains undeployed, resulting in little to no communication in the bands between 380 MHz and 850 MHz. The direction of communication is also affecting the power density, for example in the GSM-900 band, 880 MHz - 915 MHz is assigned to uplink communication (mobile to base tower), and 925 MHz - 960 MHz to downlink communication (base tower to mobile). To accurately measure the power density over a large range of frequency bands, considering the examples above, it is essential to have a resolution better than 200 kHz below 1 GHz and better than 1 MHz above 1 GHz. The design of a receiver with adequate selectivity and sensitivity is discussed below.

7.9.2 Tuned Oscillator Receiver

Signals of interest for RF energy harvesting start as low as 40 MHz from VHF TV broadcasts, which are also the frequency bands with the highest power density to retain compatibility with older television sets. As such, the bandwidth of AEM Waves should range from ca. 40 MHz to around 2.5 GHz, which is the last ISM band before the 5 GHz band. Frequencies above 2.5 GHz are typically used for satellite communications, (traffic) radar and 5 GHz wifi, but energy harvesting from these bands has not been demonstrated yet in practical applications and will therefore not be considered in the current version of AEM Waves because of the added hardware implementation complexity to double the frequency range to 5 GHz [307, 285].

To measure the RF power density per band, 2 approaches have been considered: tuning to the desired band with a traditional tuned oscillator receiver, and a superheterodyne receiver. Although a tuned oscillator works well for frequencies below 400 MHz and for small deviations in tuning frequency, it becomes impractical to design a tuned oscillator receiver that can be tuned anywhere between 40 MHz to 2.5 GHz without switched capacitor arrays for coarse tuning, and varicap arrays for fine tuning. The design complexity of such a topology in combination with its non-linear behavior poses challenges on its own. Since no switched capacitor and/or switched varicap design has previously been documented in literature, and it would be doubtful to achieve the desired selectivity, it was decided not to implement a tuned oscillator receiver but opt for a superheterodyne receiver instead.

7.9.3 Superheterodyne Receiver

The underlying principle of superheterodyne receivers is to use frequency mixing to convert a high frequency (HF) input signal into a fixed frequency intermediate signal (IF) using a local oscillator (LO). Since IF can be arbitrarily chosen, it can be set to a frequency low enough to allow more convenient processing than the original carrier frequency. The technique has been extensively documented, and is used in nearly all modern radio receivers to eliminate the tuning problems present in traditional tuned oscillator receivers. The block diagram is shown in figure 7.42. After a band selection filter, the incoming RF signal is amplified by a low noise amplifier (LNA) and subsequently fed into a mixer, which in turn is driven by a voltage controlled oscillator (VCO) acting as the local oscillator (LO). The mixer output consists of the sum and difference of the RF input signal and the LO, while preserving any data (i.e. carrier modulation) that may be present. The mixer output, a signal with the IF and many undesired mixer products, is then filtered to remove the mixer image and adjacent frequency bands. In a classic superheterodyne receiver topology, the IF signal would then be demodulated to extract the data, but in AEM Waves the filtered IF signal is passed into an RMS detector to convert the RF signal into a DC output which is then sampled by an ADC.

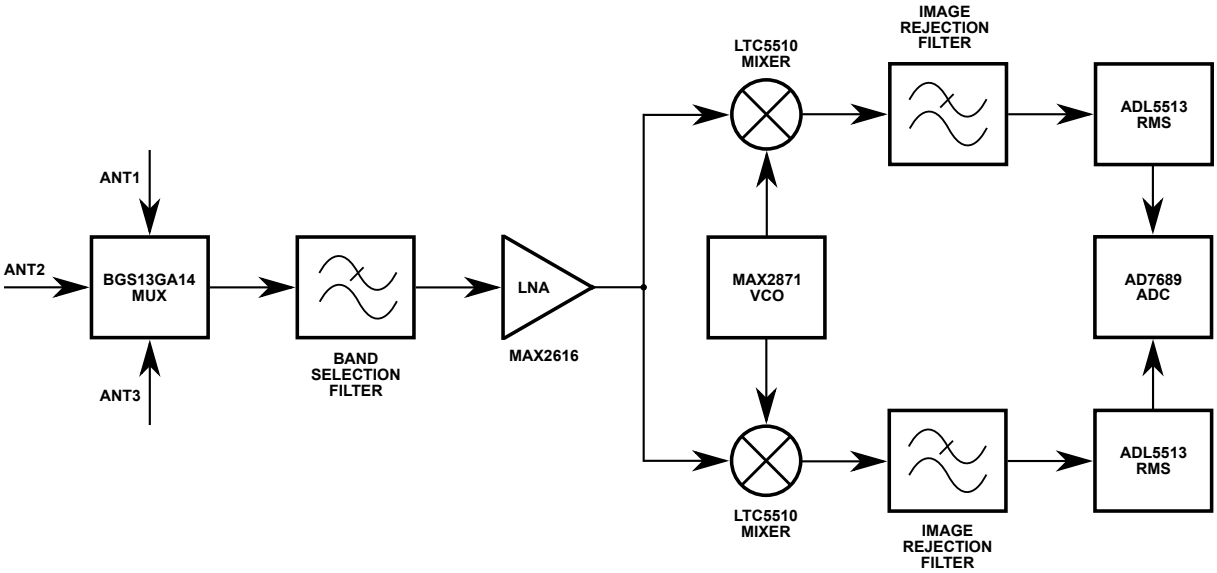

Figure 7.42: RF front-end of AEM Waves as a superheterodyne receiver with IQ mixer.

Many designs for superheterodyne receivers exist, ranging from discrete implementations with Schottky diodes as mixers, to highly integrated implementations on a die such as those in the ESP8266 and ESP32 series microcontrollers with wifi and BLE front-end. The design and development of a full custom superheterodyne receiver is out of scope of AEM Waves, and the system architecture was therefore based on the design of the CCC 2015 Rad1o Badge, which is an open source hackable SDR development board with a frequency range between 50 MHz and 4 GHz. The Rad1o Badge in turn is based on the HackRF One with a range from 1 MHz to 6 GHz. The RF signal path for AEM Waves was primarily derived from the CCC 2015 Rad1o Badge, with a few modifications.

Antennas

Because the physical size and shape of an antenna is determined by the wavelength(s) it is designed for, it is impractical to use a single antenna for the entire 50 MHz - 2.5 GHz frequency range. The CCC Rad1o Badge solves the problem by providing a hardware jumper as a 0 Ω 0603 resistor that allows the user to either select an Inverted F planar PCB antenna (PIFA), or connect an external antenna to an SMA connector. The same strategy was followed for AEM Waves, but instead of a hardware jumper that needs to be resoldered, an RF multiplexer is inserted in the signal path to dynamically connect any of 3 antennas to the LNA. Unlike the Inverted F planar PCB antenna on the Rad1o Badge, 3 identical SMA connectors are supplied on the PCB to connect external antennas, and no integrated antenna is provided. The layout is shown in figure 7.43. The multiplexer of type BGS13GA14 (IC1) has an input and output impedance of 50 Ω and can therefore be connected directly to the SMA connectors using PCB microstrips with a characteristic impedance of 50 Ω. A TVS-diode for ESD protection (D1 .. D3) is provided on each SMA connector. The BGS13GA14 offers the theoretical functionality to connect multiple antennas at the same time by asserting more than one of the V1 - V3 inputs. However, this would also connect the antennas to each other, leading to undesirable reflections and unpredictable behavior. The multiplexer is rated for frequencies between 100 MHz and 6 GHz.

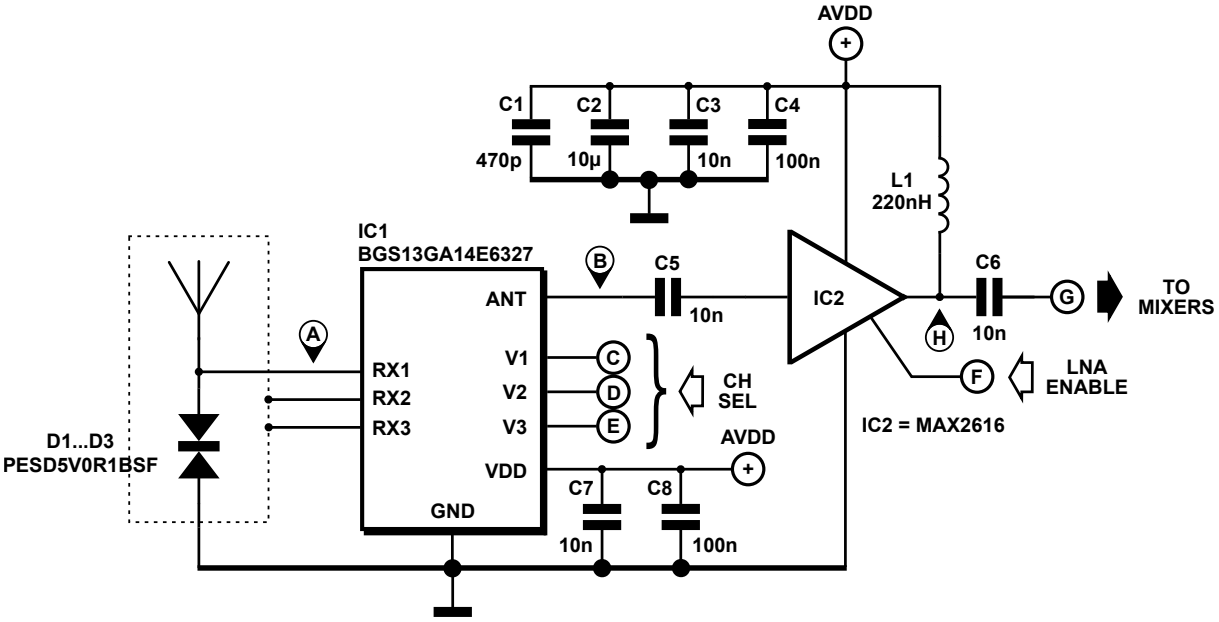

Figure 7.43: RF multiplexer with up to 3 antennas connected to SMA connectors simultaneously, with RF signal amplified by an integrated LNA.

Antennas suitable for use with AEM Waves can be found in any of 6 categories: wire antennas (including monopole, dipole and loop antennas), traveling wave antennas (helical, Yagi-Uda and spiral antennas), reflector antennas, microstrip antennas (including patch antennas and planar inverted F antennas), log-periodic antennas, and aperture antennas (with most notably vivaldi antennas and slot antennas). There is no limitation to the types or combinations of antennas that can be used, but with only 3 SMA connections available, care must be taken to select a combination of complementary antennas whose frequency response overlaps to cover the entire spectrum of interest. In general, an antenna can be made more broadband by increasing the volume it occupies, for example the bandwidth of a dipole antenna can

be increased by increasing the radius of the dipole. The drawback is that the antenna may become physically large, making its use impractical. The antenna designs proposed below have a favorable trade-off between bandwidth and physical size.

Yagi-Uda Antenna Yagi-Uda antennas are well known because they have been widely used to receive television broadcasts in the HF to UHF bands (ca. 3 MHz up to 3 GHz), although they suffer from a small bandwidth (typically 1 % - 5 % of the center frequency). A Yagi-Uda antenna can be constructed from a single feed dipole (the driving element), complemented by a number of additional elements that either reflect or help transmit the RF energy in a particular direction. The length of the feed element is typically between 0.45λ and 0.48λ making it relatively bulky for low frequencies. Yagi-Uda antennas are difficult to design without the help of an RF simulator, but since they have been extensively studied, ample sets with design parameters have been published. Although narrowband in comparison to the other antenna types discussed below, Yag-Uda antennas can be designed for frequencies below 100 MHz, where the other antenna types struggle.

Spiral Antenna Spiral antennas have a large bandwidth, and a fractional bandwidth (FBW) up to 30:1. The fractional bandwidth is calculated as the fraction between the bandwidth and the center frequency: $FBW = 2\frac{f_h - f_l}{f_h + f_l}$. With FBW $\approx$ 30:1 it is possible to achieve an antenna design with a reasonable sensitivity in a frequency range between 100 MHz and ca. 3 GHz, which makes it well suited as receptor antenna for AEM Waves. The radiation pattern of spiral antennas has a peak radiation direction perpendicular to the plane of the spiral, with a half power beam width (HPBW) between 70° and 90°. These properties make them a favorable choice in applications where very wideband antennas are required but not much space is available, such as GPS receivers. The design of a spiral antenna follows the general polar function

$$r = R_0 e^{a\theta} \tag{7.47}$$

where R_0 is a constant setting the initial radius of the spiral and a the rate at which the antenna fans out, making it *grow* exponentially. If a is too large then the spiral will be too dense and attenuate the signal because it acts as a capacitor, but if a is too small then it will act more like a dipole than a spiral and lose its wideband properties. Therefore, the value $a = 0.22$ is chosen as compromise. The frequency range of a spiral antenna is constrained by its inner and outer radii, r_1 and r_2, where r_1 is measured from the center of the spiral to the center of the first turn, and r_2 is measured from the center of the spiral to the center of the outermost turn. The frequency band can be calculated as

$$\frac{c}{2\pi r_1} \leq f_{BW} \leq \frac{c}{2\pi r_2} \tag{7.48}$$

where c is the universal speed of light constant. The complexity of the spiral is determined by the number of turns N, which has been found through experimentation to be optimal for $0.5 \leq N \leq 3$.

Patch Antenna The advantage of patch antennas (formally known as microstrip antennas) is their simplicity, which allows them to be integrated on PCBs (as with the planar inverted F patch antenna commonly used for wifi and BLE communications at 2.45 GHz). The thickness of the PCB is not critical, but should not be thinner than 0.025λ to avoid degradation of performance. The center frequency f_c can be calculated as

$$f_c = \frac{1}{2L\sqrt{\varepsilon_0 \varepsilon_r \mu_0}} \tag{7.49}$$

with η_r the permittivity of the PCB substrate, which is ca. 4.35 at 500 MHz and 4.34 at 1 GHz, and L the length of the antenna. Thus, the patch antenna should have a length equal to one half of the wavelength within the substrate. The width W determines the output impedance of the antenna, its bandwidth (with larger antennas having a greater bandwidth), and the radiation pattern. The width can be calculated as

$$W = \frac{c}{2f_0\sqrt{\frac{\varepsilon_r+1}{2}}} \tag{7.50}$$

with f_0 the desired resonance frequency of the antenna.

Table 7.8: Comparison of patch antenna sizes on a 4 layer FR4 PCB (thickness 360 μm, $\varepsilon_r = 4.35$.

Frequency (MHz)	Width	Length
50	1.8 m	1.4 m
100	917 mm	719 mm
200	458 mm	359 mm
433	211 mm	166 mm
868	105 mm	82 mm
900	102 mm	80 mm
1800	51 mm	40 mm
2450	37 mm	29 mm

As demonstrated in table 7.8, a rectangular patch antenna is only convenient at frequencies above 1 GHz. Space saving improvements can be made to shrink a patch antenna to a smaller size than dictated by the dimensions in table 7.8, as is the case with a planar inverted F patch antenna, but with a degradation of performance as a result.

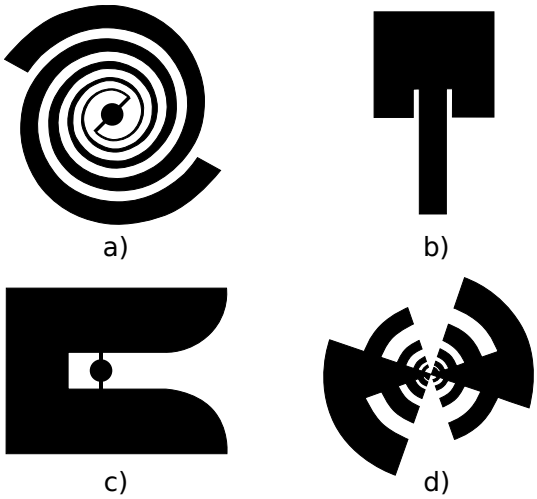

Figure 7.44: Suitable wideband antenna designs for AEM Waves. a) spiral antenna [96], b) patch antenna [279], c) vivaldi antenna [196], d) log-periodic antenna [43].

Log-periodic Antenna Similar to spiral antennas, log-periodic antennas have the potential to achieve a very wide bandwidth. The bandwidth is theoretically infinite, but practically the lower frequency f_l is

limited by the size of the largest structure in the antenna, and the higher frequency f_h by the precision of the smallest structure. The working principle of a log-periodic antenna is that it is built up from individual elements which are increasing in length by a multiplicative factor k. If one element radiates at a given frequency, it will also radiate at all multiples of k. In a typical antenna, k is then chosen so that the frequency bands overlap, essentially creating a wideband antenna by combining multiple narrower bands together. Hence the reason why the bandwidth is only limited by the number and size of the elements in the array. Also log-periodic antennas can be made as a planar PCB antenna, as a log-periodic tooth antenna or as a log-periodic dipole antenna using vias on the PCB. [33]

Vivaldi Antenna Vivaldi antennas are recognizable for their U-shape, often with tapered inner edges. The feed of this antenna is symmetrical towards the center gap, and the DC short circuit acts as a parallel inductor for RF frequencies. The shape is defined by the function

$$f(x) = \pm Ae^{px} \tag{7.51}$$

where p is the tapering factor. Because Vivaldi antennas can be considered a special case of patch antennas, parameters like shpae, dielectric constant and thickness of substrate play a role in the antenna's bandwidth and frequency response. The feed point determines f_h and the size of the aperture f_l, but as with most antenna designs, the design effort is largely empirical. [120]

LNA

The signal received by the antennas is in the order of μV, and before it can be practically processed it needs to be amplified. A low noise amplifier (LNA) is inserted in the RF signal path for this purpose. The MAX2616 is a linear broadband amplifier with proven performance on the CCC Rad1o Badge, with bandwidth between 40 MHz and 4 GHz and a good frequency response ($<$ 0.5 dB in the range 1 GHz - 4 GHz). In the band of interest, 50 MHz to 2.5 GHz, the power gain is constant and equal to 18.4 dB $\pm$ 0.2 dB. The circuit is presented in figure 7.43, using a high stability NP0 coupling capacitor of 10 nF to feed the antenna signal into the internally biased amplifier input. The output of the LNA is biased with a 220 nH inductor. The LNA can be enabled from the microcontroller (input F).

Mixer

The frequency down conversion is done in a dual mixer configuration, using the LTC5510 from Linear Technology with a bandwith up to 6 GHz. The mixer pair is driven by a MAX2871 VCO, acting as quadrature local oscillator (LO), thus producing 2 sinusoidal excitation signals 90° out of phase: $I\cos(2\pi f_L Ot)$ and $Q\sin(2\pi f_{LO}t)$. In this application, low-side injection is used to achieve a low-side down converter. Expressed as a Fourier series, each local oscillator can be presented as

$$S_{LO} = \frac{4}{\pi}\left[\sin\omega_{LO}t - \frac{1}{3}\sin 3\omega_{LO}t + \frac{1}{5}\sin 5\omega_{LO}t - ...\right] \tag{7.52}$$

When mixed with an RF input signal with ω_{RF}, the IF signal expressed as a Fourier series becomes

$$S_{IF} = \frac{4}{\pi}\left[\sin\omega_{RF}t\sin\omega_{LO}t - \frac{1}{3}\sin\omega_{RF}t\sin 3\omega_{LO}t + \frac{1}{5}\sin 5\omega_{RF}t\sin 5\omega_{LO}t - ...\right] \tag{7.53}$$

Pairing the products together and simplifying, the resulting IF signal is

$$S_{IF} = \frac{2}{\pi}\left[\sin(\omega_{RF}+\omega_{LO})t + \sin(\omega_{RF}-\omega_{LO})t + ...\right] \tag{7.54}$$

The higher order components are harmonics and omitted from the equation. The series demonstrates that when the LO is fed into the mixers together with the RF input signal, 2 side bands are formed: $\omega_{RF} - \omega_{LO}$ and $\omega_{RF} + \omega_{LO}$. The MAX2871 is controlled such that a LO is produced with a frequency that is 10 MHz below the desired RF frequency, down converting the RF band of interest to a 10 MHz carrier which can then be processed as IF. The complete circuit with quadrature VCO and mixers is shown in figure 7.45. Although a single VCO would suffice to detect RF signals at arbitrary frequencies by mixing them with the LO, the IF would be 0 if LO and RF are 180° out of phase. The IQ demodulation using quadrature LO signals resolves this problem since there is a phase shift of 90° between I and Q, and thus the original amplitude can be computed in software.

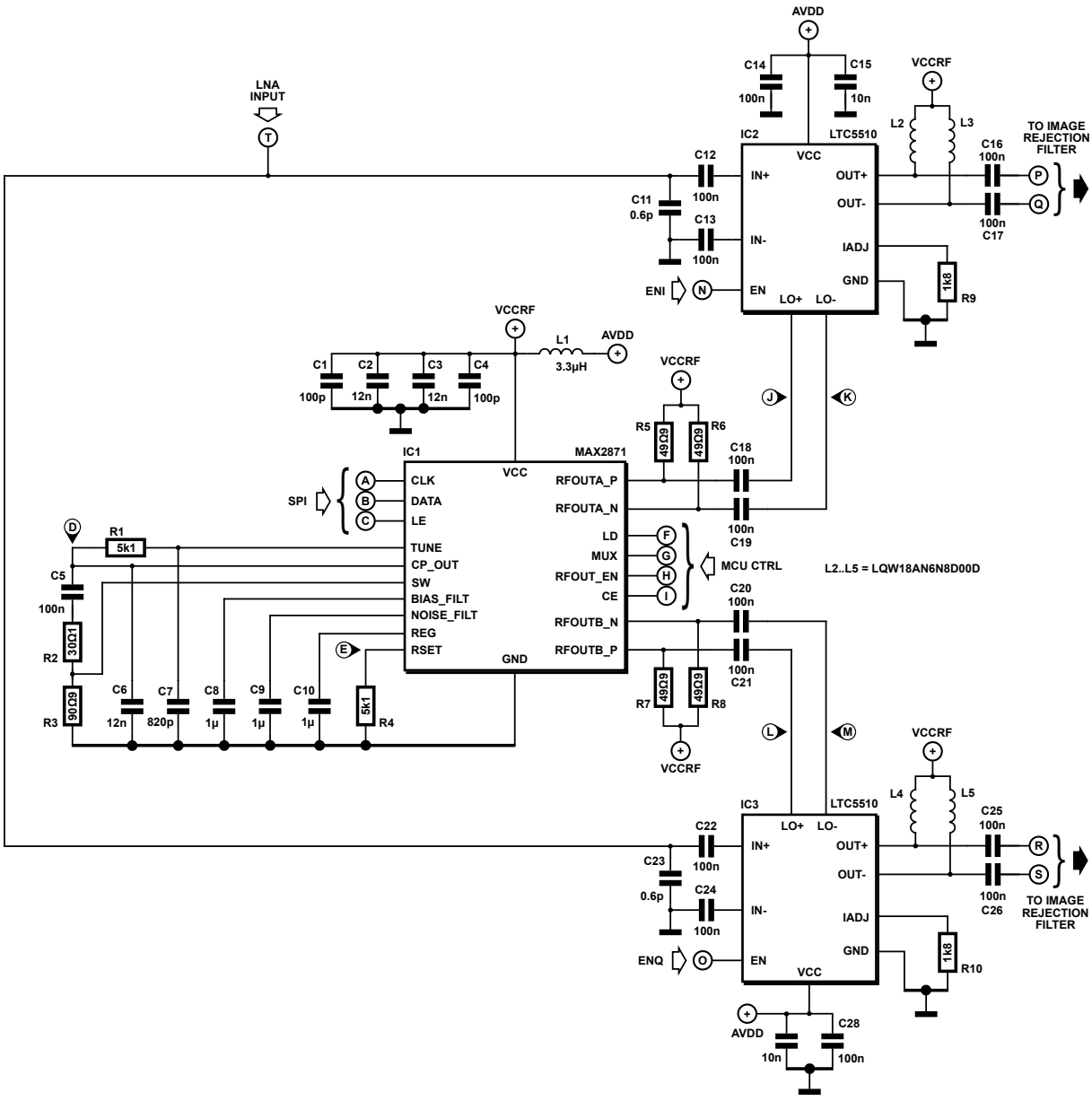

Figure 7.45: Circuit of the IQ mixer, using 2 LTC5510 integrated RF mixers and a MAX2871 VCO as LO.

Crystal Filter

The IF output signals of the mixers contain all mixer products, including the desired signal in the 10 MHz band. Removal of these undesired mixer products is necessary to achieve selectivity, and thus a band pass filter with a pass band of ca. 200 kHz is required, with little to no attenuation of the 10 MHz band of interest. Since the gain bandwidth of low noise amplifiers (i.e. RF grade opamps) is limited, it is expensive to design active R(L)C filters with this approach, and would induce additional noise in every stage. Quartz crystals commonly have a Q-factor greater than 10^4 or 10^5, beyond what is achievable with conventional resonators built from capacitors and inductors. A better solution is to make use of passive crystal filters. Using crystal filters in this application has 2 advantages: they have a high selectivity (in turn allowing for a higher dynamic range of the measurement), and are straight forward to design for a given pass band. In AEM Waves, a crystal filter was therefore chosen as IF filter, replacing the ceramic resonator filter in the Rad1o Badge design. The choice between a crystal filter and ceramic resonator filter is made based on cost and PCB area: ceramic resonator filters are smaller and cheaper than crystal filters, but perform worse.

The use of crystal filters for IF filtering in superheterodyne receivers has been extensively documented in literature, and most famously used in the Rohde & Schwartz EK-070 VLF/HF receiver, with a bandwidth up to 30 MHz but using a crystal filter with a bandwidth of only 12 kHz. Several software tools are available, and AADE Filter Designer (originally commercial but released as freeware recently, runs well under WINE) was used to tweak existing crystal filter designs to a 5 pole filter with pass band at 10 MHz. The filter design is shown in figure 7.46.

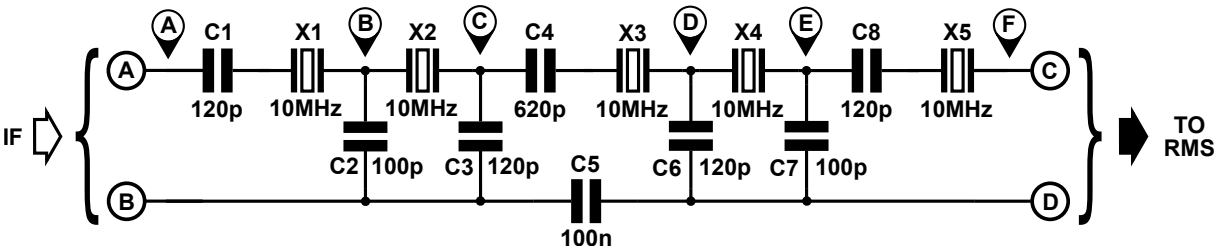

Figure 7.46: A 5 pole passive crystal filter used for IF filtering of the mixer products. The filter has a pass band of ca. 15 kHz at 10 MHz. The frequency response is shown in figure 7.48. Each crystal forms a resonant mesh with the capacitors to its side (C2, C3, C6 and C7), and the resonance frequency of these meshes is then tuned with series capacitors (C1, C4, C8) to achieve the desired response.

Although the pass band is dictated by the resonance frequency of the crystals, building a crystal filter with multiple poles is more challenging because the specifications of the individual crystals need to be matched as closely as possible. The electrical equivalent of a quartz crystal is shown in figure 7.47, and consists of an RLC series branch (with Rs, Ls and Cs) and a parallel capacitor Cp. The values shown in figure 7.47 are those for the chosen crystal, Abracon ABM3-10.0000MHZ. Due to variations in the manufacturing process, however, the natural component spread on the values affects the characteristics of any filter relying on matched crystals. The value of Cs in particular is small compared to Cp, and therefore prone to deviations.

Suitable crystals can be selected by matching their parallel and series resonance frequencies (f_p and f_s, there is no physical difference between a *series* and a *parallel* crystal), as well as their Q-factor.

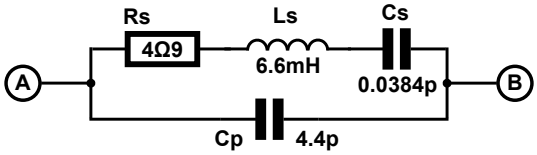

Figure 7.47: Model of an Abracon ABM3-10.0000MHZ quartz crystal trimmed to a resonance frequency of 10 MHz. Note the high value of Ls in comparison to the small value of Cs, which causes deviations in the crystal's frequency response.

In a tuned circuit, Q can be expressed as $Q = \frac{f}{BW_{3dB}}$ where BW_{3dB} is the 3 dB bandwidth and f the resonance frequency of the crystal (10.0000 MHz for the Abracon ABM3 crystal). Since $Q = \frac{X}{R}$, the components in figure 7.47 can be calculated by measuring R and then solving for X, which is the reactance of Ls and Cs (equal in a resonant circuit). This is a cumbersome process since 5 matched crystals are required per filter and per channel, totaling 10 per AEM Waves module. A usable alternative to measuring individual crystals purchased in bulk, is to build the filter using surface mount crystals. Because sequential crystals in the same tape are likely to be cut from the same crystal, they have a higher probability of having matching f_p, f_s and Q-factor than through hole bulk crystals. The performance of the filter is shown in 7.48, for the resonant input A, and for the 5 poles B, C, D, E and F. Point F is the output of the filter, with a pass band of ca. 10 kHz and a center frequency slightly above 10 MHz (10.004 MHz). An ideal crystal filter would have a flat response in the pass band, but variations in the crystals create 3 additional poles in the frequency response, at respectively 10.002 MHz, 10.004 MHz and 10.006 MHz. Unlike ceramic resonators, which tend to be sensitive to temperature, quartz as a material remains largely unaffected by temperature drifts.

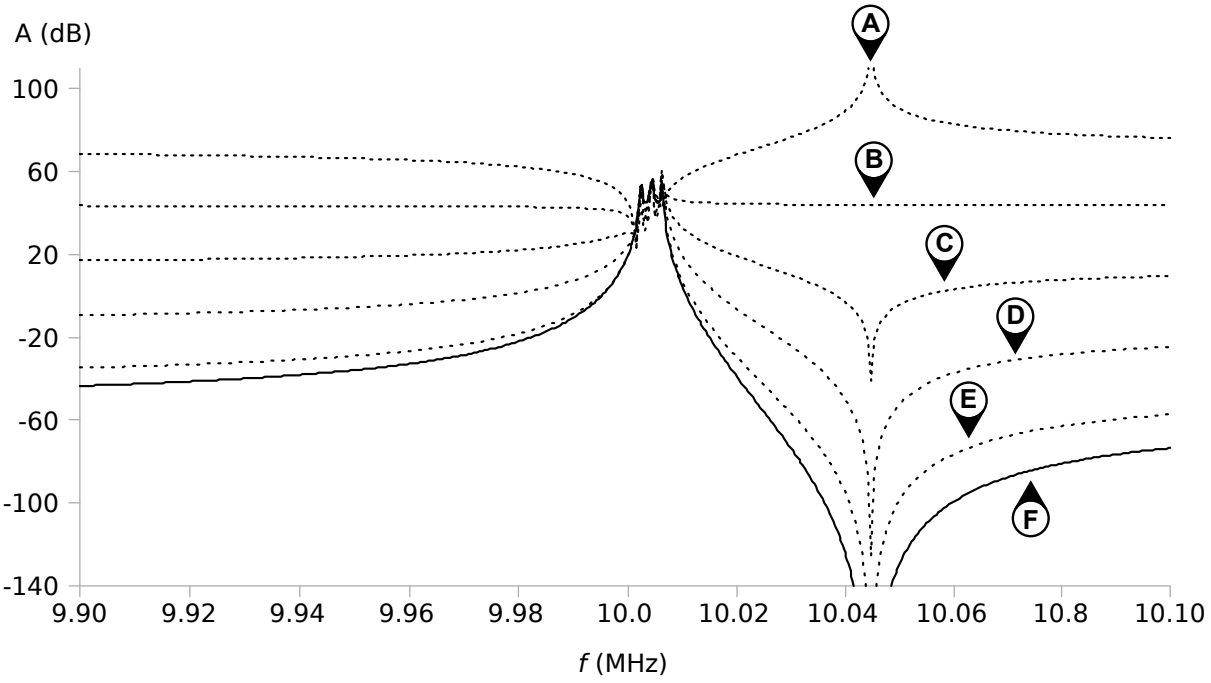

Figure 7.48: Frequency response of the 5 pole crystal filter shown in figure 7.46, with a 10 kHz wide pass band slightly beyond 10 MHz.

A convenient property of this filter is that mixer products beyond the 10 MHz pass band are more strongly attenuated than frequencies below, i.e. the crystal filter shows a dominant low pass filter behavior rather than a high pass filter. The effect is caused by the parallel crystal electrode capacitor, Co, and can be compensated for by adding resonating inductors in parallel with each capacitor (Hayward et al.). The value of Co can be approximated as $C_o = 220 \cdot C_s$, which is derived from the technique to cut the quartz crystal physically. It allows a convenient estimation of the frequency difference Δf between parallel and series resonance:

$$\Delta f \approx \frac{f \cdot C_s}{2C_o} \tag{7.55}$$

Because the effect of Co improves the filter's role for image rejection, and the additional inductors make the cicuit more complex, the compensation has been omitted. The performance strongly depends on the capacitors, which need to be rated for RF applications. Dipped silver mica capacitors are recommendable.

RMS Detector

To effectively measure the power density at 10 MHz IF, within the 10 kHz wide pass band of the crystal filter, the filter output can either be measured directly or processed further. The CCC Rad1o Bagde, as an SDR application, tackles the problem by directly sampling the 10 MHz signal to retrieve the information it contains. Following Shannon's sampling theorem, this requires a 20 MS/s ($20 \cdot 10^6$ samples per second) ADC or better, and significant processing power to process data at such a high throughput. The Rad1o Badge implements a 22 MS/s ADC (MAX5864) with parallel interface to an FPGA to solve the problem, but the approach is expensive and ultimately unnecessary for AEM Waves since not the encoded data is of interest here but the signal level itself. It was therefore decided to replace the analog front-end provided by the MAX5864 with an Analog Devices ADL5513, which is a demodulating logarithmic amplifier with a bandwidth up to 4 GHz and a dynamic range of 80 dB for a sensitivity of -70 dBm. This device is commonly used in RSSI measurement systems of WLAN and radar applications, and well suited for quantizing the power density of the 10 MHz IF signal. The circuit is shown in figure 7.49.

The output filter is integrated in the ADL5513 and configured through a filter capacitor (C5) connected to the CLPF (low pass filter capacitor). The value of C5 can be calculated as

$$C_5 = \frac{1}{2 \cdot \pi \cdot 1.5\,\mathrm{k\Omega} \cdot BW} - 3.0\,\mathrm{pF} \tag{7.56}$$

The bandwidth BW is set to a frequency equal to 10 % of the minimum input frequency, ensuring that the output ripple of the demodulated log output, which is at twice the input frequency, is adequately filtered. For BW = 10 % (10 MHz $\pm$ 5 kHz), the filter configuration yields C5 = 103 pF. The output of the ADL5513 is fed into an AD7689 ADC channel, so the voltage drop caused by the 10 Ω output impedance of the ADL5513 is negligible. The reference voltage of 2.048 V for the AD7689 is provided by an MCP1501, and fed into the REFIN input, similarly to the other AEM modules.

Calibration

Each stage in the RF signal path shown in figure 7.42 suffers from its own non-linear behavior, which can be estimated theoretically by calculating the transfer functions of each individual stage and then

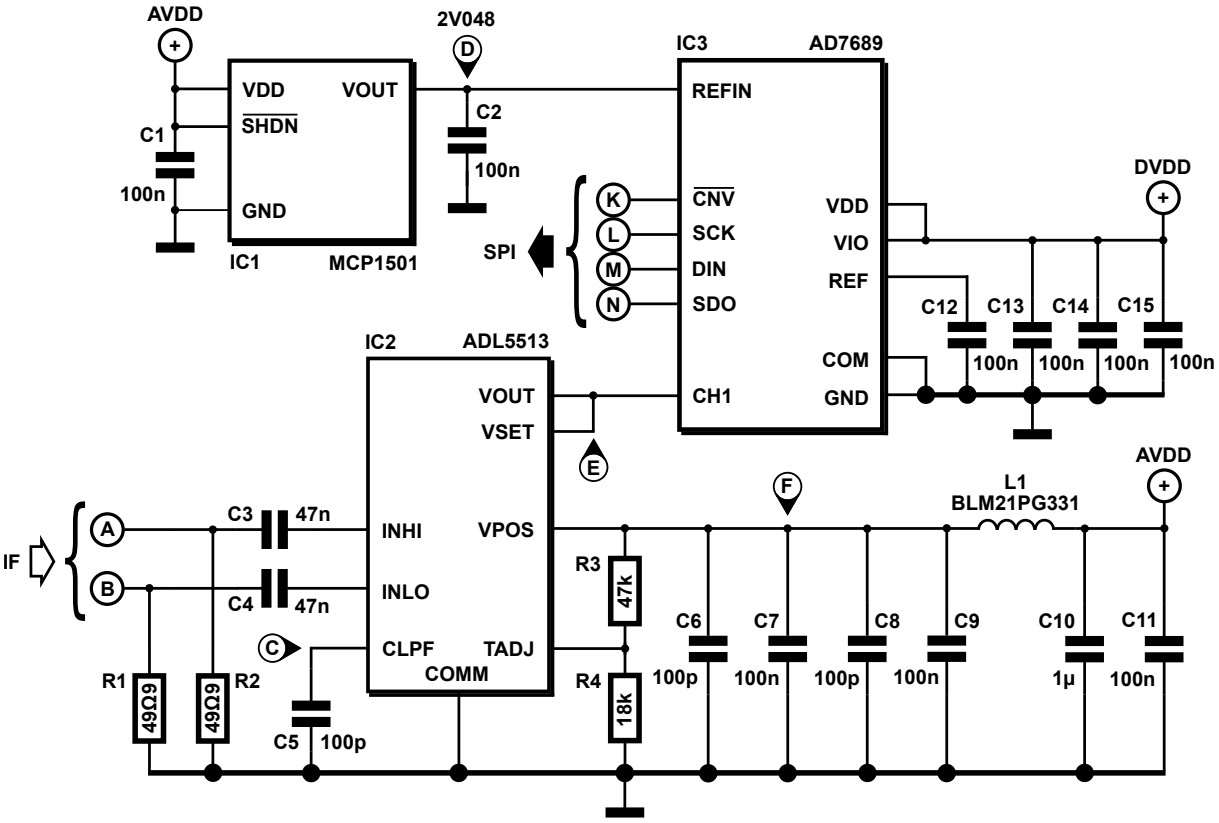

Figure 7.49: Analog RF front-end using ADL5513 as logarithmic amplifier to convert the 10 MHz IF signal to DC with a 80 dB dynamic range, and AD7689 16-bit ADC for quantisation of the input signal.

combining them to find the transfer function of the complete RF signal path. However, since the wave behavior of signals above 30 MHz should be accounted for, it is impractical to quantize the error of open loop measurements with this approach. A better solution is measuring the performance closed loop by applying a known signal (i.e. an RF input with known frequency and amplitude) and then measuring the response with the AD7689. The ratio between the applied signal amplitude and the measured signal amplitude results in a frequency dependent correction factor that allows normalization of the measurements through a simple multiplication instead of non-linear estimations. A second advantage using this approach is that the known excitation signal can either be applied directly to the RF multiplexer inputs, or with a suitable antenna, to any of the 3 antennas connected to AEM Waves. This in turn allows to benchmark the performance of each antenna at a given frequency, by calculating the AD7689 output difference between a direct input excitation (i.e. signal generator attached to SMA connectors) and indirect excitation (transferring the signal through the antennas). With a finite number of samples in a frequency sweep, the coefficients for normalization correction can be stored as a look up table (LUT) in EEPROM (24AA025UID) as part of the AEM Waves calibration procedure. The flow chart is shown in figure 7.50.

The process is started by the Raspberry Pi SoC connected to AEM Waves, and controlling an arbitrary wave generator feeding a appropriate wideband antenna in a suitable RF anechoic chamber, which in turn radiates onto a receiving antenna connected to one of the AEM Waves SMA connectors. The Raspberry Pi initiates the calibration procedure by instructing the wave generator to generate a given frequency, initially starting at 50 MHz (1). The RF energy is transfered to the receiving antenna (2)

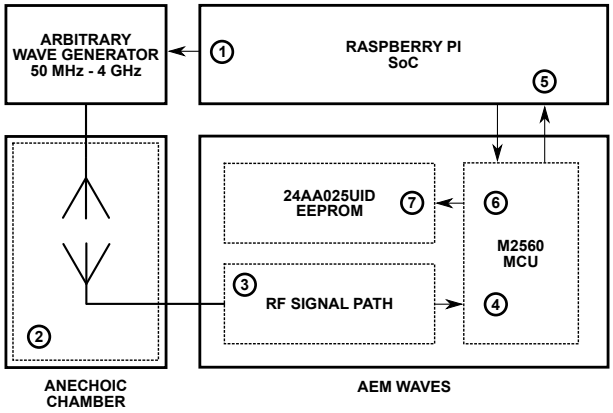

Figure 7.50: Calibration procedure for AEM Waves, using an RF anechoic chamber with arbitrary wave generator for reference signal generation.

and processed in the RF signal path on AEM Waves, causing attenuations due to non ideal antenna frequency response, non linearity of LNA, and losses in filters (3). The data for I and Q channels is then sampled by the AD7689 and converted to an RMS value proportional to the input RF signal (4). This value is subsequently communicated back to the Raspberry Pi (5), closing the feedback loop, and allowing to compute the antenna losses and AEM Waves losses itself. The correction ratio for the applied frequency is computed by the Raspberry Pi and communicated back to AEM Waves together with the test frequency (6) where it is stored in EEPROM memory (7). The calibration procedure then repeats with the next frequency, until the entire band is calibrated.

7.9.4 RF Energy Harvester

An RF energy harvester is essentially an RF to DC converter, or in other words a high speed rectifier. Since antennas produce an AC signal, a transformer can optionally be used to multiply the amplitude of the RF signal to reduce rectification losses, or to match impedance between antenna and rectification circuit. Alternatively, a single ended 50 $Omega$ load can be used to terminate the antenna transmission line, and a voltage multiplier such as a Cockcroft-Walton circuit used to increase the amplitude of the RF signal. A waveguide such as a PCB transmission line (stripline or microstrip) is necessary to avoid RF losses before the multiplier/rectification circuit is reached. The efficiency of conversion is determined by the voltage drop over the rectifier diodes, which should be minimized.

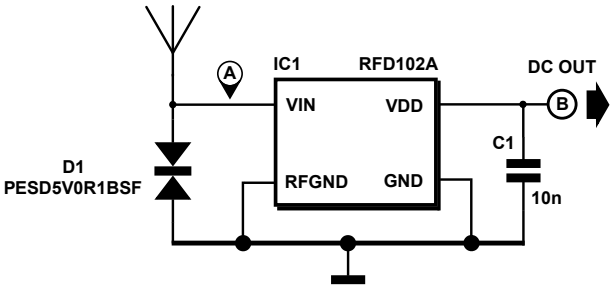

Figure 7.51: RF voltage multiplyer and RF to DC rectifier with integrated impedance matching designed for RF energy harvesting applications.

The voltage multiplier and impedance matching network can either be implemented with discrete components, but are also available as integrated solutions. Examples are the RFD120A from RF Diagnostics, as shown in figure 7.51, or the P2110 from PowerCast. The RFD120A is designed for ambient RF energy harvesting, and does not provide any kind of voltage regulation aside from a shunt regulator to clamp the output voltage in case of overload on the RF input. This is not a problem since in practical applications it will be necessary to charge an energy storage device rather than powering an embedded system directly as is the case with vibration, light or thermal energy harvesters. Passive RF to DC converters thus do not include any kind of voltage regulators, because their quiescent current alone would exceed the current sourcing capabilities of antennas in most applications. The PowerCast P2110 however is a designed for wireless power transfer applications as opposed to ambient RF energy harvesting. The P2110 is a complete BoB with castellated holes, designed to be soldered to an application as a module, and does include a voltage regulator. Unlike the RFD120A which implements all required RF circuitry on a single die, the P2110 makes use of discrete diodes for rectification of the RF signal and includes an on-board DC/DC buck converter. Since in the case of active RF power transmission there is no *need* to benchmark the environment (since the available RF power can simply be found in the transmitter's datasheet), no PowerCast solutions are currently implemented on AEM Waves which instead focuses solely on passive RF energy harvesting from already available RF signal sources for wireless communication.

7.9.5 Digital Control

AEM Waves shares its digital logic with Rev. 2 AEM modules, featuring an ATMega2650 as microcontroller and a 24AA025UID EEPROM to store calibration data for the I and Q channels. The analog front-end is implemented with a single AD7689, of which 2 channels are used for respectively I and Q after RMS detection (see figure 7.49), and one channel for the RF energy harvester signal path including RFD102A RF to DC converter and the subsequent electronic load, with a circuit identical to that of AEM Vibrations rev. 2 (figure 7.11). The block diagram of AEM Waves is shown in figure 7.52.

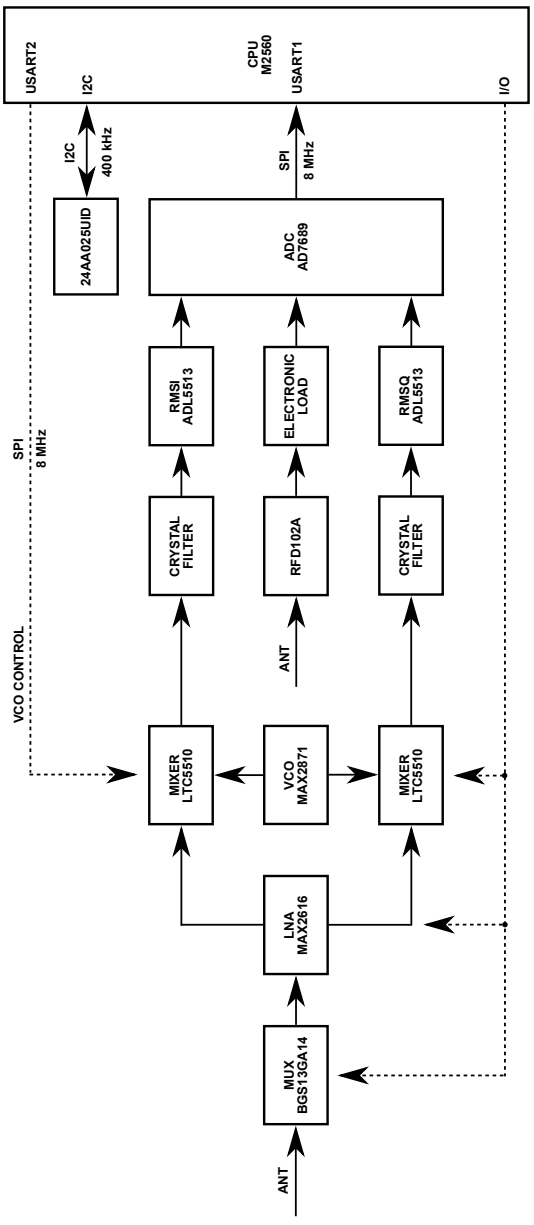

Figure 7.52: Block diagram of AEM Waves, with a single AD7689 ADC for measuring both channels of the IQ receiver and the input of the RFD102A RF to DC converter. The MAX2871 VCO is controlled by the MCU through SPI, while enables and channel selections are IO lines (dotted).

The RF front-end is directly configurable in software since RF multiplexer, LNA and mixers are connected to digital IO of the microcontroller. The VCO generating the quadrature LO signals is configured through SPI to speed up frequency sweeps across the band of interest.

7.10 Conclusion

Benchmarking ambient energy in a real world environment along with the performance of that harvester in the same environment is the cornerstone of complementary balanced energy harvesting: without adequate numeric data on harvester characteristics or ambient energy, it is impossible to properly select and dimension one or more harvesters to power the system. The Ambient Energy Monitor is capable of fulfilling both tasks: it serves as a modular and portable test platform that is capable of measuring ambient energy of any kind, provided the correct AEM modules are connected to it. At the same time, it acts as a test bench for actual energy harvesters, which can be tested directly in the environment they are intended to be deployed in. With a flexible power path, allowing the user to compare different DC/DC converters with or without maximum power point tracking to each other, the AEM is the first practical implementation of an ambient energy measurement station. It supersedes discrete sensors, instead using sensor fusion to achieve superior results while using lower cost components. The AEM modules effectively make theoretical environment modeling obsolete, because the numeric data generated through benchmarking is more accurate than any theoretical estimation.

As a proof of concept, 4 modules were developed to illustrate the nearly infinite extendability of the AEM platform. Modules are currently available for the 3 most promising sources of ambient energy, photovoltaics, thermoelectrics and vibrations, as well as RF energy as a base for comparison. Development was heavily tailored towards the creation of a sustainable environmental monitoring system, translating into a collection of open source hardware and software design resources that allow anyone with knowledge in embedded electronic systems to adapt, extend and expand the existing AEM project. In its current state, as documented in this chapter, all resources are available to make a seamless transition to a community supported initiative with the best potential for large scale and global adoption of the technology. Design resources can be found in Appendix A.

Future Work and Conclusions

The design of autonomous systems powered by decentralized energy harvesters used to be a tedious and time-consuming endeavor, involving the manual comparison of harvester performance followed by lengthy calculations to obtain approximations for harvester sizes. The resulting inaccuracy tempted designers to routinely overdimensioning harvesters, leading to unnecessary waste of natural resources and increased environmental costs.

The methodology for Complementary Balanced Energy Harvesting established in this work offers a streamlined and automated alternative for most of the manual design efforts, effectively superseding it as a faster and more accurate design methodology. Because Complementary Balanced Energy Harvesting covers each step in the design process, applying it to new systems is straight-forward and less prone to human error. The harvester model developed for this purpose, parameterizing harvester behavior as a product of maximum power output, size, and efficiency, splits the design effort in 8 distinctly different and manageable tasks:

1. Characterization of the maximum power output under different environmental conditions was automated using specialized benchmarking apparatus for each type of energy harvester. The benchmarking process is automated, requiring no manual labor except for mounting each harvester in the device, and removing it again after the benchmark process completed. Rather than complex formulas attempting to replicate the behavior of harvesters as scientifically correct as possible, the output of the benchmarks is numeric data. This allows an easy comparison of harvester performance. The designs for testing photovoltaic cells, TEGs/TECs, and piezoelectric transducers were presented as a proof-of-concept in chapter 5.

2. Harvester performance acquired through benchmarking can be stored numerically and combined into datasets per harvester type. A mathematical model was presented in chapter 5 to synthesize harvester performance as 1, 2 or 5-dimensional data structures for photovoltaics, thermoelectrics and piezoelectrics, respectively. A scalable database structure was introduced for this purpose, with the potential to become a shared resource among embedded systems designers so that harvesters only need to be characterized once, after which they remain available in the dataset for all to use.

3. The ambient environment in which the system is intended to be deployed can now be measured automatically using the hardware and software developed in the Ambient Energy Monitor project. The AEM Core, complemented by AEM Modules for various types of ambient energy, is able to benchmark the ambient environment autonomously. The compact and modular topology of the AEM makes it a convenient portable solution that can be installed effortlessly in nearly any environment imaginable. The collected ambient energy data follows the same structure as datasets in the harvester performance database, enabling algorithms to determine which harvesters fit best in a specific environment.

4. While Complementary Balanced Energy Harvesting works with a single harvester, it was conceived from the start as a method to combine different harvesters together, potentially eliminating the need for local energy storage completely. The mathematical models presented in chapter 4 demonstrate feasibility of the approach, and illustrate the advantages with real-world examples. Combining datasets of harvester performance and available ambient energy allows direct computation of the individual gain of each harvester, optimizing the harvester configuration in an iterative process that can also be completely automated.

5. As a secondary function, the AEM Modules each support external energy harvesters to be measured alongside ambient energy. Although optional in functionality, it provides a shortcut in the design methodology if the type of harvester is already known in advance. The design process can immediately proceed with dimensioning, since accurate harvester efficiency is calculated over the entire duration of the environmental benchmarking cycle. Using a switched power path, the harvester can be tested with different DC/DC converters and maximum power point trackers directly.

6. After the selection of one harvester or multiple harvesters in a complementary balanced configuration, their size can be calculated. The energy balance model presented in chapter 4 can be used to dimension harvester sizes algorithmically, with or without local energy storage. The energy budget of the powered system, either measured or calculated following the guidelines discussed in chapter 6, can be matched to the harvester profiles, obtaining the most optimal sizes for each harvester.

7. If the minimum harvester size predicted by the model is larger than is convenient, the choice can be made for local storage. Chapter 6 compared several possible storage media, including non-rechargeable batteries, solid-state and thin-film batteries, and EDLCs. Calculation of the required storage capacity was integrated in the energy balance, to make the inclusion of local storage in the design transparent from the designer's perspective.

8. The only manual effort in the design of the autonomous application is the layout of the power path between harvester(s) and the system it powers. Depending on the complexity of the design, several optimizations may be possible using switched power rails and parallel DC/DC converters. The Complementary Balanced Energy Harvesting design methodology also provides assistance in this stage, by measuring performance of different power path configurations on AEM modules, and comparing the performance of DC/DC converters as explained in chapter 6.

Whereas design efforts before the introduction of Complementary Balanced Energy Harvesting required embedded systems designers to have a good knowledge of the available energy harvesting technologies, physical characteristics of environments and so on, the design procedure is now almost completely automated and scalable. Instead of a lengthy manual design process, Complementary Balanced Energy Harvesting splits the problem into different parts and solves them sequentially by applying algorithms to numeric data obtained throughout the different steps. Almost no knowledge about the physics of energy harvesters is required to reach usable results by applying the Complementary Balanced Energy Harvesting design process. This advantage has far reaching consequences: energy harvesting as an alternative to batteries now becomes available to all electronics designers, instead of only a few well informed experts on the matter. The quality of the solutions no longer depends on the knowledge and experience of the designer, but on the volume of datasets algorithms can build solutions with. The more Complementary Balanced Energy Harvesting as a design methodology is used, the larger the collection of harvester performance datasets grows, and the better designs algorithms can suggest. Harvester energy payback and environmental costs are factored in automatically, rather than being an afterthought as was often the case

before Complementary Balanced Energy Harvesting.

Countless applications for Complementary Balanced Energy Harvesting are readily available, particularly where autonomous systems with a long lifetime are unable to be wired to a power network, or too expensive to be wired to a power network. Sensor and detection systems, monitoring and control modules etc. are prime examples of small embedded systems that have modest energy needs. Chapter 6 also demonstrated that Complementary Balanced Energy Harvesting can just as well be applied to autonomous systems with an average power consumption ranging from W to kW order of magnitude. There are no limitations regarding power levels in the mathematical harvester or energy balance models, and they can be scaled up to any power level required. DC/DC converters with power outputs ranging from mW to 60 W were discussed in chapter 6 to interface systems with higher power demands than conventional energy harvesting powered systems. This opens up the potential to convert a previously untapped range of applications to decentralized energy harvesting. Sustainable and renewable energy technologies, be it on a megawatt or milliwatt scale, will fulfill a central role in the sustainable economic models of the future, in which Complementary Balanced Energy Harvesting will play an important role. The single most important conclusion of this thesis is perhaps: **any electronic system can be made wireless and autonomous using energy harvesting**, provided there is sufficient space to install energy harvesters, and environmental energy is available. In other words, one should not ask the question *if* it is possible to power a system with energy harvesting, but rather which harvesters are best suited to make that happen, and how large they physically need to be.

The journey towards a society with autonomous electronics without batteries has only just begun, and a lot of work still remains to be done. Because photovoltaics, thermoelectics and piezoelectrics currently offer the best potential as energy harvesters, most of the examples were emphasizing these harvester types. Only for these types does appropriate benchmarking apparatus currently exist, as discussed in chapter 5, so new hardware needs to be developed to characterize micro turbines for water and wind, RF energy harvesters, TENGs, and so on. The rudimentary database needs to be expanded to accommodate these new harvester datasets, and be rolled out to a crowd sourced, globally accessible knowledge base on energy harvester performance. New peer-to-peer network technologies such as blockchain offer opportunities to share and contribute to such databases while simultaneously preserving authenticity of the data itself. The datasets of DC/DC converters and energy storage media also need to be expanded and published, possibly reaching out to energy harvester, semiconductor and capacitor manufacturers to take their responsibility in providing datasets in a similar manner they already provide circuit board footprints for their parts. A lot of work remains to be done for the AEM project as well: existing modules need thorough testing, and a community needs to be built around AEM to support, maintain and expand the existing open source hardware and software frameworks. AEM modules for other types of ambient energy such as wind or motion need to be developed and added to the inventory of 4 existing AEM modules. The Ambient Energy Monitor remains only relevant as long as the hardware it is built on is up-to-date with the latest industry developments. Empowering the energy harvesting community to disseminate the technology of the AEM resources and build upon their foundations to create the hardware and software tools to support Complementary Balanced Energy Harvesting into the future, remains perhaps the most important work to be done.

List of Publications

2017 **Analysis of Thermoelectric Coolers as Energy Harvesters for Low Power Embedded Electronic Applications**, Verbelen Y. et al., Int. Journal of Energy and Power Engineering, vol. 4, no. 3, p.310-319, 2017.

2016 **Automated Test Chamber for Indoor Photovoltaics**, Verbelen Y. et al., 5th Int. Conf. on Renewable Energy Research and Applications (ICRERA), p. 143-148, 2016.

2016 **Parametrization of Piezoelectric Vibration Energy Harvesters for Low Power Embedded Systems**, Verbelen Y. et al., Int. Journal of Electrical, Computer, Energetic, Electronic and Communications Engineering, vol. 10, no. 6, p. 798-805, 2016.

2014 **Resource Considerations for Durable Large Scale Renewable Energy Harvesting Applications**, Verbelen Y. et al., 2nd Int. Conf. on Renewable Energy Research and Applications, p. 401-406, 2014.

2014 **Towards a Complementary Balanced Energy Harvesting Solution for Low Power Embedded Systems**, Verbelen Y. et al., Microsystem Technologies, vol. 20, no. 4, p. 1007-1021, 2014.

2013 **Parametrization of Ambient Energy Harvesters for Complementary Balanced Electronic Applications**, Verbelen Y. et al., Smart Sensors, Actuators and MEMS IV, vol. 8763, 2013.

Bibliography

[1] M. M. Ababneh, S. Perez, H. Cabra, and S. Thomas, *Design of a novel mini notched turbine with optimized power management circuit*, 2017 8th International Renewable Energy Congress (IREC), March 2017, pp. 1–6.

[2] M. A. Abouzied, K. Ravichandran, and E. Sánchez-Sinencio, *A Fully Integrated Reconfigurable Self-Startup RF Energy-Harvesting System With Storage Capability*, IEEE Journal of Solid-State Circuits **52** (2017), no. 3, 704–719.

[3] B. Achzet, A. Reller, V. Zepf, C. Rennie, and M. Ashfield, *Materials critical to the energy industry - An introduction*, Tech. report, University of Ausburg, 2011.

[4] James Adams, *Emergency Medicine: Clinical Essentials*, 2 ed., Saunders, September 2012.

[5] Mr Nikunj Adroja, Prof Shruti B.Mehta, and Mr Pratik Shah, *Review of thermoelectricity to improve energy quality*, vol. Vol. 2 - Issue 3 (March-2015), JETIR, March 2015.

[6] Muhammad Alkali, Mohamed Edries, Arifur Khan, Masui Hirokazu, and Minkwon Cho, *Preliminary Study of Electric Double Layer Capacitor as an Energy Storage of Simple Nanosatellite Power System*, October 2014.

[7] Erik W. Allen, *Process water treatment in Canadas oil sands industry: Target pollutants and treatment objectives*, Journal of Environmental Engineering and Science **7** (2008), no. 2, 123–138.

[8] E. Alsema, *Energy Requirements and CO_2 Mitigation Potential of PV Systems*, Photovoltacis and the Environment, Workshop Proceedings, July 1998.

[9] Véronique Amstutz, Kathryn E. Toghill, Francis Powlesland, Heron Vrubel, Christos Comninellis, Xile Hu, and Hubert H. Girault, *Renewable hydrogen generation from a dual-circuit redox flow battery*, Energy & Environmental Science **7** (2014), no. 7, 2350–2358.

[10] John Androulakis, Chia-Her Lin, Hun-Jin Kong, Ctirad Uher, Chun-I Wu, Timothy Hogan, Bruce A. Cook, Thierry Caillat, Konstantinos M. Paraskevopoulos, and Mercouri G. Kanatzidis, *Spinodal Decomposition and Nucleation and Growth as a Means to Bulk Nanostructured Thermoelectrics: Enhanced Performance in Pb1-xSnxTe-PbS*, Journal of the American Chemical Society **129** (2007), no. 31, 9780–9788.

[11] G. B. Ansell, M. A. Modrick, J. M. Longo, K. R. Poeppeimeler, and H. S. Horowitz, *Structure of calcium manganese oxide $Ca_2Mn_3O_8$*, Acta Crystallographica Section B: Structural Crystallography and Crystal Chemistry **38** (1982), no. 6, 1795–1797.

[12] Sebastian Anthony, *Freevolt: Perpetual, free RF energy harvesting to power the Internet of Things*, September 2015.

[13] Yoichi Aoki, *Photovoltaic performance of Organic Photovoltaics for indoor energy harvester*, Organic Electronics **48** (2017), no. Supplement C, 194–197.

[14] Pietro Apostoli and Simona Catalani, *Metal ions affecting reproduction and development*, Metal Ions in Life Sciences **8** (2011), 263–303.

[15] Natalie B. Aquino, Mary B. Sevigny, Jackielyn Sabangan, and Maggie C. Louie, *The role of cadmium and nickel in estrogen receptor signaling and breast cancer: metalloestrogens or not?*, Journal of Environmental Science and Health. Part C, Environmental Carcinogenesis & Ecotoxicology Reviews **30** (2012), no. 3, 189–224.

[16] Arenst Andreas Arie and Joong Kee Lee, *Preparation of Capacitor's Electrode from Coconut Shell*, Advanced Materials Research **875-877** (2014), 1585–1589.

[17] Arveni, *T. Rex: Most Powerful Vibration Energy Harvester*, 2013.

[18] John Asafu-Adjaye and Dominic Byrne, *Dataset for analysing the relationships among economic growth, fossil fuel and non-fossil fuel consumption*, Data in Brief **10** (2017), no. Supplement C, 17–19.

[19] John Asafu-Adjaye, Dominic Byrne, and Maximiliano Alvarez, *Economic growth, fossil fuel and non-fossil consumption: A Pooled Mean Group analysis using proxies for capital*, Energy Economics **60** (2016), no. Supplement C, 345–356.

[20] Daniel D. Athayde, Douglas F. Souza, Alysson M. A. Silva, Daniela Vasconcelos, Eduardo H. M. Nunes, o C. Diniz da Costa, JoãLeBoulbar, and Wander L. Vasconcelos, *Review of perovskite ceramic synthesis and membrane preparation methods*, Ceramics International **42** (2016), no. 6, 6555–6571.

[21] Ezzat G. Bakhoum, *Very high energy-density ultracapacitor apparatus and method*, April 2016, International Classification H01G9/145, H01G9/00, H01G9/15, H01G9/04; Cooperative Classification Y02T10/7022, H01G11/86, H01G11/82, H01G11/46, H01G11/32, H01G11/26, Y02E60/13, H01G9/15, H01G9/155.

[22] D. Balan and A. Chirap, *Analysis of an eco-friendly sensor node powered by unconventional energy sources*, 2014 RoEduNet Conference 13th Edition: Networking in Education and Research Joint Event RENAM 8th Conference, September 2014, pp. 1–4.

[23] Edward B. Barbier, *The Concept of Sustainable Economic Development*, Environmental Conservation **14** (1987), no. 2, 101–110.

[24] G. Bathree, *Protocols/code for controlling the Photosynq device*, January 2017, original-date: 2013-07-24T14:34:51Z.

[25] Davy Van Belle, *Development of a modular test environment for low power indoor photovoltaic cells*, unpublished thesis, 2014.

[26] Brian Benchoff, *Crowdfunding Follies: Debunking The Batteriser*, June 2015.

[27] Gary Bennett, *Space Nuclear Power: Opening the Final Frontier*, 4th International Energy Conversion Engineering Conference and Exhibit (IECEC) (San Diego, CA), American Institute of Aeronautics and Astronautics, June 2006, DOI: 10.2514/6.2006-4191.

[28] Gary L. Bennett, Richard J. Hemler, and Alfred Schock, *Space nuclear power - An overview*, Journal of Propulsion and Power **12** (1996), no. 5, 901–910.

[29] Sophia Bennett, *How to Recycle Fibreglass*, Recycle Nation (2014).

[30] Wolfgang Berger, Franz-Georg Simon, Karin Weimann, and Erik A. Alsema, *A novel approach for the recycling of thin film photovoltaic modules*, Resources, Conservation and Recycling **54** (2010), no. 10, 711–718.

[31] Martin Bertau, Heribert Offermanns, Ludolf Plass, Friedrich Schmidt, and Hans-Jürgen Wernicke, *Methanol: The Basic Chemical and Energy Feedstock of the Future*, Springer-Verlag Berlin Heidelberg, 2014.

[32] P. Besson, P. McVey White, C. Dominguez, P. Voarino, P. Garcia-Linares, M. Lemiti, H. Schriemer, K. Hinzer, and M. Baudrit, *Spectrally-resolved measurement of concentrated light distributions for Fresnel lens concentrators*, Optics Express **24** (2016), no. 2, A397–A407.

[33] Joseph Bevelacqua, *Antenna arrays: performance limits and geometry optimization*, Ph.D. thesis, Arizona State University, May 2008.

[34] Donald I. Bleiwas, *Byproduct mineral commodities used for the production of photovoltaic cells*, USGS Numbered Series 1365, U.S. Geological Survey, 2010.

[35] Ingolfur Blühdorn, *Sustaining the unsustainable: Symbolic politics and the politics of simulation*, Environmental Politics **16** (2007), no. 2, 251–275.

[36] D. Bol, E. H. Boufouss, D. Flandre, and J. De Vos, *A 0.48mm^2 5 μW-10mW indoor/outdoor PV energy-harvesting management unit in a 65nm SoC based on a single bidirectional multi-gain/multi-mode switched-cap converter with supercap storage*, ESSCIRC Conference 2015 - 41st European Solid-State Circuits Conference (ESSCIRC), September 2015, pp. 241–244.

[37] U. Bossel, *Does a Hydrogen Economy Make Sense?*, Proceedings of the IEEE **94** (2006), no. 10, 1826–1837.

[38] Katherine Bourzac, *A 25-Year Battery*, November 2009.

[39] C. R. Bowen, J. Taylor, E. Le Boulbar, D. Zabek, and V. Yu. Topolov, *A modified figure of merit for pyroelectric energy harvesting*, Materials Letters **138** (2015), no. Supplement C, 243–246.

[40] C. R. Bowen, J. Taylor, E. LeBoulbar, D. Zabek, A. Chauhan, and R. Vaish, *Pyroelectric materials and devices for energy harvesting applications*, Energy & Environmental Science **7** (2014), no. 12, 3836–3856.

[41] Michael Boxwell, *The Solar Electricity Handbook - 2017 Edition: A simple, practical guide to solar energy - designing and installing solar photovoltaic systems.*, Greenstream Publishing, January 2017, Google-Books-ID: ko5cMQAACAAJ.

[42] Brian A Boye, Roger A Falconer, and Kunle Akande, *Integrated water management solutions from cloud to coast: application to ribble basin*, Proceedings of the 35th IAHR World Congress, vol. 4, IAHR Chengdu, China, 2013, p. 1e12.

[43] Kent Britain, *Designing PCB Log Periodic Antennas*, Tech. report, 2008.

[44] Andrew S. Brown and Martin A. Green, *Impurity photovoltaic effect: Fundamental energy conversion efficiency limits*, Journal of Applied Physics **92** (2002), no. 3, 1329–1336.

[45] Bruno Bruger, Klaus Kiefer, Christoph Kost, Sebastian Nold, Simon Philipps, Ralf Preu, Jochen Rentsch, Thomas Schlegl, Gerhard Stryi-Hipp, Gerhard Willeke, Harry Wirth, Ingo Brucker, Andreas HÃd'berle, and Werner Warmuth, *Photovoltaics Report*, Tech. report, Fraunhofer Institute for Solar Energy Systems, ISE, Freiburg, July 2017.

[46] A. Buonanno, M. D'Urso, and D. Pavone, *An ultra wide-band system for RF Energy harvesting*, Proceedings of the 5th European Conference on Antennas and Propagation (EUCAP), April 2011, pp. 388–389.

[47] Paul Burgess, *Variation in Light Intensity at Different Latitutes and Seasons, Effects of Cloud Cover, and the Amounts of Direct and Diffused Light*, September 2009.

[48] E. A. J Burke and C Kieft, *Second occurrence of makedonite, $PbTiO_3$, Långban, Sweden*, Lithos **4** (1971), no. 2, 101–104.

[49] S. Butera, M. D. C. Whitaker, A. B. Krysa, and A. M. Barnett, *Investigation of a temperature tolerant InGaP (GaInP) converter layer for a ^{63}Ni betavoltaic cell*, Journal of Physics D: Applied Physics **50** (2017), no. 34, 345101.

[50] Sabah K. Bux, Michael T. Yeung, Eric S. Toberer, G. Jeffrey Snyder, Richard B. Kaner, and Jean-Pierre Fleurial, *Mechanochemical synthesis and thermoelectric properties of high quality magnesium silicide*, Journal of Materials Chemistry **21** (2011), no. 33, 12259–12266.

[51] Brown William C, George Roscoe H, Heenan Neil I, and Wonson Roger C, *Microwave to dc converter*, March 1969, U.S. Classification 244/158.1, 244/1.00R, 307/151, 191/1.00R, 318/16; International Classification H02M11/00, H02J17/00; Cooperative Classification H02M11/00, H02J17/00; European Classification H02M11/00, H02J17/00.

[52] Renato Caliò, Udaya Bhaskar Rongala, Domenico Camboni, Mario Milazzo, Cesare Stefanini, Gianluca de Petris, and Calogero Maria Oddo, *Piezoelectric Energy Harvesting Solutions*, Sensors **14** (2014), no. 3, 4755–4790.

[53] José Rui Camargo and Maria Claudia Costa de Oliveira, *Principles of Direct Thermoelectric Conversion*, (2011).

[54] Yuliang Cao, Lifen Xiao, Maria L. Sushko, Wei Wang, Birgit Schwenzer, Jie Xiao, Zimin Nie, Laxmikant V. Saraf, Zhengguo Yang, and Jun Liu, *Sodium Ion Insertion in Hollow Carbon Nanowires for Battery Applications*, Nano Letters **12** (2012), no. 7, 3783–3787.

[55] J. M. Carrasco, L. G. Franquelo, J. T. Bialasiewicz, E. Galvan, R. C. PortilloGuisado, M. A. M. Prats, J. I. Leon, and N. Moreno-Alfonso, *Power-Electronic Systems for the Grid Integration of Renewable Energy Sources: A Survey*, IEEE Transactions on Industrial Electronics **53** (2006), no. 4, 1002–1016.

[56] Vinod R. Challa, M. G. Prasad, Yong Shi, and Frank T. Fisher, *A vibration energy harvesting device with bidirectional resonance frequency tunability*, Smart Materials and Structures **17** (2008), no. 1, 015035.

[57] M. V. S. Chandrashekhar, Christopher I. Thomas, Hui Li, M. G. Spencer, and Amit Lal, *Demonstration of a 4h SiC betavoltaic cell*, Applied Physics Letters **88** (2006), no. 3, 033506.

[58] Chieh Chang, Van H. Tran, Junbo Wang, Yiin-Kuen Fuh, and Liwei Lin, *Direct-Write Piezoelectric Polymeric Nanogenerator with High Energy Conversion Efficiency*, Nano Letters **10** (2010), no. 2, 726–731.

[59] Ming-Hui Chang, Han-Pang Huang, and Shu-Wei Chang, *A New State of Charge Estimation Method for $LiFePO_4$ Battery Packs Used in Robots*, Energies **6** (2013), no. 4, 2007–2030.

[60] Min Chen and G. A. Rincon-Mora, *Accurate electrical battery model capable of predicting runtime and I-V performance*, IEEE Transactions on Energy Conversion **21** (2006), no. 2, 504–511.

[61] Shu Wen Chen, Xia Cao, Ning Wang, Long Ma, Hui Rui Zhu, Magnus Willander, Yang Jie, and Zhong Lin Wang, *An Ultrathin Flexible Single-Electrode Triboelectric-Nanogenerator for Mechanical Energy Harvesting and Instantaneous Force Sensing*, Advanced Energy Materials **7** (2017), no. 1.

[62] Yana Chervona, Adriana Arita, and Max Costa, *Carcinogenic metals and the epigenome: understanding the effect of nickel, arsenic, and chromium*, Metallomics: Integrated Biometal Science **4** (2012), no. 7, 619–627.

[63] Adrian Chirila, Stephan Buecheler, Fabian Pianezzi, Patrick Bloesch, and Christina Gretener, *Highly efficient Cu(In,Ga)Se_2 solar cells grown on flexible polymer films*, Nature Materials **10** (2011), no. 11, 857–861.

[64] P. T. Chiu, D. C. Law, R. L. Woo, S. B. Singer, D. Bhusari, W. D. Hong, A. Zakaria, J. Boisvert, S. Mesropian, R. R. King, and N. H. Karam, *35.8% space and 38.8% terrestrial 5j direct bonded cells*, 2014 IEEE 40th Photovoltaic Specialist Conference (PVSC), June 2014, pp. 0011–0013.

[65] A Young Choi, Chang Jun Lee, Jiwon Park, Dogyun Kim, and Youn Tae Kim, *Corrugated Textile based Triboelectric Generator for Wearable Energy Harvesting*, Scientific Reports **7** (2017).

[66] In Chung, Byunghong Lee, Jiaqing He, Robert P. H. Chang, and Mercouri G. Kanatzidis, *All-solid-state dye-sensitized solar cells with high efficiency*, Nature **485** (2012), no. 7399, 486–489.

[67] Elif Şahin, Mustafa Şahin, Yüksel Oğuz, and Yilmaz Güven, *Analyses of Nuclear Power Plant Waste In Terms of Environmental Policies*, El-Cezeri Journal of Science and Engineering **3** (2016), no. 3.

[68] A. Cuadras, M. Gasulla, and V. Ferrari, *Thermal energy harvesting through pyroelectricity*, Sensors and Actuators A: Physical **158** (2010), no. 1, 132–139.

[69] Angel Cuadras, *Pyroelectric conversion: harvesting energy from temperature fluctuations*, January 2007.

[70] Canan Dagdeviren, Zhou Li, and Zhong Lin Wang, *Energy Harvesting from the Animal/Human Body for Self-Powered Electronics*, Annual Review of Biomedical Engineering **19** (2017), no. 1, 85–108.

[71] Dragan Damjanovic, *Ferroelectric, dielectric and piezoelectric properties of ferroelectric thin films and ceramics*, Reports on Progress in Physics **61** (1998), no. 9, 1267.

[72] Prithiviraj Damodaran, *Invisible Innovation with Micro-energy harvesting*, September 2014.

[73] K. K. Das, S. N. Das, and S. A. Dhundasi, *Nickel, its adverse health effects & oxidative stress*, The Indian Journal of Medical Research **128** (2008), no. 4, 412–425.

[74] Leonard David, *50 Years of Nuclear-Powered Spacecraft: It All Started with Satellite Transit 4a*, Space.com (2011).

[75] Katherine Derbyshire, *Wafer-based Solar Cells Aren't Done Yet*, Renewable Energy World (2009).

[76] Valerio DiInnocenzo, Ajay Ram Srimath Kandada, Michele De Bastiani, Marina Gandini, and Annamaria Petrozza, *Tuning the Light Emission Properties by Band Gap Engineering in Hybrid Lead Halide Perovskite*, Journal of the American Chemical Society **136** (2014), no. 51, 17730–17733.

[77] Jefferson Dixon, Aravindh Rajan, Steven Bohlemann, Dusan Coso, Ajay D. Upadhyaya, Ajeet Rohatgi, Steven Chu, Arun Majumdar, and Shannon Yee, *Evaluation of a Silicon ^{90}Sr Betavoltaic Power Source*, Scientific Reports **6** (2016), srep38182.

[78] Brian Dodson, *New lithium/sulfur battery doubles energy density of lithium-ion*, Tech. report, December 2013.

[79] AG Drachmann, *Heron's windmill*, Centaurus **7** (1961), no. 2, 145–151.

[80] Swapnil Dubey, Jatin Narotam Sarvaiya, and Bharath Seshadri, *Temperature Dependent Photovoltaic (PV) Efficiency and Its Effect on PV Production in the World - A Review*, Energy Procedia **33** (2013), no. Supplement C, 311–321.

[81] Jeffrey S. Dukes, *Burning Buried Sunshine: Human Consumption of Ancient Solar Energy*, Climatic Change **61** (2003), no. 1-2, 31–44.

[82] B.W. Eakins and G.F. Sharman, *Volumes of the World's Oceans from ETOPO1*, Tech. report, NOAA National Geophysical Data Center, Boulder, CO, 2010.

[83] Betul Bektas Ekici, *A least squares support vector machine model for prediction of the next day solar insolation for effective use of PV systems*, Measurement **50** (2014), no. Supplement C, 255–262.

[84] Karin M. Ekström, *Waste Management and Sustainable Consumption: Reflections on Consumer Waste*, Routledge, December 2014, Google-Books-ID: GXLfBQAAQBAJ.

[85] H. M. El-Shafei, *Assessment of liver function among nickel-plating workers in Egypt*, Eastern Mediterranean Health Journal **17** (2011), no. 6, 490–494.

[86] John Emsley, *Nature's Building Blocks: An A-Z Guide to the Elements*, OUP Oxford, August 2011, Google-Books-ID: 2EfYXzwPo3UC.

[87] A. Ö Ercan, O. Sunay, and I. F. Akyildiz, *RF Energy Harvesting and Transfer for Spectrum Sharing Cellular IoT Communications in 5G Systems*, IEEE Transactions on Mobile Computing **PP** (2017), no. 99.

[88] Bozena Erdmann, Bas Willibrord De Wit, Armand Michel Marie Lelkens, Arthur Robert Van Es, and Ludovicus Marinus Gerardus Maria Tolhuizen, *Electro-mechanical energy harvesting switch*, January 2017, International Classification H01H13/50, H02K7/18; Cooperative Classification H02K7/1853, H01H2239/076, Y10T307/977, H01H13/50, H02K7/1892.

[89] A. Erkan, Seyit O. Ural Gurdal, Hwi-Yeol Park, Sahn Nahm, and Kenji Uchino, *High Power ($Na_{0.5}K_{0.5}$)NbO_3-Based Lead-Free Piezoelectric Transformer*, Japanese Journal of Applied Physics **50** (2011), no. 2R, 027101.

[90] A. Erturk, J. Hoffmann, and D. J. Inman, *A piezomagnetoelastic structure for broadband vibration energy harvesting*, Applied Physics Letters **94** (2009), no. 25, 254102.

[91] Verbelen Yannick et al., *Manufacturing electronics: how to do it fast and low-cost*, August 2015.

[92] M.A. Ezzat, *Impact of a future Qattara salt-water lake on the Nubian Sandstone aquifer system in the Western Desert, Egypt*, Proceedings of the Exeter Symposium on Improvements of Methods of Long Term Prediction of Variations in Groundwater Resources and Regimes Due to Human Activity, vol. 136, July 1982, pp. 297–314.

[93] Arturo Fajardo Jaimes and Fernando Rangel de Sousa, *Simple modeling of photovoltaic solar cells for indoor harvesting applications*, Solar Energy **157** (2017), no. Supplement C, 792–802.

[94] Feng-Ru Fan, Zhong-Qun Tian, and Zhong Lin Wang, *Flexible triboelectric generator*, Nano Energy (2012).

[95] Xinming Fan, Zhanhong Yang, Runjuan Wen, Bin Yang, and Wei Long, *The application of Zn-Al-hydrotalcite as a novel anodic material for Ni-Zn secondary cells*, Journal of Power Sources **224** (2013), no. Supplement C, 80–85.

[96] M. Fantuzzi, D. Masotti, and A. Costanzo, *A Novel Integrated UWB and UHF One-Port Antenna for Localization and Energy Harvesting*, IEEE Transactions on Antennas and Propagation **63** (2015), no. 9, 3839–3848.

[97] Amir Yadollah Faraji and Aliakbar Akbarzadeh, *Design of a Compact, Portable Test System for Thermoelectric Power Generator Modules*, Journal of Electronic Materials **42** (2013), no. 7, 1535–1541.

[98] R. A. Fernando, *Strategic Corporate Sustainability - Key Approaches for Creating Strategies for Environmental Sustainability*, Vision **21** (2017), no. 2, vii–ix.

[99] N. Flourentzou, V. G. Agelidis, and G. D. Demetriades, *VSC-Based HVDC Power Transmission Systems: An Overview*, IEEE Transactions on Power Electronics **24** (2009), no. 3, 592–602.

[100] Zsolt Forgacs, Peter Massányi, Norbert Lukac, and Zoltan Somosy, *Reproductive toxicology of nickel - review*, Journal of Environmental Science and Health. Part A, Toxic/Hazardous Substances & Environmental Engineering **47** (2012), no. 9, 1249–1260.

[101] Kyriaki Fotopoulou and Brian W. Flynn, *Wireless Power Transfer in Loosely Coupled Links: Coil Misalignment Model*, IEEE Transactions on Magnetics **47** (2011), no. 2, 15.

[102] Hannah Francis, *Batteriser battery life extender: scam or saviour?*, The Sydney Morning Herald (2015).

[103] Michael Freunek, Monika Müller, Tolgay Ungan, William Walker, and Leonhard M. Reindl, *New Physical Model for Thermoelectric Generators*, Journal of Electronic Materials **38** (2009), no. 7, 1214–1220.

[104] Vasilis M. Fthenakis, *End-of-life management and recycling of PV modules*, Energy Policy **28** (2000), no. 14, 1051–1058.

[105] Vasilis M Fthenakis, *Life cycle impact analysis of cadmium in CdTe PV production*, Renewable and Sustainable Energy Reviews **8** (2004), no. 4, 303–334.

[106] Vasilis M. Fthenakis and Hyung Chul Kim, *CdTe photovoltaics: Life cycle environmental profile and comparisons*, Thin Solid Films **515** (2007), no. 15, 5961–5963.

[107] Chenguang Fu, Shengqiang Bai, Yintu Liu, Yunshan Tang, Lidong Chen, Xinbing Zhao, and Tiejun Zhu, *Realizing high figure of merit in heavy-band i-type half-Heusler thermoelectric materials*, Nature Communications **6** (2015), ncomms9144.

[108] Tiezheng Fu, Xianqiang Yue, Haijun Wu, Chenguang Fu, Tiejun Zhu, Xiaohua Liu, Lipeng Hu, Pingjun Ying, Jiaqing He, and Xinbing Zhao, *Enhanced thermoelectric performance of PbTe bulk materials with figure of merit zT >2 by multi-functional alloying*, Journal of Materiomics **2** (2016), no. 2, 141–149.

[109] Ryoji Funahashi and Masahiro Shikano, *$Bi_2Sr_2Co_2O_y$ whiskers with high thermoelectric figure of merit*, Applied Physics Letters **81** (2002), no. 8, 1459–1461.

[110] Kishor Purushottam Gadkaree and Atul Kumar, *High voltage EDLC electrodes containing CO_2 activated coconut char*, April 2016, International Classification H01G11/24, C01B31/10, H01G11/44, H01G11/34; Cooperative Classification C01B32/336, C01B32/30, C01P2006/16, Y02E60/13, C01P2004/61, H01G11/34, H01G11/24, H01G11/44, C01P2006/14, C01B31/10.

[111] Moacir Gadotti, *Education for sustainability - A critical contribution to the Decade of Education for Sustainable Development*, (2016).

[112] Iwona Gajda, John Greenman, Chris Melhuish, and Ioannis Ieropoulos, *Small Scale Ceramic MFCs for Efficient Energy Harvesting from Wastewater and Full System Development*, Meeting Abstracts **MA2016-01** (2016), no. 36, 1796–1796.

[113] A. Ghazanfari, H. Tabassum, and E. Hossain, *Ambient RF energy harvesting in ultra-dense small cell networks: performance and trade-offs*, IEEE Wireless Communications **23** (2016), no. 2, 38–45.

[114] G. Godillot, P. L. Taberna, B. Daffos, P. Simon, C. Delmas, and L. Guerlou-Demourgues, *High power density aqueous hybrid supercapacitor combining activated carbon and highly conductive spinel cobalt oxide*, Journal of Power Sources **331** (2016), no. Supplement C, 277–284.

[115] Lewis Gomez De Arco, Yi Zhang, Cody W. Schlenker, Koungmin Ryu, Mark E. Thompson, and Chongwu Zhou, *Continuous, Highly Flexible, and Transparent Graphene Films by Chemical Vapor Deposition for Organic Photovoltaics*, ACS Nano **4** (2010), no. 5, 2865–2873.

[116] T. E. Graedel, E. M. Harper, N. T. Nassar, Philip Nuss, Barbara K. Reck, and B. L. Turner, *Criticality of metals and metalloids*, Proceedings of the National Academy of Sciences of the United States of America **112** (2015), no. 14, 4257–4262.

[117] Pascal Granger, Vasile I. Parvulescu, Serge Kaliaguine, and Wilfrid Prellier, *Perovskites and Related Mixed Oxides: Concepts and Applications*, Wiley, January 2016.

[118] Martin A. Green, Keith Emery, Yoshihiro Hishikawa, Wilhelm Warta, Ewan D. Dunlop, Dean H. Levi, and Anita W. Y. Ho-Baillie, *Solar cell efficiency tables (version 49)*, Progress in Photovoltaics: Research and Applications **25** (2017), no. 1, 3–13.

[119] Kevin Greene, *Technological innovation and economic progress in the ancient world: M. I. Finley re-considered*, The Economic History Review **53** (2000), no. 1, 29–59.

[120] Fang Guangyou, *New design of the antipodal Vivaldi antenna for a GPR system*, Microwave and Optical Technology Letters **44** (2005), no. 2, 136–139.

[121] Hang Guo and A. Lal, *Nanopower betavoltaic microbatteries*, Transducers, Solid-State Sensors, Actuators and Microsystems, 12th International Conference on, 2003, vol. 1, June 2003, pp. 36–39 vol.1.

[122] Hengyu Guo, Zhen Wen, Yunlong Zi, Min-Hsin Yeh, Jie Wang, Liping Zhu, Chenguo Hu, and Zhong Lin Wang, *A Water-Proof TriboelectricâĂŞElectromagnetic Hybrid Generator for Energy Harvesting in Harsh Environments*, Advanced Energy Materials **6** (2016), no. 6.

[123] Ioannis Hadjipaschalis, Andreas Poullikkas, and Venizelos Efthimiou, *Overview of current and future energy storage technologies for electric power applications*, Renewable and Sustainable Energy Reviews **13** (2009), no. 6, 1513–1522.

[124] Salah El Haggar, *Sustainable Industrial Design and Waste Management: Cradle-to-Cradle for Sustainable Development*, Academic Press, July 2010, Google-Books-ID: smVRv6DYoYcC.

[125] Lester Haines, *iFind: Critics slam Kickstarter campaign for miraculous battery-free phone finder*, June 2014.

[126] Anna-Lena Hansen, Torben Dankwort, Markus Winkler, Jeffrey Ditto, Dave C. Johnson, Jan D. Koenig, Kilian Bartholomé, Lorenz Kienle, and Wolfgang Bensch, *Synthesis and Thermal Instability of High-Quality Bi_2Te_3/Sb_2Te_3 Superlattice Thin Film Thermoelectrics*, Chemistry of Materials **26** (2014), no. 22, 6518–6522.

[127] Benjamin J. Hansen, Ying Liu, Rusen Yang, and Zhong Lin Wang, *Hybrid Nanogenerator for Concurrently Harvesting Biomechanical and Biochemical Energy*, ACS Nano **4** (2010), no. 7, 3647–3652.

[128] T. C. Harman, M. P. Walsh, B. E. Laforge, and G. W. Turner, *Nanostructured thermoelectric materials*, Journal of Electronic Materials **34** (2005), no. 5, L19–L22.

[129] Barbara Harriss-White and Elinor Harriss, *Unsustainable Capitalism: The Politics of Renewable Energy in the UK*, Socialist Register **43** (2009), no. 43.

[130] Qing He, Xinhua Mao, and Dongliang Chu, *Output Performance Analysis on a Two-degrees-of-Freedom Bistable Piezoelectric Vibration Generator*, International Journal of Online Engineering (iJOE) **11** (2015), no. 6, 22–69.

[131] James R. Hein, Andrea Koschinsky, and Alex N. Halliday, *Global occurrence of tellurium-rich ferromanganese crusts and a model for the enrichment of tellurium*, Geochimica et Cosmochimica Acta **67** (2003), no. 6, 1117–1127.

[132] Jonathan E. Helmreich, *Gathering Rare Ores: The Diplomacy of Uranium Acquisition, 1943-1954*, Princeton University Press, July 2014, Google-Books-ID: 9vD_AwAAQBAJ.

[133] Joseph P. Heremans, Vladimir Jovovic, Eric S. Toberer, Ali Saramat, Ken Kurosaki, Anek Charoenphakdee, Shinsuke Yamanaka, and G. Jeffrey Snyder, *Enhancement of Thermoelectric Efficiency in PbTe by Distortion of the Electronic Density of States*, Science **321** (2008), no. 5888, 554–557.

[134] R. Hettich and K. O. Kortanek, *Semi-Infinite Programming: Theory, Methods, and Applications*, SIAM Review (2006).

[135] Allon I. Hochbaum, Renkun Chen, Raul Diaz Delgado, Wenjie Liang, Erik C. Garnett, Mark Najarian, Arun Majumdar, and Peidong Yang, *Enhanced thermoelectric performance of rough silicon nanowires*, Nature **451** (2008), no. 7175, 163–167.

[136] C. Honsberg, W. A. Doolittle, M. Allen, and C. Wang, *GaN betavoltaic energy converters*, Conference Record of the Thirty-first IEEE Photovoltaic Specialists Conference, 2005., January 2005, pp. 102–105.

[137] A. Hood, C. C. M. Gutjahr, and R. L. Heacock, *Organic Metamorphism and the Generation of Petroleum*, AAPG Bulletin **59** (1975), no. 6, 986–996.

[138] T. Hosono, Y. Matsuzawa, M. Kuramoto, Y. Momose, H. Tatsuoka, and H. Kuwabara, *Simple Fabrication of Mg2si Thermoelectric Generator*, Solid State Phenomena **93** (2003), 447–452.

[139] A. C. C. Hua and B. Z. W. Syue, *Charge and discharge characteristics of lead-acid battery and $LiFePO_4$ battery*, The 2010 International Power Electronics Conference - ECCE ASIA, June 2010, pp. 1478–1483.

[140] Mark Huggins, Robert E. McCracken, Jason P. Whitmire, and Mike Hornick, *Wireless power distribution system and method*, February 2016, International Classification H05B37/02, H02J7/02; Cooperative Classification H05B37/0218, H02J7/025.

[141] Pengfei Huo, Yang Liu, Ruiqi Na, Xingrui Zhang, Shuling Zhang, and Guibin Wang, *Quaternary ammonium functionalized poly(arylene ether sulfone)/poly(vinylpyrrolidone) composite membranes for electrical double-layer capacitors with activated carbon electrodes*, Journal of Membrane Science **505** (2016), no. Supplement C, 148–156.

[142] Junho Hwang, Sho Kataoka, Akira Endo, and Hirofumi Daiguji, *Enhanced energy harvesting by concentration gradient-driven ion transport in SBA-15 mesoporous silica thin films*, Lab on a Chip **16** (2016), no. 19, 3824–3832.

[143] Nextreme Thermal Solutions Inc., *eTEG HV37 Power Generator Datasheet*, 2012.

[144] Kashif Ishaque and Zainal Salam, *A review of maximum power point tracking techniques of PV system for uniform insolation and partial shading condition*, Renewable and Sustainable Energy Reviews **19** (2013), no. Supplement C, 475–488.

[145] Basel I. Ismail and Wael H. Ahmed, *Thermoelectric Power Generation Using Waste-Heat Energy as an Alternative Green Technology*, Recent Patents on Electrical & Electronic Engineering (Formerly Recent Patents on Electrical Engineering) **2** (2009), no. 1, 27–39.

[146] H. Jabbar, Y. S. Song, and T. T. Jeong, *RF energy harvesting system and circuits for charging of mobile devices*, IEEE Transactions on Consumer Electronics **56** (2010), no. 1, 247–253.

[147] Philip Jackson, Roland Würz, Dimitrios Hariskos, Erwin Lotter, Wolfram Witte, and Michael Powalla, *Effects of heavy alkali elements in Cu(In,Ga)Se_2 solar cells with efficiencies up to 22.6%*, Physica status solidi (RRL) - Rapid Research Letters **10** (2016), no. 8, 583–586.

[148] Bernard Jaffe, *Piezoelectric Ceramics*, Elsevier, December 2012, Google-Books-ID: GJC_MBEM4VMC.

[149] Steffen Jenner and Alberto J. Lamadrid, *Shale gas vs. coal: Policy implications from environmental impact comparisons of shale gas, conventional gas, and coal on air, water, and land in the United States*, Energy Policy **53** (2013), no. Supplement C, 442–453.

[150] Wenzhao Jia, Gabriela Valdés-Ramírez, Amay J. Bandodkar, Joshua R. Windmiller, and Joseph Wang, *Epidermal Biofuel Cells: Energy Harvesting from Human Perspiration*, Angewandte Chemie International Edition **52** (2013), no. 28, 7233–7236.

[151] Stella Job, *Recycling composites commercially*, Reinforced Plastics **58** (2014), no. 5, 32–38.

[152] David L. Jones, *uCurrent*, April 2009.

[153] Jong Hoon Jung, Minbaek Lee, Jung-Il Hong, Yong Ding, Chih-Yen Chen, Li-Jen Chou, and Zhong Lin Wang, *Lead-Free $NaNbO_3$ Nanowires for a High Output Piezoelectric Nanogenerator*, ACS Nano **5** (2011), no. 12, 10041–10046.

[154] G. D. Kamalapur and R. Y. Udaykumar, *Rural electrification in India and feasibility of Photovoltaic Solar Home Systems*, International Journal of Electrical Power & Energy Systems **33** (2011), no. 3, 594–599.

[155] N.S. Kardeshev, *On the inevitability and the possible structures of supercivilizations*, Proceedings of the Symposium: Search for Extraterrestrial Life: Recent Developments (Boston, MA), June 1984, pp. 497–504.

[156] Yukitoshi Kashimoto, Kyoji Hata, Hirohiko Suwa, Manato Fujimoto, Yutaka Arakawa, Takeya Shigezumi, Kunihiro Komiya, Kenta Konishi, and Keiichi Yasumoto, *Low-cost and Device-free Activity Recognition System with Energy Harvesting PIR and Door Sensors*, Adjunct Proceedings of the 13th International Conference on Mobile and Ubiquitous Systems: Computing Networking and Services (New York, NY, USA), MOBIQUITOUS 2016, ACM, 2016, pp. 6–11.

[157] Yoshiyuki Kawaharada, Ken Kurosaki, Masayoshi Uno, and Shinsuke Yamanaka, *Thermoelectric properties of $CoSb_3$*, Journal of Alloys and Compounds **315** (2001), no. 1, 193–197.

[158] Erin N. Kelly, Jeffrey W. Short, David W. Schindler, Peter V. Hodson, Mingsheng Ma, Alvin K. Kwan, and Barbra L. Fortin, *Oil sands development contributes polycyclic aromatic compounds to the Athabasca River and its tributaries*, Proceedings of the National Academy of Sciences of the United States of America, vol. 106, October 2009, pp. 22346–22351.

[159] A. U. Khan, N. Vlachos, and Th. Kyratsi, *High thermoelectric figure of merit of $Mg_2Si_{0.55}Sn_{0.4}Ge_{0.05}$ materials doped with Bi and Sb*, Scripta Materialia **69** (2013), no. 8, 606–609.

[160] Usman Khan and Sang-Woo Kim, *Triboelectric Nanogenerators for Blue Energy Harvesting*, ACS Nano **10** (2016), no. 7, 6429–6432.

[161] A. Khodayari, S. Pruvost, G. Sebald, D. Guyomar, and S. Mohammadi, *Nonlinear pyroelectric energy harvesting from relaxor single crystals*, IEEE Transactions on Ultrasonics, Ferroelectrics, and Frequency Control **56** (2009), no. 4, 693–699.

[162] Byeong Jo Kim, Dong Hoe Kim, Seung Lee Kwon, So Yeon Park, Zhen Li, Kai Zhu, and Hyun Suk Jung, *Selective dissolution of halide perovskites as a step towards recycling solar cells*, Nature Communications **7** (2016).

[163] Miso Kim, Mathias Hoegen, John Dugundji, and Brian L. Wardle, *Modeling and experimental verification of proof mass effects on vibration energy harvester performance*, Smart Materials and Structures **19** (2010), no. 4, 045023.

[164] Myeongjin Kim, Jaeho Choi, Ilgeun Oh, and Jooheon Kim, *Design and synthesis of ternary Co_3O_4/carbon coated TiO_2 hybrid nanocomposites for asymmetric supercapacitors*, Physical Chemistry Chemical Physics **18** (2016), no. 29, 19696–19704.

[165] Taeho Kim, Namho Lee, Hyun Kyu Jung, and Ji Hyun Kim, *Enhancement of energy performance in betavoltaic cells by optimizing self-absorption of beta particles*, International Journal of Energy Research **40** (2016), no. 4, 522–528.

[166] Pattareeya Kittidachachan, Lefteris Danos, Thomas J. J. Meyer, Nicolas Alderman, and Tom Markvart, *Photon Collection Efficiency of Fluorescent Solar Collectors*, CHIMIA International Journal for Chemistry **61** (2007), no. 12, 780–786.

[167] K. Knapp and T.L. Jester, *An Empirical Perspective on the Energy Payback Time for PV Modules*, Solar 2000 Conference, June 2000, pp. 16–21.

[168] John J. C. Kopera, *Inside the Nickel Metal Hydride Battery*, Tech. report, 2004.

[169] S. Korla, R. A. Leon, I. N. Tansel, A. Yenilmez, A. Yapici, and M. Demetgul, *Design and testing of an efficient and compact piezoelectric energy harvester*, Microelectronics Journal **42** (2011), no. 2, 265–270.

[170] Roy D. Kornbluh, Ron Pelrine, Harsha Prahlad, Annjoe Wong-Foy, Brian McCoy, Susan Kim, Joseph Eckerle, and Tom Low, *From Boots to Buoys: Promises and Challenges of Dielectric Elastomer Energy Harvesting*, Electroactivity in Polymeric Materials, Springer, Boston, MA, 2012, DOI: 10.1007/978-1-4614-0878-9_3, pp. 67–93.

[171] R. Kötz, P. W. Ruch, and D. Cericola, *Aging and failure mode of electrochemical double layer capacitors during accelerated constant load tests*, Journal of Power Sources **195** (2010), no. 3, 923–928.

[172] Lia Kouchachvili and Michio Ikura, *Pyroelectric conversion-Effects of P(VDF-TrFE) preconditioning on power conversion*, Journal of Electrostatics **65** (2007), no. 3, 182–188.

[173] Kunihito Koumoto, Ryoji Funahashi, Emmanuel Guilmeau, Yuzuru Miyazaki, Anke Weidenkaff, Yifeng Wang, and Chunlei Wan, *Thermoelectric Ceramics for Energy Harvesting*, Journal of the American Ceramic Society **96** (2013), no. 1, 1–23.

[174] I. Krikidis, *From wireless power transfer to wireless powered communications*, 2017 24th International Conference on Telecommunications (ICT), May 2017, pp. 1–114.

[175] M. Kroener, K. Allinger, M. Berger, E. Grether, F. Wieland, S. Heller, and P. Woias, *A water-powered Energy Harvesting system with Bluetooth Low Energy interface*, Journal of Physics: Conference Series **773** (2016), no. 1, 012040.

[176] Peter Krogstrup, Henrik Ingerslev Jørgensen, Martin Heiss, Olivier Demichel, Jeppe V. Holm, Martin Aagesen, Jesper Nygard, and Anna Fontcuberta i Morral, *Single-nanowire solar cells beyond the Shockley-Queisser limit*, Nature Photonics **7** (2013), no. 4, 306–310.

[177] Tom Krupenkin and J. Ashley Taylor, *Reverse electrowetting as a new approach to high-power energy harvesting*, Nature Communications **2** (2011), 448.

[178] Yan R. Kucherov, *Piezo-pyroelectric energy converter and method*, July 1997.

[179] P. Kuhn, P. Schmidt, F. Meyer, G. v Boegel, and A. Grabmaier, *Comparison of Energy Harvesting via Modulation Schemes for Passive Sensor RFID*, Smart SysTech 2016; European Conference on Smart Objects, Systems and Technologies, July 2016, pp. 1–6.

[180] Elizabeth B. Kujawinski, Melissa C. Kido Soule, David L. Valentine, Angela K. Boysen, Krista Longnecker, and Molly C. Redmond, *Fate of Dispersants Associated with the Deepwater Horizon Oil Spill*, Environmental Science & Technology **45** (2011), no. 4, 1298–1306.

[181] Brijesh Kumar, Keun Young Lee, Hyun-Kyu Park, Seung Jin Chae, Young Hee Lee, and Sang-Woo Kim, *Controlled Growth of Semiconducting Nanowire, Nanowall, and Hybrid Nanostructures on Graphene for Piezoelectric Nanogenerators*, ACS Nano **5** (2011), no. 5, 4197–4204.

[182] Sunil Kumar, Deepti Chaudhary, Punit Kumar Dhawan, R. R. Yadav, and Neeraj Khare, *Bi_2Te_3-MWCNT nanocomposite: An efficient thermoelectric material*, Ceramics International **43** (2017), no. 17, 14976–14982.

[183] T. L. Nguyen, H. Choi, S.-J. Ko, M. A. Uddin, B. Walker, S. Yum, J.-E. Jeong, M. H. Yun, T. J. Shin, S. Hwang, J. Y. Kim, and H. Y. Woo, *Semi-crystalline photovoltaic polymers with efficiency exceeding 9% in a 300 nm thick conventional single-cell device*, Energy & Environmental Science **7** (2014), no. 9, 3040–3051.

[184] M. Labudovic and Jin Li, *Modeling of TE cooling of pump lasers*, IEEE Transactions on Components and Packaging Technologies **27** (2004), no. 4, 724–730.

[185] Suvi Lehtimäki, Miao Li, Jarno Salomaa, Juho Pörhönen, Antti Kalanti, Sampo Tuukkanen, Petri Heljo, Kari Halonen, and Donald Lupo, *Performance of printable supercapacitors in an RF energy harvesting circuit*, International Journal of Electrical Power & Energy Systems **58** (2014), 42–46.

[186] Eli S. Leland and Paul K. Wright, *Resonance tuning of piezoelectric vibration energy scavenging generators using compressive axial preload*, Smart Materials and Structures **15** (2006), no. 5, 1413.

[187] Martin Leslie, *Using Trig Functions to Model Daylight Hours*, 2009.

[188] Shuguang Li, Jianping Yuan, and Hod Lipson, *Ambient wind energy harvesting using cross-flow fluttering*, Journal of Applied Physics **109** (2011), no. 2, 026104.

[189] Long Lin, Sihong Wang, Yannan Xie, Qingshen Jing, Simiao Niu, Youfan Hu, and Zhong Lin Wang, *Segmentally Structured Disk Triboelectric Nanogenerator for Harvesting Rotational Mechanical Energy*, Nano Letters **13** (2013), no. 6, 2916–2923.

[190] David Linden and Thomas B. Reddy, *Handbook Of Batteries*, 3 edition ed., McGraw-Hill Professional, New York, August 2001.

[191] Jenny List, *The SHA2017 Badge Revealed*, May 2017.

[192] Bo Liu, Weihong Zhu, Yueqiang Wang, Wenjun Wu, Xin Li, Baoqin Chen, Yi-Tao Long, and Yongshu Xie, *Modulation of energy levels by donor groups: an effective approach for optimizing the efficiency of zinc-porphyrin based solar cells*, Journal of Materials Chemistry **22** (2012), no. 15, 7434–7444.

[193] Jing-Quan Liu, Hua-Bin Fang, Zheng-Yi Xu, Xin-Hui Mao, Xiu-Cheng Shen, Di Chen, Hang Liao, and Bing-Chu Cai, *A MEMS-based piezoelectric power generator array for vibration energy harvesting*, Microelectronics Journal **39** (2008), no. 5, 802–806.

[194] Q. Liu, J. Wu, P. Xia, S. Zhao, W. Chen, Y. Yang, and L. Hanzo, *Charging Unplugged: Will Distributed Laser Charging for Mobile Wireless Power Transfer Work?*, IEEE Vehicular Technology Magazine **11** (2016), no. 4, 36–45.

[195] Weiguo Liu, Bin Jiang, and Weiguang Zhu, *Self-biased dielectric bolometer from epitaxially grown Pb(Zr,Ti)O_3 and lanthanum-doped Pb(Zr,Ti)O_3 multilayered thin films*, Applied Physics Letters **77** (2000), no. 7, 1047–1049.

[196] Y. Liu, W. Zhou, S. Yang, W. Li, P. Li, and S. Yang, *A Novel Miniaturized Vivaldi Antenna Using Tapered Slot Edge With Resonant Cavity Structure for Ultrawideband Applications*, IEEE Antennas and Wireless Propagation Letters **15** (2016), 1881–1884.

[197] Min Lu, Guo-guang Zhang, Kai Fu, Guo-hao Yu, Dan Su, and Ji-feng Hu, *Gallium Nitride Schottky betavoltaic nuclear batteries*, Energy Conversion and Management **52** (2011), no. 4, 1955–1958.

[198] X. Lu, P. Wang, D. Niyato, D. I. Kim, and Z. Han, *Wireless Networks With RF Energy Harvesting: A Contemporary Survey*, IEEE Communications Surveys Tutorials **17** (2015), no. 2, 757–789.

[199] Adam Lucas, *Wind, Water, Work: Ancient And Medieval Milling Technology*, BRILL, 2006, Google-Books-ID: 5QgU43HVpyIC.

[200] Laihui Luo, Xijie Jiang, Yuanyuan Zhang, and Kaixuan Li, *Electrocaloric effect and pyroelectric energy harvesting of (0.94-x)$Na_{0.5}Bi_{0.5}TiO_3$-0.06$BaTiO_3$-x$SrTiO_3$ ceramics*, Journal of the European Ceramic Society **37** (2017), no. 8, 2803–2812.

[201] L. Maharjan, S. Inoue, H. Akagi, and J. Asakura, *State-of-Charge (SOC)-Balancing Control of a Battery Energy Storage System Based on a Cascade PWM Converter*, IEEE Transactions on Power Electronics **24** (2009), no. 6, 1628–1636.

[202] Christopher Malotte, *Feasibility of Energy Harvesting Using Piezoelectric Tire*, Ph.D. thesis, Arizona State University, Arizona, US, November 2012.

[203] Amir Manbachi and Richard S C Cobbold, *Development and Application of Piezoelectric Materials for Ultrasound Generation and Detection*, Ultrasound **19** (2011), no. 4, 187–196.

[204] Max Marwede and Armin Reller, *Future recycling flows of tellurium from cadmium telluride photovoltaic waste*, Resources, Conservation and Recycling **69** (2012), no. Supplement C, 35–49.

[205] John Marx, Robert Hockberger, and Ron Walls, *Rosen's Emergency Medicine - Concepts and Clinical Practice*, 8 ed., Saunders, August 2013.

[206] Stephan Mathieu, *Indoor solar energy harvesting: a platform to (finally) get some numbers*, December 2011.

[207] N. C. McDonald and J. M. Pearce, *Producer responsibility and recycling solar photovoltaic modules*, Energy Policy **38** (2010), no. 11, 7041–7047.

[208] Chris Meehan, *Solar PV Production May Break 50 Gigawatt Barrier in 2014*, The Clean Energy Authority (2013).

[209] Ayushi Mehta, Neha Aggrawal, and Anjali Tiwari, *Solar roadways: The future of roadways*, International Advanced Research Journal in Science, Engineering and Technology (IARJSET) **2** (2015).

[210] Xiaochang Miao, Sefaattin Tongay, Maureen K. Petterson, Kara Berke, Andrew G. Rinzler, Bill R. Appleton, and Arthur F. Hebard, *High Efficiency Graphene Solar Cells by Chemical Doping*, Nano Letters **12** (2012), no. 6, 2745–2750.

[211] M. A. Migliorato, J. Pal, R. Garg, G. Tse, H. Y.s. Al-Zahrani, U. Monteverde, S. Tomić, C-K. Li, Y-R. Wu, B. G. Crutchley, I. P. Marko, and S. J. Sweeney, *A review of non linear piezoelectricity in semiconductors*, AIP Conference Proceedings **1590** (2014), no. 1, 32–41.

[212] P. D. Mitcheson, E. M. Yeatman, G. K. Rao, A. S. Holmes, and T. C. Green, *Energy Harvesting From Human and Machine Motion for Wireless Electronic Devices*, Proceedings of the IEEE **96** (2008), no. 9, 1457–1486.

[213] S. Monfray, O. Puscasu, G. Savelli, U. Soupremanien, E. Ollier, C. Guerin, L. G. Fréchette, E. Léveille, G. Mirshekari, C. Maitre, P. Coronel, K. Domanski, P. Grabiec, P. Ancey, D. Guyomar, V. Bottarel, G. Ricotti, F. Boeuf, F. Gaillard, and T. Skotnicki, *Innovative thermal energy harvesting for zero power electronics*, 2012 IEEE Silicon Nanoelectronics Workshop (SNW), June 2012, pp. 1–4.

[214] Seyyed Mohsen Mousavi Ehteshami, Mohsen Asadnia, Swee Ngin Tan, and Siew Hwa Chan, *Paper-based membraneless hydrogen peroxide fuel cell prepared by micro-fabrication*, Journal of Power Sources **301** (2016), no. Supplement C, 392–395.

[215] F. M. Mulder, B. M. H. Weninger, J. Middelkoop, F. G. B. Ooms, and H. Schreuders, *Efficient electricity storage with a battolyser, an integrated Ni-Fe battery and electrolyser*, Energy & Environmental Science **10** (2017), no. 3, 756–764.

[216] Akira Nakajima and Takashi Sakaguchi, *Recovery of uranium by tannin immobilized on matrices which have amino group*, Journal of Chemical Technology & Biotechnology **47** (1990), no. 1, 31–38.

[217] A. Namadmalan, *Self-Oscillating Tuning Loops for Series Resonant Inductive Power Transfer Systems*, IEEE Transactions on Power Electronics **31** (2016), no. 10, 7320–7327.

[218] Imogen E. Napper and Richard C. Thompson, *Release of synthetic microplastic plastic fibres from domestic washing machines: Effects of fabric type and washing conditions*, Marine Pollution Bulletin **112** (2016), no. 1, 39–45.

[219] Ashcon Navid and Laurent Pilon, *Pyroelectric energy harvesting using Olsen cycles in purified and porous poly(vinylidene fluoride-trifluoroethylene) [P(VDF-TrFE)] thin films*, Smart Materials and Structures **20** (2011), no. 2, 025012.

[220] NEA, *Uranium 2016: Resources, Production and Demand*, Organisation for Economic Co-operation and Development, Paris, December 2016.

[221] Action Nechibvute, Albert Chawanda, and Pearson Luhanga, *Piezoelectric Energy Harvesting Devices: An Alternative Energy Source for Wireless Sensors*, Smart Materials Research **2012** (2012), no. 853481, 13, DOI: 10.1155/2012/853481.

[222] Nelson L. Nemerow, *Environmental Engineering: Environmental Health and Safety for Municipal Infrastructure, Land Use and Planning, and Industry*, John Wiley & Sons, January 2009.

[223] H. T. Nguyen and J. M. Pearce, *Estimating potential photovoltaic yield with r.sun and the open source Geographical Resources Analysis Support System*, Solar Energy **84** (2010), no. 5, 831–843.

[224] Thomas Nilsen, *Nuclear lighthouses to be replaced*, Bellona.org (2003).

[225] P. Nintanavongsa, U. Muncuk, D. R. Lewis, and K. R. Chowdhury, *Design Optimization and Implementation for RF Energy Harvesting Circuits*, IEEE Journal on Emerging and Selected Topics in Circuits and Systems **2** (2012), no. 1, 24–33.

[226] Dusit Niyato, Ekram Hossain, Dong In Kim, Vijay Bhargava, and Lotfollah Shafai, *Wireless-Powered Communication Networks*, Cambridge University Press, November 2016, Google-Books-ID: iQhQDQAAQBAJ.

[227] Karen J. Nordell, Elizabeth M. Boatman, and George C. Lisensky, *A Safer, Easier, Faster Synthesis for CdSe Quantum Dot Nanocrystals*, Journal of Chemical Education **82** (2005), no. 11, 1697.

[228] Ryan O'Hayre, Suk-Won Cha, Fritz B. Prinz, and Whitney Colella, *Fuel Cell Fundamentals*, John Wiley & Sons, May 2016, Google-Books-ID: O2JYCwAAQBAJ.

[229] L.C. Olsen and Donald W. Douglas, *Betavoltaic energy conversion*, Energy Conversion **13** (1973), no. 4, i.

[230] Randall B. Olsen, *Pyroelectric energy converter and method*, March 1987, U.S. Classification 322/2.00A, 310/308; International Classification H02N10/00, H02N1/08, H01L37/02; Cooperative Classification H01L37/02, H02N1/08, H02N10/00; European Classification H01L37/02, H02N10/00, H02N1/08.

[231] Randall B. Olsen and Diane Evans, *Pyroelectric energy conversion: Hysteresis loss and temperature sensitivity of a ferroelectric material*, Journal of Applied Physics **54** (1983), no. 10, 5941–5944.

[232] Gabriel D. Oreggioni, Bhawna Singh, Francesco Cherubini, Geoffrey Guest, Carine Lausselet, Mauro Luberti, Hyungwoong Ahn, and Anders H. StrÃÿmman, *Environmental assessment of*

biomass gasification combined heat and power plants with absorptive and adsorptive carbon capture units in Norway, International Journal of Greenhouse Gas Control **57** (2017), no. Supplement C, 162–172.

[233] S. R. Ovshinsky, M. A. Fetcenko, and J. Ross, *A Nickel Metal Hydride Battery for Electric Vehicles*, Science **260** (1993), no. 5105, 176–181.

[234] R. Pandey and R. J. Holmes, *Organic Photovoltaic Cells Based on Continuously Graded Donor-Acceptor Heterojunctions*, IEEE Journal of Selected Topics in Quantum Electronics **16** (2010), no. 6, 1537–1543.

[235] J. A. Paradiso and T. Starner, *Energy scavenging for mobile and wireless electronics*, IEEE Pervasive Computing **4** (2005), no. 1, 18–27.

[236] Deep Patel, Rohan Mehta, Rhythm Patwa, Sahil Thapar, and Shivani Chopra, *RF Energy Harvesting*, International Journal of Engineering Trends and Technology **16** (2014), no. 8, 382–385.

[237] Yanzhong Pei, Aaron LaLonde, Shiho Iwanaga, and G. Jeffrey Snyder, *High thermoelectric figure of merit in heavy hole dominated PbTe*, Energy & Environmental Science **4** (2011), no. 6, 2085–2089.

[238] Yanzhong Pei, Xiaoya Shi, Aaron LaLonde, Heng Wang, Lidong Chen, and G. Jeffrey Snyder, *Convergence of electronic bands for high performance bulk thermoelectrics*, Nature **473** (2011), no. 7345, 66–69.

[239] E. Peled, A. Gorenshtein, M. Segal, and Y. Sternberg, *Rechargeable lithium-sulfur battery*, Journal of Power Sources **26** (1989), no. 3, 269–271.

[240] M. Perez, S. Boisseau, P. Gasnier, J. Willemin, M. Geisler, and J. L. Reboud, *A cm scale electret-based electrostatic wind turbine for low-speed energy harvesting applications*, Smart Materials and Structures **25** (2016), no. 4, 045015.

[241] Meredith Perry, *Receiver communications for wireless power transfer*, November 2012, U.S. Classification 367/135; International Classification H04B1/06; Cooperative Classification B60L11/1838, B60L11/182, H04R23/00, H02J50/15, H02J50/80, H01F38/14, G10K11/346, H02J5/005, Y02T90/122, G10K11/18, G10K11/26, G10K11/341, H03C3/02, H03C5/00, H02J7/025, H02J17/00, H02J7/0052, H04R17/00, H04R19/00, H04B11/00, Y02E60/12; European Classification H04B11/00.

[242] Adele Peters, *This Startup Uses A Particle Accelerator To Make Solar Panels Much, Much Cheaper*, December 2016.

[243] S. J. Pickering, *Recycling technologies for thermoset composite materials - current status*, Composites Part A: Applied Science and Manufacturing **37** (2006), no. 8, 1206–1215.

[244] Howard E. Pollard, *Solar cell assembly*, March 2000, U.S. Classification 136/256, 136/293, 257/E27.123, 136/244; International Classification H01L31/048, H01L31/042, H01L27/142, B64G1/44, H01L31/05; Cooperative Classification H01L31/048, B64G1/443, H01L31/0508, H01L31/0443, Y10S136/293, H01L27/142, Y02E10/50; European Classification H01L31/048, H01L31/05, H01L27/142.

[245] Marc Poulshock, *Micro Thermoelectric Generator Targets ZigBee*, 2007.

[246] Xiong Pu, Mengmeng Liu, Linxuan Li, Chi Zhang, Yaokun Pang, Chunyan Jiang, Lihua Shao, Weiguo Hu, and Zhong Lin Wang, *Efficient Charging of Li-Ion Batteries with Pulsed Output Current of Triboelectric Nanogenerators*, Advanced Science **3** (2016), no. 1.

[247] O. Puscasu, S. Monfray, G. Savelli, C. Maitre, J. P. Pemeant, P. Coronel, K. Domanski, P. Grabiec, P. Ancey, P. J. Cottinet, D. Guyomar, V. Bottarel, G. Ricotti, I. Bimbaud, F. Boeuf, F. Gaillard, and T. Skotnicki, *An innovative heat harvesting technology (HEATec) for above-Seebeck performance*, 2012 International Electron Devices Meeting, December 2012, pp. 12.5.1–12.5.4.

[248] Matthew R. Leyden, Luis K. Ono, Sonia R. Raga, Yuichi Kato, Shenghao Wang, and Yabing Qi, *High performance perovskite solar cells by hybrid chemical vapor deposition*, Journal of Materials Chemistry A **2** (2014), no. 44, 18742–18745.

[249] R. M. Raghavendra, K. P. S. S. Praneeth, and Soma Dutta, *Preparation and Characterization of $BaTiO_3$-$PbZrTiO_3$ Coating for Pyroelectric Energy Harvesting*, Journal of Electronic Materials **46** (2017), no. 1, 101–106.

[250] Christopher M. Reddy, J. Samuel Arey, Jeffrey S. Seewald, Sean P. Sylva, Karin L. Lemkau, Robert K. Nelson, Catherine A. Carmichael, Cameron P. McIntyre, Judith Fenwick, G. Todd Ventura, Benjamin A. S. Van Mooy, and Richard Camilli, *Composition and fate of gas and oil released to the water column during the Deepwater Horizon oil spill*, Proceedings of the National Academy of Sciences **109** (2012), no. 50, 20229–20234.

[251] Bailey Elizabeth Richert, *Building innovation ecosystems to drive carbon neutral sustainability goals*, Thesis, Massachusetts Institute of Technology, 2016.

[252] A. Richter, M. Hermle, and S. W. Glunz, *Reassessment of the Limiting Efficiency for Crystalline Silicon Solar Cells*, IEEE Journal of Photovoltaics **3** (2013), no. 4, 1184–1191.

[253] Wolfgang Richter, *Kostenlos Energie ernten*, Technology Review (2015).

[254] Zein S. Rizk and Arden D. Davis, *Impact of the Proposed Qattara Reservoir on the Moghra Aquifer of Northwestern Egypt*, Ground Water **29** (1991), no. 2, 232–238.

[255] Scott Roberts, *Reality Check: First Solar and Tellurium*, Seeking Alpha (2007).

[256] Verbruggen Robin, *Design of an intelligent open source reflow oven*, June 2017.

[257] S. Rödel, T. Krätzig, and L. Meyer, *Testing and developing energy harvester systems for operation of energy-self-sufficient measurement and control units in drinking water supply*, Water Science and Technology: Water Supply **16** (2016), no. 2, 263–273.

[258] Stephen A. Roen, *Solar powered portable calculator*, April 1977, U.S. Classification 361/679.09, 713/321, 136/291, 320/101, 250/215, 361/679.55, 136/206; International Classification G06F15/02; Cooperative Classification G06F15/0216, Y10S136/291; European Classification G06F15/02C.

[259] Niko Roorda, *Fundamentals of Sustainable Development*, Taylor & Francis, July 2017, Google-Books-ID: wEUrDwAAQBAJ.

[260] R. L. Rudnick and S. Gao, *Composition of the Continental Crust*, Treatise on Geochemistry **3** (2003), 659.

[261] Sven Rühle, *Tabulated values of the Shockley-Queisser limit for single junction solar cells*, Solar Energy **130** (2016), no. Supplement C, 139–147.

[262] W. Ruppel and P. Wurfel, *Upper limit for the conversion of solar energy*, IEEE Transactions on Electron Devices **27** (1980), no. 4, 877–882.

[263] Bhargav M. M. S. R. S, Ratna Kishore V, Anbuudayasankar S. P, and Balaji K, *Power generation by high head water in a building using micro hydro turbine - a greener approach*, Environmental Science and Pollution Research **23** (2016), no. 10, 9381–9390.

[264] Hitoshi Sai, Takuya Matsui, and Koji Matsubara, *Stabilized 14.0%-efficient triple-junction thin-film silicon solar cell*, Applied Physics Letters **109** (2016), no. 18, 183506.

[265] Yasuyoshi Saito, Hisaaki Takao, Toshihiko Tani, Tatsuhiko Nonoyama, Kazumasa Takatori, Takahiko Homma, Toshiatsu Nagaya, and Masaya Nakamura, *Lead-free piezoceramics*, Nature **432** (2004), no. 7013, 84–87.

[266] Michael Saliba, Taisuke Matsui, Konrad Domanski, Ji-Youn Seo, Amita Ummadisingu, Shaik M. Zakeeruddin, Juan-Pablo Correa-Baena, Wolfgang R. Tress, Antonio Abate, Anders Hagfeldt, and Michael Grätzel, *Incorporation of rubidium cations into perovskite solar cells improves photovoltaic performance*, Science **354** (2016), no. 6309, 206–209.

[267] Saomoto Sato, *World's Highest Conversion Efficiency of 26.33% Achieved in a Crystalline Silicon Solar Cell*, Tech. report, Kaneka Corporation, September 2016.

[268] V. Sauvant-Moynot, J. Bernard, R. Mingant, A. Delaille, F. Mattera, S. Mailley, J.-L. Hognon, and F. Huet, *ALIDISSI, a Research Program to Evaluate Electrochemical Impedance Spectroscopy as a SoC and SoH Diagnosis Tool for Li-ion Batteries*, Oil & Gas Science and Technology - Revue de Institut Français du Pétrole **65** (2010), no. 1, 79–89.

[269] H. Schmidt and C. Glaesser, *Multitemporal analysis of satellite data and their use in the monitoring of the environmental impacts of open cast lignite mining areas in Eastern Germany*, International Journal of Remote Sensing **19** (1998), no. 12, 2245–2260.

[270] Gael Sebald, Daniel Guyomar, and Amen Agbossou, *On thermoelectric and pyroelectric energy harvesting*, Smart Materials and Structures **18** (2009), no. 12, 125006.

[271] Gael Sebald, Sebastien Pruvost, and Daniel Guyomar, *Energy harvesting based on Ericsson pyroelectric cycles in a relaxor ferroelectric ceramic*, Smart Materials and Structures **17** (2008), no. 1, 015012.

[272] Michael W. Shafer, Eric R. Morgan, and Gregory Hahn, *Energy Harvester for Wildlife Monitor*, December 2016, International Classification A01K11/00, A01K61/00, G06F1/26, H02K7/18, A61B5/00, F01D15/10; Cooperative Classification A01K61/90, A61B5/0022, A01K11/008, H02K7/1823, F01D15/10, G06F1/266, A01K61/001.

[273] Faisal Karim Shaikh and Sherali Zeadally, *Energy harvesting in wireless sensor networks: A comprehensive review*, Renewable and Sustainable Energy Reviews **55** (2016), no. Supplement C, 1041–1054.

[274] Michael W. Shannon, Stephen W. Borron, and Michael Burns, *Haddad and Winchester's Clinical Management of Poisoning and Drug Overdose*, 4 edition ed., Saunders, Philadelphia, June 2007.

[275] Manish Sharma, Aditya Chauhan, Rahul Vaish, and Vishal Singh Chauhan, *Pyroelectric materials for solar energy harvesting: a comparative study*, Smart Materials and Structures **24** (2015), no. 10, 105013.

[276] N. S. Shenck and J. A. Paradiso, *Energy scavenging with shoe-mounted piezoelectrics*, IEEE Micro **21** (2001), no. 3, 30–42.

[277] William Shockley and Hans J. Queisser, *Detailed Balance Limit of Efficiency of p-n Junction Solar Cells*, Journal of Applied Physics **32** (1961), no. 3, 510–519.

[278] A. K. Shukla, M. K. Ravikumar, and T. S. Balasubramanian, *Nickel/iron batteries*, Journal of Power Sources **51** (1994), no. 1, 29–36.

[279] Zhi Wei Sim, Roger Shuttleworth, Martin J. Alexander, and Bruce D. Grieve, *Compact Patch Antenna Design for Outdoor RF Energy Harvesting in Wireless Sensor Networks*, Progress In Electromagnetics Research **105** (2010), 273–294 (English).

[280] Philip C. Singer and Werner Stumm, *Acidic Mine Drainage: The Rate-Determining Step*, Science **167** (1970), no. 3921, 1121–1123.

[281] John J. Smithrick and Doris L. Britton, *NASA Lewis advanced individual pressure vessel (IPV) nickel/hydrogen technology*, Journal of Power Sources **47** (1994), no. 3, 233–249.

[282] G. Jeffrey Snyder and Alemayouh H. Snyder, *Figure of Merit ZT of a Thermoelectric Device from Materials Properties*, Energy & Environmental Science (2017).

[283] H. A. Sodano, G. Park, and D. J. Inman, *Estimation of Electric Charge Output for Piezoelectric Energy Harvesting*, Strain **40** (2004), no. 2, 49–58.

[284] Henry A. Sodano, Daniel J. Inman, and Gyuhae Park, *Generation and Storage of Electricity from Power Harvesting Devices*, Journal of Intelligent Material Systems and Structures **16** (2005), no. 1, 67–75.

[285] C. Song, Y. Huang, J. Zhou, P. Carter, S. Yuan, Q. Xu, and Z. Fei, *Matching Network Elimination in Broadband Rectennas for High-Efficiency Wireless Power Transfer and Energy Harvesting*, IEEE Transactions on Industrial Electronics **64** (2017), no. 5, 3950–3961.

[286] Min-Kyu Song, Yuegang Zhang, and Elton J. Cairns, *A Long-Life, High-Rate Lithium/Sulfur Cell: A Multifaceted Approach to Enhancing Cell Performance*, Nano Letters **13** (2013), no. 12, 5891–5899.

[287] P. C. Souers, *Hydrogen Properties for Fusion Energy*, University of California Press, 1986, Google-Books-ID: I2K6DKA1IMwC.

[288] T. Soyata, L. Copeland, and W. Heinzelman, *RF Energy Harvesting for Embedded Systems: A Survey of Tradeoffs and Methodology*, IEEE Circuits and Systems Magazine **16** (2016), no. 1, 22–57.

[289] Douglas W. Stephan, George A. Olah, Alain Goeppert, and G. K. Surya Prakash, *Beyond Oil and Gas: The Methanol Economy, Second Updated and Enlarged Edition.*, Energy Technology **1** (2013), no. 12, 777–777.

[290] Paul C. Stern, Kathryn B. Janda, Marilyn A. Brown, Linda Steg, Edward L. Vine, and Loren Lutzenhiser, *Opportunities and insights for reducing fossil fuel consumption by households and organizations*, Nature Energy **1** (2016), no. 5, nenergy201643.

[291] Galen Stucky, Brian Evanko, Nicholas Parker, David Vonlanthen, David AUSTON, Shannon Boettcher, Sang-Eun Chun, Xiulei Ji, Bao Wang, Xingfeng Wang, and Raghu Subash Chandrabose, *Energy storage device including a redox-enhanced electrolyte*, August 2017, International Classification H01G11/32, H01G11/04, H01G11/16, H01G9/00, H01G11/02, H01G11/62; Cooperative Classification H01G11/62, H01G11/04, H01G11/02, H01G11/16, Y02E60/13, H01G11/32.

[292] Min Sun, Lin-Feng Zhai, Wen-Wei Li, and Han-Qing Yu, *Harvest and utilization of chemical energy in wastes by microbial fuel cells*, Chemical Society Reviews **45** (2016), no. 10, 2847–2870.

[293] J. Tan, K. Kalantar-zadeh, W. Wlodarski, S. Bhargava, D. Akolekar, A. Holland, and G. Rosengarten, *Thermoelectric properties of bismuth telluride thin films deposited by radio frequency magnetron sputtering*, vol. 5836, International Society for Optics and Photonics, July 2005, pp. 711–719.

[294] Lee Tan and Yao Chi-lung, *Abundance of chemical elements in the earth's crust and its major tectonic units*, International Geology Review **12** (1970), no. 7, 778–786.

[295] X. Tang, T. Lin, and L. Zuo, *Design and Optimization of a Tubular Linear Electromagnetic Vibration Energy Harvester*, IEEE/ASME Transactions on Mechatronics **19** (2014), no. 2, 615–622.

[296] Yuguo Tao and Ajeet Rohatgi, *High-Efficiency Front Junction n-Type Crystalline Silicon Solar Cells*, InTech Open Science, 2017.

[297] J.-M. Tarascon and M. Armand, *Issues and challenges facing rechargeable lithium batteries*, Nature **414** (2001), no. 6861, 359–367.

[298] Jefferson W. Tester, Elisabeth M. Drake, Michael J. Driscoll, Michael W. Golay, and William A. Peters, *Sustainable Energy: Choosing Among Options*, second edition edition ed., The MIT Press, Cambridge, MA, September 2012.

[299] Marc Thele, Oliver Bohlen, Dirk Uwe Sauer, and Eckhard Karden, *Development of a voltage-behavior model for NiMH batteries using an impedance-based modeling concept*, Journal of Power Sources **175** (2008), no. 1, 635–643.

[300] Oskar Thorin, *Power Line Induction Energy Harvesting Powering Small Sensor Nodes*, 2016.

[301] K. J. Tielrooij, J. C. W. Song, S. A. Jensen, A. Centeno, A. Pesquera, A. Z. Elorza, M. Bonn, L. S. Levitov, and F. H. L. Koppens, *Photoexcitation cascade and multiple hot carrier generation in graphene*, 2013 Conference on Lasers Electro-Optics Europe International Quantum Electronics Conference CLEO EUROPE/IQEC, May 2013, pp. 1–1.

[302] De Kegel Tim, *Ontwikkeling van een testbed voor piezo-elektrische energy harvesters*, unpublished thesis, 2015.

[303] D. M. Toma, J. del Rio, M. Carbonell-Ventura, and J. M. Masalles, *Underwater energy harvesting system based on plucked-driven piezoelectrics*, OCEANS 2015 - Genova, May 2015, pp. 1–5.

[304] R. A. Tomlinson, *The Perachora Waterworks: Addenda*, The Annual of the British School at Athens **71** (1976), 147–148.

[305] A. Torres, I. De Marco, B. M. Caballero, M. F. Laresgoiti, M. J. Chomón, and G. Kondra, *Recycling of the solid residue obtained from the pyrolysis of fiberglass polyester sheet molding compound*, Advances in Polymer Technology **28** (2009), no. 2, 141–149.

[306] Lee Torrey, *A trap to harness the Sun*, Reed Business Information, July 1980, Google-Books-ID: vfQxekunC3QC.

[307] Le-Giang Tran, Hyouk-Kyu Cha, and Woo-Tae Park, *RF power harvesting: a review on designing methodologies and applications*, Micro and Nano Systems Letters **5** (2017), 14.

[308] Terry M. Tritt and M. A. Subramanian, *Thermoelectric Materials, Phenomena, and Applications: A Bird's Eye View*, MRS Bulletin **31** (2006), no. 3, 188–198.

[309] Lars Ole Valoen and Mark I. Shoesmith, *The effect of PHEV and HEV duty cycles on battery and battery pack performance*, November 2007, pp. 4–5.

[310] Lars Ole Valøen and Mark I Shoesmith, *The effect of phev and hev duty cycles on battery and battery pack performance*, PHEV 2007 Conference, 2007, pp. 4–5.

[311] Tijs A. van den Broek, Michel L. Ehrenhard, David J. Langley, and Aard J. Groen, *Dotcauses for sustainability: combining activism and entrepreneurship*, Journal of Public Affairs **12** (2012), no. 3, 214–223.

[312] R. Venkatasubramanian, E. Siivola, T. Colpitts, and B. O'Quinn, *Thin-film thermoelectric devices with high room-temperature figures of merit*, Nature **413** (2001), no. 6856, 597–602.

[313] Y. Verbelen, D. Van Belle, N. Blondeel, S. De Winne, A. Braeken, and A. Touhafi, *Automated test chamber for indoor photovoltaics*, 2016 IEEE International Conference on Renewable Energy Research and Applications (ICRERA), November 2016, pp. 143–148.

[314] Y. Verbelen and A. Touhafi, *Resource considerations for durable large scale renewable energy harvesting applications*, 2013 International Conference on Renewable Energy Research and Applications (ICRERA), October 2013, pp. 401–406.

[315] Yannick Verbelen, An Braeken, Serge Kubera, Abdellah Touhafi, Jo Vliegen, and Nele Mentens, *Implementation of a Server Architecture for Secure Reconfiguration of Embedded Systems*, ARPN Journal of Systems and Software **1** (2011), no. 9, 270–279.

[316] Yannick Verbelen, An Braeken, and Abdellah Touhafi, *Parametrization of ambient energy harvesters for complementary balanced electronic applications*, 2013, pp. 8763 – 8.

[317] Yannick Verbelen, Sam De Winne, Niek Blondeel, Peeters Ann, An Braeken, and Abdellah Touhafi, *Analysis of thermoelectric coolers as energy harvesters for low power embedded applications*, International Journal of Electrical, Computer, Energetic, Electronic and Communication Engineering **11** (2017), no. 3, 295 – 302.

[318] Yannick Verbelen, Tim Dekegel, Ann Peeters, Klara Stinders, Niek Blondeel, Sam De Winne, An Braeken, and Abdellah Touhafi, *Parametrization of piezoelectric vibration energy harvesters for low power embedded systems*, International Journal of Electrical, Computer, Energetic, Electronic and Communication Engineering **10** (2016), no. 6, 798 – 805.

[319] Verbelen Yannick, *Energy Harvesting for Smart Autonomous Electronics 2*, August 2017.

[320] R. D. Vidic, S. L. Brantley, J. M. Vandenbossche, D. Yoxtheimer, and J. D. Abad, *Impact of Shale Gas Development on Regional Water Quality*, Science **340** (2013), no. 6134, 1235009.

[321] Alessandro Vinco, Rashid Siddique, Davide Brunelli, and Wensi Wang, *AA-Battery Sized Energy Harvesting Power Management Module for Indoor Light Wireless Sensor Applications*, Applications in Electronics Pervading Industry, Environment and Society, Lecture Notes in Electrical Engineering, Springer, Cham, 2016, DOI: 10.1007/978-3-319-20227-3_12, pp. 91–97.

[322] B. von Roedern, H.S. Ullal, and K. Zweibel, *Polycrystalline Thin-Film Photovoltaics: From the Laboratory to Solar Fields*, NREL, May 2006.

[323] A. De Vos, *Detailed balance limit of the efficiency of tandem solar cells*, Journal of Physics D: Applied Physics **13** (1980), no. 5, 839.

[324] A. De Vos and H. Pauwels, *On the thermodynamic limit of photovoltaic energy conversion*, Applied physics **25** (1981), no. 2, 119–125.

[325] Marcel Šúri, Thomas A. Huld, Ewan D. Dunlop, and Heinz A. Ossenbrink, *Potential of solar electricity generation in the European Union member states and candidate countries*, Solar Energy **81** (2007), no. 10, 1295–1305.

[326] Alan Edward Waltar and Albert Barnett Reynolds, *Fast Breeder Reactors*, Alan E. Waltar, 1981, Google-Books-ID: 4m6o1jMcIIIC.

[327] Sihong Wang, Long Lin, and Zhong Lin Wang, *Nanoscale Triboelectric-Effect-Enabled Energy Conversion for Sustainably Powering Portable Electronics*, Nano Letters **12** (2012), no. 12, 6339–6346.

[328] Sihong Wang, Long Lin, Yannan Xie, Qingshen Jing, Simiao Niu, and Zhong Lin Wang, *Sliding-Triboelectric Nanogenerators Based on In-Plane Charge-Separation Mechanism*, Nano Letters **13** (2013), no. 5, 2226–2233.

[329] Wei Wang, Mark T. Winkler, Oki Gunawan, Tayfun Gokmen, Teodor K. Todorov, Yu Zhu, and David B. Mitzi, *Device Characteristics of CZTSSe Thin-Film Solar Cells with 12.6% Efficiency*, Advanced Energy Materials **4** (2014), no. 7.

[330] Zhiyong Wang, Nan Li, Zujin Shi, and Zhennan Gu, *Low-cost and large-scale synthesis of graphene nanosheets by arc discharge in air*, Nanotechnology **21** (2010), no. 17, 175602.

[331] Zhong Lin Wang, *Triboelectric Nanogenerators as New Energy Technology for Self-Powered Systems and as Active Mechanical and Chemical Sensors*, ACS Nano **7** (2013), no. 11, 9533–9557.

[332] RunJuan Wen, ZhanHong Yang, Xinming Fan, Zhiyong Tan, and Bin Yang, *Electrochemical performances of ZnO with different morphology as anodic materials for Ni/Zn secondary batteries*, Electrochimica Acta **83** (2012), no. Supplement C, 376–382.

[333] C. E. Whitlock, *Surface Meteorology and Solar Energy Data Set for Renewable Energy Industry Use*, NASA, October 2000.

[334] Josiah Wiley and Edward Neal Koop, *Energy harvesting damper control and method of operation*, June 2017, International Classification H02K7/14, F04D15/00, F24F5/00, H02J7/00; Cooperative Classification F24F5/0021, H02J7/0029, Y02E60/147, H02J7/007.

[335] C. B. Williams and R. B. Yates, *Analysis of a micro-electric generator for microsystems*, Sensors and Actuators A: Physical **52** (1996), no. 1, 8–11.

[336] Jeff Wilson, *A Solar Powered Automatic Water Condenser For Under $100*, January 2016.

[337] Frank Wisotzky and Peter Obermann, *Acid mine groundwater in lignite overburden dumps and its prevention - the Rhineland lignite mining area*, Ecological Engineering **17** (2001), no. 2, 115–123.

[338] H. J. Wu, L.-D. Zhao, F. S. Zheng, D. Wu, Y. L. Pei, X. Tong, M. G. Kanatzidis, and J. Q. He, *Broad temperature plateau for thermoelectric figure of merit ZT>2 in phase-separated* $PbTe_{0.7}S_{0.3}$, Nature Communications **5** (2014), ncomms5515.

[339] Hongfei Wu, Kai Sun, Junjun Zhang, and Yan Xing, *A TEG Efficiency Booster with Buck-Boost Conversion*, Journal of Electronic Materials **42** (2013), no. 7, 1737–1744.

[340] Jianguo Wu, Jianhui Huang, Xingguo Han, Xianming Gao, Fangliang He, Mingxi Jiang, Zhigang Jiang, Richard B. Primack, and Zehao Shen, *The Three Gorges Dam: an ecological perspective*, Frontiers in Ecology and the Environment **2** (2004), no. 5, 241–248.

[341] Y. Wu, Z. Huang, Y. Hu, Z. Peng, X. Li, and F. Wang, *Electret materials for enhanced performance of triboelectric energy scavenging from wind flow*, 2017 19th International Conference on Solid-State Sensors, Actuators and Microsystems (TRANSDUCERS), June 2017, pp. 363–366.

[342] J. Xie, X.P. Mane, C.W. Green, K.M. Mossi, and Kam K. Leang, *Performance of Thin Piezoelectric Materials for Pyroelectric Energy Harvesting*, Journal of Intelligent Material Systems and Structures **21** (2010), no. 3, 243–249.

[343] Wenjie Xie, Xinfeng Tang, Yonggao Yan, Qingjie Zhang, and Terry M. Tritt, *Unique nanostructures and enhanced thermoelectric performance of melt-spun BiSbTe alloys*, Applied Physics Letters **94** (2009), no. 10, 102111.

[344] Yinjiao Xing, Wei He, Michael Pecht, and Kwok Leung Tsui, *State of charge estimation of lithium-ion batteries using the open-circuit voltage at various ambient temperatures*, Applied Energy **113** (2014), no. Supplement C, 106–115.

[345] Bin Yang, Chengkuo Lee, Wenfeng Xiang, Jin Xie, Johnny Han He, Rama Krishna Kotlanka, Siew Ping Low, and Hanhua Feng, *Electromagnetic energy harvesting from vibrations of multiple frequencies*, Journal of Micromechanics and Microengineering **19** (2009), no. 3, 035001.

[346] Bin Yang, Zhanhong Yang, Ruijuan Wang, and Tingting Wang, *Layered double hydroxide/carbon nanotubes composite as a high performance anode material for Ni-Zn secondary batteries*, Electrochimica Acta **111** (2013), no. Supplement C, 581–587.

[347] S.L. Yang, J. Zhang, and X.J. Xu, *Influence of the Three Gorges Dam on downstream delivery of sediment and its environmental implications, Yangtze River*, Geophysical Research Letters **34** (2007), no. 10.

[348] Weiqing Yang, Jun Chen, Guang Zhu, Xiaonan Wen, Peng Bai, Yuanjie Su, Yuan Lin, and Zhonglin Wang, *Harvesting vibration energy by a triple-cantilever based triboelectric nanogenerator*, Nano Research **6** (2013), no. 12, 880–886.

[349] Z. Yang, Q. Duan, J. Zhong, M. Mao, and Z. Xun, *Analysis of improved PSO and perturb observe global MPPT algorithm for PV array under partial shading condition*, 2017 29th Chinese Control And Decision Conference (CCDC), May 2017, pp. 549–553.

[350] Zhengbao Yang, Alper Erturk, and Jean Zu, *On the efficiency of piezoelectric energy harvesters*, Extreme Mechanics Letters **15** (2017), no. Supplement C, 26–37.

[351] Verbelen Yannick, *Design and prototyping*, September 2016.

[352] Yoshisaburo Yoshida, *Solar battery powered electronic calculator*, June 1980, U.S. Classification 320/101, 136/291, 320/112, 713/321, 250/215, 361/679.21; International Classification G06F15/02, H01L31/04, H01L31/02, G06F1/26, H05K5/03; Cooperative Classification G06F1/26, G06F15/0216, Y10S136/291, Y02E10/50, H01L31/02021; European Classification G06F1/26, G06F15/02C, H01L31/02H2B.

[353] D. Zabek, J. Taylor, and C. R. Bowen, *Characterization and Modeling of Meshed Electrodes on Free Standing Polyvilylidene Difluoride (PVDF) Films for Enhanced Pyroelectric Energy Harvesting*, IEEE Transactions on Ultrasonics, Ferroelectrics, and Frequency Control **63** (2016), no. 10, 1681–1689.

[354] Jingwei Zhang, *Rectennas for Wireless Energy Harvesting*, Microwave Power Transmission and Reception **1** (1980).

[355] Q. Zhang, N. Wang, P. Zhou, C. Chen, H. San, K. Wang, and X. Chen, *A betavoltaic microbattery using zinc oxide nanowires under build in potential difference*, 2016 IEEE 29th International Conference on Micro Electro Mechanical Systems (MEMS), January 2016, pp. 1177–1180.

[356] Li-Dong Zhao, Shih-Han Lo, Yongsheng Zhang, Hui Sun, Gangjian Tan, Ctirad Uher, C. Wolverton, Vinayak P. Dravid, and Mercouri G. Kanatzidis, *Ultralow thermal conductivity and high thermoelectric figure of merit in SnSe crystals*, Nature **508** (2014), no. 7496, 373–377.

[357] Guang Zhu, Jun Chen, Ying Liu, Peng Bai, Yu Sheng Zhou, Qingshen Jing, Caofeng Pan, and Zhong Lin Wang, *Linear-Grating Triboelectric Generator Based on Sliding Electrification*, Nano Letters **13** (2013), no. 5, 2282–2289.

[358] Guang Zhu, Caofeng Pan, Wenxi Guo, Chih-Yen Chen, Yusheng Zhou, Ruomeng Yu, and Zhong Lin Wang, *Triboelectric-Generator-Driven Pulse Electrodeposition for Micropatterning*, Nano Letters **12** (2012), no. 9, 4960–4965.

[359] Fangping Zhuo, Qiang Li, Jinghan Gao, Qingfeng Yan, Yiling Zhang, Xiaoqing Xi, and Xiangcheng Chu, *Phase transformations, anisotropic pyroelectric energy harvesting and electrocaloric properties of (Pb,La)(Zr,Sn,Ti)O_3 single crystals*, Physical Chemistry Chemical Physics **19** (2017), no. 21, 13534–13546.

[360] H. Zibetta and W. Palz, *Energy Payback Time of Photovoltaic Modules*, International Journal of Solar Energy **10** (1991), no. 3-4, 211–216.

[361] Helin Zou, D. M Rowe, and Gao Min, *Growth of p- and n-type bismuth telluride thin films by co-evaporation*, Journal of Crystal Growth **222** (2001), no. 1, 82–87.

[362] Peter Zweifel, Aaron Praktiknjo, and Georg Erdmann, *Uranium and Nuclear Energy*, Energy Economics, Springer Texts in Business and Economics, Springer, Berlin, Heidelberg, 2017, DOI: 10.1007/978-3-662-53022-1_11, pp. 247–267.

List of Figures

1.1 The 4 steps to complete the design of an autonomous system powered by ambient energy: harvester characterization (1), ambient energy benchmarking (2), energy budget estimation (3) and power path design (4). 7

3.1 Evolution of Te market prices in the last decade, showing a near exponential increase of the element's market value. [255] 30

4.1 Yield of a photovoltaic cell as a function of the efficiency μ_h which varies over a 3 day time interval. The applicate denotes the output power P for any harvester size μ_h assuming the maximum power output p_h is constant ($\mu_h p_h \in \Re^+$). 37

4.2 A system with 2 independent harvester outputs P_h^1 (1) and P_h^2 (2) profits from the harvested energy from both harvesters simultaneously (3), decreasing its dependency on a single harvester and increasing the systems reliability. 41

4.3 Effect of adding a storage medium to the system; both curves represent a harvester of the same type with same η_h but different μ_h since a system without storage (1) must generate at least as much power as required by the electronics (P_s) while for the version with storage (2) the average is sufficient. 43

4.4 Three-dimensional representation of the optimization problem as function of time t and the two harvester sizes μ_{h_1} and μ_{h_2}. Any cross section at any given time t_s is a line with equation $\mu_{h_1} p_{h_1} \eta_{h_1}(t_s) + \mu_{h_2} p_{h_2} \eta_{h_2}(t_s) = P_s$. 46

4.5 Optimization problem for 3 cross sections at $t_s, t_u, t_v \in [0, T]$, with equation of the line given for t_s. 47

4.6 Graphical representation of the optimization problem for a system powered by 2 harvesters with output efficiencies following a square wave and a sine arc. As shown, $0 \leq \eta_{h_1}, \eta_{h_2} \leq 1$ and $\mu_{h_1}, \mu_{h_2} = 1$. Continuous curves represent η_{h_1} and η_{h_2} while dotted curves correspond to the power ratios. Note the high values on a log scale for $\frac{\eta_{h_2}}{\eta_{h_1}}$ as a result of division by a very small value during the low period halves of the square wave. 49

4.7 Graphical optimization problem for 2 harvesters, one having a zero point within the interval. Note the logarithmic scale. 50

4.8 Optimization problem for 3 harvesters: h_5 has an exponential output, h_6 an attenuated impulse and h_7 a sinusoidal output. 52

4.9 Approximated evolution of harvester efficiency over a one year period. 55

4.10 Cross section of a generic ambient energy powered embedded system using a combination of different energy types and harvesters. The outside surface of the system is covered with photovoltaic cells (1) which are mechanically joined (3) to piezoelectric film to generate energy from impulses on the systems surface. The inside volume is not critical, and can be filled with RF or magneto-mechanical harvesters (4). Room for a capacitor or battery for energy storage is also provided (5). 56

5.1 Reproduction of indoor light spectra by subtraction using filters (a) or by addition (b). The resulting spectra a discrete and not identical, ideally $\lambda_2 [\lambda_1 (E_0)] \approx E_{a+b}$. 63
5.2 Block diagram of the test chamber. The logic is implemented on the embedded development platform *mbed* based on an LPC1768 microcontroller running at 50 MHz. The primary control loop stabilizes the illuminance using a MAX44004 lux sensor. The secondary loop controls the load impedance of the cell, allowing the measurement of the cells voltage and current to calculate the instantaneous power output. The experiments are controlled by Mablab software, responsible for execution of the experiment and collecting data. 64
5.3 Detail of the variable impedance generator used to load the cell under test. A PWM signal generated by the microcontroller (left) is actively filtered (IC1B) to set the desired cell voltage. The signal is fed into a comparator (IC1A), causing the partial conduction of an N-MOSFET which acts as a variable resistance. The current through the MOSFET's drain-source channel is measured as a voltage over a low value shunt resistor (R4) and digitized by high side current sense amplifier INA226 (IC2). The current measurements are sent back to the microcontroller (right). 66
5.4 Stabilization of the illumination in the test chamber as a response on a step function of 500 lx. Stabilization time (less than 1 % error over 10 samples) is up to 85 % longer for the 6.5 klx - 7.0 klx step than for the 0.5 klx - 1.0 klx step. Since illumination higher than 2 klx rarely occur in indoor environments, these delays are not a problem. The initial step to 0.5 klx experiences an overshoot of approx. 5.6 klx due to instability of the dimmers at low illumination levels. At very low illumination levels (< 150 lx) this effect may cause longer stabilization delays. 67
5.5 Illumination distribution map for an incandescent light source at an intensity of 7 klx, expressed as deviations to the average illumination level. The largest deviation accounts for approx. 1 klx, corresponding to an error of up to 14 %. Care must be taken when positioning the cell under test to keep the error to a minimum. Larger cells will suffer from uneven energy distribution. x and y units are physical measurement points, distributed over the entire active surface of approx. 30 x 30 cm. 68
5.6 Comparison of the behavior of a monocrystalline cell of type SLMD960H121 (active area: 1200 mm^2) in the left graph, with an amorphous cell of type Panasonic AM-1815 (active area: 2408 mm^2) in the right graph, for different types of artificial light, under 150 lx, 300 lx and 1000 lx. 69
5.7 Performance difference for different types of a-Si cells under 300 lx: a FJWTY001 flexible cell, a Panasonic AM-1815 marketed as "indoor" cell and a Panasonic AM-8701 marketed as "outdoor" cell. 70
5.8 Performance difference between a rigid a-Si cell for indoor use (AM-1815CA) and a flexible a-Si cell (FJWTY001) at 2000 lx. 71
5.9 Comparison of IV curves for a SLMD960H12L monocrystalline cell under 150 lx. . . . 72

5.10 Power output in the MPP for a crystalline cell of type SLMD960H121 (left graph), and an amorphous cell of type AM-1815 (right graph) for an illumination sweep between 100 lx and 1000 lx. 73
5.11 Heated bed constructed with a PCB trace on standard 1.6 mm FR4 as planar resistor. TEG and forced air cooled heat sink are dismounted, heat sink visible on the left of the setup. Insert: a close-up of the LM35 temperature sensor monitoring the hot side of the TEG, fitting into a cavity of the ceramic plate (not shown) on which the TEG is mounted. 75
5.12 Relative error on the temperature measurement over the operational range between room temperature. 76
5.13 Schematic diagram of the DAQ module, showing digital control (PIC24F16KA102), a current sense amplifier (INA226) connected over I^2C, and a DAC (MCP4921) connected over SPI. A local feedback loop is implemented with a OPA1641/OPA1644A opamp as direct MOS driver. 77
5.14 Experiment in progress (side view): a two stage TEG mounted between a stone heated bed (hot side) and an aluminum heat sink with heat pipes and forced air cooling (cold side). Electrical connections visible in the foreground. 78
5.15 Visualization of maximum power point (MPP) for 3 commercial TEGs. Note that the MPP is roughly equal to half the open circuit voltage V_{oc}. 78
5.16 DC/DC conversion stage effect on end-to-end power output for a TEC2-19006. 79
5.17 Comparison of the power outputs of various Mide vibration energy harvesters under a load of 1 g at their respective resonance frequencies. 81
5.18 Block diagram of the benchmarking platform with an AD 10650/W8 subwoofer as vibration source, TDA2003 as amplifier and MPU6050 as vibration sensor. 82
5.19 Schematic diagram of the TDA2003 based amplifier circuit driving the subwoofer. 83
5.20 Frequency response of the Philips AD 10650/W8 subwoofer. 84
5.21 Test bench setup with subwoofer and accelerometer. 85
5.22 Frequency response of the subwoofer as accelerometer samples in time domain (top graph, a.) and in frequency domain (bottom graph, b.). 86
5.23 Frequency response of the subwoofer as function of the input voltage for different frequencies. 86
5.24 Power output of a V21BL vibration harvester as a function of vibration amplitude and frequency. 87
5.25 Exponential approximation of the resonance frequency f_r with maximum power output $P_{max,a}$. 88
5.26 Database example for piezoelectric energy harvesters, with 3 harvesters $h_1..h_3$ displayed as overlapping point clouds. 89

6.1 Ragone chart comparing power density and energy density for different energy storage devices. Elcos refer to aluminum electrolytic capacitors or tantalum capacitors [291, 141, 164, 110, 21, 214, 114, 228]. 93
6.2 Block diagrams of isolated converter with transformer (top) and synchronous polyphase flyback converter (bottom). 97

6.3 First prototype of the EDLC voltage booster. From left to right: LED bar for visual charge indication and controller, local 5 V buck regulator, input current transformer and rectification, custom Ranlo flyback transformer, N-MOSFET synchronous rectifier, single channel buck regulator with push-pull N-MOSFET power stage and passive flyback diode, and LC output filter. For hardware reference and BOM, see Appendix A. 98
6.4 Synchronous boost converter stage based on Linear Technology's LTC3787 controller, featuring constant voltage control (feedback input, point A) and constant current control (shunt resistor R2). There are 2 identical channels 180° out of phase, and the pins duplicated in the second channel are marked with an **x**: BOOSTx, TGx, SWx, BGx and the differential shunt inputs RSx. T2 acts as the primary switch to charge up inductor L1, and T1 acts as a synchronous rectifier (ideal diode) to decrease losses in the usual flyback diode. D1 and C8 form a bootstrap circuit to allow a half bridge with all 2 N-channel MOSFETs. 99
6.5 Buck-boost regulator built around the Texas Instruments TPS55065 switched mode controller with integrated H-bridge. Capacitors C4 and C5 are part of a dual bootstrap circuit for an N-channel H-bridge. Booststrap diodes are integrated in the IC. 100
6.6 Transformerless ELDC booster prototypes. Rev. 1.0 (left) requires manual configuration with jumpers at the bottom of the board. Improved version Rev. 2.0 (right) features automatic range adjustment, rotary switch for cell configuration, and JST output connector for digital and analog control. Charge controller is a PLCC on the lower right of the board. 101
6.7 Typical discharge curves for popular secondary cell types: $LiFePO_4$, NiFe, LiS and NiMH. [299, p. 639, fig. 11][278, p. 34, fig. 5][239, p. 270, fig. 1][344, p. 109, fig. 3] 104
6.8 Topologies of buck, boost and inverting regulators with a single switch and PWM controller. Note that for buck and inverting regulators P-MOSFETs are commonly preferred over N-MOSFETs for high side switching to avoid bootstrap circuits. 107
6.9 Principal components of a buck regulator: input capacitor C_{in}, output capacitor C_{out}, MOSFET, inductor and flyback diode. Comparator and voltage reference provide voltage mode feedback to adjust PWM duty cycle of the MOSFET switch. 108
6.10 Supply current in active regulation in comparison to maximum output current of monolithic DC/DC converters. Gradient indicates power efficiency, with devices in lightly shaded areas performing better than devices in strongly shaded areas. The line approximates the current state of the art for monolithic DC/DC converters for different output current magnitudes. 114
6.11 A 4 phase synchronous oscillator (LTC6902) feeding a clock signal to 4 identical, 90° phase shifted buck stages with an LTC3845 controller and N-MOS half bridge for synchronous rectification. The Hall sensor based current sensing is shared among the 4 buck stages. 116
6.12 A 40 A over current detection module using an ACS722 hall sensor. 117
6.13 Top side of the prototype. Left to right: digital and analog control interface (output voltage and current, as 6-pin JST connector, galvanically isolated enable input, ACS722 hall current sensor, local 5 V buck regulator, 4 phase buck stage (oscillator on bottom side of the PCB), synchronous rectifier with 4 N-channel MOSFETs and ceramic dump resistor, and input tank capacitor bank. 118
6.14 LT4320 based synchronous rectifier with 4 N-MOSFETs providing superiorr efficiency over passive full bridge rectifiers. 119

6.15 Embedded architecture of the Influencair air quality sensing module, with an ESP8266 as general purpose IoT MCU and SDS011 particle sensor. 120
6.16 The 4 principal power consumption modes of the Influencair module: ① refreshing SDS011 particle sensor, ② particle, humidity and temperature measurement, ③ wireless LoRa transmission, ④ idle state of minimal power consumption. 122
6.17 Comparison of active power consumption proportions (right) and idle power consumption (left) for the active components. 123
6.18 Detailed architecture with PV energy harvester, Li-ion battery charger and supervisor system, triple voltage regulator with LDO and SEPIC for 3.3 V generation and boost regulator for 5 V regulation, and the system load as presented in figure 6.15. Dotted lines denote control and monitoring, the right side connections represent a data bus between sensors, actuators, and the ESP8266 microcontroller (top right). 124
6.19 Tying 2.8 V LDO output and 3.3 V SEPIC outputs together through a passively controlled P-MOSFET bridge. 125
6.20 Linear, SEPIC and boost regulators for power rail generation. On battery side only ceramic capacitors are used to minimize leakage losses. 126
6.21 CN3065 Li-ion battery charger with DW01-P battery monitor. An external MPPT circuit is implemented by controlling the charge current of the CN3065 with a feed-forward LM10. 127
6.22 Variation of average insolation levels in Brussels as a function of the seasons. 131
6.23 Comparison of insolation levels in Brussels, Belgium, in different seasons. Dotted line represent measured averages, colored curves a sinusoidal fit through the measured data. Horizontal lines denote half sines. 132
6.24 Switched mode battery charger with a CN3306 charge controller implementing a boost regulator and integrated MPPT. 135
6.25 Charge efficiency comparison between the linear CN3065 (left steep curves) and switched mode CN3306 battery chargers. Solid curves show a charge current of 100 mA, dotted curves a charge current of 10 mA. 136

7.1 Block diagram of the digital control systems common to all AEM modules. The central Atmega2560 AVR interfaces with analog parts (left) and retrieves samples, time stamps them, adds a unique ID and subsequently transmits them to the host over a UEXT interface. JTAG is provided for bootloader programming. Once a bootloader is in place in the designated memory space (see figure 7.2), debugging and reprogramming can be done over USB (top right). 144
7.2 Organization of memory space on the AEM modules, with Atmega2560 on the left and 24AA025UID on the right. Ca. 256 kB flash memory and 8 kB SRAM is available on the AVR, complemented by 512 bytes EEPROM internally and another 512 externally in the 24AA05UID. Blocks are not to scale. 145
7.3 Digital interface between Raspberry Pi 3 host and AEM Aggregator add-on module. Used pins are marked, grey pins indicate power connections. Redesigning AEM-Aggregator for use with different host systems is trivial as long as the same IO pins are available. . . 148
7.4 Rev. 1.0 of the AEM Aggregator prototype. ① transceivers for channels 1 and 2, ② I^2C multiplexer controller ③ UART multiplexer controller, ④ flash memory with UUID, ⑤ channel 1 IDC connector, ⑥ channel 2 IDC connector, ⑦ RTC with backup battery holder (not mounted). 149

7.5 Equivalent circuit for MiniSense 100 connected to an LTC6088 buffer, with clamping diodes. . . . 152
7.6 Interfacing the MiniSense 100 to the AD7689 ADC using a virtual ground to allow postive and negative input voltage swings. . . . 153
7.7 Interfacing the CEB-20D64 with the AD7689 ADC. Amplification and a low pass filter is required due to the higer frequency response but smaller amplitude than the MiniSense 100. . . . 154
7.8 Input buffer and double stage amplifer for the 1005919-1 ultrasonic acoustic vibration sensor. . . . 155
7.9 Amplifier and filter front-end for the PKGS-00LDP1-R shock sensors. . . . 156
7.10 Bias and active filter for the 801S high durability shock sensor. . . . 156
7.11 Vibration energy harvester based on LTC3588 set to 2.5V output voltage, with precision electronic load to measure . . . 158
7.12 Block diagram of the improved electronic load control system. . . . 158
7.13 Vibration energy harvester based on LTC3588 set to 2.5V output voltage, with precision electronic load to measure. . . . 159
7.14 Relative sensitivity for both Si1145 photodiodes: visible light (VIS) to the left, and infrared (IR) to the right. . . . 166
7.15 Regression fit for the Si1145 visible light (VIS) photodiode, for polynomials with order 2 to 10. . . . 166
7.16 Relative spectra of ambient light sources, including natural sunlight and 4 artificial sources: xenon lamps, fluorescent lamps (TL/CFL), incandescent lamps with tungsten filament (including halogen bulbs) and cool white LEDs with light temperature of 6000 K. . . . 167
7.17 Regression fits for fluorescent light sources (FL) and white LEDs, showing polynomial orders between 2 (parabola) and 10. . . . 168
7.18 Comparison of relative wavelength sensitivity of 8 commercial sensor devices. For devices with more than one photodiode, each diode response is listed separately. . . . 172
7.19 Block diagram of AEM Light, with a dual power path for LTC3105 and SPV1040 using analog multiplexers. . . . 173
7.20 Analog front-end for GUVA-S12SD, with current amplifier and second order LPF. . . . 174
7.21 Frequency response of the amplifier, showing current amplifier stage in gray and complete amplifier in black. Phase shifts are denoted with a dotted line. . . . 175
7.22 Static power point tracking with LTC3105 using trimpot for MPP configuration. . . . 179
7.23 Static power point tracking with LTC3105, using a digital potentiometer for MPP configuration. . . . 180
7.24 Control mechanism for MPP configuration of LTC3105, using digital potentiometer (Rev. 2) and DAC (Rev. 3). A library with MPP voltages for different cells is stored locally in the 24AA025UID EEPROM. . . . 181
7.25 Analog front-end for fixed power point tracking using the LTC3105 boost controller. MPP voltage set directly through MCP4921 DAC. Includes overload protection and auto ranging between 4 mA and 40 mA range, with digital outputs for range indication and sampling suspension (I and J). Waveforms for schmitt trigger, integrator, pulse extender and comparator are shown in the lower right corner. . . . 182
7.26 Hysteresis mechanism switching between 1 kΩ and 100 Ω shunt resistor. . . . 184

7.27 Rev. 3.0 of the AEM Light prototype. ① light energy harvester with LTC3105 MPPCT, ② power supply and ESD protection, ③ TCS3472, VEML6070, TSL25911, and MAX44009, ④ analog front-end with precision electronic load, ⑤ GUVA-S12SD with amplifier and ADPD2212. 185
7.28 PV energy harvesting circuit with true maximum power point tracking (perturb and observe), implemented with an SPV1040 DC/DC converter. 187
7.29 Active overload protection with bidirectional N-MOSFET switch, disconnecting DUT above 4.3 V. 187
7.30 Block diagram of Revision 1 (R1) and Revision 2 (R2) of AEM Thermal. On Revision 2, only the LTC3108 signal path is implemented, and the analog switches were omitted. Component selection differences between both revisions are marked where relevant. . . . 189
7.31 Sequence to retrieve ambient air temperature data from 4 Si7051 I^2C temperature sensors. 190
7.32 Block diagram of Revision 2 (R2) and Revision 3 (R3) of AEM Thermal. On Revision 2, only the LTC3108 signal path is implemented, and the analog switches were omitted. Component selection differences between both revisions are marked where relevant. . . . 191
7.33 Common mode noise attenuation by second order RLC filtering. Points A, B and C refer to nodes in figure 7.32. 192
7.34 Block diagram of Revision 2 (R2) and Revision 3 (R3) of AEM Thermal. On Revision 2, only the LTC3108 signal path is implemented, and the analog switches were omitted. Component selection differences between both revisions are marked where relevant. . . . 193
7.35 Comparison of different Si705X series temperature sensors and their effect on the measurement error of a temperature gradient, in combination with the MAX31855. 194
7.36 Analog front-end for TEG energy harvesting using the LTC3108 as ultra low input step-up converter. The negative bias for the AD7705 ADC is generated by a dedicated power supply, shown in figure 7.37. 197
7.37 Generation of a -1.5 V negative offset bias for the AD7705 ADC, using a switched mode Cúk converter (IC1) followed by a linear regulator (IC2) for ripple removal. 198
7.38 Rev. 2.0 of the AEM Thermal prototype. ① thermal energy harvester with LTC3108 step-up converter, ② voltage reference and negative bias supply ③ ambient temperature sensor controller, ④ digital processing, ⑤ digital power supply, ⑥ SMA connector for thermocouple, amplifier and ADC. 199
7.39 Start-up sequence of the LTC3108 with a 1:100 transformer (7.5 μH primary, 75 mH secondary) and capacitor values shown in figure 7.36. The left axis denotes voltage on the transformer secondary in [V], the right side shows the current through the secondary winding in [mA]. Responses shown for TEG input voltages between 10 mV and 50 mV. . 200
7.40 Start-up sequence of the LTC3108 with decoupled V_{aux} and V_{store} for faster start-up transient behavior. Solid line shows voltage over a 1 μF capacitor between V_{aux} and ground, dotted line shows the voltage over a 4.7 μF storage capacitor connected between V_{store} and ground. Curves given for DC input voltages between 0 and 200 mV in 20 mV intervals. V_{aux} tracks V_{store} above its output voltage set point, until the LTC3108 rated maximum of ca. 5.5 V (internally limited). 201
7.41 Alternative signal path for thermal energy harvesting using a TEG, with the TI BQ25570 as integrated buck-boost DC/DC converter. Capacitor C5 acts as storage element between boost and buck stage instead of a battery. 202
7.42 RF front-end of AEM Waves as a superheterodyne receiver with IQ mixer. 204

7.43 RF multiplexer with up to 3 antennas connected to SMA connectors simultaneously, with RF signal amplified by an integrated LNA. . . . 205
7.44 Suitable wideband antenna designs for AEM Waves. a) spiral antenna [96], b) patch antenna [279], c) vivaldi antenna [196], d) log-periodic antenna [43]. . . . 207
7.45 Circuit of the IQ mixer, using 2 LTC5510 integrated RF mixers and a MAX2871 VCO as LO. . . . 210
7.46 A 5 pole passive crystal filter used for IF filtering of the mixer products. The filter has a pass band of ca. 15 kHz at 10 MHz. The frequency response is shown in figure 7.48. Each crystal forms a resonant mesh with the capacitors to its side (C2, C3, C6 and C7), and the resonance frequency of these meshes is then tuned with series capacitors (C1, C4, C8) to achieve the desired response. . . . 211
7.47 Model of an Abracon ABM3-10.0000MHZ quartz crystal trimmed to a resonance frequency of 10 MHz. Note the high value of Ls in comparison to the small value of Cs, which causes deviations in the crystal's frequency response. . . . 212
7.48 Frequency response of the 5 pole crystal filter shown in figure 7.46, with a 10 kHz wide pass band slightly beyond 10 MHz. . . . 212
7.49 Analog RF front-end using ADL5513 as logarithmic amplifier to convert the 10 MHz IF signal to DC with a 80 dB dynamic range, and AD7689 16-bit ADC for quantisation of the input signal. . . . 214
7.50 Calibration procedure for AEM Waves, using an RF anechoic chamber with arbitrary wave generator for reference signal generation. . . . 215
7.51 RF voltage multiplyer and RF to DC rectifier with integrated impedance matching designed for RF energy harvesting applications. . . . 215
7.52 Block diagram of AEM Waves, with a single AD7689 ADC for measuring both channels of the IQ receiver and the input of the RFD102A RF to DC converter. The MAX2871 VCO is controlled by the MCU through SPI, while enables and channel selections are IO lines (dotted). . . . 217
53 Voltage reference and virtual ground generation. . . . 270
54 Arduino UNO add-on module (*"shield"*) with AD7689, featuring ESD input protection (D1 and D2), TVS on power rail (T1) and integrated analog power supply. . . . 271
55 Simplified AD7689 flowchart. Dotted functions represent configuration. . . . 273
56 Captured full duplex communication between ADC and MCU, showing SCK in red, SS in green, MOSI in yellow and MISO in brown. Note the 16 cycles per frame for normal operation, and the 32 cycles for the last feedback frame. . . . 274
57 Performance comparison when controlling 4 identical AD7689 devices, as counted against ADC clock cycles at 8 MHz. . . . 278
58 UML public class diagram of AD7689 communication on application level. Main denotes the parent container, running either BTestApp for deployment on Atmega328 or YTestApp for deployment on AEM modules. The implementation of AD7689 is presented in detail in figure 55. The interface YSPI is implemented for hardware SPI resources or USART in MSPIM mode, HWSPI or USARTSPI respectively. . . . 279
59 Serial programming and debugging interface over USB, including generation of system reset signal. . . . 282
60 Linear passive filter to derive AVDD from DVDD at 3.3 V. . . . 284
61 Active power supply using switched DC/DC boost converter and linear voltage regulators. Modifications for AEM Light variant shown in dotted boxes. . . . 285

List of Tables

5.1 Comparison of TEC1-12706, CP2-12706 and TEC2-19006 TEG properties. 77
5.2 Power density analysis for three commercial, consumer grade TECs. 79

6.1 Comparison of EDLCs for local energy storage. Last column showing an equivalent battery capacity for a 3.6 V Lithium Ion battery. 95
6.2 Comparison of solid state and thin film batteries. 101
6.3 Comparison of secondary chemical cell types with wet electrodes. Self discharge is indecated per month. 103
6.4 Performance comparison of monolithic DC/DC converters. 113
6.5 Power consumption of the active components in the Influencair design. 120

7.1 Comparison of 4 linear CCDs as potential candidates for a spectrometer. 162
7.2 Calculated coefficient table for light source types as 10th order polynomial fits. 169
7.3 Comparison of commercial light sensors considered for application in AEM-Light. . . . 171
7.4 Comparison of commercial PV energy harvesters considered for application in AEM-Light. 176
7.5 Comparison of commercial PV cell specifications at illumination of 1 kW/m^2. 177
7.6 Comparison of commercial temperature sensors for ambient air temperature measurement, with an accuracy of ± 2 K or better, and temperature range between -40°C and 85°C. 195
7.7 Comparison of common thermocouples for high temperature ranges. Cold-junction sensitivity for range between 0°C and 70°C. 196
7.8 Comparison of patch antenna sizes on a 4 layer FR4 PCB (thickness 360 μm, $\varepsilon_r = 4.35$. 207

List of Acronyms

a-Si	Amorphous Silicon
AC	Alternating Current
ACS	Allegro Current Sensor
AD	Analog Devices
ADC	Analog to Digital Converter
AEM	Ambient Energy Monitor
AM	Amplitude Modulation
API	Application Programming Interface
ASCII	American Standard Code for Information Interchange
BLDC	Brushless Direct Current
BLE	Bluetooth Low Energy
BMS	Battery Management System
BoB	Break-out Board
BOM	Bill of Materials
CBEH	Complementary Balanced Energy Harvesting
CC	Creative Commons
CCC	Chaos Communication Congress/Camp
CCD	Charge Coupled Device
CDC	Communications Device Class
CDMA	Code Division Multiple Access
CFD	Computational Fluid Dynamics
CFL	Cold Fluorescent Light
CIGS	Copper Indium Gallium Selenide

CM CircuitMaker

CPHA Clock Phase

CPOL Clock Polarity

CPU Central Processing Unit

CRC Cyclic Redundancy Check

CSV Comma Separated Values

CZTSSe Copper Zinc Tin Sulfur Selenide

DAC Digital to Analog Converter

DAQ Data Acquisition

DC Direct Current

DSP Digital Signal Processing

DSSC Dye Sensitized Solar Cell

DUT Device Under Test

EDA Electronic Design Automation

EDLC Electrolytic Double Layer Capacitor

EDGE Enhanced Data rates for GSM Evolution

EEPROM Electrically Erasable and Programmable Read Only Memory

Elco Electrolytic Capacitor

EMI Electro Magnetic Interference

EOL End of Life

ESD Electrostatic Discharge

ESR Equivalent Series Resistance

FBW Fractional Bandwidth

FET Field Effect Transistor

FFT Fast Fourier Transformation

FPGA Field Programmable Gate Array

GPIO General Purpose Input/Output

GPRS General Packet Radio Service

GPS Global Positioning System

GSM Global System for Mobile communication

GUI Graphical User Interface

GUID Globally Unique Identification

HF High Frequency

HPBW Half Power Bandwidth

HPF High Pass Filter

HVDC High Voltage Direct Current

I2C Inter Integrated Circuit Communication

IC Integrated Circuit

IDC Insulation Displacement Connector

IDE Integrated Development Environment

IF Intermediate Frequency

IoT Internet of Things

IPM Institute for Physical Measurement Techniques

IPS Infinite Power Solutions

IR Infrared

ISA Industry Standard Architecture

ISE Institute for Solar Energy systems

ISR Interrupt Service Routine

JST Japanese Solderless Terminal

JTAG Joint Test Action Group

LDO Low Drop-Out

LDR Light Dependent Resistor

LED Light Emitting Diode

LNA Low Noise Amplifier

LO Local Oscillator

LPF Low Pass Filter

LTC Linear Technology Circuit

LTE Long Term Evolution

LUT Look Up Table

mc-Si Monocrystalline Silicon

MCP Microchip

MCU Microcontroller Unit

MEMS Micro Electromechanical System

MISO Master In, Slave Out

MIT Massachusetts Institute of Technology

MLCC Multi Layer Ceramic Capacitor

MOSFET Metal Oxide Semiconductor Field Effect Transistor

MOSI Master Out, Slave In

MPP Maximum Power Point

MPPC Maximum Power Point Control

MPPT Maximum Power Point Tracker

MPPV Maximum Power Point Voltage

MSPIM Master Serial Peripheral Interface Mode

MTBF Mean Time Before Failure

NJTPAC NanJing Top Power ASIC Corporation

NREL National Renewable Energy Laboratory

NTC Negative Temperature Coefficient

OEM Original Equipment Manufacturer

pc-Si Polycrystalline Silicon

PCB Printed Circuit Board

PDF Probability Distribution Function

PEG Pyroelectric Generator

PID Proportional Integral Derivative

PIFA Printed circuit board Inverted F Antenna

PLL Phase Locked Loop

PMMA Polymethyl Methacrylate

PPTC Polymeric Positive Temperature Coefficient

PV Photovoltaic

PVDF Polyvinylidene Difluoride

PWM Pulse Width Modulation

PZ Piezoelectric

PZT Lead Zirconate Titanate

RAM Random Access Memory

RF Radio Frequency

RFD Radio Frequency Diagnostics

RFI Radio Frequency Interference

RFID Radio Frequency Identification

RSSI Received Signal Strength Indicator

RTC Real Time Clock

RTG Radioisotope Thermoelectric Generator

SAR Successive Approximation Register

SCL Serial Clock Line

SDA Serial Data/Address

SDR Software Defined Radio

SEPIC Single ended Primary Inductor Converter

SMA Sub Miniature Antenna

SMbus System Management Bus

SMD Surface Mounted Device

SoC State of Charge

SoH State of Health

SPI Serial Peripheral Bus

SPL Sound Pressure Level

SRAM Static Random Access Memory

SS Slave Select

TEC Thermoelectric Cooler

TEG Thermoelectric Generator

TENG Triboelectric Nanogenerator

TGS Triglycine Sulfate

TI Texas Instruments

TQFP Thin Quad Flat Package

TVS Transient Voltage Suppressor

UART Universal Asynchronous Receiver/Transmitter

UEXT Universal Extension

UHF Ultra High Frequency

USART Universal Synchronous/Asynchronous Receiver/Transmitter

USB Universal Serial Bus

UVLO Under Voltage Lock-Out

VCO Voltage Controlled Oscillator

VHF Very High Frequency

VLSI Very Large Scale Integration

Voc Open Circuit Voltage

VUB Vrije Universiteit Brussel

WCDMA Wideband Code Division Multiple Access

WDT Watchdog Timer

WHO World Health Organization

WLAN Wireless Local Area Network

YSPI Yannick's Serial Peripheral Interface

ZT Figure of Merit

Appendices

A Design Resources

This appendix serves as a listing of the open source hardware and software developed for, and discussed within the context of this thesis. The open nature of the design resources listed below is paramount to continuity of the project, and readers are encouraged to fork the repositories and contribute to hardware and software.

A.1 Hardware

The hardware is available in the CircuitMaker online repository, and can be accessed through a project's public identifier, or directly through the URL. All designs share the same URL base
https://workspace.circuitmaker.com/Projects/Details/Yannick-Verbelen/
to which the project name (also marked in bold below) should be added.

AEM

The general repository for Ambient Energy Monitor related hardware can be found at https://workspace.circuitmaker.

Ambient energy benchmarking modules:

- Vibration module: **AEM-Vibrations**
- Thermal module (TEG/PEG): **AEM-Thermal**
- Natural and artificial light module: **AEM-Light**
- RF module: **AEM-Waves**

AEM Aggregator for Raspberry Pi 3: **AEM-Aggregator**

USB dongle for programming the first AEM board revisions (legacy):
USB2UART-Dongle
USB adapter for UEXT (legacy): **AEM-UART-Adapter**

AD7689 16 bit, 8 channel data acquisition shield for Arduino UNO:
16-Bit-8-Channel-DAQ-Shield

OpenObservatory, third revision: **WeatherStation-3**
BoB for Si1145: **Si1145-breakout-board**
BoB for MQ135 (includes socket): **MQ-135-breakout-board**

Power Path Design

The following power rail designs were discussed in the chapter on power path design.

- 4 channel polyphase buck module: **Charging-Station**
- 3 A buck regulator: **LM2596-3A-Arduino-Power-Supply**
- SX1308 boost regulator and TP6042 battery charger: **Portable-Power-2**

The EDLC designs:

- Flyback design with transformer: **EDLC-ZPM**
- Single ended dual phase boost converter: **EDLC-ZPM-2**
  BoB for charge controller: **8-SOIC-to-8-SSOP-adapter**

All revisions of the Influencair prototypes: **Influencair-Node**

A.2 Software

The software repositories can be found on GitHub.

- Main repository for the AEM project:
  https://github.com/ArticCynda/AEM
  UART dongle firmware:
  https://github.com/ArticCynda/uart-dongle
- OpenObservatory firmware and device drivers:
  https://github.com/ArticCynda/OpenObservatory
- Influencair firmware:
  https://github.com/CivicLabsBelgium/Air-Quality-Brussels
- Bob's repository for AEM related Raspberry Pi firmware:
  https://github.com/gratefulfrog/SPI

B Analog Front-end

Interfacing analog sensors and measuring the power output of energy harvesters, as well as monitoring the stability of the modules itself, requires a suitable analog front-end. Although all mid to high end microcontrollers possess an integrated ADC, few satisfy the strict requirements of a data acquisition system. An analog front-end external to the microcontroller is therefore necessary, and many ADCs are available on the market to fill the void between sensors and microcontroller.

B.1 Application-specific ADC Selection

One of the perks of designing a completely new system such as the AEM hardware framework is that there are few design rules constraining the selection process of individual parts. That includes ADCs, which can be selected to optimally satisfy the requirements of each AEM module individually. For example on AEM-Vibrations, a higher sample rate than on AEM-Thermal is required since vibrations are sinusoidal signals with frequencies up to a few kHz, while temperature changes so slowly that it nearly appears a DC signal (keeping thermal inertia in mind for practical thermal energy harvesting applications). An effort was made to identify requirements for each AEM module, and select the best suited ADC for each situation, keeping other factors such as price and solderability into consideration. This resulted in 5 different ADC devices types across the 4 AEM module designs (Vibrations, Thermal, Light, and Waves). The selected devices are

- Analog Devices AD7705 and Analog Devices AD7689 for AEM-Vibrations
- Intersil ISL26102 for AEM-Light
- Analog Devices AD7705 and Analog Devices ADS1118 for AEM-Thermal
- Analog Devices AD7705 for AEM-Waves

After development of the respective embedded software drivers was started, it was discovered that the time and resources required to develop driver software was underestimated from a project management perspective. Several factors obstruct or slow the development process significantly: the diversity in footprints, lack of break-out boards (BOB), absence of suitable development platforms, and time critical constraints of the devices themselves preventing efficient use of break points and other in circuit debugging. The development time required for the AD7689 driver alone, the first one started, exceeded the planning by a factor 5. Consequently it was decided to change strategy, and instead of choosing the best suitable ADC for each application, an ADC was selected that suits all ADC requirements on all boards, with the exception of AEM-Waves. It is faster and less frustrating to respin the boards, than to spend an unpredictable amount of time on driver software development. Considering the importance of refactoring, having a small number of parts that need driver software is also preferable, since the efforts needed to maintain a code base for each ADC individually would quickly become unmanageable.

B.2 AD7689

The AD7689, for which driver development was already in progress, is a defendable choice: it combines 16 bit resolution with 250 kS/s ($25 \cdot 10^4$ samples per second) sample rate, with a total of 8 channels. These channels can be configured for single ended measurements with reference to ground or a virtual ground (= common), either unipolar or bipolar, or for differential measurements. Hence, the AD7689 can measure 4 differential signals or 8 single ended signals. A sample rate of max. 250 kS/s corresponds to a maximal sample frequency of 31.3 kHz per channel (or 62.5 kHz for differential inputs). According to Shannon's sampling theorem, the highest allowed frequency component is half of that, but a margin of

10 % is advisable for oversampling, thus leading to an effective maximum frequency of 14.1 kHz. This is more than sufficient for vibration energy harvesting, where vibrations of interest are usually below 5 kHz. Thermal and Light energy harvesting modules have slower varying signals, so their specifications will also suffice for AEM-Light and AEM-Thermal. The dynamic range of the ADC is 93.8 dB, allowing for wide variations in input amplitude, with a SnR (signal to noise ratio) of 93.5 dB at 20 kHz.

B.3 Voltage Reference

The samples returned by the ADC are raw values referenced to an internal or external reference voltage. It is necessary to scale these samples to the reference voltage to convert them to meaningful voltages. Due to the large number of sensors on each AEM module, and the complexity of a floating point multiplication and division, a powerful microcontroller would be necessary to keep up with the data stream, if maximum resolution were to be achieved. Unfortunately, such microcontrollers add complexity to the board in terms of power supply constraints, and produce additional noise which is undesirable given the high impedance characteristics of the some of the sensors. This problem was resolved by adding an additional 2.048 V precision voltage reference to the design. When referencing a 16 bit sample to a 2.048 V reference, which is an exact power of 2, complex floating point operations are reduced to simple and fast binary shift operations since

$$V_s = \frac{S \cdot 2.048}{2^{16}} = \frac{S \cdot 2^{11}}{10^3 \cdot 2^{16}} = \frac{S}{10^3 \cdot 2^5} = S >> 5\,[\mathrm{mV}] \tag{57}$$

The 2.048 V reference is generated from a 1.23 V band gap reference using a Microchip MCP1501 precision voltage reference. This voltage is buffered and divided by two to serve sensors as virtual ground with an absolute potential of 1.024 V. The implementation is show in figure 53. The AD7689 is equipped with a 4.096 V and 2.5 V internal reference generator, but these are only used for testing purposes and not for sensor operation.

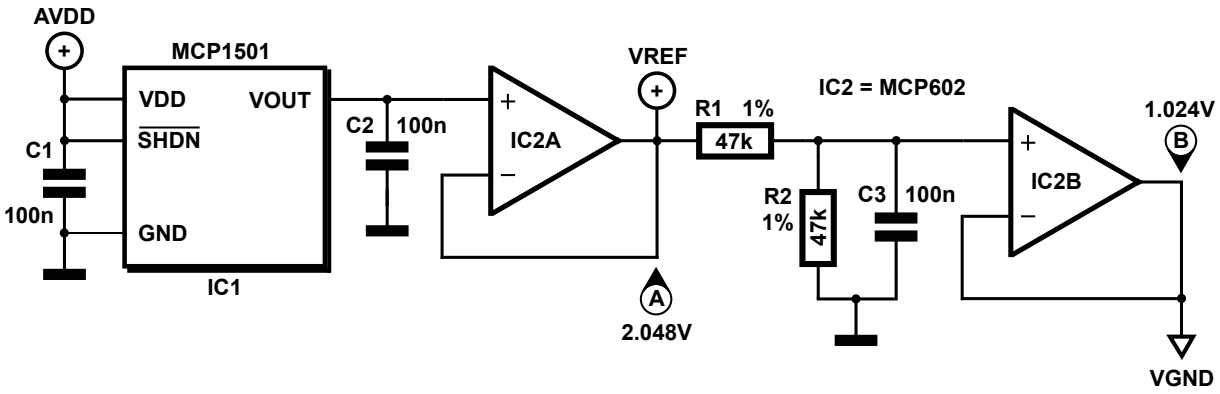

Figure 53: Voltage reference and virtual ground generation.

The AD7689 interfaces with a microcontroller through a serial connection compatible with SPI (Serial Peripheral Interconnect). The maximum throughput is specified at 30 MHz, but to limit noise of harmonics, communication runs at the minimum required frequency to sustain stable operation at 250 kS/s, which is 8 MHz. Voltage reference connections (REFIN for external input reference, REF for reference output and COM) are bypassed to shunt noise to the analog ground. A ferrite bead is used to connect analog and digital ground under the ADC device.

B.4 DAQ Shield

The lack of a convenient development platform for the AD7689 makes development of driver software more difficult, but also complicates system level testing. On custom hardware such as the AEM modules, there are 4 uncertainties hindering streamlined development:

- Hardware problems in circuit design (logical errors)
- Hardware problems in manufacturing (soldering issues, short circuits, defective components)
- Timing issues and delays caused by the microcontroller
- Bugs in embedded software and/or driver software

Developing software directly on an AEM module, where any of the issues above may occur alone or stacked, is too challenging. A better approach is to isolate the ADC and develop the driver software separately, to reduce or eliminate the effect of unknown factors on the driver development. Since no existing development board for the AD7689 turned out suitable, a new one was designed and manufactured. The design is shown in figure 54. The board is designed as an expansion module for the Arduino UNO prototyping board, with long female pin headers that allow it to be stacked on top of an Arduino UNO. The Arduino UNO is the most commonly used microcontroller development board, and its wide adoption reduces the chance of encountering unknown problems, since every aspect of it has been numerously reviewed and documented. Stacking the ADC board on top through a board to board connector interface eliminates the chance of bad contacts in wiring, offering a reliable interface to the AD7689. Functional blocks of the DAQ shield are marked in figure 54. The main blocks are the AD7689 itself and its supporting power supply, generating a noise free 5 V power supply. A two stage supply topology, discussed in the power supply section below, was implemented here before it was adopted on AEM modules. Remaining components on the board include overload and TVS protection on all input channels, and a LED driver to indicate data transfer on the SPI bus. As with all other hardware, the design is open source and available under a Creative Commons license.

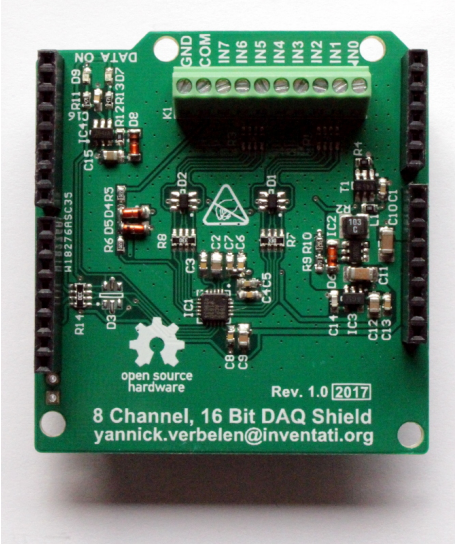

Figure 54: Arduino UNO add-on module (*"shield"*) with AD7689, featuring ESD input protection (D1 and D2), TVS on power rail (T1) and integrated analog power supply.

B.5 Driver Development

The AD7689 can operate in both single shot mode, taking a single sample at a time, or in sequencer mode, sampling each channel sequentially. Acquisition always starts with channel 0, and runs up to the highest channel specified by the 3 INx bits set in the configuration register of the device. The ADC does not have its own oscillator, and all timing is directed by the the SPI communication, more specifically the signaling on the Slave Select (SS) line. The SS line generates the timing framework to take a sample, perform the analog to digital conversion, and move the results to the output buffer. Falling edges on SS act as clock edges to the ADC to initiate each step in the internal state machine. This results in a fairly complex pipelined data structure where 2 cycles elapse between sampling data and sending the output to the microcontroller:

- Cycle 1: command is latched into the ADC and immediately afterwards, input channels are sampled.
- Cycle 2: analog to digital conversion is performed.
- Cycle 3: digital data available for retrieval.

The advantage of such a pipelined data flow is that all functional blocks (sample & hold, SAR, command processor) are used to maximum capacity, unlike a non-pipelined architecture where the sample & hold and SAR would idle until the converted sample is read. The sampling rate of 250 kS/s, which is high compared to other ADCs in the same price range, would not be possible without such a pipelined data structure. It does have its drawbacks on the software driver side, unfortunately, because timing is critical. For example, the time between two successive cycles must be long enough to perform a sample acquisition and an analog to digital conversion in parallel, but short enough to prevent the previous sample in the buffer to be overwritten by the next one before it could be read out. The output buffer is only 16 bits (2 bytes), containing only a single converted sample. It is important to emphasize that this sample corresponds to a measurement that was made 2 cycles ago.

Because of the complexity of the timing criticality and considerable complexity of the AD7689, developing a robust yet transparent software driver is a challenging endeavor. The driver must be compatible with different microcontrollers within the AVR family (Atmega328p for the DAQ shield to allow testing, and Atmega2560 for AEM modules), handle different microcontroller clock frequencies without needing manual reconfiguration, and be compatible with both hardware SPI and MSPIM, as discussed below. A primary requirement remains the ease of use and transparent operation, as well as the refactorability of the code. The simplified functional flow chart of the AD7689 driver is shown in figure 55, with the top part indicating the preprocessing stage and bottom part the post processing on retrieved data. Since the AD7689 is directly connected to the microcontroller (MOSI and MISO offering bidirectional full duplex data flow), the communication is essentially a loop with a 2 byte data buffer on microcontroller side, and an identical data buffer on ADC side. After data is loaded in the buffers on either side, the master (microcontroller) dictates the transfer rate by issuing clock cycles to the ADC. A total of 16 clock cycles is generated to transfer 2 bytes from the ADC to the MCU, and simultaneously also the 2 bytes from the MCU to the ADC. The operation *Shift SPI Transaction* in figure 55 thus indicates both receiving and transmitting 2 bytes simultaneously.

Self Test

The AD7689 supports readback of the command register, which is implemented as a self test function in the driver. When enabled in the ADC command register, the ADC returns the contents of the command register instead of a converted sample immediately after the second cycle, without additional delay. In

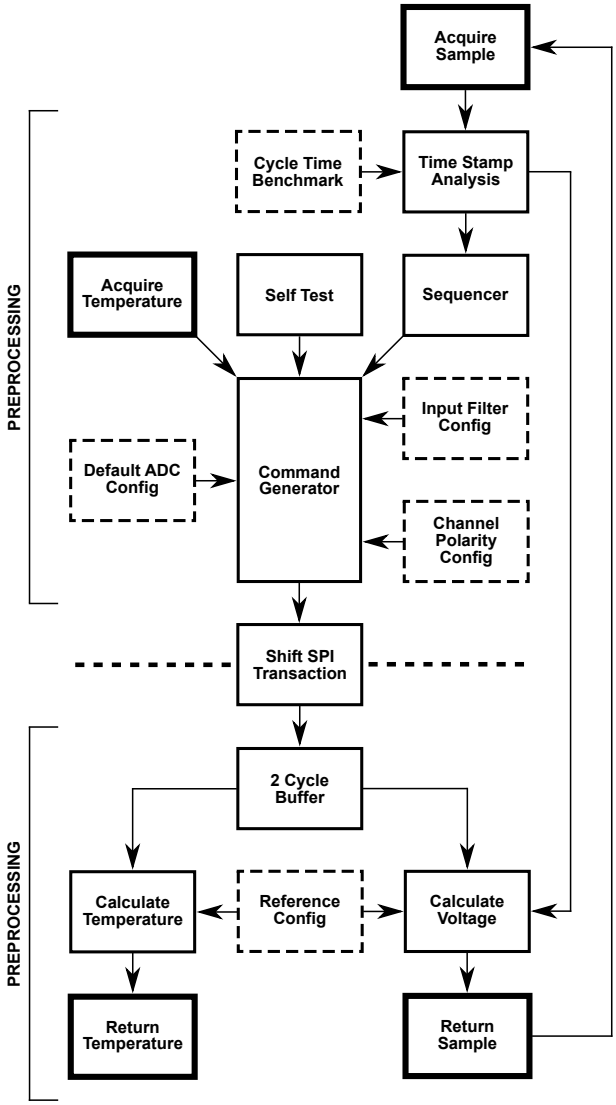

Figure 55: Simplified AD7689 flowchart. Dotted functions represent configuration.

readback mode, the AD7689 thus returns 32 bits, the first 16 bits being the converted sample and the last 16 bits the contents of the command register 2 cycles ago. The self test function in the driver first configures the AD7689 for readback, then skips a dummy cycle before reading out the second dummy cycle followed by the command register contents. If those contents match the original command, the test is considered successful, and proves that the ADC is responding, and that the 4 digital interface lines (MISO, MOSI, SCK and SS) are properly connected. After a self test, 2 more cycles are skipped to flush the command register. Conveniently, the self test function returns only a boolean value indicating whether the test succeeded or failed, allowing testing of the ADC with a single line of code.

Single Shot and Sequencer

The AD7689 supports 2 operation modes: *single shot mode*, in which a single channel is sampled recurringly, and *sequencer mode* in which sampling loops automatically through all active channels. The first

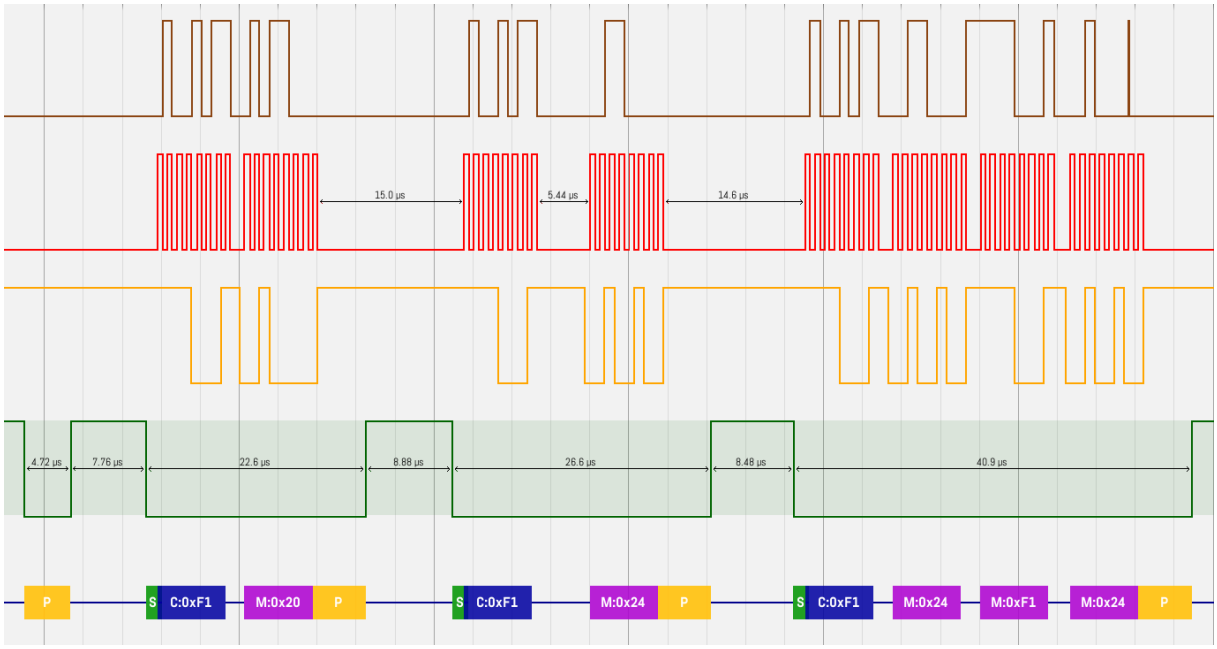

Figure 56: Captured full duplex communication between ADC and MCU, showing SCK in red, SS in green, MOSI in yellow and MISO in brown. Note the 16 cycles per frame for normal operation, and the 32 cycles for the last feedback frame.

active channel is always channel 0, the last active channel can be set by the user. Although the least complex to implement in software, single shot mode only reaches the maximum sample speed of 250 kS/s when a single channel is sampled repeatedly. When changing the channel by altering the command register, 2 cycles will pass before the first sample is available. The actual sample rate is thus much lower than the theoretically achievable sample rate of 250 kS/s. To avoid burdening the application level with the question whether single shot or sequencer mode is the better choice for a given set of input channels, the driver software configures the AD7689 in sequencer mode by default, with all channels up to the highest channel specified by the user being sampled sequentially. The samples are read out continuously and stored in a sample vector in microcontroller memory together with a time stamp indicating their age. If the application level makes a request for a specific channel, the driver software calculates the time it would take to make a new measurement of that channel based on a timing benchmark made during the initialization phase. If taking a new sample takes longer than the time since the previous sample in memory, the previous sample is returned, as shown in figure 55 on the right. If the time stamp indicates the measurement is outdated however, the sequencer will be activated and a new sample acquired, then returned to the application level. Ideally, the driver is set to sequence the ADC continuously, ensuring the samples in buffer are always up to date. However, this generates continuous traffic on the SPI bus, which is undesirable if the bus is shared with other SPI devices. To mitigate this problem, the sequencing can also be triggered on request, decreasing the load on the SPI bus but also resulting in higher sample ages. The time stamps are recorded and returned to the calling application level together with the sample values themselves however, so there is no confusion about the moment samples were taken. At the application level, measurements are made by calling the *AcquireChannel* function, which activates the sequencer when necessary and returns the sample together with its optional time stamp. AcquireChannel returns a voltage, which is calculated from the raw sample data using the reference voltage and channel

polarity set during the initialization phase. Support for an integrated anti-aliasing filter is included, which can be turned on or off by the user. Activating the filter turns it on for all channels.

Temperature Calibration

The AD7689 includes a semiconductor temperature sensor, designed to compensate measurements for temperature drifts. The temperature can be read as stand alone value (using the AD7689 as a temperature sensor with SPI interface), or the temperature can be sampled by the sequencer as a virtual additional channel. The driver software implements both strategies, and keeps the latest temperature together with its appropriate time stamp in its buffer. When sampling only temperature, the sequencer is disabled. At application level, temperature is read by calling the *AcquireTemperature* function, similar to *AcquireChannel* for measuring input channels.

B.6 SPI

The digital interface of the AD7689, and in general any high speed ADC, is SPI. In a typical setup connecting an ADC with a microcontroller or microprocessor, the characteristics of SPI as a data transmission interface are intentionally kept simple to reduce the overhead on either side and speed up data transmission. In its bare form, SPI is more a communication principle than a bus protocol. With only a shift register on either side, data transmission is full duplex since at every clock cycle of the SCK line, one bit is transferred in either direction. The clock phase and polarity, CPHA and CPOL respectively, are hardware dependent on the slave side, and specified as CPHA = 0 and CPOL = 0 for the AD7689, which corresponds to SPI mode 0. Since the AD7689 has a 16 bit resolution, it has a 16 bit output register, and thus takes 16 MCU clock cycles (assuming one bit is transferred at every MCU cycle, i.e. SPI clock speed equals MCU clock speed) to transfer 2 bytes from MCU to ADC and vice versa. The ADC frame starts counting when the slave select line SS is pulled low, and the AD7689 requires an additional 0.8 μs to complete pipelined operations per frame, corresponding to 6 clock cycles at 8 MHz. Thus, it takes a total of 22 clock cycles at that clock frequency before another transaction can take place. This is shown in figure 57 in the column on the right. Retrieving sample data from the IO buffer and loading a new command into this buffer takes another clock cycle each, adding up to a total of 24 clock cycles before a new transaction can start.

It is important to understand that transmission of the 16 bits is controlled by a hardware SPI resource, and does the CPU itself. Thus, after moving the data to the output buffer and initiating the transfer, the CPU is free for other operations. For the AD7689, Bathree et al. suggest to put the CPU in a busy wait loop until a receive flag is set by the hardware SPI core of the MCU, indicating a completed transaction and availability of data [24]. Despite its simplicity, this approach is wasteful with regard to CPU power, since a majority of time will be spent waiting for the transaction to be completed. Note that in situations where the CPU clock frequency is higher than the SPI clock frequency, proportionally even more CPU power is wasted idling. Since particularly on AEM-Vibrations relatively demanding timing constraints exist in comparison to the AEM modules, it is undesirable to waste CPU cycles that could be used to increase the sample rate or run calculations instead of waiting.

MSPIM

In systems where multiple slaves communicating over SPI need to be interfaced with a single master, they are often merged onto the same SPI bus by tying all MOSI, MISO and SCK lines together, and providing a separate Slave Select (SS) line for each device. Any output is governed by a tristate buffer,

controlled by this SS line. Whenever the active low SS line is unasserted, it remains floating high, and the unaddressed SPI device is physically disconnected from the bus. For this reason, low end microcontrollers usually only have a single SPI hardware resource integrated. And although this approach enables multiple ADCs to share the same bus, identical ones if desired, it does not result in a nett gain in sample frequency because only one device can be controlled at any given time. The processing time of 0.8 μs is too short to multiplex 2 AD7689s on the same bus at full speed.

A solution offered by AVR class devices is their USART resource, *Universal Synchronous/Asynchronous Receiver and Transmitter*, in addition to the already existing hardware SPI core. The purpose of USART is to provide a flexible communications core that can be used either asynchronously (standard UART, RS232 etc.) or synchronously in master mode, where the core provides the clock for a connected slave. In other words, the USART hardware resources can be dynamically configured to operate either as UART or SPI cores. When configured for synchronous operation, the cores are defined as MSPIM (Master SPI Mode). This allows design flexibility from a system level perspective because the Atmega2560 is equipped with 4 USART resources and 1 SPI resource. In applications where fewer than 4 UART connections are necessary, unused USART resources may be traded in for MSPIM resources, or simply used as GPIO pins. When all USART resources are configured in MSPIM mode, a theoretical 5 SPI devices may be connected simultaneously to the Atmega2560, all on their designated bus. The Atmega328 used for prototyping code using the previously discussed DAQ shield, in comparison, only has a single USART resource in addition to a hardware SPI resource.

The efficiency gain from connecting different ADCs on different dedicated bus interfaces is shown in figure 57 in the left column. In this example, 4 different AD7689 devices are controlled from a single core CPU, but due to the USART/SPI resources taking responsibility to coordinate data transfer, the CPU can control them effectively in parallel. The volume of data that can be transferred is increased by 400 % in comparison the a topology where 4 ADCs would share the same SPI bus. The only difference in implementation from a software point of view is that the transfer control routine can no longer poll the receive flag, because this would lock the CPU as explained before. Instead, an interrupt driven approach is implemented to trigger reading and writing data from/to buffers in an interrupt service routine (ISR). Only one interrupt is required, as shown in figure 57, because the delays are identical for each AD7689 device, and as such, the time shift is also constant.

YSPI

The flexibility of combining USART in MSPIM mode with hardware SPI resources increases the complexity on the application level because different USART resources have different register names, different addresses, different pin numbers, different ports they belong to, etc. A proper software framework to control AD7689 devices regardless of which USART or SPI resource they are physically connected to, is therefore necessary to encapsulate the complexity of the implementation and hide the hardware details from the application layer. The class diagram of the C++ implementation is shown in figure 58. On the hardware level, an abstract class YSPI represents a generic SPI resource, which can be a USART or SPI resource. Two classes implement YSPI, one to use hardware SPI cores with appropriate registers (hwSPI) and another to use USART cores in MSPIM mode (usartSPI). The constructor of usartSPI takes as argument the USART resource that should be used, on the Atmega2560 any value between 0 and 3 since available USART resources are numbered from USART0 to USART3. A separate MCU definition file holds a list with registers and register addresses necessary to control and configure USART and SPI resources on different microcontrollers of the AVR family. Currently, Atmega256 and Atmega328 are

supported, respectively for AEM modules and DAQ shield debugging. An instance of either class is then called by the AD7689 driver itself, which in turn is controlled by the application.

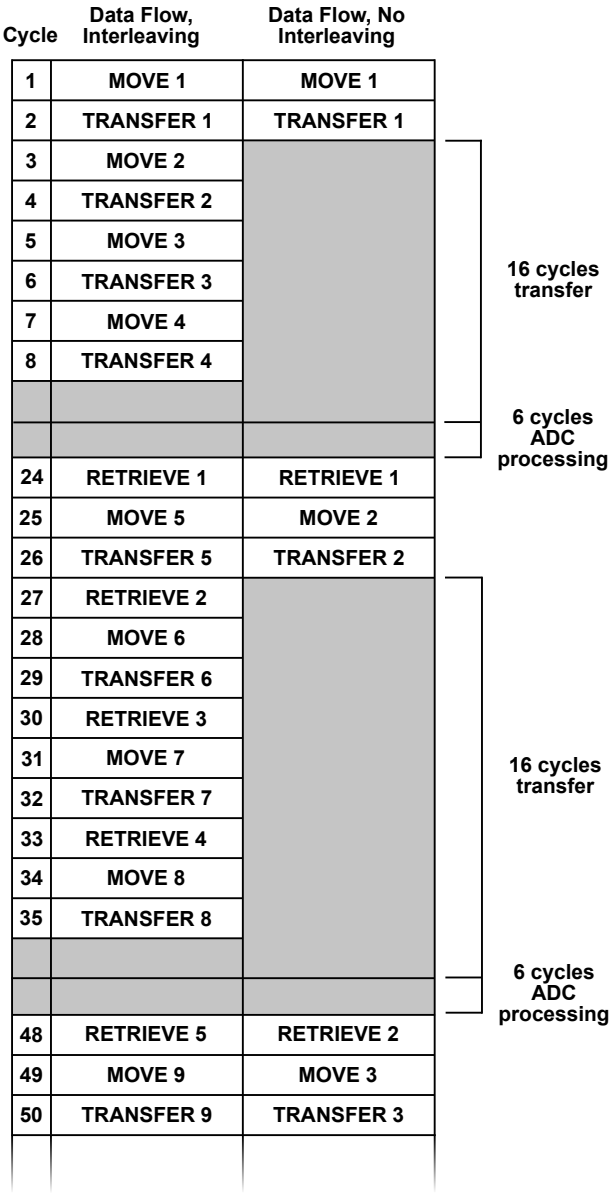

Figure 57: Performance comparison when controlling 4 identical AD7689 devices, as counted against ADC clock cycles at 8 MHz.

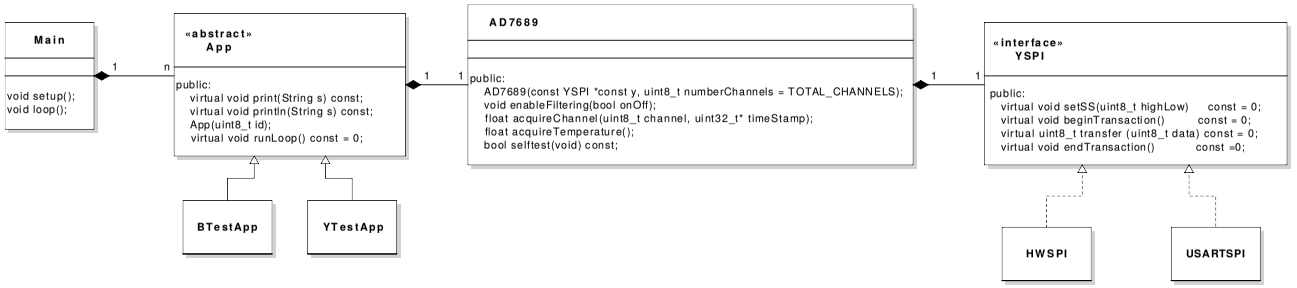

Figure 58: UML public class diagram of AD7689 communication on application level. Main denotes the parent container, running either BTestApp for deployment on Atmega328 or YTestApp for deployment on AEM modules. The implementation of AD7689 is presented in detail in figure 55. The interface YSPI is implemented for hardware SPI resources or USART in MSPIM mode, HWSPI or USARTSPI respectively.

Implementation notes

The software framework presented in figure 58 is the first open source MSPIM implementation to the author's knowledge, despite MSPIM being documented in AVR datasheets. Consequentially, few development boards for AVR micrcontrollers make the required clock pins available, preventing prototyping efforts with YSPI. Aside from the AEM modules, only IteadStudio currently provides a development board with SCK pins broken out.

C Connectivity

All AEM modules are equipped with 3 digital connectors: a JTAG connector, a UEXT connector, and depending on the revision, a UART or USB connector.

C.1 JTAG

A 6 pin JTAG interface is available as a shrouded IDC connector, allowing direct reconfiguration of the Atmel Atmega2560 microcontroller. The interface can be used to write flash memory, i.e. to burn a bootloader or write user firmware directly. With the AVR JTAG ICE Mk II and other JTAG programmers that support it, it is also possible to debug software directly on the AEM modules through breakpoints. Currently, no JTAG board definition files are available for the AEM modules, and thus JTAG hardware debugging is not supported.

Two distinct approaches exist to get firmware loaded on an SMD microcontroller: either burning the firmware before soldering the IC to the PCB, or burning it after assembly. Burning firmware before assembly can be done using an appropriate IC socket, and some chip vendors (i.e. Digikey) offer this as a service to customers. A notable drawback however is that no recovery is possible in case the bootloader gets corrupted, in which case the board is effectively bricked. Desoldering the microcontroller, which has a 0.5 mm pitch TQFP package, is complex, prone to failure, and therefore not a pleasant undertaking. To avoid risking bricking modules indefinitely, it was opted to equip all modules with a standard JTAG interface instead to allow post reflow programming and reprogramming at any given time. Recovering a bricked module then only requires to hook up a suitable programmer to restore the bootloader and/or run a self test program. There is no physical connector layout defined in the JTAG standard, but shrouded and unshrouded headers in 6, 8 or 10 pin versions are the most common. AVR recommends a 6 pin connector layout. Rather than a double row 6 pin header, it was decided to choose a shrouded IDC connector instead which is pin compatible but has the additional advantage that it is impossible to polarize the connector incorrectly into the socket because of the notch sticking out on one side. IDC connectors are widely available and low cost, unlike pogo connectors which are harder to come by and much more expensive (30 - 40 EUR are no exceptions).

The JTAG interface shares several physical pins with the SPI interface on the Atmega2560, and are therefore multiplexed. Series resistors are included to lower slew rate in an effort to reduce EMI produced by the fast SPI communication, and also prevent shorting lines in case a JTAG programmer would be connected simultaneously with a UEXT peripheral. AEM modules are capable of powering JTAG programmers through the JTAG connector, with a maximum of 250 mA at 3.3 V. A polyfuse (PPTC) is responsible for short circuit protection and, if the need for it arises, compensation of voltage level differences between JTAG programmer and the module's on board power supply. Although powering a module through the JTAG programmer is supported in theory, the AVR JTAG ICE Mk II is not able to

supply enough current to boot up the board in most experiments. The AEM module thus needs to be externally powered for the JTAG ICE Mk II to be able to access the Atmega2560.

C.2 UEXT

The UEXT interface (Universal EXTension) was chosen for communication between AEM energy harvesting modules and an Aggregator module. The UEXT standard was defined by Olimex, and provides power and serial data in a single connector. UEXT connectors officially only support 3.3 V power, and all AEM modules comply to this specification, although third party hardware is available on the market with UEXT connectors using 5 V power rails instead of 3.3 V. AEM modules are not compatible with this 5 V UEXT hardware, but tolerant to it because of adequate input protection (PPTC + varistor/TVS). Aside from power, UEXT specifies 3 serial interface buses: 4 wire SPI (MOSI, MISO, SCK and SS), I2C (SCL and SDA), and UART (RX and TX). These 8 physical connections combined with a 3.3 V and ground connection result in a 10 pin connector. The standard defines 10 pin right angle shrouded headers, to which 10 pin female board to board connectors can be fitted, or IDC cables. Both are supported by AEM modules, and TVS protection is in place to enable unshielded ribbon cables to be used. The UEXT standard does not require all 3 buses to be wired on slave devices such as the AEM modules. Earlier revision of AEM modules implement only the SPI bus, while later revisions implement all 3. A switch matrix on the Aggregator board determines which buses are routed to the host.

C.3 UART

AEM-Vibrations and AEM-Thermal revisions 1 and 2 are equipped with a dedicated 4 pin right angle header acting as a UART interface to the board. This header carries 3 signals: transmission (TX), reception (RX) and reset (RST). The latter is required to reset the microcontroller into bootloader mode, enabling the reflashing of firmware through the bootloader to avoid needing the JTAG programmer during development. Because the UEXT connector supports UART but does not have undesignated contacts to carry a reset signal, it is not possible to reset the board through the UEXT connector without additional hardware components. One solution to his problem is the addition of an I^2C expander IC such as the PCA9536. This allows the reset signal to be generated on the module side, using the I^2C bus of the UEXT connector. The IC has a fixed I^2C address of 0x41 which can be addressed to set 4 independent I/O pins. While a low cost solution on the module side, the software implementation on the computer side becomes more complex because the programmer tools, AVRdude and AVaRICE, need to be altered to send a reset pulse through this uncommon interface. To avoid a lengthy software development process, it was decided to resolve the problem through hardware instead, by including the additional 4 pin header.

To enable easier development, a USB dongle was designed to interface directly with AEM modules. The dongle carries a UEXT connector which can be connected directly to AEM modules for serial debugging, in which case the dongle acts as a master. The dongle acts as a USB to UART bridge using the famous CH340G, and does not implement the SPI or I^2C bus of the UEXT specification. Instead, it uses its MOSI line to generate a reset pulse, which can easily be rewired to the 4 pin header by splitting a ribbon cable. Since the direction of MOSI is always output for the master side and input for the slave side, no data direction conflicts are possible if the dongle were to be connected to a UEXT slave implementing SPI. The SS line on the dongle side is pulled high (inverse logic) to disable any SPI device on a slave side. The dongle design offers numerous improvements over existing similar hardware, such as the FTDIfriend from Adafruit. The most significant improvements are

- On board voltage regulator, capable of supplying 500 mA of current to a slave at 3.3 V.

- Full USB 2.0 support, maximum UART speed of 460 kHz.
- ESD protection on USB inputs and outputs.
- Short circuit protection on all outputs.

The dongle enumerates as a standard ACM device in Linux, which eliminates the need for an additional driver. An additional advantage is that the dongle also works on a Rasperry Pi or similar single board computers with a Linux operating system, allowing remote configuration of AEM modules in the field as long as they are properly interfaced.

C.4 USB

After evaluation of the UART approach, it became apparent that the concept is suboptimal. Although the pinout is printed on the underside of each board, past experiences have learned that custom connectors such as the 4 pin UART connector are almost universally a bad idea because they are prone to miswiring. Keeping the negligible cost of the part count on the dongle presented above in consideration, it was decided to merge both together. Integrating the dongle hardware onto the AEM modules equips them with their own USB connector, making connection to the host computer easier because only a standard USB cable is required instead of a less common UEXT ribbon cable. The circuitry of the dongle was inherited nearly completely, aside from minor changes in power supply layout and ESD protection. The circuit is elaborated in figure 59.

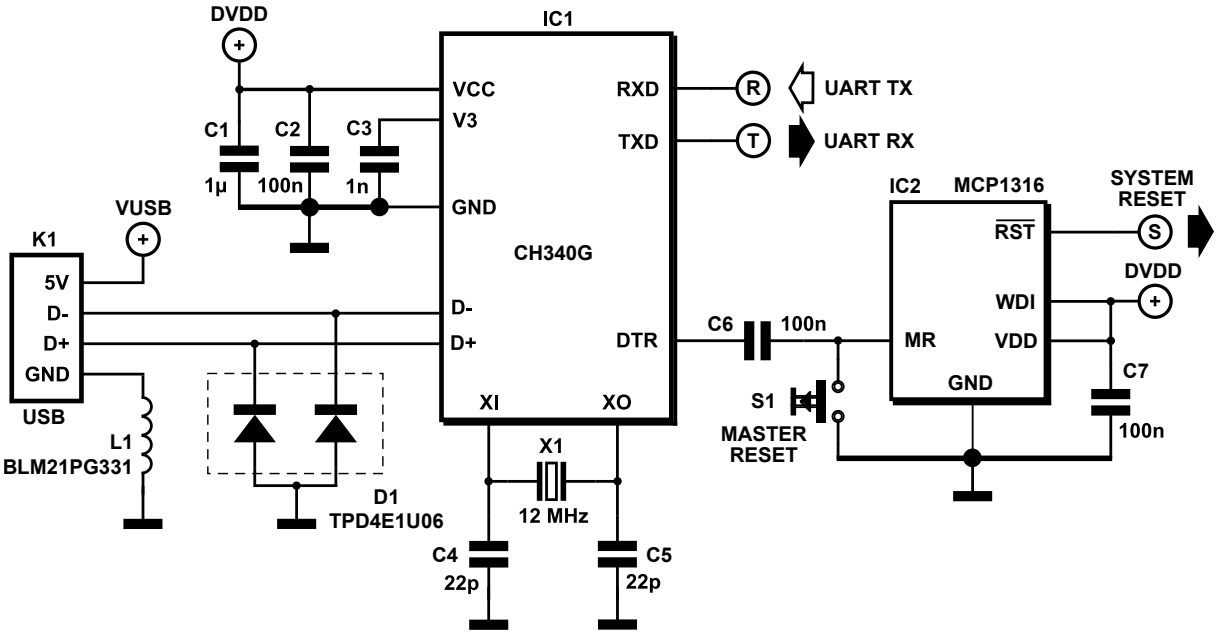

Figure 59: Serial programming and debugging interface over USB, including generation of system reset signal.

The CH340G from DreamCity Innovations integrates all necessary filtering on USB lines and the required 1.5 kΩ pull-up resistor to comply to the USB 2.0 standard. TVS diodes are not strictly necessary, but included to allow interfacing AEM modules with an unshielded USB cable. A crystal oscillator with integrated multiplier generates a 48 MHz USB clock. USB communication runs at 3.3 V, and the CH340G can therefore directly be powered from DVDD. The UART lines RX and TX are interfaced to

the Atmega2560 microcontroller directly, while the reset pulse is fed to a MCP1316 rail monitor. This voltage supervisor from Microchip monitors the DVDD supply rail continuity and resets the system if instabilities are detected on the DVDD rail, if the CH340G gives a reset pulse to reboot the Atmega2560 into bootloader mode, or when the user resets the board manually with the Master Reset button S1. This push button is colored red on all AEM modules to indicate its reset function uniformly. The choice for the CH340G as USB to UART bridge IC deserves elaboration, since the OpenObservatory project makes use of the Microchip MCP2200 instead. Although the MCP2200 is functionally almost identical to the CH340G, it is physically larger and less robust than the CH340G. It requires a configuration utility that is only compatible with the Microsoft Windows operating system, and thus incompatible with the open source philosophy of the AEM project. These three arguments have motivated the change of hardware controller from MCP2200 to CH340G.

D Power Supply

Power supply design is a critical element of any mixed signal design, and the AEM modules are no exception to this rule. In addition to a 2.048 V precision voltage reference and the 1.024 V virtual ground derived from it, a properly regulated and decoupled digital and analog power supply of 3.3 V is required. The reference was experimentally verified on AEM Waves with an AN8008 precision volt meter and is accurate within ± 1 mV. The analog 3.3 V power rail supplies low noise power to sensitive analog parts, primarily voltage reference, ADCs, amplifiers and electronic load for energy harvester benchmarking. The digital 3.3 V power rail is responsible for powering all the remaining circuitry: central microcontroller, memory, and IO connectivity. Two revisions of the AEM module power supply were designed: a linear higher order passive filter, and an active design with voltage regulators.

D.1 Passive Filtering

The circuit for the first revision is shown in figure 60. This design was used on the first 2 revisions of AEM-Vibrations, AEM-Thermal and AEM-Light. These modules have UEXT connectivity, in addition to a 4 pin UART connector. The modules are powered through the UEXT connector, supplying 3.3 V from the host. This supply is considered a digital supply, carrying considerable digital noise. As seen in figure 60, the interface consists of a fuse to disconnect the power rail in case of a surge current or overload. D1 was added for transient voltage suppression (TVS) and reverse polarization protection. C2 acts as a tank capacitor, in conjunction with multi layer ceramic capacitor (MLCC) C3 forming a passive low pass filter in combination with F1 which is a polyfuse (PPTC - polymeric PTC). In normal operation, F1 acts as a resistive impedance of 5 Ω - 20 Ω, and peaks to 10 kΩ - 100 kΩ after tripping current has been exceeded. The cut-off frequency of the formed low pass filter thus varies between ca. 86 Hz and ca. 350 Hz. This is adequate, since filtering is not critical for the digital power supply (DVDD). However, DVDD still contains a significant amount of digital noise from the host, as well as noise contributed by the digital components attached to the DVDD rail on the AEM module itself. This noise is detrimental for the performance of analog sections on the modules, and requires additional filtering to be removed.

To attenuate noise over a frequency range as wide as possible, it was chosen to cascade 2 CLC pi filters. The first filter consists of C3, L1 and FL1, the second one of FL1, L2 and C4. L1 and L2 are ferrite beads from Murata, with a characteristic impedance at 100 MHz of 330 Ω±25 %, a rated current up to 1.5 A and a maximum DC resistance of 70 mΩ. FL1 is a feed through capacitor, designed for filtering applications on high speed signal lines and DC power supplies. Its nominal capacitance is 220 nF ±20 %, with a maximum DC resistance of 30 mΩ. This low ESR improves its performance in filtering applications.

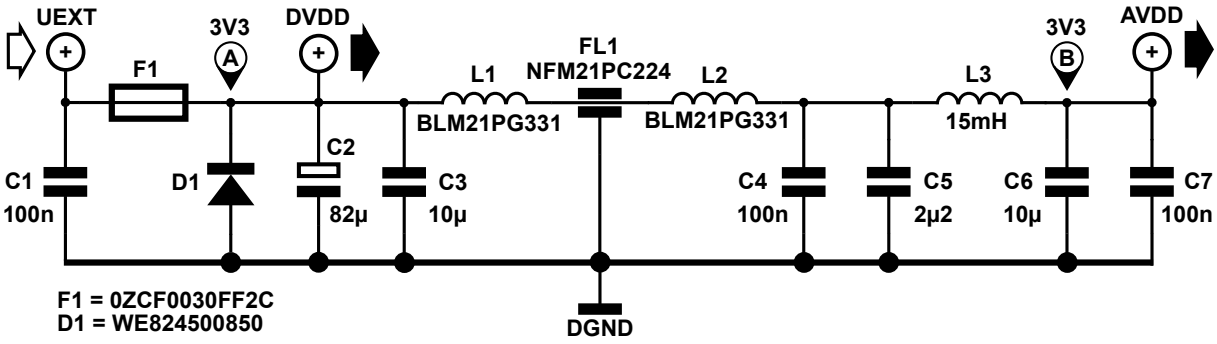

Figure 60: Linear passive filter to derive AVDD from DVDD at 3.3 V.

Although this 4th order low pass filter topology performs well for digital switching noise, it provides little attenuation for 50 Hz - 100 Hz noise caused by power lines or lighting. Particularly for AEM-Vibrations, where 50 Hz - 100 Hz is an interesting frequency range for piezoelectric energy harvesters, it is essential to remove external noise covering this frequency range. An additional pi filter with high value inductor was added for this purpose. Filtering the 50 Hz frequency component requires very high capacitance values however, 680 μF or more for a passive LC filter with 15 mH inductor.

D.2 Performance

The layout in figure 60 was first implemented and tested on AEM-Vibrations Revision 2. It was found that DVDD complied to all the set requirements regarding ripple and ground bounce. Unfortunately, two problems were observed on the AVDD rail:

- Insufficient filtering of the 50 Hz power line frequency component present on DVDD.
- Excessive voltage drop over the filters due to their resistive impedance, causing a voltage difference up to 350 mV between DVDD and AVDD.

To resolve these issues, it was attempted to increase C6 to 1000 μF as tank capacitor, and replace C7 with an ultra low ESR tantalum type. This allows lowering L3 from 15 mH to 33 μH, drastically lowering its series resistance. Although the voltage difference was decreased to 150 mV, this lack of stability remains unacceptable, and a passive filter design was therefore abandoned in favor of a design with active voltage regulators.

D.3 Active Filtering

To improve noise attenuation and output voltage stability, and simultaneously reduce dependence on large tank capacitors and/or bulky filter inductors, an active filter was designed with two cascaded voltage regulators, shown in figure 61. When powered over UEXT, a 3.3 V power supply is connected to the top left UEXT connector, and the overload protection part is identical to that of figure 60. The digital power rail DVDD was stable in the passive topology, and was carried over for simplicity. To stabilize the 3.3 V digital rail (point B) and filter digital noise away, the passive cascaded pi and LC filter topology from figure 60 was replaced by voltage regulators IC2 and IC3.

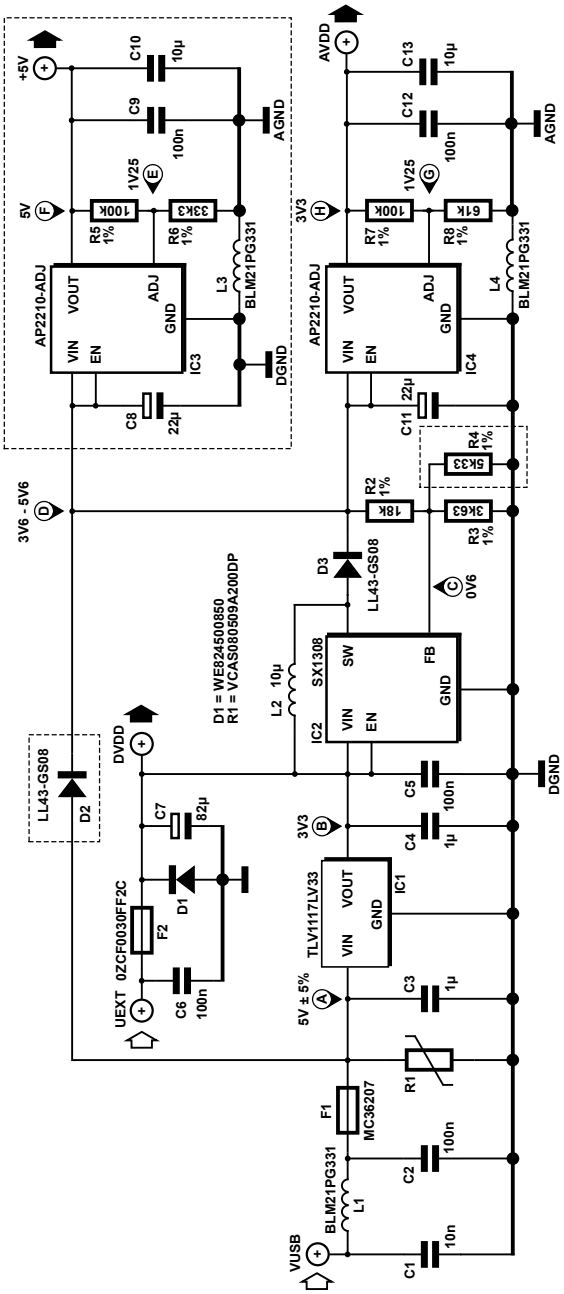

Figure 61: Active power supply using switched DC/DC boost converter and linear voltage regulators. Modifications for AEM Light variant shown in dotted boxes.

In the first stage, the 3.3 V digital power rail is boosted to ca. 3.6 V by IC2 (point D). It is a low cost integrated boost controller with internal voltage reference of 0.6 V and oscillator of 2 MHz. Since it is equipped with an internal low $R_{DS(on)}$ P-channel MOSFET, the only required external components are switching inductor L1, flyback diode D1, and output tank capacitor C8. In addition, voltage divider R2/R3 closes the feedback loop and sets the output voltage. Calculation of the resistor values is trivial, since an internal comparator regulates the output voltage to converge point C to the internal reference of 0.6 V. The value of the inductor L1 is not critical, its exact value will be decisive for the current ripple on the output, but since the output voltage is not used directly, it is unimportant. The intermediate voltage rail of 3.6 V (point D) is contaminated with the original digital noise, in addition to the 2 MHz switching noise of IC2 itself. This is subsequently removed in a second stage, constructed around linear low dropout (LDO) regulator IC3. This regulator IC is specifically designed for sensitive analog applications. C13 acts as a tank capacitor. The analog output voltage (point E) of 3.3 V not only exhibits superior stability in comparison to the passive approach described above, but also better filtering characteristics in the low frequency range (50 Hz - 100 Hz). The remaining noise in this frequency range was found to be so low on point H that it could not be reliably measured (<2 mVpp). As proof of concept, the topology was implemented on the AD7689 DAQ shield as analog power supply before being integrated in AEM modules. The only notable difference is regulation to AVDD = 5 V instead of AVDD = 3.3 V. A second modification in comparison to the passive design of figure 60 is the separation of analog and digital ground directly at the power supply. This was previously done with ferrite beads under ADCs individually, but this approach turned out complex. A shielded analog ground plane on an internal layer of a 4 layer PCB is a better solution, that is less prone to picking up external noise. Bypass capacitors are distributed over the board to provide the necessary filtering as a low ESR path. The role of C11 becomes more important to reduce ground bounce when large currents are drawn through ferrite bead L3. It is of paramount importance to choose L1 with a parasitic DC resistance as low as possible, to avoid AGND being significantly higher than DGND. AEM-Vibrations was upgraded to a USB interface in Revision 2.2 (see section Connectivity). Since it is more convenient to reconfigure and power the module through USB at the same time, rather than requiring the UEXT interface to supply power ot it, modifications to the power supply design were added to accommodate 5 V USB power. These modifications are shown at the bottom left side of figure 61, with 5 V digital USB power rail connected to VUSB. According to USB specifications, an error margin of ±5 % is allowed, ranging power levels between 4.75 V and 5.25 V. C1 and L1 ensure compliance with USB specifications (a minimum capacitive load of 10 nF is required for USB 2.0). PPTC F1 and varistor R1 protect the input against overloads, sourcing ca. 5 V on point A to the power supply circuit. The digital power rail DVDD is directly derived from the USB power rail with a general purpose linear regulator of type 1117, the surface mount equivalent of a classic LM317 with integrated voltage divider configured for an output voltage of 3.3 V (IC1). C3 and C4 provide tank capacitance and bypassing, respectively. Since it would be inefficient to first regulate down to 3.3 V to boost up to 3.6 V again in the first stage of the active filter, a bypass for IC1 was added through D2. Flyback diode D1 and D2 form a logical OR, sourcing the highest voltage (minus forward voltage drop) to point D. Since the voltage divider R2/R3 is configured for an output voltage of ca. 3.6 V, connecting 4.4 V - 4.8 V (depending on type of diode used) to point D reduces the duty cycle of IC2 to 0, effectively disabling the boost stage. IC3 thus proceeds to regulate the USB input voltage down to analog voltage rail AVDD. When the module is powered by USB, both linear regulators IC1 and IC3 operate in parallel, and IC2 is disabled.

D.4 Variants

The analog front-end of all AEM modules operates at 3.3 V, which is generated by LDO IC4. A notable exception is AEM Light, which operates the analog front-end at both 3.3 V and 5 V to ensure compliance with PV cells with a maximum power point voltage (MPPV) of up to 4.096 V. A variant to the power supply circuit is therefore devised, which also generates the additional 5 V power rail. In figure 61, the three sections that are added or removed in the AEM Light variant are marked with dotted boxes. Parallel resistor R4 is added to raise the output voltage of the SX1308 to ca. 5.6 V, which allows a dropout voltage of 0.6 V for IC3. The voltage divider 18k/3k36 configures the output to 3.6 V, but it can be changed by mounting R4 with a value calculated as follows:

$$V_{out} = \frac{1}{0.6} \cdot \frac{3k63 \cdot R_4}{3k63 + R_4} \cdot \left[\frac{3k63 \cdot R_4}{3k63 + R_4} + 18k \right]^{-1} \tag{58}$$

Solving the equation for R4 with an output voltage of 5.6 V yields a resistor of 5.33 kΩ. With R4 in place, the voltage on point D will always be higher than the USB input voltage and therefore, D2 can never be forward biased. This diode may thus be omitted since it will never conduct in the variant mode. A third modification is the addition of a secondary output LDO in parallel with the existing one. Both LDOs are identical, but their output voltages are configured differently, for respectively 5 V (IC3) and 3.3 V (IC4). The feedback input regulates to 1.25 V, allowing easy dimensioning of the feedback resistor dividers, respectively R5/R6 and R7/R8. It should be noted that fixed output versions exist of the AP2210 LDO (respectively AP2210-3.3 and AP2210-5.0), but it was chosen to use the adjustable version to reduce number of different components on the board (reduced BOM complexity), and eliminate the chance of accidentally switching both regulators, leading to potentially disastrous consequences for sensitive parts on AEM Light. All resistors depicted in figure 61 are critical for power rail accuracy, and need to be 1 % tolerance resistors or better.

D.5 Alternative Topology

A variation to the topology presented in figure 61 is to move the voltage regulator for DVDD (IC1) to a parallel configuration with IC3, deriving both DVDD and AVDD from the intermediate 3.6 V-5 V power rail on point D. Although this has the notable added advantage of improved voltage stability and noise reduction on DVDD as well, it does increase the power handling requirements of IC2 by a factor 3. Since the EMI being generated by the fast switching current through L1 is proportional to the current, this would lead to an increase of the EMI being generated by the power supply as a whole by ca. a factor 3. This is a highly undesirable drawback for a noise sensitive application, and therefore, this alternative strategy has not been implemented. A secondary side effect is the reduced efficiency of such an approach, generating more waste heat, which may be problematic for the AEM-Thermal module's on board temperature sensors. One solution to deal with both problems is covering noisy components in the power supply with electromagnetic shielding. Such shields are readily available, for example from Laird Technologies, but custom sizes can also easily be manufactured using sheet metal and a manual press brake. However, this adds complexity to the board that is not strictly necessary, and the covered components make prototyping more difficult because they are rendered inaccessible. It was therefore decided to omit EM shielding from the SX1308 and its inductor.

Index

a-Si PV, 5
absorption, 16
absorption coefficient, 22
accelerometer, 9
AD7689, 267
ADC, 65
AEM, 40
AEM Aggregator, 267
AEM Light, 267
AEM Thermal, 267
AEM Vibrations, 267
AEM Waves, 267
ambient energy, 5, 61
ambient energy benchmarking, 6
Ambient Energy Monitor, 40, 267, 268
ambient energy source, 35
amorphous silicon, 16
antenna, 23
appendix, 267
artificial light, 63
Avaaz, 1

band gap, 16, 22
Banki turbine, 5
battery management, 124
battery management system, 102
betavoltaic energy harvesting, 22
bicycle dynamo, 5
biofuel, 3
bioharvester, 23
Bluetooth Low Energy, 11
boost regulator, 65, 107, 110
brown-out voltage, 107
buck regulator, 65, 107
buck-boost regulator, 123, 125

capacitor, 61
Carnot efficiency, 18
CdTe, 17
cell balancing, 102
ceramic, 77
CFD simulation, 6
charge current, 126
charge density, 20
charge/discharge cycle, 93
chemical energy harvesting, 23
CIGS, 17, 27
Colpitts oscillator, 11
commercial availability, 17
complementary balanced energy harvesting, 6, 23, 36, 91
composite material, 2
concentrated photovoltaics, 16
Conservation of Energy, Law of, 15
conversion efficiency, 19
copper phthalocyanine, 27
correction factor, 39
coupling factor, 20
crystal radio, 5
CZTSSe, 17

decentralization, 4
Deep Water Horizon, 33
Deepwater Horizon, 3
device under test, 63
Dragonlink RC, 11
dropout voltage, 126
DSSC, 17, 27

EDLC, 10, 93
EDLC booster, 268
electrolysis, 92
electrolyte, 93
electrolytic capacitor, 93
electromagnetic induction, 22
embedded system, 91

end-of-life, 94
energ harvesting from humans, 23
energy budget estimation, 6
energy carrier, 3
energy harvester, 12, 15, 61
energy scavenging, 4
energy storage, 91
EnOcean, 12
environmental impact, 17
equivalent series resistance, 108
Ericsson heat cycle, 21
ESP8266, 119

Faraday induction law, 22
fibreglass, 2
filter, spectral, 62
firmware, 268
fluorescent lamp, 63
fossil fuel, 1
Francis turbine, 5
fuel cell, 92

galena, 30
gallium, 27
Garzweiler quarry, 3
geothermal energy, 2
GitHub, 268
Glonass, 5
Gorlov turbine, 5
governance, 30
graphene, 27, 29, 32
graphite, 28
Greenpeace, 1
gyrator, 64

Hall sensor, 117
halogen lamp, 63
hardware, 267
harvester characterization, 6, 61
harvester selection, 6
heat flow, 17
heat flux, 13
HVDC, 4
hydroelectricity, 4
hydrogen economy, 3, 92

illumination, 65
incandescent lamp, 63
indium, 27
inductive power transfer, 4
Influencair, 118, 268
input impedance, 93
insolation, 16
inverting regulator, 107
ionizing radiation, 22
irradiation, 16
isotope, 22

kapton, 21, 58
Kardashev scale, 2
kinetic energy harvesting, 22

landfill, 2, 31
landfill mining, 31, 32
langasite, 21
lead zirconate titanate, PZT, 19
life span, 17
light spectrum, 65
light spectrum, indoor, 62
lignite, 1
LoRa, 11, 121
luminosity, 63

Matlab, 64
MAX44004, 64
MAX440094, 64
maximum output power, 57
maximum power point, 17, 61, 65
maximum power point voltage, 125
memory effect, 102
MEMS, 9, 29
metal halide lamp, 62
methanol economy, 3
microcontroller, 5, 43, 64, 119
microwave energy harvesting, 23
monocrystalline silicon, 16
MQ-135, 267
multi sourced energy harvesting, 38
multijunction photovoltaics, 16

nanofiber, 20
nanostructure, 18
nanotechnology, 29
nanowire, 19, 29
Narrowband 4G, 11
nuclear battery, 22
nuclear fission, 2
nuclear fusion, 2

nuclear lighthouse, 5
nuclear waste, 3, 22

on-die battery, 100
open circuit voltage, 17
open source, 267
OpenObservatory, 267, 268
optical power transfer, 4
organic photovoltaics, 27
output regulation, 96
overcharging, 93
overdischarge, 102

parametrization, 57
particle sensor, 120
PEG, 21, 25
Pelton turbine, 5
permittivity, 19
perovskite, 17, 28, 31
photovoltaic cell, 15, 56, 65
photovoltaic energy harvesting, 15, 27, 61
piezoelectric coefficient, 19
piezoelectric effect, 19
piezoelectric energy harvesting, 19, 29, 31
piezoelectric transducer, 29
platinum, 27
polycrystalline silicon, 16
polyester, 2
polymethyl methacrylate, PMMA, 21, 58
polyphase regulator, 115
polyvinyldifluoride, PVDF, 19, 21, 29
power output, 36
power path controller, 91
power regulation, 96
power supply optimization, 6
PowerCast, 12
precautionary principle, 3
probability distribution function, 92
production concentration, 30
publications, 223
PV cell, 2, 61
PV energy, 2
PV powered calculator, 5
pyroelectric coefficient, 21
pyroelectric effect, 21
pyroelectric energy harvesting, 21, 31

Qattara Depression Project, 3

quality factor, 20
quantum dots, 29
quartz, 19, 21

Raspberry Pi, 267
rectenna, 23
rectification, 23
recycling, 31
recycling rate, 30
renewable energy, 2
reserve distribution, 30
resonance frequency, 20
resource management, 3, 4, 25
RF energy harvesting, 23
RF power transfer, 4
RFID, 4
ripple voltage, 107
RTC, 41, 110
RTG, 5, 8, 22
ruthenium, 27

saturation, 109
Seebeck coefficient, 17
Seebeck effect, 17
SEPIC converter, 123
serial communication, 65
shale gas, 1
Shockley-Queisser limit, 16, 22
Si1145, 267
Sigfox, 11
smart highway, 12
software, 267
software repository, 268
Solar Roadways, 12
solar spectrum, 61
solid state battery, 99
spectral sensitivity, 15
spectrometer, 63
sphalerite, 30, 32
spring constant, 20
steam, 13
step-down converter, 107
step-up converter, 110
Sterling engine, 17, 21
substitutability, 30
substrate, 27
sugar, 19, 23
Suosemi, 123

sustainability, 2, 31
sustainable economy, 1
sweep test, 72

tar sand, 1
TEG, 12, 17, 22, 25, 28, 30, 58, 61, 73
TENG, 20, 25, 37
thermal conductivity, 17
thermocouple, 77
thermoelectric capacitance, 21
thermoelectric energy harvesting, 5, 13, 17, 28, 73
thermoelectric generator, 17
thermopile, 18
thin film battery, 101
thin film photovoltaics, 27
Three Gorges Dam, 3
tip mass, 20
titanate, 21
Torex Semi, 123
tourmaline, 19
Transit 4A, 5
transmission power, 23
triboelectric effect, 20
triboelectric energy harvesting, 20
triboelectric polarity, 20
trichlorosilane, 28
triglycine sulfate, TGS, 21
tritium, 22

uranium, 2, 30
USB dongle, 267

vacuum permittivity, 20
valence band, 16
Vanguard 1, 5
vibration energy harvesting, 80
Voltree, 24

water mill, 1
water turbine, 5
wave energy, 13
wavelength sensitivity, 16
wearable electronics, 23
wind mill, 1
wind turbine, 2, 38
Wireless Belgium, 121
wireless power transfer, 4

xenon lamp, 62

Young modulus, 19

Z-Wave, 11
zenith, 62

View publication stats